Trinity College Dublin
Coláiste na Tríonóide, Baile Átha Cliath
The University of Dublin

The Role of Mitochondrial Uncoupling Protein 3 in T Cell Function

A thesis submitted to Trinity College Dublin for the degree of Doctor of Philosophy

By

Emma O'Connor, B.A., M.Sc.

January 2019

Supervisors:

Prof. Richard K. Porter and Prof. Patrick T. Walsh

School of Biochemistry and Immunology,
Trinity Biomedical Sciences Institute,
Trinity College Dublin,
The University of Dublin

Declaration

I declare that this thesis has not been submitted as an exercise for a degree at this or any other university and it is entirely my own work. I agree to deposit this thesis in the University's open access institutional repository or allow the library to do so on my behalf, subject to Irish Copyright Legislation and Trinity College Library conditions of use and acknowledgement.

_____

Emma O'Connor

Summary

Uncoupling proteins (UCPs) are members of the mitochondrial anion carrier superfamily that can mediate the transfer of protons into the mitochondrial matrix from the intermembrane space. Our laboratory has reported evidence of UCP1 and UCP3 expression in thymocytes and spleen mitochondria, while Krauss *et al*. (2002) reported expression of UCP2 in thymocytes. Thymocytes develop into mature T cells before exiting the thymus and travelling to the periphery where they wait to carry out an immune response. Expression of all three UCPs in thymocytes suggests their importance in thymic function, as well as a potential role in T cell selection, maturation, metabolism and/or function. Using quantitative RT-PCR, we have demonstrated that *Ucp1*, *Ucp2* and *Ucp3* are expressed in peripheral naive $CD4^+$ T cells at the mRNA level before being markedly downregulated following cell activation under different polarizing conditions, the only exception being the expression of *Ucp2* in regulatory T cells (T_{reg} cells) which is not significantly altered following T cell activation until 120 h post-stimulation when it is significantly increased. Overall, the downregulation of *Ucp*s in response to T cell activation is suggestive of a role for them in naive T cell maintenance. As our laboratory has previously provided evidence of an altered T cell profile in both thymus and spleen of *Ucp3*$^{-/-}$ mice, we investigated the role of UCP3 in $CD4^+$ T cell metabolism and function using the Seahorse XF Cell Mito Stress Test, flow cytometry and ELISAs. Following *Ucp3* ablation, non-polarized, activated T cells (T_H0 cells) produced significantly more IL-2, which was reflected by an increase in CD25 and CD69 expression as well as an increase in cell proliferation. However, this was also followed by a decrease in cell viability and IFN-γ production 72 h post-stimulation. IL-2 promotes T cell activation, growth and survival but it is also known to prime T cells for activation-induced cell death (AICD). In this regard, it is thought that the increased IL-2 levels observed in *Ucp3*$^{-/-}$ T_H0 cells are promoting early T cell activation but also subsequently inducing AICD. Interestingly, although *Ucp3*$^{-/-}$ T_H0 cells underwent early activation, *Ucp3* ablation did not have a major impact on T cell metabolism. IL-2 can influence the generation of T_H17 cells, a subset of T cells that are highly pro-inflammatory, and T_{reg} cells; high levels of IL-2 promote T_{reg} cell generation while inhibiting the generation of T_H17 cells. In line with this, the altered IL-2 expression observed between *Ucp3*$^{+/+}$ and *Ucp3*$^{-/-}$ T_H0 cells appears to have a crucial impact on the generation of T_H17 and T_{reg} cells *in vitro*. An increased frequency of $FoxP3^+$ T_{reg} cells was generated *in vitro* from *Ucp3*$^{-/-}$ mice compared to *Ucp3*$^{+/+}$ mice, while *Ucp3*$^{-/-}$ T_H17 cells

generated *in vitro* displayed lower cell survival/viability and decreased IL-17A production compared to their *Ucp3*$^{+/+}$ counterparts. These results were also mirrored *in vivo*. *Ucp3*$^{-/-}$ mice immunized with keyhole limpet hemocyanin and cholera toxin displayed a higher frequency of FoxP3^{+}CD25^{+} T_{reg} cells and significantly less production of IL-17A during antigen recall response compared to *Ucp3*$^{+/+}$ mice. We postulate that UCP3 is acting to restrict the activation of naive T cells. UCP3 may be acting as a rheostat to dampen signals following T cell receptor and CD28 co-receptor ligation, thereby preventing early activation and AICD. The fact that *Ucp3* ablation alters the T_H17:T_{reg} cell balance *in vivo* as well as *in vitro* implicates UCP3 as a potential target for the treatment of T_H17 cell-mediated forms of autoimmunity.

Acknowledgements

How do I even begin to thank my supervisors? Richie, thank you so much for your patience, your guidance, your enthusiasm, your sense of humour and for letting me travel with this Ph.D. almost every year since the start! You were a super supervisor! Also, thank you so much for giving me the opportunity to do a Ph.D. in the first place. I don't think I would have ever considered doing one, had you not asked me to apply and I'm very glad you did. Pat, thank you so much for sharing your infinite knowledge with me over the last four years. You made me feel like my Ph.D. was always on track and going okay every time I met you (even if it really wasn't but I appreciated and needed that!). There was many a time I was thinking of giving up but I always changed my mind after meeting you again and felt reassured. You made me hang on and keep going more than you'll ever know. Thank you both so much. It goes without saying that I wouldn't have finished this Ph.D. or made half as good an attempt at it, were it not for the two of you. Most students only get to have one supervisor, I was so lucky to have two, and two amazing ones at that!

Mary, Marilena and Caitriona, thank you for being such a lovely lab group for me to be part of. Mary, I've done my entire Ph.D. with you in the group and can honestly say I have never met a more intelligent, hard-working and gas woman in all my life! I've so much admiration for you. Marilena, I don't think you ever realised how much I enjoyed your sense of humour. You always made me laugh and God knows we need that trying to get through a Ph.D.! In my future job(s), if there isn't someone like you around that quotes 'Friends' every day and shouts about the 'left phalange' when a catastrophe happens, I'll be very disappointed! Caitriona, newest member of the group! Once you started with us, it was like you had always been in our lab group. You took to everything so fast and learned techniques in record time! You're an unbelievable worker. Thank you so much for all your help. You've become such an instrumental member of the team and I've no doubt that you will excel at whatever you do in the future.

I owe a very big thank you to Gemma, Yasmina and Eirini for all your help, particularly with the *Rag1*$^{-/-}$ experiments. Gemma especially, sorry for all my annoying e-mails over the last few years. I'm sure you'll be delighted I won't be pestering you anymore! The three of you were always so friendly and welcoming to me whenever I popped out to the National Children's Research Centre and it was a pleasure to work with the three of you, even for such a brief time.

I cannot forget to thank past members of my lab groups: Clare, Martina and Fintan but particularly Shane, Ania and Rachel who were invaluable in getting me set up and teaching me the ropes of T cell culture.

To past and present members of the 6th floor reading room: Sinead, Rachel, Jill, Gillian, Ewelina, Ciara, Rebecca, Stefania, Claire, Magda, Maurizio, Tania, Vinnie, Sarah P., Mashael, Nick, Brian, Joan, Paddy, Siobhan, Sandra, Sarah C., Jade, Jenny, Kasia, Paula and Dominic (I hope I'm not forgetting anyone!), thank you all so much for the laughs and for making the reading room such a friendly space. I have made some amazing friends over the last four years.

I would like to express my sincere gratitude to all of the guys, past and present, in the Comparative Medicine Unit for your unwavering support: Laavanya, Mark C., Phillip, Aoife, Rustam, Sylvie, José, Caroline and Anne. An extra big thank you extends to Mark T. and Ciarán. The two of you helped me out so much, particularly when I first started. You were both excellent teachers showing me the ropes and I can't thank you enough for your patience and guidance.

I am very grateful to Barry and Gavin for your help with flow and confocal. I'm sure I was the most annoying and pestering person you've both ever been unfortunate enough to deal with but you were both so professional and patient and I appreciated your help so much.

A sincere thank you to Natalia, Ed, Kingston and Caroline for your help and guidance with the *in vivo* work. It would never have happened without you!

Liam and Noel, what would I have done without you? What would the SCHOOL do without you? The two of you are such gents and were like superheroes, appearing within minutes of something breaking down!

Ailish, Jane and Orla, thank you for all of your help with registration, grants, orders, *etc*.

Thank you to everyone who has been involved in the School Office during my time here: Gabby, Sara, Mary-Pat, Miriam, Isobel and, finally, David, who I will always remember.

Thank you to Liam M^{c}Carthy and all the staff in the Teaching Lab, particularly Brian for printing out my posters!

To all of my friends from home, school, college and everywhere else: I became a hermit because of this Ph.D. You all did without me for far too long but never stopped being the best loyal friends a girl could have and were always there for me when I left my Ph.D. cave and needed a distraction. I am so excited to start LIVING again and to have a great time with all of you (Lisa and Aoife, hurry home from your travels)!

Myles/Moyles/Milly/Bebe, thank you for being my rock. You put up with my rants, my tears and my hermit-ness through all of this. Thank you for being by my side the entire time, for getting me through it and keeping me sane. You're alright, you know that? Think I'll keep you.

Mam, Dad, Aileen, Christine (git) and Seán, thank you for making it possible for me to do a Ph.D. Thank you for keeping me fed and watered. Thank you for dropping me. Thank you for collecting me. Thank you for walking Murph for me. Thank you for putting up with me. Thank you for cheering me up. Thank you for encouraging me. Thank you for being an amazing, loving family.

For my mam and dad

Table of Contents

List of Figures

List of Tables

Abbreviations and Acronyms

2,4-DNP	2,4-dinitrophenol
7-AAD	7-aminoactinomycin D
°C	degrees Celsius
ϵ	extinction coefficient
α	alpha
β	beta
γ	gamma
Δ	delta
ΔA	change in absorbance per minute
ε	epsilon
κ	kappa
µg	microgram
µL	microlitre
µm	micrometre
µM	micromolar
A	absorbance at a particular wavelength
ADP	adenosine diphosphate
AICD	activation-induced cell death
AML1	acute myeloid leukaemia 1 protein
AMP	adenosine monophosphate
AMPK	5’ adenosine monophosphate-activated protein kinase
ANOVA	analysis of variance
AP-1	activator protein-1
APC	antigen-presenting cell
APC	allophycocyanin
APS	ammonium persulphate
ATP	adenosine triphosphate
BAT	brown adipose tissue
BCA	bicinchoninic acid
Bcl-2	B cell lymphoma-2
Bcl-X_L	B cell lymphoma-extra large
BCL11B	B cell lymphoma 11 B
BLIMP-1	B lymphocyte-induced maturation protein-1

BMCP1	brain-specific mitochondrial carrier protein 1
bp	base pair
BSA	bovine serum albumin
C	concentration of nucleic acid
c-FLIP	cellular (FADD-like IL-1 beta converting enzyme)-inhibitory protein
c-Myc	cellular myelocytomatosis oncogene
Ca^{2+}	calcium cation
cAMP	cyclic adenosine monophosphate
CBP	(cyclic adenosine monophosphate-response element-binding protein)-binding protein
CD3	cluster of differentiation co-receptor 3
CD4	cluster of differentiation co-receptor 4
CD8	cluster of differentiation co-receptor 8
CD25	cluster of differentiation co-receptor 25
CD28	cluster of differentiation co-receptor 28
CD40	cluster of differentiation co-receptor 40
CD40L	cluster of differentiation co-receptor 40 ligand
CD44	cluster of differentiation co-receptor 44
CD62L	cluster of differentiation co-receptor 62 ligand
CD69	cluster of differentiation co-receptor 69
CD80	cluster of differentiation co-receptor 80
CD86	cluster of differentiation co-receptor 86
CD95	cluster of differentiation co-receptor 95
CD95L	cluster of differentiation co-receptor 95 ligand
CD178	cluster of differentiation co-receptor 178
CD223	cluster of differentiation co-receptor 223
cDNA	complimentary deoxyribonucleic acid
cm	centimetre
CMU	Comparative Medicine Unit
CNS	central nervous system
CO_2	carbon dioxide
CoA	coenzyme A
CoASH	coenzyme A with a sulfhydryl functional group
CPT1A	carnitine palmitoyltransferase 1A

CPT2	carnitine palmitoyltransferase 2
CREB	cyclic adenosine monophosphate-response element-binding protein
cRPMI	complete Roswell Park Memorial Institute 1640 medium
CT	cholera toxin
CTL	cytotoxic T lymphocyte
Cys	cysteine
DAMP	damage-associated molecular pattern
DC	dendritic cell
DCF	2’,7’-dichlorofluorescein
DCFDA	2’,7’-dichlorofluorescein diacetate
dH_2O	distilled water
DMSO	dimethyl sulfoxide
DNA	deoxyribonucleic acid
dNTP	deoxynucleotide triphosphate
DPBS	Dulbecco’s Phosphate Buffered Saline
DTNB	5,5’-dithiobis(2-nitrobenzoic acid)
DTT	DL-dithiothreitol
EAE	experimental autoimmune encephalomyelitis
ECAR	extracellular acidification rate
EDTA	ethylenediaminetetraacetic acid
EGR1	early growth response 1
EGR2	early growth response 2
EGR3	early growth response 3
ELISA	enzyme-linked immunosorbent assay
ETC	electron transport chain
EtOH	ethanol
FA	fatty acid
FAD	flavin adenine dinucleotide
FADD	Fas-associated death domain
$FADH_2$	reduced flavin adenine dinucleotide
FAO	fatty acid beta-oxidation
FasL	Fas ligand
FBS	foetal bovine serum
FCCP	carbonyl cyanide-p-trifluoromethoxyphenylhydrazone
FFA	free fatty acid

FITC	fluorescein isothiocyanate
FLICE	(Fas-associated death domain)-like IL-1 beta converting enzyme
FoxP2	forkhead box P2
FoxP3	forkhead box P3
FSC	forward scatter
FSC-A	forward scatter-area
FSC-W	forward scatter-width
g	g-force
g	grams
GATA-3	GATA-binding protein 3
GDP	guanosine diphosphate
GLUT	glucose transporter
GLUT1	glucose transporter 1
GM-CSF	granulocyte-macrophage colony-stimulating factor
GMP	guanosine monophosphate
G_s protein	stimulatory guanosine triphosphate-binding protein
GTP	guanosine triphosphate
h	hour
H^+	proton
H_2O	water
H_2O_2	hydrogen peroxide
HIF1α	hypoxia-inducible factor 1 alpha
His	histidine
HNE	4-hydroxy-trans-2-nonenal
HPRA	Health Products Regulatory Authority
Hprt	Hypoxanthine phosphoribosyl transferase
HRP	horseradish peroxidase
HSL	hormone-sensitive triacylglycerol lipase
IBD	inflammatory bowel disease
IFN-γ	interferon-gamma
Ig	immunoglobulin
IL-1	interleukin-1
IL-1β	interleukin-1 beta
IL-2	interleukin-2
IL-2R	interleukin-2 receptor

IL-2Rα	interleukin-2 receptor alpha subunit
IL-4	interleukin-4
IL-5	interleukin-5
IL-6	interleukin-6
IL-6R	interleukin-6 receptor
IL-6Rα	interleukin-6 receptor alpha subunit
IL-6Rβ	interleukin-6 receptor beta subunit
IL-10	interleukin-10
IL-12	interleukin-12
IL-12Rβ2	interleukin-12 receptor beta 2 subunit
IL-13	interleukin-13
Il-17	interleukin-17
IL-17A	interleukin-17A
IL-17F	interleukin-17F
IL-21	interleukin-21
IL-22	interleukin-22
IL-23	interleukin-23
IL-35	interleukin-35
IMS	intermembrane space
iT_{reg}	inducible regulatory T cell
Jak	Janus kinase
JAX®	Jackson Laboratory
kDa	kiloDalton
kg	kilogram
KLH	keyhole limpet hemocyanin
KO	knockout
l	path length of spectrophotometer cuvette
LAG3	lymphocyte activation gene 3
LAP	latency-associated peptide
LAST	Laboratory Animal Science and Training
LPS	lipopolysaccharide
M	molar
mA	milliamp
MALT	mucosa-associated lymphoid tissue
MDMA	3,4-methylenedioxymethamphetamine

MFI	median fluorescence intensity
mg	milligram
Mg^{2+}	magnesium cation
MHC	major histocompatibility complex
MIM	mitochondrial inner membrane
min	minute
mL	millilitre
mM	millimolar
MM	mitochondrial matrix
Mn^{2+}	manganese cation
MOM	mitochondrial outer membrane
M_r	molecular weight
mRNA	messenger ribonucleic acid
MS	multiple sclerosis
mTOR	mammalian target of rapamycin
N	Normal
NaCl	sodium chloride
NAD^+	nicotinamide adenine dinucleotide
NADH	reduced nicotinamide adenine dinucleotide
NADPH	nicotinamide adenine dinucleotide phosphate
NE	norepinephrine
Nec-1	necrostatin-1
NEFA	non-esterified fatty acid
NF-κB	nuclear factor kappa light chain-enhancer of activated B cells
NFAT	nuclear factor of activated T cells
NFATc1	nuclear factor of activated T cells, cytoplasmic 1
NFATc2	nuclear factor of activated T cells, cytoplasmic 2
ng	nanogram
NK cell	natural killer cell
NLR	nucleotide-binding oligomerisation domain-like receptor
nm	nanometre
nmol	nanomole
NO	nitric oxide
NOD	nucleotide-binding oligomerisation domain
NPC	no primary control

NRF2	nuclear factor-erythroid 2-related factor 2
NST	non-shivering thermogenesis
nT_{reg}	naturally occurring regulatory T cell
O_2	oxygen
O_2^-	superoxide anion
OCR	oxygen consumption rate
OCT1	octamer-binding protein 1
OCT2	octamer-binding protein 2
OH^-	hydroxyl radical
OxPhos	oxidative phosphorylation
PAMP	pathogen-associated molecular pattern
PCR	polymerase chain reaction
PD-1	programmed cell death protein 1
PDHe1α	pyruvate dehydrogenase e1 alpha subunit
PE	R-phycoerythrin
PE-Cy5	R-phycoerythrin-Cyanine 5
PE-Cy7	R-phycoerythrin-Cyanine 7
PerCP eFluor™ 710	Peridinin chlorophyll protein eFluor™ 710
PerCP-Cy™5.5	Peridinin chlorophyll protein-Cyanine 5.5
pg	picogram
PGC1α	peroxisome proliferation activating receptor gamma coactivator 1 alpha
P_i	phosphate
PKA	protein kinase A
PKC	protein kinase C
PMA	phorbal 12-myristate 13-acetate
PMF	proton-motive force
pmol	picomole
PPAR	peroxisome proliferation activating receptor
PPARγ	peroxisome proliferation activating receptor gamma
PPARδ	peroxisome proliferation activating receptor delta
PRDM1	PR domain zinc finger protein 1
PRDM16	PRD1-BF1-RIZ1 homologous domain-containing protein-16
PRR	pattern recognition receptor
PVDF	polyvinylidene difluoride

QH_2	ubiquinol
Rag1	recombination-activating gene 1
RBC	red blood cell
RhoA	Ras homologue gene family, member A
rhTGF-β1	recombinant human transforming growth factor-beta 1
rIFN-γ	recombinant interferon-gamma
rIL-2	recombinant interleukin-2
rIL-6	recombinant interleukin-6
rIL-10	recombinant interleukin-10
rIL-12	recombinant interleukin-12
rIL-17A	recombinant interleukin-17A
RIPA	radio immunoprecipitation assay
RNA	ribonucleic acid
RNS	reactive nitrogen species
RORγt	retinoic acid receptor-related orphan receptor gamma t
ROS	reactive oxygen species
RPMI	Roswell Park Memorial Institute 1640 medium
RT	room temperature
RT-PCR	reverse transcription polymerase chain reaction
RUNX1	runt-related transcription factor 1
RXR	retinoid X receptor
s	second
SCID	severe combined immunodeficiency
SDS	sodium dodecyl sulphate
SDS-PAGE	sodium dodecyl sulphate polyacrylamide gel electrophoresis
siRNA	small interfering ribonucleic acid
SKM	skeletal muscle
SLE	systemic lupus erythematosus
SOD	superoxide dismutase
Sod2	superoxide dismutase 2
SSC	side scatter
SSC-A	side scatter-area
SSC-W	side scatter-width
STAT3	signal transducer and activator of transcription 3
STAT4	signal transducer and activator of transcription 4

STAT5	signal transducer and activator of transcription 5
T_3	triiodothyronine
T-bet	T-box transcription factor TBX21
TCA	tricarboxylic acid
TCR	T cell receptor
TBSI	Trinity Biomedical Sciences Institute
TEMED	tetramethylethylenediamine
TGF-β	transforming growth factor-beta
T_H cell	T helper cell
TLR	Toll-like receptor
TLR4	Toll-like receptor 4
TMB	3,3',5,5'-tetramethylbenzidine
TNBH	5-thionitrobenzene
TNF	tumour necrosis factor
TNF-α	tumour necrosis factor-alpha
TNF-β	tumour necrosis factor-beta
T_{reg} cell	regulatory T cell
UCP	uncoupling protein
UCP1	uncoupling protein 1
UCP2	uncoupling protein 2
UCP3	uncoupling protein 3
Ucp3$_L$	uncoupling protein 3 long form
Ucp3$_S$	uncoupling protein 3 short form
UCP4	uncoupling protein 4
UCP5	uncoupling protein 5
Ucp5$_L$	uncoupling protein 5 long form
Ucp5$_S$	uncoupling protein 5 short form
Ucp5$_{SI}$	uncoupling protein 5 short form with insert
UNG	uracil-deoxyribonucleic acid glycosylase
UV	ultraviolet
V	volt
v/v	volume per unit volume
w/v	weight per unit volume
WAT	white adipose tissue
WT	wildtype

Z-VAD Z-VAD-FMK

Chapter 1:

Introduction

Chapter 1

Introduction

1.1 Metabolism

A fundamental property of living organisms is that they harness energy from their environment in order to drive thermodynamically unfavourable processes (Brand, 2000). The energy used by animals is sourced from food, while plants harness energy from the sun. In animal cells, most of the energy produced is derived from three fuel sources: glucose, glutamine and fatty acids (FAs). These fuel sources are digested and metabolized, forming adenosine triphosphate (ATP). The displacement from equilibrium of the hydrolysis of ATP to adenosine diphosphate (ADP) and phosphate (P_i; Figure 1.1) provides significant Gibbs free energy for useful work, such as maintaining ion gradients, transporting substrates and proteins across membranes, protein synthesis and muscle movement. All cells of the body need ATP to fuel cellular processes and, due to this displacement from equilibrium, it is the primary chemical energy currency of the cell (Pebay-Peyroula *et al*., 2003). The majority of ATP in a cell is produced within the mitochondria and an average 70 kilogram (kg) man produces approximately 50 kg of ATP per day (Pebay-Peyroula *et al*., 2003).

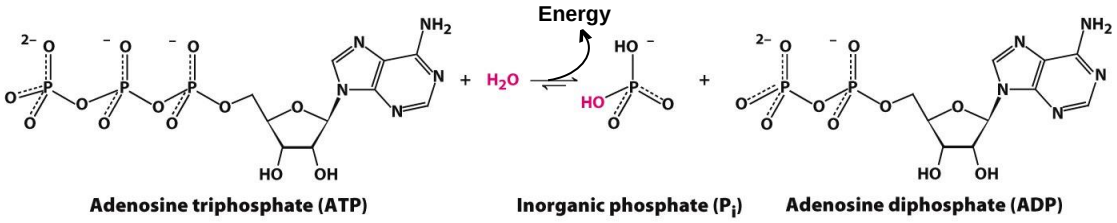

Figure 1.1: The hydrolysis of ATP, forming ADP and P_i

Adapted from Berg *et al*. (2012). H_2O: water.

1.1.1 Mitochondria

Mitochondria (singular: mitochondrion) arose when an ancient prokaryotic lineage supposedly evolved a nucleus, giving rise to a eukaryote, and then endocytosed a bacterium. This intracellular bacterium co-existed inside the eukaryote in symbiosis, creating the first acquired or original mitochondrion (Henze and Martin, 2003). Mitochondria are present in all known eukaryotic cells (except for erythrocytes). They are interesting in that they contain mitochondrial deoxyribonucleic acid (DNA) that codes for 13 proteins, 2 ribosomal ribonucleic acids (RNAs) and 22 transfer RNAs, all of which are essential for mitochondrial replication. This mitochondrial DNA is a vestige from the DNA of the original bacterium from which mitochondria evolved. Mitochondrial density in cells is dependent on ATP demand – the more energy required for a specific cell, the more mitochondria present.

Structurally, mitochondria consist of two membranes: a mitochondrial outer membrane (MOM), which is thought to be left over from the original endocytosis event, and an extensively folded mitochondrial inner membrane (MIM; Figure 1.2A). The foldings and convolutions of the MIM, called cristae (Plecitá-Hlavatá *et al*., 2008), are required to substantially increase its surface area. Both membranes have highly distinct properties; while both are made up of a phospholipid bilayer and proteins, the MOM is freely permeable to small molecules and ions, whereas the MIM is practically impermeable to most small molecules and ions, including protons. The MIM, therefore, houses a number of transporters, proteins and enzymes, such as the ADP/ATP translocase, to transport specific molecules across this impermeable barrier. Together, the two membranes create two separate compartments within mitochondria: the intermembrane space (IMS) and the mitochondrial matrix (MM; Figure 1.2B). The IMS lies between the two membranes, while the MM is the inner most part of the organelle bound by the MIM. The MM is home to a number of soluble enzymes involved in oxidative metabolism, as well as substrates, nucleotide cofactors, inorganic ions, the mitochondrial genetic machinery, DNA, RNA and ribosomes. Mitochondria range in size from 0.5 to 1 micrometre (μm) in diameter and tend to form columnar reticular networks undergoing constant fission and fusion (Figure 1.2C; Plecitá-Hlavatá *et al*., 2008).

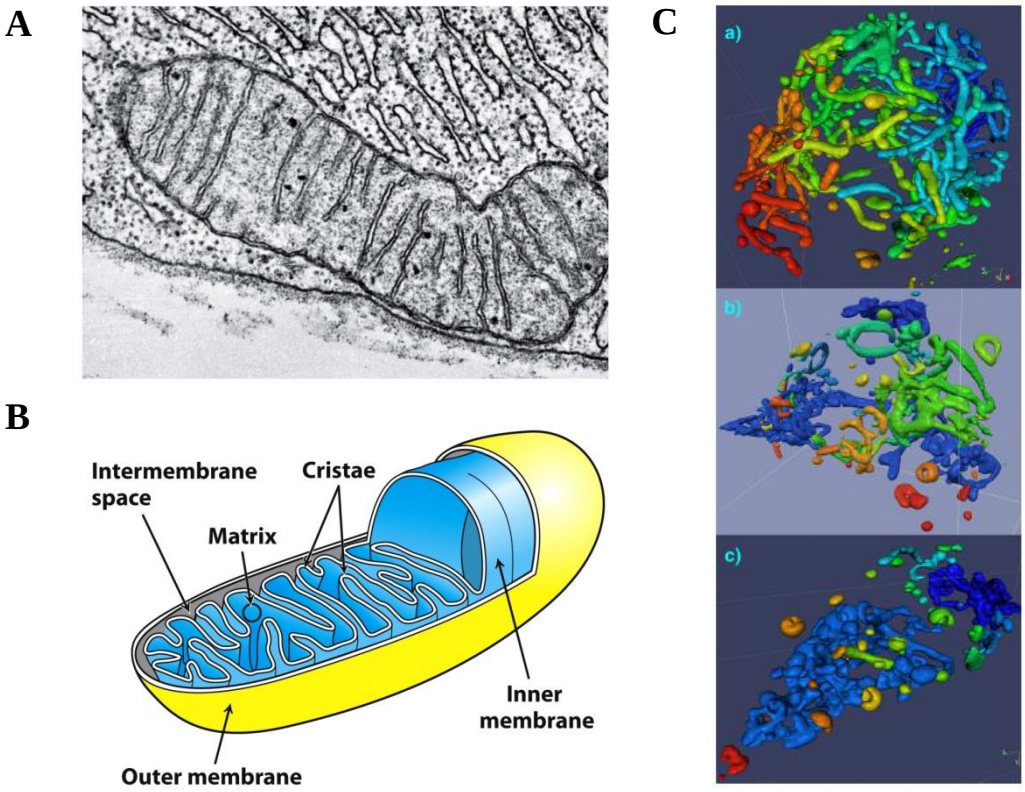

Figure 1.2: Simplified structure of the mitochondrion

Electron micrograph (A) and schematic representation (B) of a mitochondrion. Taken from Berg *et al*. (2012). (C) 4Pi microscopy images of originally highly interconnected mitochondrial reticulum in INS-1E cells that have disintegrated following addition of 20 micromolar (µM) rotenone (panel a), 1 µM carbonyl cyanide-p-trifluoromethoxyphenylhydrazone (FCCP; panel b) and both agents (panel c). Taken from Plecitá-Hlavatá *et al*. (2008).

1.1.2 Glycolysis

Glucose is a simple sugar and the basic building block of polysaccharides. Importantly, it acts as a carbon fuel source for the generation of cellular ATP by being metabolized via two integrated pathways: glycolysis and oxidative phosphorylation (OxPhos; Zheng, 2012). Glycolysis is the first process that occurs in the metabolism of glucose. Taking place in the cytoplasm, it is the sequence of reactions that converts one molecule of glucose to two molecules of pyruvate, with the concomitant net production of two molecules of ATP (Zheng, 2012) and two molecules of reduced nicotinamide adenine dinucleotide (NADH; Figure 1.3). The first step of glycolysis occurs following the entry of glucose into the cell through specific transport proteins. It is phosphorylated by hexokinase to form glucose-6-phosphate, which is notable for two reasons: glucose-6-phosphate cannot pass through the membrane because it is not a substrate for glucose transporters (GLUTs) and is, thus, trapped in the cell for processing, and the addition of a phosphoryl group acts to destabilize glucose, subsequently facilitating its further metabolism. Glucose-6-phosphate is then processed down the glycolytic pathway, undergoing numerous biochemical reactions until it has been converted to two molecules of pyruvate. Pyruvate is further processed to lactate under anaerobic or hypoxic conditions (lactic acid fermentation) and is excreted from the cell or, under aerobic conditions, pyruvate can be transported into the mitochondria by the mitochondrial pyruvate carrier to be oxidized to carbon dioxide (CO_2) and acetyl coenzyme A (acetyl CoA) by pyruvate dehydrogenase. In some cases, the conversion of pyruvate into lactate may also occur in normoxia (Chang *et al*., 2013), which will be discussed in more detail later. As glycolysis does not require oxygen (O_2), it can occur under anaerobic conditions.

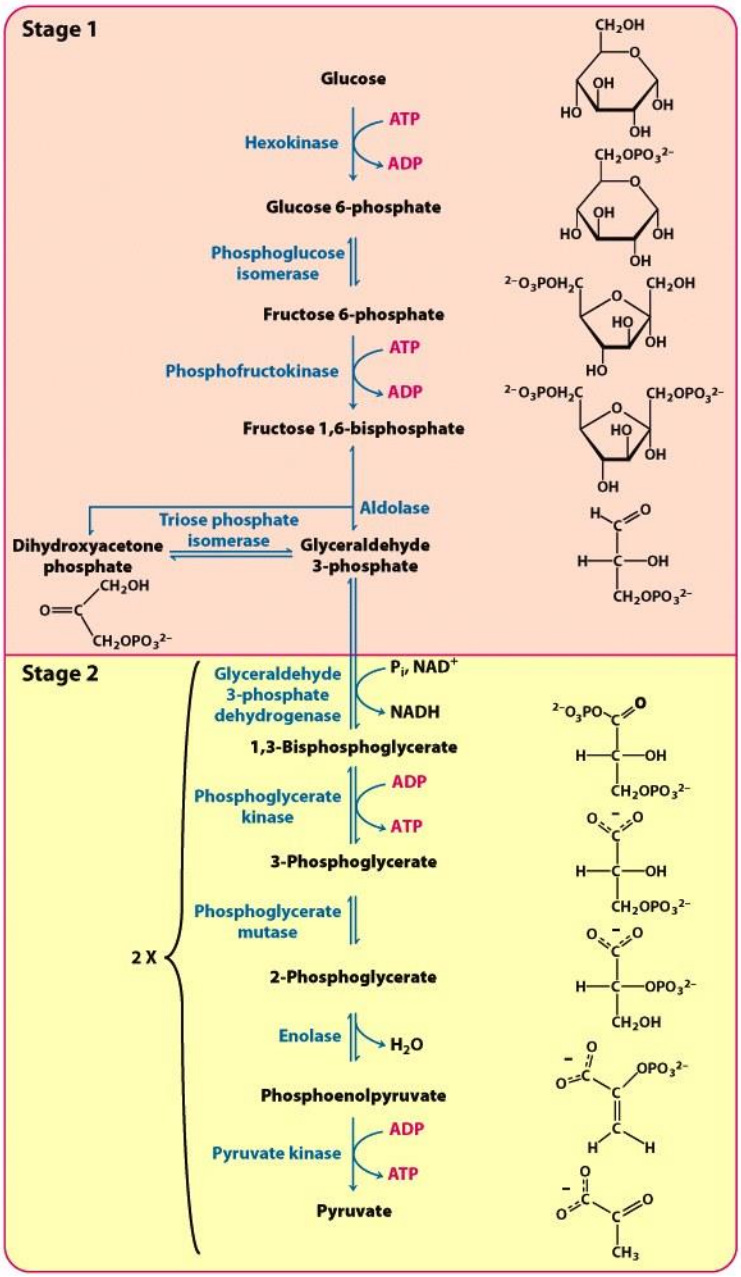

Figure 1.3: Reactions of the glycolytic pathway

Glycolysis can be divided into two stages; during stage 1, glucose is destabilised and cleaved into two interconvertible three-carbon molecules while during stage 2, those molecules are used to produce ATP. Enzymes involved in the glycolytic pathway are displayed in blue font. The consumption and production of ATP at different steps of the glycolytic pathway are displayed in pink font. Taken from Berg *et al*. (2012).

1.1.3 FA Oxidation

Some cells can use FAs as a fuel source for energy rather than carbohydrates containing glucose, as FAs are a rich source of ATP. For example, the oxidation of one palmitic acid molecule yields a net production of 129 ATP molecules in comparison to 36 ATP molecules from the complete oxidation of glucose. FAs can be broken down via beta (β)-oxidation. The metabolism of non-esterified long-chain FAs present in the cytoplasm requires several steps to transport them into the MM, where FA β-oxidation (FAO) takes place (Schrauwen *et al*., 2001). In the cytoplasm, FAs are firstly converted to their esterified form, fatty acyl-CoA, by an enzyme called fatty acyl-CoA synthetase (Schrauwen *et al*., 2001, 2002, 2003, 2006). Fatty acyl-CoA (and non-esterified FAs; NEFAs) can easily cross the MOM; however, the MIM is impermeable to long-chain fatty acyl-CoA and NEFAs. The acyl-CoA ester is converted to acyl-carnitine by carnitine palmitoyltransferase 1A (CPT1A) located at the MOM (Schrauwen *et al*., 2001, 2002). Acyl-carnitine crosses the MIM in exchange for carnitine, is reconverted to acyl-CoA in the MM by CPT2 and subsequently enters the FAO and tricarboxylic acid (TCA) cycles as FAs can only undergo FAO in their esterified form (Schrauwen *et al*., 2001, 2002, 2006). In contrast to long-chain FAs, medium-chain FAs do not need to be esterified to CoA esters in the cytoplasm (Schrauwen *et al*., 2003). Medium-chain FAs bypass CPT1A and can be esterified to their respective CoA esters inside the MM before being diverted to FAO (Schrauwen *et al*., 2003). Once inside the MM, CoA esters then undergo the series of reactions of FAO (Figure 1.4), resulting in the generation of acetyl CoA and reducing equivalents [NADH, a proton (H^+) and reduced flavin adenine dinucleotide ($FADH_2$)] for the mitochondrial electron transport chain.

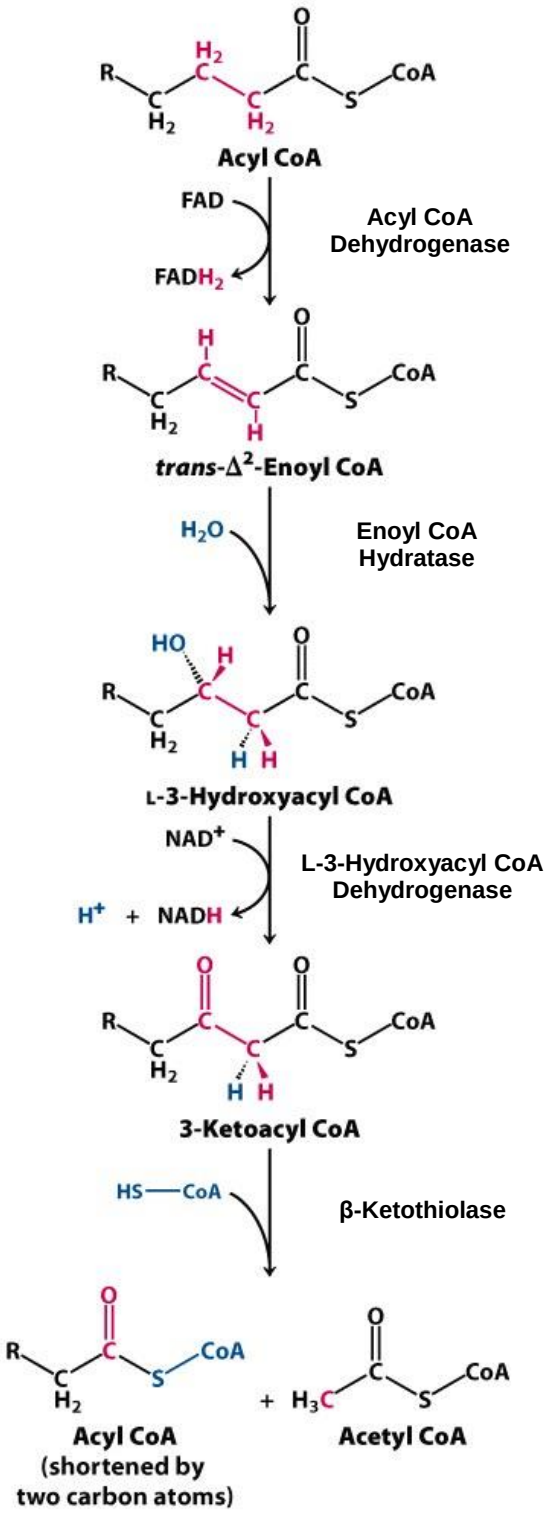

Figure 1.4: Sequence of reactions of FAO

FAs are degraded by the repetition of a four-reaction sequence consisting of oxidation, hydration, oxidation and thiolysis. Adapted from Berg *et al*. (2012).

1.1.4 Glutaminolysis

The metabolism of the amino acid glutamine involves its conversion to alpha (α)-ketoglutarate, an intermediate of the TCA cycle. The conversion of glutamine to α-ketoglutarate involves two main steps: the hydrolysis of the amino group of glutamine by glutaminase in mitochondria, yielding glutamate and ammonium, and the conversion of glutamate to α-ketoglutarate by glutamate dehydrogenase, glutamate pyruvate transaminase or glutamate oxaloacetate transaminase, a component of the malate-aspartate shuttle (Figure 1.5; Jin *et al*., 2016). Once converted to α-ketoglutarate, it may enter the TCA cycle in the MM.

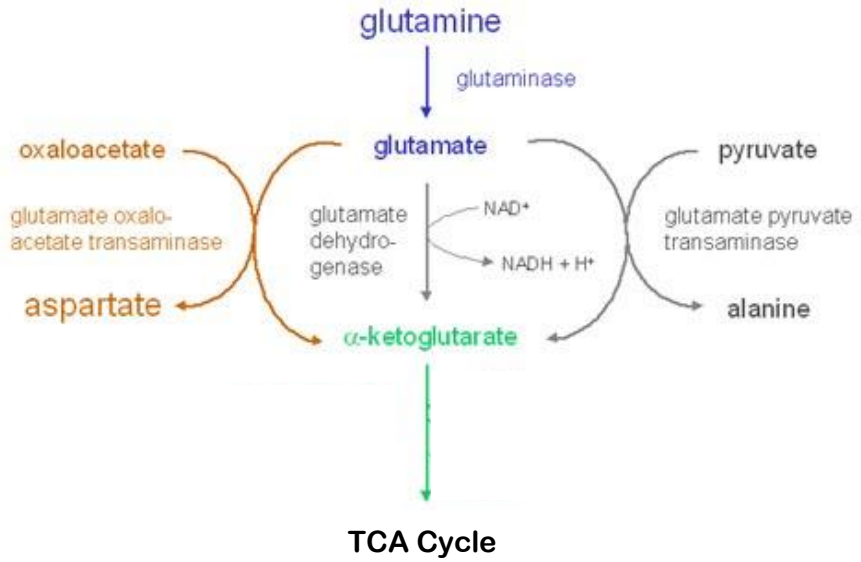

Figure 1.5: The glutaminolysis pathway

During glutamine metabolism, the amino group of glutamine is hydrolysed by glutaminase, forming glutamate and ammonium. Glutamate can be converted to α-ketoglutarate by one of three different reactions and enter the TCA cycle. Image taken and adapted from [http://www.metabolic-database.com/html/glutaminolysis_energy_scheme.html].

1.1.5 The TCA Cycle

One of the main functions of mitochondria is to continue the metabolism of acetyl CoA generated from pyruvate and FAO. This oxidation is achieved through the TCA cycle. The reactions of the TCA cycle, also known as the citric acid cycle or Kreb's cycle, occur in the MM. Under aerobic conditions, acetyl CoA combines with four-carbon oxaloacetate to yield a six-carbon tricarboxylic acid catalysed by citrate synthase. Citrate then undergoes a series of oxidizing reactions denoted the TCA cycle (Figure 1.6). During the cycle, the six-carbon compound releases CO_2 twice in two successive oxidative decarboxylations. Overall, two carbon atoms enter the cycle as acetyl units and two carbon atoms leave the cycle in the form of two molecules of CO_2. The reducing equivalents generated, namely NADH, H^+ and $FADH_2$, are used to produce ATP by OxPhos. Succinyl CoA synthetase also produces guanosine triphosphate (GTP; which is converted to ATP) by substrate level phosphorylation.

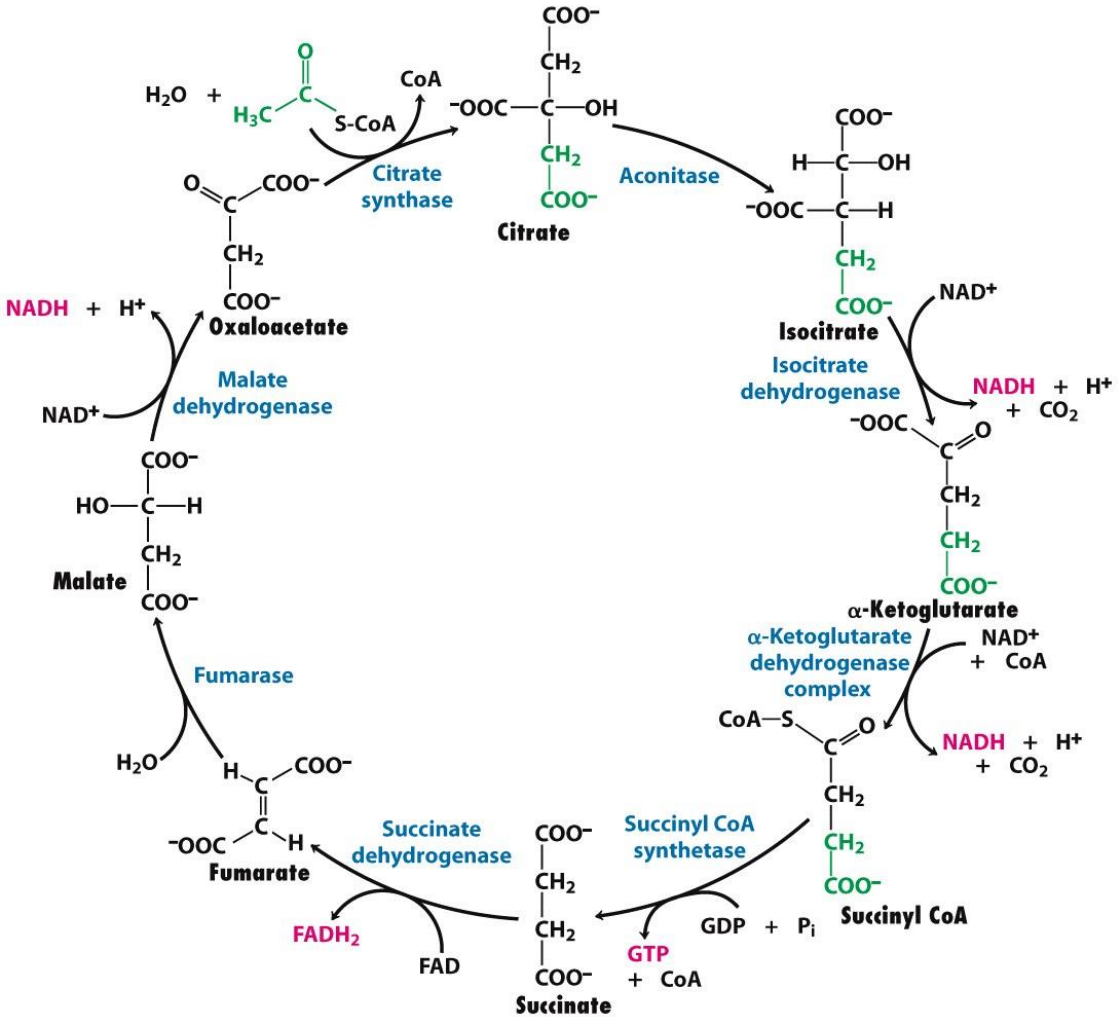

Figure 1.6: Reactions of the TCA cycle

Enzymes involved in the TCA cycle are displayed in blue font. The reducing equivalents NADH and $FADH_2$, produced at certain steps of the TCA cycle, are displayed in pink font. Taken from Berg *et al*. (2012). GDP: guanosine diphosphate.

1.1.6 OxPhos

The main bulk of ATP for a cell is formed at the MIM where OxPhos takes place. OxPhos is the terminal process of cellular respiration in eukaryotes. It utilises the energy released from the oxidation of nutrients to create an electrochemical gradient across the MIM. This gradient drives F_1F_0-ATP synthase, the enzyme responsible for catalysing the synthesis of ATP, resulting in a large amount of ATP being made available to the cell. This process was first described by Peter Mitchell in the 1960s and is best summarized by his proposed chemiosmotic theory (Mitchell, 1961).

As previously mentioned, the energy harnessed up to this point from the oxidation of fuel substrates during glycolysis, FAO and the TCA cycle is in the form of electrons that were transferred to nicotinamide adenine dinucleotide (NAD^+) and flavin adenine dinucleotide (FAD) to form NADH plus H^+ and $FADH_2$, respectively. During OxPhos, these electron carriers in turn pass the electrons to a series of enzyme complexes embedded in the MIM, referred to as the electron transport chain (ETC; Krauss *et al*., 2005). The ETC consists of four complexes: NADH-Q oxidoreductase (Complex I), succinate-Q reductase (Complex II), Q-cytochrome c oxidoreductase (Complex III) and cytochrome c oxidase (Complex IV). Electrons of NADH-linked substrates in the MM are donated to Complex I, while electrons of $FADH_2$-linked substrates are donated further up the ETC at an electron entry site in Complex II. Electrons are transferred from Complexes I and II to the mobile lipid-soluble carrier, ubiquinone, which is reduced to ubiquinol (QH_2). From QH_2, the electrons are passed to Complex III followed by the water (H_2O)-soluble mobile carrier cytochrome c and, finally, to Complex IV. Here, they are transferred to molecular O_2 at the haem a_3-Cu_B binuclear centre, reducing it to H_2O (Krauss *et al*., 2005). The pass of electrons along this chain is obligatorily coupled with the translocation of protons from the MM, across the MIM and into the IMS by three of the protein complexes: Complex I, Complex III and Complex IV (Krauss *et al*., 2005). This creates a transmembrane pH and electrochemical gradient. The potential energy provided by this gradient, referred to as the proton-motive force (PMF), is used to drive the synthesis of ATP from ADP and P_i by the flow of protons down the gradient back to the MM through ATP synthase (Complex V; Stock *et al*., 2000). In short, ATP synthesis by mitochondria is coupled to O_2 consumption via the PMF (summarized in Figure 1.7). As previously mentioned, the MIM contains an ADP/ATP translocase. This exchanges ADP from the cytoplasm for the ATP synthesized during OxPhos (Pebay-Peyroula *et al*., 2003). The ATP is translocated to the cytoplasm and other cellular locations where it can be used by the cell for different cellular processes. OxPhos

generates a net production of approximately 34 molecules of ATP per glucose molecule, making this form of glucose metabolism extremely resourceful in terms of energy production (Zheng, 2012).

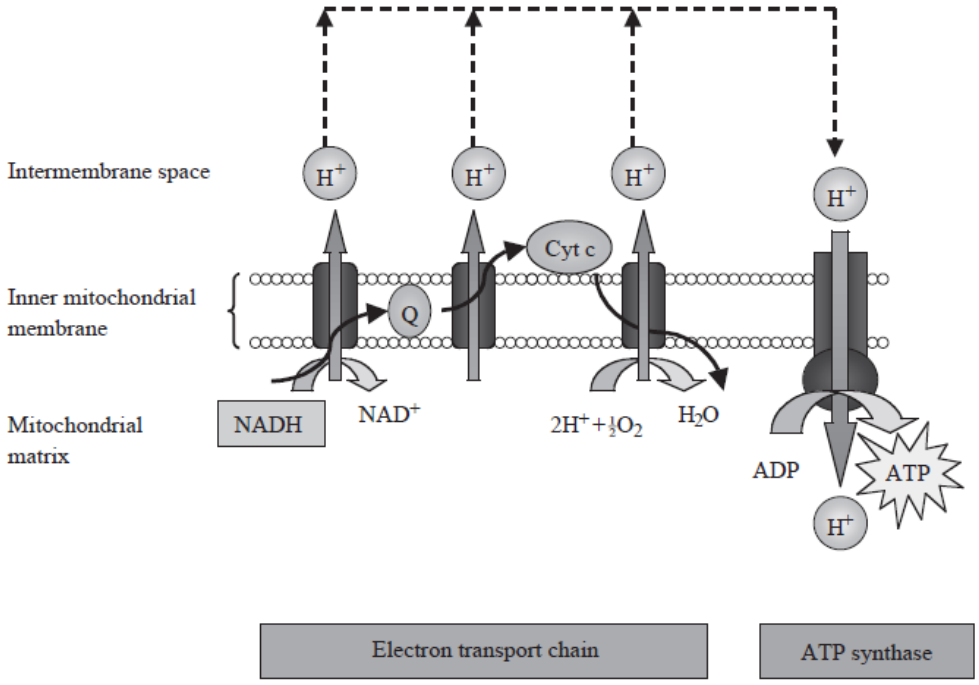

Figure 1.7: The process of OxPhos

The cellular metabolism of substrates, such as glucose and FAs, generates electrons in the form of the reduced hydrogen carriers, NADH plus H^+ and $FADH_2$. NADH and $FADH_2$ donate electrons to the ETC which comprises protein complexes that are located in the MIM. Electrons are ultimately transported to molecular O_2 which is reduced to H_2O. As electrons are transferred along the ETC, protons are pumped from the MM into the IMS. This generates a proton gradient across the MIM which is used to synthesize ATP. Protons can cross the MIM and return to the MM via ATP synthase, thereby providing energy for the conversion of ADP to ATP. ATP is then made available to the cell for various processes that require energy. Adapted from Schrauwen *et al*. (2002). Cyt C: cytochrome c. Q: ubiquinone.

1.2 Reactive O_2 Species

A by-product of all normally functioning mitochondria and a consequence of the generation of the proton electrochemical gradient is the continual involuntary release of free electrons from the ETC. These electrons have the potential to partially reduce O_2, forming intracellular reactive O_2 species (ROS). ROS is the collective term for the chemical species formed upon the incomplete reduction of molecular O_2 and includes the superoxide anion (O_2^-), hydrogen peroxide (H_2O_2) and the hydroxyl radical (OH^-), all of which are powerful oxidants. The major sites of intracellular ROS generation by the ETC are predominantly Complexes I and III (Drahota *et al*., 2002; Brand *et al*., 2004; Murphy, 2009).

In some cases, the generation of ROS can be deliberate. For example, phagocytes generate ROS as a host defence mechanism and ROS can also participate in cell signalling. However, the occurrence of ROS is generally considered to be an unintended consequence of aerobic metabolism (Lambeth, 2002). Free radicals can cause harm to cells if not removed quickly. ROS cause damage to cellular components, particularly nuclear and mitochondrial DNA as ROS are produced at the MIM, but also RNA, lipids and proteins (Brand, 2000; Schrauwen *et al*., 2006). This leads to impaired function, increased somatic mutation and, hence, degeneration and ageing (Brand, 2000; Brand *et al*., 2004). Importantly, all cells have powerful antioxidants, such as O_2^- dismutase (SOD), and physiological ROS defence mechanisms in place to counteract ROS production by mitochondria and reduce oxidative damage (Ježek and Hlavatá, 2005). For example, O_2^-, the parental form of ROS, can be enzymatically converted to H_2O_2 by SOD (Brand *et al*., 2004). The H_2O_2 produced by SOD conversion of O_2^- can be reduced to O_2 and H_2O by catalase or glutathione peroxidase (Brand *et al*., 2004).

1.3 Mitochondrial Proton Leak

ATP synthesis is described as being 'coupled' to O_2 consumption via the PMF. However, O_2 consumption by mitochondria is never perfectly coupled to ATP synthesis due to a degree of permeability of the MIM as the membrane potential rises (Porter, 2001). This leads to a non-specific diffusion process termed 'basal proton leak' (Brand, 1990; Brand *et al*., 1994; Rolfe *et al*., 1994; Harper *et al*., 2001). Basal proton leak occurs in all mitochondria and, while its mechanism is still not fully understood, it is believed to involve the passive diffusion of protons across the MIM back into the MM without any enzymatic involvement (Brand, 2000). Basal proton leak is physiologically important as it can account for up to 25 % of resting O_2 consumption of whole animals, contributing significantly to basal metabolism and energy expenditure (Porter, 2001).

In addition to naturally occurring basal proton leak across the MIM, proton leak can occur in other ways. One can have artificially-induced proton leak and protein-mediated proton leak. Artificially-induced proton leak occurs with the use of uncoupling agents: compounds whose mode of action abolishes the link between oxidation and phosphorylation, allowing electron transport to proceed without coupled ATP synthesis (Brand, 2000). Examples of chemical uncouplers include 2,4-dinitrophenol (2,4-DNP) and FCCP, which are lipophilic weak acids that can cross the MIM in either a protonated or unprotonated state. The artificial uncoupler sets up a catalytic cycle that dissipates the proton electrochemical gradient and allows substrate oxidation to proceed without providing the driving force for coupled ATP synthesis (Brand, 2000). Protein-mediated proton leak has historically been associated with brown adipocytes whose mitochondria were discovered to contain an uncoupling protein (UCP) responsible for the catalysis of proton leak that can supersede basal proton leak.

1.3.1 Brown Adipose Tissue and Non-Shivering Thermogenesis

Brown adipose tissue (BAT) is made up predominantly of brown adipocytes containing multiple small lipid droplets (Cannon and Nedergaard, 2004; Betz and Enerbäck, 2015; Cohen and Spiegelman, 2016). It is so-called due to its high mitochondrial content, the cytochromes within which give biological material its 'brown' colour (Betz and Enerbäck, 2015; Cohen and Spiegelman, 2016). Significant stores of BAT are found in interscapular, subscapular, axillary, perirenal and periaortic regions of rodents, hibernators and new-born mammals incapable of shivering, including humans (Palou *et al*., 1998; Cohen and Spiegelman, 2016). For a long time, it was thought that BAT in humans was rapidly lost

postnatally. However, following positron emission tomography studies using fluorodeoxyglucose, it is now accepted that adult humans possess small amounts of BAT in cervical, supraclavicular, paravertebral, mediastinal, perirenal and axillary regions (Cypess *et al*., 2009; Virtanen *et al*., 2009; Enerbäck, 2010). Additionally, this BAT can increase in mass following cold exposure (Nedergaard *et al*., 2007; Saito *et al*., 2009; Muzik *et al*., 2013; Betz and Enerbäck, 2015; Trayhurn, 2017). Whether BAT in adult humans can make more than a minor contribution to thermogenesis and overall energy expenditure is uncertain. The main function of BAT is to carry out the process of non-shivering thermogenesis (NST), an adaptation of increased thermogenic activity that protects mammals against a drop in body temperature and, in some cases, from body weight gain during chronic over-eating (Cohen and Spiegelman, 2016). The mechanism of NST allows animals to increase their heat production by raising their basal metabolic rate and, thus, defend their core body temperature against acute cold exposure (Betz and Enerbäck, 2015).

In response to cold exposure, shivering-derived thermogenesis, as well as NST, are initiated (Suzuki *et al*., 1997; Betz and Enerbäck, 2015). Shivering thermogenesis occurs through constant nerve stimulation of skeletal muscle (SKM), causing the muscle fibres to contract and relax (Behrens and Himms-Hagen, 1977). Gradually, as the period of cold acclimation continues, NST replaces shivering thermogenesis as the major source of heat production in the body. During NST, densely innervated BAT is stimulated by the sympathetic nervous system (Betz and Enerbäck, 2015; Cohen and Spiegelman, 2016). Upon stimulation, UCP1, the protein responsible for carrying out NST in BAT, exerts its thermogenic effect by dissipating the proton electrochemical gradient generated by the ETC of BAT mitochondria (Chouchani *et al*., 2017). It does this by mediating the passive re-entry of protons through the MIM into the MM from the IMS (Figure 1.8; Klaus *et al*., 1991). As protons return to the MM by means other than ATP synthase, the potential energy from substrate oxidation that is conserved in the proton gradient is not fixed chemically as ATP and, instead, is released as heat (Chouchani *et al*., 2017). BAT is highly vascular which allows for rapid deployment and distribution of this generated heat throughout the whole body (Nedergaard *et al*., 2007; Betz and Enerbäck, 2015). A concomitant decrease in the ATP yield of OxPhos is observed. ATP synthesis is thereby 'uncoupled' from substrate oxidation and O_2 consumption. This process of uncoupling in BAT enables fuel to be oxidized for the direct production of heat in thermoregulation. As a consequence, in an effort to restore the proton electrochemical gradient, oxidative

metabolism in BAT can proceed at a maximum rate, resulting in an increased metabolic flux oxidizing more fuel and enabling its mitochondria to produce more heat (Chouchani *et al*., 2017). During a prolonged stimulus, NST can be enhanced through an increase in the number of mature brown adipocytes, an increase in the mitochondrial content of brown adipocytes, an increase in mitochondrial enzymes that enhance the oxidative capacity of BAT and, predominantly, an increase in the UCP1 content of BAT mitochondria (Ricquier *et al*., 1986; Betz and Enerbäck, 2015), which mainly determines the heat-producing capacity of BAT (Silva and Rabelo, 1997; Trayhurn, 2017). NST plays a critical role in thermoregulation and in overall energy balance (Palou *et al*., 1998).

The mechanism of thermogenesis can also occur in UCP1-containing brown in white (brite) adipose tissue, also known as beige fat, found predominantly in subcutaneous regions (Wu *et al*., 2012; Betz and Enerbäck, 2015; Cohen and Spiegelman, 2016; Trayhurn, 2017). Beige adipocytes are a wholly different cell type to brown adipocytes, developing from a distinct white adipocyte lineage and from the 'browning/beiging' of said white adipocytes undergoing 'trans-differentiation' (Berardi and Chou, 2014; Qiu *et al*., 2014; Betz and Enerbäck, 2015; Min *et al*., 2016; Chouchani e*t al*., 2017; Trayhurn, 2017). Similar to BAT, beige fat UCP1 expression is significantly enhanced following cold exposure and hormonal stimulation by the sympathetic nervous system (Wu *et al*., 2012; Harms and Seale, 2013; Rosenwald *et al*., 2013).

Wildtype (WT) mice have been shown to be able to defend their body temperature by first generating heat through shivering, as described above, and then, following an acclimation period of about three days, they gradually replace shivering with NST via stimulated BAT containing active UCP1. *Ucp1*$^{-/-}$ mice cannot defend their core body temperature, having to rely completely on shivering (Enerbäck *et al*., 1997; Golozoubova *et al*., 2001, 2006; Feldmann *et al*., 2009). As the energy from food is released as heat during uncoupling rather than being stored and used in the body, the uncoupling of mitochondria has also been shown to reduce body fat, with *Ucp1*$^{-/-}$ mice demonstrating an obese phenotype (Feldmann *et al*., 2009). In fact, the previously mentioned uncoupling agent, 2,4-DNP, had been used for this purpose for many years (Tainter *et al*., 1933; Parascandola, 1974). 2,4-DNP was introduced as an anti-obesity drug in the 1930s with some considerable success, though reports of side effects (cataracts) and deaths from overdose led to it being removed from the market by the U.S. Food and Drug Administration in 1938 (Parascandola, 1974; Grundlingh *et al*., 2011; Harms and Seale, 2013).

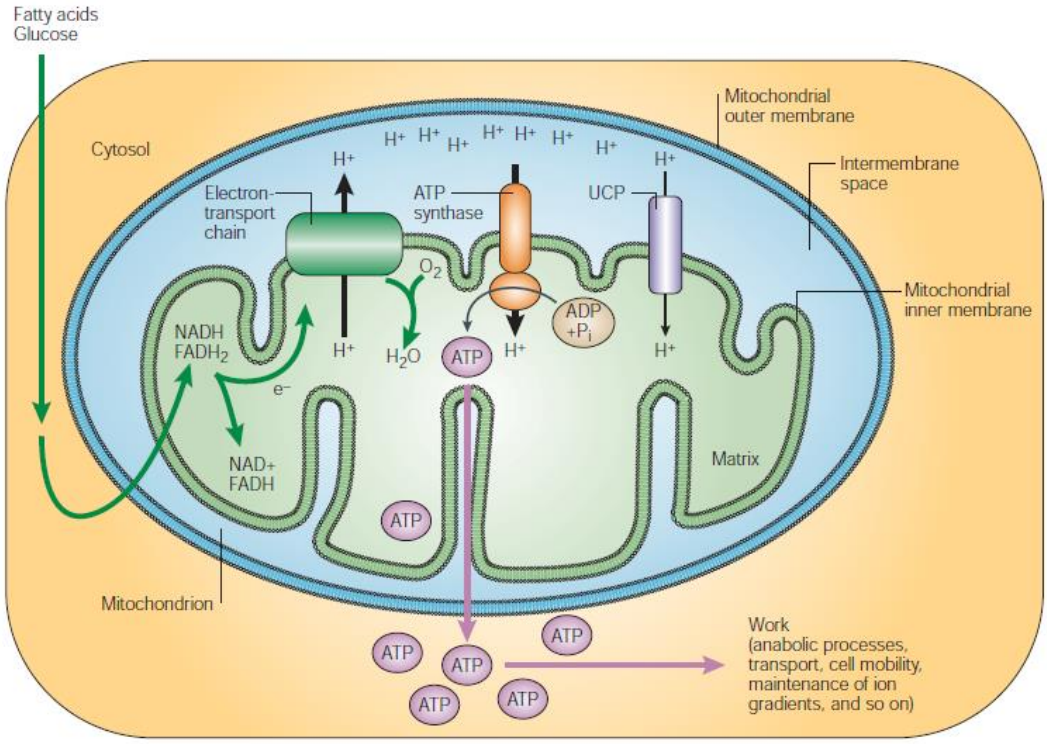

Figure 1.8: Generation of the proton electrochemical gradient by the ETC and its dissipation by UCP1

In stimulated BAT mitochondria, protons in the IMS may re-enter the MM via ATP synthase (as in normal mitochondria), thereby providing energy for the conversion of ADP to ATP, or through UCP1. In the latter case, the energy derived from oxidized substrates and stored in the proton electrochemical gradient is dissipated as heat (thermogenesis) instead of being fixed chemically as ATP. Taken from Krauss *et al*. (2005).

1.3.2 UCP1

The protein responsible for dissipating the proton electrochemical gradient during NST, UCP1, was discovered in the 1970s by Heaton *et al*. (1978) and, for a long time, its expression was thought to be a unique feature of BAT until its discovery in white adipose tissue (WAT) and SKM in 1998 (Yoshida *et al*.). The amino acid sequence of UCP1 is highly conserved between species (Figure 1.9) and highly homologous to that of several ubiquitous MIM carriers, including the ADP/ATP translocase, the phosphate carrier and the oxoglutarate carrier (Klingenberg, 1990; Klaus *et al*., 1991). This made it evident early on after its discovery that this 32 kiloDalton (kDa) protein is a member of the mitochondrial anion carrier superfamily. Similar to its family members, the 306 amino acid-long monomer contains six transmembrane α-helices and has both C and N termini protruding into the IMS (Figure 1.10; Klingenberg, 1990; Klingenberg and Huang, 1999). As a tripartite structure, the protein can be divided into three symmetrical sections of about 100 amino acids in length, each containing two of the six transmembrane helices (Klingenberg, 1990; Boss *et al*., 1998; Palou *et al*., 1998; Klingenberg and Huang, 1999). Within each domain, the two transmembrane helices are separated on the matrix side of the MIM by a stretch of approximately 40 nucleotide residues arranged in a hydrophilic loop (Klingenberg and Huang, 1999). The three loops on the matrix side of the MIM together arrange in a pocket, the significance of which is seen in its affinity for purine nucleotide binding, which is an essential aspect of UCP1 inhibition and will be discussed in more detail later.

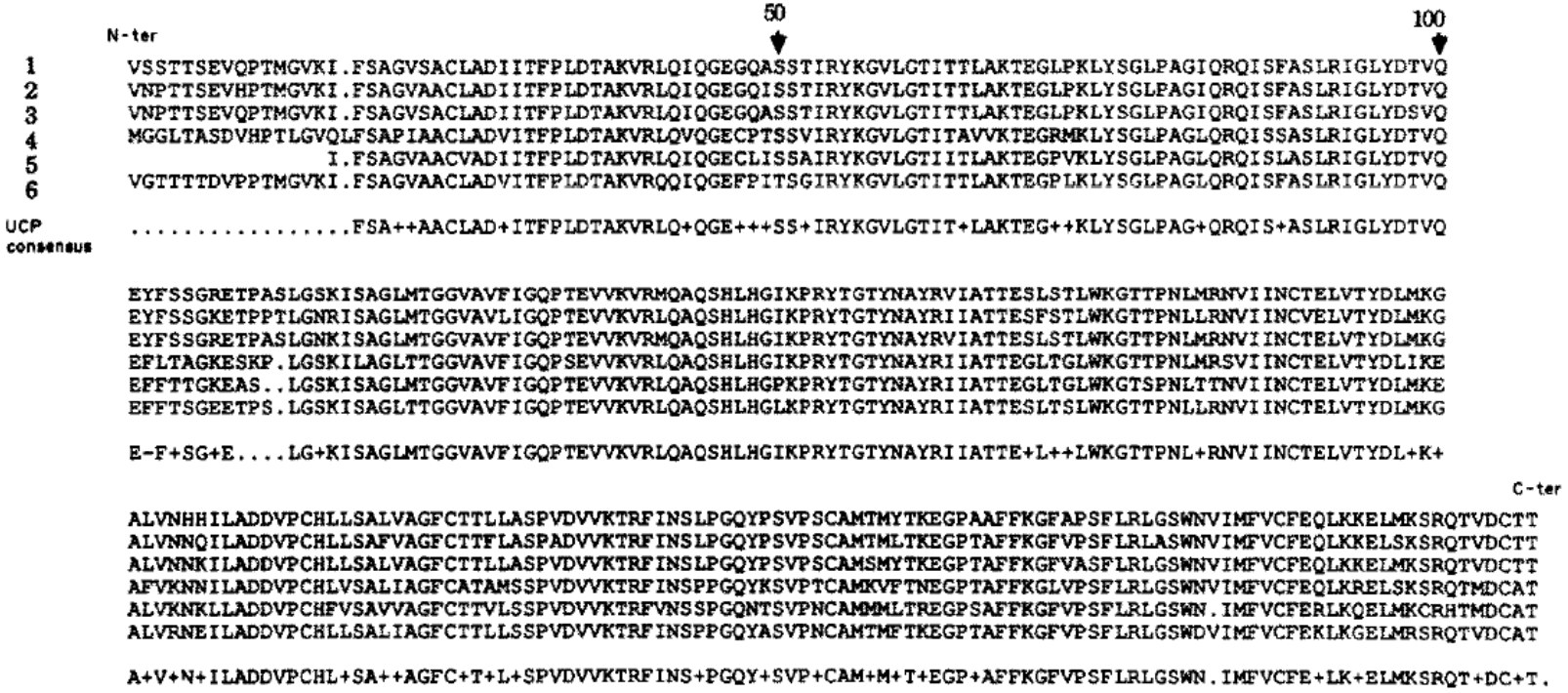

Figure 1.9: UCP1 is highly conserved among species

Alignment of UCP1 amino acid sequences from rat (1), hamster (2), mouse (3), human (4), bovine (5) and rabbit (6). In the consensus sequences, the sign + indicates a lower level of homology. Taken from Klaus *et al*. (1991).

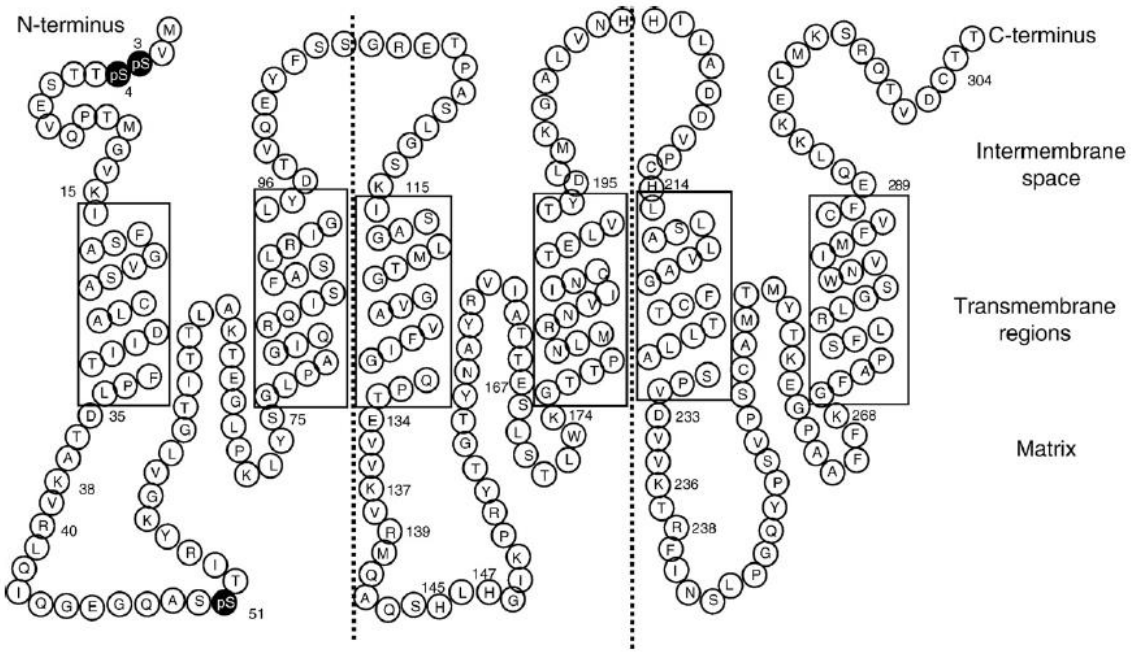

Figure 1.10: Tripartite structural model of UCP1 in the MIM

UCP1 (306 amino acids long) has been proposed to constitute three symmetrical membrane-spanning domains, each comprising about 100 amino acids, and to contain six amphiphilic transmembrane α-helices, represented by rectangles. The dotted lines help visualize the tripartite structure. Taken from Carroll *et al*. (2008).

1.3.2.1 UCP1 Regulation - Expression

The expression of the *Ucp1* gene is mainly regulated at the transcriptional level. Norepinephrine (NE) is the main positive regulator of *Ucp1* messenger RNA (mRNA) generation, protein synthesis and activity (Ricquier *et al*., 1984, 1986; Palou *et al*., 1998). Acting via β-adrenergic receptors and cyclic adenosine monophosphate (cAMP), NE is released from sympathetic nerve terminals that stimulate BAT in response to cold exposure or chronic overeating (Ricquier *et al*., 1984, 1986; Palou *et al*., 1998). The major adrenoceptor mediating the effects of NE in mature brown adipocytes is the β_3-adrenergic receptor in mice and the β_1-adrenergic receptor in humans (Nedergaard and Cannon, 2010); α_1-, α_2- and β_2-adrenoceptors may also be involved, although to a lesser extent (Palou *et al*., 1998; Thonberg *et al*., 2002). Activation of the β_1-, β_2-, β_3- and α_1-adrenergic receptors by NE, as well as inhibition of the α_2-adrenergic receptor, has been shown to increase the expression of *Ucp1* (Boss *et al*., 1998). β-adrenoceptors are coupled via stimulatory GTP-binding proteins (G_s proteins) to adenylyl cyclase; their stimulation by NE leads to an increase in cAMP synthesis that in turn stimulates protein kinase A (PKA) activity (Thonberg *et al*., 2002; Hoffmann *et al*., 2015). Key downstream targets of PKA phosphorylation include the transcription factor cAMP-response element-binding protein (CREB), which stimulates transcription of the *Ucp1* gene (Figure 1.11A; Nedergaard *et al*., 2001; Thonberg *et al*., 2002). Another activator of *Ucp1* transcription of physiological relevance is triiodothyronine (T_3). T_3 acts synergistically with NE since NE stimulation markedly increases thyroxine deiodinase activity of brown adipocytes, thus allowing high intracellular generation of T_3 from thyroxine (Silva and Rabelo, 1997; Palou *et al*., 1998; Betz and Enerbäck, 2015). T_3 stimulates *Ucp1* gene expression via thyroid hormone response elements (Silva and Rabelo, 1997).

Retinoic acid, the natural active form of vitamin A, has been shown to stimulate *Ucp1* gene transcription through a mechanism independent from the adrenergic pathway and to induce UCP1 appearance both in cultured brown adipocytes and in BAT of intact mice (Palou *et al*., 1998). Retinoic acid and vitamin D receptors bind to specific response elements in the genes as heterodimers with other receptors, most commonly with the so-called retinoid X receptors (RXRs). It is also known that activators of peroxisome proliferation activating receptors (PPARs), such as pioglitazone, PPARgamma (PPARγ) coactivator 1 α (PGC1α) and PRD1-BF1-RIZ1 homologous domain-containing protein-16 (PRDM16), cause *Ucp1* gene expression (Seale *et al*., 2008; Betz and Enerbäck, 2015). Sears *et al*. (1996) reported that PPARγ-RXR heterodimers are necessary for cAMP-mediated transcription of the

Ucp1 gene. Concerning UCP1 degradation, it was suggested that a post-translational regulatory mechanism exists that ensures the rapid degradation of newly synthesized molecules when the physiological stimulation ceases (Bonet *et al*., 1995). More recently, our laboratory demonstrated that the cytoplasmic proteasome is required for the ubiquitination and degradation of UCP1 in BAT and thymus mitochondria (Clarke *et al*., 2012).

1.3.2.2 UCP1 Regulation - Activation

As previously mentioned, NE is a strong physiological activator of *Ucp1* expression but also of UCP1 activity. Following NE stimulation of BAT, another key downstream target of PKA is hormone-sensitive triacylglycerol lipase (HSL) which, once phosphorylated, hydrolyses triacylglycerol stores providing free FAs (FFAs; Shih and Taberner, 1995; Palou *et al*., 1998), the natural activators of UCP1 activity. PKA also phosphorylates perilipin. Perilipin protects triacylglycerides from HSL activity and, upon phosphorylation, is deactivated which leads to its dissociation from the triglyceride droplets and, ultimately, their exposure to attack by HSL (Martinez-Botas *et al*., 2000). The uncoupling activity of UCP1 is subsequently stimulated by the presence of FFAs (which can also serve as fuel) and long-chain fatty acyl CoA esters, causing thermogenesis (Figure 1.11B). It has been found that saturated FA chain length of at least ten carbons is required to activate UCP1 uncoupling activity and this activity decreases when chains exceed sixteen carbons in length (Klingenberg and Huang, 1999; Klingenberg, 2017). Unsaturated FAs (*i.e.* contain at least one double bond between two carbon atoms) are known to be good activators of UCP1-catalyzed proton conductance [*e.g.* Oleic acid (C_{18}); Klingenberg and Echtay, 2001]. Retinoic acid is also a good activator of UCP1-induced proton transport (Klingenberg and Echtay, 2001) and, while this was originally thought to be due to retinoic acid being a physiological FA analogue, it is now thought to be due to it having properties similar to 4-hydroxy-trans-2-nonenal (HNE), a lipid peroxidation product that has been shown to activate UCP1 (Brand *et al*., 2004). Furthermore, UCP1 is phosphorylated at serine 51 which increases following cold-acclimation but it is unclear whether this covalent modification affects activity or turnover (Carroll *et al*., 2008). UCP1 may also be regulated by ROS-driven sulfenylation of a key cysteine residue, Cys253 (Chouchani *et al*., 2016).

The mechanism by which FFAs activate UCP1 has been extensively studied but remains controversial. There are a number of models of FFA stimulation of UCP1 activity currently proposed: the allosteric model (Rial *et al*., 1983), the FA proton-buffering model (Winkler

and Klingenberg, 1994), the FA cycling/protonophore model, which was originally proposed by Skulachev (1991) before being extended by Garlid *et al*. (1996, 1998, 2000, 2001), and the FA shuttling model (Fedorenko *et al*., 2012). The first model hypothesizes that FAs induce proton transport by UCP1 by causing a conformational change in the protein, without FAs interfering directly with proton translocation (Klingenberg, 2017). The FA proton-buffering model suggests a role for FAs as cofactors for the direct transport of protons by UCP1 along its aqueous channel (Winkler and Klingenberg, 1994). FAs localize to binding sites along the aqueous channel of UCP1 and catalyse the transport of protons along their acidic moieties from one FA to the next, with the final proton transfer step employing proton transferring residues until the proton is through the MIM and in the MM (Klingenberg, 2017). No such FA binding sites have been identified as of yet; however, in support of this model, the mutation of two UCP1 histidine residues (His145 and His147) causes a loss of proton transport (Bienengraeber *et al*., 1998). The FA cycling model proposes FAs as protonophores themselves and that UCP1 catalyses not the direct transport of protons but the transport of FA anionic head groups across the MIM, acting as a FA anion uniporter (Garlid *et al*., 1996). Protonated FAs would spontaneously flip-flop across the MIM to the MM, be deprotonated and actively transported back to the IMS by UCP1 (Garlid *et al*., 1996), driven by the high negative membrane potential inside the mitochondria. Once the head group reaches the IMS, it becomes protonated again and spontaneously flip-flops back to the matrix side where the cycle restarts. As a result, uncoupling and the concomitant consumption of the PMF is not taking place within the UCP1 protein but is ensured by the spontaneous diffusion of protonated FAs across the MIM. The continuation of the cycle is ensured by FA anion transport mediated by UCP1, leading overall to the apparent UCP1-mediated proton translocation (Ježek *et al*., 1997a, 1997b; Jabůrek *et al*., 2001). The FA cycling model has been supported by reported evidence of the existence of the peripheral FA binding sites (Berardi and Chou, 2014), as well as observations of the inability of so-called ‘inactive FAs’ to induce the protonophoric ability of UCP1 (Ježek *et al*., 1997b; Breen *et al*., 2013). Finally, the FA shuttling model suggests that FAs bound to UCP1 shuttle or swing in the UCP1 channel with the carboxyl group alternating between anion and acid forms, picking up protons on the cytosolic side of the MIM and releasing them on the matrix side with the FA remaining bound to UCP1 (Fedorenko *et al*., 2012).

1.3.2.3 UCP1 Regulation - Inhibition

UCP1 activity can be inhibited by the binding of free [not in complex/chelated with magnesium or manganese cations (Mg^{2+} or Mn^{2+}, respectively)] purine nucleotide di- or tri-phosphates [mainly ATP under cellular conditions but also guanosine diphosphate (GDP), GTP and ADP; Figure 1.11B; Klingenberg, 2017], whereas monophosphates, such as guanosine monophosphate (GMP) and AMP, are poor ligands (Klingenberg and Huang, 1999). The purine nucleotide binding site on UCP1 has been well characterized (Heaton *et al*., 1978), *i.e.* the outer facing hydrophilic cavity mentioned previously, formed by the three loops of UCP1 in the MM (Zhu *et al*., 2013; Klingenberg, 2017). UCP1 is predicted to behave as a homodimer in the MIM (Boss *et al*., 1998; Palou *et al*., 1998), with only one nucleotide binding per dimer (Klingenberg, 1984; Klingenberg and Huang, 1999). More recently, however, it has been shown that monomeric UCP1 may also exist and bind a single nucleotide (Lee *et al*., 2015). Purine nucleotides are made up of a purine base, a sugar moiety and at least one phosphate group. The α-phosphate group binds deep inside the protein to three arginine residues on helices 2, 4 and 6 and the sugar base moiety interacts with the third matrix loop which connects helices 5 and 6 (Klingenberg and Huang, 1999; Porter, 2001). Purine nucleotide binding to UCP1 is believed to induce a conformational change in the protein affecting glycine 281 (Berardi and Chou, 2014), which may be responsible for its inhibitory activity by occluding the FA binding site (Klingenberg and Huang, 1999). Nucleotide binding to UCP1 is pH dependent, with decreasing affinity as the pH exceeds approximately 7.2 (Klingenberg, 2017). BAT mitochondria of normothermic and otherwise untreated animals are largely coupled due to a low FFA concentration and inhibition of UCP1 by high concentrations of ATP. When BAT is stimulated during cold exposure, the endogenous ATP concentration is depleted, resulting in the dissociation of pre-bound ATP from UCP1. This dissociation, coupled with the liberation of activating FFAs, increases proton transport activity through UCP1, *i.e.* uncoupling (Huang and Klingenberg, 1995). The mechanism of FFAs overcoming nucleotide-mediated UCP1 inhibition has not yet been fully elucidated, although Fedorenko *et al*. (2012) have claimed that FFAs directly compete with purine nucleotides to bind UCP1.

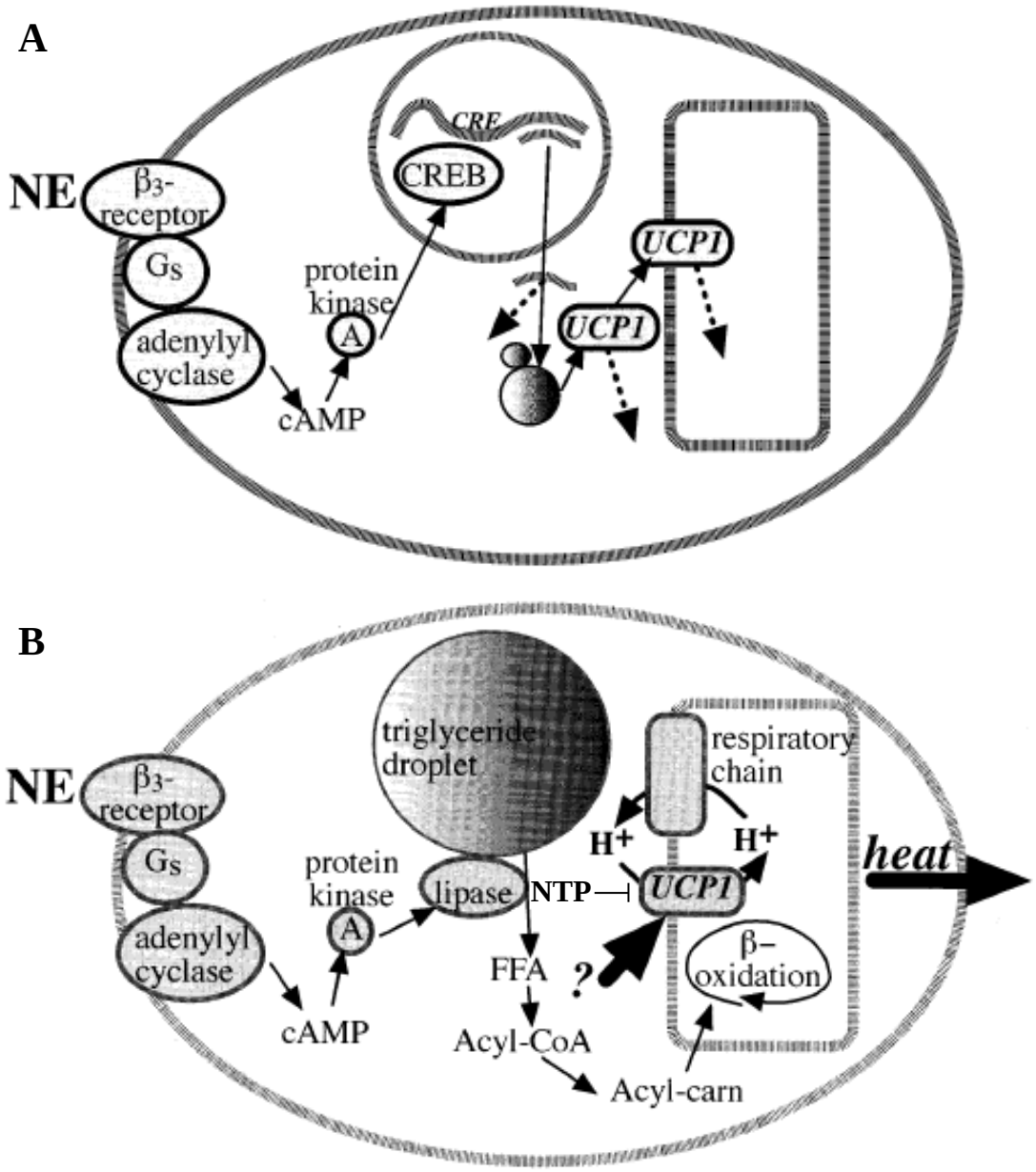

Figure 1.11: Hormonally-induced expression and regulation of UCP1

(A) NE induces an increase in *Ucp1* synthesis in mitochondria of brown adipocytes. Degradative pathways are indicated by broken arrows. (B) Activation/inhibition of UCP1. NE acts on β-receptors and leads to lipolysis via cAMP. The proton conductance of UCP1, which is normally blocked by purine nucleotides, is induced by the resultant FFAs. Adapted from Nedergaard *et al*. (2001). Acyl-carn: acyl-carnitine. NTP: nucleotide triphosphate.

1.4 Discovery of UCP1 Homologues

Since the discovery of UCP1 in the 1970s, other mitochondrial UCPs of the MIM have been reported. In 1997, two UCPs were discovered a couple of months apart: UCP2 by Fleury *et al*. (and a short time later by Gimeno *et al*.) and UCP3 by Boss *et al*. (and a few months later by Vidal-Puig *et al*. and Gong *et al*.). With molecular weights (M_r) of approximately 33.2 and 34 kDa, UCP2 and UCP3 consist of 309 and 312 amino acids, respectively (Fleury *et al*., 1997; Harper *et al*., 2001). As expected, UCP2 and UCP3 have the highest predicted amino acid sequence homology to the archetypical UCP, UCP1, than any other member of the mitochondrial anion carrier superfamily (Figure 1.12), at 59 and 57 %, respectively (Krauss *et al*., 2005), and are 73 % identical to each other (Hilse *et al*., 2016). Their degree of homology to mitochondrial carriers other than UCP1 is approximately 30 % in comparison (Fleury *et al*., 1997; Boss *et al*., 1998; Vidal-Puig *et al*., 2000). The six membrane-spanning α-helix structure of UCP1 is highly conserved amongst UCP2 and UCP3, including the three mitochondrial carrier protein motifs, consistent with roles as ion transporters of the MIM (Boss *et al*., 1997; Fleury *et al*., 1997). However, UCP3 differs from UCP1 and UCP2 in that it has two isoforms, while they have no known isoforms. Alternative splicing results in two mRNA transcripts referred to as the short (*Ucp3*$_S$) and long (*Ucp3*$_L$) forms (Harper *et al*., 2001). *Ucp3*$_S$ and *Ucp3*$_L$ correspond to proteins of 275 and 312 amino acids in length, respectively (Harper *et al*., 2001). *Ucp3*$_S$ lacks the sequences corresponding to the last (sixth) transmembrane region and putative nucleotide binding site. There is some doubt as to whether *Ucp3*$_S$ is translated into a functional protein and findings suggest that only *Ucp3*$_L$ is expressed in mice and humans (Harper *et al*., 2001). The amino acid sequences of human and mouse UCP2 are 95 % identical to each other (Fleury *et al*., 1997), while those of UCP3 are 87 % identical (Solanes *et al*., 1997).

More UCPs have been found since the discovery of UCP2 and UCP3. These include UCP4, which is a 36 kDa protein of 323 amino acids (Mao *et al*., 1999), UCP5, also termed brain-specific mitochondrial carrier protein 1 (BMCP1; Sanchis *et al*., 1998; Yu *et al*., 2000), and plant UCPs, which have been discovered in potato tubers and tomatoes (Costa *et al*., 1999; Considine *et al*., 2003). UCP4 is 29, 33 and 34 % homologous to UCP1, UCP2 and UCP3, respectively, and transcripts have been found in both foetal and adult brain tissues (Mao *et al*., 1999; Yu *et al*., 2000). *Ucp5* mRNA has been found in brain, testis, heart, liver and kidney (Yu *et al*., 2000). *Ucp5* has three isoforms: a short form (*Ucp5*$_S$), a short form with insert (*Ucp5*$_{SI}$) and a long form (*Ucp5*$_L$; Yu *et al*., 2000).

The non-photosynthetic soil amoeboid protozoan, *Acanthamoeba catellanii*, has been shown to express an UCP (Jarmuszkiewicz *et al*., 1999) and a protein has been identified in the SKM of chickens, ducklings and hummingbirds (avian UCP) that shares approximately 70 % amino acid identity with both UCP2 and UCP3 (Raimbault *et al*., 2001; Vianna *et al*., 2001; Toyomizu *et al*., 2002). UCP1, UCP2 and UCP3, together with plant UCPs, represent the core of the UCP family (Laloi *et al*., 1997). While UCP4 and UCP5 were considered to be members of the family of mitochondrial UCPs in earlier days (Sanchis *et al*., 1998; Mao *et al*., 1999), more recent studies do not include them anymore but, rather, suggest they are precursors to UCP1, UCP2 and UCP3 today (Hanák and Ježek, 2001).

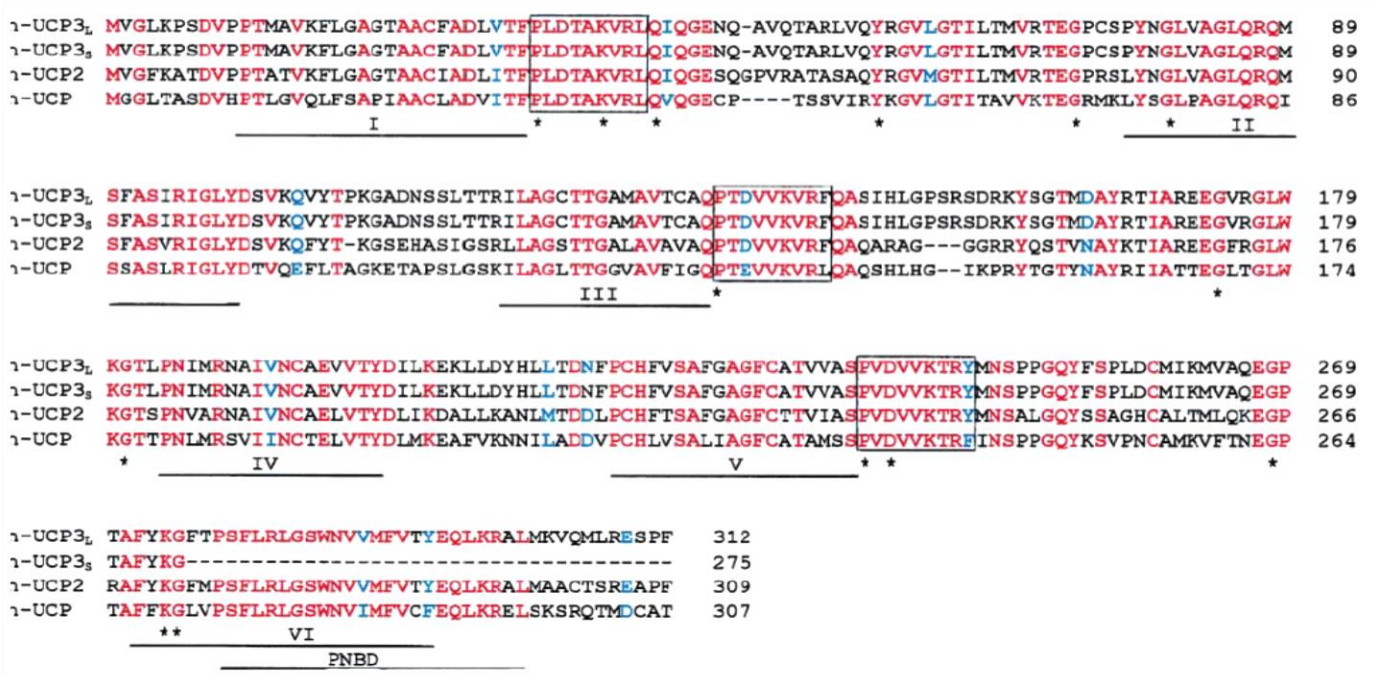

Figure 1.12: Multiple amino acid sequence alignment of UCP1, UCP2, UCP3$_L$ and UCP3$_S$

The diagram shows alignment of human UCP3$_L$, UCP3$_S$, UCP2 and UCP1 (UCP). The sequences are presented in single letter code. Gaps introduced into the sequences to optimize alignments are illustrated with a dash. Identical and similar amino acids are highlighted in red and blue, respectively. Transmembrane α-helices are underlined and numbered in Roman numerals (I – VI). The three signature tripartite structure motifs common to mitochondrial anion transporters are boxed. Asterisks denote the 14 amino acid residues that are completely conserved in mitochondrial carrier proteins. PNBD: potential nucleotide binding domain. Taken from Boss *et al*. (1997).

1.4.1 Expression of UCP2 and UCP3

UCP2 is expressed ubiquitously in a number of tissues. *Ucp2* mRNA has been reported in placenta, prostate, ovary, leukocytes (Gong *et al*., 1997), Kupffer cells of the liver (Larrouy *et al*., 1997), BAT, uterus, intestines (Ricquier and Bouillaud, 2000), pancreatic β-cells (Zhang *et al*., 2001), SKM, heart, brain, kidney, lungs, WAT, spleen, thymus, testis, stomach and spinal cord (Rupprecht *et al*., 2012). In comparison, UCP2 protein has been reported in intestine, WAT (Pecqueur *et al*., 2001), pancreatic β-cells (Zhang *et al*., 2001), BAT, uterus, ovary (Rousset *et al*., 2003), spleen, lung, stomach, brain, thymus, kidney, heart, liver, lymph nodes and leukocytes (Rupprecht *et al*., 2012). However, there are many conflicting reports on the presence and expression of *Ucp2* mRNA and protein in different tissues. Similar to UCP1, UCP3 was thought to be exclusively expressed in one tissue, SKM, following its discovery (Boss *et al*., 1997). UCP3 has since been reported in BAT (Cunningham *et al*., 2003), spleen, thymus, reticulocytes, monocytes, lymphocytes (Carroll and Porter, 2004), pancreatic β-cells (Azzu *et al*., 2010) and heart (Hilse *et al*., 2018).

Our laboratory has reported evidence of UCP1 and UCP3 expression in murine thymocytes and spleen mitochondria (Carroll and Porter, 2004; Carroll *et al*., 2004; Carroll *et al*., 2005; Adams *et al*., 2008a, 2008b; Kelly and Porter, 2011), while Krauss *et al*. (2002) reported evidence of UCP2 expression in thymocytes. Thymocytes are derived from lymphoid progenitor cells and develop into mature T cells in the thymus before migrating to peripheral lymphoid tissues, such as the spleen, where they wait to be activated by cells of the innate immune system and subsequently carry out an immune response (Krammer *et al*., 2007). Thus, we were curious to explore the potential expression and role, if any, of UCPs in peripheral T cells of the immune system.

1.5 The Immune System

In order to survive and thrive, organisms need to protect themselves from invading pathogens such as bacteria, viruses, fungi and parasites that have the potential to cause infection and disease. Organisms possess mechanical and chemical barriers to prevent pathogens from gaining access to the body. The skin acts as a physical barrier but also secretes sweat and acids containing antimicrobial substances to chemically hinder pathogen invasion. Cavity surfaces of the body, such as the nose and lungs, are covered with antimicrobial mucus and/or filamentous layers that capture and excrete possibly harmful organisms. Furthermore, commensal organisms in the gut and bacteria on the skin secrete bacteriocines and acids and compete with intruders for vital nutrients (Janeway and Medzhitov, 2002). This normal bacterial flora provides a further layer of protection. If a pathogen breaches these barriers, the next line of defence is the immune system.

Identifying and clearing foreign pathogens and harmful or dead cells is the immune system's main purpose. The immune system responds upon encountering an antigen. Antigens are three dimensional molecules that trigger a specific immune response. They can be extraneous antigens, such as components of bacterial cell walls, capsules, pili and flagella, as well as viruses, fungi and protozoa, or they can be particles of food and dust. They can also be 'self'-antigens. The central quality of the immune system is its ability to distinguish between self- and non-self-antigens, *i.e.* what is harmful and what is helpful, and to display tolerance as too much immune reactivity towards self-antigens can result in autoimmunity. Antigens can be made up of protein, DNA, RNA, carbohydrates or lipids and can enter the body by various routes: for example, through breaks in the skin and mucous membranes, through direct injection, as with a bite or needle or through organ transplants and skin grafts. When an antigen is detected, active immune cells are recruited to the site of infection by the release of chemical homing factors called chemokines and specialized chemical mediators called cytokines from the detecting cell. Cytokines are small soluble regulatory proteins produced by cells of the immune system that allow intercellular communication and cell recruitment. The complex web of signals among all cell types of the immune system is referred to as the cytokine network.

1.5.1 Cells of the Immune System

The immune system comprises a variety of cell populations that are responsible for the detection and elimination of pathogenic organisms, as well as the clearance of harmful or damaged cells and debris. All cells of the immune system are derived from pluripotent,

haematopoietic stem cells in the bone marrow (Schwarz and Bhandoola, 2006). Leukocytes differentiate in two different pathways to cells of the myeloid or lymphoid lineage. The myeloid line produces mononuclear and polymorphonuclear leukocytes as well as platelets, mast cells and erythrocytes. Of the mononuclear myeloid cells, monocytes circulate for several days before leaving the blood following activation and entering tissues to mature into phagocytic macrophages or dendritic cells (DCs). Macrophages and DCs are tissue-resident cells and are continuously replenished by the pool of circulating monocytes (Pulendran and Ahmed, 2006). The polymorphonuclear cells, granulocytes, are made up of neutrophils, eosinophils and basophils and display a granular cytoplasm. The lymphoid pathway gives rise to lymphocytes, the smallest of the leukocytes. Lymphocytes include T and B cells with specific receptors and Natural Killer (NK) cells (Schwarz and Bhandoola, 2006). T and B cells are distinguishable by their site of differentiation. Lymphoid progenitor cells are processed in the thymus to become T cells and in the bone marrow to become B cells (Schwarz and Bhandoola, 2006). These lymphoid cells are non-phagocytic and are agranular – their cytoplasm appears uniform under a light microscope in comparison to granulocytes.

1.5.2 The Innate Immune System

The immune system can be classically divided into two distinct factions: the innate immune system and the adaptive immune system, which both respond when an antigen is encountered. The innate immune response is the body's first line of defence against invading microbes. In a healthy individual, the innate immune system is functional from birth and protects efficiently against harmful microorganisms without the need for prior exposure to any pathogen. It is the first to respond to a bacterial, viral, fungal or parasitic challenge and is responsible for mounting an immediate but generalized, non-specific inflammatory response. The innate immune response recognises antigens associated with microbes and this detection triggers a response in which innate cells attempt to wall off and attack the invader in a non-specific manner and halt its spread. While this type of immunity protects against a broad variety of infectious agents, it is an unspecific and short-lived response.

The innate immune system comprises various innate cell types: NK cells, DCs, mast cells, granulocytes and macrophages, along with their soluble effector substances (Janeway and Medzhitov, 2002). Macrophages, DCs and neutrophils specialize in phagocytosis and destruction of microorganisms in intracellular vesicles with bactericidal reagents. Upon

phagocytosing a bacterium or other particle, these cells often display an increase in O_2 consumption, leading to the production of ROS. This so-called respiratory burst gives rise to a significant amount of ROS, like O_2^- and H_2O_2, produced primarily by nicotinamide adenine dinucleotide phosphate (NADPH) oxidases of the Nox/Duox family of proteins (Lambeth, 2002). Neutrophils and eosinophils are capable of diapedesis (leaving blood vessels) and phagocytosing pathogens upon encountering them. Basophils release vasoactive amines (histamine, bradykinin, slow-reacting substance of anaphylaxis) and eosinophil chemotactic factor from granules, while eosinophils release anti-histamines to neutralise those released from basophils and control the immune response. NK cells identify infected cells and efficiently kill them directly (hence the name). Viruses can only replicate within a host cell, thus, causing alterations to the host cell membrane that are detected by NK cells and allow the NK cell to kill the host cell. The activities of innate immune cells and the chemicals they secrete lead to redness and swelling at sites of injury and account for the fever, body aches and other flu-like symptoms that accompany many infections.

Innate immune cells possess a variety of pattern recognition receptors (PRRs) on their cell surface or intracellularly (Medzhitov, 2001; Kang *et al*., 2016). PRRs may also be secreted into the bloodstream and tissue fluids (Janeway and Medzhitov, 2002). Among the best characterized PRRs are the Toll-like receptors (TLRs) and intracellular nucleotide-binding oligomerisation domain (NOD)-like receptors (NLRs). TLRs are prominent on the cell surface and membranes of lysozomes and endosomes where they detect pathogens, whereas NLRs are expressed in the cytosol and detect intracellular intruders such as viruses (Akira *et al*., 2006). Detection of pathogens is mediated via these PRRs that can recognise specific, conserved microbial patterns called pathogen-associated molecular patterns (PAMPs) or damage-associated molecular patterns (DAMPs; Medzhitov, 2001; Janeway and Medzhitov, 2002; Awate *et al*., 2013; Kang *et al*., 2016) from damaged/infected cells. PAMPs are usually shared by more than one organism and, therefore, a broad variety of potentially harmful pathogens can be identified (Medzhitov, 2001). Once a PAMP or DAMP has been detected by a PRR, a conserved host defence signalling pathway is activated, causing the expression of immune response genes and the triggering of an innate immune response. Innate cells produce and release an array of different signalling molecules depending on the range of PRRs activated by the specific PAMP or DAMP. These signalling molecules and secretion profiles act to recruit additional innate immune cells. The most prominent pro-inflammatory cytokine is

interferon-γ (IFN-γ) which triggers a full inflammatory response by directing more cells to the site of infection and activating them to destroy the microbe and secrete even more cytokines, usually until the threat is eradicated.

Once a PAMP or DAMP has been detected by a PRR, the innate immune cell is also responsible for engulfing, processing and presenting pieces of this antigen, along with the major histocompatibility complex (MHC), on its cell surface to cells of the adaptive immune system in a process termed antigen presentation (Mills, 1996). This indicates to cells of the adaptive immune system that a disease-causing agent is present. Innate cells that perform this function are known as antigen-presenting cells (APCs; Tsai and Wu, 2015). Macrophages and DCs are common APCs (Tsai and Wu, 2015). This display and presentation of antigen to cells of the adaptive immune system, combined with the cytokines they release in response to PRR engagement, work to ultimately activate and recruit B and T cells that recognize specific antigenic pieces and participate in the adaptive response. This is how the innate and adaptive immune systems and responses are connected. DCs are considered the principal link between the innate and adaptive immune systems as these cells are classed as professional APCs (Medzhitov, 2001; Janeway and Medzhitov, 2002; Tsai and Wu, 2015). Immature DCs patrol the system and, upon engulfment of a pathogen, the antigen is processed for presentation (Medzhitov, 2001). Activated DCs migrate to lymph nodes and undergo maturation, shutting off their pathogen collection properties and presenting antigen in complex with MHC and a range of other surface molecules to prime and activate naive T cells and mount the adaptive immune response (Medzhitov, 2001; Janeway and Medzhitov, 2002; Pulendran and Ahmed, 2006; Tsai and Wu, 2015). As well as their watchman function with PRRs, they can also sense pathogens indirectly via inflammatory mediators produced by various cells, including macrophages, NK cells and endothelial cells (Pulendran and Ahmed, 2006).

1.5.3 The Adaptive Immune System

Microorganisms that circumvent or overcome the innate immune response are met by the adaptive immune response, which is initiated by presentation of an antigen epitope by APCs to lymphoid B and T cells. In contrast to the innate immune system, the adaptive immune system is highly specific. It works in tandem with, and is directed by, the innate immune system but reacts with a much more delayed response to invading pathogens because it relies on specific immunity (Medzhitov, 2001). However, once activated, it can elicit a very direct and effective response that often results in an infection being cleared.

The major functions of the adaptive immune system include the recognition of specific 'non-self'-antigens in the presence of 'self'-antigens during the process of antigen presentation, the generation of responses that are adapted to maximally eliminate specific pathogens or pathogen-infected cells and the development of immunological memory in which each pathogen is 'remembered' by a signature antibody (Janeway and Medzhitov, 2002; Tsai and Wu, 2015). Immunological memory is provided by cells of the adaptive immune system that are capable of becoming 'memory cells' (Krammer *et al*., 2007). When an infection is removed, memory cells persist and are maintained in a dormant but primed state, ready to elicit a specific immune response at a much more rapid rate and ward off subsequent attacks if the same type of pathogen is encountered a second time, as the cells learn to recognize distinct invaders and their products (Pearce *et al*., 2009). This specific type of immunity is acquired over time. With each successive exposure to a particular microbe, their defensive capabilities and the magnitude of their defensive response increase (Janeway and Medzhitov, 2002). These mature lymphoid cells may live for several years and build up an antigen library, providing the body with an excellent defence system. Through memory cells and antibody production, immunological memory allows for a much faster and more vigorous response to reinfection by a known antigen.

Various cells, tissues and organs are part of the adaptive immune system. It includes the lymphatic recirculation system, the thymus, central and peripheral lymphoid organs such as the spleen, interactions with circulatory, nervous and endocrine systems, T and B cells and their products. The lymphatic system is the body's drainage system. It screens the tissues of the body for foreign antigens and is composed of lymphatic vessels and lymphatic cells. Lymphatic vessels form a one-way system that conducts lymph from local tissues and returns it to the circulatory system. Lymph is a liquid with similar composition to blood plasma that arises from fluid leaked from blood vessels into surrounding tissues. Lymph nodes contain leukocyte collections that recognize and attack foreign antigens present in the lymph. They are concentrated in the cervical, inguinal, axillary and abdominal regions. They receive lymph from afferent lymphatic vessels and drain lymph into efferent lymphatic vessels. The tonsils and mucosa-associated lymphoid tissue (MALT) physically trap foreign particles and microbes. MALT includes the appendix, lymphoid tissue of the respiratory tract and Peyer's patches in the wall of the small intestine (Broere *et al*., 2011).

When the adaptive immune response is initiated, a humoral and a cell-mediated response take place, usually in parallel. The humoral response is carried out by B cells, while T cells orchestrate the cell-mediated response. B cells differentiate into antibody-producing plasma cells (mature B cells actively fighting exogenous antigen), their major function being to produce and secrete antibodies (also called immunoglobulins; Ig) and display clonally diverse cell surface Ig receptors, providing humoral immunity (Pulendran and Ahmed, 2006). This process is, in many circumstances, aided by a specific subset of cluster of differentiation co-receptor 4 $(CD4)^+$ T cells known as T follicular helper cells, underlining the complexity and multicellular nature of adaptive immunity.

1.5.3.1 T Cell Development in the Thymus

The thymus is a primary lymphoid organ of crucial importance to the immune system as it is the site of T cell growth, maturation and immunological self-tolerance (Kelly and Porter, 2011). Its sole function is to provide an appropriate milieu within which T lymphocytes, the key players of cell-mediated immunity, can develop, proliferate and mature (Kelly *et al*., 2007). Lymphoid progenitor cells derived from haematopoietic stem cells in the bone marrow migrate through blood vessels to the thymus where they mature into thymocytes (Schwarz and Bhandoola, 2006). The most immature of thymocytes that have just entered the thymus are easily identified as they are double-negative, *i.e.* they express neither CD4 or CD8 (Fox *et al*., 2005), and account for up to 5 % of the cells present in the thymus (Lagresle *et al*., 2002; Kelly and Porter, 2011). Follicles of the thymus consist of two distinct compartments: the outer cortex and the inner medulla. Both compartments contribute a specific function to the T cell education process. Most of the cortical lymphocytes are immature and unable to carry out immune functions. Mature immunocompetent cells are found in the medulla in greater numbers. Thus, the thymus contains thymocytes that are at different stages of maturation (Kelly and Porter, 2011).

The cortex is the site of the earliest events in thymocyte development and maturation, where T cell receptor (TCR) gene rearrangement, antigen recognition (peptide:MHC complexes), positive selection and the transition from double-negative to double-positive cells take place. Most T cells express TCRs containing two chains: an α chain and a β chain. Lymphocyte progenitor cells enter the thymus expressing a pre-TCRα receptor on their surface and no β chain. The β chain undergoes genetic rearrangement during thymocyte maturation in the cortex (Lagresle *et al*., 2002; Nikolich-Žugich *et al*., 2004). After the unique β chain is transported to the surface, the pre-TCRα chain is cleaved,

leading to expression of both chains and the full TCR. Following this β chain checkpoint, the cells begin to express both CD4 and CD8 on their surface, denoting them double-positive ($CD4^+CD8^+$; Lagresle *et al*., 2002; Kelly *et al*., 2007). $CD4^+CD8^+$ cells account for up to 85 % of cells in the thymus (Kelly and Porter, 2011). The functionality of the TCR to interact with peptide:MHC complexes is then determined through positive selection. The β chain of the TCR must rearrange to form a unique receptor that maintains a level of specificity but retains enough continuity to remain a functional receptor. Only thymocytes that bind the antigen:MHC complex with adequate affinity will survive. Developing thymocytes that do not bind with adequate affinity cannot serve useful functions in the body. Signals that are marked by weak affinity result in apoptosis of the cell (Hettmann *et al*., 1999), ensuring that the remaining TCRs are functional.

The random nature of the genetic rearrangement of the TCR results in a requirement of central tolerance mechanisms to remove or inactivate cells that bear a TCR with the ability to recognise and bind strongly to self-peptides. As the migratory route of the thymocytes moves across the cortico-medullary junction towards the thymic medulla, the $CD4^+CD8^+$ thymocytes are presented with self-antigen complexed with MHC molecules on the surface of cortical epithelial cells (Hettmann *et al*., 1999) and undergo negative selection. Negative selection is crucial for rendering self-tolerance amongst T cells in the immune system and preventing autoimmunity. Cells recognising self-antigen with high avidity are eliminated, while those whose TCRs bind with low avidity to self-peptide:MHC are stimulated to survive (Hettmann *et al*., 1999). This results in attrition of up to 95 % of these cells through apoptosis (Hettmann *et al*., 1999; Kelly and Porter, 2011). The remaining 5 % of selected $CD4^+CD8^+$ cells generate either naive CD4 single-positive ($CD4^+CD8^-$) or naive CD8 single-positive ($CD4^-CD8^+$) cells and proceed to the medulla of the thymus (Kelly and Porter, 2011). A thymocyte's fate of whether to become a $CD4^+$ or $CD8^+$ T cell is determined during positive selection in the cortex, described previously. $CD4^+CD8^+$ cells that are positively selected on MHC class II molecules will become $CD4^+$ T cells and cells positively selected on MHC class I molecules will mature into $CD8^+$ T cells (Ellmeier *et al*., 1997). $CD4^+$ T cells generated in the thymus can subsequently only recognize and bind antigen in complex with MHC class II molecules, while $CD8^+$ T cells can only recognize and bind antigen in complex with MHC class I molecules.

The medulla is the location of the latter events of T cell development and maturation. Thymocytes that reach the medulla have already successfully undergone TCR gene

rearrangement, positive selection and a limited degree of negative selection. The medulla is specialized to allow thymocytes to undergo additional rounds of negative selection to remove autoreactive T cells from the mature repertoire. This ensures the almost complete depletion of autoreactive T cells and that mature T cells are self:MHC restricted. In the medulla, the lymphocytes are densely surrounded by APCs, such as macrophages and DCs (Page *et al*., 1996), and medullary thymic epithelial cells, all of which display self-antigen in complex with MHC molecules. As they signal to the incoming T cells, signals that are too strong are rendered self-reactive and those T cells are triggered to undergo apoptosis. Therefore, they are depleted from the peripheral T cell population, a crucial role of our immune system in generating tolerance and preventing autoimmunity. As can be seen, negative selection is an important component of immunological tolerance and serves to prevent the formation of self-reactive T cells that are capable of inducing autoimmune diseases in the host. In this respect, apoptosis plays a critical role in the successful selection of the thymocyte pool by deleting cells expressing an unproductive TCR or exhibiting hyper-responsiveness upon encountering self-peptide:MHC complexes (Zacharchuk *et al*., 1991; Page *et al*., 1996).

Following this rigorous selection and maturation process in the thymus, the remaining T cell population can exit the thymus, circulate in the lymph and blood stream and migrate to peripheral secondary lymphoid organs, such as the spleen and lymph nodes, as mature, immunocompetent T cells (Krammer *et al*., 2007; Kelly and Porter, 2011). T cell thymic development results in a potential repertoire of approximately 10^{13} diverse, naive αβ T cells (Nikolich-Žugich *et al*., 2004). Given that the thymus is the primary site of T cell maturation in the body and that maturation of T cells is a tightly regulated process, errors in the process of selecting functional T cells can be detrimental for an individual, leading to a variety of autoimmune diseases.

1.5.3.2 The Spleen

The spleen is a peripheral lymphoid organ similar in structure and function to the lymph nodes (Mebius and Kraal, 2005). It is comparable to a large lymph node that filters the blood and removes and recycles antibody-coated erythrocytes, bacteria, viruses, toxins and other foreign matter from the blood and lymph (Mebius and Kraal, 2005). The spleen stores almost half of the body's monocytes which, upon activation, migrate to target tissues and develop into DCs and macrophages (Pulendran and Ahmed, 2006). $CD4^+$ T cells account for approximately 20 – 25 % of cells present in the spleen, while $CD8^+$ T cells

account for approximately 10 % (Kelly and Porter, 2011). The amount of $CD4^+CD8^+$ T cells is negligible (Kelly and Porter, 2011). The remainder of cells in the spleen is composed mainly of reticulocytes and B cells (Kelly and Porter, 2011).

1.5.4 Peripheral T Cells

T cells play a critical role in the adaptive immune response to pathogens and microorganisms by lodging in peripheral secondary lymphoid tissues, awaiting activation through their TCR by APCs bearing pathogen-derived peptide antigens. APCs that have detected pathogens will migrate towards the lymph nodes to begin an adaptive response. The ability of T cells to recognize pathogen-derived fragments of proteins (foreign antigens) is mediated by the TCR. Each TCR displayed on T cells is unique and responds specifically to a limited set of peptide:MHC combinations (Broere *et al*., 2011), which accounts for the variation and specificity seen in our adaptive immune system. The antigen receptor complex expressed by T cells is composed of the TCR and CD3. Signalling by the TCR:CD3 complex is initiated by the recognition of peptide antigen in the context of MHC molecules, as well as stimulation from co-stimulatory molecules expressed on APCs (Tsai and Wu, 2015). An effective immune response by T cells is then facilitated by clonal expansion and differentiation of antigen-specific T cells into effector subsets (Pulendran and Ahmed, 2006) that are licensed to migrate into inflamed target tissues where they can launch a powerful and highly specific assault on the pathogen (Figure 1.13). Hence, T cell activation and migration is crucial for immunology.

1.5.4.1 $CD8^+$ T Cells

The roles of $CD4^+$ and $CD8^+$ T cells are quite different. $CD8^+$ T cells are classed as cytotoxic T lymphocytes (CTLs). CTLs, as the name suggests, are cytotoxic and are armed with a variety of cytolytic proteins, such as perforin and granzyme, to kill pathogen-infected cells by inducing apoptosis (Figure 1.13; Gregori *et al*., 2012). They are responsible for directly killing transformed cells or cells infected with viruses or other intracellular pathogens. Intracellular microbes, such as viruses and some specialised bacteria, can survive, proliferate and pose reservoirs of infection inside phagocytes and other host cells where they are protected from the humoral immunity mediated by B cells. CTL-mediated immunity promotes the destruction of such infected cells and the microbes residing in them. $CD8^+$ T cells express TCRs that can recognize a specific antigenic peptide bound to MHC class I molecules, which are present on all nucleated cells.

1.5.4.2 $CD4^+$ T Cells

T cells expressing CD4 are classed as T 'helper' (T_H) cells. $CD4^+$ T_H cells require antigen presentation in association with MHC class II molecules. T_H cells have a central function in the generation, maintenance and regulation of both the humoral and cellular immune response through their actions on cells of both the innate and adaptive immune systems and by guiding and controlling the immune response. They play roles in promoting the production of antibodies by B cells, stimulating macrophages to develop enhanced microbe-killing activity, recruiting neutrophils, eosinophils and basophils to sites of infection and inflammation and regulating the activities of B cells and CTLs overall. They can also 'license' DCs to express molecules that influence T cell differentiation and effectively activate CTLs by upregulating CD40 ligand (CD40L) and ligating CD40 on the DC surface (Pulendran and Ahmed, 2006; Boyman and Sprent, 2012). Many of these effects are mediated by the production of cytokines and chemokines (Figure 1.13).

In contrast to CTLs, there are a number of $CD4^+$ T cell subsets, each of which displays a unique function. The type of cell an activated $CD4^+$ T cell becomes is heavily influenced by the cytokine microenvironment at the time of activation (Figure 1.14; Park *et al*., 2005; Tsai and Wu, 2015). The signalling molecules and cytokine secretion profiles that are released by APCs are mainly responsible for directing the differentiation of T cells (Medzhitov, 2001) as they induce different nuclear factors that drive the differentiation of a specific T cell subset. Thus, these cytokine profiles are crucial for generating an adaptive immune response catered specifically towards the pathogen. Activation of $CD4^+$ T cells requires union of the TCR and co-stimulatory molecules, such as CD4, CD3 and CD28, on the T cell with MHC class II, antigenic peptide and complementary co-stimulatory molecules, such as CD80 and CD86, on the APC (Medzhitov, 2001; Janeway and Medzhitov, 2002; Pulendran and Ahmed, 2006). The T cell requires these signals simultaneously, otherwise, the T cell may be rendered anergic (Page *et al*., 1996). Once activated, these signals, in conjunction with the cytokine microenvironment, initiate a series of signalling cascades responsible for activating the transcription factors that promote T cell differentiation, proliferation and cytokine production, leading to a process of clonal expansion of the appropriate cellular profile needed to combat the infection (Nikolich-Žugich *et al*., 2004; Pulendran and Ahmed, 2006).

Secretion of cytokines is one of the hallmarks of T cell activation. Interleukin-2 (IL-2) is one of the first adaptive cytokines to be produced and secreted from all activated $CD4^+$ T cells (and to a lesser extent by $CD8^+$ T cells) in response to appropriate co-stimulation through the TCR and CD28 co-receptor by an APC displaying an antigen:MHC class II complex on its surface (Crispin and Tsokos, 2009; Boyman and Sprent, 2012; Liao *et al*., 2013). It functions by modulating the proliferation of T cells and B cells (Boyman and Sprent, 2012). The IL-2:IL-2 receptor (IL-2R) interaction stimulates T cell growth, development, proliferation and survival (Boyman and Sprent, 2012; Liao *et al*., 2013). T cell activation also results in the modulation of cell surface molecules. Prolonged T cell activation leads to downregulation of the TCR:CD3 complex, while the surface expression of other receptors, such as the CD44 adhesion receptor, is upregulated.

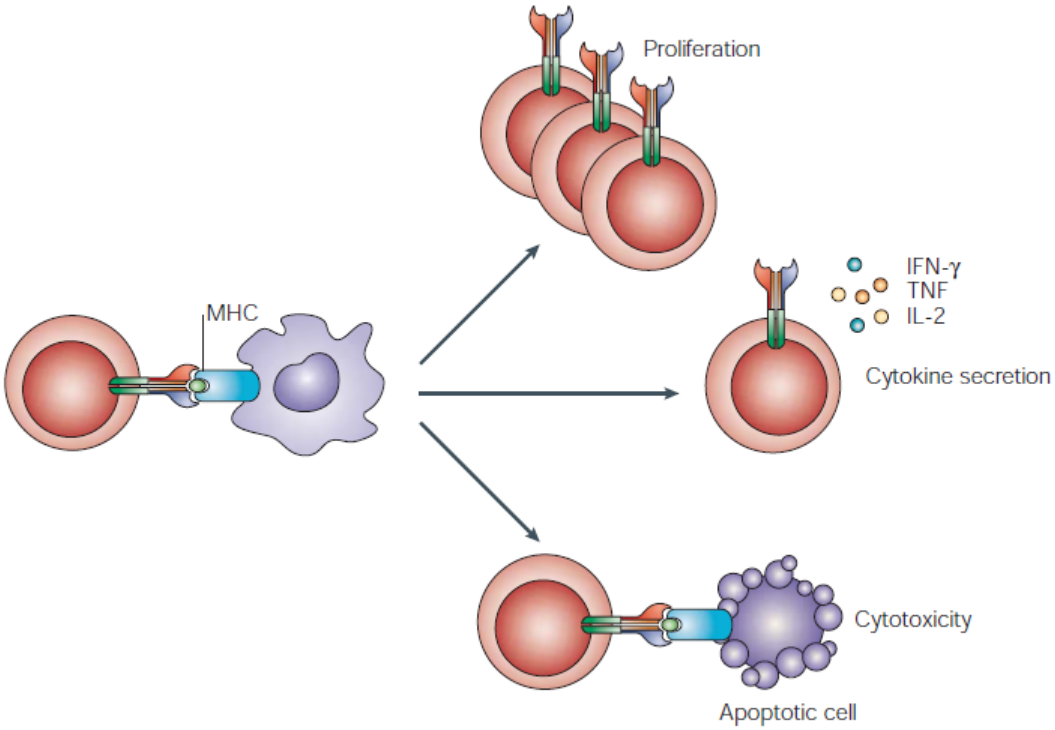

Figure 1.13: Functional diversity of antigen-specific T cells

Following antigen exposure, activated T cells have one or more distinct effector functions: proliferation/clonal expansion, cytokine secretion, which is usually mediated by activated $CD4^+$ T cells, and cytolysis, which is mediated by $CD8^+$ T cells, as well as a differential propensity for migration and homing. Taken from Nikolich-Žugich *et al*. (2004).

1.5.4.2.1 T_H1 and T_H2 Cells

The cytokine secretion profiles of APCs induce different nuclear factors that drive the differentiation of a specific T cell subset. IL-12-promoted and signal transducer and activator of transcription 4 (STAT4)-mediated induction of T-box transcription factor TBX21 (T-bet) generates a T_H1 profile and increases the production and release of IFN-γ by T_H1 cells (Figure 1.14; Pulendran and Ahmed, 2006; Boyman and Sprent, 2012; Liao *et al*., 2013). IFN-γ activates innate and adaptive effector cells, generating an immune response aimed at the cell-mediated defence against and clearance of intracellular pathogens, particularly viruses but also some bacteria (Ivanov *et al*., 2006; Liao *et al*., 2013). T_H1 cells activate and assist CTLs (Pulendran and Ahmed, 2006) through the production of IL-2 (Boyman and Sprent, 2012). GATA-binding protein 3 (GATA-3), driven by IL-4 signalling, generates a T_H2 profile (Figure 1.14; Boyman and Sprent, 2012; Liao *et al*., 2013). Activation of GATA-3 stimulates the production of cytokines such as IL-4 (in a positive feedback loop), IL-5 and IL-13 (Boyman and Sprent, 2012), inducing a response aimed at killing large extracellular pathogens, such as parasites and helminths, by T_H2 cells (Ivanov *et al*., 2006; Liao *et al*., 2013).

1.5.4.2.2 T_H17 Cells

STAT3 is predominantly activated by the presence of cytokines IL-1, IL-21, IL-23, transforming growth factor-β (TGF-β) and, most importantly, the major pro-inflammatory cytokine, IL-6, at the time of cell activation and begins differentiation towards a T_H17 profile (Figure 1.14) by driving the expression of the orphan nuclear receptor 'retinoic acid receptor-related orphan receptor γ t' (RORγt; Ivanov *et al*., 2006; Boyman and Sprent, 2012; Liao *et al*., 2013; Kuhn *et al*., 2016). TGF-β signalling promotes T_H17 cell development by inhibiting T-bet and GATA-3 (Park *et al*., 2005), the drivers of T_H1 and T_H2 fates, respectively. T_H17 cells are so-called because of their predominant secretion of IL-17A, the trademark of their cytokine production (Boyman and Sprent, 2012). As well as IL-17A, T_H17 cells produce IL-6, IL-17F, IL-22 and tumour necrosis factor-α (TNF-α; Ivanov *et al*., 2006; Boyman and Sprent, 2012; Liao *et al*., 2013; Tsai and Wu, 2015). T_H17 cells are extremely pro-inflammatory. The main function of T_H17 cells seems to be the promotion of neutrophil recruitment to sites of infection (Ivanov *et al*., 2006; Lee *et al*., 2009; Tsai and Wu, 2015). T_H17 cells also have a huge antimicrobial immune function responsible for dealing with certain bacterial, fungal and intercellular pathogens (Liao *et al*., 2013; Tsai and Wu, 2015). The highly inflammatory nature of T_H17 cells manifests in

them being a main contributor to the pathogenesis of autoimmunity (Ivanov *et al*., 2006; Liao *et al*., 2013; Tsai and Wu, 2015).

1.5.4.2.3 Regulatory T Cells

Naturally occurring regulatory T cells (nT_{reg}) develop in the thymus through contact with self-peptide:MHC class II complexes and express the signature transcription factor forkhead box P3 (FoxP3; Boyman and Sprent, 2012; Gregori *et al*., 2012; Liao *et al*., 2013). In addition, inducible regulatory T cells (iT_{reg}) can be generated from conventional $CD4^+FoxP3^-$ T cells following stimulation by antigens in peripheral lymphoid organs or during culture with anti-CD3 and TGF-β *in vitro* (Boyman and Sprent, 2012; Liao *et al*., 2013; Newton *et al*., 2016). As mentioned previously, TGF-β signalling can promote T_H17 cell development (Park *et al*., 2005). However, TGF-β can also lead to regulatory T cell (T_{reg}) differentiation (Figure 1.14; Ivanov *et al*., 2006). IL-6 blocks TGF-β-induced T_{reg} differentiation and polarizes $CD4^+$ T cells in the presence of low concentrations of TGF-β towards a T_H17 cell type, while high concentrations of TGF-β favour T_{reg} cell differentiation (Kuhn *et al*., 2016). Thus, TGF-β regulates both T_{reg} and T_H17 cell differentiation. IL-2 also plays a prominent role in the generation of T_{reg} cells as it is crucial for T_{reg} cell maintenance and homeostasis and enhances FoxP3 expression (Liao *et al*., 2013). Conditions in which IL-2 or its receptor subunits are absent lack T_{reg} cells (Crispin and Tsokos, 2009) and display a lack of peripheral immune tolerance mediated by T_{reg} cells, resulting in systemic autoimmunity (Boyman and Sprent, 2012). Additionally, where IL-2 deficiency is not absolute, T_{reg} cell function is still abnormal (Crispin and Tsokos, 2009). Interestingly, as well as being characterized by the expression of the transcription factor FoxP3, T_{reg} cells are characterized by their failure to produce significant amounts of IL-2 upon TCR-mediated stimulation (Crispin and Tsokos, 2009) and rely on the production of IL-2 by other cells (Boyman and Sprent, 2012). T_{reg} cells predominantly secrete TGF-β, IL-35 and IL-10 (Gregori *et al*., 2012; Loftus and Finlay, 2016), which can promote their own proliferation and simultaneously inhibit T_H cell activation. This acts in a feed forward loop to promote T_{reg} differentiation and expansion. T_{reg} cells are a specialized subpopulation of $CD4^+$ T cells that act to suppress T_H cells, CTLs and activation of the immune system, thereby maintaining immune system homeostasis (Pulendran and Ahmed, 2006; Boyman and Sprent, 2012; Liao *et al*., 2013). They function in contrast to the other subsets, modulating inflammation and acting as key players in sustaining self-tolerance. This helps to prevent excessive tissue damage from too

much inflammation and autoimmune responses to self-antigen, as supported by the occurrence of autoimmunity in T_{reg} deficiency (Gregori *et al*., 2012; Liao *et al*., 2013).

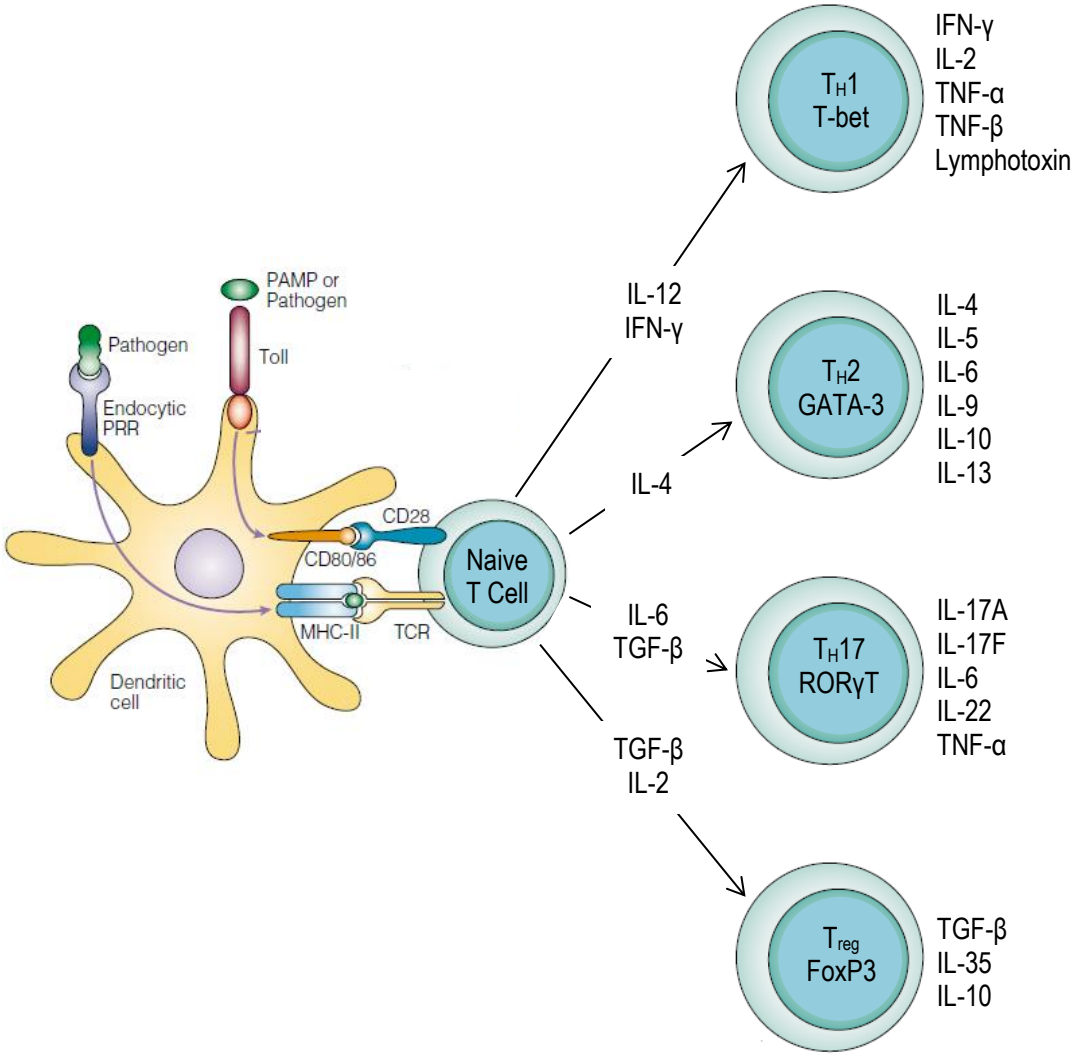

Figure 1.14: T cell differentiation following activation by an APC

Activation by an APC, in combination with the cytokine microenvironment, causes T cells to differentiate and polarize towards a particular T cell subset. Adapted from Medzhitov (2001).

1.5.5 Immune Cell Metabolism

In the past, cellular metabolism was considered a basic process required for the supply of energy to a cell. However, strong evidence has emerged in recent years that portrays a fundamental role of metabolic processes in dictating the immune response. Immune cells adopt distinct metabolic configurations that allow them to balance their requirements for energy, molecular biosynthesis and/or longevity (Loftus and Finlay, 2016). Quiescent immune cells display low rates of glucose uptake and metabolize it efficiently using OxPhos to meet their energy demands (Pearce and Pearce, 2013). When quiescent immune cells are activated to become effector cells, they switch from this relatively quiescent state to a highly active state. Effector cells require a demanding expenditure of energy as they undergo rapid clonal expansion, differentiation and initiate migratory functions (Pearce and Pearce, 2013). To compensate, they undergo a significant metabolic switch. The switch involves the transition from predominantly using OxPhos to a Warburg-like metabolism that utilises glycolysis as the primary pathway of energy generation, even though sufficient levels of O_2 are often present. Pro-inflammatory immune cells and transformed cells are known to often engage in this form of glucose metabolism termed aerobic glycolysis.

While at first glance, this may seem like a very inefficient metabolic program producing significantly less ATP than OxPhos, aerobic glycolysis is the most beneficial metabolic program for proliferating cells. As the biosynthetic demands of pro-inflammatory immune cells are often high due to their requirement for increased clonal expansion and effector molecule production, glycolysis importantly provides intermediates and important sources of carbon for biosynthetic processes, facilitating increased cell growth, the production of effector molecules and increased rates of proliferation (Loftus and Finlay, 2016). For example, glucose-6-phosphate and fructose-6-phosphate, two intermediates from the glycolytic pathway (see Figure 1.3), can be shunted into the pentose phosphate pathway to make ribose-5-phosphate, the backbone for nucleotide synthesis; dihydroxyacetone phosphate can be converted to glycerol for lipid synthesis to build membranes and 3-phosphoglycerate can be converted to the amino acid, serine. Aerobic glycolysis supports efficient biosynthesis, which is presumably why it is the characteristic metabolic profile of many effector immune cells. In support of this, pro-inflammatory immune cells have the ability to dramatically increase their transcription and expression of GLUTs, especially GLUT1, and key rate-limiting glycolytic enzymes, resulting in a consequential increase in glucose uptake and glycolytic flux, thereby producing high levels of ATP (Fox *et al*., 2005;

Jacobs *et al*., 2008; Marko *et al*., 2010; Loftus and Finlay, 2016). Additionally, not only does aerobic glycolysis provide the building blocks for biosynthetic processes, this metabolic profile also prepares an immune cell for entering metabolically restrictive microenvironments, such as hypoxic tissue, where OxPhos may not be possible (Loftus and Finlay, 2016). The pyruvate generated from increased glycolysis in effector immune cells is primarily metabolized to lactate (Chang *et al*., 2013).

In addition to the Warburg effect, proliferating cells also display enhanced glutaminolysis (Vozza *et al*., 2014). The rapid synthesis of macromolecules, as mentioned above, requires a supply of nucleotides, proteins and lipids. An increased use of glutamine is required for the success of these synthetic activities as it generates α-ketoglutarate, replenishing the pool of precursor molecules that are generated in the TCA cycle (Vozza *et al*., 2014), such as citrate which can be exported to the cytosol and used for FA synthesis. Additionally, enhanced glutaminolysis can support immune cell metabolism in restrictive microenvironments where glucose availability is limiting (Loftus and Finlay, 2016).

1.5.5.1 $CD4^+$ T Cell Metabolism

Cellular metabolism has been shown to influence the differentiation of $CD4^+$ T cells. While naive $CD4^+$ T cells are known to exist in a relatively quiescent state metabolizing low levels of glucose, FAs and amino acids using OxPhos (Fox *et al*., 2005), effector T cells, such as T_H17 cells, undergo the metabolic switch described previously, transitioning to Warburg-like aerobic glycolysis as the primary pathway of energy generation (Figure 1.15; Shi *et al*., 2011), although there may also be an increase in the global rate of OxPhos (Chang *et al*., 2013; Loftus and Finlay, 2016). This glycolytic reprogramming is mediated by a number of transcription factors, including hypoxia-inducible factor 1α (HIF1α) and cellular myelocytomatosis oncogene (c-Myc; Fox *et al*., 2005; Loftus and Finlay, 2016). Following TCR ligation and subsequent cell activation, T cells dramatically increase their rates of glucose uptake and glycolysis, producing large amounts of lactate (Marko *et al*., 2010; Wang *et al*., 2011; Chang *et al*., 2013). The effector functions of $CD4^+$ T cells rely on their ability to increase the rate of glycolysis upon activation (Chang *et al*., 2013). Indeed, inhibiting flux through the glycolytic pathway by culturing in galactose or 2-deoxy-D-glucose, a non-metabolizable glucose analogue, or by HIF1α knockdown blocks $CD4^+$ T cell proliferation (Fox *et al*., 2005), IFN-γ production (Chang *et al*., 2013) and the development of T_H17 cells but promotes the generation of T_{reg} cells (Shi *et al*., 2011). Increasing glucose uptake in TCR-stimulated $CD4^+$ T cells through transgenic expression

of GLUT1 is sufficient to promote increased numbers of IFN-γ-producing effector T cells (Michalek *et al*., 2011). It is clear that this metabolic switch, which favours efficient biosynthesis over efficient ATP production, is important to facilitate the biosynthetic demands of effector T cell subsets, thereby promoting their clonal expansion and pro-inflammatory molecule production. In addition to glucose, glutamine metabolism through glutaminolysis is also essential during T cell activation and effector T cell differentiation can be impaired if the supply of glutamine is limiting (Loftus and Finlay, 2016).

In contrast to effector T cells, T_{reg} cells rely predominantly on FAO as their primary form of energy production (Figure 1.16; Michalek *et al*., 2011). Activation of the 5' AMP-activated protein kinase (AMPK) pathway and promoting FAO promotes an increase in T_{reg} cell generation (Michalek *et al*., 2011). Treatment with rapamycin *in vivo*, an inhibitor of mammalian target of rapamycin (mTOR) which is involved in regulating glycolysis, results in increased numbers of $CD4^+CD25^+$ T_{reg} cells (Fox *et al*., 2005). Owing to their substantial dependence on FAO and use of the ETC, T_{reg} cells generate increased amounts of ROS but seem to be resistant to ROS-mediated damage and may be armed with antioxidant molecules to maintain their integrity (Newton *et al*., 2016). Undoubtedly, the metabolic profile of T cells, and indeed all immune cells, is crucial to appropriate cell function. It should be noted, however, that, more recently, doubt has been cast over the requirement of FAO for the development of T_{reg} cells (Raud *et al*., 2018).

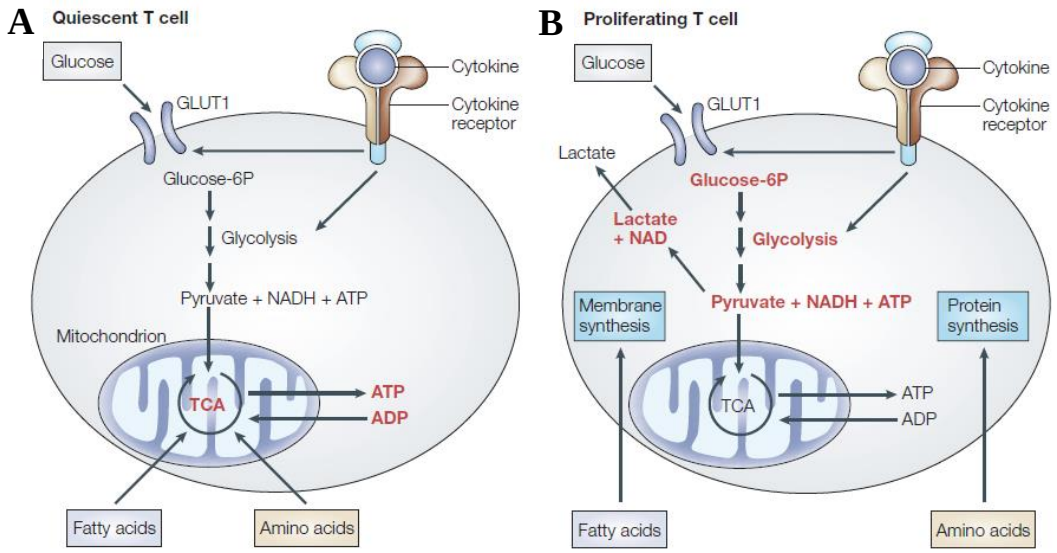

Figure 1.15: The metabolic switch of naive and proliferating T cells

(A) In quiescent T cells, most ATP is generated in the mitochondria by the conversion of pyruvate to acetyl CoA and through the use of acetyl CoA in the TCA cycle (red), followed by OxPhos. Nutrients such as FAs and amino acids can also be degraded to pyruvate, acetyl CoA or other TCA cycle intermediates to maintain ATP production. (B) Following stimulation of T cells with mitogen, the binding of growth factors such as IL-2 or the ligation of co-stimulatory molecules, such as CD28, induces a substantial increase in the glycolytic rate. NAD^+ is a required electron acceptor in this catabolic process and must be regenerated, usually by the conversion of pyruvate to lactate. Most ATP is generated by glucose catabolism (red) in proliferating T cells due to available FAs and amino acids being shunted away from the TCA cycle for membrane and protein synthesis, respectively. Taken from Fox *et al*. (2005). Glucose-6P: glucose-6-phosphate.

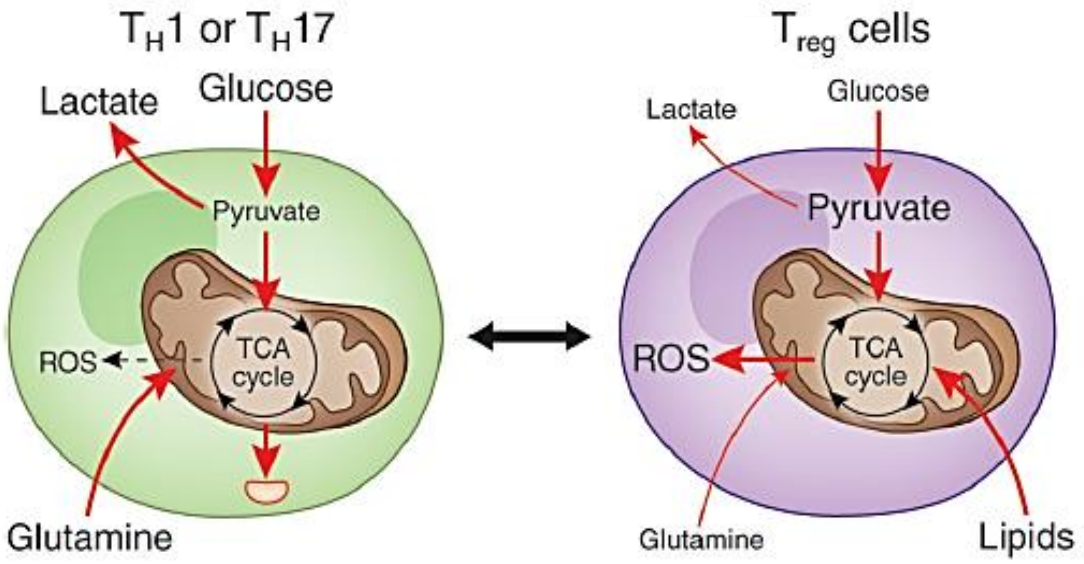

Figure 1.16: Metabolic signatures of T cell subsets

Activated $CD4^+$ T cells that differentiate into an effector T cell lineage (green), such as a T_H1 or T_H17 cell subset, are dependent mainly on carbon substrates, such as glucose and glutamine, and on utilizing glycolysis for their anabolic metabolism. In contrast, T_{reg} cells can rely on exogenous lipids and glucose-derived pyruvate that they can oxidize in the TCA cycle. Owing to their substantial dependence on FAO, T_{reg} cells generate increased amounts of ROS but are resistant to ROS-mediated damage due to antioxidant molecules potentially maintaining their integrity. Adapted from Newton *et al*. (2016).

1.6 The Role of UCPs in the Immune System

In contrast to the majority of organs in the body, the thymus does not grow with age. Rather, it is largest and most active between the late stages of gestation and early adolescence when most of the T cells an individual will carry for their lifetime are formed but diminishes in size and activity with the onset of puberty (Gui *et al*., 2012). During our childhood is when most of our immune education occurs and this timeline is paralleled with T cell 'education' in the thymus. Absence or loss of the thymus from an early age, through surgical removal for example, can result in severe immunodeficiency and a high susceptibility to infection (Gui *et al*., 2012). If the thymus is removed from adult mammals however, few effects are seen. Our laboratory has demonstrated UCP1 expression in murine thymocytes and spleen mitochondria using immunoblotting and confocal microscopy (Adams *et al*., 2008a, 2008b). UCP1 has an interesting time-dependent profile in the murine thymus that seems to be age-related. It appears UCP1 is expressed at a higher level immediately after birth and in the first few weeks of life until it starts to decline rapidly three weeks after birth, which coincides with the weaning process (Adams *et al*., 2010). During this time, most murine T cells that are required throughout life are formed and enter the circulation until needed. There is already circumstantial evidence that UCP1 does not play a thermogenic role in the thymus as thymocytes isolated from cold-acclimated animals have decreased O_2 consumption rates (OCRs; Brennan *et al*., 2006). Following acute starvation, UCP1 protein expression is decreased in BAT (Rothwell *et al*., 1984; Nedergaard *et al*., 2001), presumably to preserve energy stores, whereas its expression in thymocytes and thymus mitochondria is unchanged (Carroll *et al*., 2005). The fact that starvation decreases UCP1 expression in BAT whilst having no effect on UCP1 expression in thymus and that cold-acclimation does not increase UCP1 expression in the thymus implies that UCP1 functions differently in the thymus compared to BAT. Additionally, Clarke *et al*. (2012) observed that the half-life of UCP1 is significantly decreased 10-fold in thymocytes, with a half-life of 3 h compared to a half-life of 30 – 72 h in brown adipocytes, whilst ablation of *Ucp1* has been reported to alter the T cell profile of the thymus and periphery (Adams *et al*., 2010). This implies that there is an alternative function for UCP1 in thymocytes: a potential non-thermogenic, immunological role. However, the function of UCP1 in thymocytes is not presently known, rendering more investigation into its role in these cells necessary.

Krauss *et al*. (2002) reported evidence of UCP2 in murine thymocytes. The function of UCP2 remains under investigation but a substantial amount of research suggests that UCP2

does not play a role in thermogenesis (Matthias *et al*., 2000; Brand *et al*., 2004), while an array of other reports suggest it displays uncoupling activity (Jabůrek *et al*., 1999; Echtay *et al*., 2001). The expression of UCP2 throughout the immune system suggests a putative role for this protein in immunity and/or thermoregulatory responses to infection (fever). UCP2 may play a role in regulating ROS production as it has been reported that UCP2 expressed in macrophages dampens the generation of mitochondrial ROS and, therefore, the activation and function of these cells (Arsenijevic *et al*., 2000). It has also been established that, through an uncoupling mechanism, UCP2 plays an important role in the regulation of glucose-stimulated insulin secretion from pancreatic β cells (Zhang *et al*., 2001; Brand *et al*., 2004; Krauss *et al*., 2005; Brand *et al*., 2010). Additionally, Vozza *et al*. (2014) provided evidence that UCP2 acts as a metabolite transporter that regulates substrate oxidation in mitochondria. They have shown that UCP2 transports the four-carbon metabolites malate, oxaloacetate and aspartate from the MM into the IMS in exchange for P_i and a proton. This export of TCA cycle intermediates depletes the availability of oxaloacetate and limits the oxidation of acetyl CoA-producing substrates, thus lowering the redox pressure on the mitochondrial respiratory chain, the ATP:ADP ratio and ROS production and driving aerobic glycolysis. It also enhances glutaminolysis but prevents the mitochondrial accumulation of four-carbon metabolites derived from glutamine. In support of this finding, *Ucp2* mRNA translation is activated by glutamine (Hurtaud *et al*., 2007). However, its exact role in the immune system and in thymocytes remains to be elucidated.

Similar to UCP2, it is thought that UCP3 does not play a role in thermogenesis as none of the expected phenotypes of cold sensitivity or obesity are observed in *Ucp3*$^{-/-}$ mice (Gong *et al*., 2000; Vidal-Puig *et al*., 2000) and, although an increase in *Ucp3* gene expression has been reported in BAT of *Ucp1*$^{-/-}$ mice, no thermogenic activity has been detected (Matthias *et al*., 2000). Our laboratory has demonstrated UCP3 expression in murine thymocytes, spleen mitochondria and the lymphocyte fraction of the spleen using immunoblotting and confocal microscopy (Carroll and Porter, 2004; Kelly and Porter, 2011). The ablation of *Ucp3* has been reported to influence $CD4^+$ and $CD8^+$ T cell frequencies in the thymus and periphery, such as the spleen, by affecting the apoptotic potential of T cells (Kelly and Porter, 2011). Its role in these cells, however, as well as that of UCP1 and UCP2, has not been thoroughly investigated. Thymocytes are the precursor cells of mature T cells, while the spleen houses a significant proportion of the $CD4^+$ T cell pool following T cell exit from the thymus. Expression of all three UCPs in thymocytes suggests their importance in

thymic function, as well as a potential role in T cell selection, maturation, metabolism and/or function. Thus, we set out to examine the expression of UCPs in mature $CD4^+$ T cells, both naive and polarized subsets, and to investigate the role of UCP3 in $CD4^+$ T cell metabolism and function.

1.7 Project Objective and Aims

The objective of this project was to build upon the aforementioned empirical evidence supplied by our laboratory and others of the existence of UCP1, UCP2 and UCP3 in thymocytes. This will be carried out by investigating the possibility of their presence in mature $CD4^+$ T cells and, if present, deciphering the role of UCPs in these cells.

The aims of this project were to:

1. determine whether the UCPs UCP1, UCP2 and UCP3 are expressed in peripheral $CD4^+$ T cells
2. compare the function of $CD4^+$ T cells from WT versus UCP-deficient mice, under varying conditions
3. compare the metabolism of $CD4^+$ T cells from WT versus UCP-deficient mice, under varying conditions
4. elucidate the role, if any, of UCPs in $CD4^+$ T cell differentiation towards effector subsets

1.8 Project Hypothesis

It is hypothesized that, due to their detected expression in thymocytes, UCP1, UCP2 and UCP3 will be detected in peripheral $CD4^+$ T cells. It is predicted that *Ucp*$^{-/-}$ $CD4^+$ T cells will display an altered metabolism in the form of an increased efficiency in OxPhos, due to the absence of an UCP decreasing the mitochondrial membrane potential and uncoupling ATP synthesis from substrate oxidation. Furthermore, as metabolism is fundamental in the proper functioning of peripheral T cells, a skewed function of *Ucp*$^{-/-}$ T cells may also be observed as a secondary effect of the predicted altered metabolism of these cells.

Chapter 2:

Materials and Methods

Chapter 2

Materials and Methods

2.1 Materials

2.1.1 List of Materials Used and Suppliers

Full supplier names and addresses are given in Appendix A.

Material	Supplier
2-Mercaptoethanol	Sigma-Aldrich
2',7'-dichlorofluorescein diacetate (DCFDA)	Sigma-Aldrich
3,3',5,5'-Tetramethylbenzidine (TMB) Substrate Set	Medical Supply Company Ltd.
5,5'-Dithiobis(2-nitrobenzoic acid) (DTNB)	Sigma-Aldrich
7-Aminoactinomycin D (7-AAD)	Bio-Sciences Ltd.
Absolute Alcohol (Ethanol; EtOH)	TCD Hazardous Materials Facility
Acetic Acid, 100 %	Sigma-Aldrich
Acetyl CoA lithium salt	Sigma-Aldrich
Agarose	Sigma-Aldrich
Alexa Fluor® 647 goat anti-rabbit IgG (H + L)	Bio-Sciences Ltd.
Ammonium persulphate (APS)	Sigma-Aldrich
Annexin V Apoptosis Detection Kit	
allophycocyanin (*APC*)	Bio-Sciences Ltd.
Anti-mouse IgG (H + L), horseradish peroxidase (HRP) conjugate	MyBio Ltd.
Anti-rabbit IgG (H + L), HRP conjugate	MyBio Ltd.
Antimycin A from *Streptomyces* sp.	Sigma-Aldrich
APC anti-mouse CD44	Bio-Sciences Ltd.
APC anti-mouse IFN-γ	Medical Supply Company Ltd.
APC anti-mouse/human FoxP3	Miltenyi Biotec Ltd.
Avidin-HRP	Medical Supply Company Ltd.
BD™ CompBead Anti-Rat and Anti-Hamster Ig κ/ Negative Control Compensation Particles Set	BD Biosciences
Biotin anti-mouse IFN-γ [enzyme-linked	

immunosorbent assay (ELISA) detection]	Medical Supply Company Ltd.
Biotin anti-mouse IL-2 (ELISA detection)	Medical Supply Company Ltd.
Biotin anti-mouse IL-10 (ELISA detection)	Medical Supply Company Ltd.
Biotin anti-mouse IL-17A (ELISA detection)	Medical Supply Company Ltd.
Brefeldin A	Sigma-Aldrich
Bromophenol blue	Sigma-Aldrich
CD4 (L3T4) Microbeads, mouse	Miltenyi Biotec Ltd.
CellTrace™ Violet Cell Proliferation Kit	Bio-Sciences Ltd.
Cholera Toxin (CT) from *Vibrio cholera*	List Biological Laboratories, Inc.
cOmplete™ ULTRA Tablets, Mini, *EASY*pack Protease Inhibitor Cocktail	Sigma-Aldrich
Corning® Cell-Tak™ Cell and Tissue Adhesive	Fisher Scientific Ltd.
D-(+)-Glucose	Sigma-Aldrich
Dimethyl sulfoxide (DMSO)	Sigma-Aldrich
Distilled H_2O (dH_2O), for use with RPMI from Sigma	Bio-Sciences Ltd.
DL-Dithiothreitol (DTT)	Sigma-Aldrich
Dulbecco's Phosphate Buffered Saline (DPBS)	Bio-Sciences Ltd.
eFluor® 660 anti-mouse CD25	Bio-Sciences Ltd.
ELISA Assay Diluent (5X)	Medical Supply Company Ltd.
Ethylenediaminetetraacetic acid (EDTA)	Sigma-Aldrich
FCCP	Sigma-Aldrich
Fluorescein isothiocyanate (FITC) anti-mouse CD62 ligand (CD62L)	Bio-Sciences Ltd.
FITC anti-mouse lymphocyte activation gene 3 (LAG3)	Bio-Sciences Ltd.
Fixation buffer	Medical Supply Company Ltd.
Foetal bovine serum (FBS)	Bio-Sciences Ltd.
FoxP3/Transcription Factor Staining Buffer Set	Bio-Sciences Ltd.
GeneRuler™ DNA Ladder Mix	Fisher Scientific Ltd.
Glycerol	Sigma-Aldrich
Glycine	Sigma-Aldrich
GoTaq® Hot Start Green Master Mix	MyBio Ltd.
High Capacity complimentary DNA (cDNA) Reverse Transcription Kit	Bio-Sciences Ltd.

IL-2 monoclonal antibody (JES6-1A12), functional grade	Bio-Sciences Ltd.
Intracellular Staining Permeabilization Wash Buffer (10X)	Medical Supply Company Ltd.
Ionomycin calcium salt from *Streptomyces conglobatus*	Sigma-Aldrich
ISOLATE II RNA Mini Kit	Medical Supply Company Ltd.
Isopropanol	TCD Hazardous Materials Facility
Keyhole limpet hemocyanin (KLH), *Megathura crenulata*	Merck Millipore
L-Glutamine 200 mM (100X)	Bio-Sciences Ltd.
Leaf™ purified anti-mouse IFN-γ	Medical Supply Company Ltd.
LIVE/DEAD™ Fixable Aqua Dead Cell Stain Kit	Bio-Sciences Ltd.
LS Columns	Miltenyi Biotec Ltd.
Marvel Original Dried Skimmed Milk	Standard supermarket
Methanol	TCD Hazardous Materials Facility
MicroAmp™ Fast Optical 96-Well Reaction Plate with Barcode	Bio-Sciences Ltd.
MicroAmp™ Optical Adhesive Film	Bio-Sciences Ltd.
MidiMACS Starting Kit (LS)	Miltenyi Biotec Ltd.
MitoTracker™ Green FM	Bio-Sciences Ltd.
MitoTracker™ Red CMXRos	Bio-Sciences Ltd.
Mouse monoclonal (9H9AF5) to pyruvate dehydrogenase e1α subunit (PDHe1α)	Abcam plc
Nancy-520	Sigma-Aldrich
Necrostatin-1 (Nec-1)	Sigma-Aldrich
Oligomycin from *Streptomyces diastatochromogenes*	Sigma-Aldrich
Oxaloacetic acid	Sigma-Aldrich
Oxoid™ PBS (Dulbecco A) Tablets	Fisher Scientific Ltd.
Pacific Blue™ anti-mouse CD69	Medical Supply Company Ltd.
PageRuler™ Plus Prestained Protein Ladder	Bio-Sciences Ltd.
R-phycoerythrin (PE) anti-mouse CD8a	BD Biosciences
PE anti-mouse CD25	Bio-Sciences Ltd.

PE anti-mouse FasL (CD178)	Medical Supply Company Ltd.
PE anti-mouse IL-2	Bio-Sciences Ltd.
PE anti-mouse IL-17A	Medical Supply Company Ltd.
PE anti-mouse/rat FoxP3	Bio-Sciences Ltd.
PE-Cyanine (PE-Cy)5 anti-mouse CD8a	Bio-Sciences Ltd.
PE-Cy7 anti-mouse CD4	Medical Supply Company Ltd.
Pen Strep	Bio-Sciences Ltd.
Peridinin chlorophyll protein-Cy™5.5 (PerCP-Cy™5.5) anti-mouse CD69	BD Biosciences
PerCP-eFluor™ 710 anti-mouse Ki-67	Bio-Sciences Ltd.
PerCP-eFluor™ 710 anti-mouse latency-associated peptide (LAP)	Bio-Sciences Ltd.
Phorbal 12-myristate 13-acetate (PMA)	Sigma-Aldrich
PhosSTOP™ *EASY*pack Phosphatase Inhibitor Cocktail Tablets	Sigma-Aldrich
Pierce™ BCA Protein Assay Kit	Bio-Sciences Ltd.
Polyvinylidene difluoride (PVDF) membrane	Sigma-Aldrich
Proteinase K from *Tritirachium album*	Sigma-Aldrich
ProtoGel™	Bio-Sciences Ltd.
Purified anti-mouse CD3epsilon (ε)	Medical Supply Company Ltd.
Purified anti-mouse CD28	Medical Supply Company Ltd.
Purified anti-mouse IFN-γ (ELISA capture)	Medical Supply Company Ltd.
Purified anti-mouse IL-2 (ELISA capture)	Medical Supply Company Ltd.
Purified anti-mouse IL-4	Medical Supply Company Ltd.
Purified anti-mouse IL-10 (ELISA capture)	Medical Supply Company Ltd.
Purified anti-mouse IL-17A (ELISA capture)	Medical Supply Company Ltd.
Rabbit anti-mouse UCP3	Eurogentec
Recombinant human TGF-β1 (rhTGF-β1)	ImmunoTools GmbH
Recombinant mouse IFN-γ (rIFN-γ; ELISA standard)	Medical Supply Company Ltd.
rIL-2 (carrier-free)	Medical Supply Company Ltd.
rIL-2 (ELISA standard)	Medical Supply Company Ltd.
rIL-6 (carrier-free)	Medical Supply Company Ltd.
rIL-10 (ELISA standard)	Medical Supply Company Ltd.
rIL-12 (carrier-free)	Medical Supply Company Ltd.

rIL-17A (ELISA standard)	Medical Supply Company Ltd.
Red Blood Cell (RBC) Lysing Buffer	
Hybri-Max™	Sigma-Aldrich
Roswell Park Memorial Institute (RPMI) 1640	
Medium 1X + GlutaMAX™ Supplement	Bio-Sciences Ltd.
RPMI 1640 medium, with L-glutamine, without	
glucose and sodium bicarbonate	Sigma-Aldrich
Rotenone	Sigma-Aldrich
Seahorse XF24 FluxPak	Agilent Technologies
Sodium chloride (NaCl)	Sigma-Aldrich
Sodium deoxycholate	Sigma-Aldrich
Sodium dodecyl sulphate (SDS)	Sigma-Aldrich
Sodium pyruvate	Sigma-Aldrich
Sulphuric acid solution	VWR
TaqMan® Gene Expression Assays	Bio-Sciences Ltd.
TaqMan® Universal Polymerase Chain Reaction	
(PCR) Master Mix	Bio-Sciences Ltd.
Tetramethylethylenediamine (TEMED)	Sigma-Aldrich
TrackIt™ Cyan/Yellow Loading Buffer	Bio-Sciences Ltd.
Triton™ X-100	Sigma-Aldrich
Trizma® Base	Sigma-Aldrich
Tween® 20	Sigma-Aldrich
UltraComp eBeads™ Compensation Beads	Bio-Sciences Ltd.
UltraPure™ DNase/RNase-Free dH_2O	Bio-Sciences Ltd.
Unmodified DNA oligonucleotides	Eurofins Genomics
Western Chemiluminescent HRP Substrate	Merck Millipore
Z-VAD-FMK (Z-VAD)	Merck Millipore

2.1.2 Reagent Recipes

1X Running Buffer

dH_2O

200 millimolar (mM) glycine

25 mM Tris

0.1 % [weight per unit volume (w/v)] SDS

pH 8.3

Stored at 4 degrees Celsius (°C)

1X TBS-T

dH_2O

20 mM Tris

150 mM NaCl

pH 7.6

0.1 % [volume per unit volume (v/v)] Tween® 20

Stored at 4°C

1X Wet Transfer Buffer

dH_2O

25 mM Tris

195 mM glycine

20 % (v/v) methanol

pH 8.3

Stored at 4°C

4X Sample Buffer

dH_2O

240 mM Tris

40 % (v/v) glycerol

8 % (w/v) SDS

pH 6.8

Stored at room temperature (RT)

Complete RPMI (cRPMI)

RPMI

10 % (w/v) FBS

1 % (w/v) Pen Strep

2 mM L-glutamine

0.0003 % (v/v) 2-mercaptoethanol

Stored at 4°C

DNA Extraction Buffer

Nuclease-free dH_2O

100 mM Tris, pH 8.5

5 mM EDTA

0.2 % (w/v) SDS

200 mM NaCl

500 micrograms (μg).millilitre $(mL)^{-1}$ proteinase K

Stored at -20°C in 1 mL aliquots

MACS Buffer

DPBS

2 % (w/v) FBS

2 mM EDTA

Stored at 4°C

Marvel-TBS-T

TBS-T

5 % (w/v) Marvel

PBS-Tween

dH_2O

Oxoid™ PBS (Dulbecco A) Tablets

0.05 % (v/v) Tween® 20

Stored at RT

Radio Immunoprecipitation Assay (RIPA) Lysis Buffer

dH_2O

150 mM NaCl

1 % (v/v) Triton™ X-100

0.5 % (w/v) Sodium deoxycholate

0.1 % (w/v) SDS

50 mM Tris, pH 8.0

1 mM EDTA

cOmplete™ ULTRA Tablets, Mini, *EASY*pack Protease Inhibitor Cocktail

PhosSTOP™ *EASY*pack Phosphatase Inhibitor Cocktail Tablets

Stored at 4°C

TAE Buffer

dH_2O

40 mM Tris

1 mM EDTA

1 mM acetic acid

Stored at RT

Tris-DTNB

dH_2O

100 mM Tris

1 mM DTNB

Made up fresh on day of experiment and kept at 4°C

Tris-Triton™ X-100

dH_2O

200 mM Tris

0.2 % (v/v) Triton™ X-100

Made up fresh on day of experiment and kept at 4°C

2.2 Methods

2.2.1 Animals

All animals were maintained in compliance with the Health Products Regulatory Authority (HPRA) regulations and with the approval of the University of Dublin's ethical review board. Experiments were performed under license from HPRA and in strict accordance with regulations laid out by Laboratory Animal Science and Training (LAST) – Ireland and the European Union [(Protection of Animals Used for Scientific Purposes) Regulations 2012 (S.I. number 543 of 2012) and Directive 2010/63/EU].

WT and *Ucp* knockout (KO) mice were bred in-house in the Comparative Medicine Unit (CMU), Trinity Biomedical Sciences Institute (TBSI), Trinity College Dublin. *Recombination-activating gene 1* (*Rag1*)$^{-/-}$ mice were bred in the CMU, Trinity Translational Medicine Unit, Trinity Centre for Health Sciences, St. James' Hospital, Dublin. All KO mice were viable and fertile. Mice were housed in individually ventilated cages in a specific pathogen-free facility at RT. A standard 12 h light/dark cycle was in place and animals had access to H_2O and standard laboratory rodent chow *ad libitum*.

WT C57BL/6J mice were used for *Ucp1* and *Ucp2* gene expression experiments. *Ucp3*$^{-/-}$ mice were generated by Vidal-Puig *et al*. in 2000. *Ucp3*$^{-/-}$ mice were originally provided to our laboratory by Prof. Pádraic Fallon (TBSI, Trinity College Dublin), who obtained them from the Jackson Laboratory (JAX®; strain number 005937). *Ucp3*$^{-/-}$ mice were of a mixed genetic background of C57BL/6J and two 129S sublines, 129S4/SvJae and 129S1/SvlmJ. Thus, WT littermates of *Ucp3*$^{-/-}$ mice were used as controls. *Rag1*$^{-/-}$ mice were bred on a C57BL/6J background.

WT and *Ucp* KO mice were confirmed to be homozygous by PCR genotyping of ear punch or tail clip DNA samples (tail clips were taken *post mortem* only). At the time of sacrifice, mice were euthanized by CO_2 asphyxiation followed by cervical dislocation. For all experiments, KO mice and WT controls were age- and sex-matched.

2.2.2 Genotyping

2.2.2.1 Isolation of Genomic DNA

Ear punches and tail clips were stored at -20°C in 1.5 mL tubes until ready to carry out DNA isolation. 1 mL of DNA extraction buffer per DNA sample was thawed at RT. An ear punch or tail clip was placed in the tube containing thawed DNA extraction buffer and incubated overnight in a water bath [Type JB2; Grant Instruments (Cambridge) Ltd., Cambridgeshire, U.K.] at 55°C, until digestion of the tissue sample was complete. The sample was vortexed briefly (Top Mix FB15024; Fisher Scientific, Hampton, NH, U.S.A.) and centrifuged (5417r; Eppendorf, Hamburg, Germany) at 14 000 g-force (*g*) and 4°C for 10 minutes (min). Without disturbing the pellet of undigested hair and debris at the bottom of the tube, 475 microlitres (µL) of the supernatant were transferred to a new, labelled 1.5 mL tube containing 950 µL of ice-cold 100 % EtOH. The sample in EtOH was vortexed briefly and centrifuged as above. The supernatant was removed and the pelleted DNA was resuspended in 30 µL of nuclease-free dH_2O. Any remaining EtOH was evaporated by incubation of the sample on a heating block (SBH130; Stuart®, Staffordshire, U.K.) at 65°C for 15 min with the lid open. DNA samples were stored at -20°C until ready for genotyping.

2.2.2.2 NanoDrop® Quantification of Nucleic Acids

The concentration of isolated RNA or genomic DNA was quantified using a NanoDrop® ND-1000 Spectrophotometer (Thermo Fisher Scientific, Waltham, MA, U.S.A.) and ND-1000 software (version 3.7.1). 2 µL of nuclease-free dH_2O were used to calibrate the spectrophotometer and act as a 'blank' sample. 2 µL of undiluted DNA or RNA samples, which were kept on ice, were loaded onto the spectrophotometer and the absorbance was measured at 260 and 280 nanometres (nm), the absorption maxima for nucleic acids and aromatic groups in proteins, respectively. Absorbance was also measured at 230 nm for RNA samples only. The nucleic acid concentration was calculated using the Beer-Lambert law which relates the amount of light absorbed to the concentration of the absorbing molecule:

$A = \epsilon Cl$, where:

A = absorbance at a particular wavelength (260 nm)

C = concentration of nucleic acid

l = path length of the spectrophotometer cuvette [typically 1 centimetre (cm)]

ϵ = the extinction coefficient

[ϵ for DNA and RNA is 0.02 and 0.025 $(\mu g.mL)^{-1}$ cm^{-1}, respectively]

Concentration values were recorded as well as the A_{260}/A_{280} ratio which is used as a quality control to assess purity. An A_{260}/A_{280} ratio of 1.8 – 2.1 indicates highly purified nucleic acids. Lower values may indicate high protein levels in a preparation. High protein levels, as well as other chemical contaminants, can cause PCR inhibition. The A_{260}/A_{230} ratio was recorded for RNA samples only. This is a ratio of RNA to impurities.

2.2.2.3 PCR for Genotyping of WT and *Ucp* KO Mice

The genotyping protocols from the JAX® mice database for strains B6.129S4-*Ucp2*^{tm1Lowl}/J (strain number 005934) and B6;129S4-*Ucp3*^{tm1Lowl}/J (strain number 005937) were used with some alterations. The GoTaq® Hot Start Green Master Mix was used to carry out PCR. Primers used are detailed in Table 2.1. The PCR reaction mixture was prepared on ice in 0.2 mL 8-tube PCR strips, according to Table 2.2. The volume of each DNA sample required to load 50 nanograms (ng) of DNA was calculated from the concentration of each sample measured using the NanoDrop® ND-1000 Spectrophotometer in Section 2.2.2.2 and added to the tube. The total volume of each reaction was brought to 25 µL using nuclease-free dH_2O and reactions were mixed thoroughly by pipetting. A negative control was created by adding nuclease-free dH_2O in place of the DNA sample. The reactions were gently tapped to mix, placed in a thermal cycler (PTC-200 DNA Engine® Peltier Thermal Cycler; Bio-Rad Laboratories Ltd., Hertfordshire, U.K. or Swift™ MiniPro Thermal Cycler; ESCO® Technologies, Inc., St. Louis, MO, U.S.A.) and the appropriate PCR program was initiated. The programs for PCR are outlined in Table 2.3. Following the PCR reaction, samples were either analysed immediately by agarose gel electrophoresis (Section 2.2.2.4) or stored at -20°C.

Table 2.1: Primers used for genotyping experiments

Primer	Primer Sequence (5' – 3')	Melting Temperature (°C)	Annealing Temperature (°C)
Ucp1 WT Forward	TTTGGTGGGAAAGAAAGCTG	55.3	54
Ucp1 WT Reverse	TAGTGGCCCTAGGGAAAACC	59.4	54
Ucp1 KO Forward	GGGGTAGTATGCAAGAGAGGTG	62.1	58
Ucp1 KO Reverse	CCTACCCGCTTCCATTGCTCA	61.8	58
Ucp2 WT Forward	GCGTTCTGGGTACCATCCTA	59.4	57
Ucp2 WT Reverse	GCTCTGAGCCCTTGGTGTAG	61.4	57
Ucp2 KO Forward	CTTGGGTGGAGAGGCTATTC	59.4	55
Ucp2 KO Reverse	AGGTGAGATGACAGGAGATC	57.3	55
Ucp3 WT	GCACTGCGGCCTGTTTTG	58.2	56
Ucp3 Common	ACCCTCTGTCGCCACCATAGT	61.8	56/57
Ucp3 KO	CCTCCACTCATGATCTATAGATC	58.9	57

Table 2.2: Components of the PCR reaction mixture

Component	Concentration/Amount
GoTaq® Hot Start Green Master Mix	1X
Forward primer	1 µM
Reverse/common primer	1 µM
DNA template	50 ng
Nuclease-free dH_2O	Bring total volume to 25 µL

Table 2.3: Thermal cycler program for *Ucp* genotyping

Step	Temperature (°C)	Time (min)	
1 – Denaturation	94	2	
2 – Denaturation	94	0.5	Repeat for 35 cycles
3 – Annealing	See Table 2.1	1	
4 – Extension	72	1	
5	72	5	
6	4	Hold	

2.2.2.4 Agarose Gel Electrophoresis

Nancy-520 was warmed to RT. For genotyping experiments and reverse transcription (RT)-PCR experiments, 1.5 or 2.5 % (w/v) agarose gels were prepared by boiling 1.5 or 2.5 grams (g), respectively, of agarose in 100 mL of TAE Buffer for 3 min using a microwave, until dissolved. A pre-stained gel was made by adding 10 µL of Nancy-520 to the agarose-TAE solution while it was still liquid but cooling down. The mixture was swirled to ensure an even mixture immediately before pouring into a gel tray containing 20-well combs. The gel was covered with tinfoil to protect from light and left to solidify for approximately 20 min. Once solid, the gel was mounted into an electrophoresis chamber (Gibco-BRL Horizon® 11 – 14 Horizontal Gel Electrophoresis Apparatus; Thermo Fisher Scientific, Waltham, MA, U.S.A.) and covered with TAE buffer. PCR product samples (if frozen) and a GeneRuler™ DNA Ladder Mix were thawed on ice. TrackIt™ Cyan/Yellow Loading Buffer was added to RT-PCR samples (Section 2.2.4) at a 1 in 12 dilution. Genotyping samples did not require a loading buffer as they were prepared using GoTaq® Hot Start Green Master Mix which contains blue and yellow dye. 3 µL of the GeneRuler™ DNA Ladder Mix and 8 µL of samples were loaded onto the gel. The gel was exposed to a voltage for at least 30 min while covered with tinfoil to minimize gel exposure to light. The voltage used and the expected size of the PCR products detected on the gel are indicated in Table 2.4. Directly after the run, Nancy-520-stained DNA bands were made visible with ultraviolet (UV) light using a Kodak® GEL Logic 200 Imaging System (Carestream Health Inc., Rochester, NY, U.S.A.). Gels were photographed and images were obtained using Kodak® ID Image Analysis software (version 3.6; Eastman Kodak Company, Rochester, NY, U.S.A.). Examples of agarose gels for *Ucp1*, *Ucp2* and *Ucp3* genotyping are displayed in Appendix B.

Table 2.4: Voltages used and expected PCR product sizes during agarose gel electrophoresis

Primer	Voltage Used [volts (V)]	PCR Product Size [base pairs (bp)]
Genotyping Experiments		
Ucp1 WT	110	378
Ucp1 KO	110	400
Ucp2 WT	130	156
Ucp2 KO	130	280
Ucp3 WT	90	600
Ucp3 KO	90	300
Quantitative RT-PCR Experiments		
Ucp1	80	73
Ucp2	90	137
Ucp3	80	69
Hypoxanthine phosphoribosyl transferase (Hprt)	80	82

2.2.3 Cell Isolation and Culture

2.2.3.1 Isolation of Thymocytes

Thymocytes were isolated according to the method of Buttgereit and Brand (1995) but with some minor alterations. Briefly, the thymus was removed, trimmed free of connective tissue and BAT and transferred to cold DPBS. Under sterile conditions, the thymus was poured onto a wet nylon mesh cell strainer (70 µm) over a 50 mL tube. It was rinsed once with cold cRPMI and, using the plunger of a 2.5 mL syringe, gently ground and homogenized through the strainer until a fine suspension of thymocytes was obtained. cRPMI was poured three times through the cell strainer to wash any remaining cells into the tube, forming a homogenous cell solution free of clumps. The cell suspension was centrifuged (Sorvall® Legend™ T Benchtop Centrifuge; Thermo Fisher Scientific, Waltham, MA, U.S.A.) at 420 *g* for 5 min at RT and the supernatant was discarded. The pellet was resuspended in 2 mL of warm (37°C) RBC Lysing Buffer Hybri-Max™ and the

tube was placed in a heated water bath at 37°C for 2 min to lyse erythrocytes. After that time, the RBC Lysing Buffer was diluted to a total volume of 15 mL with cRPMI to terminate the lysis process and the tube was centrifuged as before. The supernatant was discarded and the cell pellet was resuspended in 20 mL of cRPMI.

2.2.3.2 Isolation of Lymph Node Cells

Inguinal lymph nodes were removed, trimmed free of connective tissue and transferred to cold DPBS. Under sterile conditions, the lymph nodes were poured onto a wet nylon mesh cell strainer (70 µm) over a 50 mL tube. They were rinsed once with cold cRPMI and, using the plunger of a 2.5 mL syringe, gently ground and homogenized through the strainer until a fine suspension of lymph node cells was obtained. cRPMI was poured three times through the cell strainer to wash any remaining cells into the tube, forming a homogenous cell solution free of clumps. The cell suspension was centrifuged at 420 *g* for 5 min at RT and the supernatant was discarded. The pellet was resuspended in 3 mL of cRPMI.

2.2.3.3 Isolation of Spleen Cells

Spleen cells were isolated according to the method of Mills (1996) but with some minor alterations. Briefly, the spleen was removed from the mouse abdominal cavity, trimmed free of connective tissue and transferred to cold DPBS. Under sterile conditions, the spleen was poured onto a wet nylon mesh cell strainer (70 µm) over a 50 mL tube. It was rinsed once with cold cRPMI and, using the plunger of a 2.5 mL syringe, gently ground and homogenized through the strainer until a fine suspension of spleen cells was obtained. cRPMI was poured three times through the cell strainer to wash any remaining cells into the tube, forming a homogenous cell solution free of clumps. The cell suspension was centrifuged at 420 *g* for 5 min at RT and the supernatant was discarded. The pellet was resuspended in 2 mL of warm (37°C) RBC Lysing Buffer and the tube was placed in a heated water bath at 37°C for 2 min to lyse erythrocytes. After that time, the RBC Lysing Buffer was diluted to a total volume of 15 mL with cRPMI to terminate the lysis process and the tube was centrifuged as above.

2.2.3.4 Isolation of $CD4^+$ T Cells

Following erythrocyte lysis of the splenocyte suspension, the supernatant was discarded and the splenocyte pellet was resuspended in 180 µL of MACS buffer and 20 µL of CD4 Microbeads. Cells were incubated at 4°C in the dark for 15 min before the solution was diluted to a total volume of 15 mL with MACS buffer and the tube centrifuged at 420 *g* for

5 min at RT. The supernatant was discarded and the pellet was resuspended in 3 mL of MACS buffer. $CD4^+$ T cells were isolated from the cell suspension by positive selection using the MidiMACS Starting Kit and LS columns, according to the manufacturer's instructions. Briefly, the column was rinsed with 5 mL of MACS buffer before the 3 mL of cell suspension were added to the column through a wet nylon mesh cell strainer (70 µm). The column was washed through the cell strainer 3 times with 3 mL of MACS buffer. 5 mL of MACS buffer were added directly to the column which was then removed from the MidiMACS Starting Kit and the plunger was used to force the positively selected $CD4^+$ T cells out of the column into a fresh 50 mL tube. The solution was diluted to a total volume of 15 ml with cRPMI, centrifuged as before and the T cell pellet was resuspended in 3 mL of cRPMI.

2.2.3.5 Cell Counting

10 µL of cell suspension were loaded onto a clean glass haemocytometer with a cover slip. The number of viable cells (bright) and dead cells (dark) were distinguished using an inverted, contrasting microscope (Leica DM IL; Leica Microsystems GmbH, Wetzlar, Germany). Viable cells were counted in 4 large corner squares of the haemocytometer grid, as highlighted in Figure 2.1, and the mean was calculated. The total number of viable cells in the cell suspension was calculated by multiplying the mean cell number by 10^4 to determine the concentration of cells per mL and then by the number of mL of cell suspension.

Total cell count = mean cell number in 4 corner squares x 10^4 x 3 mL

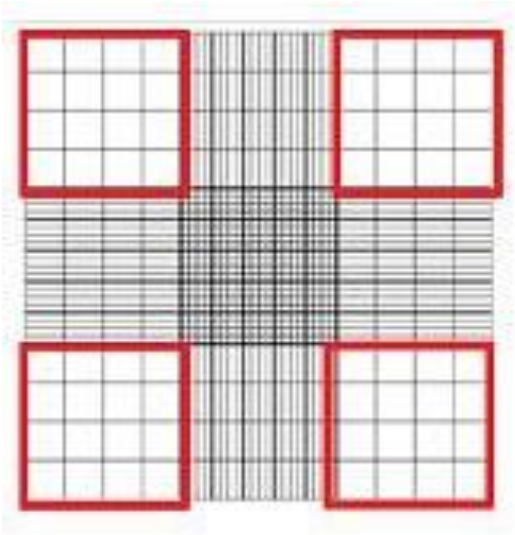

Figure 2.1: Grid used to perform cell counts with a haemocytometer
Image taken and adapted from [http://www.humanimmunologyportal.com/protocols/performing-cell-counts-with-a-hemacytometer/].

2.2.3.6 Cell Seeding and $CD4^+$ T Cell Polarization and Culture

A 96-well, round-bottomed plate was coated with 50 µL of anti-CD3 and anti-CD28 at different concentrations in DPBS to activate naive T cells. The concentration of antibodies depended on the desired T cell subset (see Table 2.5). Where indicated, anti-CD3 and/or anti-CD28 were titrated during experiments. The plate was incubated at 37°C and 5 % CO_2 (Steri-Cycler™ CO_2 Incubator; Thermo Fisher Scientific, Waltham, MA, U.S.A.) for 2 – 3 h, while splenocytes and primary T cells were being isolated as previously described (Sections 2.2.3.3 – 2.2.3.5) so that the antibodies would become plate-bound.

Table 2.5: Concentrations of anti-CD3 and anti-CD28 used to activate $CD4^+$ T cells

T Cell Subset	Anti-CD3 Concentration ($\mu g.mL^{-1}$)	Anti-CD28 Concentration ($\mu g.mL^{-1}$)
Naive	0	0
T_H0	1	2
T_H1	5	5
T_H17	5	5
T_{reg}	1	1

Depending on the total cell count, the cell suspension was either diluted with cRPMI or centrifuged at 420 *g* for 5 min at RT and resuspended in a smaller volume so that the cell density was 2 000 000 cells.mL^{-1}. The wells of the 96-well plate were washed with 100 µL of DPBS and cells were seeded in 100 µL at a density of 200 000 cells per well. 100 µL of cRPMI containing the appropriate mix of cytokines and/or antibodies at a 2X concentration were added to each well and the plate was incubated for up to 120 h at 37°C and 5 % CO_2. The cytokines and antibodies and their working concentrations required to induce polarization towards each T cell subset are outlined in Table 2.6. Where indicated, cells were incubated in the presence of 10 µM of the pan-caspase inhibitor Z-VAD, 10 µM of the necrosis inhibitor Nec-1 or 0.03 % (v/v) DMSO. For the IL-2 neutralisation assay, T_H17 and T_{reg} cells were incubated in the presence of 10 µg.mL^{-1} of anti-IL-2 (clone JES6-1A12). To confirm the successful polarization of each T cell subset, IFN-γ and IL-17A ELISAs were carried out as in Section 2.2.7. This allowed one to ensure that cells under T_H0 and T_H1 polarizing conditions were secreting a high amount of IFN-γ and a low amount, if any, of IL-17A, that cells under T_H17 polarizing conditions were secreting a high amount of IL-17A and a low amount, if any, of IFN-γ and that cells under T_{reg} polarizing conditions were secreting neither IFN-γ nor IL-17A.

Table 2.6: Cytokines and/or antibodies and their working concentrations required to induce T cell polarization

T Cell Subset	rIL-12 (ng.mL^{-1})	Anti-IL-4 (ng.mL^{-1})	rIL-6 (ng.mL^{-1})	Anti-IFN-γ (µg.mL^{-1})	rhTGF-β1 (ng.mL^{-1})	rIL-2 (ng.mL^{-1})
T_H0	-	-	-	-	-	-
T_H1	10	10	-	-	-	-
T_H17	-	20	20	10	2.5	-
T_{reg}	-	-	-	-	5	+/-10

2.2.4 Quantitative RT-PCR

2.2.4.1 Brown Adipocyte Isolation

Interscapular BAT was removed from the mouse, trimmed free of WAT and transferred to cold DPBS. Under sterile conditions, BAT was poured onto a wet nylon mesh cell strainer (70 µm) over a 50 mL tube. It was rinsed once with cold cRPMI and, using the plunger of a 2.5 mL syringe, gently ground and homogenized through the strainer until a fine

suspension of brown adipocytes was obtained. cRPMI was poured three times through the cell strainer to wash any remaining cells into the tube, forming a homogenous cell solution free of clumps. The cell suspension was centrifuged at 420 *g* for 5 min at RT and the supernatant was discarded. The pellet was resuspended in 1 mL of DPBS, transferred to a labelled 1.5 mL tube and centrifuged at 210 *g* for 5 min at RT. The supernatant was decanted and the pellet was resuspended in 300 µL of Lysis Buffer RLY and stored at -80°C until ready to begin the RNA isolation process (Section 2.2.4.2).

2.2.4.2 Isolation of RNA

RNA isolation was carried out using the ISOLATE II RNA Mini Kit as per the manufacturer's instructions with some minor alterations. Approximately 1 000 000 naive $CD4^+$ T cells or 4 – 5 wells of cells stimulated for the desired amount of time were taken per sample. Cells were placed in a 1.5 mL tube and centrifuged at 210 *g* for 5 min at RT. The supernatant was decanted or aliquoted into a labelled 1.5 mL tube and stored at -20°C to be analysed by ELISA at a later time. The pellet was resuspended in 300 µL of Lysis Buffer RLY and stored at -80°C until ready to continue the isolation process.

On the day of RNA isolation, frozen lysates were thawed and pipetted up and down to dissolve any precipitate present. The lysate was loaded onto the ISOLATE II Filter in a 2 mL collection tube and centrifuged for 1 min at 11 000 *g* and 4°C. The filter was discarded and 300 µL of 70 % EtOH were added to the collection tube. The sample was mixed by pipetting until dissolved and transferred to the ISOLATE II RNA Mini Column in a 2 mL collection tube. Columns were centrifuged for 30 seconds (s) at 11 000 *g* and 4°C and placed into a new 2 mL collection tube. 350 µL of Membrane Desalting Buffer MEM were added to the sample and columns were centrifuged for 1 min at 11 000 *g* and 4°C to dry the column membrane. 95 µL of DNase I in Reaction Buffer for DNase I RDN were added to the centre of the silica membrane in the column and samples were incubated at RT for 15 min. The column was washed with 200 µL of Wash Buffer RW1 and centrifuged for 30 s at 11 000 *g* and 4°C before being placed in a new 2 mL collection tube. 600 µL of Wash Buffer RW2 were added and the column was centrifuged for 30 s at 11 000 *g* and 4°C. The flow-through was discarded and the column was returned to the same collection tube. 250 µL of Wash Buffer RW2 were added and the column was centrifuged for 2 min at 11 000 *g* and 4°C to dry the membrane completely. Without touching any flow-through at the bottom of the collection tube, the column was carefully removed and placed into a labelled, nuclease-free 1.5 mL collection tube. 60 µL of RNase-free H_2O were added to the centre of

the silica membrane and columns were centrifuged for 1 min at 11 000 *g* and 4°C. The column was discarded and the collection tube was closed and incubated on ice or at -20°C until ready for RT-PCR. Sample RNA concentration was measured using a NanoDrop® ND-1000 Spectrophotometer, as in Section 2.2.2.2.

2.2.4.3 Reverse Transcription

The High Capacity cDNA Reverse Transcription Kit was used to reverse transcribe isolated RNA into cDNA. Reverse transcription reactions were set up in 0.2 mL 8-tube PCR strips on ice as in Table 2.7. A maximum volume of 14.2 µL of each RNA sample could be used. The sample with the lowest concentration, as measured in Section 2.2.2.2, was used as the 'limiting sample'. Thus, the total amount of cDNA that could be added from the limiting sample was calculated and the volume required to add the same amount of RNA from every other sample was calculated and used. The total volume of each reaction was brought to 20 µL using nuclease-free H_2O and reactions were mixed thoroughly by pipetting. Negative controls were created by adding nuclease-free H_2O in place of the reverse transcriptase enzyme. The 'no enzyme' control samples were used to evaluate levels of genomic DNA in the RNA preparations and to ensure that samples were not contaminated with genomic DNA which could lead to false positive results. The PCR strips were sealed and kept on ice until ready to be loaded into the thermal cycler. The program outlined in Table 2.8 was used to carry out reverse transcription. Following reverse transcription, PCR strips were stored at -20°C until ready to perform PCR (Section 2.2.4.4).

Table 2.7: Components of the reverse transcription reaction mixture

Component	Volume per Reaction (µL)
10X Reverse Transcription Buffer	2
25X deoxynucleotide triphosphate (dNTP) Mix	0.8
10X Reverse Transcription Random Primers	2
Multiscribe™ Reverse Transcriptase	1

Table 2.8: Thermal cycler program for reverse transcription

Step	Temperature (°C)	Time (min)
1	25	10
2	37	120
3	85	5
4	4	Hold

2.2.4.4 PCR

TaqMan® Gene Expression Assays for *Ucp1*, *Ucp2*, *Ucp3* and *Hprt* (ID numbers: Mm01244861_m1, Mm00627599_m1, Mm00494077_m1 and Mm00446968_m1, respectively) and the TaqMan® Universal PCR Master Mix were used to perform PCR. PCR reactions were set up in triplicate in a MicroAmp™ Fast Optical 96-Well Reaction Plate on ice, as in Table 2.9. cDNA was diluted 1 in 2 with nuclease-free dH_2O before being added. The 'no enzyme' negative controls from the reverse transcription step (Section 2.2.4.3) as well as a 'no template' negative control were also included. The 'no template' negative control contained all components of the reaction mixture except for nuclease-free dH_2O in place of cDNA sample. This control sample was used to verify that no PCR reagent had become contaminated with DNA. Reaction plates were sealed with MicroAmp® Optical Adhesive Film and placed in a thermocycler (Applied Biosystems® 7500 Fast Real-Time PCR System; Thermo Fisher Scientific, Waltham, MA, U.S.A.). The program outlined in Table 2.10 was used to carry out PCR using 7500 Fast SDS software (version 1.4.1). Following PCR amplification, plates were stored at -20°C until ready to carry out agarose gel electrophoresis, as in Section 2.2.2.4. The relative expression level of each mRNA was calculated using the comparative C_T method, as described by Schmittgen and Livak (2008), by normalizing the amount of the target gene to the endogenous reference gene (*Hprt*) and relating this to the 'calibrator' sample (naive T cells at time 0). Briefly, C_T values were first normalized by subtracting the mean C_T value of *Hprt* mRNA of each sample from the C_T value of the target mRNA in the same sample. The mean normalized C_T value of the target mRNA in the naive $CD4^+$ T cell sample was then subtracted from the normalized values of the remaining samples. The resulting values were used to calculate the fold-change of gene expression relative to the naive $CD4^+$ T cells at the time of isolation (time 0). The equations are summarized as follows:

$C_{T\ target\ gene} - C_{T\ endogenous\ reference\ gene}$ = delta (Δ)C_T

$\Delta C_{T\ test\ sample} - \Delta C_{T\ calibrator\ sample} = \Delta\Delta C_T$

$2^{\wedge -\Delta\Delta CT}$ = fold-change relative to calibrator sample

Table 2.9: Components of the PCR reaction mixture following reverse transcription

Component	Volume per Reaction (µL)
2X TaqMan® Universal PCR Master Mix	10
20X TaqMan® Gene Expression Assay	1
cDNA template diluted in nuclease-free dH_2O	9

Table 2.10: Thermal cycler program for PCR

Step	Temperature (°C)	Time (min)	
1 – Uracil deoxyribonucleic acid glycosylase (UNG) incubation	50	2	
2 – Polymerase activation	95	10	
3 – Denaturation	95	0.25	Repeat for 40 cycles
4 – Annealing/extension	60	1	
5	72	10	

2.2.5 Sodium Dodecyl Sulphate-Polyacrylamide Gel Electrophoresis

Sodium Dodecyl Sulphate-Polyacrylamide Gel Electrophoresis (SDS-PAGE) is a method of resolving denatured, negatively charged proteins on a polyacrylamide gel, separating proteins based on their M_r, charge and the polyacrylamide gel pore size.

2.2.5.1 SKM Cell Protein Lysate Preparation

The skin of the hind legs of *Ucp3*$^{+/+}$ and *Ucp3*$^{-/-}$ mice was removed and the hind legs were cut off and stored in ice-cold PBS until ready for processing. The hind legs were moved from PBS to a petri dish containing ice-cold RIPA buffer. The muscle tissue was trimmed from the bone using a sharp scissors and fat and connective tissue were removed and discarded. The muscle tissue was placed in a beaker on ice and suspended in 10 times its original volume of ice-cold RIPA buffer. The muscle was minced with a sharp scissors and

homogenized using the Ultra-Turrax T25 (Janke & Kunkel IKA-Labortechnik) for 3 x 10 s bursts (medium/half maximum speed). Once thoroughly homogenized, the homogenate was left in a tube on ice for 30 min, vortexed for 15 s and sonicated for 3 x 5 s bursts (Ultrasonic Processor; Jencons (Scientific) Ltd., Leighton Buzzard, U.K.). The homogenate was incubated at 4°C overnight with constant agitation. Following the incubation, the homogenate was centrifuged at 600 g and 4°C for 15 min twice, with the supernatants kept both times and the pellet being discarded. The SKM protein lysate was then aliquoted, snap frozen and stored at -80°C until required.

2.2.5.2 SDS-PAGE Gel Preparation

Using a mini-PROTEAN® 3 Cell handcast (Bio-Rad Laboratories Ltd.), a 1.5 mm gel containing 15 and 5 % resolving and stacking solutions, respectively, was prepared as per Table 2.11. Gel solutions were thoroughly mixed by vortexing before being used. The resolving gel was pipetted into the glass chamber followed by 1 mL of isopropanol to ensure the resolving gel remained hydrated and level. The gel was left to set for approximately 25 min. When the resolving gel had hardened, the isopropanol was poured off and the top of the gel was rinsed with dH_2O. 5 % stacking gel was prepared as per Table 2.11 and pipetted onto the dry resolving gel. Following the insertion of a 10-pronged comb to generate 10 wells in which the lysates would be placed, the stacking gel was left to set for approximately 25 min. Once set, gels (still in chamber plates) were used immediately or wrapped in wet tissue and stored at 4°C for up to 3 days.

Table 2.11: Components of resolving and stacking gels for SDS-PAGE

Component	Volume (mL)
15 % Resolving Gel	
H_2O	1.7
1.5 M Tris, pH 8.8	1.9
10 % (w/v) SDS, pH 7	0.075
ProtoGel™	3.75
10 % (w/v) APS	0.075
TEMED	0.003
5 % Stacking Gel	
H_2O	2.1
1 M Tris, pH 6.8	0.38
10 % (w/v) SDS, pH 7	0.03
ProtoGel™	0.5
10 % (w/v) APS	0.03
TEMED	0.003

2.2.5.3 Protein Quantification Using the Bicinchoninic Acid Assay

A bicinchoninic acid (BCA) assay was performed to quantify the total protein concentration in lysate samples, as described by Smith *et al*. (1985), using the Pierce™ BCA Protein Assay Kit as per the manufacturer's instructions. A stock solution of 2 milligrams (mg).mL^{-1} of bovine serum albumin (BSA) was diluted with dH_2O to generate a standard curve of a range of concentrations, as indicated in Table 2.12. Lysate samples were diluted 1:5 (citrate synthase assay samples) or 1:20 (SKM lysate samples) with dH_2O before analysis so that the final concentrations of the samples would fall within the range of the standard curve. 10 µL of standard solutions and sample dilutions were pipetted into a 96-well, flat-bottomed plate in triplicate, as well as 10 µL of dH_2O in triplicate to act as blank wells. 200 µL of a working solution of Reagent A and Reagent B (1:50 Reagent A:Reagent B) were added to each well and the plate was covered with cling film and incubated for 30 min at 37˚C in a non-CO_2 incubator (TB53; ALC International). The plate was placed in a SpectraMax Plus 384 microplate reader (Molecular Devices, San Jose, CA, U.S.A.) and the absorbance of the samples in each well was measured at 562 nm using SoftMax Pro software (version 6.4.2; Molecular Devices). The amount of protein present

in the samples was determined using the standard curve. Concentration values were then multiplied by the appropriate dilution factor.

Table 2.12: Dilutions of BSA performed to generate a standard curve for the BCA assay

Vial	dH_2O (µL)	BSA (µL)	Final BSA Concentration ($\mu g.mL^{-1}$)
A	0	300 of stock BSA	2000
B	125	375 of stock BSA	1500
C	325	325 of stock BSA	1000
D	175	175 of vial B	750
E	325	325 of vial C	500
F	325	325 of vial E	250
G	325	325 of vial F	125
H	400	100 of vial G	25
I	400	0	0

2.2.5.4 SDS-PAGE Sample Preparation

Using the protein concentration of each lysate sample calculated using the BCA assay (Section 2.2.5.3), an average of 20 µg of SKM lysate samples, respectively, was diluted in sample buffer as per Table 2.13 so that the final concentration of the sample buffer was 1X. Samples were vortexed briefly, centrifuged briefly and boiled at 100°C in a heating block for 10 min. The SDS-PAGE gel was placed into the mini-PROTEAN® 3 Cell System and 1X running buffer was added to fill the chamber. Following a further brief vortex and centrifugation step, samples were mixed by pipetting and 45 µL were loaded into wells of the prepared SDS-PAGE gel, along with 7 µL of protein ladder.

Table 2.13: Sample preparation for SDS-PAGE

Component	Volume (µL)
Protein lysate	20 µg
4X sample buffer	12.5
1 M DTT	5
1 % (w/v) bromophenol blue	0.5
dH_2O	Bring total volume to 50 µL

2.2.5.5 SDS-PAGE

The mini-PROTEAN® 3 Cell System was exposed to 90 V (PowerPac™ Basic; Bio-Rad Laboratories Ltd.) and electrophoresed until the samples had passed through the stacking gel and reached the resolving gel. At this point, the voltage was increased to 120 V and the samples were electrophoresed until the bromophenol blue dye (migration front) had reached the bottom of the gel. Gels were then prepared for immunodetection (Section 2.2.5.6).

2.2.5.6 Immunodetection

Following SDS-PAGE, the running buffer used was discarded and a 'wet' transfer was carried out immediately to prevent proteins eluting from the gel over time. Resolved proteins were transferred onto PVDF membrane (Immobilon-P^{SQ}; Millipore). The transfer was carried out by removing the stacking gel and soaking the gel, 6 pieces of filter paper (7.5 x 8.5 cm) and 2 sponges in ice-cold transfer buffer in a casserole dish for 10 min. PVDF membrane (7.5 x 8.5 cm) was activated with 100 % methanol for 1 min before being added to the casserole dish containing transfer buffer to soak. The sponges, filter paper, membrane and gel were arranged in a transfer sandwich in a Bio-Rad Mini-Trans Blot cassette as follows: sponge, filter paper x 3, membrane, gel, filter paper x 3, sponge. The cassette was placed in the transfer apparatus submerged in 1X transfer buffer with an ice pack to keep contents cold and the transfer was performed at 200 milliamps (mA) for 1 h.

Following transfer, the PVDF membrane was washed by rocking in TBS-T for 5 min at RT. The TBS-T was discarded and the washing was repeated twice. The PVDF membrane was incubated in Marvel-TBS-T with constant agitation for 1 h at RT to prevent non-specific binding. Afterwards, the membrane was put in a 50 mL Falcon tube containing 5

mL of Marvel-TBS-T and the required antibody at the appropriate dilution, as indicated in Table 2.14. The membrane was incubated overnight at 4°C with constant agitation. The rabbit anti-mouse UCP3 polypeptide antibody was custom made for our laboratory. Peptide synthesis, conjugation of peptides to BSA and injection of rabbits was undertaken by Eurogentec (Belgium). Polyclonal antibodies in the resulting rabbit anti-sera were previously affinity-purified on a protein A column. The peptide to which the antibody is raised is amino acids 141 – 156: TGGERKYRGTMDAYRC.

Following overnight incubation in primary antibody, the PVDF membrane was washed by rocking in TBS-T for 5 min at RT. The TBS-T was discarded and the washing step was repeated twice. The PVDF membrane was incubated in 5 mL of Marvel-TBS-T containing the required secondary antibody at the appropriate dilution as indicated in Table 2.14 for 1 h at RT with constant agitation.

Table 2.14: Antibodies used for immunoblotting

Primary Antibody	**Dilution**	**M_r**
Rabbit anti-mouse UCP3	1:500	33
Mouse anti-mouse PDHe1α	1:1 000	43
Secondary Antibody	**Dilution**	
Goat anti-rabbit IgG-HRP	1:2 500	-
Goat anti-mouse IgG-HRP	1:2 500/1:5 000	-

The PVDF membrane was washed by rocking in TBS-T for 5 min. The TBS-T was discarded and the washing step was repeated twice. Visualization of protein bands was performed using the Immobilon™ Western Chemiluminescent HRP Substrate kit for detecting HRP-labelled antibody by means of the HRP-catalysed oxidation of luminol under alkaline conditions. In a 15 mL Falcon tube, the oxidizing reagent and enhanced luminol reagent were mixed at a 1 in 2 dilution to make 1 mL and then slowly pipetted over the membrane and left for approximately 1 min. Membranes were developed using a ChemiDoc™ MP Imaging System (Bio-Rad Laboratories Ltd.) with Image Lab™ software (V. 5.0, Bio-Rad Laboratories Ltd.).

2.2.6 Flow Cytometry

2.2.6.1 Sample Preparation

Following cell isolation and stimulation for the desired time if required, approximately 1 000 000 cells or 4 wells of cells were taken per flow cytometry sample. Cells were placed in a labelled 5 mL round-bottomed, polystyrene tube. If required, 20 µL of each sample were taken and added together to a new tube to create a 7-AAD or MitoTracker™ Red CMXRos compensation control sample. This tube was not stained with any antibody:fluorophore conjugate during subsequent steps and, instead, was treated with DPBS, annexin V binding buffer or fixation buffer only, where appropriate. Tubes were centrifuged at 420 *g* for 5 min at RT. Supernatants were decanted or aliquoted into labelled 1.5 mL tubes and stored at -20°C to be analysed by ELISA at a later time.

2.2.6.1.1 Sample Restimulation

For intracellular cytokine analysis, sample pellets were resuspended in 1 mL of cRPMI containing PMA, ionomycin and brefeldin A at the concentrations indicated in Table 2.15. PMA is a protein kinase C (PKC) agonist that mimics antigen activation of the TCR:CD3 complex and triggers TCR pathways, while ionomycin causes a calcium (Ca^{2+}) flux and brefeldin A blocks exocytosis of intracellular cytokines. Unstimulated control samples were resuspended in 1 mL of cRPMI containing brefeldin A only. Tubes were lightly capped to allow CO_2 entry and tubes were incubated at 37°C with 5 % CO_2 for 6 h. After this time, samples were washed with 0.5 mL of DPBS and centrifuged at 420 *g* for 5 min at RT. Supernatants were decanted and the pellet was stained for viability detection as in Section 2.2.6.1.2. If samples were not being analysed for intracellular cytokine production, restimulation was not required. In this case, pellets were resuspended in 1 mL of cRPMI, washed immediately with 0.5 mL of DPBS (not after 6 h) and centrifuged as above.

Table 2.15: Concentrations of compounds used for sample restimulation

Sample	PMA ($ng.mL^{-1}$)	Ionomycin ($\mu g.mL^{-1}$)	Brefeldin A ($\mu g.mL^{-1}$)
Stimulated	10	1	5
Unstimulated control	-	-	5

2.2.6.1.2 Sample Staining for Viability Detection

Pellets were resuspended in 200 µL of LIVE/DEAD™ Fixable Aqua Dead Cell Stain diluted in DPBS as per the manufacturer's instructions and incubated on ice for 20 min in the dark. 20 µL of each sample were taken during incubation and added together to a new tube to create a LIVE/DEAD™ compensation control sample. This tube was not stained with any other antibody:fluorophore conjugate during subsequent steps and, instead, was treated with DPBS, fixation buffer or permeabilization buffer only, where appropriate. Samples were washed with 1 mL of DPBS, centrifuged (Sorvall® T 6000D; Thermo Fisher Scientific, Waltham, MA, U.S.A.) at 420 *g* for 5 min at RT and supernatants were decanted. This step was skipped if samples were to be co-stained with PE:anti-CD95L, 7-AAD and *APC*:Annexin V (Sections 2.2.6.1.3 and 2.2.6.1.4, respectively).

2.2.6.1.3 Cell Surface Marker Labelling

All cell surface marker staining was carried out before fixation (Section 2.2.6.1.6). Sample pellets were resuspended in 50 µL of DPBS containing one or a mixture of the antibody:fluorophore conjugates listed in Table 2.16. Concentrations used were those recommended by the manufacturer. Compensation control samples were resuspended in DPBS only. Samples were incubated on ice for 20 min in the dark, washed with 1 mL of DPBS and centrifuged at 420 *g* for 5 min at RT. Supernatants were decanted.

Table 2.16: Concentration of antibody:fluorophore conjugates used for cell surface marker labelling

Antibody:Fluorophore Conjugate	Concentration ($\mu g.mL^{-1}$)
PE-Cy7:anti-CD4	2.5
eFluor® 660/PE:anti-CD25	2.5/4
PE:anti-CD95L	2.5
PE/Pe-Cy5:anti-CD8	4
APC:anti-CD44	4
FITC:anti-CD62L	10
PerCP-Cy™5.5/Pacific Blue™:anti-CD69	4/10
PerCP-eFluor™ 710:anti-LAP	10
FITC:anti-LAG3	20

2.2.6.1.4 Sample Staining for Early Apoptosis, Apoptosis and Necrosis Detection

Pellets were washed in 1 mL of 1X annexin binding buffer from the Annexin V Apoptosis Detection Kit *APC*, centrifuged at 420 *g* for 5 min at RT and supernatants were decanted. Cells were resuspended in 50 µL of 1X binding buffer containing 5 µL of *APC*:Annexin V and incubated in the dark at RT for 15 min. Cells were washed again in 1X binding buffer and centrifuged as above. Supernatants were decanted and cell pellets were resuspended in 50 µL of 1X binding buffer containing 1 $\mu g.mL^{-1}$ of 7-AAD and incubated on ice for 30 min. Volume was increased to 250 µL with 1X binding buffer and samples were analysed on a flow cytometer immediately without fixing.

2.2.6.1.5 Mitochondrial Labelling for Flow Cytometry

Sample pellets that had been stained with LIVE/DEAD™ and PE-Cy7:anti-CD4 were resuspended in 50 µL of DPBS containing 100 nM MitoTracker™ Green FM, 100 nM MitoTracker™ Red CMXRos or 10 µM DCFDA. Samples stained with MitoTracker™ Green FM and MitoTracker™ Red CMXRos were incubated on ice for 20 min before being washed with 1 mL of PBS and centrifuged at 420 *g* for 5 min at RT. Supernatants were decanted and MitoTracker™ Green FM-labelled samples were resuspended in 250 µL of DPBS and analysed on a flow cytometer immediately without fixing. MitoTracker™ Red CMXRos-labelled samples were fixed as in Section 2.2.6.1.6 before being analysed on a flow cytometer. DCFDA-labelled samples were incubated for 10 min at 37°C. Volume was increased to 250 µL and samples were analysed on a flow cytometer immediately without fixing.

2.2.6.1.6 Sample Fixation and Permeabilization

Sample pellets were resuspended in 200 µL of Fixation Buffer and incubated on ice for 30 min in the dark unless FoxP3, Ki-67 or UCP3 were being investigated. If FoxP3, Ki-67 or UCP3 were being analysed, samples were resuspended in 200 µL of fixing buffer from the FoxP3/Transcription Factor Staining Buffer Set as per the manufacturer's instructions. Following incubation, if intracellular cytokines were being analysed, samples were washed with 0.5 mL of 1X Intracellular Staining Permeabilization Wash Buffer. If FoxP3, Ki-67 or UCP3 were being detected, samples were washed with 0.5 mL of permeabilization buffer from the FoxP3/Transcription Factor Staining Buffer Set as per the manufacturer's instructions. Samples were centrifuged at 420 *g* for 5 min at RT and supernatants were decanted. If no intracellular cytokines or transcription factors were being analysed,

samples were washed with 0.5 mL of DPBS following fixation, centrifuged as before and resuspended in 0.25 mL of DPBS, ready to be analysed on a flow cytometer.

2.2.6.1.7 Intracellular Cytokine Labelling

Sample pellets were resuspended in 50 µL of 1X Intracellular Staining Permeabilization Wash Buffer containing one or a mixture of the antibody:fluorophore conjugates listed in Table 2.17. Concentrations used were those recommended by the manufacturer. The LIVE/DEAD™ compensation control sample was resuspended in permeabilization buffer only. Samples were incubated on ice for 20 min in the dark, washed with 0.5 mL of 1X Intracellular Staining Permeabilization Wash Buffer and centrifuged at 420 *g* for 5 min at RT. Supernatants were decanted and pellets were resuspended in 0.25 mL of DPBS, ready to be analysed on a flow cytometer.

Table 2.17: Concentration of antibody:fluorophore conjugates used for intracellular cytokine labelling

Antibody:Fluorophore Conjugate	Concentration ($\mu g.mL^{-1}$)
PE:anti-IL-2	4
APC:anti-IFN-γ	10
PE:anti-IL-17A	2.5

2.2.6.1.8 FoxP3, Ki-67 and UCP3 Labelling

Sample pellets were resuspended in 50 µL of permeabilization buffer from the FoxP3/Transcription Factor Staining Buffer Set containing PE/*APC*:anti-FoxP3, PerCP-eFluor™ 710:anti-Ki-67 or rabbit anti-mouse UCP3 at the concentrations indicated in Table 2.18. The LIVE/DEAD™ compensation control sample was resuspended in permeabilization buffer only. A 'no primary-control' (NPC) was also made by incubating a portion of cells in permeabilization buffer only without anti-mouse UCP3. Samples were incubated on ice for 20 min in the dark. Following incubation, samples were washed with 0.5 mL of permeabilization buffer and centrifuged at 420 *g* for 5 min at RT. Supernatants were decanted and samples for FoxP3 and Ki-67 analysis were resuspended in 0.25 mL of DPBS, ready to be analysed on a flow cytometer. Samples for UCP3 detection (including the NPC control) were resuspended in 50 µL of permeabilization buffer containing Alexa Fluor® 647 goat anti-rabbit IgG (H + L) at a 1:500 dilution. The LIVE/DEAD™

compensation control sample was resuspended in permeabilization buffer only. Samples were incubated on ice for 20 min in the dark. Following incubation, samples were washed with 0.5 mL of permeabilization buffer and centrifuged at 420 *g* for 5 min at RT. Supernatants were decanted and samples were resuspended in 0.25 mL of DPBS, ready to be analysed on a flow cytometer.

As a positive control for FoxP3 staining, approximately 1 000 000 naive T cells were taken at the time of $CD4^+$ T cell isolation. These were stained on the day with LIVE/DEAD™ and PE-Cy7:anti-CD4, fixed and permeabilized as in Sections 2.2.6.1.2, 2.2.6.1.3 and 2.2.6.1.6, respectively, before being stained with PE:anti-FoxP3 as described previously. Approximately 10 % of the splenic $CD4^+$ T cell population is $FoxP3^+$ (Hori *et al*., 2003; Huang *et al*., 2004).

Table 2.18: Concentration of anti-FoxP3, anti-Ki-67 and anti-mouse UCP3 used for flow cytometry

Antibody:Fluorophore Conjugate	Concentration ($\mu g.mL^{-1}$)
PE/*APC*:anti-FoxP3	2.5
PerCP-eFluor™ 710:anti-Ki-67	0.6
Rabbit anti-mouse UCP3	1:500 dilution

2.2.6.2 Sample Preparation for the Proliferation Assay

Following $CD4^+$ T cell isolation and cell counting (Sections 2.2.3.3 – 2.2.3.5), WT and KO cells were divided into two samples: one to be stained with CellTrace™ Violet and the other to be left as an unstained, negative control. Samples were centrifuged at 420 *g* for 5 min at RT. The supernatant was discarded and pellets were resuspended in 1 mL of DPBS. The centrifugation step was repeated as above and the supernatant was discarded. Cell pellets were resuspended in 5 mL of warm DPBS containing 1 µM CellTrace™ Violet or warm DPBS only. Tubes were wrapped in tinfoil to protect from light and incubated in a water bath at 37°C for 10 min. 10 mL of cRPMI were added to each tube to stop the labelling process and remove any free dye remaining in the solution. Samples were incubated on ice for 15 min still protected from light and were then centrifuged as before. The supernatant was decanted and cells were resuspended in the appropriate volume of media to have cells at a density of 2 000 000 cells.mL^{-1}. 1 000 000 cells were taken from

the labelled and unlabelled samples and fixed immediately with Fixation Buffer as in Section 2.2.6.1.6. These were stored at 4°C wrapped in tinfoil until flow cytometry sample processing when they would be used as a compensation control. The remaining cells were plated as in Section 2.2.3.6 at a density of 200 000 cells per well for 72 h. Following incubation, 4 – 5 wells of cells were taken per sample. Cells were placed in a labelled 5 mL round-bottomed, polystyrene tube, centrifuged at 420 *g* for 5 min at RT and the supernatant was decanted. Samples were then prepared for flow cytometry as in Sections 2.2.6.1.1 – 2.2.6.1.6.

CellTrace™ Violet contains a cell-permeant, non-fluorescent ester of an amine-reactive fluorescent molecule that enters cells by diffusion through the plasma membrane. Upon entry into the cell, the non-fluorescent molecule is converted to a fluorescent derivative by cellular esterases. The active succinimydyl ester covalently binds to amine groups in proteins, resulting in long-term dye retention within the cell. Through subsequent cell divisions, daughter cells receive approximately half of the fluorescent label of their parent cells, allowing the analysis of the fluorescence intensities of cells labelled and grown. Analysis of the level of fluorescence in the cell populations by flow cytometry permits the determination of the number of generations through which a cell has progressed since the label was applied. The labelled and unlabelled unstimulated (naive) cells mentioned above were used as compensation controls. Labelled, unstimulated cells provide a fluorescence measurement of non-dividing lymphocytes, while unlabelled, unstimulated cells act as a negative control. Unlabelled, stimulated cells were also used as an additional control as they provide a measure of the auto-fluorescence of activated, proliferating lymphocytes, which is usually higher than that of resting lymphocytes. Using these controls, one can calculate the cell division number of the proliferating, labelled lymphocytes.

2.2.6.3 Flow Cytometry Sample Processing

Compensation controls for flow cytometry experiments were created using the Anti-Rat and Anti-Hamster Ig kappa (κ)/Negative Control Compensation Particles Set or UltraComp eBeads™. When using the Compensation Particles Set, one drop of Ig κ beads was mixed with one drop of the negative control (FBS) beads in a 1.5 mL tube and diluted with 300 µL of DPBS. 100 µL of this solution were added to a labelled 5 mL round-bottomed, polystyrene tube and stained with the appropriate antibody:fluorophore conjugate. When using the UltraComp eBeads™, 1 drop was added to a labelled 5 mL round-bottomed,

polystyrene tube and stained with the antibody:fluorophore conjugate. Tubes were incubated on ice for 10 min in the dark before being diluted with 150 µL of DPBS.

All samples were kept at 4°C and protected from light by being covered in tinfoil until processing. Flow cytometry was carried out using a BD FACSCanto™ II or BD LSRFortessa™ (BD Biosciences, CA, U.S.A.). A forward scatter (FSC) threshold of 15 000 was used to exclude debris during sample processing. Samples were vortexed immediately before analysis (Lab Dancer; VWR, Radnor, PA, U.S.A.) and processed using BD FACSDiva™ software (version 8.0; BD, Franklin Lakes, NJ, U.S.A.). Compensation was set up using the LIVE/DEAD™, 7-AAD, MitoTracker™ Red CMXRos, CellTrace™ Violet and bead compensation control samples, where appropriate. During sample processing, gates were created in order to exclude doublets, dead cells and $CD4^-$ cells, as indicated in Table 2.19 and depicted in the gating strategy in Figure 2.2. A stopping gate of 10 000 (viable, if viability dye was used) $CD4^+$ cells was used for each sample.

Table 2.19: Gating strategy during flow cytometry sample processing

Axes (X vs. Y)	Gated Population
FSC-area (A) vs. side scatter (SSC)-A	Total cell population (excluding debris)
FSC-A vs. FSC-width (W)	Singlets (lower FSC-W)
SSC-A vs. SSC-W	Singlets (lower SSC-W)
LIVE/DEAD™ vs. SSC-A	Viable cells (lower LIVE/DEAD™ signal)
PE-Cy7:anti-CD4 vs. SSC-A	$CD4^+$ cells (higher PE-Cy7 signal)

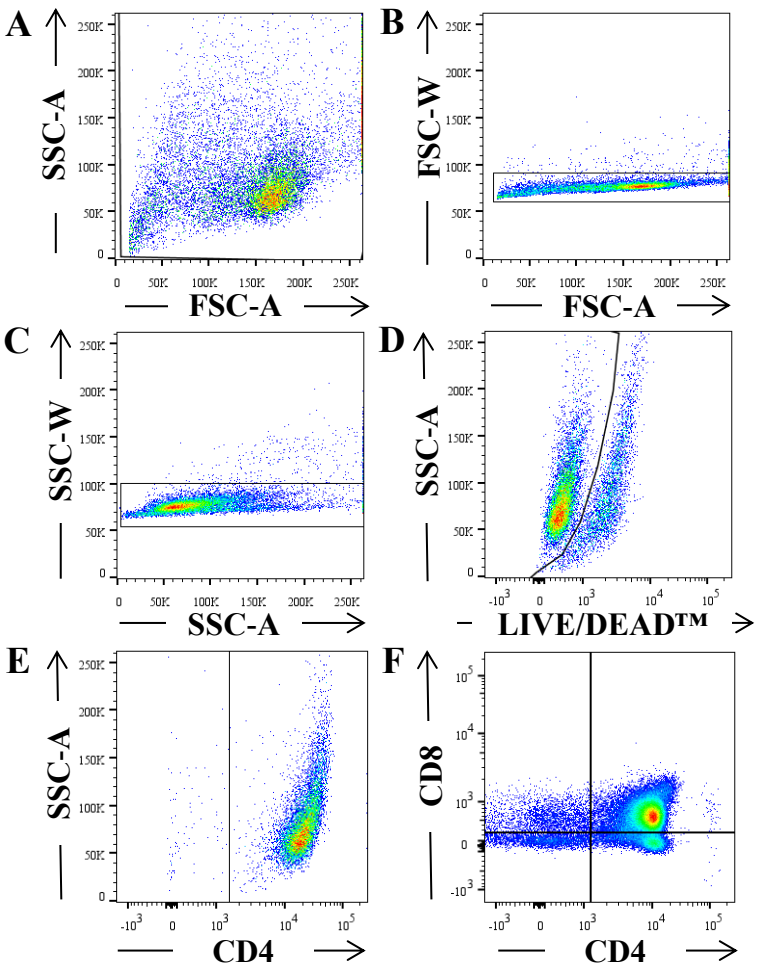

Figure 2.2: Gating strategy used during flow cytometry

Doublets, dead cells and $CD4^-$ cells were excluded during flow cytometry by the gates displayed in B – E. Where indicated, dead cells may not have been excluded with LIVE/DEAD™, such as during flow cytometry analysing 7-AAD and Annexin V staining. (F) Anti-CD8 was used to gate the $CD4^+CD8^-$ population for thymocyte samples only.

2.2.7 ELISA

Cell supernatants were taken at designated time points, transferred to 1.5 mL tubes and stored at -20°C until ready to use. A 96-well ELISA plate was coated with 50 µL per well of the appropriate capture antibody diluted in DPBS to the concentration indicated in Table 2.20. The plate was sealed with cling film and incubated at 4°C overnight.

The ELISA plate was rinsed 5 times in PBS-Tween solution and allowed to soak for 60 s during each rinse before being blotted on absorbent paper to remove any residual buffer. 100 µL of 1X ELISA assay diluent were added to each well to block non-specific binding. The plate was sealed with cling film and incubated for 1 h at RT before being rinsed as before. Standards were diluted with ELISA assay diluent to the concentrations indicated in Table 2.20. This was used as the top standard concentration and was serially diluted to create a standard curve of 8 different concentrations in duplicate. The lowest concentration of the standard curve was 0 picograms (pg).mL^{-1}, for which ELISA assay diluent only was used. Supernatant samples were diluted with ELISA assay diluent (1 in 2, 1 in 5, 1 in 10 and/or 1 in 20) and 50 µL were added to empty wells. 50 µL of ELISA assay diluent were plated in 3 separate wells to act as blanks for spectrophotometer calibration. The plate was sealed with cling film and incubated at 4°C overnight.

The ELISA plate was rinsed as before and coated with 50 µL per well of detection antibody diluted in ELISA assay diluent to the concentrations indicated in Table 2.20. The plate was sealed with cling film and incubated for 1 h at RT before being rinsed as before. 50 µL of Avidin-HRP diluted with ELISA assay diluent (1 in 3 000) were added to each well and the plate was sealed with cling film and incubated for 30 min at RT. Following incubation, the ELISA plate was rinsed 7 times in PBS-Tween solution and allowed to soak for 120 s during the first rinse and 60 s during each subsequent rinse before being blotted on absorbent paper to remove any residual buffer. Substrates A and B of the TMB Substrate Set were mixed at a 1 in 2 dilution and 50 µL were added to each well. The plate was incubated at RT for up to 30 min whilst being continuously monitored for the appearance of a blue colour. When the blue colour could be seen gradually in standard curve wells, 25 µL of 2 Normal (N) sulphuric acid were added quickly to each well to stop the reaction. The absorbance of each well was measured at 450 nm using a microplate reader. The standard curve was used to calculate the cytokine concentration in each well containing supernatant samples. Concentration values were then multiplied by the appropriate dilution factor.

Table 2.20: Concentration of capture and detection antibodies and recombinant protein standards used during ELISAs

Antibody	Concentration
IL-2 capture antibody	0.5 µg.mL^{-1}
rIL-2 standard	250 pg.mL^{-1}
IL-2 detection antibody	0.5 µg.mL^{-1}
IFN-γ capture antibody	0.25 µg.mL^{-1}
rIFN-γ standard	2000 pg.mL^{-1}
IFN-γ detection antibody	0.5 µg.mL^{-1}
IL-17A capture antibody	1 µg.mL^{-1}
rIL-17A standard	1000 pg.mL^{-1}
IL-17A detection antibody	0.5 µg.mL^{-1}
IL-10 capture antibody	4 µg.mL^{-1}
rIL-10 standard	2000 pg.mL^{-1}
IL-10 detection antibody	0.5 µg.mL^{-1}

2.2.8 Citrate Synthase Specific Activity Assay

2.2.8.1 Cell Lysate Preparation

The citrate synthase assay was carried out as previously described by Spinazzi *et al*. (2012) with some minor alterations. Briefly, cells were taken at the desired time point and centrifuged at 420 *g* for 5 min at RT. The supernatant was decanted or aliquoted into labelled 1.5 mL tubes and stored at -20°C to be analysed by ELISA at a later time. The cell pellet was resuspended in 1 mL of cRPMI, transferred to a labelled 1.5 mL tube and centrifuged at 1 000 *g* and 4°C for 5 min. The supernatant was discarded and the pellet was resuspended in 1 mL of DPBS and centrifuged as before. This was repeated once. The supernatant was discarded and the pellet was resuspended in 100 µL of cold 0.2 % (v/v) Tris-Triton™ X-100 to lyse cells. Samples were placed on ice and agitated on a rocker for 10 min. The sample was centrifuged at 20 820 *g* and 4°C for 10 min and the pellet was discarded by transferring the supernatant to a new, labelled 1.5 mL tube on ice. Total protein concentration of each lysate sample was quantified using the BCA assay, as described in Section 2.2.5.3.

2.2.8.2 Citrate Synthase Assay

Cuvettes were prepared for spectrophotometric analysis as in Table 2.21. The volume of each lysate sample required to add 40 µg of protein was calculated and added to the cuvette along with dH_2O to bring the total volume in the cuvettes up to 950 µL. The citrate synthase assay was performed using a flatbed recorder (BD12E; Kipp & Zonen B.V., Delft, the Netherlands) and a Libra S12 UV/Vis spectrophotometer (Biochrom, Cambridge, U.K.). Chart speed was set to 1 $cm.min^{-1}$ and the range was set to 0.2 V. The spectrophotometer was first calibrated by using a cuvette containing Tris-Triton™ X-100 only as a blank control. The cuvettes were mixed by inversion using parafilm to prevent spillages and the baseline activity was recorded at 412 nm for at least 2 min. The reaction was started by adding 50 µL of freshly prepared, cold 10 mM oxaloacetic acid. The cuvettes were again mixed by inversion and the increase in absorbance was monitored for at least 3 min.

The free CoA and acetyl CoA used in the citrate synthase reaction do not have convenient absorptions of any magnitude in the range of UV wavelengths measured accurately by spectrophotometers. Therefore, the citrate synthase reaction is coupled to a second, faster reaction between CoASH (CoA with a sulfhydryl functional group) and DTNB which produces a coloured product, 5-thionitrobenzene (TNBH), whose absorption can be measured. The rate of appearance of the yellow colour under these conditions is then a measure of the rate of the citrate synthase reaction which itself is a measure of the amount of citrate synthase present and an indirect measurement of mitochondrial abundance. The change in absorbance per min (ΔA) was determined for each sample and the enzymatic activity of citrate synthase was calculated according to the following equation:

Enzymatic activity [nanomoles (nmol).min^{-1}.mg^{-1}] = (ΔA x 1000) / [(ϵ x volume of sample in mL) x (sample protein concentration in $mg.mL^{-1}$)]
where ϵ for TNBH is 13.6 $mM^{-1}.cm^{-1}$.

Table 2.21: Citrate synthase assay reaction mixture

Component	Volume (µL)
Tris-Triton™ X-100	500
DTNB-Tris	100
10 mM acetyl CoA	30
Lysate sample	40 µg of protein
dH_2O	Bring total volume up to 950 µL

2.2.9 Seahorse XF Cell Mito Stress Test

2.2.9.1 Preparation of XF24 Sensor Cartridge

The Seahorse XF24 FluxPak includes 18 XF24 sensor cartridges, 20 XF24 cell culture microplates and one bottle of XF calibrant solution. Each well of the sensor cartridge was filled with 1 mL of XF calibrant 24 h before the experiment in order to hydrate the cartridge sensors. The cartridge was labelled and incubated at 37°C overnight in a non-CO_2 incubator. The Seahorse XF24 Analyzer (Agilent Technologies, Santa Clara, CA, U.S.A.) was turned on and left on overnight so that it warmed to 37°C for use the following day.

2.2.9.2 Preparation of XF24 Cell Culture Microplate

Cells are required to be in an adherent monolayer for assay on the Seahorse XF24 Analyzer. T cells are normally grown in suspension and do not naturally settle to the bottom of a microplate well under gravity, requiring centrifugation to settle down. Thus, Corning® Cell-Tak Cell and Tissue Adhesive was used to adhere T cells to the bottom of the wells of the XF24 cell culture microplates (Rogers *et al*., 2011; Wang *et al*., 2011). Cell-Tak is a non-immunogenic extracellular matrix protein preparation isolated from the marine mussel, Mytilus edulis (Rogers *et al*., 2011). On the day of the experiment, a solution of Cell-Tak was prepared at 22.4 $\mu g.mL^{-1}$ in 0.1 molar (M) sodium bicarbonate as per the manufacturer's instructions. Each well of the cell microplate was layered with 50 µL. The plate was incubated at RT under sterile conditions with the lid left off for a minimum of 20 min. Each well was washed with 200 µL of sterile dH_2O twice before being left to dry at RT for a further 30 min under sterile conditions with the lid off.

2.2.9.3 Preparation of Media for Seahorse XF Cell Mito Stress Test

Low- or non-buffered media is required for measuring the extracellular acidification rate (ECAR) so as to prevent sodium bicarbonate, the buffer present in most media, from masking any changes in the extracellular acidity. RPMI 1640 medium with L-glutamine but without glucose and sodium bicarbonate was used as the assay medium for the Seahorse XF Cell Mito Stress Test experiments. This was prepared as per the manufacturer's guidelines, supplemented with 11.11 mM glucose and warmed to 37°C in a water bath.

2.2.9.4 Seeding Density Optimization

Cells were harvested direct from spleens or from 96-well plates at the desired time point and centrifuged at 420 *g* for 5 min at RT. The supernatant was decanted or aliquoted into labelled 1.5 mL tubes and stored at -20°C to be analysed by ELISA at a later time. The cell pellet was washed in 5 mL of warm assay media and cells were counted as in Section 2.2.3.5. Five different cell densities were plated in the first experiment to determine the optimal seeding density for use with the Seahorse XF Cell Mito Stress Test: 250 000, 500 000, 750 000, 1 000 000 and 1 250 000 WT cells per well. After counting, cells were divided into five samples containing the designated number of cells and centrifuged as above. The supernatants were decanted and the cell pellets were resuspended in the volume of warm assay media required to have cells at the correct cell density for seeding. 100 µL of assay medium containing no cells were pipetted into the background correction/control wells (A1, B4, C3, D6) of the Cell-Tak-coated XF24 cell culture microplate, as in Figure 2.3. Background wells were used to correct for artefacts, such as temperature fluctuations and buffering capacity, that can affect O_2 and pH and that are not due to changes in metabolism. 100 µL of the cell suspension were pipetted along the side of each well, excluding the background correction wells. The cell plate was centrifuged (5804 R; Eppendorf, Hamburg, Germany) at 400 *g* for 5 min at RT and with zero braking to help cells to adhere to the layer of Cell-Tak at the bottom of each well. To balance the centrifuge, a "dummy" plate was created by adding 100 µL of dH_2O to each well of another XF24 cell culture microplate. The plates were turned to face the opposite direction and re-centrifuged as above to promote even cell distribution and reduce edge effects. The plates were incubated at 37°C in a non-CO_2 incubator for 25 – 30 min to allow the cells to completely attach to the culture surface. This was then visually confirmed using an inverted, contrasting microscope.

The optimal seeding density was determined firstly by visual assessment; cells should be at 50 – 90 % confluence and evenly distributed within each individual well. Subsequently, 3 basal measurements were taken during a short trial assay. The mean basal OCR was used to assess seeding density as the cells were offered an unlimited supply of substrate and had not yet been treated with mitochondrial inhibitors. A basal OCR and ECAR between 100 – 400 $pmol.min^{-1}$ and 20 – 120 $mpH.min^{-1}$, respectively, were desired, as per the manufacturer's recommendations. A cell seeding density of 500 000 cells per well was chosen for all subsequent Seahorse experiments.

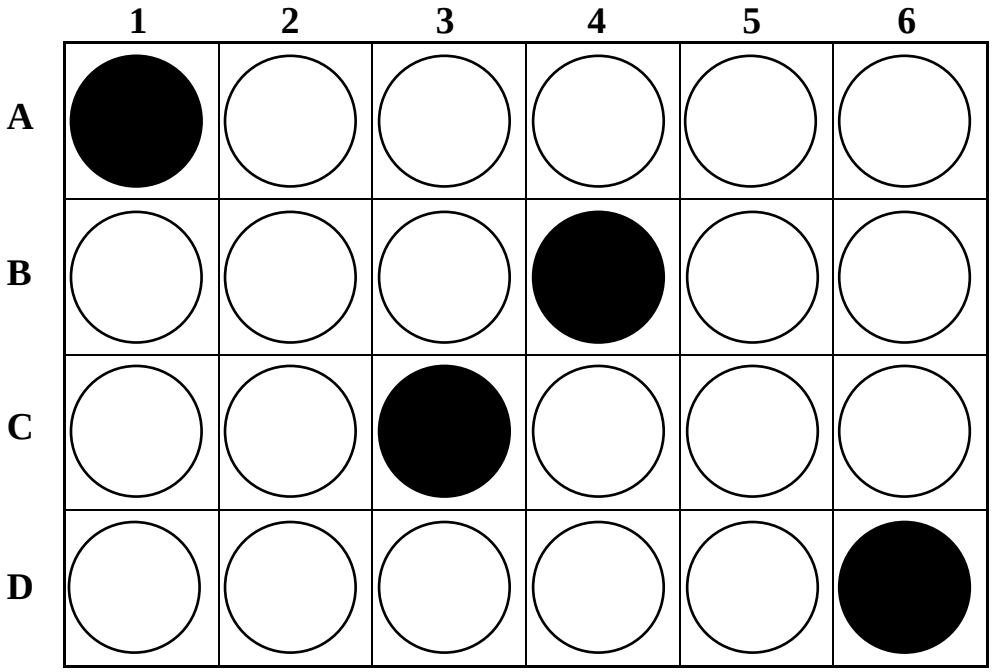

Figure 2.3: Wells of the XF24 cell culture microplate used for background correction

2.2.9.5 Compound Preparation and Concentration Optimization

The compounds oligomycin, FCCP, antimycin A and rotenone were prepared at 10X concentrations so that, following injection, they would be at a 1X working concentration in each well. Compounds were titrated in assay media in separate experiments initially to determine the optimal concentration of each to use for the Seahorse XF24 Cell Mito Stress Test. Four working concentrations of oligomycin were tested: 0, 0.5, 1 and 2 µM. For the oligomycin optimization assay, 3 basal rate measurements followed by compound injection from port A and 3 more rate measurements were taken to determine the optimal concentration. 1 µM was chosen as the optimal working concentration.

Six working concentrations of FCCP were tested: 0, 0.125, 0.25, 0.5, 1 and 2 µM. The FCCP optimization assay was carried out as follows: 3 basal rate measurements were taken followed by injection of 1 µM oligomycin (final concentration) from port A, 3 rate measurements, titrated FCCP injection from port B and 3 more rate measurements. However, it was noticed that the OCR did not reach that of the basal rate following FCCP injection. Thus, the FCCP optimization experiment was repeated firstly with 1.5 mM sodium pyruvate supplementation in the media and an injection of 1.5 mM FCCP and then without a preceding injection of oligomycin, using media instead and following it with injection of 0.5, 1, 1.5 or 2 µM FCCP. In the latter experiment, the OCR successfully reached and surpassed that of the basal rate. Thus, 1.5 µM was chosen as the optimal working concentration of FCCP and it was decided that during experiments, wells would be treated with either oligomycin or FCCP followed by an antimycin A and rotenone mix so that the full effect of FCCP could be observed.

Two working concentrations of rotenone were tested mixed with 1 µM antimycin A: 0.1 and 1 µM. The rotenone optimization assay was carried out as follows: 3 basal rate measurements were taken followed by compound injection from port A (1 µM oligomycin, working concentration), 3 rate measurements, compound injection from port B (1.5 µM FCCP, working concentration), 3 rate measurements, compound injection from port C (antimycin A and titrated rotenone mix) and 3 more rate measurements. 0.1 µM rotenone was chosen as the optimal working concentration. The compounds used during the Seahorse XF24 Cell Mito Stress Test, their concentrations and their functions are outlined in Table 2.22.

Table 2.22: Compounds used during the Seahorse XF Cell Mito Stress Test

Compound	Concentration (µM)	Function
Oligomycin	1	Complex V (ATP synthase) inhibitor
FCCP	1.5	Mitochondrial uncoupler
Rotenone	0.1	Complex I inhibitor
Antimycin A	1	Complex III inhibitor

Injection compounds were pre-warmed to 37°C for approximately 15 min before being loaded into the XF24 sensor cartridge hydrated with calibrant from the previous day. The cartridge has 4 injection ports labelled A, B, C and D, as shown in Figure 2.4. Including the ports of background correction wells, 56 µL of 10X oligomycin or FCCP were loaded into each port A and 62 µL of the 10X antimycin A and rotenone mix were loaded into each port B to take into account the change in volume following each injection. The cartridge was incubated at 37 °C in a non-CO_2 incubator for approximately 30 min.

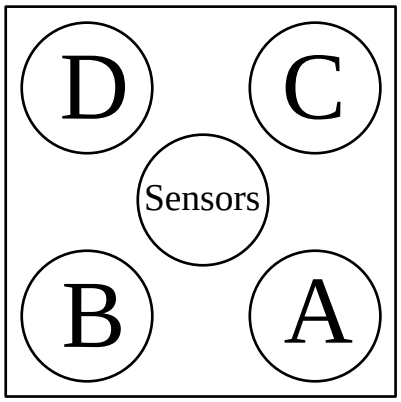

Figure 2.4: Injection port layout of the XF24 sensor cartridge

2.2.9.6 Measurement of OCR and ECAR during the Seahorse XF Cell Mito Stress Test

The Seahorse XF24 Analyzer was calibrated using the hydrated XF24 sensor cartridge containing the 10X compounds. The calibration process takes approximately 25 – 30 min. During this time, 400 µL of warm assay media were added gently to the side of each well of the XF24 cell culture microplate to bring the final volume up to 500 µL. Care was taken to avoid disturbing the cell monolayer. Cells were checked under the microscope for seeding uniformity and to ensure that no cells had detached or been washed away. The cell plate was returned to the non-CO_2 incubator at 37°C until calibration was finished. Following calibration, the utility plate (bottom half) of the XF24 sensor cartridge was replaced with the XF24 cell culture microplate in the Seahorse XF Analyzer and the assay was started. The protocol of the Seahorse XF24 Cell Mito Stress Test involves a cycle of 3 min of mixing, 2 min of waiting and 3 min of measuring, repeated twice. This was followed by injection of port A, 3 of the cycles described above, injection of port B and 3 more cycles, as outlined in Table 2.23.

Table 2.23: Seahorse XF Cell Mito Stress Test protocol

Step	Action	Time (min)
1	Mix	3
2	Wait	2
3	Measure	3
4	Mix	3
5	Wait	2
6	Measure	3
7	Mix	3
8	Wait	2
9	Measure	3
10	Inject port A (Oligomycin/FCCP)	-
11	Mix	3
12	Wait	2
13	Measure	3
14	Mix	3
15	Wait	2
16	Measure	3
17	Mix	3
18	Wait	2
19	Measure	3
20	Inject port B (Rotenone and Antimycin A)	-
21	Mix	3
22	Wait	2
23	Measure	3
24	Mix	3
25	Wait	2
26	Measure	3
27	Mix	3
28	Wait	2
29	Measure	3
30	End	

Cycle

2.2.9.7 Calculation of Metabolic Parameters from Seahorse Data

The basal OCR and ECAR of cells were used to calculate the OCR/ECAR ratio. Non-mitochondrial respiration was measured following the addition of rotenone and antimycin A mix. Basal mitochondrial OCR, proton leak and maximal respiration were calculated by subtracting non-mitochondrial respiration from the basal OCR, the OCR following oligomycin injection and the OCR following FCCP injection, respectively. ATP-linked respiration was calculated by subtracting proton leak from the basal mitochondrial OCR. The coupling efficiency was calculated by expressing the ATP-linked mitochondrial OCR as a percentage of the basal mitochondrial OCR. Spare respiratory capacity was calculated by subtracting the basal mitochondrial OCR from the maximal respiration. This was also calculated as a percentage of the basal rate.

2.2.10 Adoptive Transfer to *Rag1*$^{-/-}$ Mice

WT and *Ucp3*$^{-/-}$ CD4^{+} T cells from female donor mice were isolated as in Sections 2.2.3.3 – 2.2.3.5 and stained with CellTrace™ Violet as in Section 2.2.6.2. Cells were resuspended in PBS at a density of 20 000 000 cells.mL^{-1} and 2 000 000 cells (100 µL volume) were injected intraperitoneally into *Rag1*$^{-/-}$ host mice. After 7 days, splenocytes were isolated from host mice as in Section 2.2.3.3 and prepared for flow cytometry as in Section 2.2.6. Transferred cells were detected through gating on CD4^{+} expression and subsequently analysed for relative rates of proliferation through CellTrace™ Violet dilution. Fresh WT CD4^{+} T cells stained or unstained with CellTrace™ Violet were prepared 2 days before the isolation day and incubated in a 96-well plate at 37°C and 5 % CO_2 with no stimulating antibodies or polarizing cytokines for use as a CellTrace™ Violet compensation control.

2.2.11 *In Vivo* Immunization of *Ucp3*$^{+/+}$ and *Ucp3*$^{-/-}$ Mice

WT and *Ucp3*$^{-/-}$ mice were immunized subcutaneously with 1 µg of KLH alone or 1 µg of KLH plus 1 µg of CT in a 200 µL volume of sterile DPBS (100 µL in each flank) on days 0 and 14. On day 21, lymph node cells and splenocytes were isolated as in Sections 2.2.3.2 and 2.2.3.3, respectively, and counted as in Section 2.2.3.5, with the exception that splenocyte and lymph node cell samples were diluted 1 in 50 and 1 in 5, respectively, for counting. Splenocyte samples were diluted to 10 000 000 cells.mL^{-1} and 200 µL were transferred to labelled 5 mL round-bottomed, polystyrene tubes for flow cytometry. Cells were prepared for FoxP3 expression analysis as in Sections 2.2.6.1 and 2.2.6.3.

96-well round-bottomed plates were coated the night before tissue isolation with 25 µL of anti-CD3 at a concentration of 0.2 $\mu g.mL^{-1}$ in cRPMI without FBS and left at 4°C overnight to allow the antibody to become plate-bound. Some wells were also plated with 25 µL of cRPMI without FBS and without anti-CD3 to act as negative controls. For *ex vivo* antigen-specific recall response analysis, the remaining splenocyte and lymph node cells were diluted to densities of 2 000 000 and 1 000 000 $cells.mL^{-1}$, respectively, and plated in 200 µL volumes (400 000 and 200 000 cells per well, respectively) in 96-well plates for 72 h in the presence of cRPMI alone, 0.2 $\mu g.mL^{-1}$ of anti-CD3 as described above or 2, 10 or 50 $\mu g.mL^{-1}$ of KLH. After 72 h, supernatants were collected to analyse cytokine secretion by ELISA as in Section 2.2.7. Lymph node cells receiving the same *in vitro* stimulation and from mice that received the same immunization were pooled together and prepared for flow cytometry as for splenocyte cells described previously.

2.2.12 Statistical Analysis

Data are presented as mean ± the standard error of measurement unless otherwise indicated. Flow cytometry data were analysed using FlowJo® software (version 10.0.7; FlowJo® LLC, Ashland, OR, U.S.A.). All other data were analysed using GraphPad Prism® software for Windows (version 5; GraphPad Software, Inc., La Jolla, CA, U.S.A.). Statistical significance was detected and quantified using a two-tailed, unpaired *t* test or a one-way or two-way, repeated measures or non-repeated measures analyses of variance (ANOVA) with a *post hoc* Bonferroni or Dunnet test, where indicated. A p value of < 0.05 was used to indicate significance where detected. Experiments were performed three times unless otherwise stated.

Chapter 3:

Ucp Expression in $CD4^+$ T Cells and the Role of UCP3 in $CD4^+$ T Cell Function

Chapter 3

Ucp Expression in CD4$^+$ T Cells and the Role of UCP3 in CD4$^+$ T Cell Function

3.1 Introduction

Following its discovery in the 1970s by Heaton *et al*. (1978), UCP1 was thought to be exclusively expressed in and associated with BAT for a number of years until its discovery in WAT and SKM in 1998 (Yoshida *et al*.). UCP2 is expressed ubiquitously in a number of tissues. *Ucp2* mRNA has been reported in placenta, prostate, ovary, leukocytes (Gong *et al*., 1997), Kupffer cells of the liver (Larrouy *et al*., 1997), BAT, uterus, intestines (Ricquier and Bouillaud, 2000), pancreatic β-cells (Zhang *et al*., 2001), SKM, heart, brain, kidney, lungs, WAT, spleen, thymus, testis, stomach and spinal cord (Rupprecht *et al*., 2012). UCP2 protein has been reported in intestine, WAT (Pecqueur *et al*., 2001), pancreatic β-cells (Zhang *et al*., 2001), BAT, uterus, ovary (Rousset *et al*., 2003), spleen, lung, stomach, brain, thymus, kidney, heart, liver, lymph nodes and leukocytes (Rupprecht *et al*., 2012). However, there are many conflicting reports on the presence and expression of *Ucp2* mRNA and protein in different tissues. Similar to UCP1, UCP3 was thought to be exclusively expressed in one tissue, SKM, following its discovery (Boss *et al*., 1997). However, UCP3 protein (and transcripts) has since been reported in BAT (Cunningham *et al*., 2003), spleen, thymus, reticulocytes, monocytes, lymphocytes (Carroll and Porter, 2004), pancreatic β-cells (Azzu *et al*., 2010) and heart (Hilse *et al*., 2018).

Our laboratory has reported evidence of UCP1 and UCP3 expression in murine thymocytes and spleen mitochondria (Carroll and Porter, 2004; Carroll *et al*., 2004; Carroll *et al*., 2005; Adams *et al*., 2008a, 2008b; Kelly and Porter, 2011), while Krauss *et al*. (2002) reported evidence of UCP2 expression in thymocytes. Thymocytes are derived from lymphoid progenitor cells and develop into mature T cells in the thymus before migrating to peripheral lymphoid tissues, such as the spleen, where they wait to be activated by cells of the innate immune system to carry out an immune response (Krammer *et al*., 2007). Classically, αβ T cells have been divided into two distinct populations of CD4$^+$ and CD8$^+$ T cells. CD4$^+$ T cells play a central role in the defence against pathogens through their actions on cells of both the innate and adaptive immune systems and by guiding and controlling the immune response. They play roles in promoting the production of antibodies by B cells, stimulating macrophages to develop enhanced microbe-killing

activity, recruiting neutrophils, eosinophils and basophils to sites of infection and inflammation and regulating the activities of B cells and CTLs overall. $CD4^+$ T cells also 'license' DCs to effectively activate CTLs by causing them to upregulate CD40 on their cell surface and ligating it with $CD4^+$ T cell-expressed CD40L (Pulendran and Ahmed, 2006; Boyman and Sprent, 2012). Many of these effects are mediated by the production of cytokines and chemokines, small soluble regulatory proteins that allow intercellular communication and cell recruitment.

Our laboratory has demonstrated that *Ucp3* ablation alters the T cell profiles of both thymus and spleen (Kelly and Porter, 2011). The expression of UCPs in thymocytes, along with this finding, suggests the importance of UCPs in thymic function, as well as a potential role in T cell selection, maturation, metabolism and/or function. Thus, we decided to investigate the expression of UCPs in mature $CD4^+$ T cells, both naive cells, non-polarized and polarized subsets, and the role of UCP3 in $CD4^+$ T cell function, the results of which are presented in this chapter.

3.2 Results

3.2.1 *Ucp1*, *Ucp2* and *Ucp3* Transcription is Downregulated in Activated $CD4^+$ T Cells

Following the discovery by our laboratory and Krauss *et al*. (2002) of UCP expression in thymocytes and spleen mitochondria (Carroll and Porter, 2004; Carroll *et al*., 2004; Carroll *et al*., 2005; Adams *et al*., 2008a, 2008b; Kelly and Porter, 2011), we set out to explore the expression of *Ucp1*, *Ucp2* and *Ucp3* in $CD4^+$ T cells using quantitative RT-PCR. This was performed on primary $CD4^+$ T cells following isolation and on cells activated under various stimulatory conditions to induce non-polarized (T_H0) cells and T_H1, T_H17 and T_{reg} cell subsets. Samples were prepared after various lengths of time to determine the relative changes in expression as cells differentiate upon polarization. Samples were taken and analysed every 24 h for 3 days in the case of T_H0, T_H1 and T_H17 cells and for 5 days in the case of T_{reg} cells. Using the comparative C_T method to calculate relative gene expression, cDNA converted from mRNA corresponding to the *Ucp* gene of interest was first normalised to *Hprt* as an endogenous control to account for variability in the initial concentration and quality of the total RNA and in the conversion efficiency of the reverse transcription reaction. Gene expression was then measured by the quantitation of normalised cDNA of the *Ucp* gene of interest relative to that of the naive T cell sample.

Ucp1 expression is significantly decreased in T_H0 cells within 24 h of stimulation compared to naive T cells and remains at a significantly lower level up to 72 h later (Figure 3.1A). Figure 3.1B displays a representative agarose gel for *Ucp1* in naive T cell and T_H0 cell cDNA from the RT-PCR experiments, as well as BAT cDNA as a positive control. Similar to the results of T_H0 cells, the relative expression of *Ucp1* in T_H1 (Figure 3.2), T_H17 (Figure 3.3) and T_{reg} (Figure 3.4) cells compared to naive T cells is significantly decreased within 24 h following stimulation and remains significantly lower until 72 h post-stimulation in the case of T_H1 and T_H17 cells and 120 h post-stimulation in the case of T_{reg} cells.

Ucp2 expression is significantly decreased in T_H0 cells within 24 h of stimulation compared to naive T cells and remains at a significantly lower level up to 72 h later (Figure 3.5A). Figure 3.5B displays a representative agarose gel for *Ucp2* in naive T cell and T_H0 cell cDNA from the RT-PCR experiments. Similar to the results of T_H0 cells, the relative expression of *Ucp2* in T_H1 (Figure 3.6) and T_H17 (Figure 3.7) cells compared to naive T cells is significantly decreased within 24 h following stimulation and remains significantly

lower until 72 h post-stimulation. However, the expression of *Ucp2* in activated T cells did not decrease as low as *Ucp1* gene expression following activation; expression appeared to be approximately halved. While *Ucp2* gene expression appears to decrease within 24 h in T_{reg} cells in a similar manner to that of T_H0 and effector T cells, this is not statistically significant (Figure 3.8). In contrast, the *Ucp2* expression level in T_{reg} cells boomerangs and is actually significantly higher than that of naive T cells 120 h post-stimulation.

Ucp3 expression is significantly decreased in T_H0 cells within 24 h of stimulation compared to naive T cells and remains at a significantly lower level up to 72 h later (Figure 3.9A). Figure 3.9B displays a representative agarose gel for *Ucp3* in naive T cell and T_H0 cell cDNA from the RT-PCR experiments. Similar to the results of T_H0 cells, the relative expression of *Ucp3* in T_H1 (Figure 3.10), T_H17 (Figure 3.11) and T_{reg} (Figure 3.12) cells compared to naive T cells is significantly decreased within 24 h following stimulation and remains significantly lower until 72 h post-stimulation in the case of T_H1 and T_H17 cells and 120 h post-stimulation in the case of T_{reg} cells. The expression of *Ucp3* in the four T cell subsets analysed displays a similar pattern to that of *Ucp1*, significantly decreasing within 24 h of activation and remaining significantly lower until the final time point.

As our data suggest that *Ucp1*, *Ucp2* and *Ucp3* are expressed in naive $CD4^+$ T cells before being downregulated following cell activation (excluding *Ucp2* in T_{reg} cells), we decided to compare the transcription of the three *Ucp* genes in naive $CD4^+$ T cells before cell activation. *Ucp2* expression is significantly higher than both *Ucp1* and *Ucp3* expression in naive $CD4^+$ T cells (Figure 3.13A), being over 8 000-fold higher in expression than *Ucp1* and almost 600-fold higher in expression compared to *Ucp3*. In contrast, *Ucp1* and *Ucp3* expression are not significantly different. Figure 3.13B displays a representative agarose gel for *Ucp1*, *Ucp2* and *Ucp3* in naive T cell cDNA from the RT-PCR experiments. Together, these data demonstrate that *Ucp1*, *Ucp2* and *Ucp3* are expressed in peripheral naive $CD4^+$ T cells, with *Ucp2* being expressed at a much higher level, and are downregulated in response to T cell activation. Judging from this downregulation, with *Ucp2* in T_{reg} cells being the only exception, UCPs may have an important role in naive T cell maintenance in addition to their perceived role in thymic function and T cell selection mentioned previously.

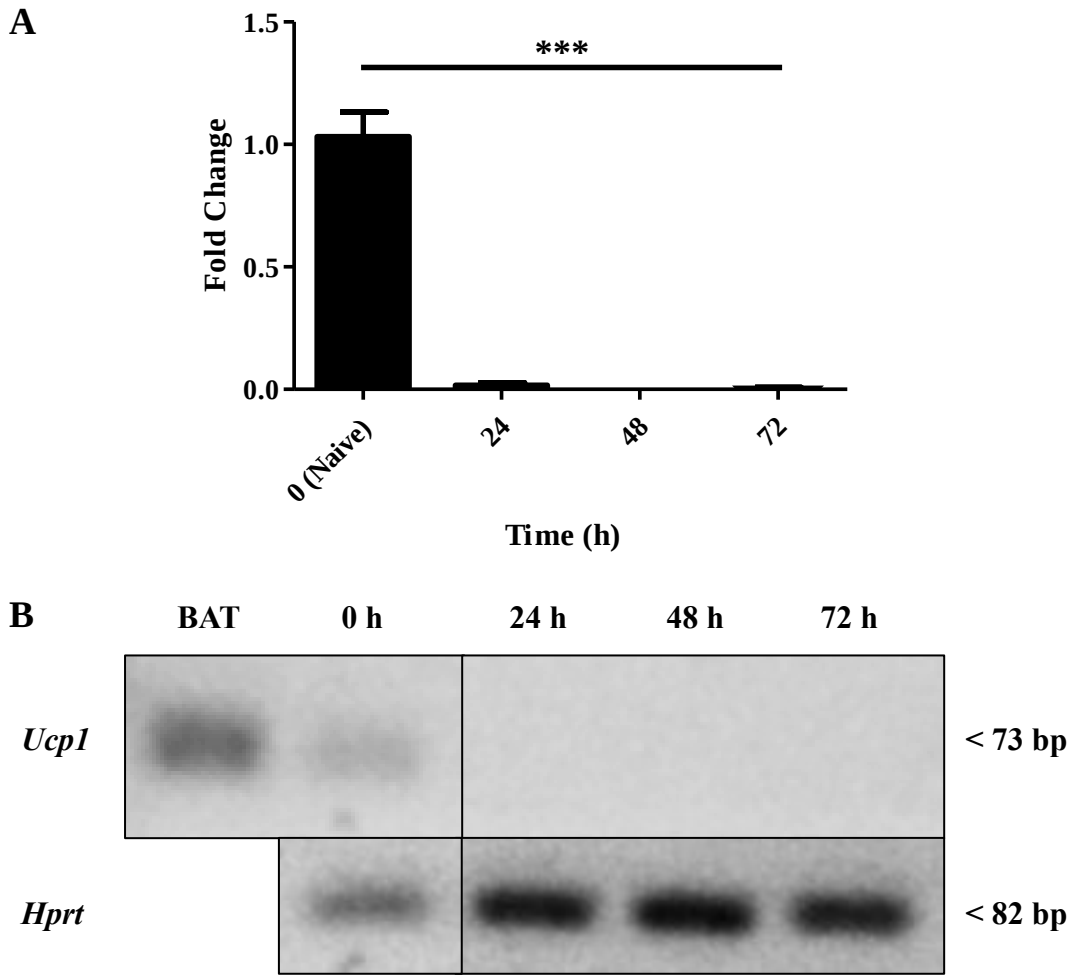

Figure 3.1: *Ucp1* gene expression is downregulated in T_H0 cells

Primary $CD4^+$ T cells were isolated from a suspension of splenocytes and analysed for RT-PCR immediately. T_H0 cells were generated by incubating naive T cells in the presence of 1 and 2 $\mu g.mL^{-1}$ of anti-CD3 and anti-CD28, respectively, for the time indicated before being used for RT-PCR. (A) RT-PCR analysis of *Ucp1* gene expression in T_H0 cells relative to naive T cells. RT-PCR was performed three times in triplicate. Data were analysed using a one-way repeated measures ANOVA with a *post hoc* Dunnet test to quantify significance where detected. *** = $p < 0.001$. (B) Representative agarose gel of naive T cell cDNA and T_H0 cell cDNA prepared at the times indicated, displaying *Ucp1* and *Hprt* at 73 and 82 bp, respectively.

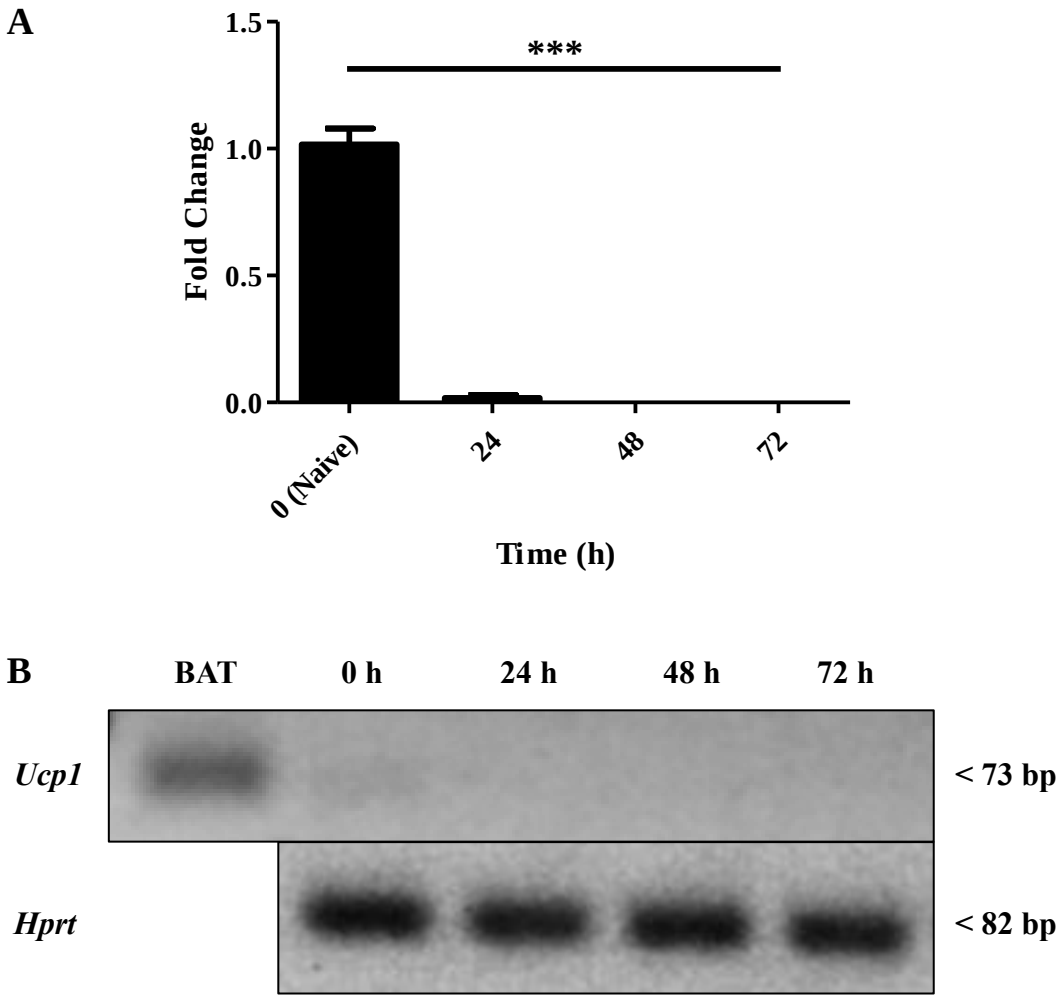

Figure 3.2: *Ucp1* gene expression is downregulated in T_H1 cells

Primary $CD4^+$ T cells were isolated from a suspension of splenocytes and analysed for RT-PCR immediately. T_H1 cells were generated by incubating naive T cells in the presence of 5 $\mu g.mL^{-1}$ of anti-CD3 and anti-CD28 and 10 $ng.mL^{-1}$ of anti-IL-4 and rIL-12 for the time indicated before being used for RT-PCR. (A) RT-PCR analysis of *Ucp1* gene expression in T_H1 cells relative to naive T cells. RT-PCR was performed three times in triplicate. Data were analysed using a one-way repeated measures ANOVA with a *post hoc* Dunnet test to quantify significance where detected. *** = $p < 0.001$. (B) Representative agarose gel of naive T cell cDNA and T_H1 cell cDNA prepared at the times indicated, displaying *Ucp1* and *Hprt* at 73 and 82 bp, respectively.

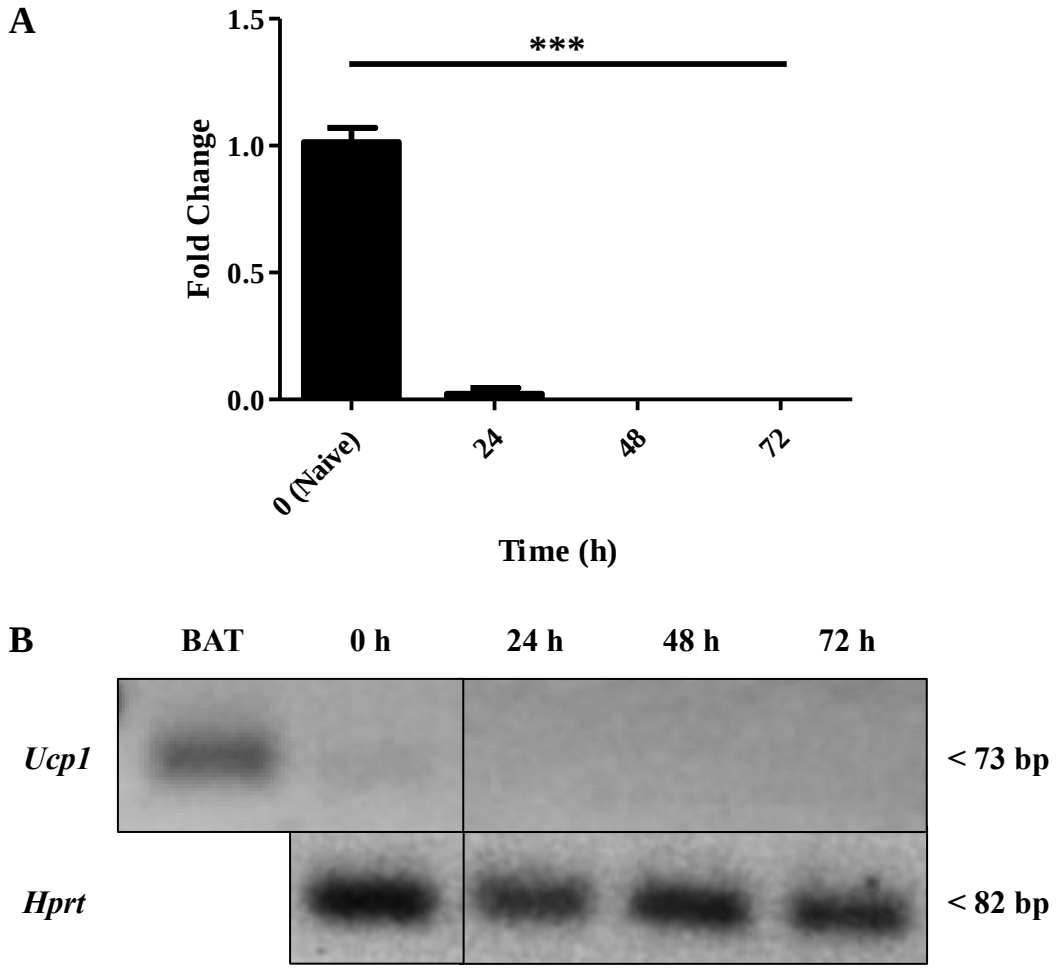

Figure 3.3: *Ucp1* gene expression is downregulated in T_H17 cells

Primary $CD4^+$ T cells were isolated from a suspension of splenocytes and analysed for RT-PCR immediately. T_H17 cells were generated by incubating naive T cells in the presence of 5 µg.mL^{-1} of anti-CD3 and anti-CD28, 20 ng.mL^{-1} of anti-IL-4 and rIL-6, 10 µg.mL^{-1} of anti-IFN-γ and 2.5 ng.mL^{-1} of rhTGF-β1 for the time indicated before being used for RT-PCR. (A) RT-PCR analysis of *Ucp1* gene expression in T_H17 cells relative to naive T cells. RT-PCR was performed three times in triplicate. Data were analysed using a one-way repeated measures ANOVA with a *post hoc* Dunnet test to quantify significance where detected. *** = $p < 0.001$. (B) Representative agarose gel of naive T cell cDNA and T_H17 cell cDNA prepared at the times indicated, displaying *Ucp1* and *Hprt* at 73 and 82 bp, respectively.

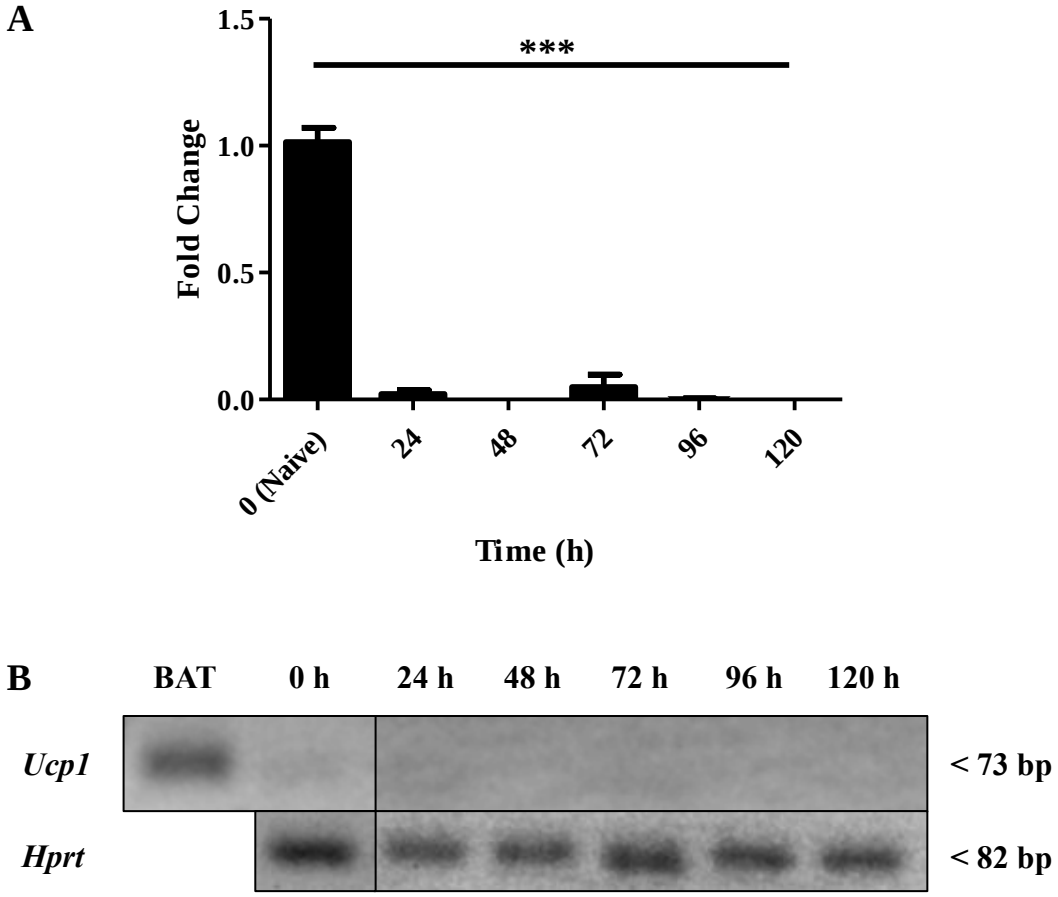

Figure 3.4: *Ucp1* gene expression is downregulated in T_{reg} cells

Primary $CD4^+$ T cells were isolated from a suspension of splenocytes and analysed for RT-PCR immediately. T_{reg} cells were generated by incubating naive T cells in the presence of 1 µg.mL^{-1} of anti-CD3 and anti-CD28, 5 ng.mL^{-1} of rhTGF-β1 and 10 ng.mL^{-1} of rIL-2 for the time indicated before being used for RT-PCR. (A) RT-PCR analysis of *Ucp1* gene expression in T_{reg} cells relative to naive T cells. RT-PCR was performed three times in triplicate. Data were analysed using a one-way repeated measures ANOVA with a *post hoc* Dunnet test to quantify significance where detected. *** = $p < 0.001$. (B) Representative agarose gel of naive T cell cDNA and T_{reg} cell cDNA prepared at the times indicated, displaying *Ucp1* and *Hprt* at 73 and 82 bp, respectively.

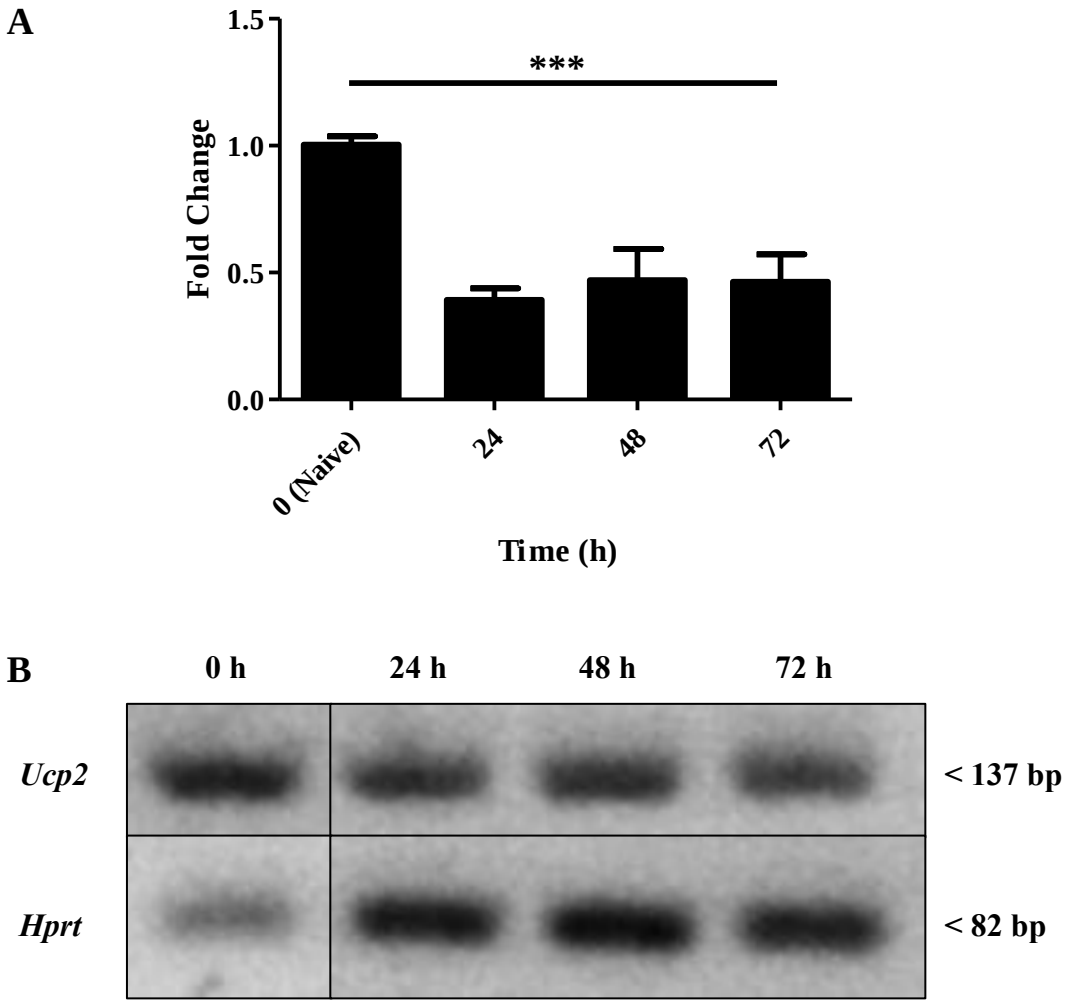

Figure 3.5: *Ucp2* gene expression is downregulated in T_H0 cells

Primary $CD4^+$ T cells were isolated from a suspension of splenocytes and analysed for RT-PCR immediately. T_H0 cells were generated by incubating naive T cells in the presence of 1 and 2 $\mu g.mL^{-1}$ of anti-CD3 and anti-CD28, respectively, for the time indicated before being used for RT-PCR. (A) RT-PCR analysis of *Ucp2* gene expression in T_H0 cells relative to naive T cells. RT-PCR was performed three times in triplicate. Data were analysed using a one-way repeated measures ANOVA with a *post hoc* Dunnet test to quantify significance where detected. *** = $p < 0.001$. (B) Representative agarose gel of naive T cell cDNA and T_H0 cell cDNA prepared at the times indicated, displaying *Ucp2* and *Hprt* at 137 and 82 bp, respectively.

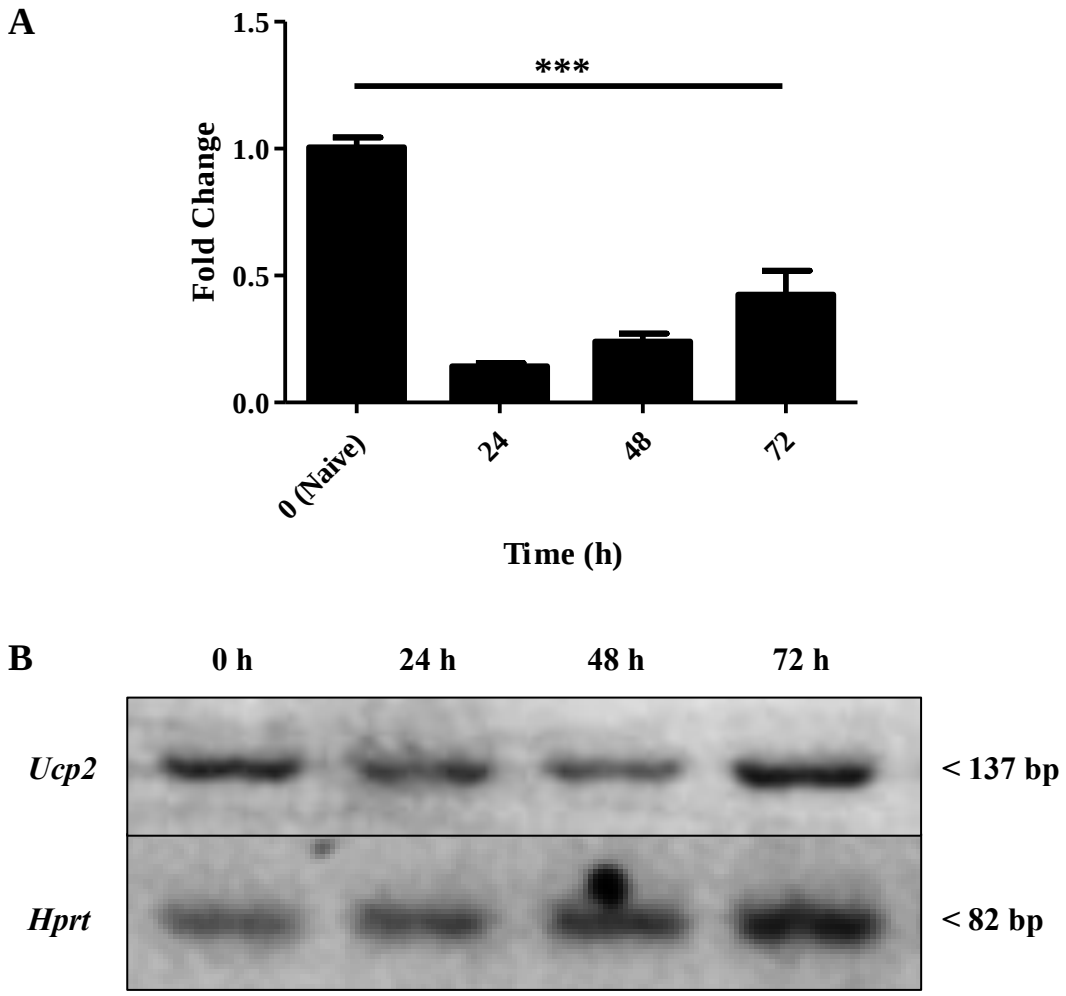

Figure 3.6: *Ucp2* gene expression is downregulated in T_H1 cells

Primary $CD4^+$ T cells were isolated from a suspension of splenocytes and analysed for RT-PCR immediately. T_H1 cells were generated by incubating naive T cells in the presence of 5 $\mu g.mL^{-1}$ of anti-CD3 and anti-CD28 and 10 $ng.mL^{-1}$ of anti-IL-4 and rIL-12 for the time indicated before being used for RT-PCR. (A) RT-PCR analysis of *Ucp2* gene expression in T_H1 cells relative to naive T cells. RT-PCR was performed three times in triplicate. Data were analysed using a one-way repeated measures ANOVA with a *post hoc* Dunnet test to quantify significance where detected. *** = $p < 0.001$. (B) Representative agarose gel of naive T cell cDNA and T_H1 cell cDNA prepared at the times indicated, displaying *Ucp2* and *Hprt* at 137 and 82 bp, respectively.

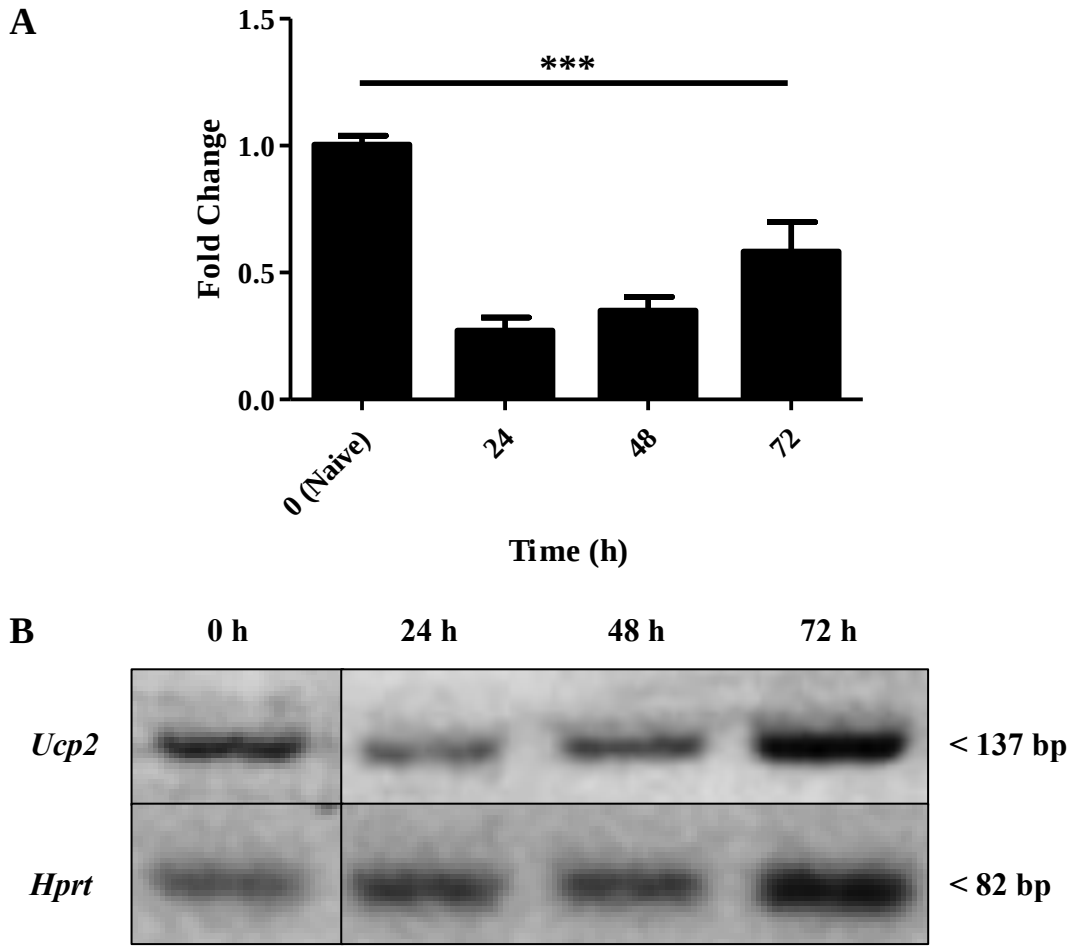

Figure 3.7: *Ucp2* gene expression is downregulated in T_H17 cells

Primary $CD4^+$ T cells were isolated from a suspension of splenocytes and analysed for RT-PCR immediately. T_H17 cells were generated by incubating naive T cells in the presence of 5 µg.mL^{-1} of anti-CD3 and anti-CD28, 20 ng.mL^{-1} of anti-IL-4 and rIL-6, 10 µg.mL^{-1} of anti-IFN-γ and 2.5 ng.mL^{-1} of rhTGF-β1 for the time indicated before being used for RT-PCR. (A) RT-PCR analysis of *Ucp2* gene expression in T_H17 cells relative to naive T cells. RT-PCR was performed three times in triplicate. Data were analysed using a one-way repeated measures ANOVA with a *post hoc* Dunnet test to quantify significance where detected. *** = $p < 0.001$. (B) Representative agarose gel of naive T cell cDNA and T_H17 cell cDNA prepared at the times indicated, displaying *Ucp2* and *Hprt* at 137 and 82 bp, respectively.

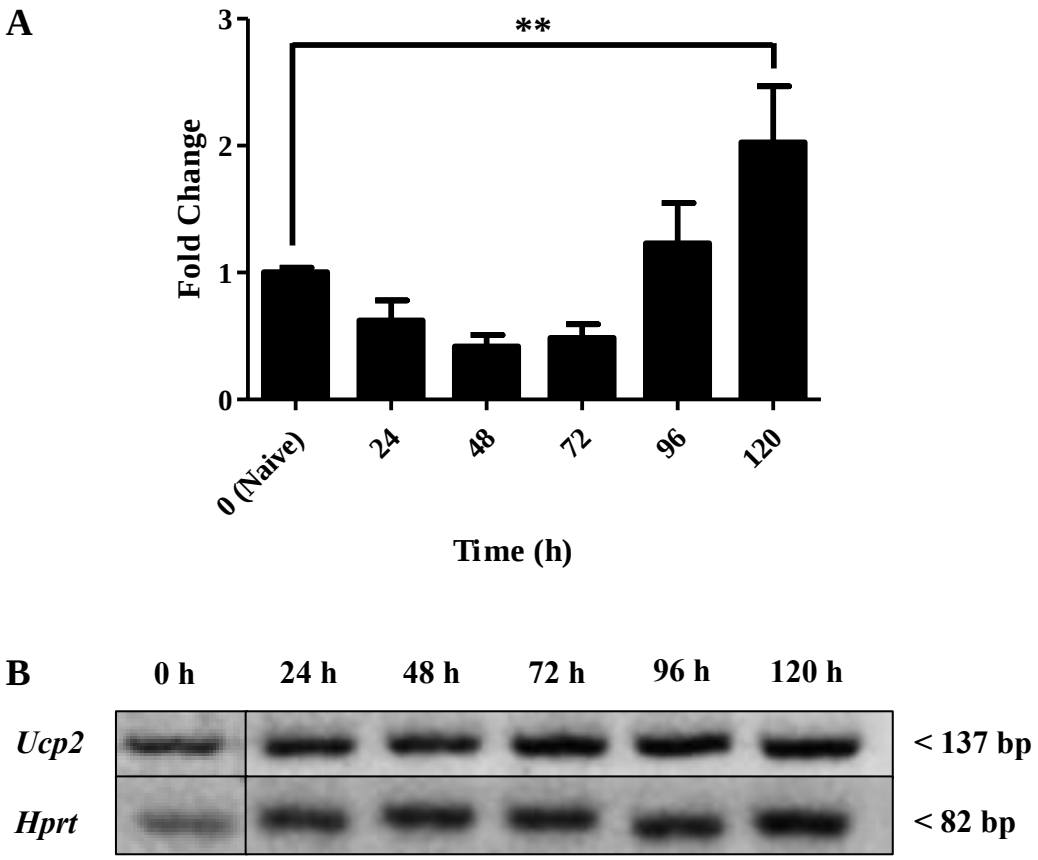

Figure 3.8: *Ucp2* gene expression becomes upregulated in T_{reg} cells

Primary $CD4^+$ T cells were isolated from a suspension of splenocytes and analysed for RT-PCR immediately. T_{reg} cells were generated by incubating naive T cells in the presence of 1 µg.mL^{-1} of anti-CD3 and anti-CD28, 5 ng.mL^{-1} of rhTGF-β1 and 10 ng.mL^{-1} of rIL-2 for the time indicated before being used for RT-PCR. (A) RT-PCR analysis of *Ucp2* gene expression in T_{reg} cells relative to naive T cells. RT-PCR was performed three times in triplicate. Data were analysed using a one-way repeated measures ANOVA with a *post hoc* Dunnet test to quantify significance where detected. ** = $p < 0.01$. (B) Representative agarose gel of naive T cell cDNA and T_{reg} cell cDNA prepared at the times indicated, displaying *Ucp2* and *Hprt* at 137 and 82 bp, respectively.

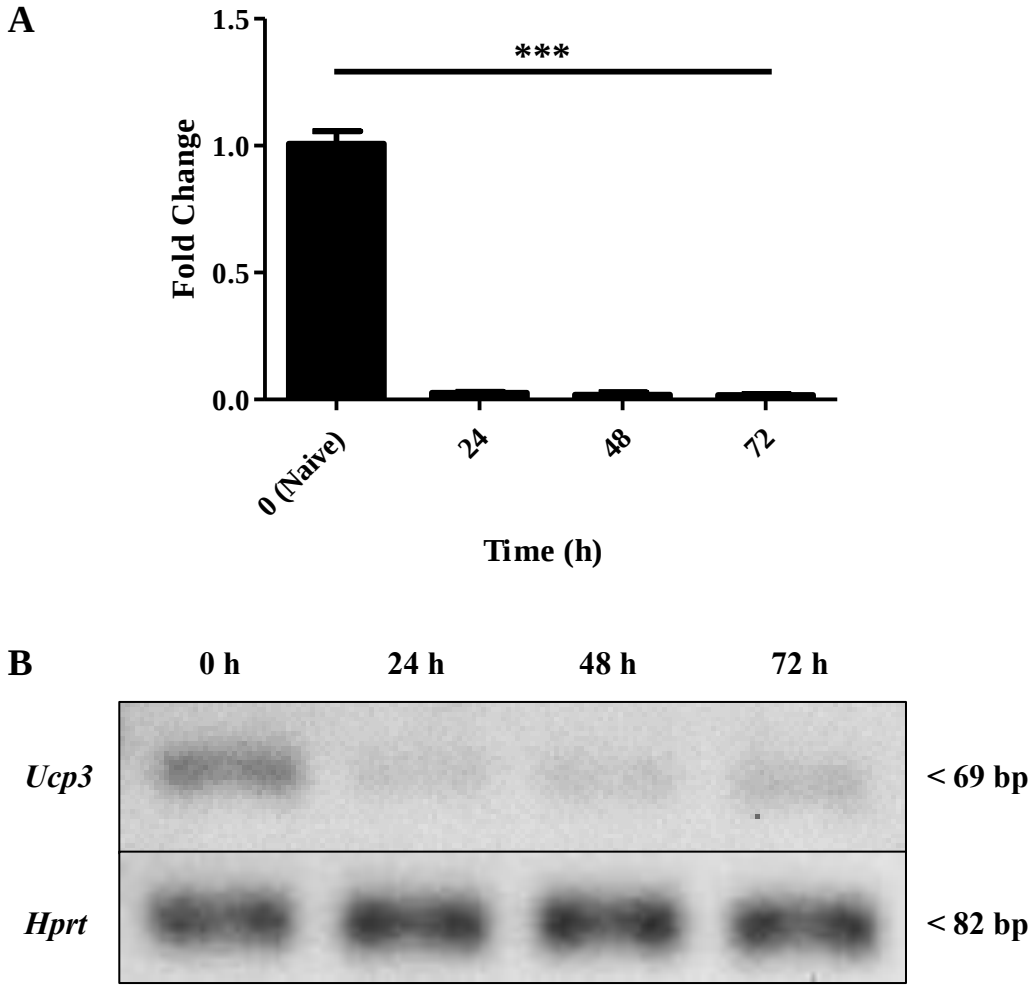

Figure 3.9: *Ucp3* gene expression is downregulated in T_H0 cells

Primary $CD4^+$ T cells were isolated from a suspension of splenocytes and analysed for RT-PCR immediately. T_H0 cells were generated by incubating naive T cells in the presence of 1 and 2 $\mu g.mL^{-1}$ of anti-CD3 and anti-CD28, respectively, for the time indicated before being used for RT-PCR. (A) RT-PCR analysis of *Ucp3* gene expression in T_H0 cells relative to naive T cells. RT-PCR was performed three times in triplicate. Data were analysed using a one-way repeated measures ANOVA with a *post hoc* Dunnet test to quantify significance where detected. *** = $p < 0.001$. (B) Representative agarose gel of naive T cell cDNA and T_H0 cell cDNA prepared at the times indicated, displaying *Ucp3* and *Hprt* at 69 and 82 bp, respectively.

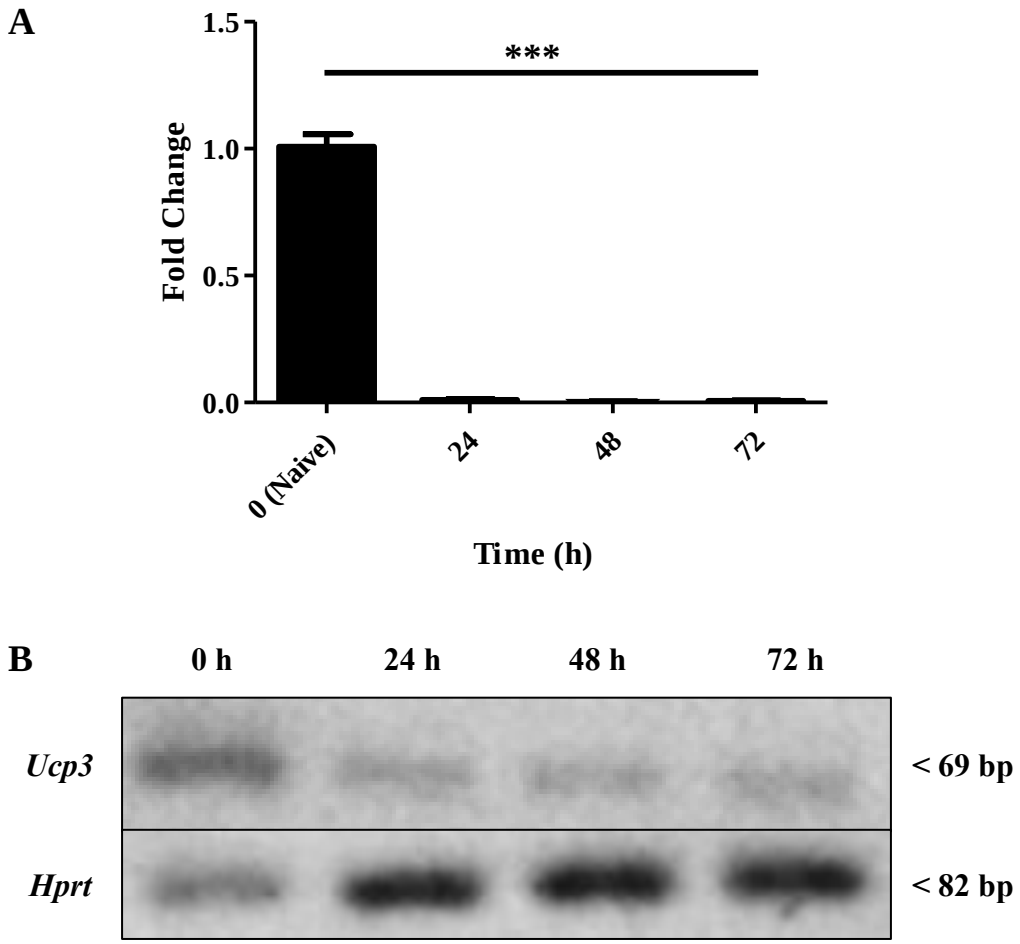

Figure 3.10: *Ucp3* gene expression is downregulated in T_H1 cells

Primary $CD4^+$ T cells were isolated from a suspension of splenocytes and analysed for RT-PCR immediately. T_H1 cells were generated by incubating naive T cells in the presence of 5 µg.mL^{-1} of anti-CD3 and anti-CD28 and 10 ng.mL^{-1} of anti-IL-4 and rIL-12 for the time indicated before being used for RT-PCR. (A) RT-PCR analysis of *Ucp3* gene expression in T_H1 cells relative to naive T cells. RT-PCR was performed three times in triplicate. Data were analysed using a one-way repeated measures ANOVA with a *post hoc* Dunnet test to quantify significance where detected. *** = $p < 0.001$. (B) Representative agarose gel of naive T cell cDNA and T_H1 cell cDNA prepared at the times indicated, displaying *Ucp3* and *Hprt* at 69 and 82 bp, respectively.

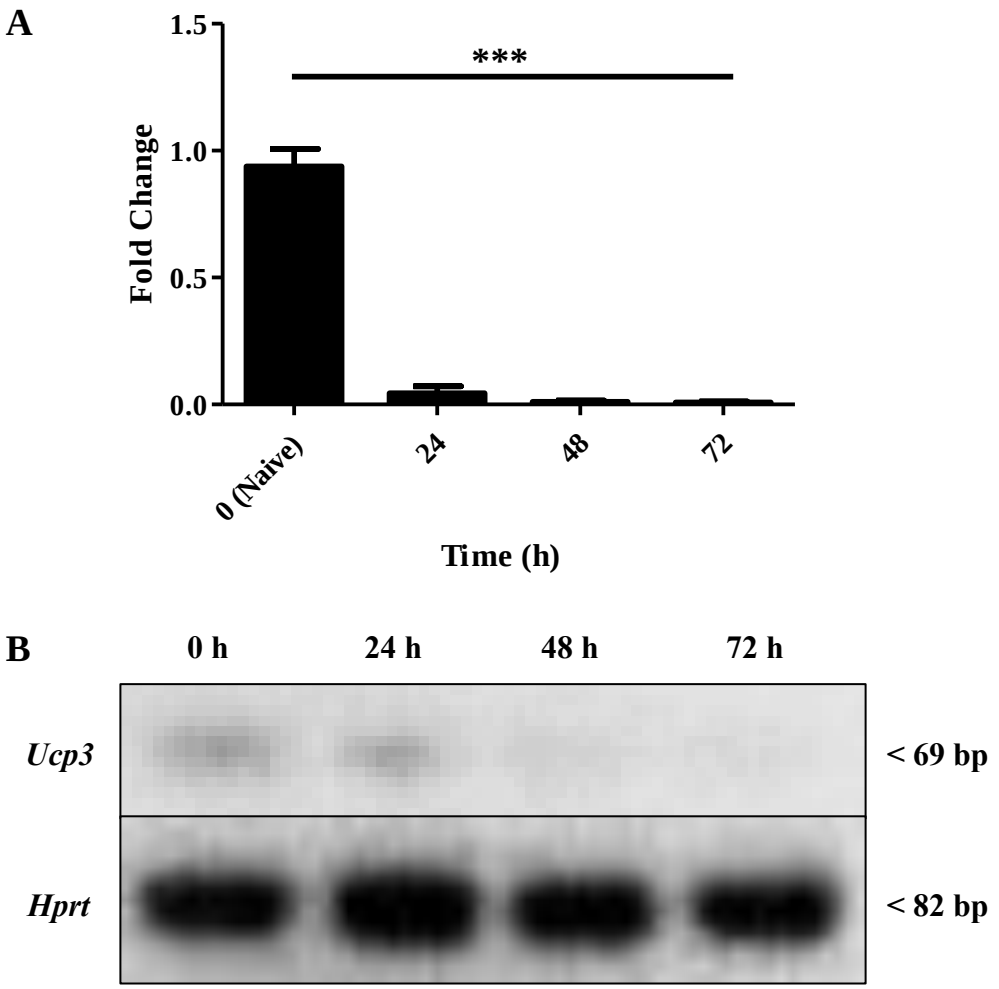

Figure 3.11: *Ucp3* gene expression is downregulated in T_H17 cells

Primary $CD4^+$ T cells were isolated from a suspension of splenocytes and analysed for RT-PCR immediately. T_H17 cells were generated by incubating naive T cells in the presence of 5 µg.mL^{-1} of anti-CD3 and anti-CD28, 20 ng.mL^{-1} of anti-IL-4 and rIL-6, 10 µg.mL^{-1} of anti-IFN-γ and 2.5 ng.mL^{-1} of rhTGF-β1 for the time indicated before being used for RT-PCR. (A) RT-PCR analysis of *Ucp3* gene expression in T_H17 cells relative to naive T cells. RT-PCR was performed three times in triplicate. Data were analysed using a one-way repeated measures ANOVA with a *post hoc* Dunnet test to quantify significance where detected. *** = $p < 0.001$. (B) Representative agarose gel of naive T cell cDNA and T_H17 cell cDNA prepared at the times indicated, displaying *Ucp3* and *Hprt* at 69 and 82 bp, respectively.

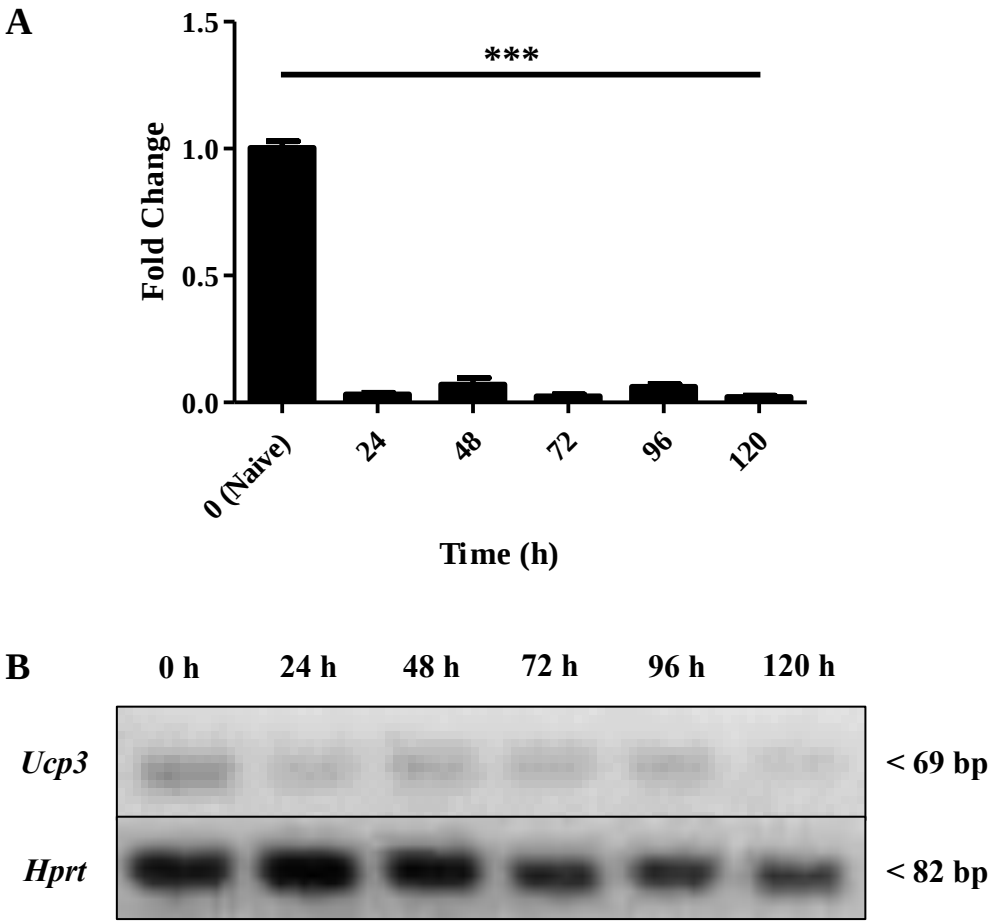

Figure 3.12: *Ucp3* gene expression is downregulated in T_{reg} cells

Primary $CD4^+$ T cells were isolated from a suspension of splenocytes and analysed for RT-PCR immediately. T_{reg} cells were generated by incubating naive T cells in the presence of 1 µg.mL^{-1} of anti-CD3 and anti-CD28, 5 ng.mL^{-1} of rhTGF-β1 and 10 ng.mL^{-1} of rIL-2 for the time indicated before being used for RT-PCR. (A) RT-PCR analysis of *Ucp3* gene expression in T_{reg} cells relative to naive T cells. RT-PCR was performed three times in triplicate. Data were analysed using a one-way repeated measures ANOVA with a *post hoc* Dunnet test to quantify significance where detected. *** = $p < 0.001$. (B) Representative agarose gel of naive T cell cDNA and T_{reg} cell cDNA prepared at the times indicated, displaying *Ucp3* and *Hprt* at 69 and 82 bp, respectively.

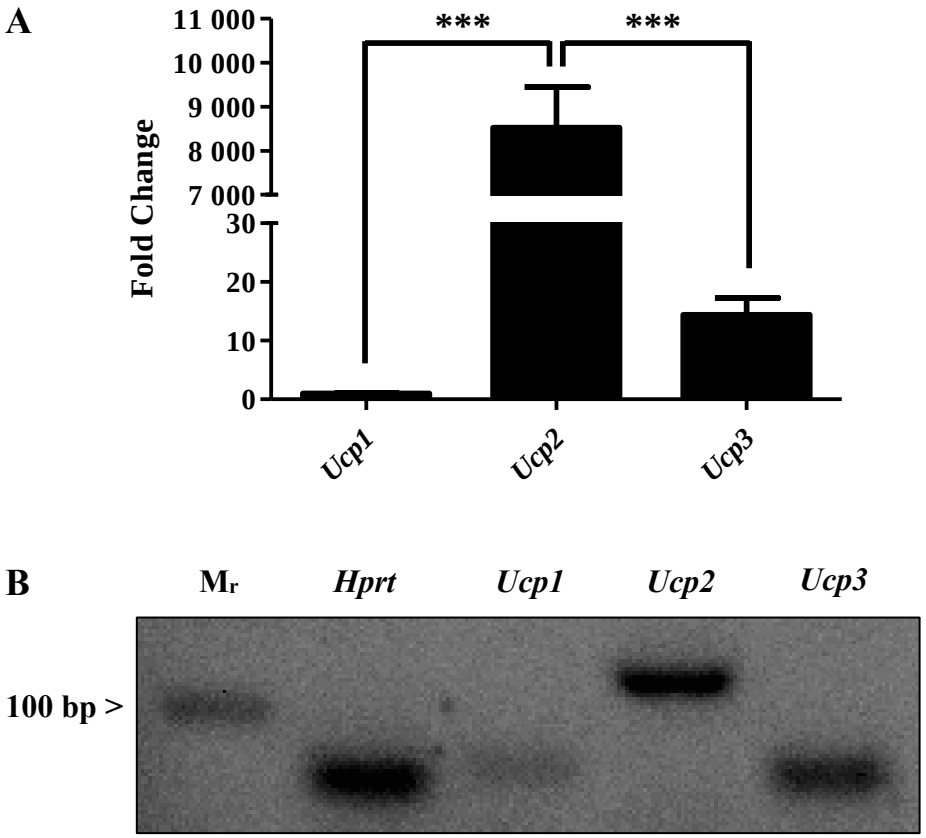

Figure 3.13: Comparison of *Ucp* gene expression in naive CD4$^+$ T cells

Primary CD4$^+$ T cells were isolated from a suspension of splenocytes and analysed for RT-PCR immediately. (A) RT-PCR analysis of *Ucp1*, *Ucp2* and *Ucp3* gene expression in naive CD4$^+$ T cells. RT-PCR was performed three times in triplicate. Data were analysed using a one-way ANOVA with a *post hoc* Bonferroni test to quantify significance where detected. *** = $p < 0.001$. (B) Representative agarose gel of naive T cell cDNA displaying *Hprt*, *Ucp1*, *Ucp2* and *Ucp3* at 82, 73, 137 and 69 bp, respectively.

3.2.2 UCP3 Protein Is Not Detected In *Ucp3*$^{-/-}$ Mice

UCP3 protein is clearly visible in thymocytes from WT mice but not in thymocytes from *Ucp3*$^{-/-}$ mice, as shown by Kelly and Porter (2011), and its deficiency alters the T cell profile of the thymus and spleen. We have demonstrated that it is expressed in naive CD4^{+} T cells at the mRNA level before being downregulated upon TCR and CD28-dependent T cell activation (Figures 3.9 – 3.12). *Ucp3*$^{+/-}$ mice breeding in our facility allowed us to easily breed *Ucp3*$^{+/+}$ mice in house as littermate controls for our experiments. C57BL/6J WT controls for *Ucp1*$^{-/-}$ and *Ucp2*$^{-/-}$ mice had to be outsourced and purchased from a supplier which, we considered, would add an unwanted level of variability to our *Ucp1* and *Ucp2* experiments. Thus, we decided to follow on from the original work of our laboratory in 2011 and pursue the role of *Ucp3* only in CD4^{+} T cells, excluding *Ucp1* and *Ucp2*.

While detection of *Ucp* transcript is useful, it is not necessarily representative of the expression of the functional entity, *i.e.* the protein (Krauss *et al*., 2005; Kendrick, 2014; Rupprecht *et al*., 2014). This has clearly been the case for UCP2, transcripts of which have been found in placenta, prostate (Gong *et al*., 1997), Kupffer cells of the liver (Larrouy *et al*., 1997), SKM, testis and spinal cord (Rupprecht *et al*., 2012) but yet protein detection has been confined to specific tissues, namely intestine, WAT (Pecqueur *et al*., 2001), pancreatic β-cells (Zhang *et al*., 2001), BAT, uterus, ovary (Rousset *et al*., 2003), spleen, lung, stomach, brain, thymus, kidney, heart, liver, lymph nodes and leukocytes (Rupprecht *et al*., 2012). Thus, having demonstrated that the expression of *Ucp3* is decreased at the mRNA level upon activation of CD4^{+} T cells, western blotting was performed to explore the expression of UCP3 protein. Despite a number of commercial antibodies being available, as well as peptide antibodies to UCP3 being developed in-house by a number of groups (Vidal-Puig *et al*., 2000; Hesselink *et al*., 2001), the sensitivity and discriminatory nature of the antibodies to other UCPs and mitochondrial transporters in general has not been satisfactorily demonstrated in many cases (Cunningham *et al*., 2003). We used a peptide antibody generated by Eurogentec exclusively for our laboratory and which we have previously characterized and shown to be sensitive and discriminatory for UCP3 over UCP1, UCP2 and other mitochondrial proteins (see Cunningham *et al*., 2003). As UCP3 is known to be expressed most abundantly in SKM, SKM cell lysates from *Ucp3*$^{+/+}$ and *Ucp3*$^{-/-}$ mice were used as positive and negative controls, respectively. PDHe1α was used as a loading control as it is a MIM protein, similar to UCP3. However, due to poor protein yields, efforts to detect UCP3 protein in T cell sample lysates were unsuccessful. Thus, Figure 3.14A displays an immunoblot for UCP3 and PDHe1α as loading control performed

on lysates from *Ucp3*$^{+/+}$ and *Ucp3*$^{-/-}$ SKM control samples only. As expected, a 33 kDa band for UCP3 was detected in the positive control lane containing protein from a *Ucp3*$^{+/+}$ SKM lysate sample. No band for UCP3 was detected in the negative control lane containing protein from the *Ucp3*$^{-/-}$ SKM lysate sample.

In order to confirm whether UCP3 protein is expressed in CD4^{+} T cells, we decided to try other avenues of investigation. We performed FACS on *Ucp3*$^{+/+}$ and *Ucp3*$^{-/-}$ naive CD4^{+} T cells. Figure 3.14B displays representative histograms of *Ucp3*$^{+/+}$ and *Ucp3*$^{-/-}$ naive CD4^{+} T cells stained with our anti-UCP3 antibody followed by a secondary goat anti-rabbit antibody conjugated to Alexa Fluor® 647. Also displayed is a histogram representing *Ucp3*$^{+/+}$ naive CD4^{+} T cells stained with secondary antibody only as a 'no primary control' (NPC). Although very small, a shift to the right in the fluorescence of the *Ucp3*$^{+/+}$ sample can be seen in comparison to the *Ucp3*$^{-/-}$ sample (as well as the NPC, as expected). This is thought to be due to the detection of UCP3 in the WT sample that is absent in the KO sample. The staining detected in the KO sample is assumed to be due to non-specific binding. This suggests that, while expression may be extremely low, UCP3 is expressed in *Ucp3*$^{+/+}$ naive CD4^{+} T cells. In line with this, there was a consistent trend for the *Ucp3*$^{+/+}$ median fluorescence intensity (MFI) values to be higher than the *Ucp3*$^{-/-}$ values, although the differences were not statistically significant (Figure 3.14C). An extremely low level of expression may have contributed to our difficulty in detecting this protein by western blot. Indeed, van der Windt and Pearce (2012) reported that effector T cells have very few mitochondria, much less than memory T cells.

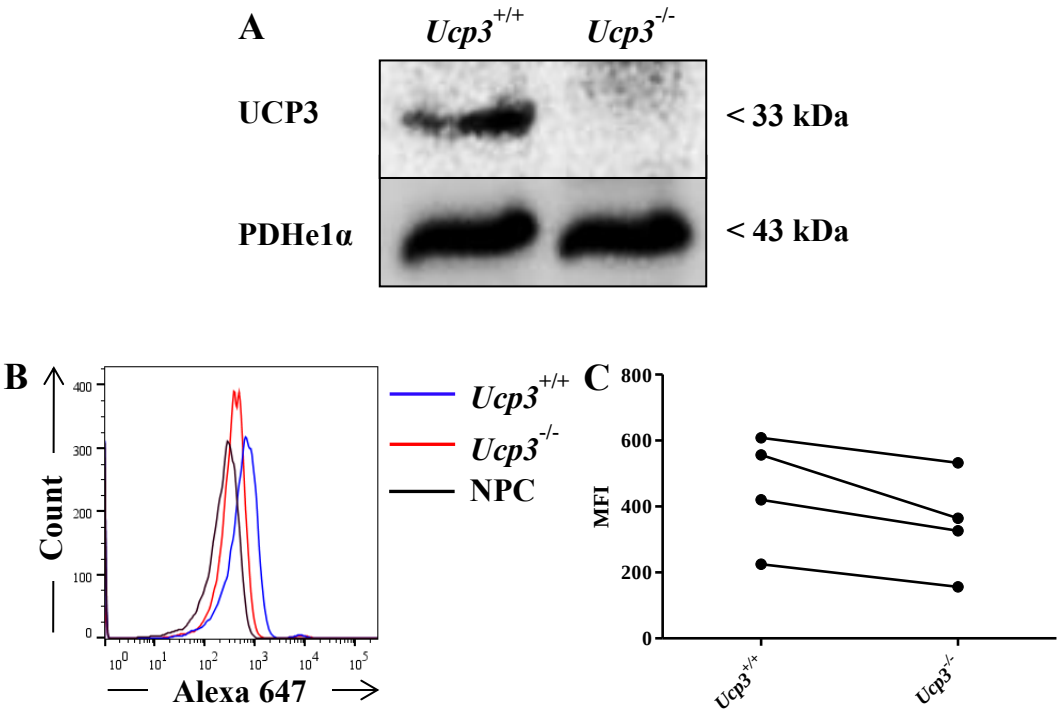

Figure 3.14: UCP3 protein detection in SKM and naive CD4$^+$ T cells

SKM cell lysates were prepared as in the text. Primary CD4$^+$ T cells were isolated from a suspension of splenocytes and analysed by flow cytometry immediately. (A) Representative immunoblot of UCP3 and PDHe1α protein in *Ucp3*$^{+/+}$ and *Ucp3*$^{-/-}$ SKM cell lysates. Immunoblot was performed three times. Lysates were resolved on a 15 % SDS-PAGE gel and transferred to a PVDF membrane for immunodetection. (B) Histogram of UCP3 detection in naive CD4$^+$ T cells by flow cytometry. Histogram is of the viable, CD4$^+$ T cell population and is representative of at least three different experiments. (C) MFI values of Alexa Fluor® 647 staining from at least three different experiments. Data were analysed using a two-tailed, unpaired *t* test to quantify significance where detected.

3.2.3 *Ucp3* Ablation Affects T_H0 Cells

We have demonstrated that *Ucp3* is expressed in naive $CD4^+$ T cells at the mRNA level before being downregulated upon TCR and CD28-dependent T cell activation (Figures 3.9 – 3.12), while UCP3 deficiency has been shown to alter the T cell profile of the thymus and spleen (Kelly and Porter, 2011). To further these findings, we next explored the effect of *Ucp3* ablation on activated, non-polarized $CD4^+$ T cell function. Primary $Ucp3^{+/+}$ and $Ucp3^{-/-}$ $CD4^+$ T cells were harvested direct from spleens and T_H0 cells were generated by incubating naive T cells in the presence of anti-CD3 and/or anti-CD28 for the indicated time. We used titrated concentrations of anti-CD3 and anti-CD28 where indicated in order to detect any subtle differences that may exist between $Ucp3^{+/+}$ and $Ucp3^{-/-}$ T_H0 cells.

IL-2 is one of the first cytokines to be produced by and secreted from all activated $CD4^+$ T cells in response to appropriate co-stimulation through the TCR and CD28 co-receptor (Crispin and Tsokos, 2009; Boyman and Sprent, 2012; Liao *et al*., 2013). As our data indicate that *Ucp3* gene expression is also under the control of these signalling pathways, we explored the effect of *Ucp3* ablation on T_H0 cell function by measuring IL-2 production 24 h post-stimulation. Flow cytometry was performed to investigate the frequency of activated T cells producing IL-2 and ELISAs were performed on cell supernatants to measure IL-2 secretion. While no differences between genotypes were detected in the presence of titrated anti-CD3 by flow cytometry (Figure 3.15A – G), IL-2 secretion was significantly greater by $Ucp3^{-/-}$ T_H0 cells than $Ucp3^{+/+}$ T_H0 cells in the presence of 1, 1.25 and 1.5 $\mu g.mL^{-1}$ of anti-CD3 (Figure 3.15H). This inconsistency between the flow cytometry and ELISA data is thought to be due to the restimulation of cells before flow cytometry analysis. PMA is used to restimulate cells for 6 h, resulting in a triggered increase in cytokine production. The difference in IL-2 production evident in the ELISA may be masked by PMA causing such an increase in cytokine production. Under anti-CD28 titration conditions, IL-2 production was higher in $Ucp3^{-/-}$ T_H0 cells than $Ucp3^{+/+}$ T_H0 cells. This was evident by flow cytometry in the form of increased percentages of PE:anti-$IL\text{-}2^+$ $Ucp3^{-/-}$ T_H0 cells compared to PE:anti-$IL\text{-}2^+$ $Ucp3^{+/+}$ T_H0 cells (Figure 3.16A – E) and by ELISA in the form of significantly higher IL-2 secretion from $Ucp3^{-/-}$ T_H0 cells in the presence of 1.5 and 2 $\mu g.mL^{-1}$ of anti-CD28 (Figure 3.16F). These data were further supported by measuring IL-2 production in the presence of titrated anti-CD3 with 2 $\mu g.mL^{-1}$ of anti-CD28 (Figure 3.17) and titrated anti-CD28 with 1 $\mu g.mL^{-1}$ of anti-CD3 (Figure 3.18). During the anti-CD3 titration with anti-CD28, more PE:anti-$IL\text{-}2^+$ $Ucp3^{-/-}$ T_H0 cells were observed than PE:anti-$IL\text{-}2^+$ $Ucp3^{+/+}$ T_H0 cells at lower concentrations of anti-CD3

stimulation (Figure 3.17A and C), while the difference disappeared in the presence of higher concentrations. IL-2 secretion was significantly higher from *Ucp3*$^{-/-}$ cells following stimulation with all concentrations of anti-CD3 with 2 μg.mL^{-1} of anti-CD28 except 0 μg.mL^{-1} (Figure 3.17G). Although no increase in the percentage of PE:anti-IL-2^{+} *Ucp3*$^{-/-}$ T_H0 cells compared to WTs was observed by flow cytometry during the anti-CD28 titration with anti-CD3 (Figure 3.18A – I), IL-2 secretion measured by ELISA was significantly higher by *Ucp3*$^{-/-}$ T_H0 cells in the presence of 2.5, 3 and 3.5 μg.mL^{-1} of anti-CD28 with 1 μg.mL^{-1} of anti-CD3 (Figure 3.18J). This discrepancy is again thought to be due to the PMA effect before flow cytometry analysis.

These data indicate that UCP3 may play a role in restricting IL-2 expression in response to TCR and CD28 co-stimulation. In order to further investigate these effects observed in *Ucp3*$^{-/-}$ T_H0 cells under different conditions, we analysed the expression of CD25 on T_H0 cells. CD25 is also known as IL-2Rα, the α subunit present in the receptor for IL-2 (Boyman and Sprent, 2012). CD25 is absent or minimally expressed on resting T cells but its transcription is potently induced following stimulation via the TCR or contact with IL-2 (Boyman and Sprent, 2012; Liao *et al*., 2013). CD25 does not appear to participate in signalling but increases affinity of the IL-2R for its ligand; IL-2 is known to stimulate the expression of CD25 following TCR activation to increase cell responsiveness in a positive feedback mechanism (Boyman and Sprent, 2012; Liao *et al*., 2013; Preston *et al*., 2015). Thus, if IL-2 is consistently upregulated in *Ucp3*$^{-/-}$ T_H0 cells, this should be mirrored by an increased expression of CD25. In order to ensure subtle differences would be detected and due to the biggest differences in IL-2 secretion between *Ucp3*$^{+/+}$ and *Ucp3*$^{-/-}$ T_H0 cells being observed during the anti-CD3 titration (Figure 3.15H), we decided to measure CD25 expression of T_H0 cells following stimulation with titrated anti-CD3 alone. CD25 expression is clearly higher in *Ucp3*$^{-/-}$ T_H0 cells compared to *Ucp3*$^{+/+}$ T_H0 cells following stimulation with lower concentrations of anti-CD3 (*i.e.* 0.25 and 0.5 μg.mL^{-1}; Figure 3.19A, B and G). Stimulation with higher concentrations results in the difference diminishing (Figure 3.19C – G). That IL-2 is produced at a significantly higher level in *Ucp3*$^{-/-}$ T_H0 cells, as well as these cells displaying increased CD25 expression, suggests that these cells are becoming activated earlier than *Ucp3*$^{+/+}$ T_H0 cells. CD69 is an early activation marker that is expressed at low levels on the surface of naive CD4^{+} T cells and increases in expression following cell activation (Preston *et al*., 2015; Kang *et al*., 2016). Hence, we measured CD69 expression to see if a concomitant increase would be observed on *Ucp3*$^{-/-}$ T_H0 cells. Indeed, a subtle increase of CD69 expression is observed in *Ucp3*$^{-/-}$

T_H0 cells following stimulation with 0.25 µg.mL^{-1} of anti-CD3 (Figure 3.20A and D) but this difference quickly disappears following stimulation with higher concentrations of anti-CD3 (Figure 3.20B – D).

Following secretion from activated CD4$^+$ T cells, IL-2 is known to modulate the proliferation of T and B lymphocytes (Boyman and Sprent, 2012). To further explore the effects of *Ucp3* ablation on T_H0 cells and the consequential increase in IL-2 production, we compared the proliferation of *Ucp3*$^{+/+}$ and *Ucp3*$^{-/-}$ T_H0 cells by staining them with CellTrace™ Violet and stimulating them for 72 h before analysing them by flow cytometry. CellTrace™ Violet labelling permits the determination of the number of generations through which a cell has progressed since the label was applied. As expected, more *Ucp3*$^{-/-}$ T_H0 cells undergo cell division than their WT counterparts following 72 h of stimulation with low concentrations of anti-CD3 (0.25 µg.mL^{-1}; Figure 3.21). To compliment these data, we also analysed Ki-67 expression of T_H0 cells 24, 48 and 72 h post-stimulation with titrated anti-CD3. Ki-67 is often used as a marker for cell proliferation as it is expressed during all active phases of the cell cycle (G_1, S, G_2 and mitosis) but is absent in quiescent cells (G_0; Scholzen and Gerdes, 2000). As *Ucp3*$^{-/-}$ T_H0 cells appeared to be undergoing cell activation earlier and proliferating more than their WT counterparts, we hypothesized that they would display increased Ki-67 expression sooner than *Ucp3*$^{+/+}$ T_H0 cells. Surprisingly, no significant difference between the Ki-67 expression of *Ucp3*$^{+/+}$ and *Ucp3*$^{-/-}$ T_H0 cells is detected after each time point (Figures 3.22 – 3.24). However, the growth fraction of a population, indicated by Ki-67 labelling, relates to the number of proliferative cells and not necessarily to the time needed for completion of an intermitotic cycle (Scholzen and Gerdes, 2000). Thus, Ki-67 labelling gives information only about the state but not the rate of proliferation (Scholzen and Gerdes, 2000). While a similar frequency of *Ucp3*$^{+/+}$ and *Ucp3*$^{-/-}$ T_H0 cells may be proliferating or about to proliferate, as indicated by Ki-67 labelling, the *Ucp3*$^{-/-}$ T_H0 cells may be proliferating at a faster rate, which would result in the data observed in Figure 3.21.

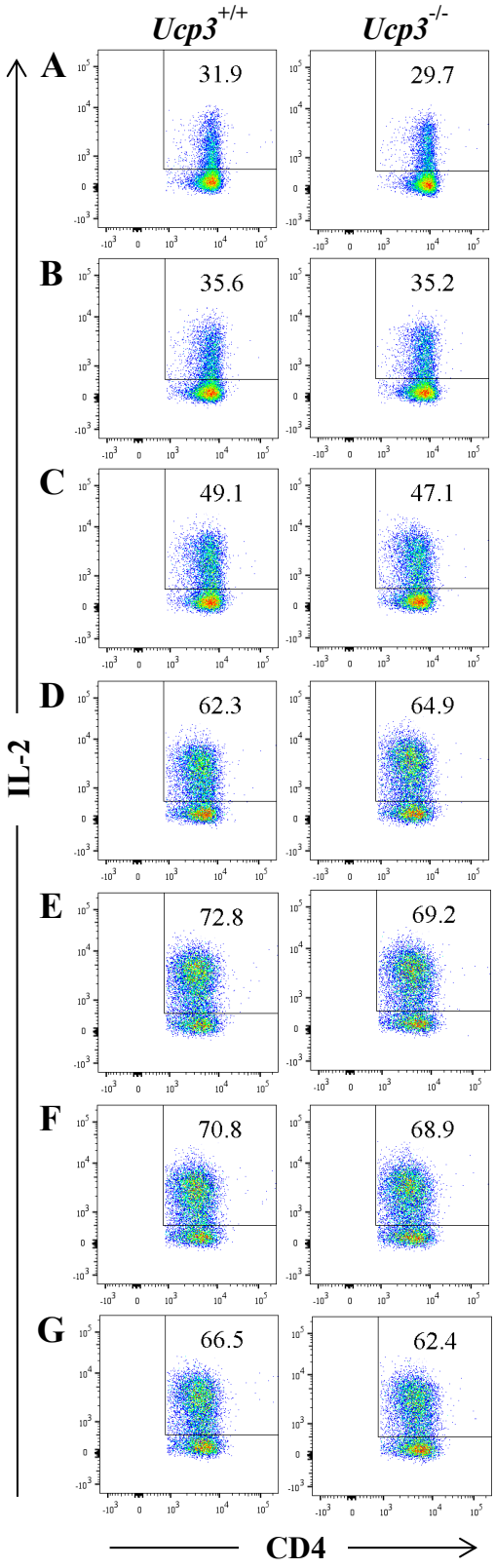

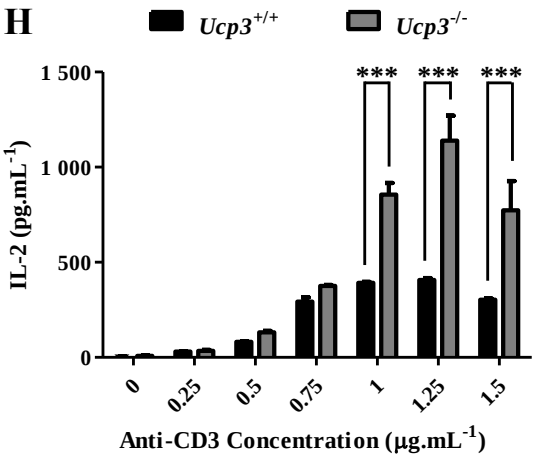

Figure 3.15: IL-2 production is increased in *Ucp3*$^{-/-}$ T_H0 cells in the presence of increasing concentrations of anti-CD3

T_H0 cells were generated by incubating naive T cells in the presence of 0 (A), 0.25 (B), 0.5 (C), 0.75 (D), 1 (E), 1.25 (F) or 1.5 (G) µg.mL^{-1} of anti-CD3 for 24 h. Cells were restimulated with PMA, ionomycin and brefeldin A for 6 h before being stained with LIVE/DEAD™, PE-Cy7:anti-CD4 and PE:anti-IL-2 and analysed on a flow cytometer. Flow cytometry was performed once. Data are presented as a percentage of the viable, CD4$^+$ T cell population. (H) IL-2 secretion of T_H0 cells 24 h post-incubation with increasing concentrations of anti-CD3. ELISA was performed once with twelve technical replicates. Data were analysed using a two-way ANOVA with a *post hoc* Bonferroni test to quantify significance where detected. *** = $p <$ 0.001.

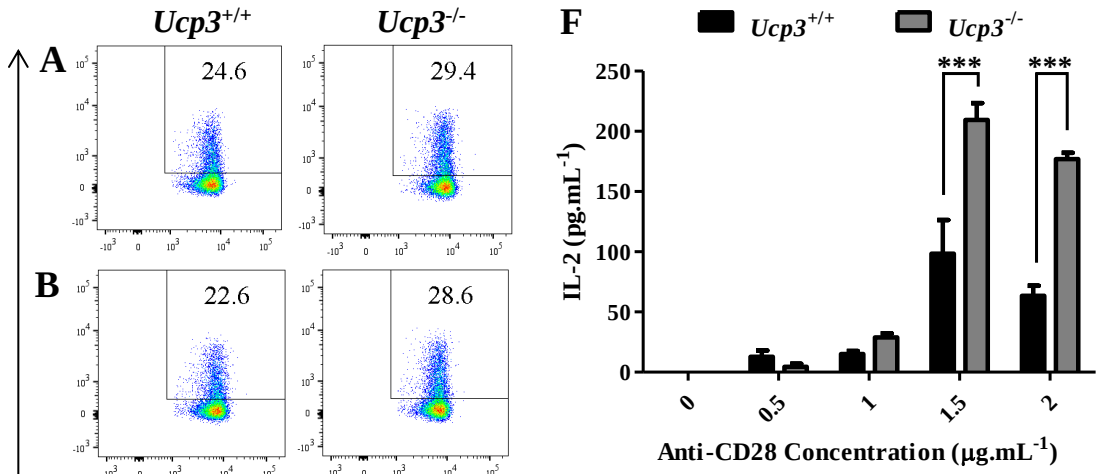

Figure 3.16: IL-2 production is increased in *Ucp3*$^{-/-}$ T_H0 cells in the presence of increasing concentrations of anti-CD28

T_H0 cells were generated by incubating naive T cells in the presence of 0 (A), 0.5 (B), 1 (C), 1.5 (D) or 2 (E) µg.mL^{-1} of anti-CD28 for 24 h. Cells were restimulated with PMA, ionomycin and brefeldin A for 6 h before being stained with LIVE/DEAD™, PE-Cy7:anti-CD4 and PE:anti-IL-2 and analysed on a flow cytometer. Flow cytometry was performed once. Data are presented as a percentage of the viable, CD4$^+$ T cell population. (F) IL-2 secretion of T_H0 cells 24 h post-incubation with increasing concentrations of anti-CD28. ELISA was performed once with twelve technical replicates. Data were analysed using a two-way ANOVA with a *post hoc* Bonferroni test to quantify significance where detected. *** = $p < 0.001$.

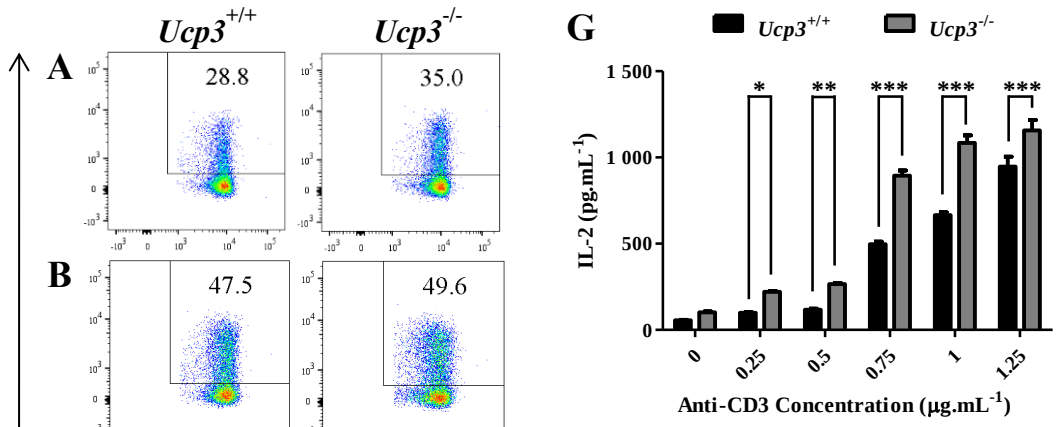

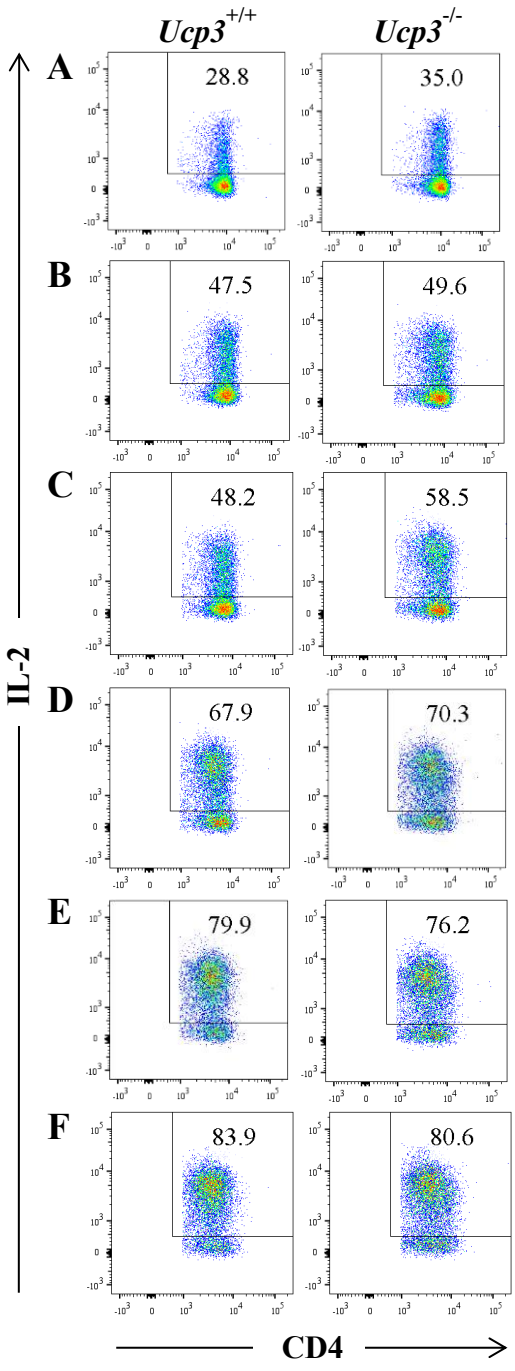

Figure 3.17: IL-2 production is increased in *Ucp3*$^{-/-}$ T_H0 cells in the presence of increasing concentrations of anti-CD3 and 2 µg.mL^{-1} of anti-CD28

T_H0 cells were generated by incubating naive T cells in the presence of 0 (A), 0.25 (B), 0.5 (C), 0.75 (D), 1 (E) or 1.25 (F) µg.mL^{-1} of anti-CD3 and 2 µg.mL^{-1} of anti-CD28 for 24 h. Cells were restimulated with PMA, ionomycin and brefeldin A for 6 h before being stained with LIVE/DEAD™, PE-Cy7:anti-CD4 and PE:anti-IL-2 and analysed on a flow cytometer. Flow cytometry was performed once. Data are presented as a percentage of the viable, CD4$^+$ T cell population. (G) IL-2 secretion of T_H0 cells 24 h post-incubation with increasing concentrations of anti-CD3 and 2 µg.mL^{-1} of anti-CD28. ELISA was performed once with twelve technical replicates. Data were analysed using a two-way ANOVA with a *post hoc* Bonferroni test to quantify significance where detected. * = $p < 0.05$. ** = $p < 0.01$. *** = $p < 0.001$.

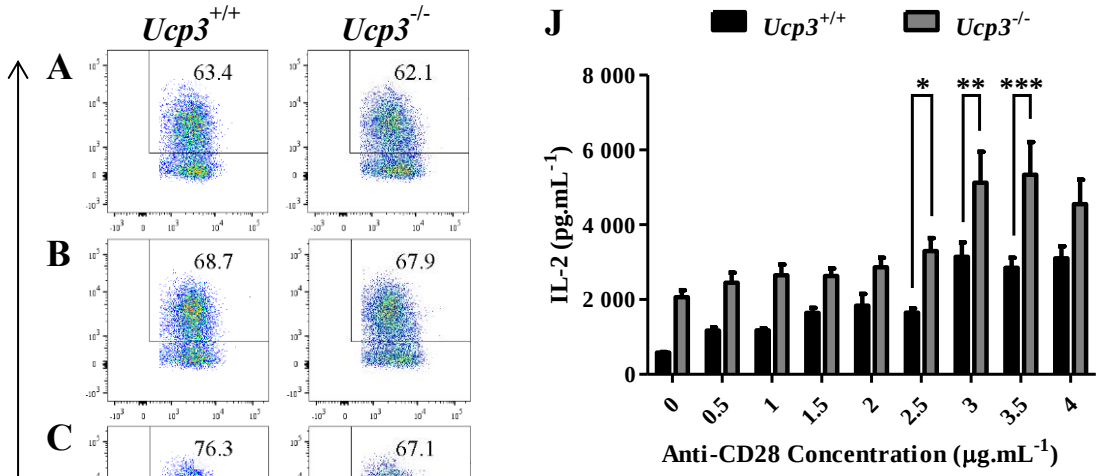

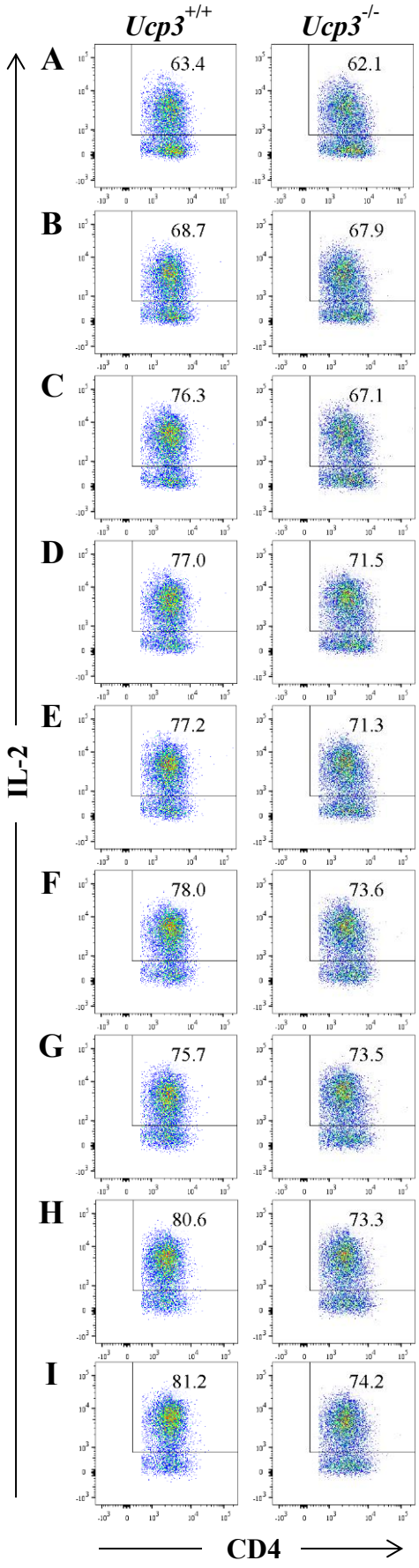

Figure 3.18: IL-2 production is increased in *Ucp3*$^{-/-}$ T_H0 cells in the presence of increasing concentrations of anti-CD28 and 1 µg.mL^{-1} of anti-CD3

T_H0 cells were generated by incubating naive T cells in the presence of 0 (A), 0.5 (B), 1 (C), 1.5 (D), 2 (E), 2.5 (F), 3 (G), 3.5 (H) or 4 (I) µg.mL^{-1} of anti-CD28 and 1 µg.mL^{-1} of anti-CD3 for 24 h. Cells were restimulated with PMA, ionomycin and brefeldin A for 6 h before being stained with LIVE/DEAD™, PE-Cy7:anti-CD4 and PE:anti-IL-2 and analysed on a flow cytometer. Flow cytometry was performed once. Data are presented as a percentage of the viable, CD4$^+$ T cell population. (J) IL-2 secretion of T_H0 cells 24 h post-incubation with increasing concentrations of anti-CD28 and 1 µg.mL^{-1} of anti-CD3. ELISA was performed once with twelve technical replicates. Data were analysed using a two-way ANOVA with a *post hoc* Bonferroni test to quantify significance where detected. * = $p < 0.05$. ** = $p < 0.01$. *** = $p < 0.001$.

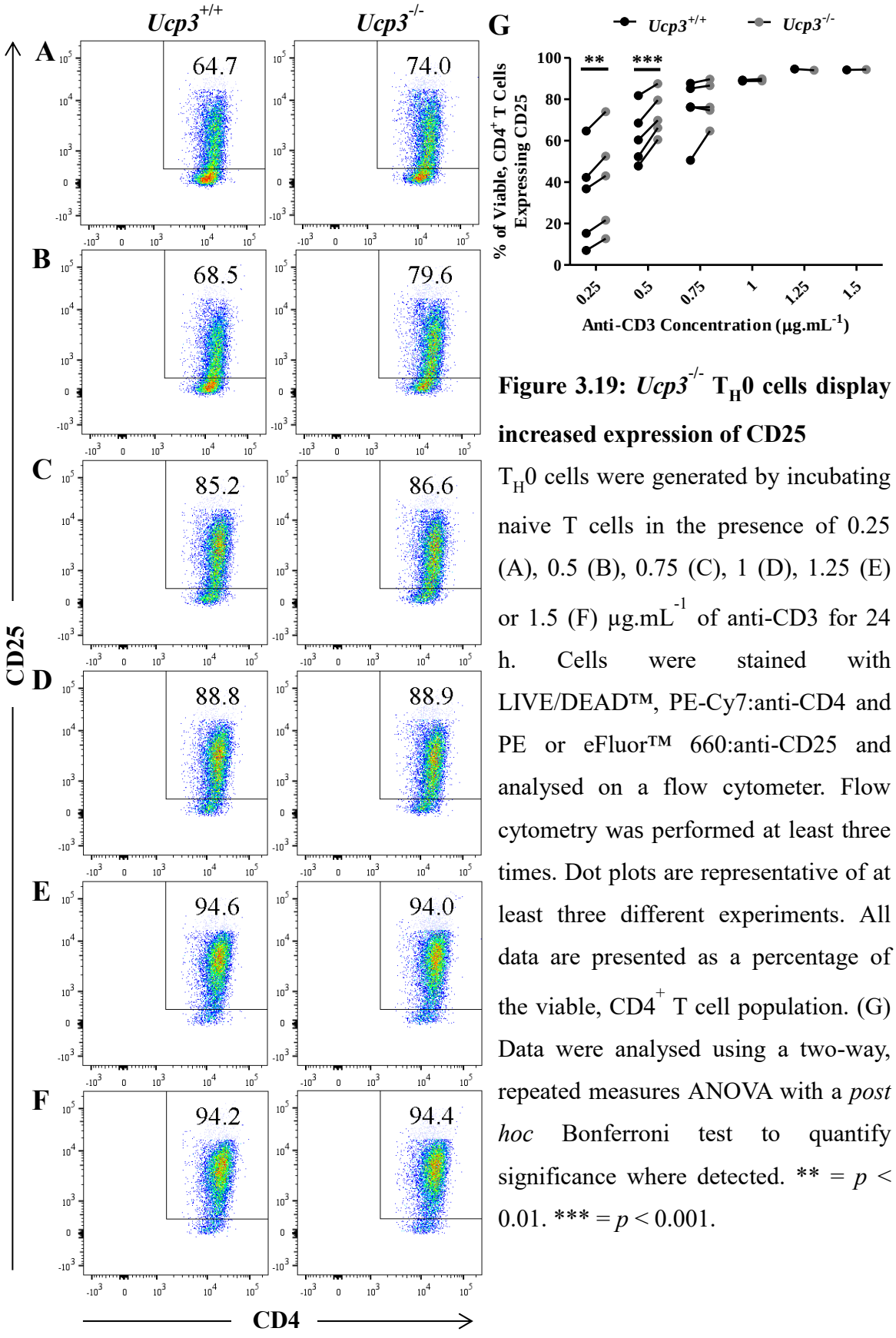

Figure 3.19: *Ucp3*$^{-/-}$ T_H0 cells display increased expression of CD25

T_H0 cells were generated by incubating naive T cells in the presence of 0.25 (A), 0.5 (B), 0.75 (C), 1 (D), 1.25 (E) or 1.5 (F) µg.mL^{-1} of anti-CD3 for 24 h. Cells were stained with LIVE/DEAD™, PE-Cy7:anti-CD4 and PE or eFluor™ 660:anti-CD25 and analysed on a flow cytometer. Flow cytometry was performed at least three times. Dot plots are representative of at least three different experiments. All data are presented as a percentage of the viable, CD4$^+$ T cell population. (G) Data were analysed using a two-way, repeated measures ANOVA with a *post hoc* Bonferroni test to quantify significance where detected. ** = $p < 0.01$. *** = $p < 0.001$.

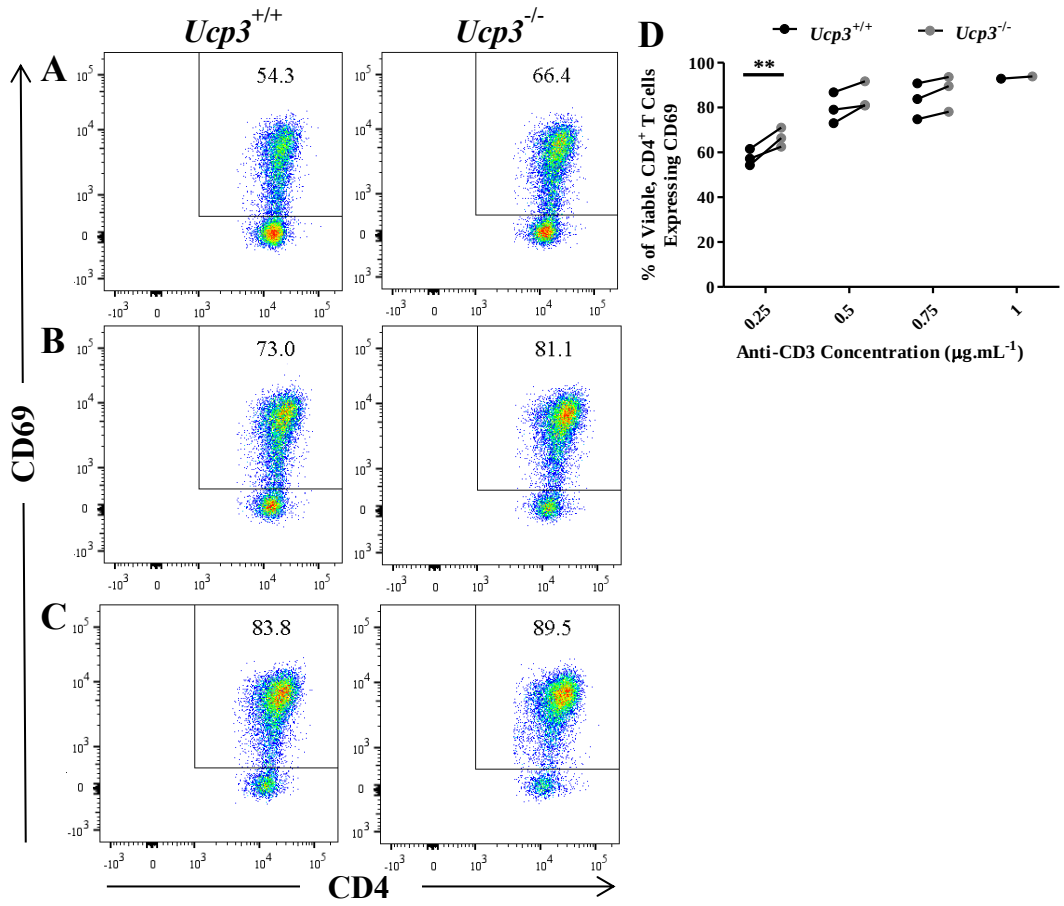

Figure 3.20: *Ucp3*$^{-/-}$ T_H0 cells display increased expression of CD69

T_H0 cells were generated by incubating naive T cells in the presence of 0.25 (A), 0.5 (B) or 0.75 (C) µg.mL^{-1} of anti-CD3 for 24 h. Cells were stained with LIVE/DEAD™, PE-Cy7:anti-CD4 and Pacific Blue™:anti-CD69 and analysed on a flow cytometer. Flow cytometry was performed at least three times. Dot plots are representative of at least three different experiments. All data are presented as a percentage of the viable, CD4$^+$ T cell population. (D) Data were analysed using a two-way, repeated measures ANOVA with a *post hoc* Bonferroni test to quantify significance where detected. ** = $p < 0.01$.

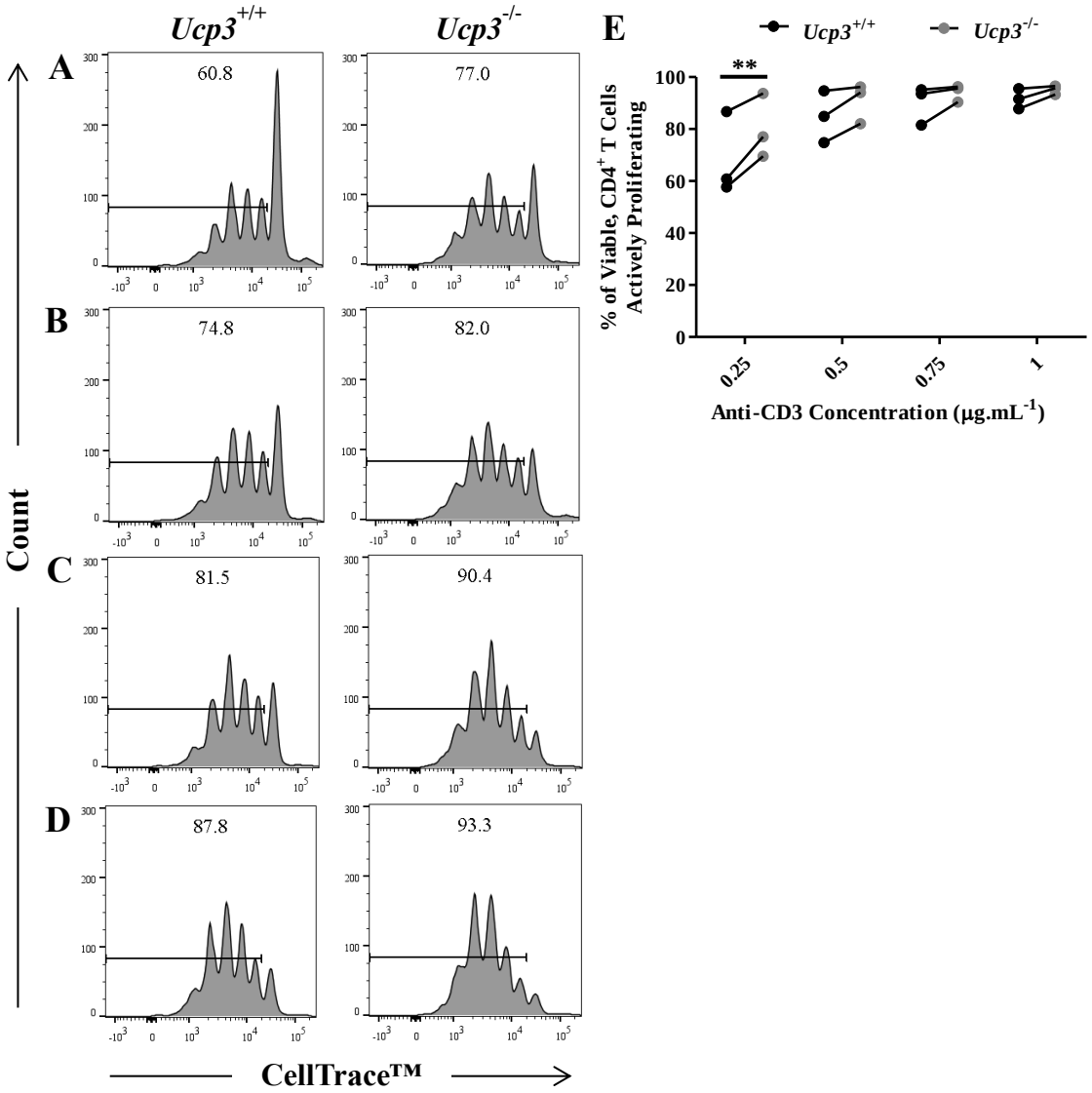

Figure 3.21: *Ucp3*$^{-/-}$ T_H0 cells display greater proliferation

T_H0 cells were generated by incubating CellTrace™-labelled naive T cells in the presence of 0.25 (A), 0.5 (B), 0.75 (C) or 1 (D) µg.mL^{-1} of anti-CD3 for 72 h. Cells were stained with LIVE/DEAD™ and PE-Cy7:anti-CD4 and analysed on a flow cytometer. Flow cytometry was performed at least three times. Histograms are representative of at least three different experiments. All data are presented as a percentage of the viable, CD4$^+$ T cell population. (E) Data were analysed using a two-way, repeated measures ANOVA with a *post hoc* Bonferroni test to quantify significance where detected. ** = $p < 0.01$.

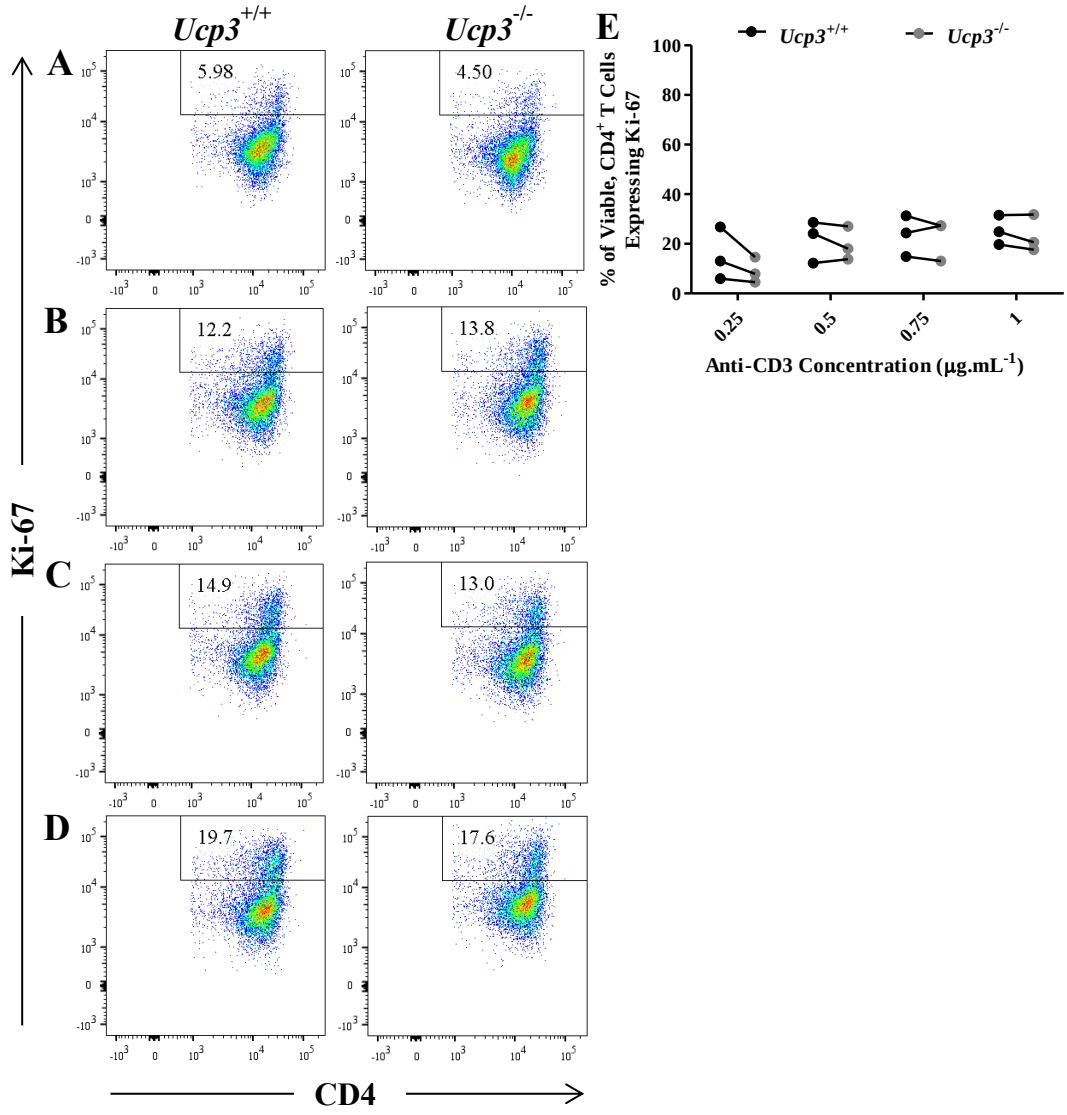

Figure 3.22: Ki-67 expression of *Ucp3*$^{+/+}$ and *Ucp3*$^{-/-}$ T_H0 cells is comparable 24 h post-stimulation

T_H0 cells were generated by incubating naive T cells in the presence of 0.25 (A), 0.5 (B), 0.75 (C) or 1 (D) µg.mL^{-1} of anti-CD3 for 24 h. Cells were stained with LIVE/DEAD™, PE-Cy7:anti-CD4 and PerCP-eFluor™ 710:anti-Ki-67 and analysed on a flow cytometer. Flow cytometry was performed at least three times. Dot plots are representative of at least three different experiments. All data are presented as a percentage of the viable, CD4$^+$ T cell population. (E) Data were analysed using a two-way, repeated measures ANOVA with a *post hoc* Bonferroni test to quantify significance where detected.

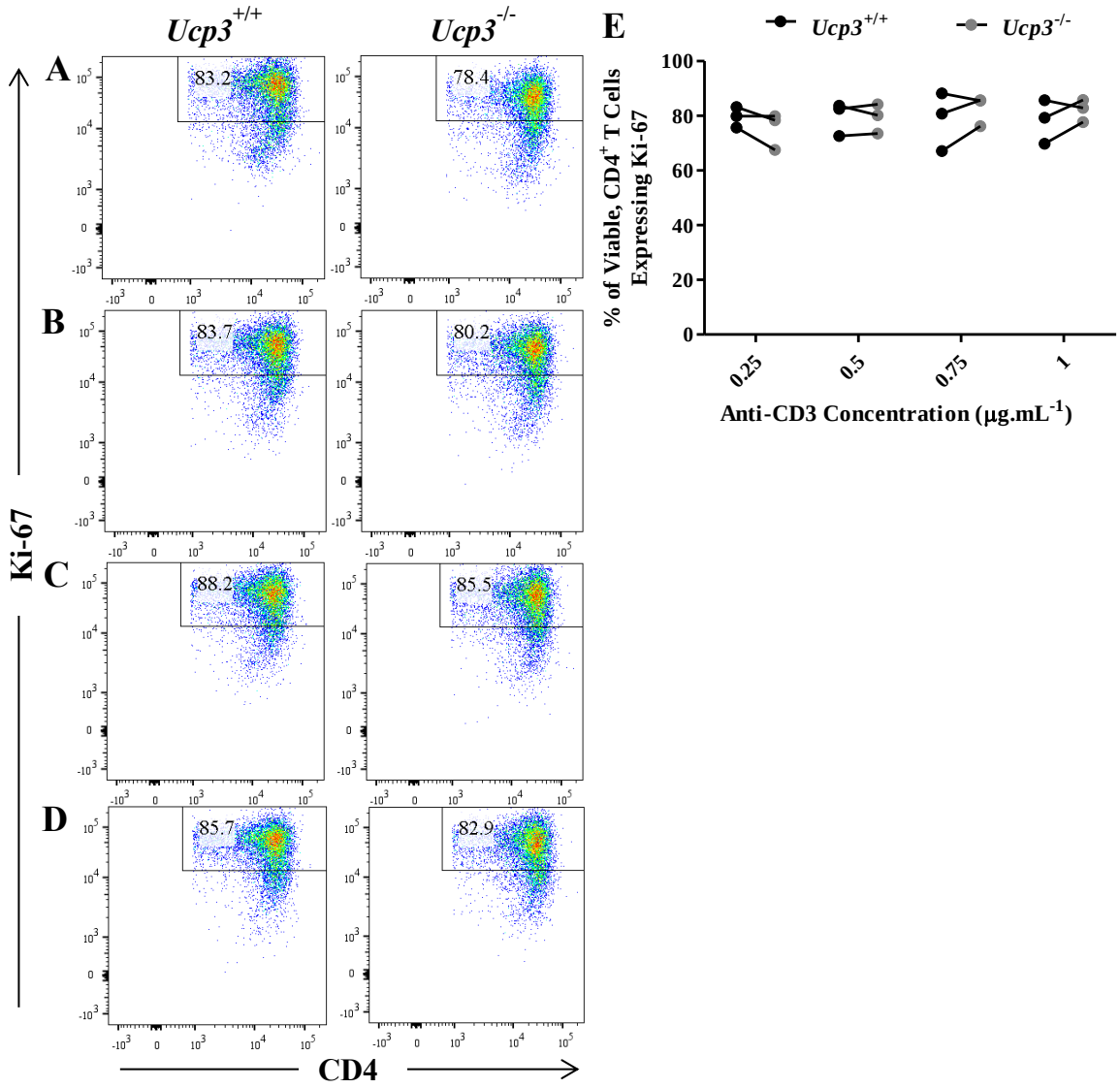

Figure 3.23: Ki-67 expression of *Ucp3*$^{+/+}$ and *Ucp3*$^{-/-}$ T_H0 cells is comparable 48 h post-stimulation

T_H0 cells were generated by incubating naive T cells in the presence of 0.25 (A), 0.5 (B), 0.75 (C) or 1 (D) µg.mL^{-1} of anti-CD3 for 48 h. Cells were stained with LIVE/DEAD™, PE-Cy7:anti-CD4 and PerCP-eFluor™ 710:anti-Ki-67 and analysed on a flow cytometer. Flow cytometry was performed at least three times. Dot plots are representative of at least three different experiments. All data are presented as a percentage of the viable, CD4$^+$ T cell population. (E) Data were analysed using a two-way, repeated measures ANOVA with a *post hoc* Bonferroni test to quantify significance where detected.

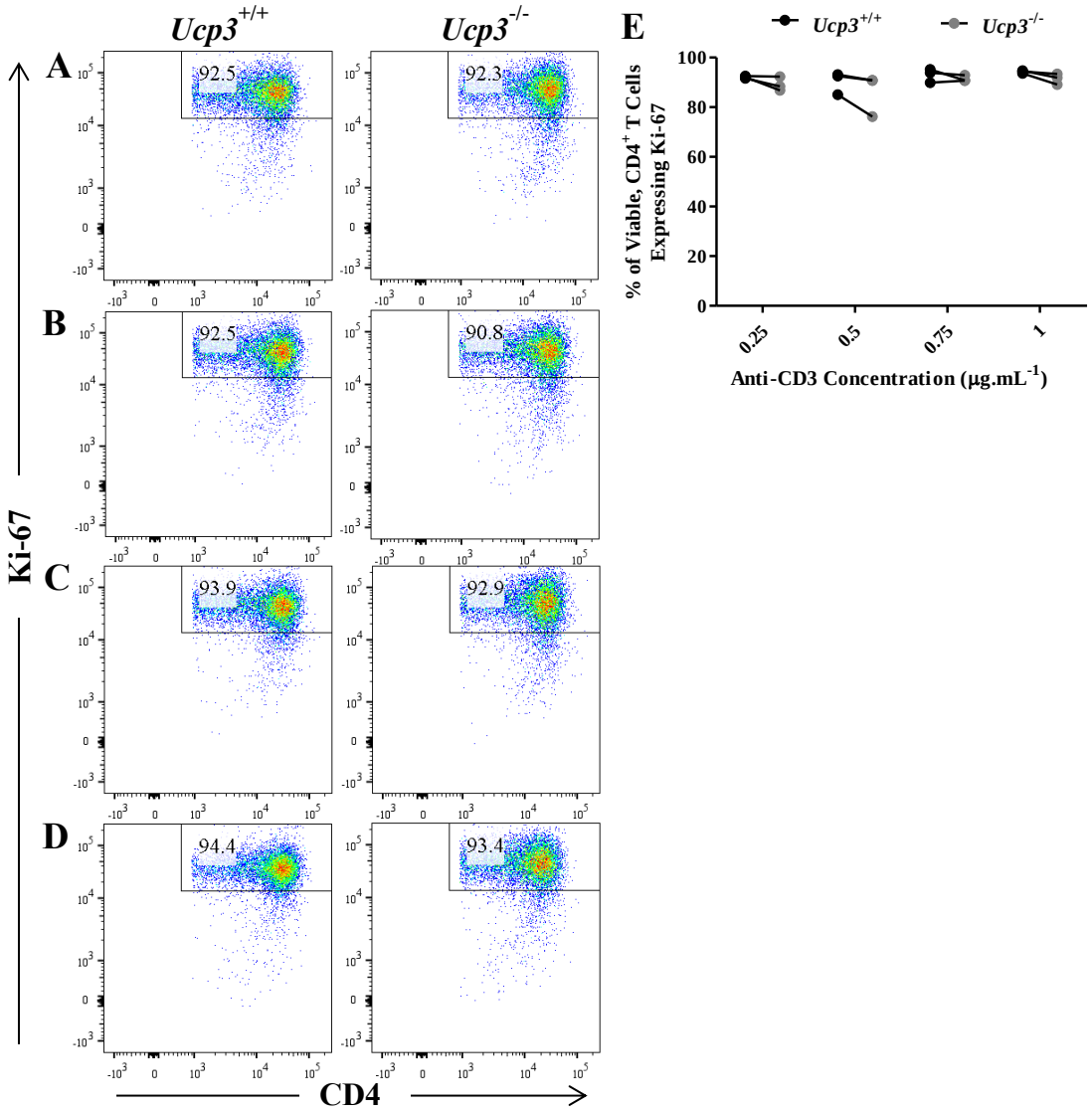

Figure 3.24: Ki-67 expression of *Ucp3*$^{+/+}$ and *Ucp3*$^{-/-}$ T_H0 cells is comparable 72 h post-stimulation

T_H0 cells were generated by incubating naive T cells in the presence of 0.25 (A), 0.5 (B), 0.75 (C) or 1 (D) µg.mL^{-1} of anti-CD3 for 72 h. Cells were stained with LIVE/DEAD™, PE-Cy7:anti-CD4 and PerCP-eFluor™ 710:anti-Ki-67 and analysed on a flow cytometer. Flow cytometry was performed at least three times. Dot plots are representative of at least three different experiments. All data are presented as a percentage of the viable, CD4$^+$ T cell population. (E) Data were analysed using a two-way, repeated measures ANOVA with a *post hoc* Bonferroni test to quantify significance where detected.

Our data convey earlier activation and increased proliferation of *Ucp3*$^{-/-}$ T_H0 cells compared to *Ucp3*$^{+/+}$ T_H0 cells and point towards a role for UCP3 in restricting TCR signalling and T cell activation. To further these results, we analysed T_H0 cell size and viability 24, 48 and 72 h post-stimulation by flow cytometry. FSC-A can be used as a measure of cell size but can also be indicative of cell growth and activation. Thus, it was predicted that earlier activated *Ucp3*$^{-/-}$ T_H0 cells displaying a large FSC would be greater in number than *Ucp3*$^{+/+}$ T_H0 cells displaying the same. Interestingly, while no significant differences in FSC are evident for the most part following 24 and 48 h of stimulation with titrated anti-CD3 (Figures 3.25 and 3.26), 72 h of stimulation with 0.25, 0.5 and 0.75 μg.mL^{-1} of anti-CD3 (Figures 3.27B – E) result in an increased number of *Ucp3*$^{+/+}$ T_H0 cells with a higher FSC rather than *Ucp3*$^{-/-}$ T_H0 cells. This was an unexpected result at first and did not seem to coincide with *Ucp3*$^{-/-}$ T_H0 cells undergoing activation earlier and, thus, having a growth 'head start'. However, after analysing the viability of these cells, it was clear that *Ucp3*$^{-/-}$ T_H0 cells are not surviving as well as *Ucp3*$^{+/+}$ T_H0 cells. T_H0 cell viability was measured by staining cells with LIVE/DEAD™ Aqua following 24, 48 or 72 h of stimulation and analysing them by flow cytometry. As IL-2 is known to promote cell survival, our hypothesis was that the increased IL-2 production from *Ucp3*$^{-/-}$ T_H0 cells would promote a concomitant increase in their viability and survival. Increased cell survival of *Ucp3*$^{-/-}$ CD4$^+$ T cells is evident 24, 48 and 72 h following no stimulation (Figures 3.28A, 3.29A and 3.30A, respectively) and 24 h post-stimulation with titrated anti-CD3 (Figure 3.28B – E). No major differences are observed following stimulation with titrated anti-CD3 for 48 h (Figure 3.29B – E) and a *decrease* in cell survival is observed following stimulation with titrated anti-CD3 for 72 h (Figure 3.30B – E). In line with this, *Ucp3*$^{-/-}$ T_H0 cells secreted significantly more IFN-γ than their WT counterparts 24 h post-stimulation (Figure 3.31A), a comparable amount 48 h post-stimulation (Figure 3.31B) and significantly less IFN-γ 72 h post-stimulation (Figure 3.32C) with 1 and 2 μg.mL^{-1} of anti-CD3 and anti-CD28, respectively.

It is apparent that *Ucp3*$^{-/-}$ T_H0 cells die prematurely, as suggested by the lower frequency of viable cells, as well as the decrease in IFN-γ production and number of cells of increased size compared to *Ucp3*$^{+/+}$ T_H0 cells. While this decrease in cell survival and cytokine production seems counterintuitive following the observations of increased IL-2 production, it is thought to be due to the triggering of a phenomenon known as activation-induced cell death (AICD). As well as acting as a T cell growth factor, IL-2 has been found to 'prime' T cells for AICD following initial expansion (Maher *et al.*, 2002; Roberts *et al.*, 2003;

Krammer *et al*., 2007; Boyman and Sprent, 2012; Liao *et al*., 2013). Thus, while initially unexpected, the above listed data are thought to be a reflection of increased AICD. To explore our hypothesis of AICD occurring and to reinforce our previous viability data (Figures 3.28 – 3.30), we analysed T_H0 cells by flow cytometry following 7-AAD and annexin V staining. 7-AAD has a strong affinity for DNA but is generally excluded from live cells. Annexin V is used to detect cells undergoing cell death due to its ability to bind to phosphatidylserine that is externalized to the outer leaflet of the cell membrane of dying cells. In combination, 7-AAD and annexin V can be used to observe the proportion of cells that are viable (negatively stained), early apoptotic (positively stained with annexin V) and apoptotic/necrotic (positively stained with both 7-AAD and annexin V). *Ucp3*$^{+/+}$ and *Ucp3*$^{-/-}$ T_H0 cells were analysed 24, 48 and 72 h post-stimulation with titrated anti-CD3. While no major differences are seen between genotypes following 24 (Figure 3.33) and 48 (Figure 3.34) h of stimulation, it is evident by 72 h post-stimulation that the frequencies of viable and apoptotic/necrotic *Ucp3*$^{-/-}$ T_H0 cells are significantly decreased and increased, respectively, in comparison to their WT counterparts (Figure 3.35), reflecting our viability data displayed in Figure 3.30.

AICD is an apoptotic form of cell death. Thus, to confirm that AICD (apoptosis) is occurring, rather than necrosis, we re-analysed 7-AAD and annexin V staining of T_H0 cells by flow cytometry 72 h post-stimulation with titrated anti-CD3 in the presence of an apoptosis inhibitor [Z-VAD-FMK (Z-VAD)], a necrosis inhibitor [Necrostatin-1 (Nec-1)] or vehicle (DMSO). If our hypothesis of AICD occurring is correct, a decrease in the frequency of the early apoptotic and apoptotic/necrotic fractions of *Ucp3*$^{-/-}$ (and *Ucp3*$^{+/+}$) T_H0 cells and a consequential increase in the viable fraction would be expected following incubation with Z-VAD. Indeed, an increase in the frequency of viable cells and a decrease in the frequency of early apoptotic and apoptotic/necrotic cells, both *Ucp3*$^{+/+}$ and *Ucp3*$^{-/-}$, are observed following culture in the presence of 10 µM Z-VAD, while no differences are noted following culture with 10 µM Nec-1 or 0.7 % (v/v) DMSO (Figures 3.36 – 3.39). Importantly, significantly lower and higher frequencies of viable and apoptotic/necrotic cells, respectively, from *Ucp3*$^{-/-}$ mice are still observed. This indicates that apoptosis is the form of cell death the cells are undergoing following stimulation and is in line with our hypothesis that *Ucp3*$^{-/-}$ T_H0 cells are primed for AICD due to their elevated production and secretion of IL-2.

AICD can be caused, at least in part, by the interaction of CD95 with CD95 ligand (CD95L), also known as Fas and FasL, respectively, the expression of which can be promoted by IL-2 signalling (Maher *et al*., 2002; Boyman and Sprent, 2012; Liao *et al*., 2013). CD95 is expressed ubiquitously in many tissues, whereas CD95L is described historically on activated T cells and is upregulated following T cell activation (Maher *et al*., 2002; Roberts *et al*., 2003). Transcription of CD95L is activated by c-Myc (Roberts *et al*., 2003). Importantly, IL-2 enhances the Janus kinase (Jak)/STAT and Akt signalling pathways which have been linked to c-Myc expression in T cells (Grumont *et al*., 2002; Preston *et al*., 2015). Thus, the increased IL-2 production of *Ucp3*$^{-/-}$ T_H0 cells could be enhancing c-Myc expression and indirectly promoting CD95L transcription, resulting in an increased susceptibility to AICD. In this regard, we measured the expression of CD95L on *Ucp3*$^{+/+}$ and *Ucp3*$^{-/-}$ T_H0 cells 24, 48 and 72 h post-stimulation and hypothesized that *Ucp3*$^{-/-}$ T_H0 cells would display a higher frequency of CD95L^{+} cells sooner than their WT counterparts. On the contrary, the opposite was observed. While no difference in expression is evident between genotypes 24 (Figure 3.40) and 48 (Figure 3.41) h post-stimulation, CD95L expression is significantly *decreased* in *Ucp3*$^{-/-}$ T_H0 cells 72 h post-stimulation with 0.25, 0.5 and 1 μg.mL^{-1} of anti-CD3 (Figure 3.42). Of the low level of CD95L expression that is observed in *Ucp3*$^{-/-}$ T_H0 cells, it responds to 10 μM Z-VAD treatment as one would expect: inhibition of apoptosis results in a decrease in CD95L expression in both *Ucp3*$^{+/+}$ and *Ucp3*$^{-/-}$ T_H0 cells 72 h post-stimulation with titrated anti-CD3, while no major effect is observed following treatment with 10 μM Nec-1, an inhibitor of necrosis, or vehicle [0.7 % (v/v) DMSO; Figures 3.43 – 3.46]. CD95L expression still remains significantly lower in *Ucp3*$^{-/-}$ cells, however. The significantly lower CD95L expression of *Ucp3*$^{-/-}$ T_H0 cells is an unexpected result, given our previous findings, and why CD95L expression of *Ucp3*$^{-/-}$ T_H0 cells would be significantly *lower* than that of *Ucp3*$^{+/+}$ T_H0 cells rather than being at a similar level, if not increased, is unclear. Nonetheless, as mentioned previously, AICD can be caused in part by the interaction of CD95 with CD95L, but can also be induced by other means, such as TNF ligation of the TNF receptor or exposure to ceramide and ROS (Maher *et al*., 2002; Roberts *et al*., 2003; Krammer *et al*., 2007). Thus, our hypothesis of *Ucp3*$^{-/-}$ T_H0 cells being more susceptible to AICD due to their elevated production of IL-2 remains.

The above data, as well as the downregulation of *Ucp3* following activation shown in Figure 3.9, convey earlier activation of *Ucp3*$^{-/-}$ T_H0 cells compared to *Ucp3*$^{+/+}$ T_H0 cells and point towards a role for UCP3 in restricting TCR signalling and CD4^{+} T cell activation

as, following *Ucp3* ablation, T cells are capable of producing more IL-2, upregulating the activation markers CD25 and CD69 and increasing their proliferation rate. Subsequently, however, it is apparent that *Ucp3*$^{-/-}$ T_H0 cells die prematurely, as suggested by the viability data, the decrease in the number of cells of increased size and the decrease in IFN-γ secretion compared to *Ucp3*$^{+/+}$ T_H0 cells. While this decrease in cell survival and cytokine production seems counterintuitive following the observations of increased IL-2 production, it is thought to be due to the triggering of AICD. Therefore, we decided to investigate how soon the expression of *Ucp3* is downregulated in *Ucp3*$^{+/+}$ T_H0 cells in order to determine the 'window' during which *Ucp3*$^{-/-}$ T_H0 cell activation is being enhanced. We examined the gene expression of *Ucp3* in T_H0 cells at time points earlier than 24 h, taking and analysing samples every 4 h for 20 h. *Ucp3* expression is significantly decreased within 4 h and remains at a significantly lower level compared to naive T cells up to 20 h later (Figure 3.47), as well as up to 72 h later as shown previously (see Figure 3.9). Figure 3.47B displays a representative agarose gel for *Ucp3* in naive T cell and T_H0 cell cDNA from the RT-PCR experiments up to 20 h post-stimulation. This indicates that *Ucp3* gene expression in $CD4^+$ T cells is decreased rapidly in response to TCR and CD28 co-receptor stimulation.

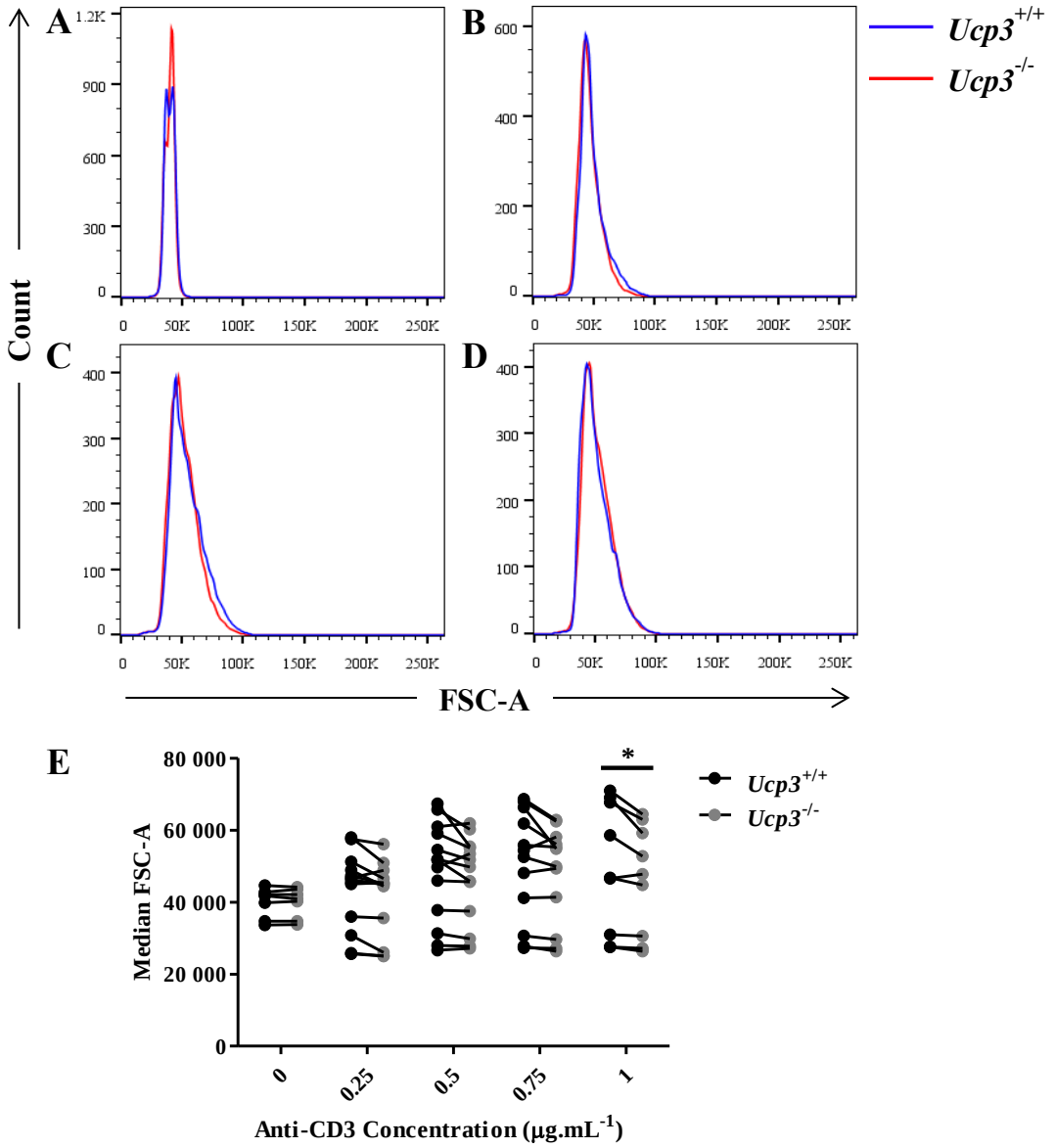

Figure 3.25: *Ucp3*$^{+/+}$ and *Ucp3*$^{-/-}$ T_H0 cell size is comparable 24 h post-stimulation

T_H0 cells were generated by incubating naive T cells in the presence of 0 (A), 0.25 (B), 0.5 (C) or 0.75 (D) µg.mL^{-1} of anti-CD3 for 24 h. Cells were stained with LIVE/DEAD™ and PE-Cy7:anti-CD4 and analysed on a flow cytometer. Flow cytometry was performed at least three times. Histograms are representative of at least three different experiments. All data presented are of the viable, CD4$^+$ T cell population. (E) Data were analysed using a two-way, repeated measures ANOVA with a *post hoc* Bonferroni test to quantify significance where detected. * = $p < 0.05$.

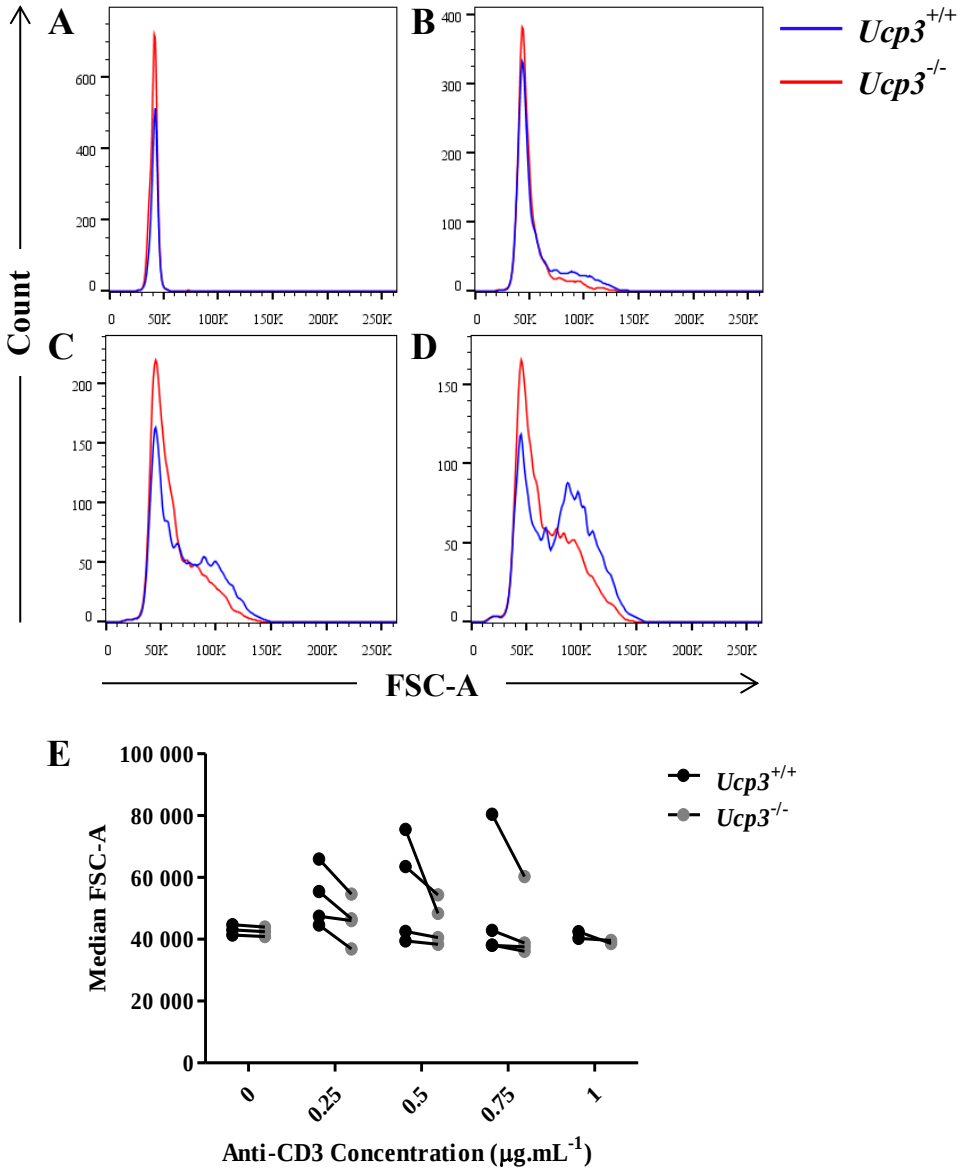

Figure 3.26: *Ucp3*$^{+/+}$ and *Ucp3*$^{-/-}$ T_H0 cell size is comparable 48 h post-stimulation

T_H0 cells were generated by incubating naive T cells in the presence of 0 (A), 0.25 (B), 0.5 (C) or 0.75 (D) µg.mL^{-1} of anti-CD3 for 48 h. Cells were stained with LIVE/DEAD™ and PE-Cy7:anti-CD4 and analysed on a flow cytometer. Flow cytometry was performed at least three times. Histograms are representative of at least three different experiments. All data presented are of the viable, CD4$^+$ T cell population. (E) Data were analysed using a two-way, repeated measures ANOVA with a *post hoc* Bonferroni test to quantify significance where detected.

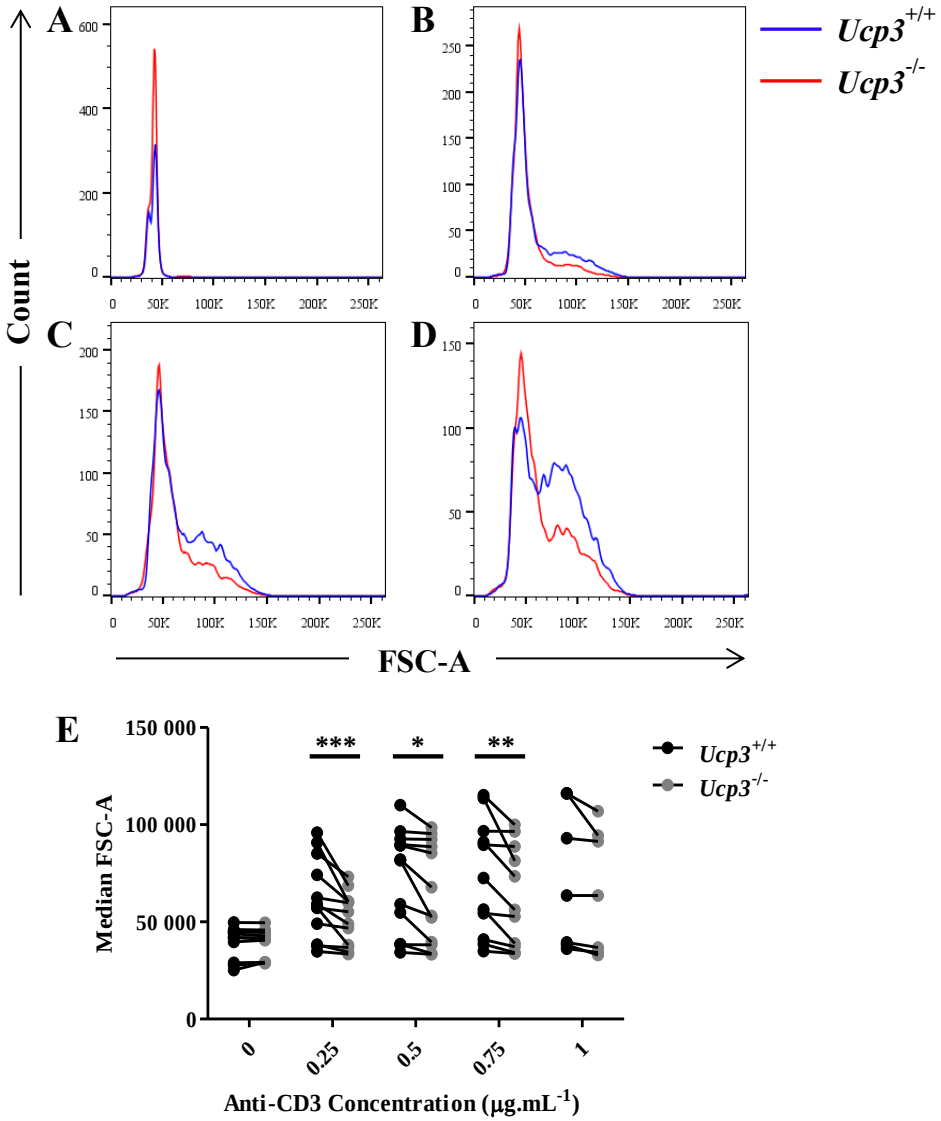

Figure 3.27: *Ucp3*$^{-/-}$ T_H0 cells display decreased cell size 72 h post-stimulation

T_H0 cells were generated by incubating naive T cells in the presence of 0 (A), 0.25 (B), 0.5 (C) or 0.75 (D) µg.mL^{-1} of anti-CD3 for 72 h. Cells were stained with LIVE/DEAD™ and PE-Cy7:anti-CD4 and analysed on a flow cytometer. Flow cytometry was performed at least three times. Histograms are representative of at least three different experiments. All data presented are of the viable, CD4$^+$ T cell population. (E) Data were analysed using a two-way, repeated measures ANOVA with a *post hoc* Bonferroni test to quantify significance where detected. * = $p < 0.05$. ** = $p < 0.01$. *** = $p < 0.001$.

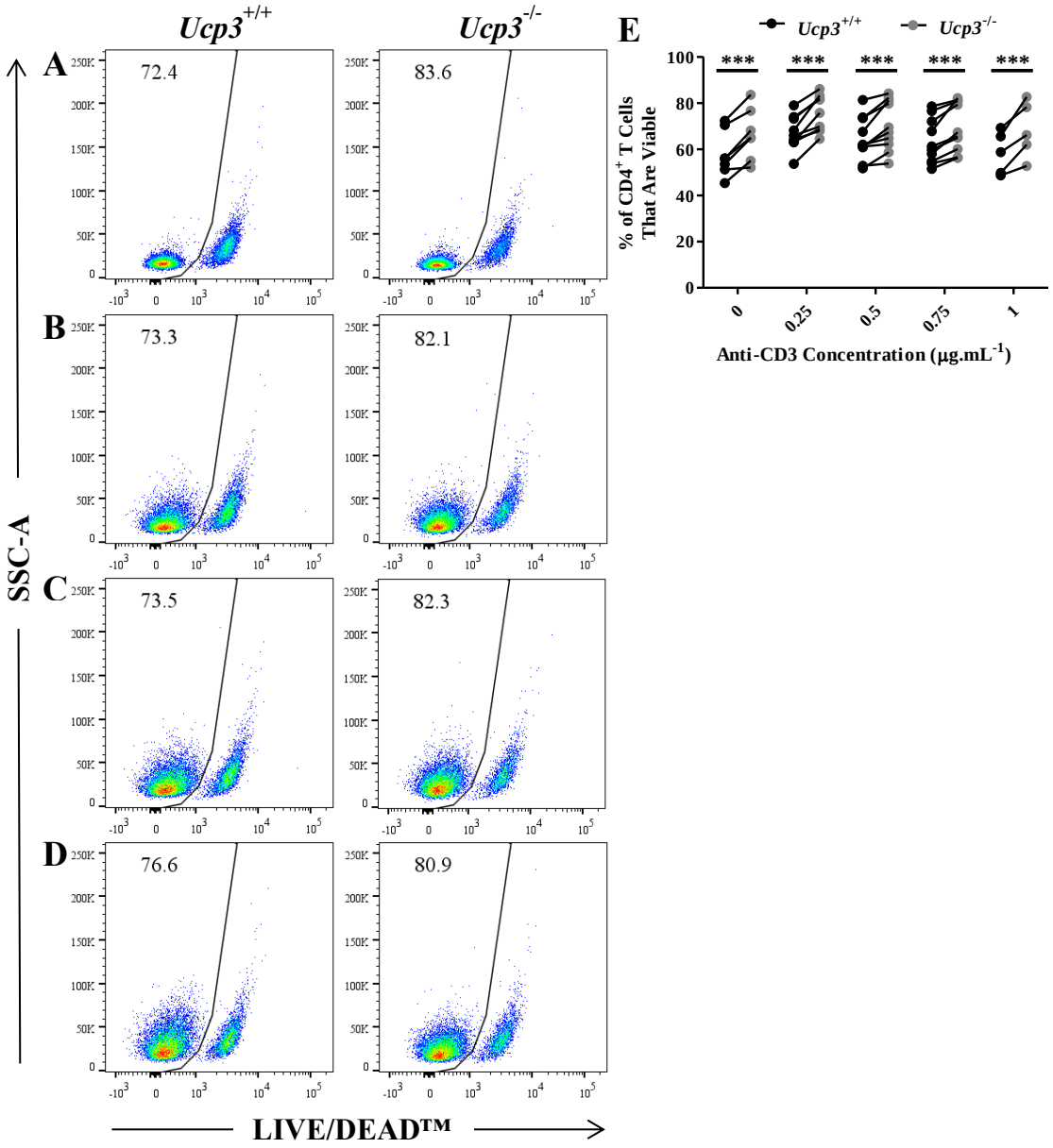

Figure 3.28: *Ucp3*$^{-/-}$ T_H0 cells are more viable 24 h post-stimulation

T_H0 cells were generated by incubating naive T cells in the presence of 0 (A), 0.25 (B), 0.5 (C) or 0.75 (D) µg.mL^{-1} of anti-CD3 for 24 h. Cells were stained with LIVE/DEAD™ and PE-Cy7:anti-CD4 and analysed on a flow cytometer. Flow cytometry was performed at least three times. Dot plots are representative of at least three different experiments. All data are presented as a percentage of the total CD4$^+$ T cell population. (E) Data were analysed using a two-way, repeated measures ANOVA with a *post hoc* Bonferroni test to quantify significance where detected. *** = $p < 0.001$.

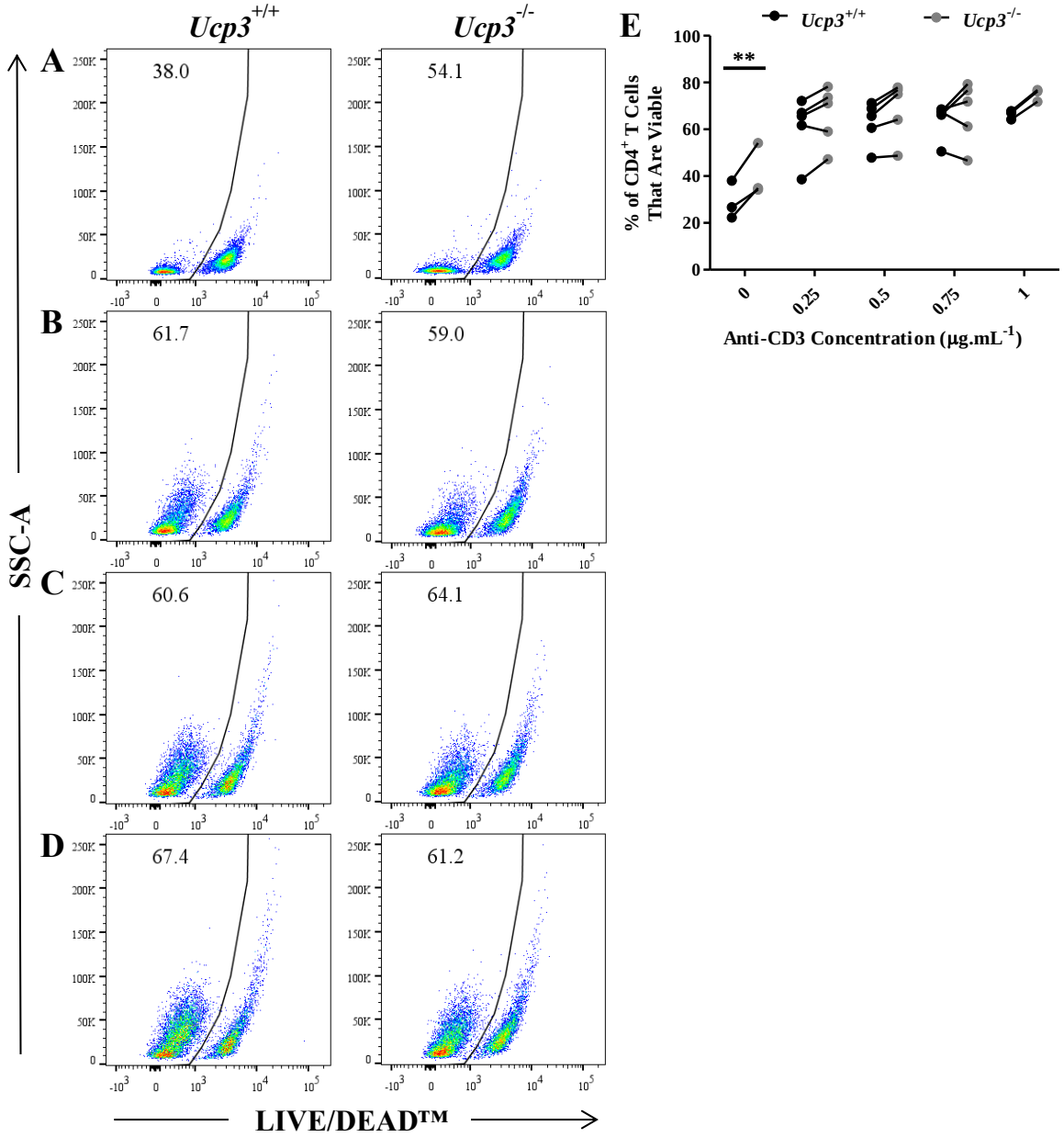

Figure 3.29: Viability of *Ucp3*$^{+/+}$ and *Ucp3*$^{-/-}$ T_H0 cells is comparable 48 h post-stimulation

T_H0 cells were generated by incubating naive T cells in the presence of 0 (A), 0.25 (B), 0.5 (C) or 0.75 (D) µg.mL^{-1} of anti-CD3 for 48 h. Cells were stained with LIVE/DEAD™ and PE-Cy7:anti-CD4 and analysed on a flow cytometer. Flow cytometry was performed at least three times. Dot plots are representative of at least three different experiments. All data are presented as a percentage of the total CD4$^+$ T cell population. (E) Data were analysed using a two-way, repeated measures ANOVA with a *post hoc* Bonferroni test to quantify significance where detected. ** = $p < 0.01$.

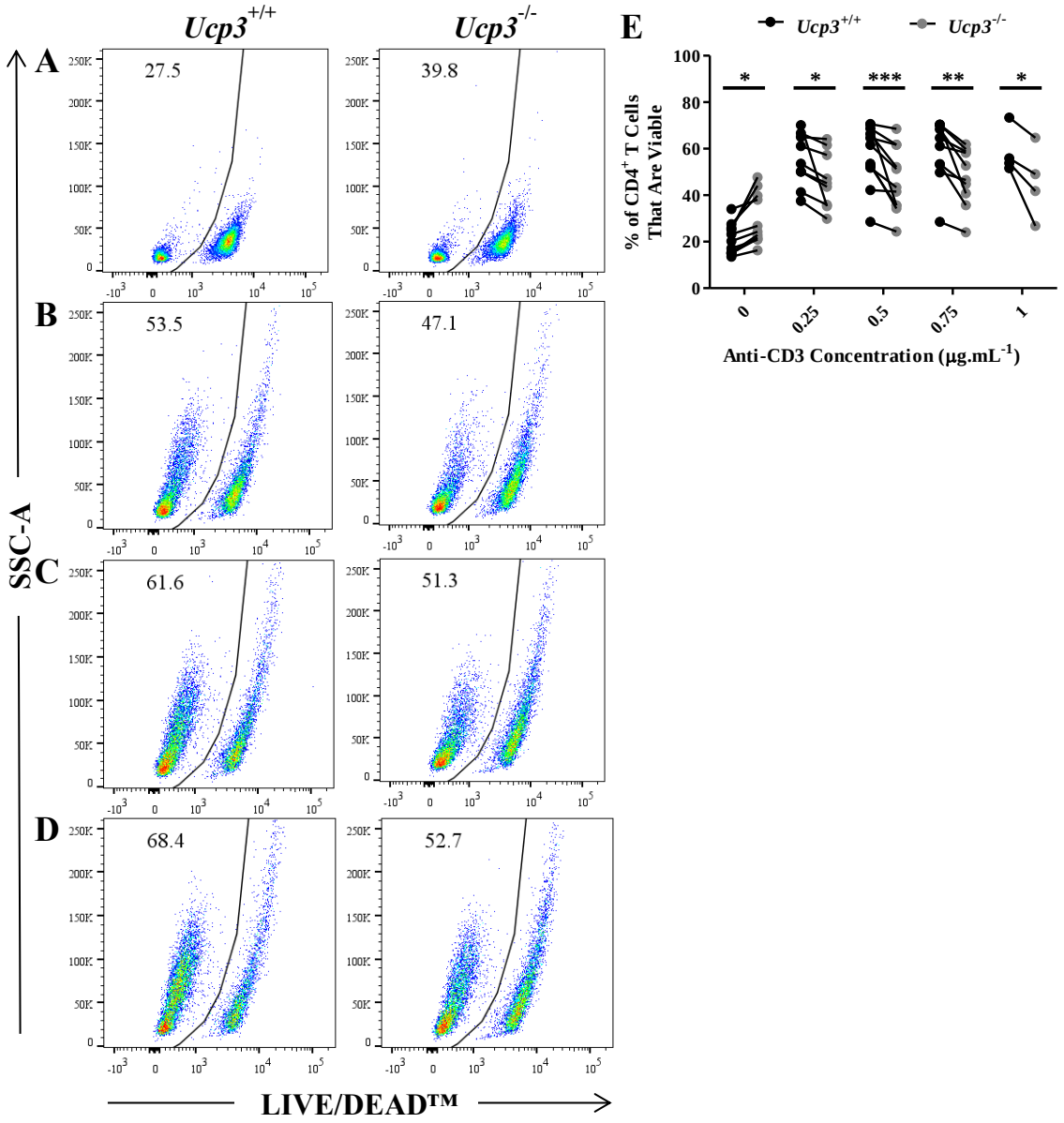

Figure 3.30: *Ucp3*$^{-/-}$ T_H0 cells are less viable 72 h post-stimulation

T_H0 cells were generated by incubating naive T cells in the presence of 0 (A), 0.25 (B), 0.5 (C) or 0.75 (D) µg.mL^{-1} of anti-CD3 for 72 h. Cells were stained with LIVE/DEAD™ and PE-Cy7:anti-CD4 and analysed on a flow cytometer. Flow cytometry was performed at least three times. Dot plots are representative of at least three different experiments. All data are presented as a percentage of the total CD4$^+$ T cell population. (E) Data were analysed using a two-way, repeated measures ANOVA with a *post hoc* Bonferroni test to quantify significance where detected. * = $p < 0.05$. ** = $p < 0.01$. *** = $p < 0.001$.

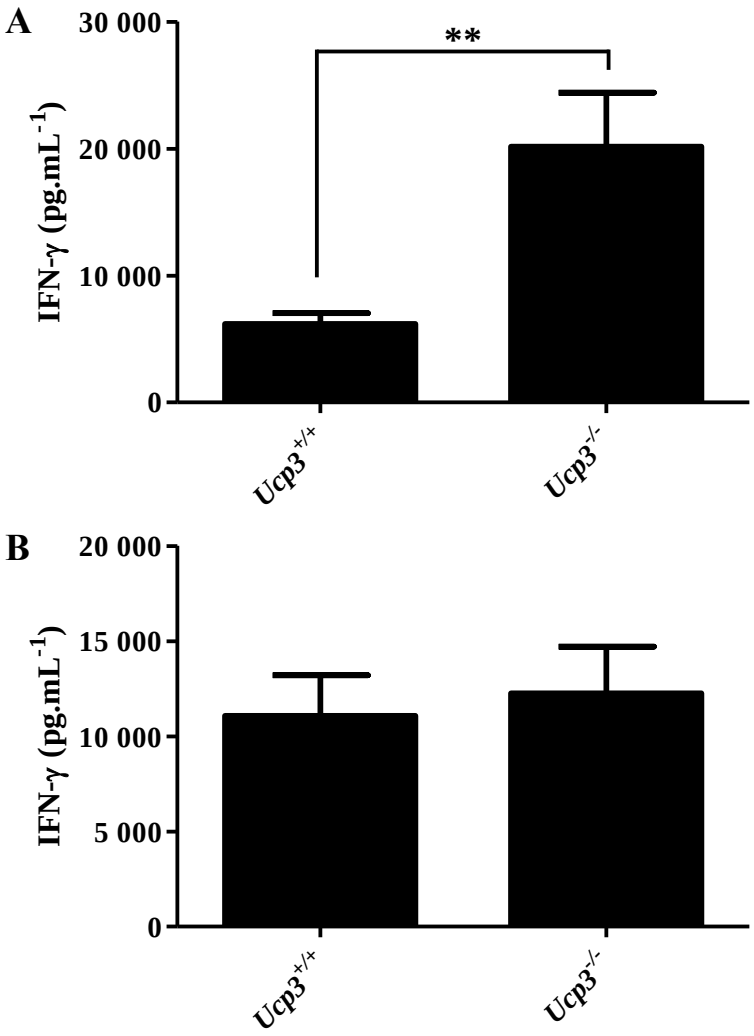

Figure 3.31: IFN-γ secretion by *Ucp3*$^{+/+}$ and *Ucp3*$^{-/-}$ T_H0 cells 24 and 48 h post-stimulation

T_H0 cells were generated by incubating naive T cells in the presence of 1 and 2 µg.mL^{-1} of anti-CD3 and anti-CD28, respectively, for (A) 24 and (B) 48 h. ELISA was performed at least three times with twelve technical replicates. Data were analysed using a two-tailed, unpaired *t* test to quantify significance where detected. ** = $p < 0.01$.

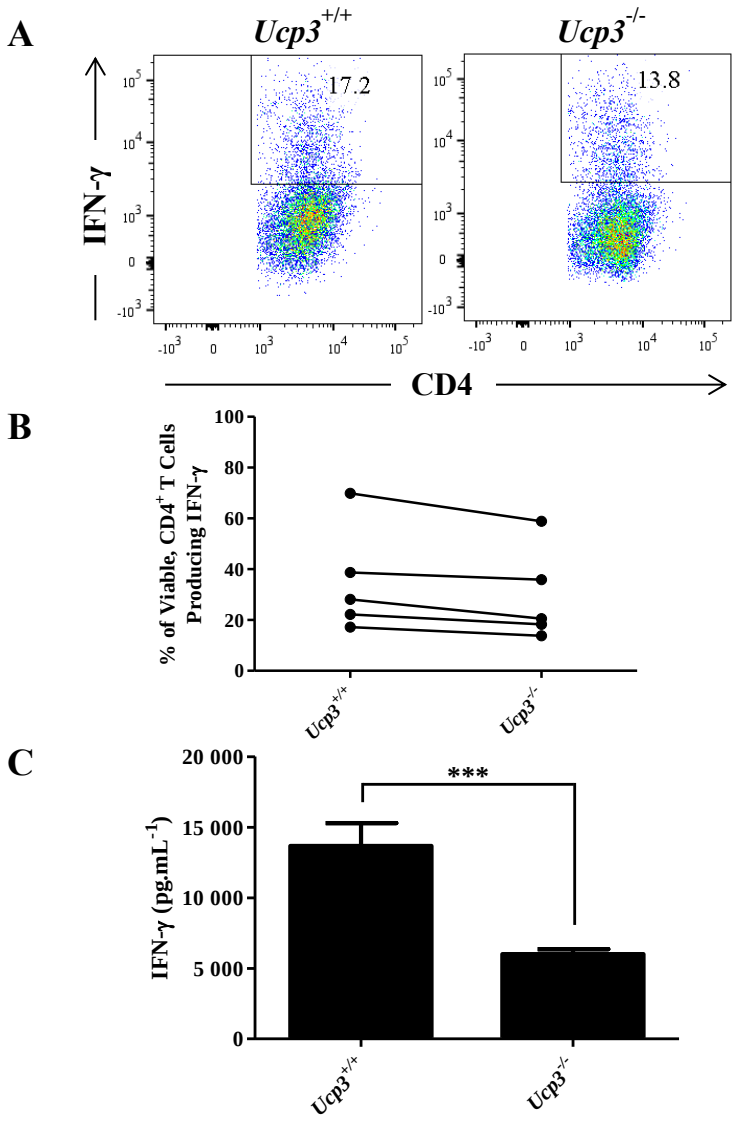

Figure 3.32: *Ucp3*$^{-/-}$ T_H0 cells secrete less IFN-γ 72 h post-stimulation

T_H0 cells were generated by incubating naive T cells in the presence of 1 and 2 µg.mL^{-1} of anti-CD3 and anti-CD28, respectively, for 72 h. (A, B) Cells were restimulated with PMA, ionomycin and brefeldin A for 6 h before being stained with LIVE/DEAD™, PE-Cy7:anti-CD4 and *APC*:anti-IFN-γ and analysed on a flow cytometer. Flow cytometry was performed at least three times. Data are presented as a percentage of the viable, CD4$^+$ T cell population. (A) Dot plots are representative of at least three different experiments. (C) IFN-γ secretion by T_H0 cells 72 h post-stimulation. ELISA was performed at least three times in sextuplicate. (B, C) Data were analysed using a two-tailed, unpaired *t* test to quantify significance where detected. *** = $p < 0.001$.

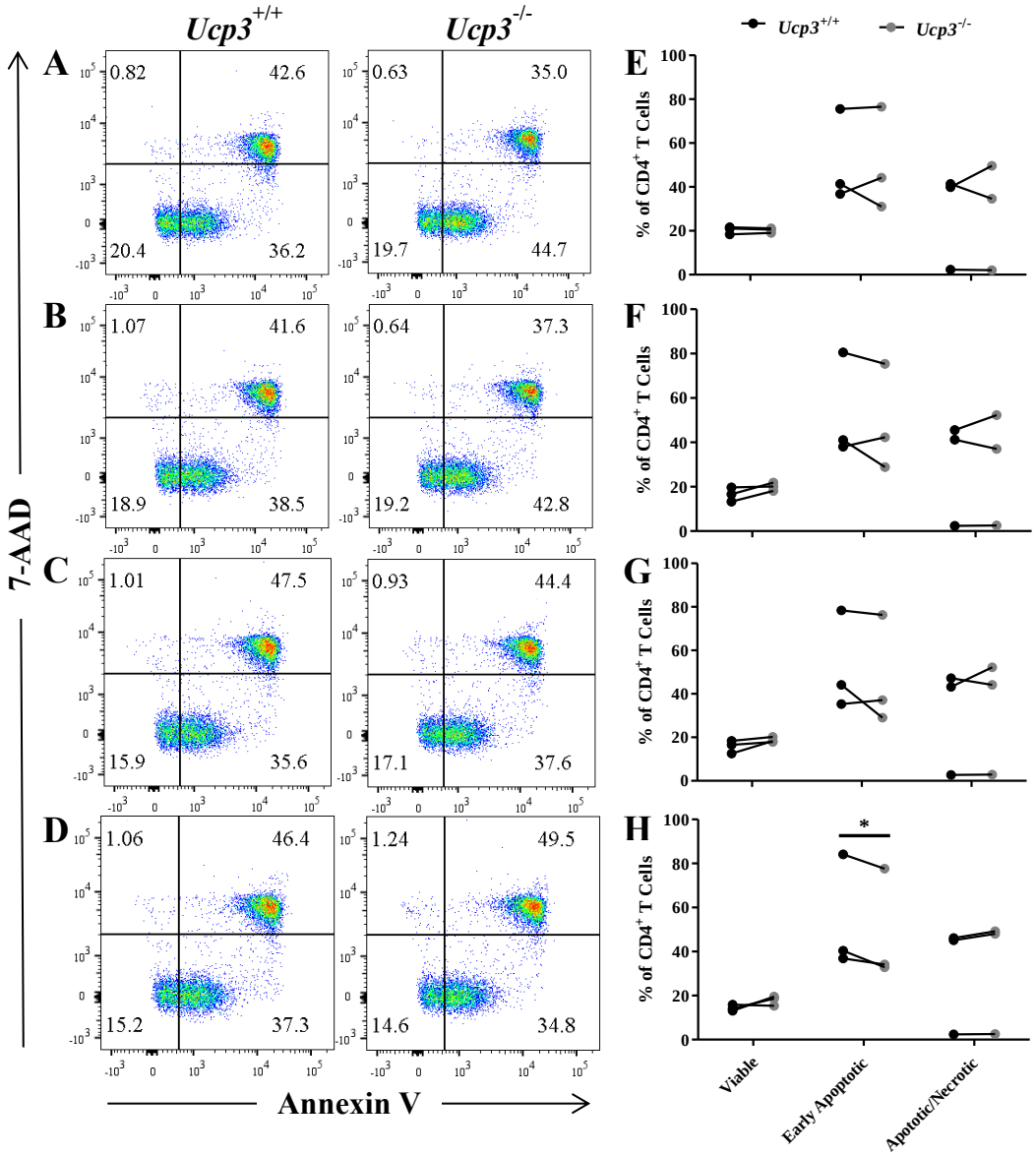

Figure 3.33: Frequencies of viable, early apoptotic and apoptotic/necrotic *Ucp3*$^{+/+}$ and *Ucp3*$^{-/-}$ T$_H$0 cells are comparable 24 h post-stimulation

T$_H$0 cells were generated by incubating naive T cells in the presence of 0.25 (A, E), 0.5 (B, F), 0.75 (C, G) or 1 (D, H) µg.mL^{-1} of anti-CD3 for 24 h. Cells were stained with PE-Cy7:anti-CD4, 7-AAD and *APC*:annexin V and analysed on a flow cytometer. Flow cytometry was performed at least three times. Dot plots are representative of at least three different experiments. All data are presented as a percentage of the total CD4$^+$ T cell population. (E – H) Data were analysed using a two-way, repeated measures ANOVA with a *post hoc* Bonferroni test to quantify significance where detected. * = $p < 0.05$.

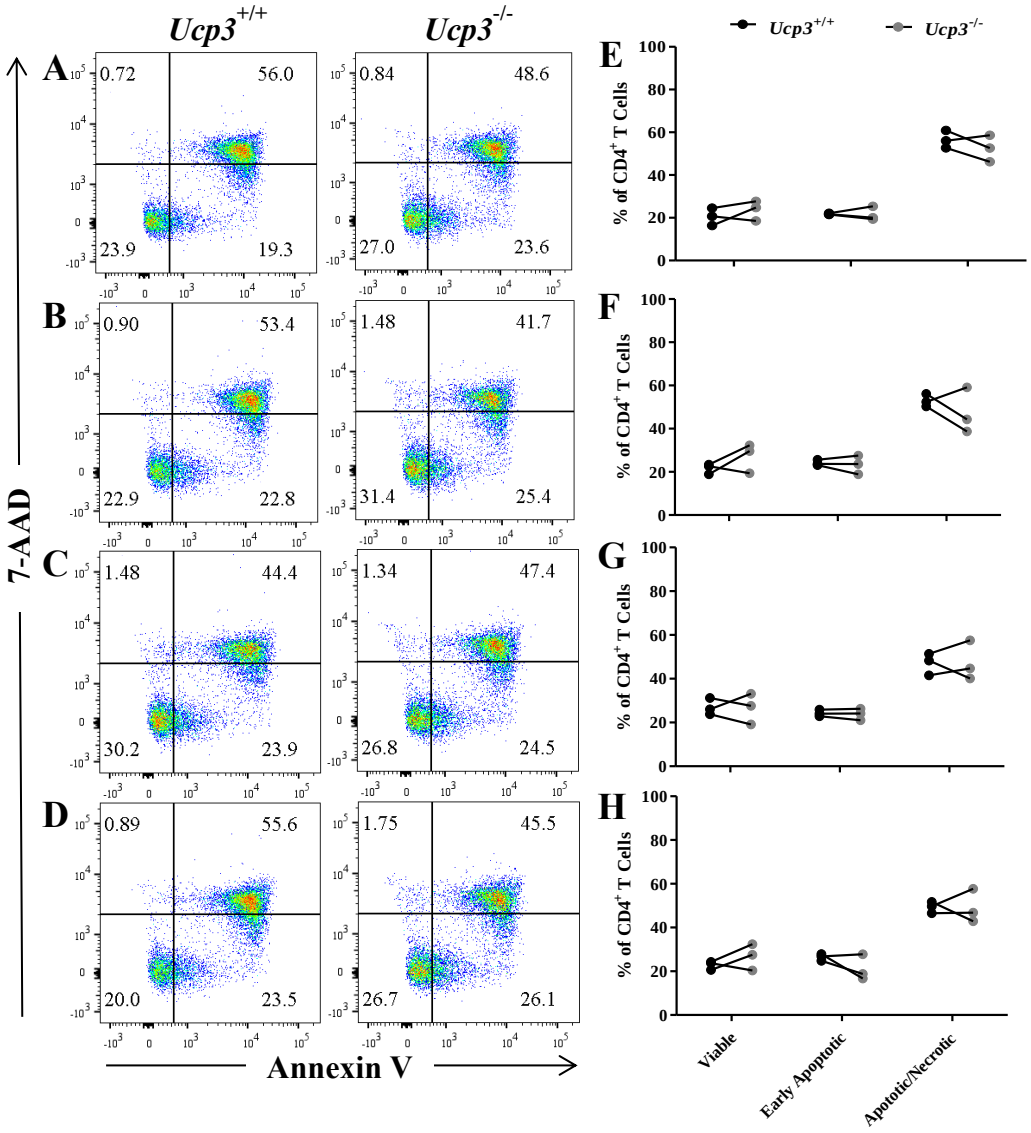

Figure 3.34: Frequencies of viable, early apoptotic and apoptotic/necrotic *Ucp3*$^{+/+}$ and *Ucp3*$^{-/-}$ T_H0 cells are comparable 48 h post-stimulation

T_H0 cells were generated by incubating naive T cells in the presence of 0.25 (A, E), 0.5 (B, F), 0.75 (C, G) or 1 (D, H) µg.mL^{-1} of anti-CD3 for 48 h. Cells were stained with PE-Cy7:anti-CD4, 7-AAD and *APC*:annexin V and analysed on a flow cytometer. Flow cytometry was performed at least three times. Dot plots are representative of at least three different experiments. All data are presented as a percentage of the total CD4$^+$ T cell population. (E – H) Data were analysed using a two-way, repeated measures ANOVA with a *post hoc* Bonferroni test to quantify significance where detected.

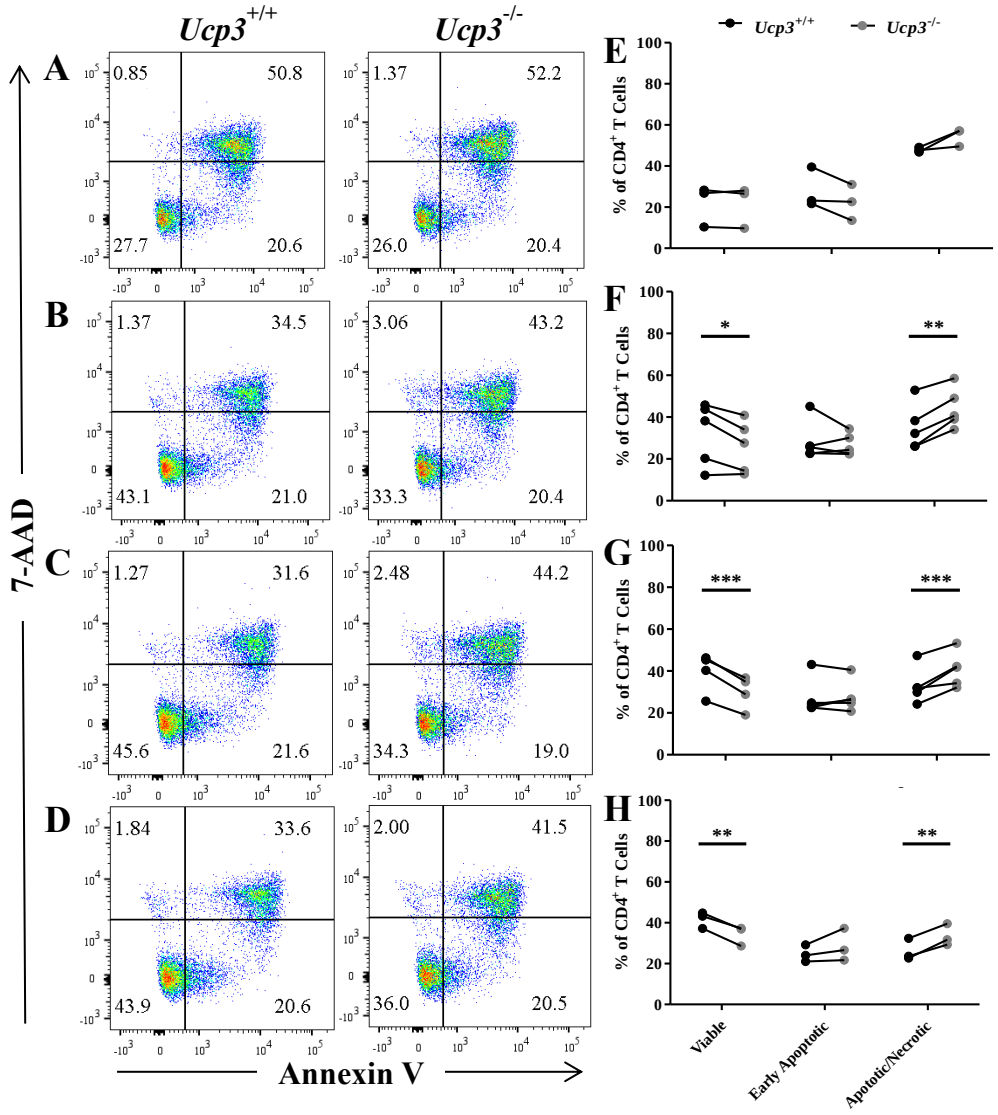

Figure 3.35: *Ucp3*$^{-/-}$ T_H0 cells display lower viability and increased cell death 72 h post-stimulation

T_H0 cells were generated by incubating naive T cells in the presence of 0.25 (A, E), 0.5 (B, F), 0.75 (C, G) or 1 (D, H) µg.mL^{-1} of anti-CD3 for 72 h. Cells were stained with PE-Cy7:anti-CD4, 7-AAD and *APC*:annexin V and analysed on a flow cytometer. Flow cytometry was performed at least three times. Dot plots are representative of at least three different experiments. All data are presented as a percentage of the total CD4$^+$ T cell population. (E – H) Data were analysed using a two-way, repeated measures ANOVA with a *post hoc* Bonferroni test to quantify significance where detected. * = $p < 0.05$. ** = $p < 0.01$. *** = $p < 0.001$.

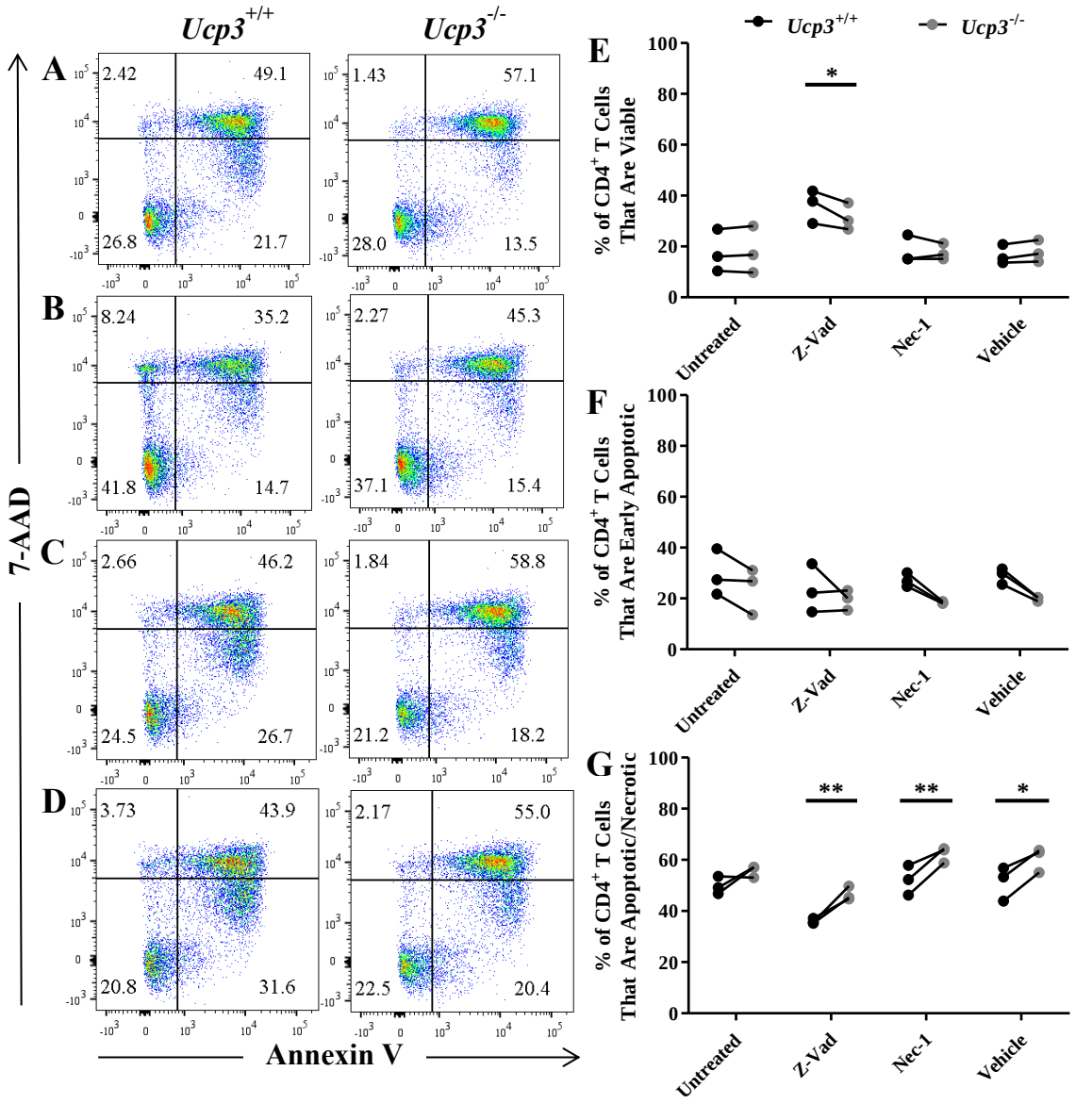

Figure 3.36: *Ucp3*$^{-/-}$ T_H0 cells display greater cell death 72 h post-stimulation with 0.25 µg.mL^{-1} of anti-CD3 in the presence of cell death inhibitors

T_H0 cells were generated by incubating naive T cells in the presence of 0.25 µg.mL^{-1} of anti-CD3 only (A) or in combination with 10 µM Z-VAD (B), 10 µM Nec-1 (C) or 0.07 % (v/v) DMSO (vehicle; D) for 72 h. Cells were stained with PE-Cy7:anti-CD4, 7-AAD and *APC*:annexin V and analysed on a flow cytometer. Flow cytometry was performed at least three times. Dot plots are representative of at least three different experiments. All data are presented as a percentage of the total CD4$^+$ T cell population. (E – G) Data were analysed using a two-way, repeated measures ANOVA with a *post hoc* Bonferroni test to quantify significance where detected. * = $p < 0.05$. ** = $p < 0.01$.

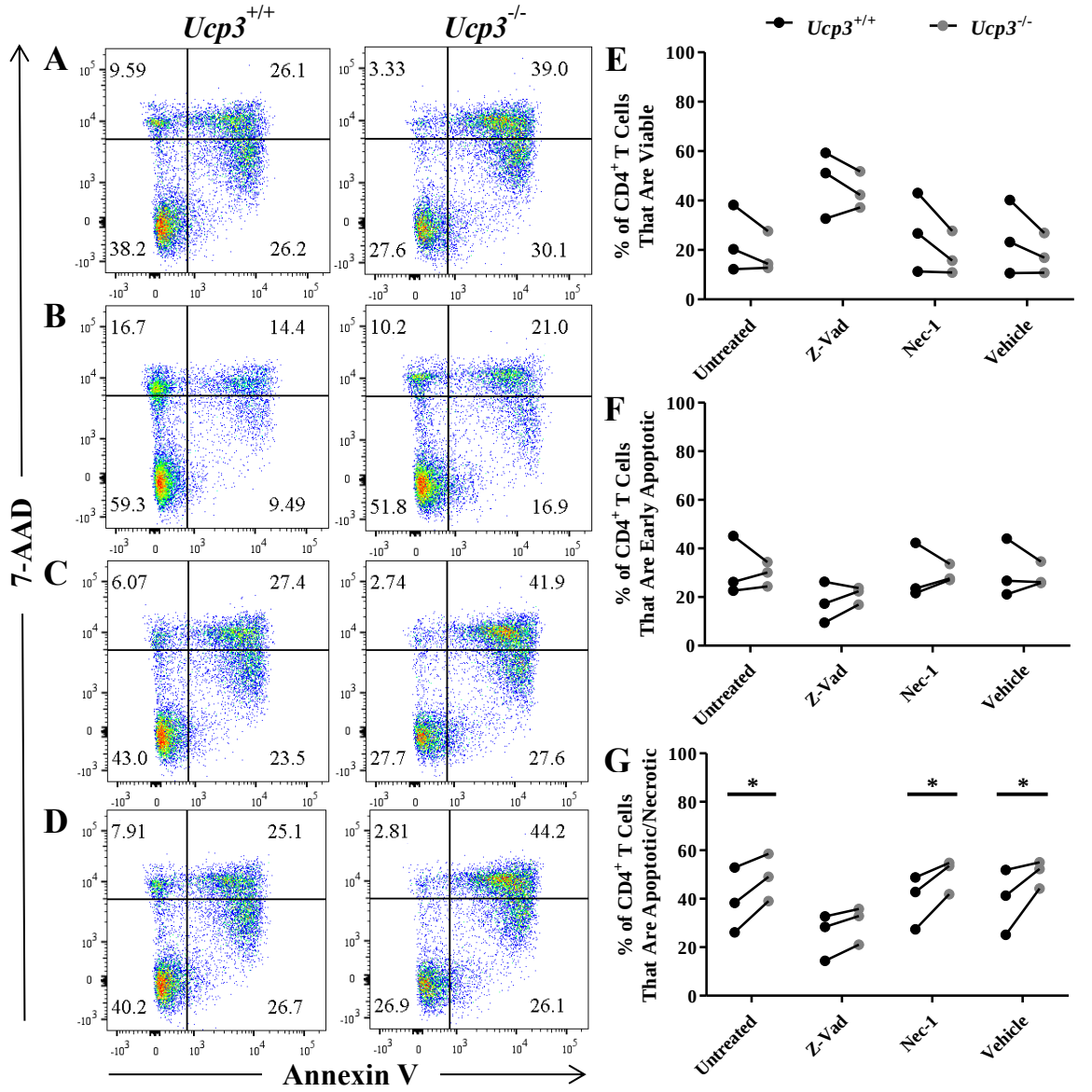

Figure 3.37: *Ucp3*$^{-/-}$ T_H0 cells display greater cell death 72 h post-stimulation with 0.5 µg.mL^{-1} of anti-CD3 in the presence of cell death inhibitors

T_H0 cells were generated by incubating naive T cells in the presence of 0.5 µg.mL^{-1} of anti-CD3 only (A) or in combination with 10 µM Z-VAD (B), 10 µM Nec-1 (C) or 0.07 % (v/v) DMSO (vehicle; D) for 72 h. Cells were stained with PE-Cy7:anti-CD4, 7-AAD and *APC*:annexin V and analysed on a flow cytometer. Flow cytometry was performed at least three times. Dot plots are representative of at least three different experiments. All data are presented as a percentage of the total CD4$^+$ T cell population. (E – G) Data were analysed using a two-way, repeated measures ANOVA with a *post hoc* Bonferroni test to quantify significance where detected. * = $p < 0.05$.

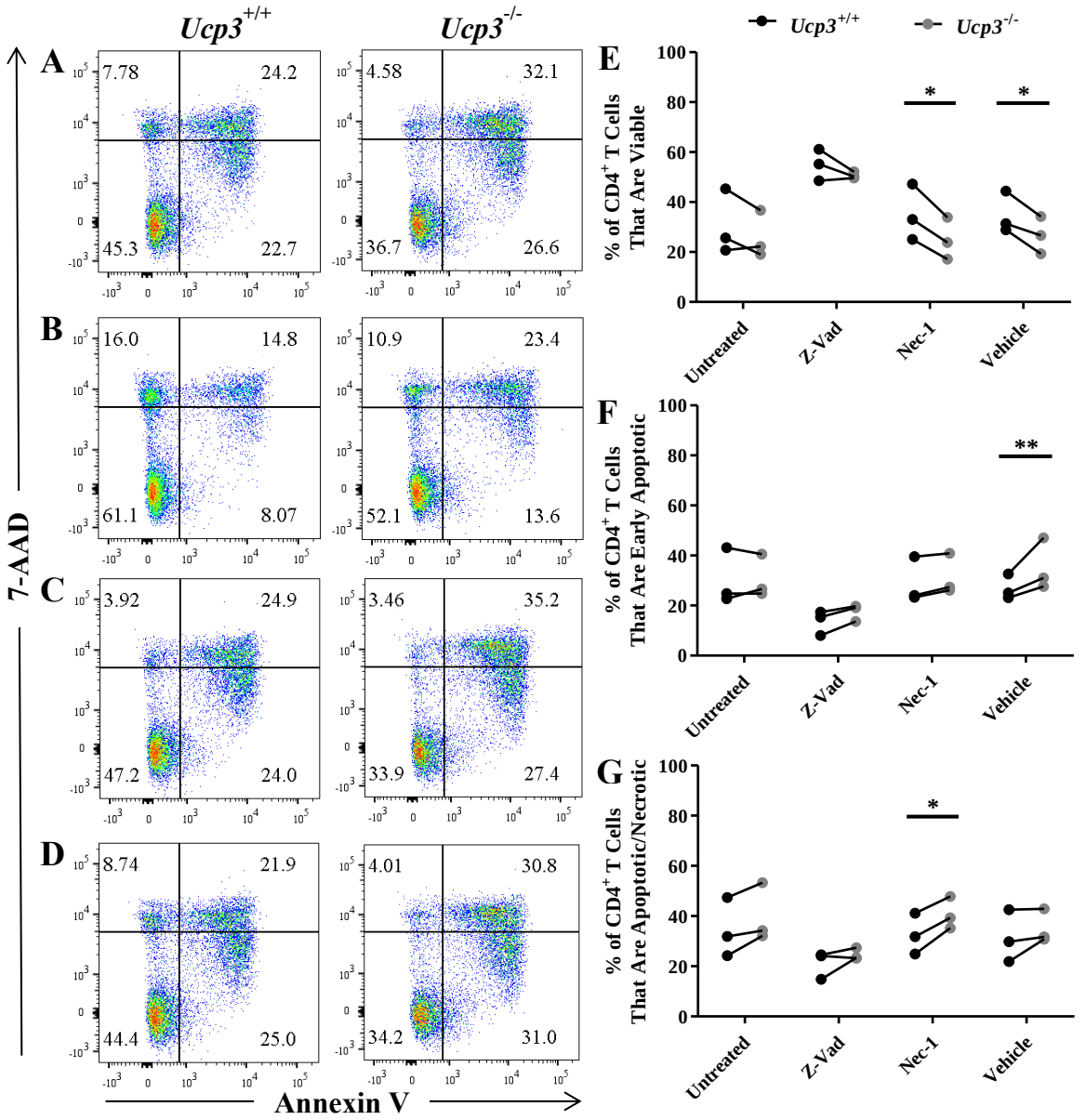

Figure 3.38: *Ucp3*$^{-/-}$ T_H0 cells display greater cell death 72 h post-stimulation with 0.75 µg.mL^{-1} of anti-CD3 in the presence of cell death inhibitors

T_H0 cells were generated by incubating naive T cells in the presence of 0.75 µg.mL^{-1} of anti-CD3 only (A) or in combination with 10 µM Z-VAD (B), 10 µM Nec-1 (C) or 0.07 % (v/v) DMSO (vehicle; D) for 72 h. Cells were stained with PE-Cy7:anti-CD4, 7-AAD and *APC*:annexin V and analysed on a flow cytometer. Flow cytometry was performed at least three times. Dot plots are representative of at least three different experiments. All data are presented as a percentage of the total CD4$^+$ T cell population. (E – G) Data were analysed using a two-way, repeated measures ANOVA with a *post hoc* Bonferroni test to quantify significance where detected. * = $p < 0.05$. ** = $p < 0.01$.

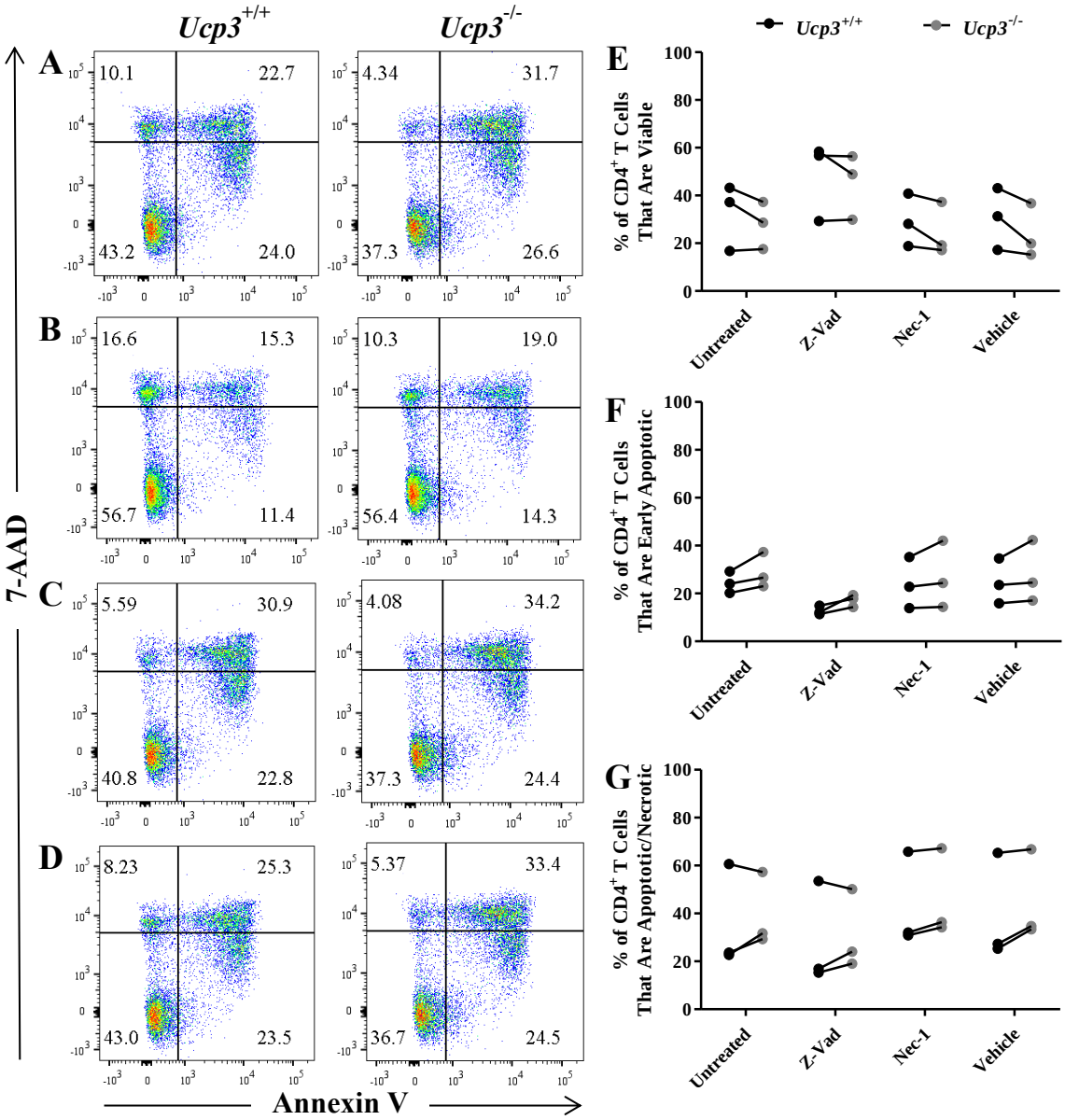

Figure 3.39: *Ucp3*$^{+/+}$ and *Ucp3*$^{-/-}$ T_H0 cell death is comparable 72 h post-stimulation with 1 µg.mL^{-1} of anti-CD3 in the presence of cell death inhibitors

T_H0 cells were generated by incubating naive T cells in the presence of 1 µg.mL^{-1} of anti-CD3 only (A) or in combination with 10 µM Z-VAD (B), 10 µM Nec-1 (C) or 0.07 % (v/v) DMSO (vehicle; D) for 72 h. Cells were stained with PE-Cy7:anti-CD4, 7-AAD and *APC*:annexin V and analysed on a flow cytometer. Flow cytometry was performed at least three times. Dot plots are representative of at least three different experiments. All data are presented as a percentage of the total CD4$^+$ T cell population. (E – G) Data were analysed using a two-way, repeated measures ANOVA with a *post hoc* Bonferroni test to quantify significance where detected.

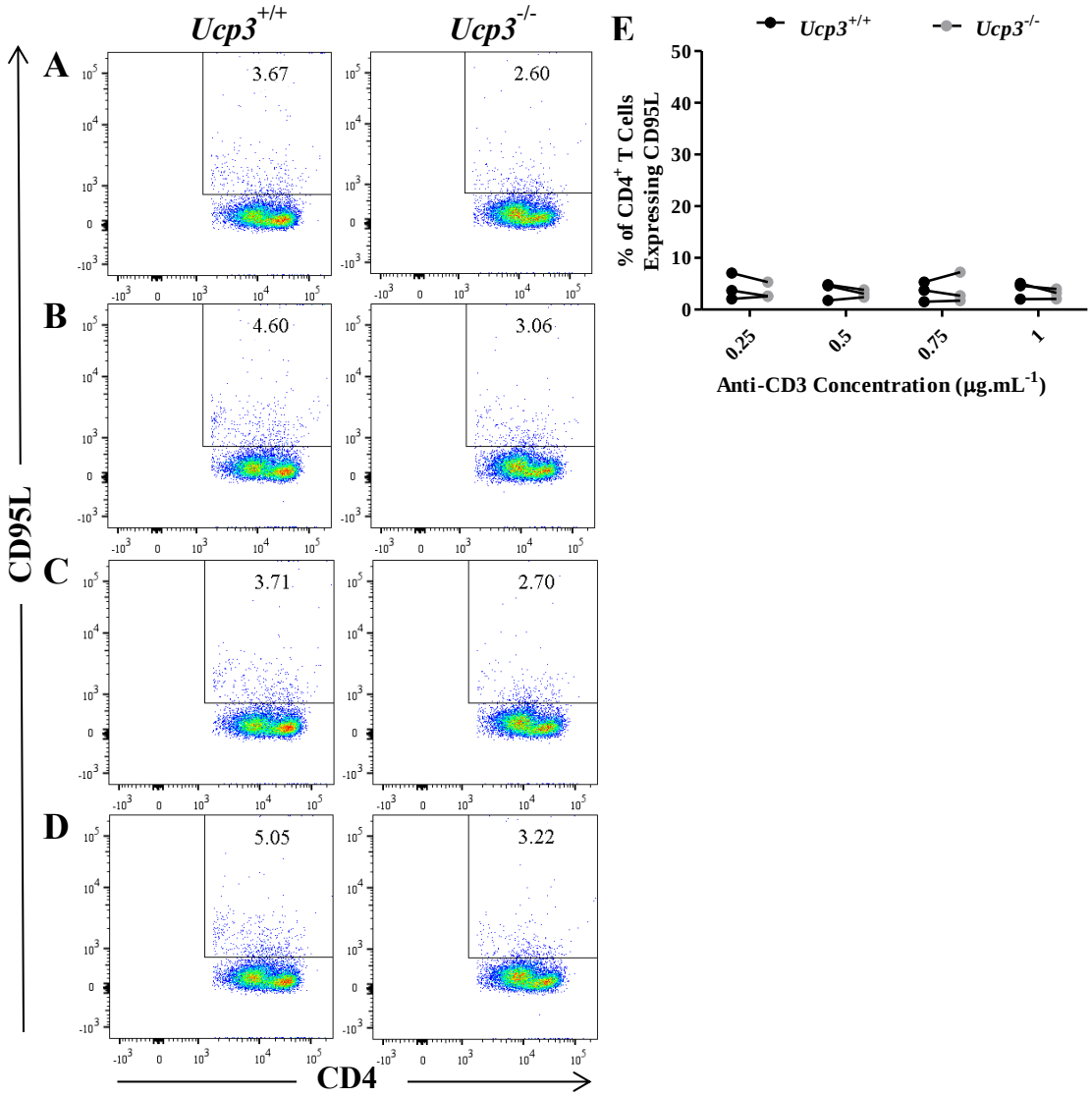

Figure 3.40: CD95L expression of *Ucp3*$^{+/+}$ and *Ucp3*$^{-/-}$ T_H0 cells is comparable 24 h post-stimulation

T_H0 cells were generated by incubating naive T cells in the presence of 0.25 (A), 0.5 (B), 0.75 (C) or 1 (D) µg.mL^{-1} of anti-CD3 for 24 h. Cells were stained with PE-Cy7:anti-CD4 and PE:anti-CD95L and analysed on a flow cytometer. Flow cytometry was performed at least three times. Dot plots are representative of at least three different experiments. All data are presented as a percentage of the total CD4$^+$ T cell population. (E) Data were analysed using a two-way, repeated measures ANOVA with a *post hoc* Bonferroni test to quantify significance where detected.

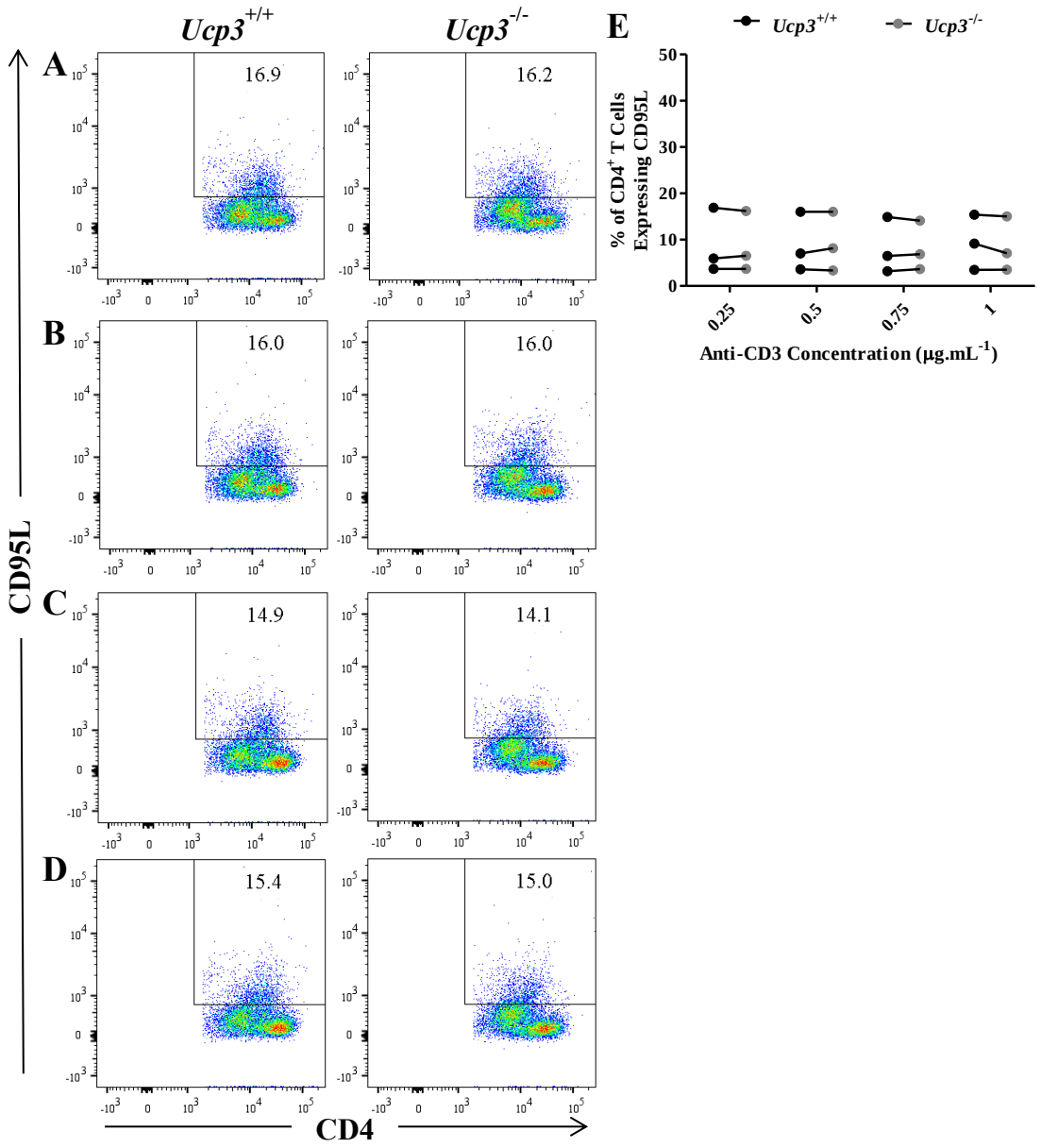

Figure 3.41: CD95L expression of *Ucp3*$^{+/+}$ and *Ucp3*$^{-/-}$ T_H0 cells is comparable 48 h post-stimulation

T_H0 cells were generated by incubating naive T cells in the presence of 0.25 (A), 0.5 (B), 0.75 (C) or 1 (D) µg.mL^{-1} of anti-CD3 for 48 h. Cells were stained with PE-Cy7:anti-CD4 and PE:anti-CD95L and analysed on a flow cytometer. Flow cytometry was performed at least three times. Dot plots are representative of at least three different experiments. All data are presented as a percentage of the total CD4$^+$ T cell population. (E) Data were analysed using a two-way, repeated measures ANOVA with a *post hoc* Bonferroni test to quantify significance where detected.

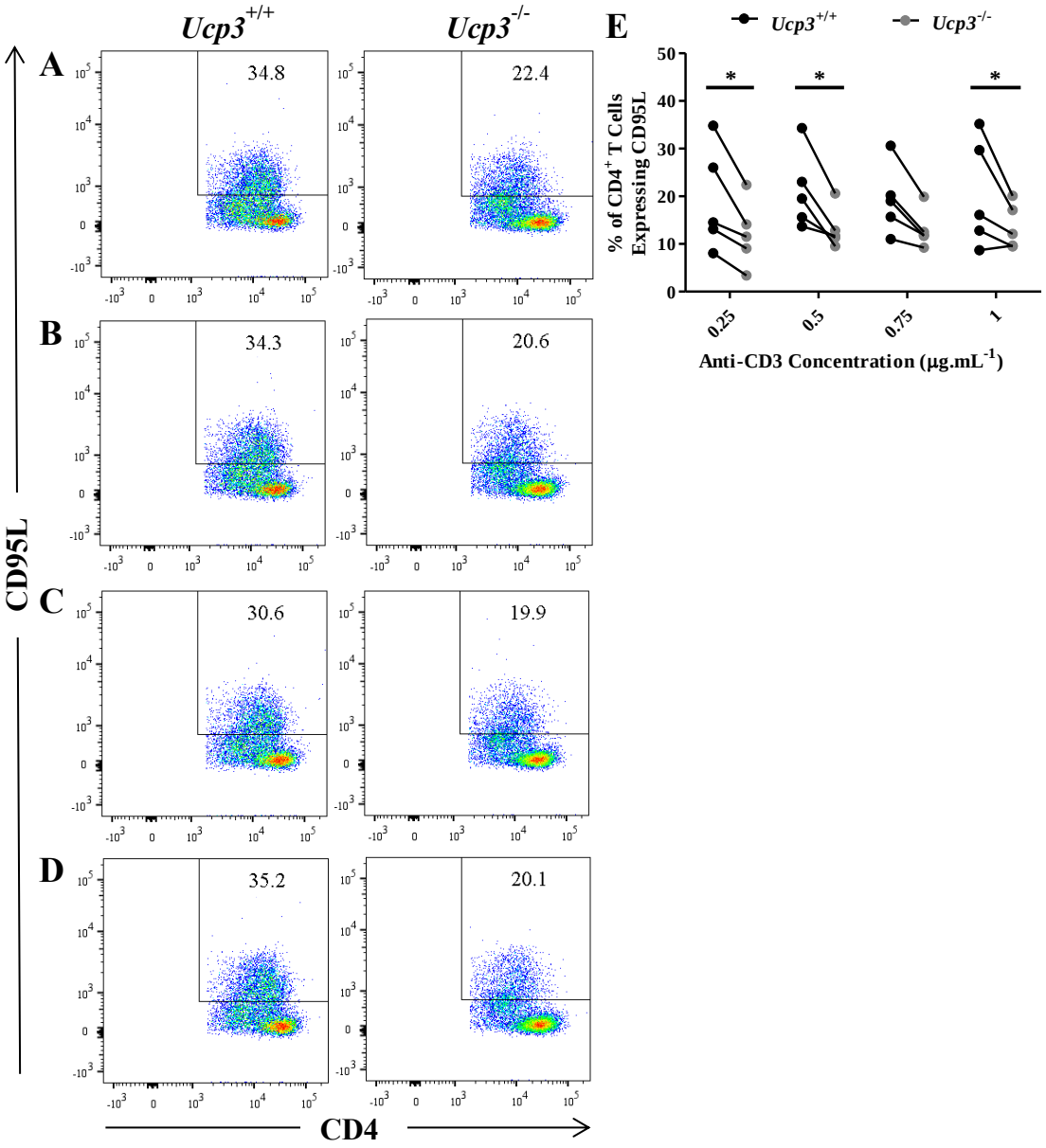

Figure 3.42: *Ucp3*$^{-/-}$ T_H0 cells display decreased CD95L expression 72 h post-stimulation

T_H0 cells were generated by incubating naive T cells in the presence of 0.25 (A), 0.5 (B), 0.75 (C) or 1 (D) µg.mL^{-1} of anti-CD3 for 72 h. Cells were stained with PE-Cy7:anti-CD4 and PE:anti-CD95L and analysed on a flow cytometer. Flow cytometry was performed at least three times. Dot plots are representative of at least three different experiments. All data are presented as a percentage of the total CD4$^+$ T cell population. (E) Data were analysed using a two-way, repeated measures ANOVA with a *post hoc* Bonferroni test to quantify significance where detected. * = $p < 0.05$.

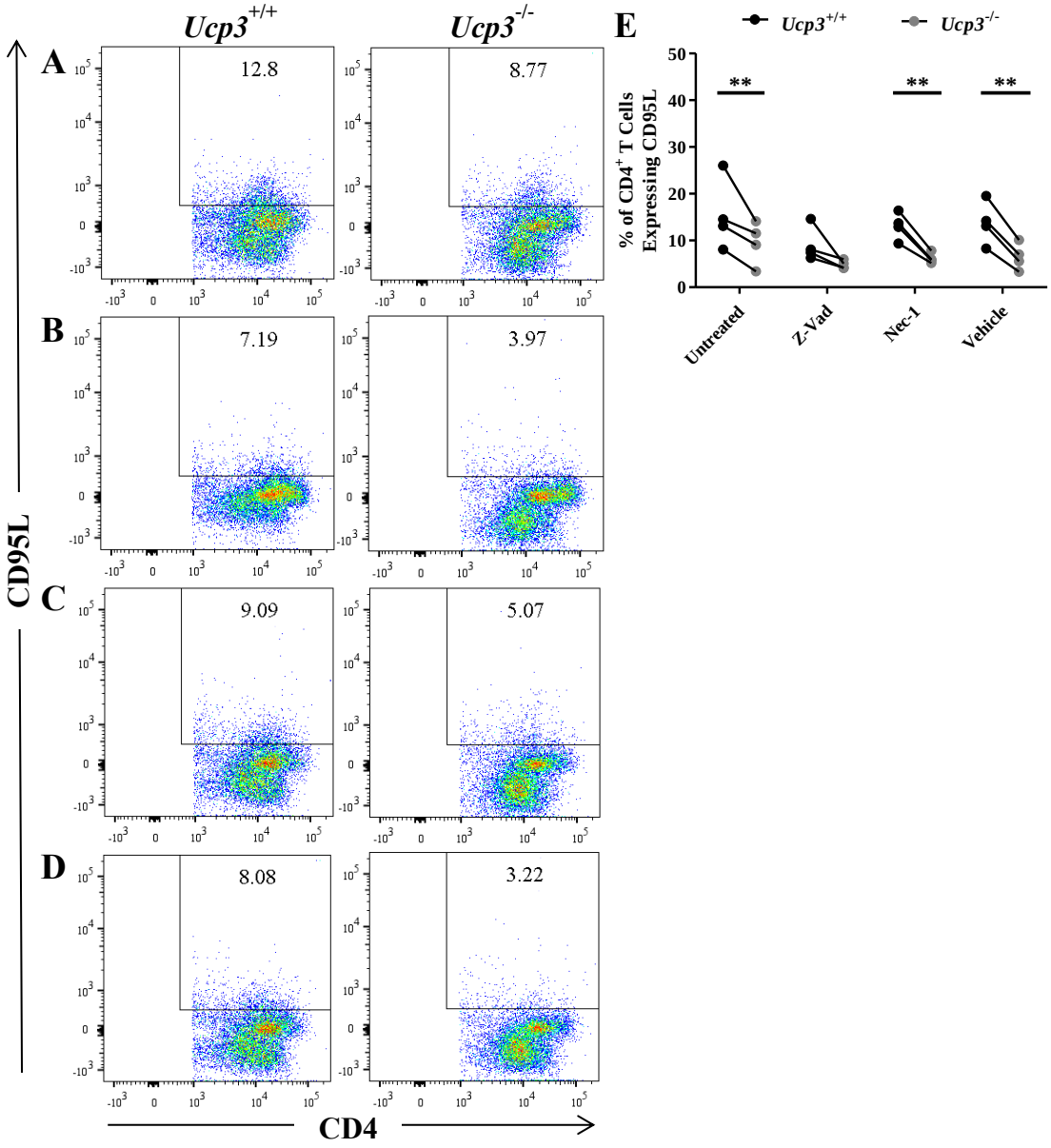

Figure 3.43: *Ucp3*$^{-/-}$ T_H0 cells display decreased CD95L expression 72 h post-stimulation with 0.25 µg.mL^{-1} of anti-CD3 in the presence of cell death inhibitors

T_H0 cells were generated by incubating naive T cells in the presence of 0.25 µg.mL^{-1} of anti-CD3 only (A) or in combination with 10 µM Z-VAD (B), 10 µM Nec-1 (C) or 0.07 % (v/v) DMSO (vehicle; D) for 72 h. Cells were stained with PE-Cy7:anti-CD4 and PE:anti-CD95L and analysed on a flow cytometer. Flow cytometry was performed at least three times. Dot plots are representative of at least three different experiments. All data are presented as a percentage of the total CD4$^+$ T cell population. (E) Data were analysed using a two-way, repeated measures ANOVA with a *post hoc* Bonferroni test to quantify significance where detected. ** = $p < 0.01$.

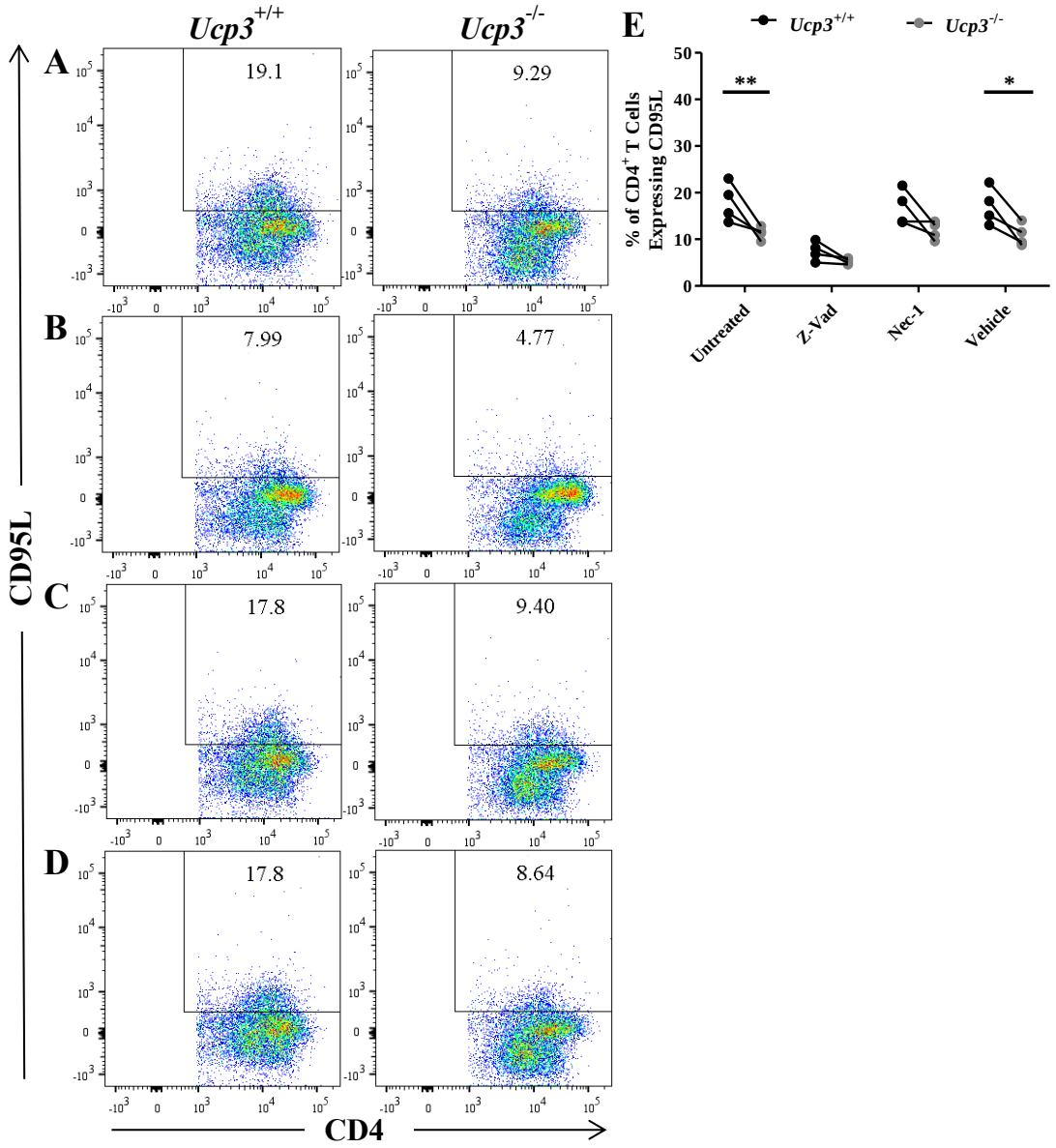

Figure 3.44: *Ucp3*$^{-/-}$ T_H0 cells display decreased CD95L expression 72 h post-stimulation with 0.5 µg.mL^{-1} of anti-CD3 in the presence of cell death inhibitors

T_H0 cells were generated by incubating naive T cells in the presence of 0.5 µg.mL^{-1} of anti-CD3 only (A) or in combination with 10 µM Z-VAD (B), 10 µM Nec-1 (C) or 0.07 % (v/v) DMSO (vehicle; D) for 72 h. Cells were stained with PE-Cy7:anti-CD4 and PE:anti-CD95L and analysed on a flow cytometer. Flow cytometry was performed at least three times. Dot plots are representative of at least three different experiments. All data are presented as a percentage of the total CD4$^+$ T cell population. (E) Data were analysed using a two-way, repeated measures ANOVA with a *post hoc* Bonferroni test to quantify significance where detected. * = $p < 0.05$. ** = $p < 0.01$.

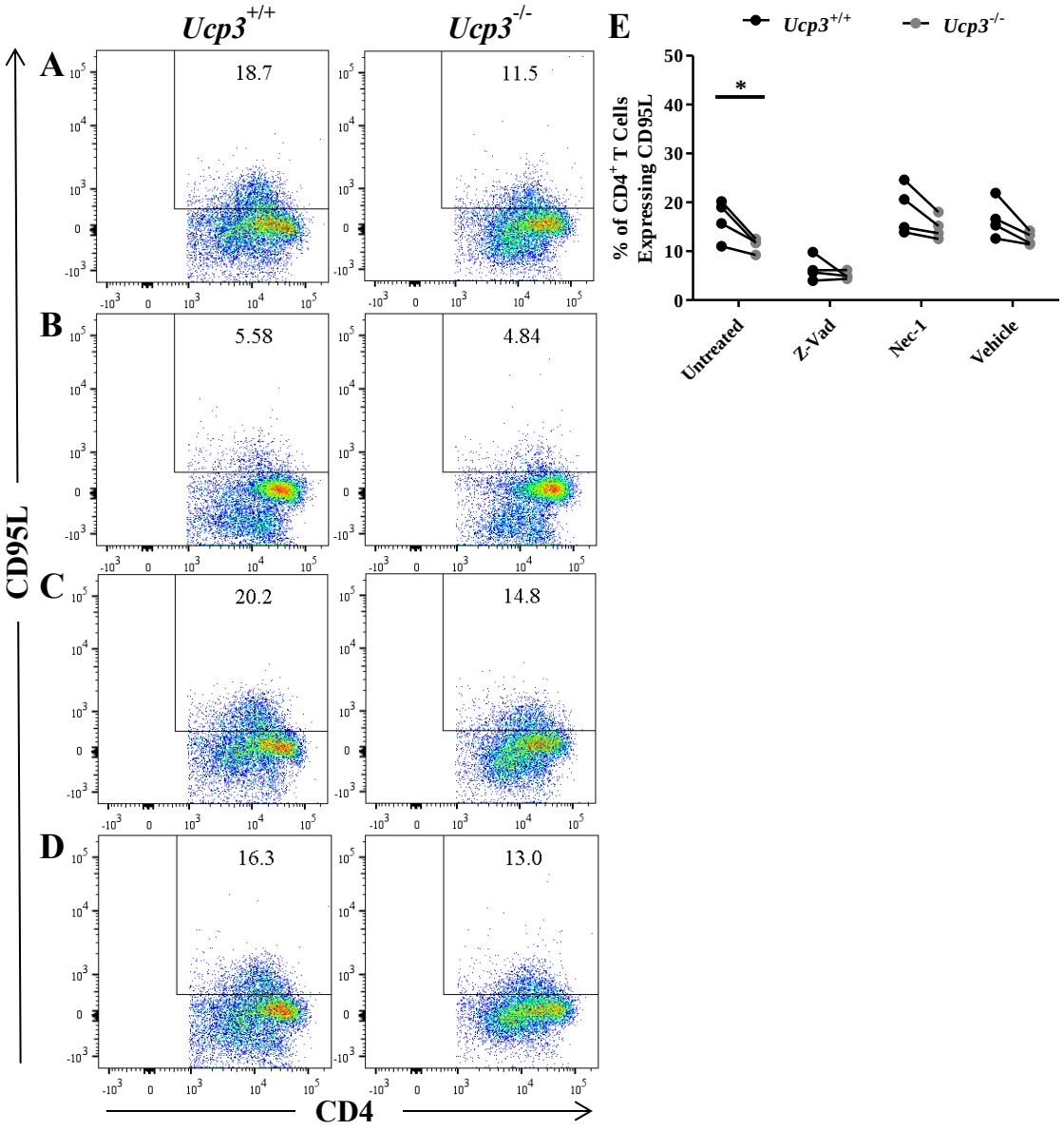

Figure 3.45: CD95L expression of *Ucp3*$^{+/+}$ and *Ucp3*$^{-/-}$ T_H0 cells is comparable 72 h post-stimulation with 0.75 µg.mL^{-1} of anti-CD3 in the presence of cell death inhibitors

T_H0 cells were generated by incubating naive T cells in the presence of 0.75 µg.mL^{-1} of anti-CD3 only (A) or in combination with 10 µM Z-VAD (B), 10 µM Nec-1 (C) or 0.07 % (v/v) DMSO (vehicle; D) for 72 h. Cells were stained with PE-Cy7:anti-CD4 and PE:anti-CD95L and analysed on a flow cytometer. Flow cytometry was performed at least three times. Dot plots are representative of at least three different experiments. All data are presented as a percentage of the total CD4$^+$ T cell population. (E) Data were analysed using a two-way, repeated measures ANOVA with a *post hoc* Bonferroni test to quantify significance where detected. * = $p < 0.05$.

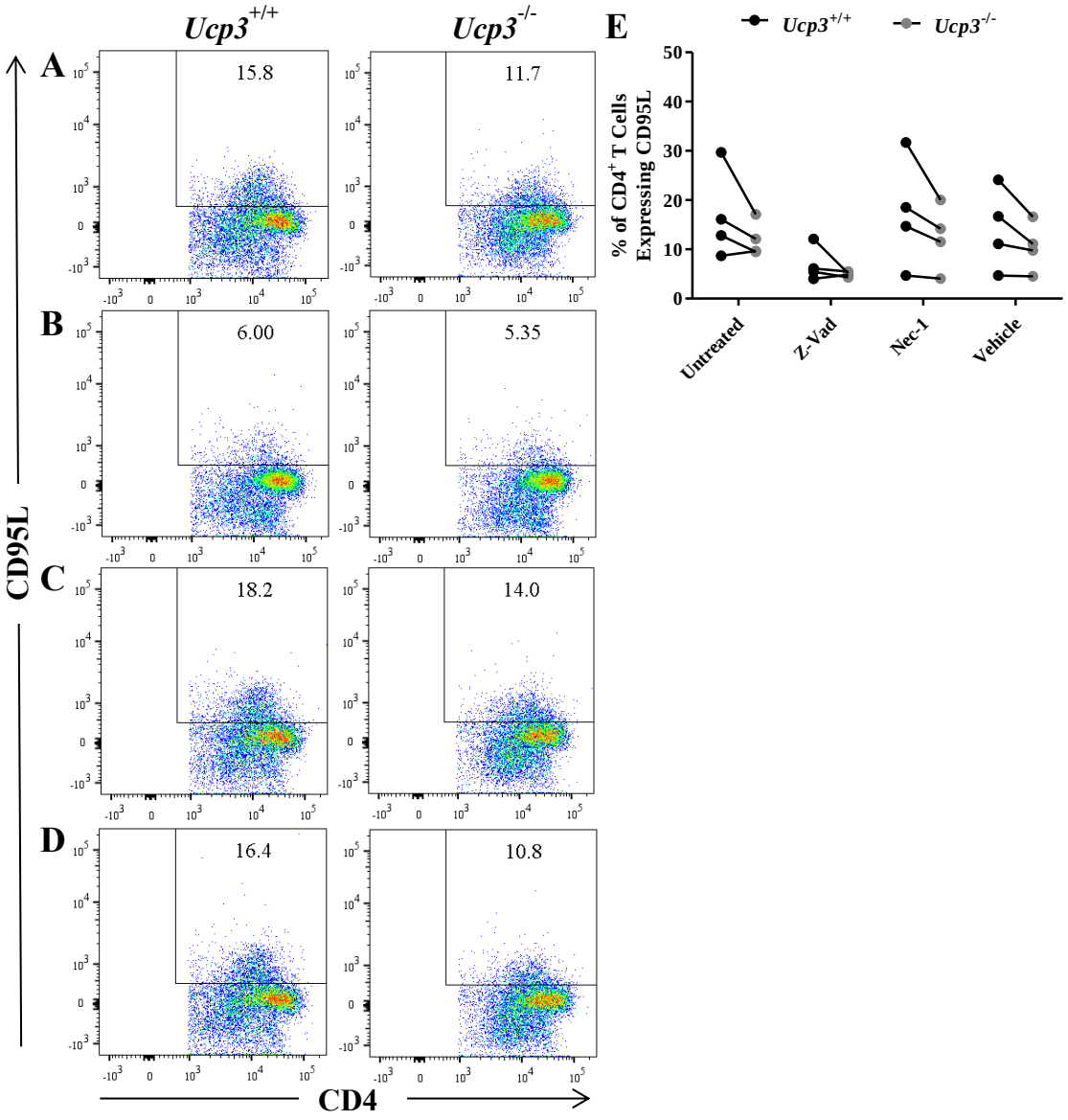

Figure 3.46: CD95L expression of *Ucp3*$^{+/+}$ and *Ucp3*$^{-/-}$ T_H0 cells is comparable 72 h post-stimulation with 1 µg.mL^{-1} of anti-CD3 in the presence of cell death inhibitors

T_H0 cells were generated by incubating naive T cells in the presence of 1 µg.mL^{-1} of anti-CD3 only (A) or in combination with 10 µM Z-VAD (B), 10 µM Nec-1 (C) or 0.07 % (v/v) DMSO (vehicle; D) for 72 h. Cells were stained with PE-Cy7:anti-CD4 and PE:anti-CD95L and analysed on a flow cytometer. Flow cytometry was performed at least three times. Dot plots are representative of at least three different experiments. All data are presented as a percentage of the total CD4$^+$ T cell population. (E) Data were analysed using a two-way, repeated measures ANOVA with a *post hoc* Bonferroni test to quantify significance where detected.

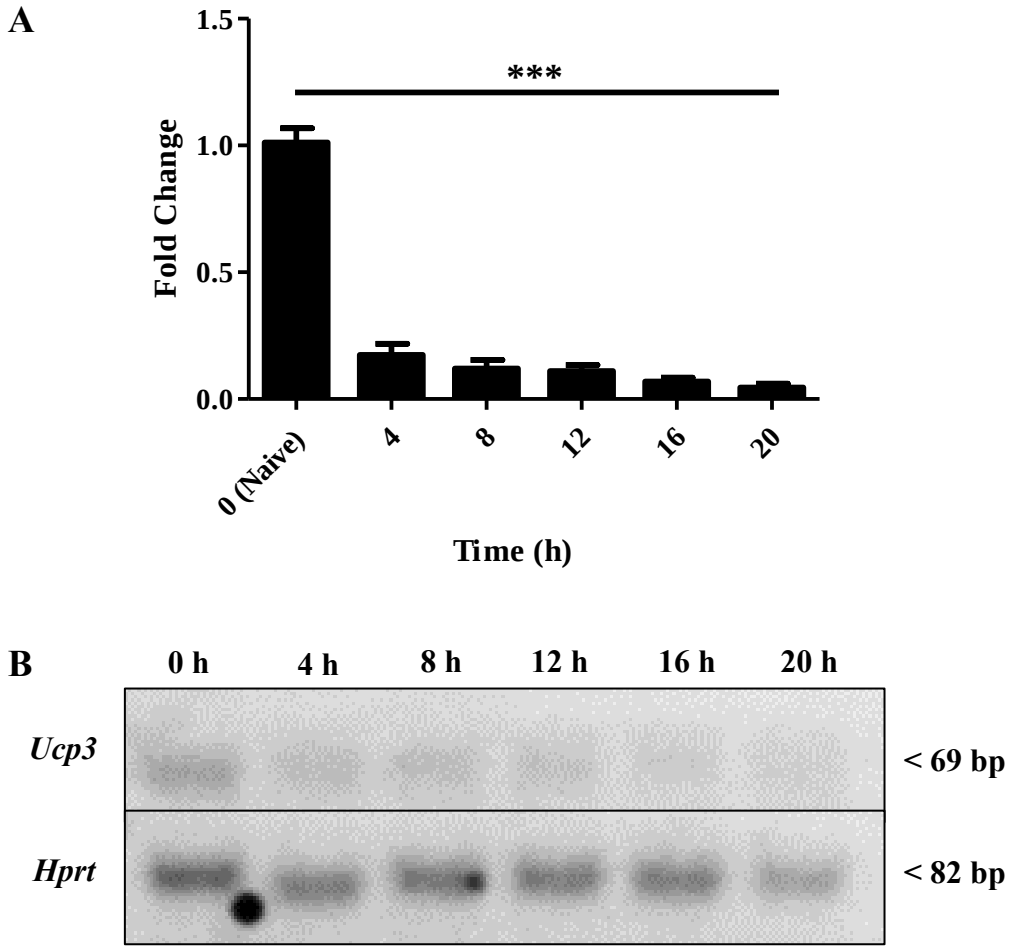

Figure 3.47: *Ucp3* gene expression is downregulated in T_H0 cells within 4 h of activation

Primary $CD4^+$ T cells were isolated from a suspension of splenocytes and analysed for RT-PCR immediately. T_H0 cells were generated by incubating naive T cells in the presence of 1 and 2 $\mu g.mL^{-1}$ of anti-CD3 and anti-CD28, respectively, for the time indicated before being used for RT-PCR. (A) RT-PCR analysis of *Ucp3* gene expression in T_H0 cells relative to naive T cells. RT-PCR was performed three times in triplicate. Data were analysed using a one-way repeated measures ANOVA with a *post hoc* Dunnet test to quantify significance where detected. *** = $p < 0.001$. (B) Representative agarose gel of naive T cell cDNA and T_H0 cell cDNA prepared at the times indicated, displaying *Ucp3* and *Hprt* at 69 and 82 bp, respectively.

3.2.4 *Ucp3* Ablation Does Not Affect $CD4^+CD8^-$ Thymocytes, Naive $CD4^+$ T Cells or T_{reg} and Memory T Cell Frequency

The effect of *Ucp*3 ablation on T_H0 cells observed in Section 3.2.3 is suggestive of a role for UCP3 in the restriction of T cell activation and TCR signalling. Therefore, we hypothesized that no effect of *Ucp3* ablation would be evident on precursor cells to $CD4^+$ T cells, *i.e.* $CD4^+CD8^-$ thymocytes, or naive $CD4^+$ T cells until they undergo activation. To explore this possibility, we analysed the viability, size, Ki-67 expression and cytokine production of these cell populations from $Ucp3^{+/+}$ and $Ucp3^{-/-}$ mice. Moreover, the above data arose from our examination of total splenic $CD4^+$ T cells. As well as naive $CD4^+$ T cells, this population also includes a portion of $CD4^+$ memory and nT_{reg} cells, which can display hyper- and hypo-responsiveness, respectively, to TCR activation *in vitro*. To ensure that the effects we have observed are not due to differences in the numbers of naive versus memory versus nT_{reg} cells in $Ucp3^{+/+}$ compared to $Ucp3^{-/-}$ mice under steady state conditions, we explored the effect of *Ucp3* ablation on the frequency of these cell populations, as well as on the parameters mentioned above by performing flow cytometry. $CD4^+$ T cells were harvested direct from spleens or inguinal lymph nodes and, along with thymocytes, were immediately labelled with LIVE/DEAD™ Fixable Aqua Dead Cell Stain, PE-Cy7:anti-CD4, PE or PE-Cy5:anti-CD8, PerCP-Cy™5.5 or Pacific Blue:anti-CD69, *APC*:anti-CD44, FITC:anti-CD62L, PerCP-eFluor™ 710:anti-Ki-67, eFluor™ 660:anti-CD25 and/or PE or *APC*:anti-FoxP3 and analysed on a flow cytometer. For intracellular cytokine production analysis, cells were stimulated with PMA, ionomycin and brefeldin A for 6 h before being labelled for flow cytometry as above, as well as with *APC*:anti-IFN-γ and PE:anti-IL-17A.

$CD4^+CD8^-$ thymocyte viability is unaffected by *Ucp3* ablation (Figure 3.48A and B). FSC-A was used as a measure of cell size. No difference in cell size is evident between $Ucp3^{+/+}$ and $Ucp3^{-/-}$ $CD4^+CD8^-$ thymocytes (Figure 3.48C and D). The expression of Ki-67, the cell cycle marker described previously, and FoxP3, the marker for nT_{reg} cells, are comparable between genotypes (Figure 3.49). Production of the cytokines IFN-γ and IL-17A following PMA stimulation are also not significantly different by $Ucp3^{+/+}$ and $Ucp3^{-/-}$ $CD4^+CD8^-$ thymocytes (Figure 3.50). Similarly, $Ucp3^{+/+}$ and $Ucp3^{-/-}$ naive $CD4^+$ T cells isolated from inguinal lymph nodes display no difference in viability and cell size (Figure 3.51) or Ki-67 and FoxP3 expression (Figure 3.52). The frequency of $FoxP3^+$ cells observed in both the $CD4^+CD8^-$ thymocyte population and the $CD4^+$ naive T cell population isolated from lymph nodes is in line with previous findings (Hori *et al*., 2003). No significant differences

in IFN-γ or IL-17A production are observed in naive $CD4^+$ T cells isolated from inguinal lymph nodes (Figure 3.53).

The viability and size of naive $CD4^+$ T cells isolated from spleen are unaffected by *Ucp3* ablation (Figure 3.54). The expression of CD69, the early activation marker described previously, is comparable between genotypes (Figure 3.55A and B). Using the expression levels of CD44 and CD62L in combination, we were able to differentiate memory $CD4^+$ T cells from naive T cells. Naive T cells display high levels of CD62L, while memory cells characteristically have a 'CD44 high and CD62L low' phenotype (Broere *et al*., 2011). The frequencies of these populations are similar in $Ucp3^{+/+}$ and $Ucp3^{-/-}$ mice (Figure 3.55C and D). FoxP3 and CD25 co-expression is indicative of T_{reg} cells (Liao *et al*., 2013). Naturally occurring $CD25^+FoxP3^+$ T_{reg} cells make up approximately 10 % of the $CD4^+$ T cell population in the murine spleen (Hori *et al*., 2003; Huang *et al*., 2004). To ensure that no differences in the T_{reg} cell frequency exist between $Ucp3^{+/+}$ and $Ucp3^{-/-}$ mice, the $CD4^+CD25^+FoxP3^+$ cell populations were analysed. No difference in T_{reg} cell frequency is detected between genotypes (Figure 3.55E and F). Likewise, no differences in Ki-67 expression or IFN-γ and IL-17A production are evident between $Ucp3^{+/+}$ and $Ucp3^{-/-}$ splenic, naive $CD4^+$ T cells (Figure 3.56). That no effect of *Ucp3* ablation is observed on $CD4^+CD8^-$ thymocytes or naive $CD4^+$ T cells isolated from both lymph nodes and spleen, including memory and nT_{reg} cells, complies with our hypothesis of UCP3 acting as a restrictor of T cell activation. It is perceivable that the impact of *Ucp3* ablation is only discernible following the T cell activation event.

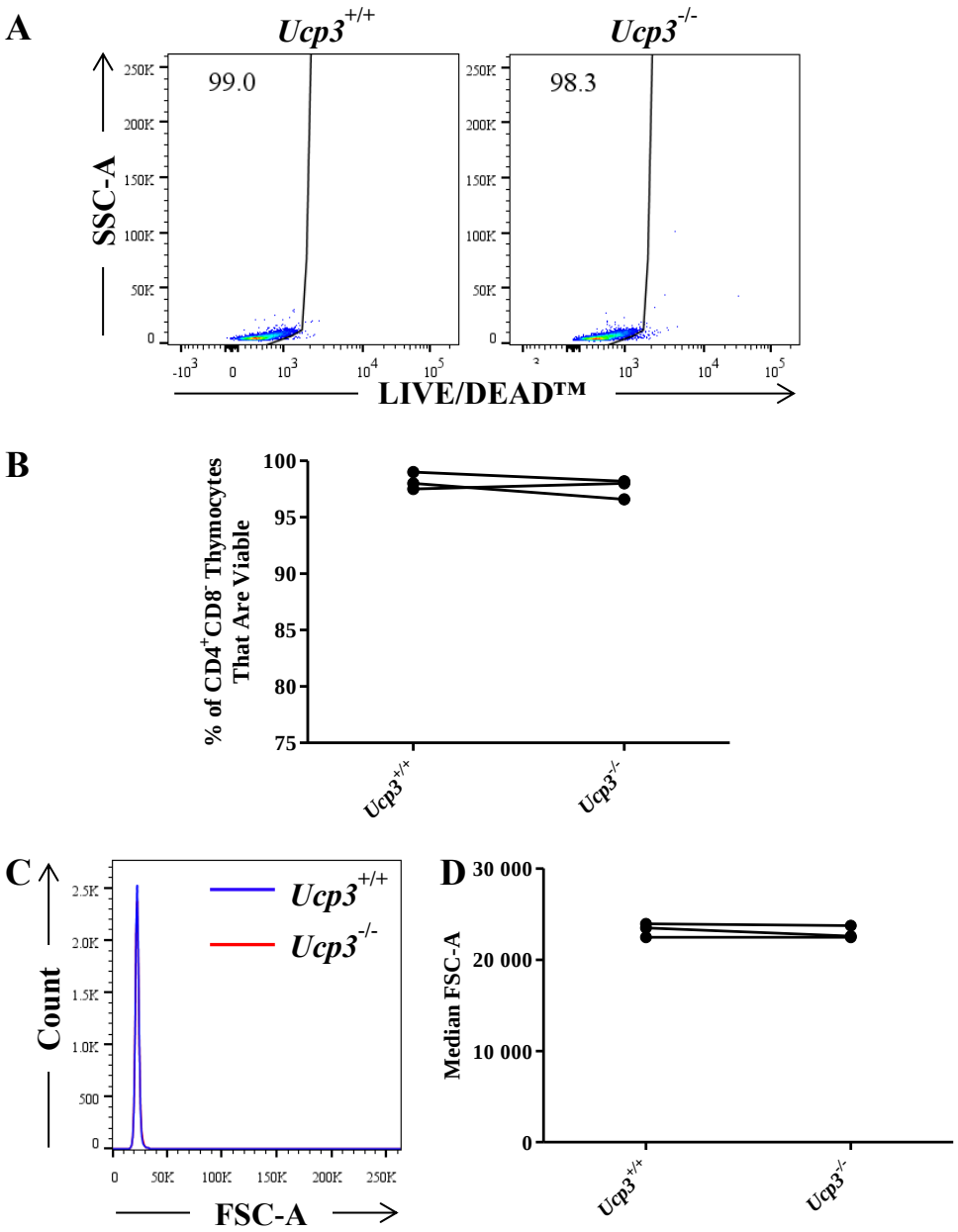

Figure 3.48: Viability and size of *Ucp3*$^{+/+}$ and *Ucp3*$^{-/-}$ CD4^{+}CD8^{-} thymocytes are comparable

Thymocytes were stained with LIVE/DEAD™, PE-Cy7:anti-CD4 and PE:anti-CD8 before being analysed on a flow cytometer. Flow cytometry was performed at least three times. Dot plots and histogram are representative of at least three different experiments. Data were analysed using a two-tailed, unpaired *t* test to quantify significance where detected. (A, B) Viability of CD4^{+}CD8^{-} thymocytes. Data are presented as a percentage of the total CD4^{+}CD8^{-} thymocyte population. (C) Histogram of viable, CD4^{+}CD8^{-} thymocyte size. (D) Size of viable, CD4^{+}CD8^{-} thymocytes.

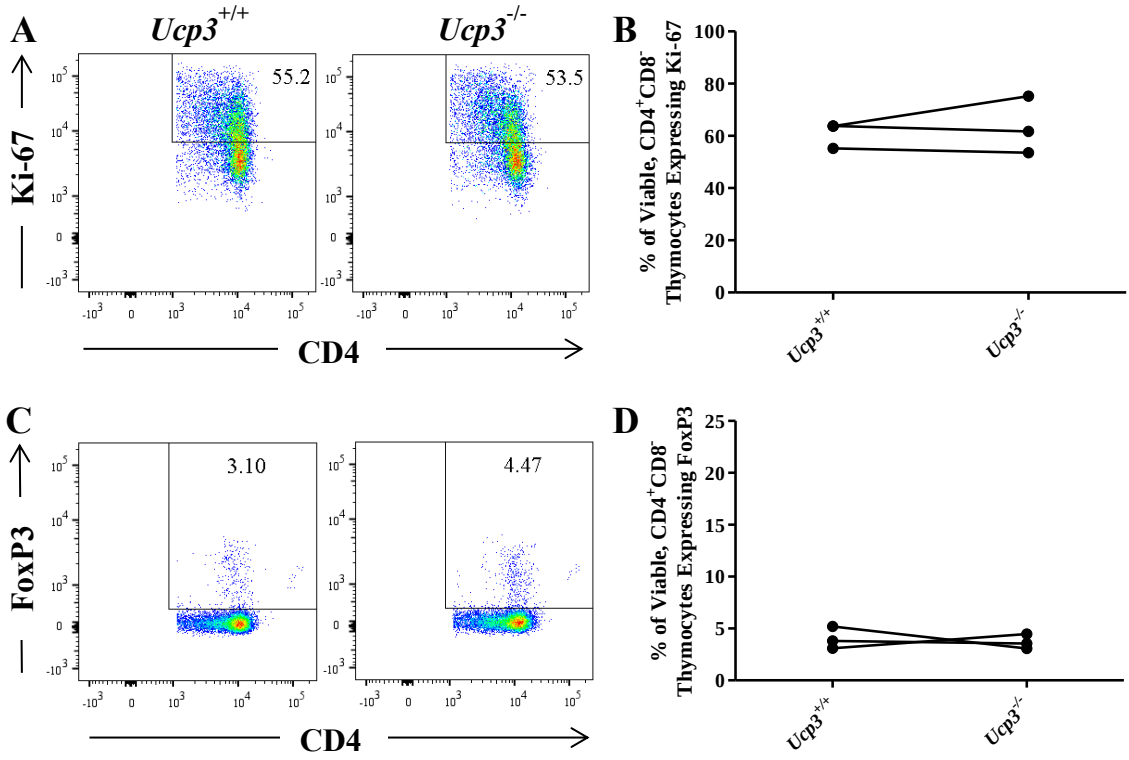

Figure 3.49: Ki-67 and FoxP3 expression of *Ucp3*$^{+/+}$ and *Ucp3*$^{-/-}$ CD4^{+}CD8^{-} thymocytes is comparable

Thymocytes were stained with LIVE/DEAD™, PE-Cy7:anti-CD4, PE:anti-CD8, *APC*:anti-FoxP3 and PerCP-eFluor™ 710:anti-Ki-67 before being analysed on a flow cytometer. Flow cytometry was performed at least three times. Dot plots are representative of at least three different experiments. All data are presented as a percentage of the viable, CD4^{+}CD8^{-} thymocyte population. Data were analysed using a two-tailed, unpaired *t* test to quantify significance where detected. (A, B) Ki-67 expression of CD4^{+}CD8^{-} thymocytes. (C, D) FoxP3 expression of CD4^{+}CD8^{-} thymocytes.

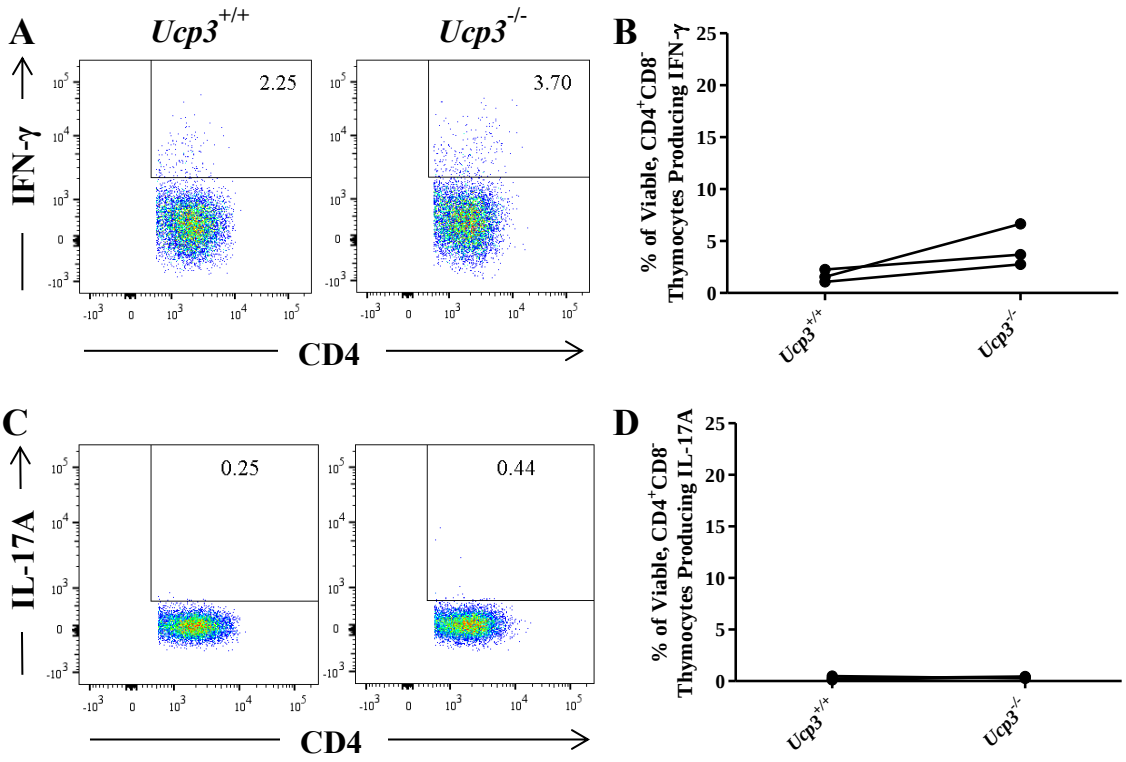

Figure 3.50: IFN-γ and IL-17A production by *Ucp3*$^{+/+}$ and *Ucp3*$^{-/-}$ CD4^{+}CD8^{-} thymocytes is negligible

Thymocytes were stimulated with PMA, ionomycin and brefeldin A for 6 h before being stained with LIVE/DEAD™, PE-Cy7:anti-CD4, PE-Cy5:anti-CD8, PE:anti-IL-17A and *APC*:anti-IFN-γ and analysed on a flow cytometer. Flow cytometry was performed at least three times. Dot plots are representative of at least three different experiments. All data are presented as a percentage of the viable, CD4^{+}CD8^{-} thymocyte population. Data were analysed using a two-tailed, unpaired *t* test to quantify significance where detected. (A, B) IFN-γ production by CD4^{+}CD8^{-} thymocytes. (C, D) IL-17A production by CD4^{+}CD8^{-} thymocytes.

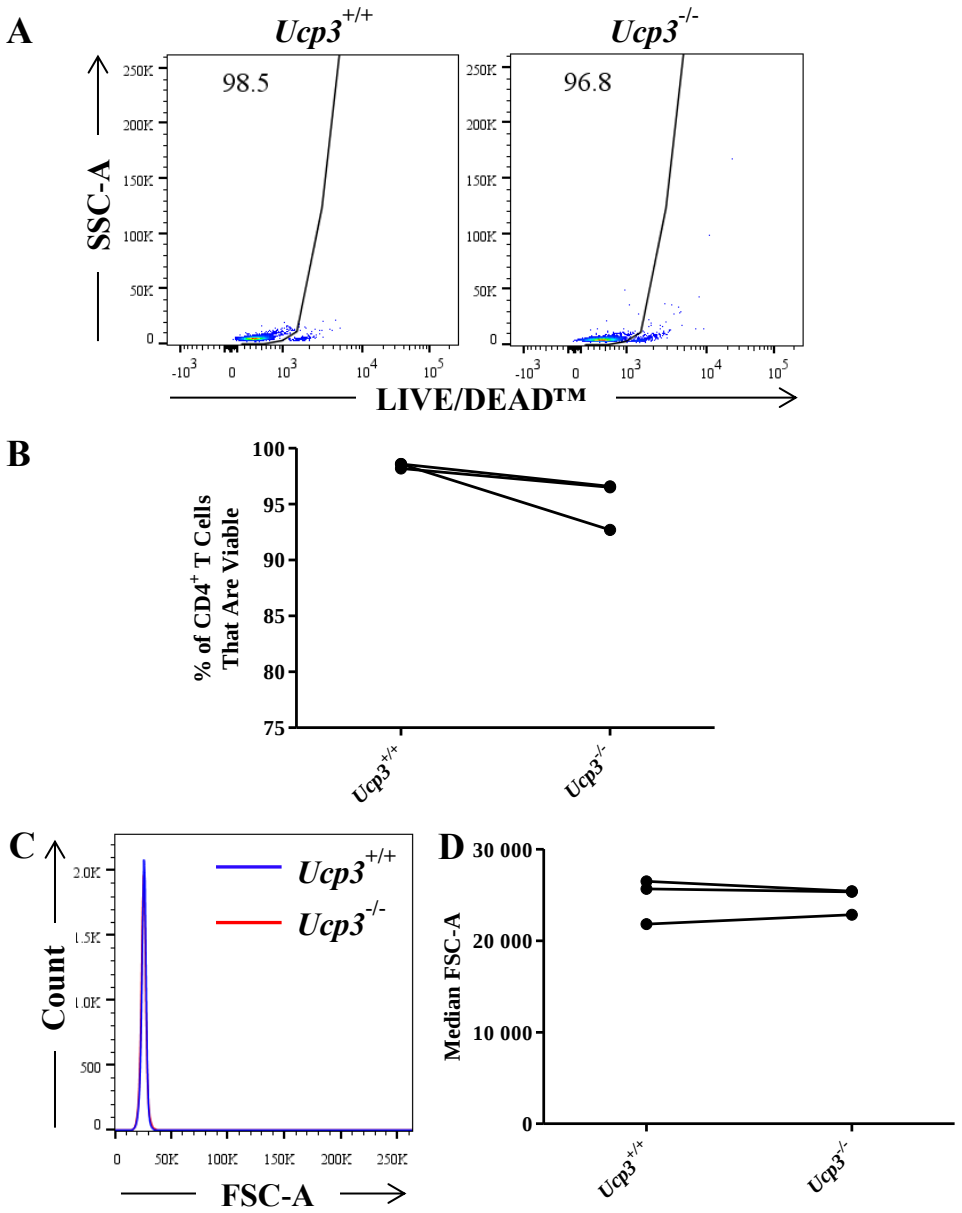

Figure 3.51: Viability and size of *Ucp3*$^{+/+}$ and *Ucp3*$^{-/-}$ naive CD4^{+} T cells from lymph nodes are comparable

Primary CD4^{+} T cells were isolated from a suspension of lymph node cells and stained with LIVE/DEAD™ and PE-Cy7:anti-CD4 before being analysed on a flow cytometer. Flow cytometry was performed at least three times. Dot plots and histogram are representative of at least three different experiments. Data were analysed using a two-tailed, unpaired *t* test to quantify significance where detected. (A, B) Viability of naive T cells. Data are presented as a percentage of the total CD4^{+} T cell population. (C) Histogram of viable, CD4^{+} T cell size. (D) Size of viable, CD4^{+} T cells.

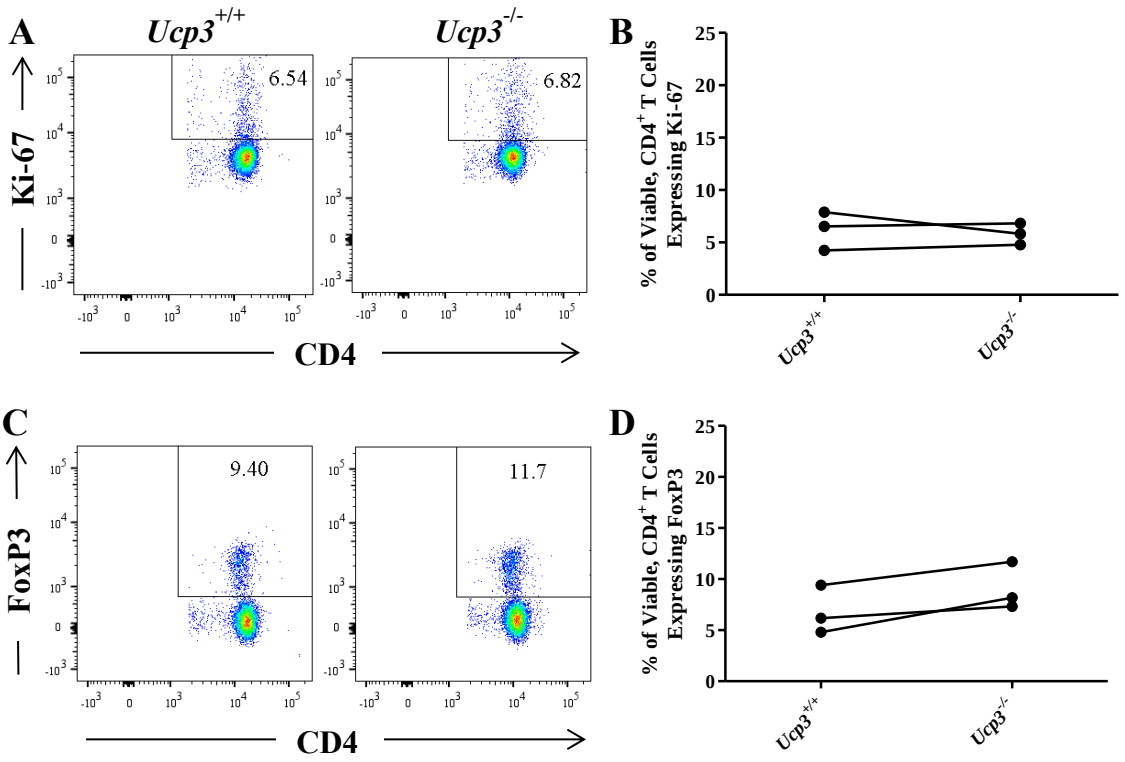

Figure 3.52: Ki-67 and FoxP3 expression of *Ucp3*$^{+/+}$ and *Ucp3*$^{-/-}$ naive CD4^{+} T cells from lymph nodes is comparable

Primary CD4^{+} T cells were isolated from a suspension of lymph node cells and stained with LIVE/DEAD™, PE-Cy7:anti-CD4, PE:anti-FoxP3 and PerCP-eFluor™ 710:anti-Ki-67 before being analysed on a flow cytometer. Flow cytometry was performed at least three times. Dot plots are representative of at least three different experiments. All data are presented as a percentage of the viable, CD4^{+} T cell population. Data were analysed using a two-tailed, unpaired *t* test to quantify significance where detected. (A, B) Ki-67 expression of naive, CD4^{+} T cells. (C, D) FoxP3 expression of naive, CD4^{+} T cells.

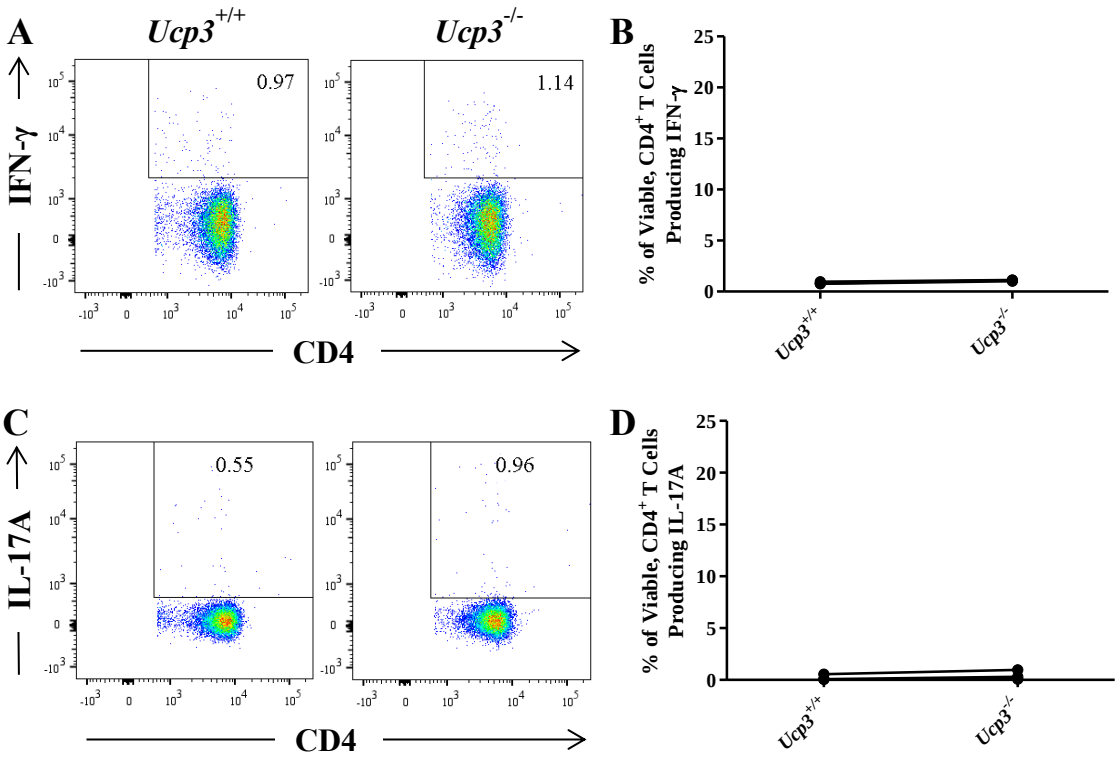

Figure 3.53: IFN-γ and IL-17A production by *Ucp3*$^{+/+}$ and *Ucp3*$^{-/-}$ naive CD4^{+} T cells from lymph nodes is negligible

Primary CD4^{+} T cells were isolated from a suspension of lymph node cells and stimulated with PMA, ionomycin and brefeldin A for 6 h before being stained with LIVE/DEAD™, PE-Cy7:anti-CD4, PE:anti-IL-17A and *APC*:anti-IFN-γ and analysed on a flow cytometer. Flow cytometry was performed at least three times. Dot plots are representative of at least three different experiments. All data are presented as a percentage of the viable, CD4^{+} T cell population. Data were analysed using a two-tailed, unpaired *t* test to quantify significance where detected. * = $p < 0.05$. (A, B) IFN-γ production by naive, CD4^{+} T cells. (C, D) IL-17A production by naive, CD4^{+} T cells.

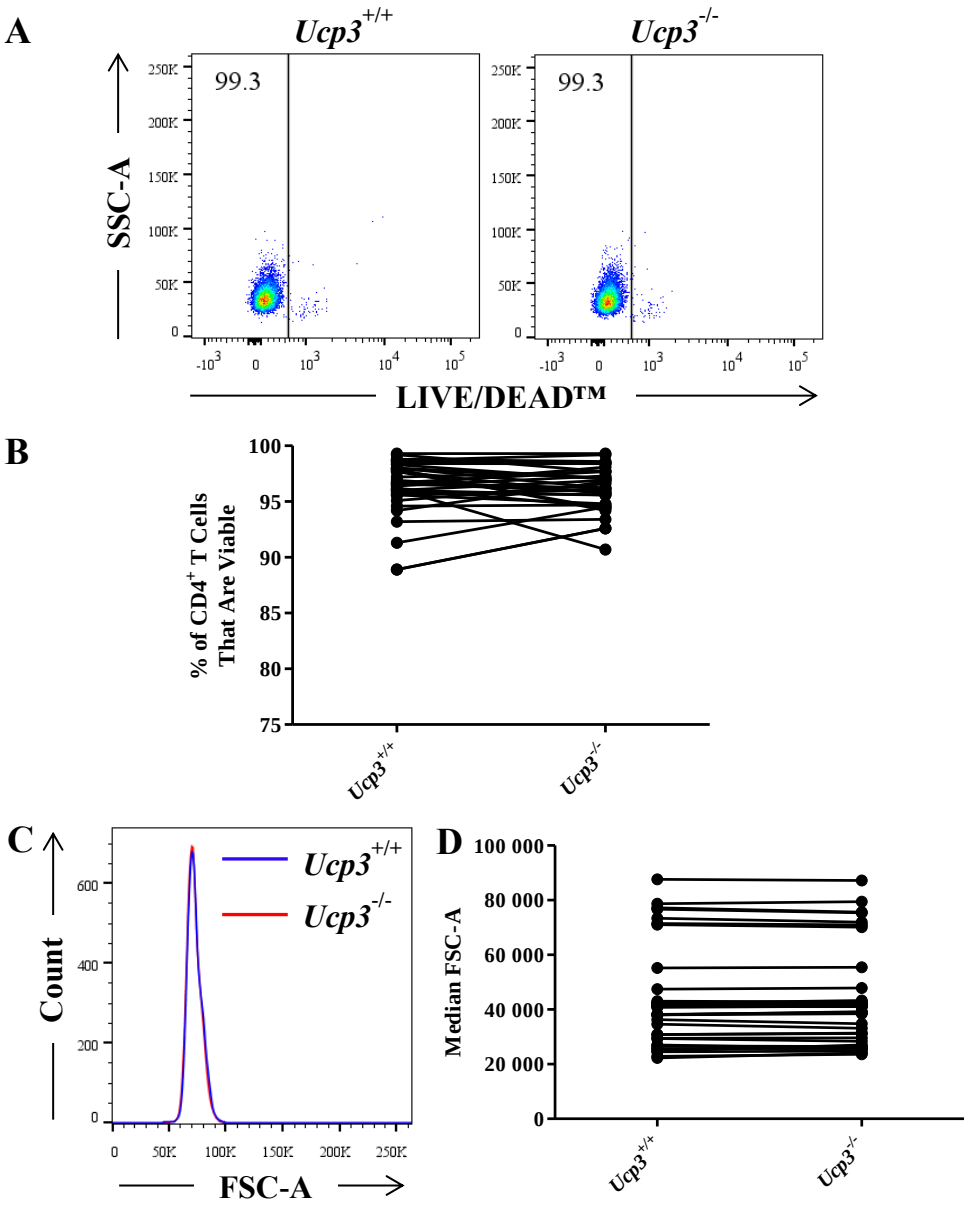

Figure 3.54: Viability and size of *Ucp3*$^{+/+}$ and *Ucp3*$^{-/-}$ splenic naive CD4^{+} T cells are comparable

Primary CD4^{+} T cells were isolated from a suspension of splenocytes and stained with LIVE/DEAD™ and PE-Cy7:anti-CD4 before being analysed on a flow cytometer. Flow cytometry was performed at least three times. Dot plots and histogram are representative of at least three different experiments. Data were analysed using a two-tailed, unpaired *t* test to quantify significance where detected. (A, B) Viability of naive T cells. Data are presented as a percentage of the total CD4^{+} T cell population. (C) Histogram of viable, CD4^{+} T cell size. (D) Size of viable, CD4^{+} T cells.

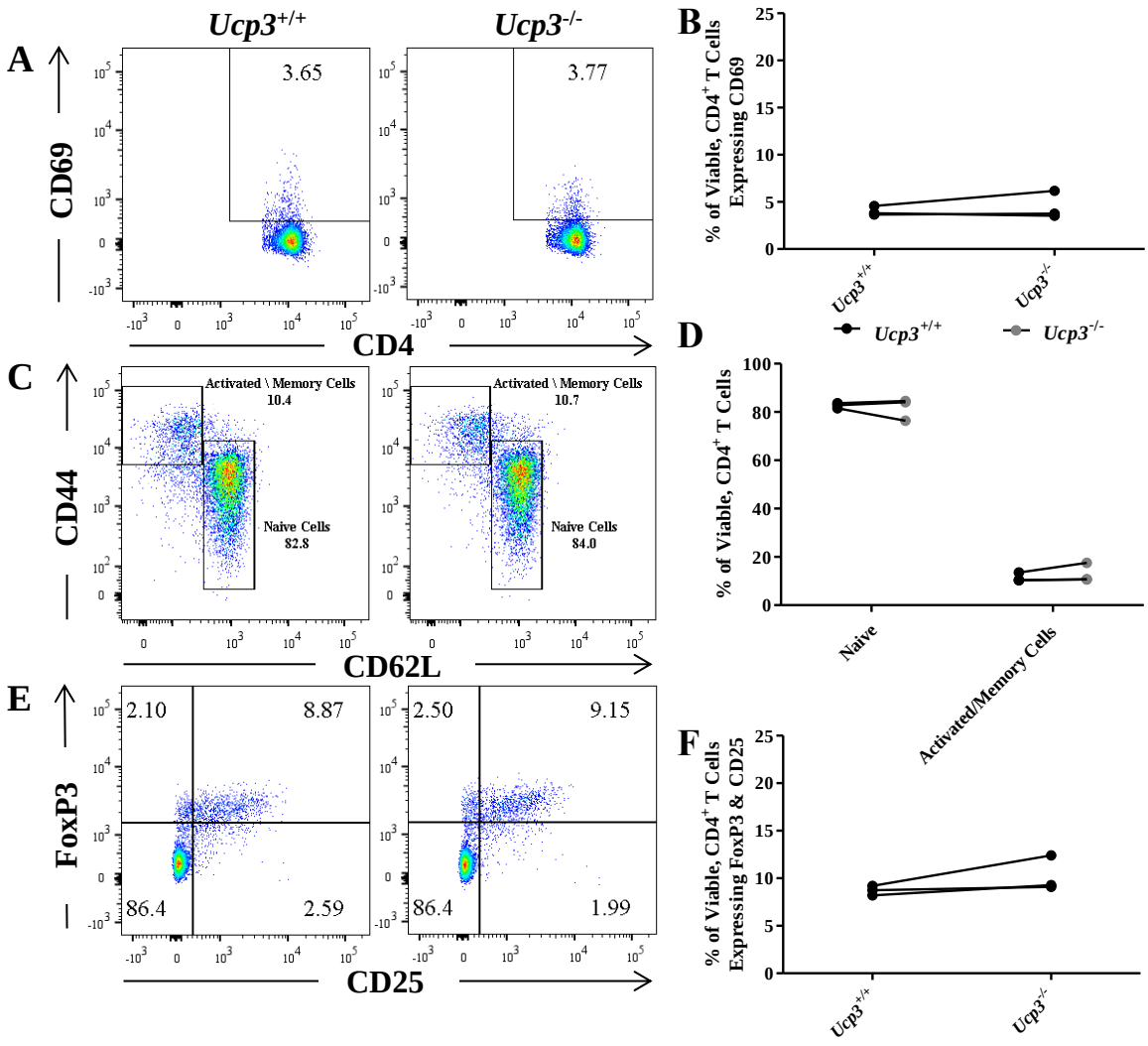

Figure 3.55: Surface marker expression of *Ucp3*$^{+/+}$ and *Ucp3*$^{-/-}$ splenic naive CD4^{+} T cells and frequency of memory and nT$_{reg}$ cells in *Ucp3*$^{+/+}$ and *Ucp3*$^{-/-}$ mice are comparable

Primary CD4^{+} T cells were isolated from a suspension of splenocytes and stained with LIVE/DEAD™, PE-Cy7:anti-CD4, PerCP-Cy™5.5:anti-CD69, *APC*:anti-CD44, FITC:anti-CD62L, eFluor™ 660:anti-CD25 and/or PE:anti-FoxP3 before being analysed on a flow cytometer. All data are presented as a percentage of the viable, CD4^{+} T cell population. Flow cytometry was performed at least three times. Dot plots are representative of at least three different experiments. (A, B) CD69 expression of naive T cells. (C, D) Frequency of naive and memory T cells. (E, F) FoxP3 and CD25 co-expression, indicative of nT$_{reg}$ cells which are CD4^{+}CD25^{+}FoxP3^{+}. Data were analysed using a two-tailed, unpaired *t* test (B, F) or a two-way repeated measures ANOVA with a *post hoc* Bonferroni test (D) to quantify significance where detected.

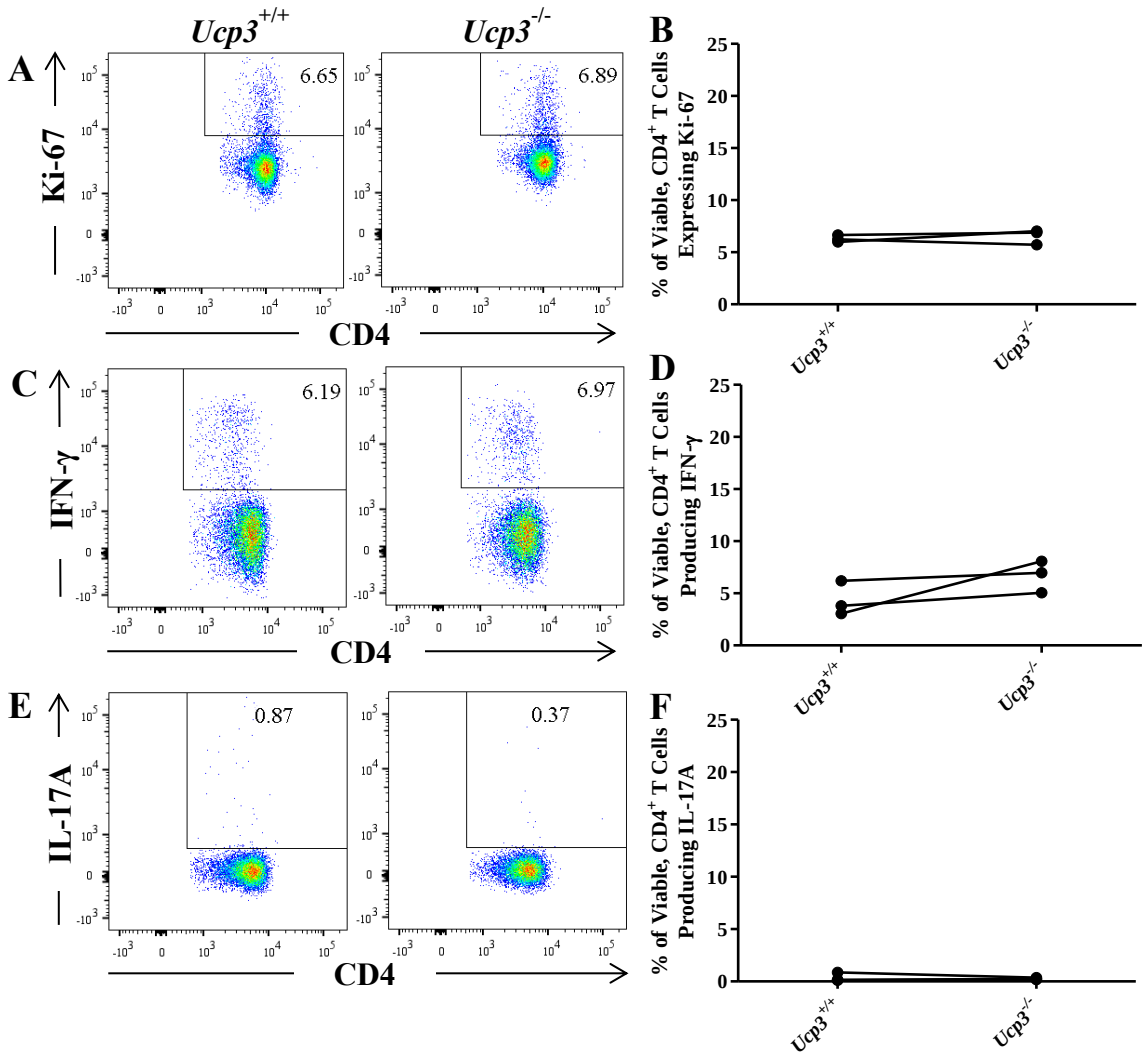

Figure 3.56: Ki-67 expression of, and IFN-γ and IL-17A production by, *Ucp3*$^{+/+}$ and *Ucp3*$^{-/-}$ splenic naive CD4^{+} T cells are comparable

Primary CD4^{+} T cells were isolated from a suspension of splenocytes and stained with LIVE/DEAD™ and PE-Cy7:anti-CD4 with PerCP-eFluor™ 710:anti-Ki-67 or *APC*:anti-IFN-γ and PE:anti-IL-17A before being analysed on a flow cytometer. For intracellular cytokine analysis, cells were first stimulated with PMA, ionomycin and brefeldin A for 6 h before being labelled. Flow cytometry was performed at least three times. Dot plots are representative of at least three different experiments. All data are presented as a percentage of the viable, CD4^{+} T cell population. Data were analysed using a two-tailed, unpaired *t* test to quantify significance where detected. (A, B) Ki-67 expression of naive, CD4^{+} T cells. (C, D) IFN-γ production by naive, CD4^{+} T cells. (E, F) IL-17A production by naive, CD4^{+} T cells.

3.2.5 *Ucp3* Ablation Does Not Affect T_H1 Cells

After observing the striking effects of *Ucp3* ablation on non-polarized, activated T (T_H0) cells, it was hypothesized that *Ucp3* ablation would also affect polarized T cell subsets. With this in mind, we investigated the function of *Ucp3*$^{-/-}$ T_H1 cells compared to *Ucp3*$^{+/+}$ T_H1 cells by measuring the production of IFN-γ, the characteristic cytokine produced by T_H1 cells, as well as T_H1 cell viability and activation (size). Primary *Ucp3*$^{+/+}$ and *Ucp3*$^{-/-}$ $CD4^+$ T cells were harvested direct from spleens and incubated for 72 h in the presence of anti-CD3, anti-CD28, anti-IL-4 and rIL-12 to generate T_H1 cells. For flow cytometry, cells were restimulated in the presence of PMA, ionomycin and brefeldin A for 6 h before being labelled with LIVE/DEAD™, PE-Cy7:anti-CD4 and *APC*:anti-IFN-γ and analysed on a flow cytometer. Supernatants of *Ucp3*$^{+/+}$ and *Ucp3*$^{-/-}$ T_H1 cells were taken 72 h post-stimulation to measure IFN-γ secretion levels by ELISA.

No differences in viability (Figure 3.57A and B) or cell size/activation (Figure 3.57C and D) were evident between *Ucp3*$^{+/+}$ and *Ucp3*$^{-/-}$ T_H1 cells. Similarly, no difference in IFN-γ production was detected between genotypes by flow cytometry (Figure 3.58A and B) or by ELISA (Figure 3.58C), in contrast to T_H0 cells. Due to the effect of *Ucp3* ablation on T_H0 cells, these results were quite surprising. On the one hand, one may have expected a decrease in viability along with a consequential decrease in IFN-γ production from the *Ucp3*$^{-/-}$ T_H1 cells, as in the *Ucp3*$^{-/-}$ T_H0 cells. Conversely, one could have also expected to observe an increase in survival and IFN-γ production from the *Ucp3*$^{-/-}$ T_H1 cells due to the increased IL-2 production observed in *Ucp3*$^{-/-}$ T_H0 cells, as IL-2 promotes cell survival and IFN-γ production (Liao *et al*., 2013), although this effect was not observed in T_H0 cells and so, seemed less likely. These data convey that, contrary to T_H0 cells, T_H1 cell generation *in vitro* is unaffected by *Ucp3* ablation.

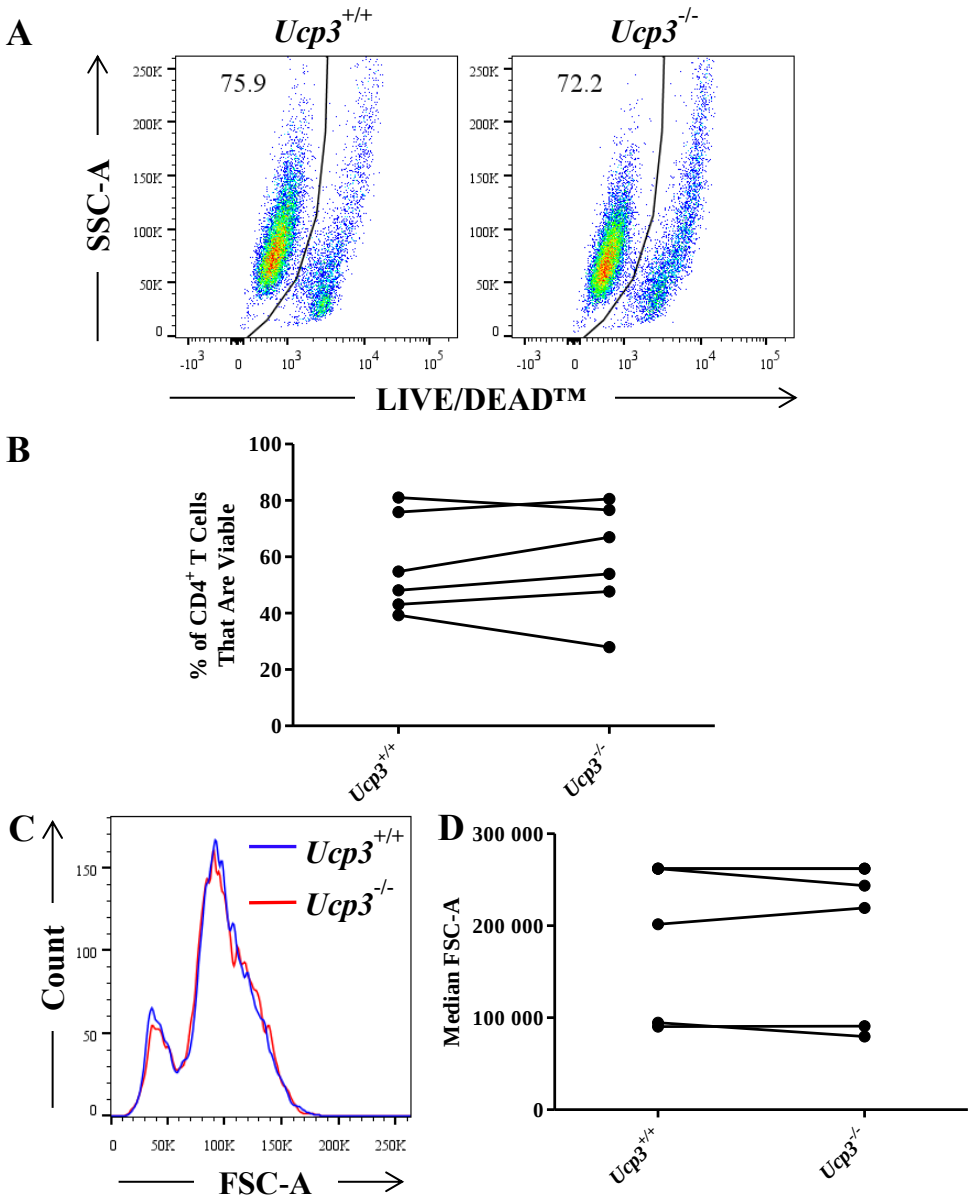

Figure 3.57: Viability and size of *Ucp3*$^{+/+}$ and *Ucp3*$^{-/-}$ T_H1 cells are comparable

T_H1 cells were generated by incubating naive T cells in the presence of 5 µg.mL^{-1} of anti-CD3 and anti-CD28 and 10 ng.mL^{-1} of anti-IL-4 and rIL-12 for 72 h. Cells were stained with LIVE/DEAD™ and PE-Cy7:anti-CD4 and analysed on a flow cytometer. Flow cytometry was performed at least three times. Dot plots and histogram are representative of at least three different experiments. Data were analysed using a two-tailed, unpaired *t* test to quantify significance where detected. (A, B) Viability of T_H1 cells. Data are presented as a percentage of the total CD4$^+$ T cell population. (C) Histogram of viable CD4$^+$ T_H1 cell size. (D) Size of viable, CD4$^+$ T_H1 cells.

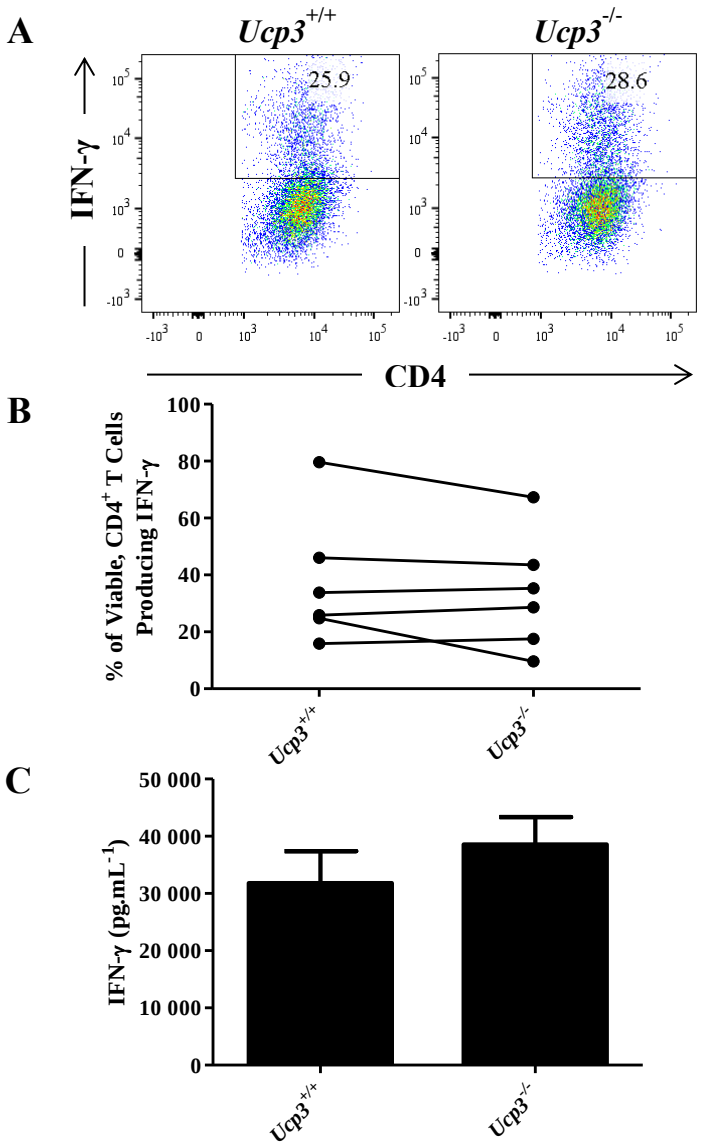

Figure 3.58: IFN-γ production by *Ucp3*$^{+/+}$ and *Ucp3*$^{-/-}$ T_H1 cells is comparable

T_H1 cells were generated by incubating naive T cells in the presence of 5 µg.mL^{-1} of anti-CD3 and anti-CD28 and 10 ng.mL^{-1} of anti-IL-4 and rIL-12 for 72 h. (A, B) Cells were restimulated with PMA, ionomycin and brefeldin A for 6 h before being stained with LIVE/DEAD™, PE-Cy7:anti-CD4 and *APC*:anti-IFN-γ and analysed on a flow cytometer. Flow cytometry was performed at least three times. Dot plots are representative of at least three different experiments. Data are presented as a percentage of the viable, CD4$^+$ T cell population. (C) IFN-γ secretion by T_H1 cells 72 h post-stimulation. ELISA was performed at least three times in sextuplicate. Data were analysed using a two-tailed, unpaired *t* test to quantify significance where detected.

3.2.6 *Ucp3* Ablation Reciprocally Affects T_H17 and T_{reg} Cells

Although no effect of *Ucp3* ablation on T_H1 cells was observed, it is known that IL-2 can play a significant role in influencing T_H17 and T_{reg} cell differentiation**.** High levels of IL-2 in the presence of high levels of TGF-β can promote the generation of T_{reg} cells and inhibit the generation of T_H17 cells, while lower levels of TGF-β in the presence of IL-6 favour T_H17 cell polarization (Laurence *et al*., 2007; Boyman and Sprent, 2012; Liao *et al*., 2013). The significantly higher production of IL-2 by *Ucp3*$^{-/-}$ T_H0 cells called for investigation into the effect of *Ucp3* ablation on T_H17 and T_{reg} cells. Primary *Ucp3*$^{+/+}$ and *Ucp3*$^{-/-}$ $CD4^+$ T cells were harvested direct from spleens and incubated for 72 h in the presence of anti-CD3, anti-CD28, anti-IL-4, anti-IFN-γ, rhTGF-β1 and rIL-6 to generate T_H17 cells. For flow cytometry using T_H17 cells, cells were restimulated in the presence of PMA, ionomycin and brefeldin A for 6 h before being labelled with LIVE/DEAD™, PE-Cy7:anti-CD4 and PE:anti-IL-17A and analysed on a flow cytometer. Primary *Ucp3*$^{+/+}$ and *Ucp3*$^{-/-}$ $CD4^+$ T cells were harvested direct from spleens and incubated for 120 h in the presence of anti-CD3, anti-CD28 and rhTGF-β1 to generate T_{reg} cells. For flow cytometry using T_{reg} cells, cells were labelled immediately with LIVE/DEAD™, PE-Cy7:anti-CD4, PE:anti-FoxP3, PerCP-eFluor™ 710:anti-LAP and FITC:anti-LAG3 and analysed on a flow cytometer. Supernatants of *Ucp3*$^{+/+}$ and *Ucp3*$^{-/-}$ T_H17 and T_{reg} cells were taken 72 and 120 h post-stimulation, respectively, to measure IL-17A and IL-10 secretion levels by ELISA, respectively.

While a trend for the *Ucp3*$^{-/-}$ T_H17 cells to have lower viability than the *Ucp3*$^{+/+}$ T_H17 cells is observed, the difference in viability is not statistically significant (Figure 3.59A and B). The size of *Ucp3*$^{-/-}$ T_H17 cells is decreased in comparison to *Ucp3*$^{+/+}$ T_H17 cells (Figure 3.59C and D). Additionally, *Ucp3*$^{-/-}$ T_H17 cells display significantly less IL-17A secretion than *Ucp3*$^{+/+}$ T_H17 cells, as measured by ELISA (Figure 3.60C), although this difference is not observed by flow cytometry (Figure 3.60A and B). No marked differences in the viability or cell size/activation of cells under T_{reg} polarizing conditions are evident (Figure 3.61). Similarly, the frequency of *Ucp3*$^{+/+}$ and *Ucp3*$^{-/-}$ $FoxP3^+$ cells under T_{reg} polarizing conditions is comparable (Figure 3.62A and B). However, although not significant, a trend for greater viability and a higher frequency of *Ucp3*$^{-/-}$ $FoxP3^+$ cells can be observed. FoxP3 expression is indicative of T_{reg} cell induction (Hori *et al*., 2003).

$FoxP3^+$ T_{reg} cells can regulate effector T cells by expressing TGF-β on their cell surface in complex with latency-associated peptide (LAP; Duan *et al*., 2011; Gregori *et al*., 2012).

LAP is a pro-peptide that is non-covalently associated to the amino terminal domain of TGF-β, forming a latent TGF-β complex (Gandhi *et al*., 2010). Thus, TGF-β production can be measured indirectly by staining for LAP and analysing by FACS. As regulatory T cells that are $FoxP3^-$ can also express LAP (Gandhi *et al*., 2010; Duan *et al*., 2011; Kuhn *et al*., 2016), we analysed the co-expression of LAP and FoxP3 on $Ucp3^{+/+}$ and $Ucp3^{-/-}$ T_{reg} cells with the expectation of observing a significantly higher level of expression in the latter population due to the trend for an increased generation of $FoxP3^+$ cells previously observed. However, no difference in the frequency of $FoxP3^+LAP^+$ $Ucp3^{+/+}$ and $Ucp3^{-/-}$ cells is apparent (Figure 3.62C and D). It has been previously reported that there is a significant amount of heterogeneity among the T_{reg} cell population and LAP^-FoxP3^+ T_{reg} cells are also known to exist (Duan *et al*., 2011). This may account for the lack of difference in LAP^+FoxP3^+ cells observed here.

Another mechanism often used by $FoxP3^+$ T_{reg} cells to suppress inflammation is the prevention of DC activation by sending inhibitory signals through the interaction of T_{reg} cell-expressed lymphocyte activation gene 3 (LAG3; also known as CD223) with MHC class II molecules on the DC surface (Gregori *et al*., 2012). LAG3 is similar to CD4 in that it binds MHC class II molecules, although it does so with greater affinity (Huang *et al*., 2004; Goldberg and Drake, 2011). LAG3 can also be expressed by activated effector T cells (Huang *et al*., 2004; Goldberg and Drake, 2011; Zhang *et al*., 2017). Therefore, similar to LAP, LAG3 expression was measured alongside FoxP3 expression of $Ucp3^{+/+}$ and $Ucp3^{-/-}$ T_{reg} cells. No significant difference in LAG3 and FoxP3 co-expression is observed between $Ucp3^{+/+}$ and $Ucp3^{-/-}$ T_{reg} cells (Figure 3.62E and F). Regulatory T cells can secrete the anti-inflammatory cytokine, IL-10, in order to modulate the activity of effector T cells. IL-10 secretion was measured in the supernatants of $Ucp3^{+/+}$ and $Ucp3^{-/-}$ cells under T_{reg} polarizing conditions for 120 h and is significantly decreased by $Ucp3^{-/-}$ cells (Figure 3.63). This was initially a surprisingly result following our observation of a trend for enhanced $FoxP3^+$ T_{reg} cell generation. However, decreased IL-10 secretion in $Ucp3^{-/-}$ cells under T_{reg} polarizing conditions may not be completely counterintuitive. IL-10 (as well as TGF-β) can be produced by Tr1 regulatory T cells which are $CD25^+FoxP3^-$ (Lavelle *et al*., 2003; Gandhi *et al*., 2010; Loftus and Finlay, 2016), rather than by $FoxP3^+$ T_{reg} cells (Duan *et al*., 2011; Gregori *et al*., 2012). Thus, while we see a trend for enhanced $Ucp3^{-/-}$ $FoxP3^+$ T_{reg} cell generation, this may be in place of Tr1 cell generation/activation, resulting in a significant decrease in the secretion of the characteristic Tr1 cell cytokine.

It appears that, while T_H1 cells are unaffected by *Ucp3* ablation, T_H17 and T_{reg} cells are crucially affected. The IL-2 differential between $Ucp3^{+/+}$ and $Ucp3^{-/-}$ T cells appears to culminate in T_{reg} cell differentiation and survival being favoured over T_H17 cell differentiation and survival. To test whether an increase in IL-2 production is indeed the cause of enhanced T_{reg} and dampened T_H17 cell generation when *Ucp3* is ablated, we repeated the above investigation with the addition of using an anti-IL-2 neutralising antibody. If excess IL-2 is the protagonist in this scenario, neutralising its activity should result in the $Ucp3^{-/-}$ cells becoming more reflective of the WT cells, *i.e.* normal T_H17 cell viability and function may be restored and T_{reg} cell generation may no longer be enhanced. In agreement with this, IL-2 neutralisation results in an increase in $Ucp3^{-/-}$ T_H17 cell viability (as well as $Ucp3^{+/+}$ T_H17 cell viability), with the frequency of viable $Ucp3^{-/-}$ cells being more similar to that of $Ucp3^{+/+}$ cells before IL-2 neutralisation (Figure 3.64). Similarly, while $Ucp3^{-/-}$ T_H17 cells are smaller in size than their WT counterparts under normal conditions, this difference is no longer observed following culture with 10 $\mu g.mL^{-1}$ of anti-IL-2 (Figure 3.65). IL-17A production is increased in both $Ucp3^{+/+}$ and $Ucp3^{-/-}$ T_H17 cells following culture with anti-IL-2, as expected, but secretion from $Ucp3^{-/-}$ cells is comparable to that of the WT level before IL-2 neutralisation and is no longer significantly decreased in comparison to $Ucp3^{+/+}$ cells (Figure 3.66).

IL-2 neutralisation had an opposing effect on T_{reg} cells in comparison to T_H17 cells. Viability decreases following anti-IL-2 treatment and is no longer significantly higher in $Ucp3^{-/-}$ T_{reg} cells (Figure 3.67), while the size of both $Ucp3^{+/+}$ and $Ucp3^{-/-}$ T_{reg} cells decreases slightly (Figure 3.68), although they were originally not significantly different. $FoxP3^+$ T_{reg} cell generation is hampered for both $Ucp3^{+/+}$ and $Ucp3^{-/-}$ cells and the significant enhancement of the generation of these $Ucp3^{-/-}$ cells is no longer evident following IL-2 neutralisation (Figure 3.69). No significant differences in LAP and LAG3 expression are observed between $Ucp3^{+/+}$ and $Ucp3^{-/-}$ T_{reg} cells following incubation with anti-IL-2, as before (Figures 3.70 and 3.71, respectively). IL-10 secretion is decreased in both $Ucp3^{+/+}$ and $Ucp3^{-/-}$ T cells under T_{reg} polarizing conditions following IL-2 neutralisation but is no longer significantly different between genotypes (Figure 3.72). These data support our previous findings of increased IL-2 production in $Ucp3^{-/-}$ T_H0 cells, our hypothesis that an increase in IL-2 production is favouring the generation of $Ucp3^{-/-}$ $FoxP3^+$ T_{reg} cells over $Ucp3^{-/-}$ T_H17 cells and highlight IL-2 as (one of) the main orchestrator(s) of the effects of *Ucp3* ablation on $CD4^+$ T cells that we have observed.

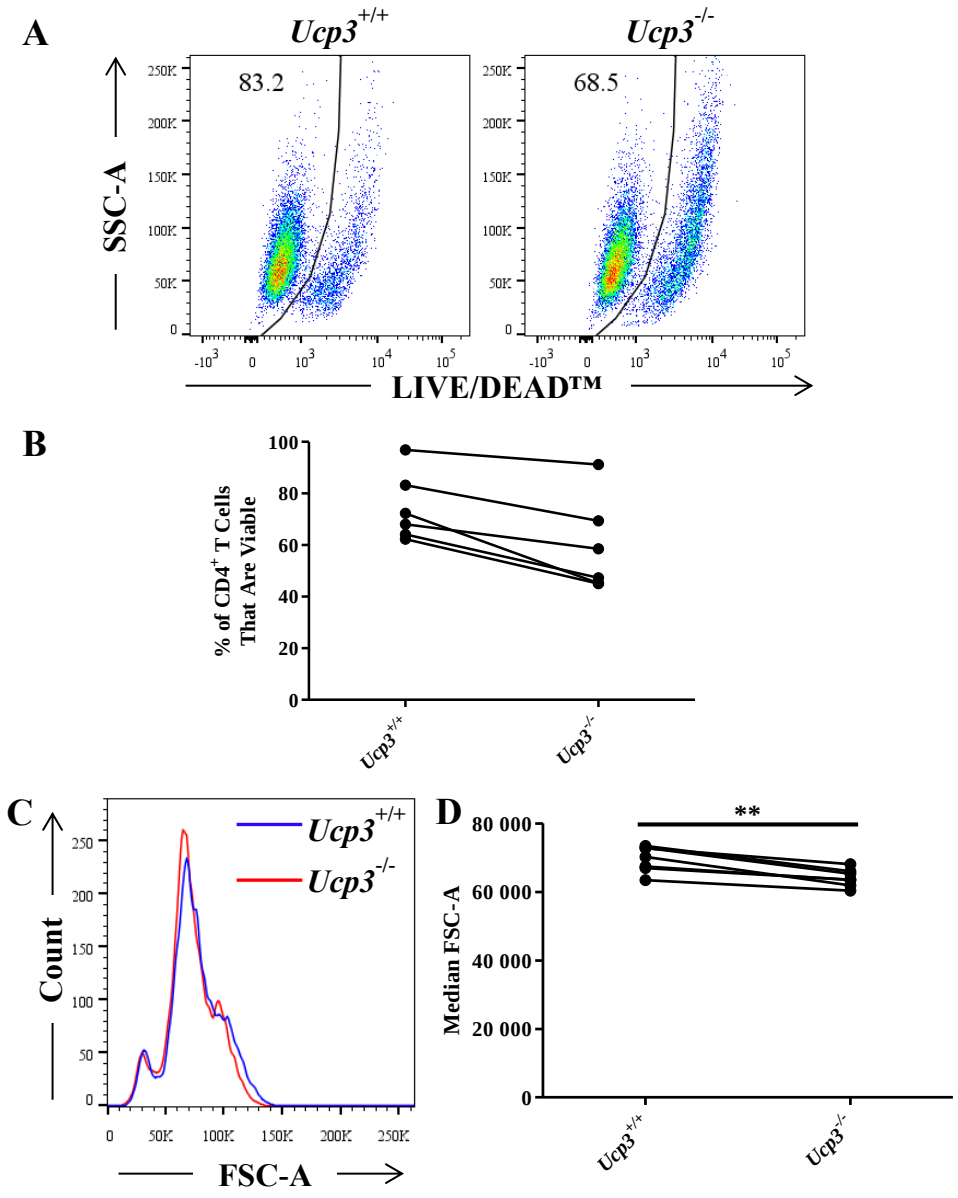

Figure 3.59: *Ucp3*$^{-/-}$ T_H17 cells display decreased cell size

T_H17 cells were generated by incubating naive T cells in the presence of 5 µg.mL^{-1} of anti-CD3 and anti-CD28, 20 ng.mL^{-1} of anti-IL-4 and rIL-6, 10 µg.mL^{-1} of anti-IFN-γ and 2.5 ng.mL^{-1} of rhTGF-β1 for 72 h. Cells were stained with LIVE/DEAD™ and PE-Cy7:anti-CD4 and analysed on a flow cytometer. Flow cytometry was performed at least three times. Dot plots and histogram are representative of at least three different experiments. Data were analysed using a two-tailed, unpaired *t* test to quantify significance where detected. ** = $p < 0.01$. (A, B) Viability of T_H17 cells. Data are presented as a percentage of the total CD4$^+$ T cell population. (C) Histogram of viable CD4$^+$ T_H17 cell size. (D) Size of viable, CD4$^+$ T_H17 cells.

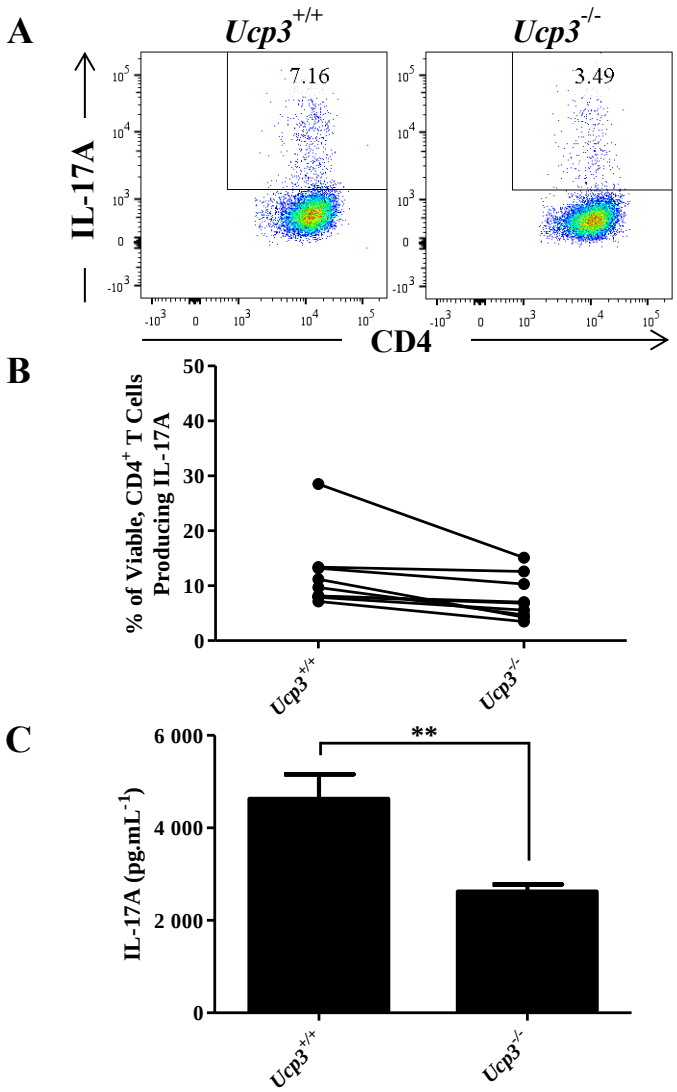

Figure 3.60: *Ucp3*$^{-/-}$ T_H17 cells secrete less IL-17A

T_H17 cells were generated by incubating naive T cells in the presence of 5 µg.mL^{-1} of anti-CD3 and anti-CD28, 20 ng.mL^{-1} of anti-IL-4 and rIL-6, 10 µg.mL^{-1} of anti-IFN-γ and 2.5 ng.mL^{-1} of rhTGF-β1 for 72 h. (A, B) Cells were restimulated with PMA, ionomycin and brefeldin A for 6 h before being stained with LIVE/DEAD™, PE-Cy7:anti-CD4 and PE:anti-IL-17A and analysed on a flow cytometer. Flow cytometry was performed at least three times. Dot plots are representative of at least three different experiments. Data are presented as a percentage of the viable, CD4$^+$ T cell population. (C) IL-17A secretion by T_H17 cells 72 h post-stimulation. ELISA was performed at least three times in sextuplicate. Data were analysed using a two-tailed, unpaired *t* test to quantify significance where detected. ** = $p < 0.01$.

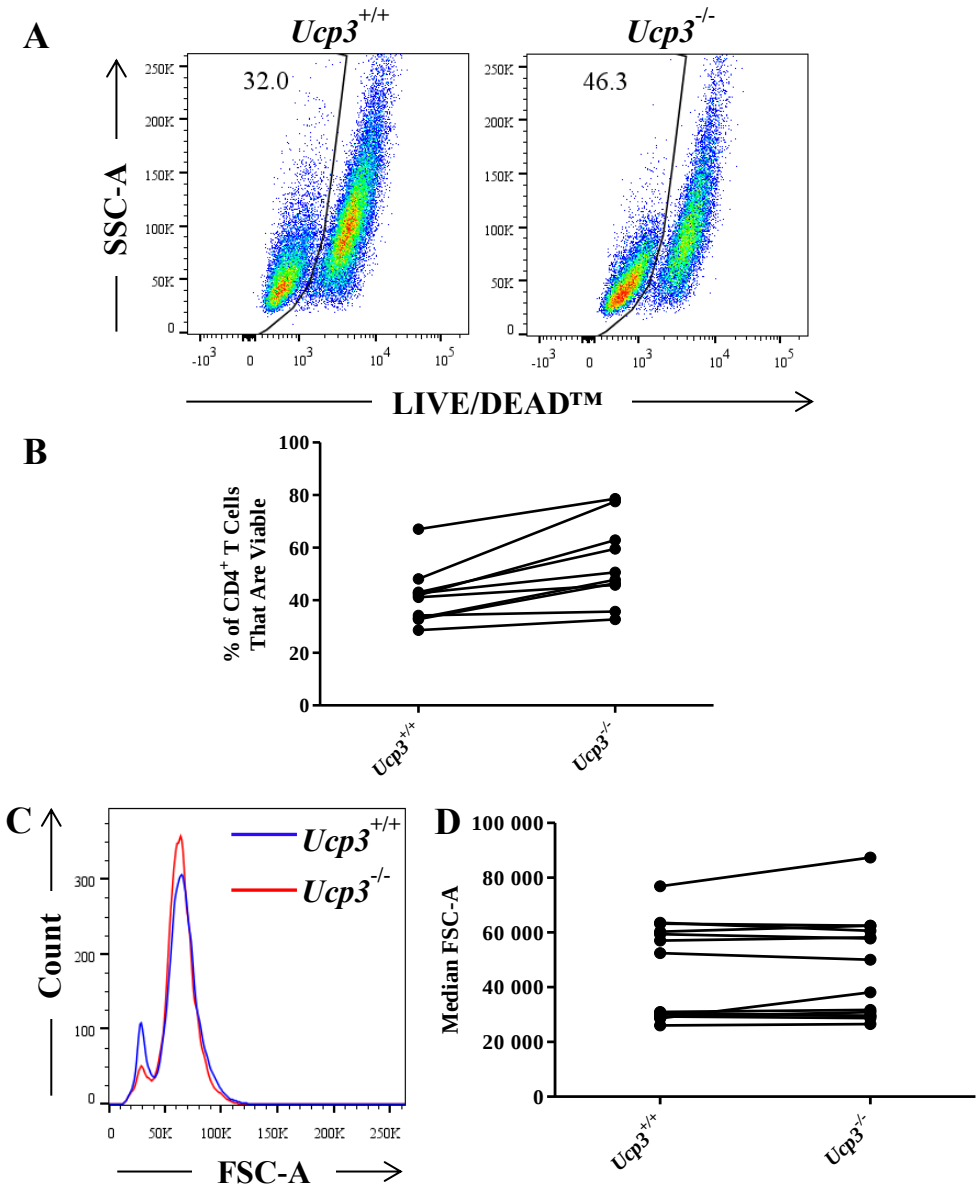

Figure 3.61: *Ucp3*$^{-/-}$ T_{reg} cells display comparable viability and cell size

T_{reg} cells were generated by incubating naive T cells in the presence of 1 µg.mL^{-1} of anti-CD3 and anti-CD28 and 5 ng.mL^{-1} of rhTGF-β1 for 120 h. Cells were stained with LIVE/DEAD™ and PE-Cy7:anti-CD4 and analysed on a flow cytometer. Flow cytometry was performed at least three times. Dot plots and histogram are representative of at least three different experiments. Data were analysed using a two-tailed, unpaired *t* test to quantify significance where detected. (A, B) Viability of T_{reg} cells. Data are presented as a percentage of the total CD4$^+$ T cell population. (C) Histogram of viable CD4$^+$ T_{reg} cell size. (D) Size of viable, CD4$^+$ T_{reg} cells.

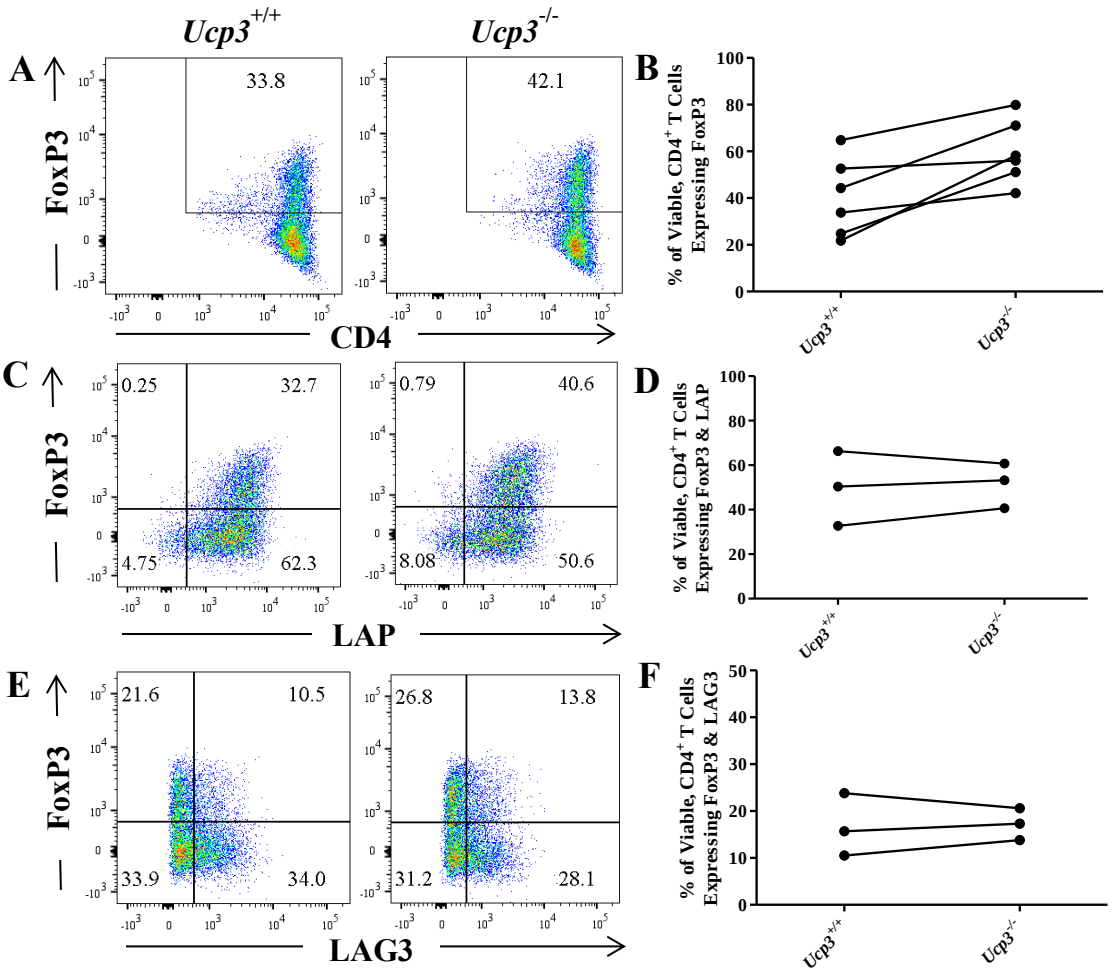

Figure 3.62: Generation of FoxP3$^+$ T_{reg} cells and LAP and LAG3 expression of *Ucp3*$^{+/+}$ and *Ucp3*$^{-/-}$ FoxP3$^+$ T_{reg} cells

T_{reg} cells were generated by incubating naive T cells in the presence of 1 µg.mL^{-1} of anti-CD3 and anti-CD28 and 5 ng.mL^{-1} of rhTGF-β1 for 120 h. Cells were stained with LIVE/DEAD™, PE-Cy7:anti-CD4, PerCP-eFluor™ 710:anti-LAP, FITC:anti-LAG3 and PE:anti-FoxP3 and analysed on a flow cytometer. Flow cytometry was performed at least three times. Dot plots are representative of at least three different experiments. Data are presented as a percentage of the viable, CD4$^+$ T cell population. Data were analysed using a two-tailed, unpaired *t* test to quantify significance where detected. (A, B) FoxP3$^+$ T_{reg} cells. (C, D) LAP and FoxP3 co-expression of viable CD4$^+$ T cells. (E, F) LAG3 and FoxP3 co-expression of viable, CD4$^+$ T cells.

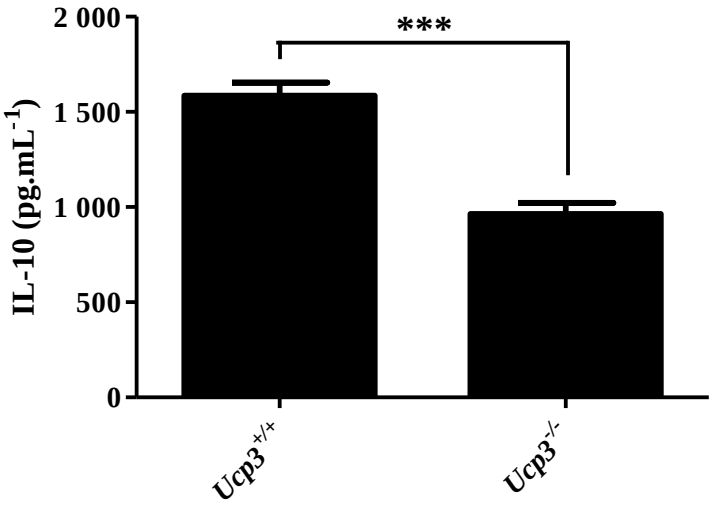

Figure 3.63: *Ucp3*$^{-/-}$ T cells under T_{reg} polarizing conditions secrete less IL-10

T_{reg} cells were generated by incubating naive T cells in the presence of 1 µg.mL^{-1} of anti-CD3 and anti-CD28 and 5 ng.mL^{-1} of rhTGF-β1 for 120 h. ELISA was performed at least three times with twelve technical replicates. Data were analysed using a two-tailed, unpaired *t* test to quantify significance where detected. *** = $p < 0.001$.

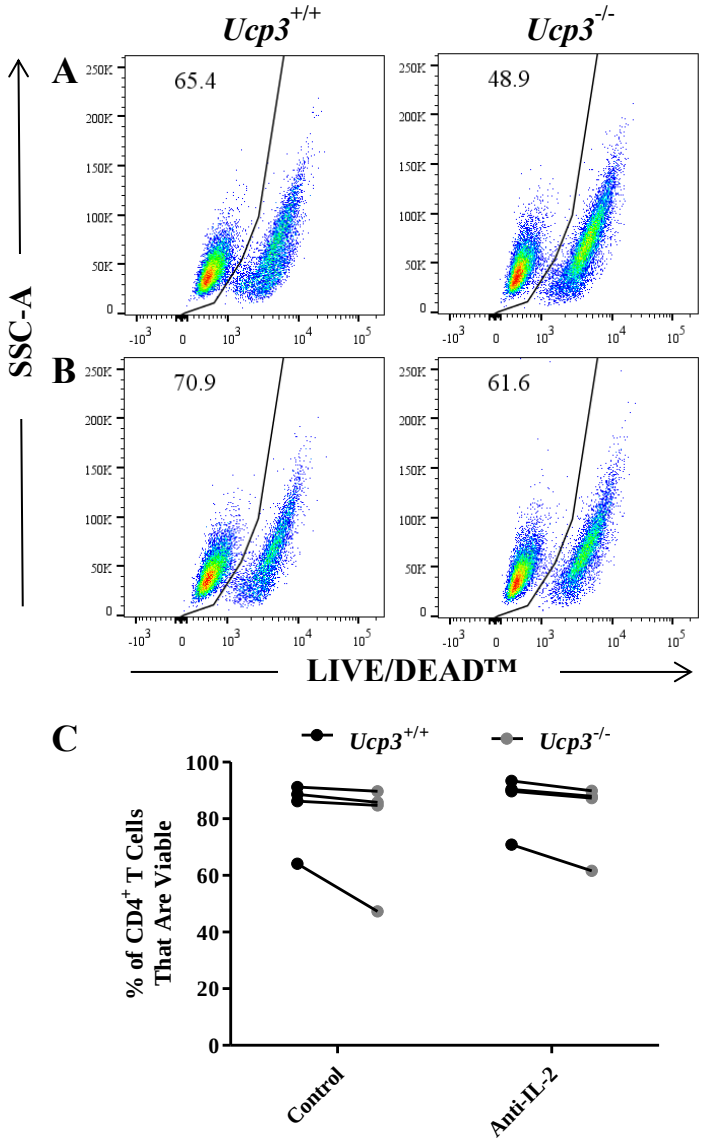

Figure 3.64: Viability of *Ucp3*$^{+/+}$ and *Ucp3*$^{-/-}$ T_H17 cells is comparable following IL-2 neutralisation

T_H17 cells were generated by incubating naive T cells in the presence of 5 µg.mL^{-1} of anti-CD3 and anti-CD28, 20 ng.mL^{-1} of anti-IL-4 and rIL-6, 10 µg.mL^{-1} of anti-IFN-γ and 2.5 ng.mL^{-1} of rhTGF-β1 without (A) or with (B) 10 µg.mL^{-1} of anti-IL-2 for 72 h. Cells were stained with LIVE/DEAD™ and PE-Cy7:anti-CD4 and analysed on a flow cytometer. Flow cytometry was performed at least three times. Dot plots are representative of at least three different experiments. Data are presented as a percentage of the total CD4$^+$ T cell population. (C) Data were analysed using a two-way, repeated measures ANOVA with a *post hoc* Bonferroni test to quantify significance where detected.

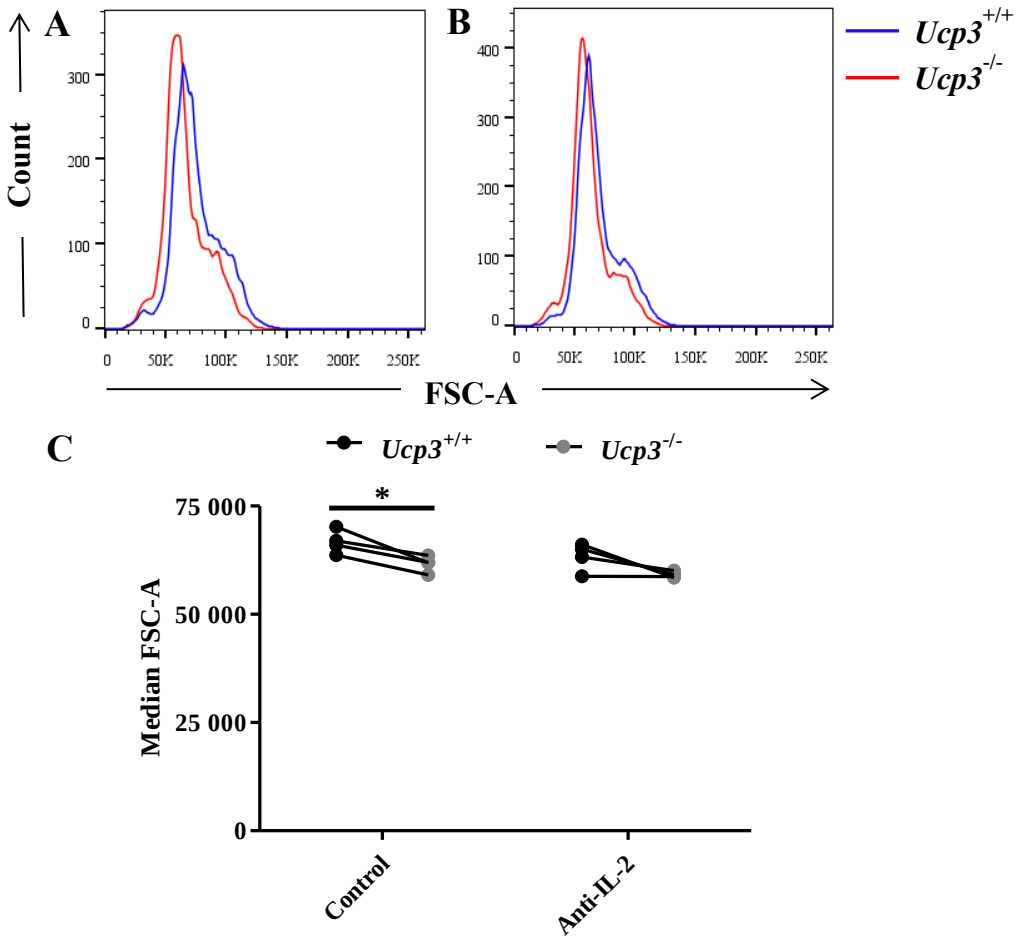

Figure 3.65: Size of *Ucp3*$^{+/+}$ and *Ucp3*$^{-/-}$ T_H17 cells is comparable following IL-2 neutralisation

T_H17 cells were generated by incubating naive T cells in the presence of 5 µg.mL^{-1} of anti-CD3 and anti-CD28, 20 ng.mL^{-1} of anti-IL-4 and rIL-6, 10 µg.mL^{-1} of anti-IFN-γ and 2.5 ng.mL^{-1} of rhTGF-β1 without (A) or with (B) 10 µg.mL^{-1} of anti-IL-2 for 72 h. Cells were stained with LIVE/DEAD™ and PE-Cy7:anti-CD4 and analysed on a flow cytometer. Flow cytometry was performed at least three times. Histograms are representative of at least three different experiments. Data are of the viable CD4$^+$ T cell population. (C) Data were analysed using a two-way, repeated measures ANOVA with a *post hoc* Bonferroni test to quantify significance where detected. * = $p < 0.05$.

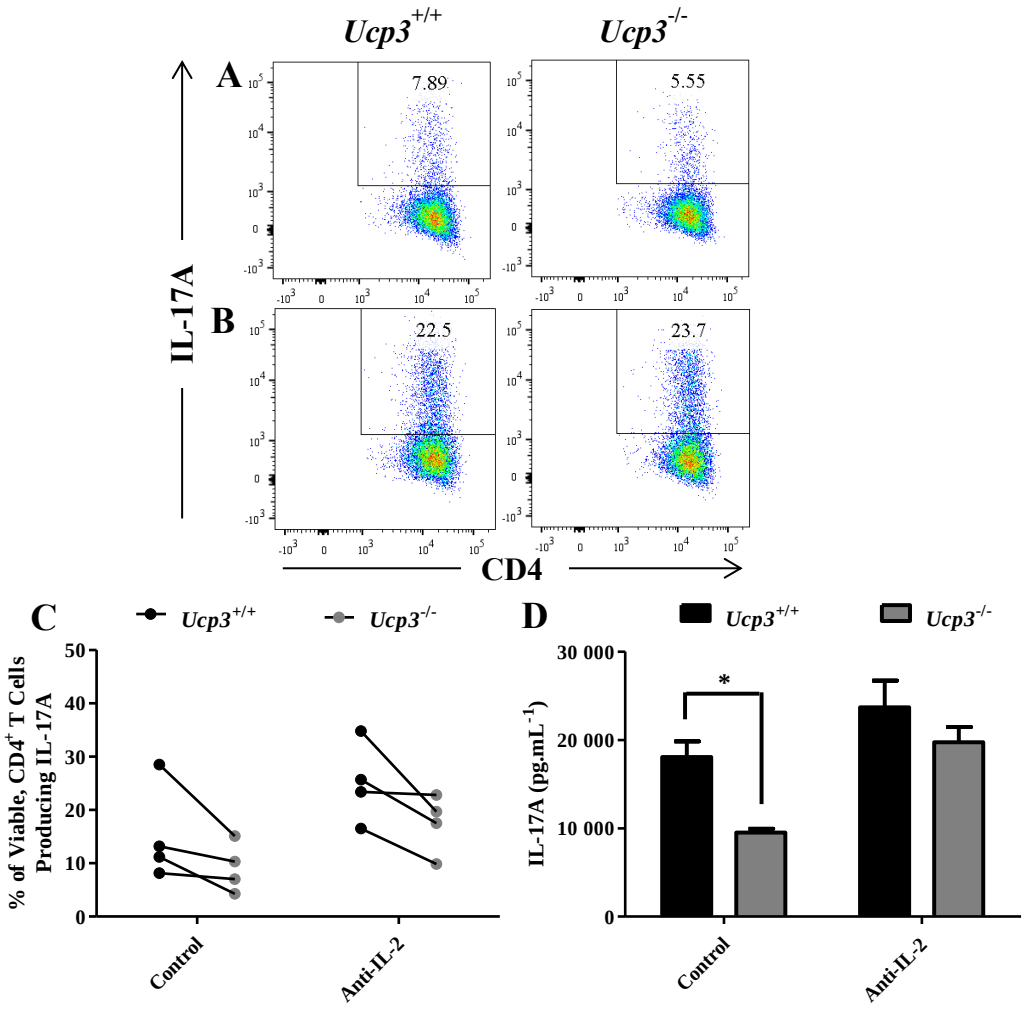

Figure 3.66: IL-17A production by *Ucp3*$^{+/+}$ and *Ucp3*$^{-/-}$ T_H17 cells is comparable following IL-2 neutralisation

T_H17 cells were generated by incubating naive T cells in the presence of 5 µg.mL^{-1} of anti-CD3 and anti-CD28, 20 ng.mL^{-1} of anti-IL-4 and rIL-6, 10 µg.mL^{-1} of anti-IFN-γ and 2.5 ng.mL^{-1} of rhTGF-β1 without (A) or with (B) 10 µg.mL^{-1} of anti-IL-2 for 72 h. (A – C) Cells were restimulated with PMA, ionomycin and brefeldin A for 6 h before being stained with LIVE/DEAD™, PE-Cy7:anti-CD4 and PE:anti-IL-17A and analysed on a flow cytometer. Flow cytometry was performed at least three times. Dot plots are representative of at least three different experiments. Data are presented as a percentage of the viable CD4$^+$ T cell population. (D) IL-17A secretion by T_H17 cells 72 h post-stimulation with or without anti-IL-2. ELISA was performed at least three times with twelve technical replicates. Data were analysed using a two-way, repeated measures (C) or non-repeated measures (D) ANOVA with a *post hoc* Bonferroni test to quantify significance where detected. * = $p < 0.05$.

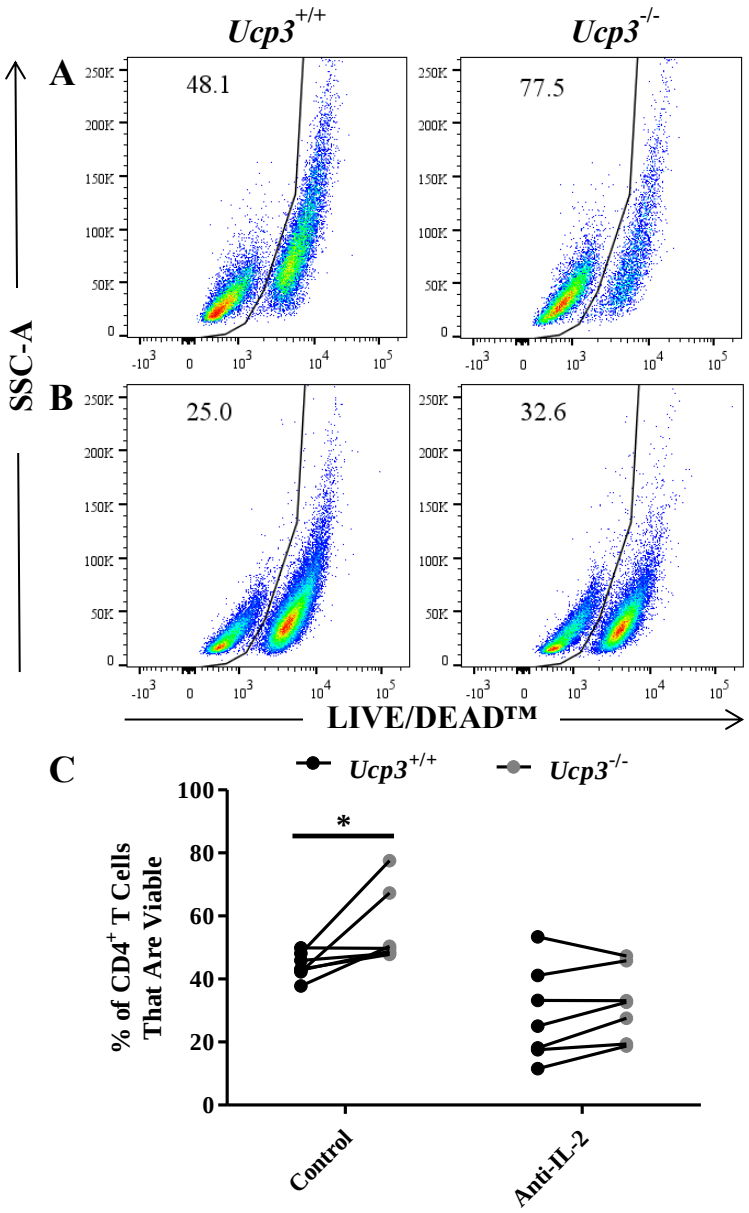

Figure 3.67: Viability of *Ucp3*$^{+/+}$ and *Ucp3*$^{-/-}$ T_{reg} cells is comparable following IL-2 neutralisation

T_{reg} cells were generated by incubating naive T cells in the presence of 1 µg.mL^{-1} of anti-CD3 and anti-CD28 and 5 ng.mL^{-1} of rhTGF-β1 without (A) or with (B) 10 µg.mL^{-1} of anti-IL-2 for 120 h. Cells were stained with LIVE/DEAD™ and PE-Cy7:anti-CD4 and analysed on a flow cytometer. Flow cytometry was performed at least three times. Dot plots are representative of at least three different experiments. Data are presented as a percentage of the total CD4$^+$ T cell population. (C) Data were analysed using a two-way, repeated measures ANOVA with a *post hoc* Bonferroni test to quantify significance where detected. * = $p < 0.05$.

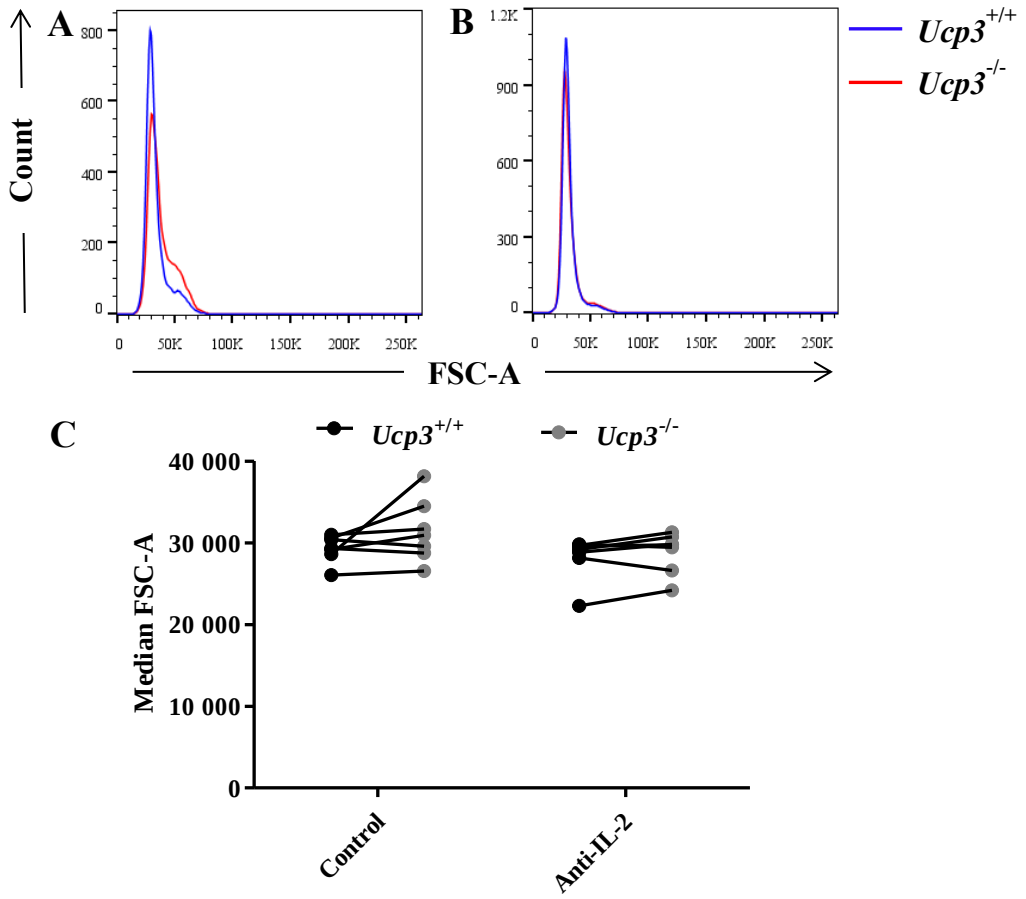

Figure 3.68: Size of *Ucp3*$^{+/+}$ and *Ucp3*$^{-/-}$ T_{reg} cells is comparable following IL-2 neutralisation

T_{reg} cells were generated by incubating naive T cells in the presence of 1 µg.mL^{-1} of anti-CD3 and anti-CD28 and 5 ng.mL^{-1} of rhTGF-β1 without (A) or with (B) 10 µg.mL^{-1} of anti-IL-2 for 120 h. Cells were stained with LIVE/DEAD™ and PE-Cy7:anti-CD4 and analysed on a flow cytometer. Flow cytometry was performed at least three times. Histograms are representative of at least three different experiments. Data are of the viable CD4^{+} T cell population. (C) Data were analysed using a two-way, repeated measures ANOVA with a *post hoc* Bonferroni test to quantify significance where detected.

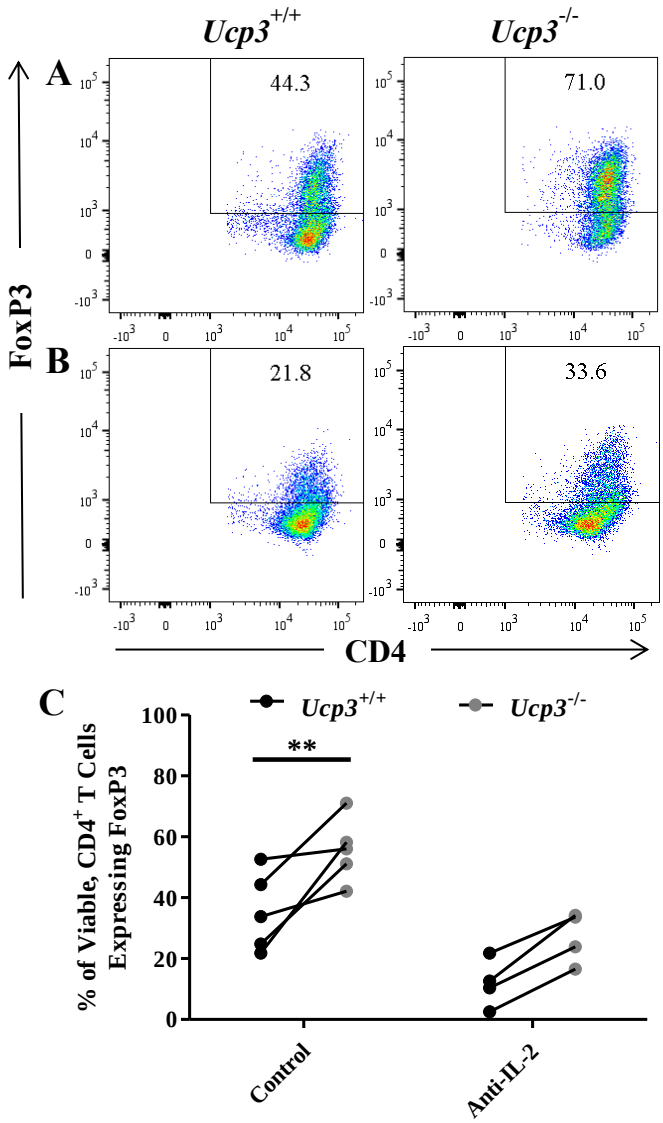

Figure 3.69: Generation of *Ucp3*$^{+/+}$ and *Ucp3*$^{-/-}$ FoxP3^{+} T$_{reg}$ cells is comparable following IL-2 neutralisation

T$_{reg}$ cells were generated by incubating naive T cells in the presence of 1 µg.mL^{-1} of anti-CD3 and anti-CD28 and 5 ng.mL^{-1} of rhTGF-β1 without (A) or with (B) 10 µg.mL^{-1} of anti-IL-2 for 120 h. Cells were stained with LIVE/DEAD™, PE-Cy7:anti-CD4 and PE:anti-FoxP3 and analysed on a flow cytometer. Flow cytometry was performed at least three times. Dot plots are representative of at least three different experiments. Data are presented as a percentage of the viable CD4^{+} T cell population. (C) Data were analysed using a two-way, repeated measures ANOVA with a *post hoc* Bonferroni test to quantify significance where detected. ** = $p < 0.01$.

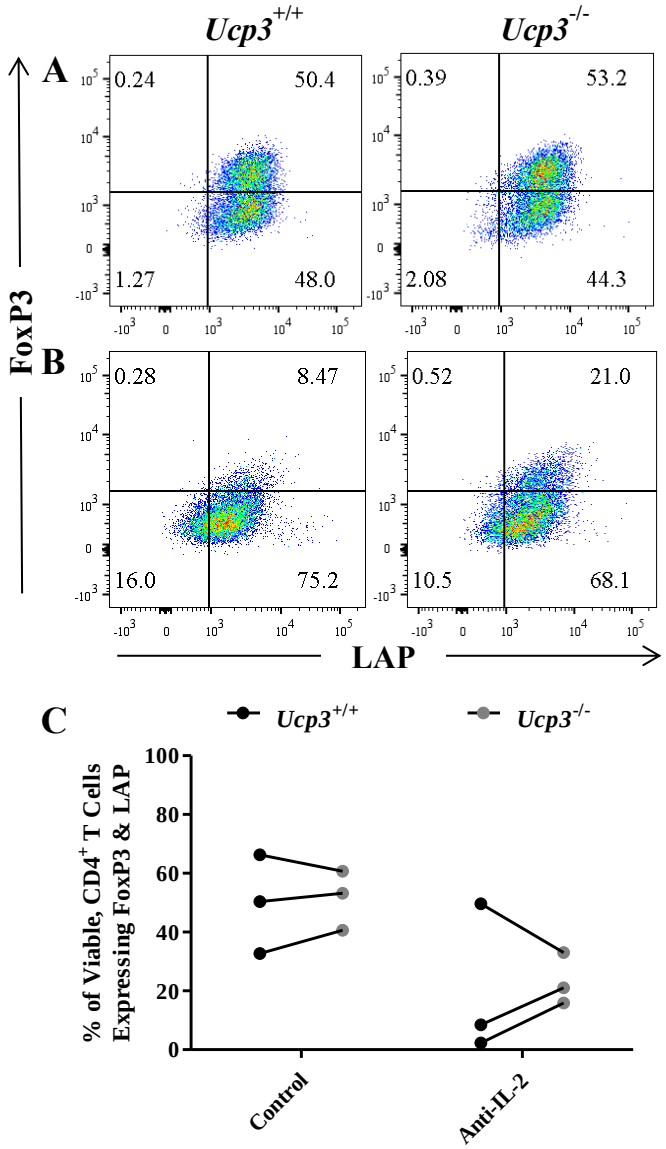

Figure 3.70: LAP expression of *Ucp3*$^{+/+}$ and *Ucp3*$^{-/-}$ FoxP3^{+} T_{reg} cells is comparable following IL-2 neutralisation

T_{reg} cells were generated by incubating naive T cells in the presence of 1 µg.mL^{-1} of anti-CD3 and anti-CD28 and 5 ng.mL^{-1} of rhTGF-β1 without (A) or with (B) 10 µg.mL^{-1} of anti-IL-2 for 120 h. Cells were stained with LIVE/DEAD™, PE-Cy7:anti-CD4, PerCP-eFluor™ 710:anti-LAP and PE:anti-FoxP3 and analysed on a flow cytometer. Flow cytometry was performed at least three times. Dot plots are representative of at least three different experiments. Data are presented as a percentage of the viable CD4^{+} T cell population. (C) Data were analysed using a two-way, repeated measures ANOVA with a *post hoc* Bonferroni test to quantify significance where detected.

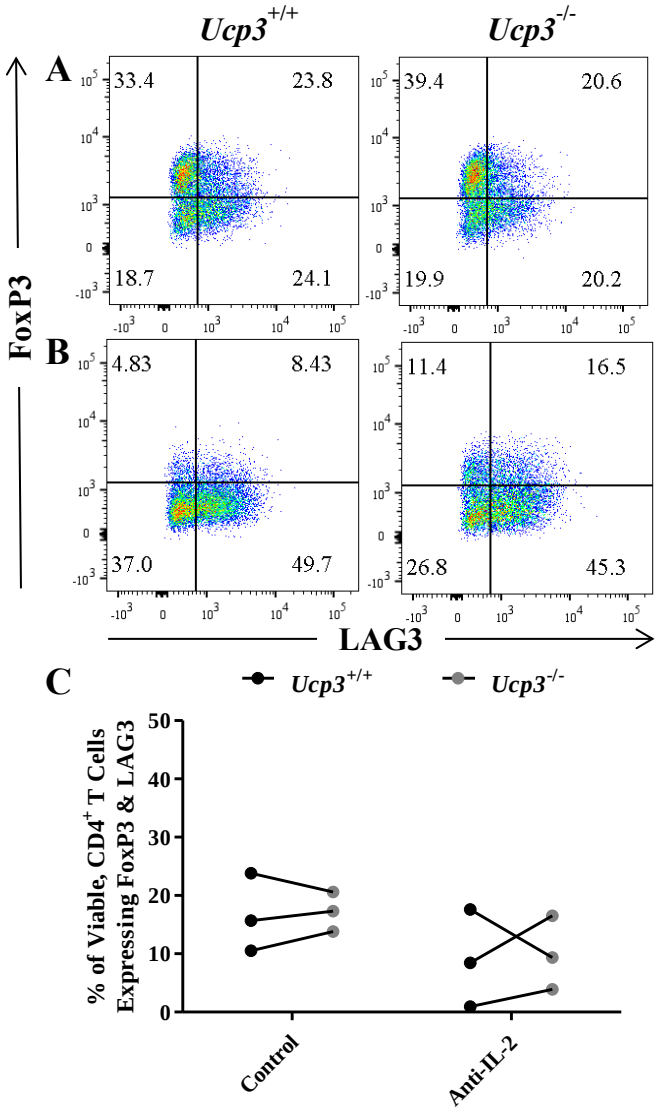

Figure 3.71: LAG3 expression of *Ucp3*$^{+/+}$ and *Ucp3*$^{-/-}$ FoxP3^{+} T_{reg} cells is comparable following IL-2 neutralisation

T_{reg} cells were generated by incubating naive T cells in the presence of 1 µg.mL^{-1} of anti-CD3 and anti-CD28 and 5 ng.mL^{-1} of rhTGF-β1 without (A) or with (B) 10 µg.mL^{-1} of anti-IL-2 for 120 h. Cells were stained with LIVE/DEAD™, PE-Cy7:anti-CD4, FITC:anti-LAG3 and PE:anti-FoxP3 and analysed on a flow cytometer. Flow cytometry was performed at least three times. Dot plots are representative of at least three different experiments. Data are presented as a percentage of the viable CD4^{+} T cell population. (C) Data were analysed using a two-way, repeated measures ANOVA with a *post hoc* Bonferroni test to quantify significance where detected.

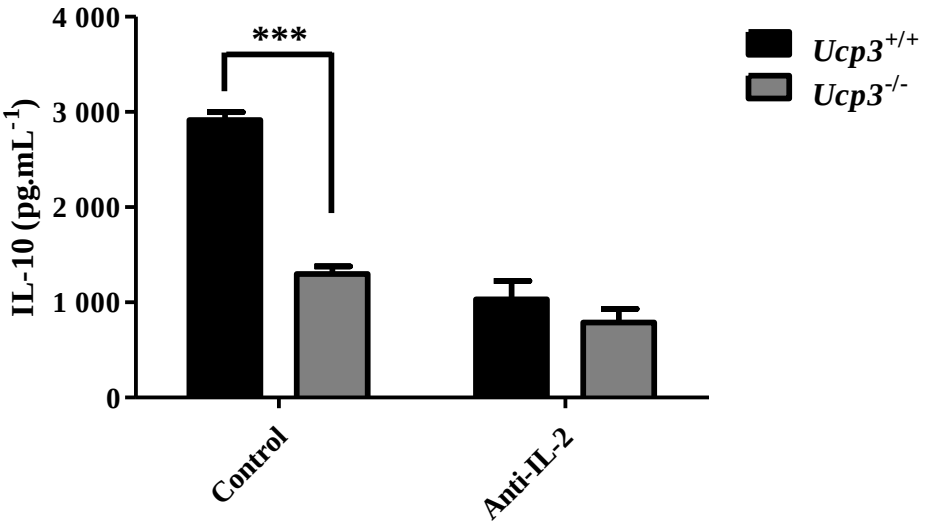

Figure 3.72: IL-10 secretion by *Ucp3*$^{+/+}$ and *Ucp3*$^{-/-}$ T cells under T_{reg} polarizing conditions is comparable following IL-2 neutralisation

T_{reg} cells were generated by incubating naive T cells in the presence of 1 µg.mL^{-1} of anti-CD3 and anti-CD28 and 5 ng.mL^{-1} of rhTGF-β1 without or with anti-IL-2 for 120 h. ELISA was performed twice with twelve technical replicates. Data were analysed using a two-way ANOVA with a *post hoc* Bonferroni test to quantify significance where detected. *** = $p < 0.001$.

3.3 Discussion

Our laboratory has reported evidence of UCP1 and UCP3 expression in murine thymocytes and spleen mitochondria (Carroll and Porter, 2004; Carroll *et al*., 2004; Carroll *et al*., 2005; Adams *et al*., 2008a, 2008b; Kelly and Porter, 2011), while Krauss *et al*. (2002) reported evidence of UCP2 expression in thymocytes. Thymocytes are derived from lymphoid progenitor cells and develop into mature T cells in the thymus before migrating to peripheral lymphoid tissues, such as the spleen (Krammer *et al*., 2007). Our laboratory has previously shown that ablation of *Ucp1* or *Ucp3* alters the T cell profile of both thymus and spleen (Adams *et al*., 2010; Kelly and Porter, 2011). Although Krauss *et al*. (2002) did not observe an effect on the T cell profile of the thymus in the absence of UCP2, the expression of UCPs in thymocytes and spleen mitochondria suggests their importance in thymic function, as well as a potential role in T cell selection, maturation, metabolism and/or function. Thus, we investigated the expression of UCPs in mature $CD4^+$ T cells and have shown that, for the most part, transcription of *Ucp*s is significantly downregulated following naive $CD4^+$ T cell activation.

Ucp1 is significantly downregulated in T_H0, T_H1, T_H17 and T_{reg} cells within 24 h of activation. To the best of our knowledge, no other research group has investigated the transcription of *Ucp1* in $CD4^+$ T cells. Transcription of *Ucp2* is also significantly reduced within 24 h in T_H0, T_H1 and T_H17 cells, although the fold-change in expression is not as extensive as that of *Ucp1*. *Ucp2* transcription in T_{reg} cells is not significantly reduced within 24 h and, in contrast, is significantly upregulated 120 h post-stimulation. T_{reg} cells display a unique and important role in the adaptive immune response that involves modulating and suppressing pro-inflammatory immune cells to prevent excessive inflammation and tissue damage (Gregori *et al*., 2012). They are also known to have a contrasting metabolic profile to effector T cells, utilising predominantly FAO rather than glycolysis (Michalek *et al*., 2011). The contrasting expression pattern of *Ucp2* in T_{reg} cells compared to that in T_H0 and effector T cells suggests that UCP2 protein may have an important role to play in T_{reg} cell generation, maintenance, metabolism and/or function.

The decrease in transcription of *Ucp1* and *Ucp2* across all subsets (excluding *Ucp2* in T_{reg} cells) suggests that their corresponding proteins, if their expression follows their transcriptional pattern, do not have a major function in activated T cells. Conversely, it is indicative of a role in the maintenance or metabolism of naive T cells. However, on closer inspection, it is clear that, while still significantly lower than in naive T cells, *Ucp2*

transcription in T_H1 and T_H17 cells seems to be increasing after 24 h. Indeed, it is possible that if these cells were incubated for as long as T_{reg} cells, *i.e.* up to 120 h post-stimulation, perhaps we would have seen a significant increase in *Ucp2* transcription by that point. This would be in line with the findings of Rupprecht *et al*. (2012) who reported the upregulation of UCP2 protein in $CD4^+$ T_H0 cells 48 h after activation, although they did not investigate UCP2 expression in polarized $CD4^+$ T cell subsets. The same group also reported a link between UCP2 expression and tissues with a high proliferative potential and reliance on glycolysis, such as T lymphocytes, hypothesizing that the expression of UCP2 is tightly connected to the cell metabolic state and changes simultaneously upon its alteration (Rupprecht *et al*., 2014). T_H1 and T_H17 cells are known to rely on glycolysis as their main pathway of energy generation so, if the hypothesis of Rupprecht *et al*. is correct, we may have seen a significant increase in *Ucp2* transcription, had we incubated the cells for a longer time point. Perhaps a decrease in *Ucp2* mRNA is observed in our work due to mRNA translation and degradation occurring at a high rate but gene transcription occurring more slowly. However, the fact that *Ucp2* transcription is significantly increased in T_{reg} cells contradicts the hypothesis of Rupprecht *et al*. as T_{reg} cells are known to rely on FAO as their primary metabolic profile and not glycolysis. It has also been suggested previously that mRNA levels do not always correspond to or accurately predict protein levels (Krauss *et al*., 2005; Kendrick, 2014; Rupprecht *et al*., 2014). However, as we did not pursue the role of UCP1 and UCP2 in $CD4^+$ T cells any further, their expression and potential roles in naive, effector or T_{reg} cells were not fully investigated.

Following on from the discovery by our laboratory of altered T cell profiles in both thymus and spleen of *Ucp3*$^{-/-}$ mice (Kelly and Porter, 2011) and with *Ucp3*$^{+/+}$ littermate controls available to us, we decided to pursue the role of UCP3 only in $CD4^+$ T cells. We have shown that the transcription pattern of *Ucp3* in T cells is quite similar to that of *Ucp1*, showing a significant decrease in all subsets tested within 24 h. Interestingly, Hilse *et al*. (2016) correlated UCP3 expression with UCP1 expression in BAT, although contradicted a role for UCP3 in BAT thermogenesis. Hence, a correlation between the expression of UCP1 and UCP3 in T cells may also be plausible and may be contributing to the similar effect on T cell profiles reported following *Ucp1* and *Ucp3* ablation, mentioned previously. This is in contrast to reports of *Ucp1* and *Ucp2* expression being inversely proportional in adipose tissue (Arsenijevic *et al*., 2000), although our data does not suggest this relationship in T cells. On further examination, it is evident that *Ucp3* transcription is significantly reduced within 4 h of activation of T_H0 cells. Much like *Ucp1* and *Ucp2*, the

downregulation of *Ucp3* transcription following T cell activation suggests a potential role in naive $CD4^+$ T cell maintenance.

To explore the effect of *Ucp3* ablation on $CD4^+$ T cells, we looked into differences in *Ucp3*$^{+/+}$ and *Ucp3*$^{-/-}$ activated T cell function under non-polarizing conditions, *i.e.* T_H0 cells. We have shown that *Ucp3* ablation indeed affects activated T cells, resulting in significantly higher IL-2 production and secretion by T_H0 cells under a number of different stimulatory conditions. IL-2 is one of the first cytokines to be produced by all activated $CD4^+$ T cells after antigen presentation to the TCR and is responsible for the promotion and modulation of T cell survival, activation, growth and proliferation (Boyman and Sprent, 2012; Liao *et al*., 2013). In addition to antigen presentation to the TCR causing an increase in expression of the IL-2R, it is also known that IL-2 stimulates the expression of CD25, the α subunit of the IL-2R, through the involvement of STAT5 binding to the *Cd25* gene locus, and subsequently increases cell responsiveness in a feedforward mechanism (Boyman and Sprent, 2012; Liao *et al*., 2013). In line with this, *Ucp3*$^{-/-}$ T_H0 cells display elevated expression of CD25, upregulation of the early activation marker CD69 and higher numbers of cells that have undergone more cell divisions. Following oligomycin (ATP synthase inhibitor) treatment of T cells, Chang *et al*. (2013) reported that mitochondrial ATP generated by OxPhos is a requirement for T cell proliferation and activation marker expression. Albeit the possibility of UCP3 eliciting uncoupling activity in $CD4^+$ T cells has not yet been explored, *Ucp3*$^{-/-}$ T cells may well be more 'coupled' if this is the case and, as such, would display more efficient OxPhos and, consequently, more efficient ATP production, which may be responsible for the observed early activation and increased proliferation of these cells. Indeed, it may have been worthwhile to measure the ATP/ADP ratio of *Ucp3*$^{+/+}$ compared to *Ucp3*$^{-/-}$ T_H0 cells in this work. On the other hand, the oligomycin treatment of activated T cells in the study by Chang *et al*. may have led to an increase in ROS production, with ROS being previously implicated in promoting T cell activation (Roth and Dröge, 1987; Los *et al*., 1995; Sena *et al*., 2013) and proliferation (Chang *et al*., 2013). 'Coupled' *Ucp3*$^{-/-}$ T_H0 cells would be presumed to have a higher mitochondrial membrane potential than *Ucp3*$^{+/+}$ T_H0 cells and, thus, may produce more ROS. The possibility of ROS influencing the activation and proliferation of *Ucp3*$^{-/-}$ T_H0 cells is explored in Chapter 4. As a side note, it is interesting that, in a similar manner, $CD4^+$ lymphocytes of *Ucp2*$^{-/-}$ mice produce higher levels of IL-2 and TNF-α (Vogler *et al*., 2006) and Pecqueur *et al*. (2008) reported that loss of *Ucp2* activated cell proliferation

specifically in murine embryonic fibroblasts and T cells. It is clear from our work that *Ucp3*$^{-/-}$ cells undergo earlier activation compared to their WT counterparts.

In line with the above findings, it was predicted that earlier activated *Ucp3*$^{-/-}$ T_H0 cells with a large FSC would be greater in number than *Ucp3*$^{+/+}$ T_H0 cells with same and that they would additionally survive better due to the increase in IL-2 production which can promote cell survival and growth (Boyman and Sprent, 2012; Liao *et al*., 2013). FSC-A was used as a measure of cell size. Increased cell size, which occurs during lymphocyte blastogenesis (Preston *et al*., 2015), is synonymous with increased cell growth and activation. However, fewer *Ucp3*$^{-/-}$ T_H0 cells are observed with a large FSC and *Ucp3*$^{-/-}$ T_H0 cell viability is decreased 72 h post-stimulation. As well as this, *Ucp3*$^{-/-}$ T_H0 cells secrete significantly less IFN-γ than their WT counterparts, which is thought to be a reflection of their decreased viability. These unexpected results did not seem to coincide with *Ucp3*$^{-/-}$ T_H0 cells undergoing activation earlier and, thus, having a growth 'head start' and IL-2-linked promotion of cell survival and IFN-γ production (Liao *et al*., 2013). While this decrease in cell survival seems counterintuitive following the observations of increased IL-2 production, it is thought to be due to the triggering of a phenomenon known as AICD, an apoptotic form of cell death. In line with this, *Ucp3*$^{-/-}$ T_H0 cell viability is increased following incubation with an inhibitor of apoptosis, with no effect observed following incubation with an inhibitor of necrosis. Moreover, IL-2 has been implicated in the priming of T cells for AICD (Maher *et al*., 2002; Roberts *et al*., 2003; Krammer *et al*., 2007; Boyman and Sprent, 2012; Liao *et al*., 2013).

AICD is important for homeostasis and the elimination of potentially harmful autoreactive cells (Liao *et al*., 2013). Failure to produce normal amounts of IL-2 upon activation is a hallmark of T cells from patients with systemic lupus erythematosus (SLE), a chronic autoimmune disease, and, indeed, SLE patients display defective AICD among other T cell defects (Crispin and Tsokos, 2009). AICD can be caused in part by the interaction of CD95 with CD95L, the expression of which can be promoted by IL-2 signalling (Maher *et al*., 2002; Boyman and Sprent, 2012; Liao *et al*., 2013). This interaction triggers the clustering of CD95 and the recruitment of the adapter protein Fas-associated death domain (FADD; Maher *et al*., 2002; Krammer *et al*., 2007). Pro-caspase 8 binds to FADD's death effector domain and is activated by self-cleavage, forming caspase 8 (Maher *et al*., 2002; Krammer *et al*., 2007). Activated caspase 8 is released into the cytosol where it mediates apoptosis by either directly activating downstream effector caspases or by indirectly activating

downstream effector caspases through cytochrome c release from mitochondria (Maher *et al*., 2002; Krammer *et al*., 2007). However, following our observation of decreased CD95L expression in *Ucp3*$^{-/-}$ T_H0 cells rather than increased expression, it is clear that AICD may be occurring by means other than the CD95:CD95L interaction. Indeed, Maher *et al*. (2002) reported that, although T cells constitutively express CD95, some apoptosis-resistant T cells can express lower levels or have defective CD95 signalling. It may be possible that *Ucp3*$^{+/+}$ T_H0 cells express lower levels of CD95 and, thus, are more resistant to CD95:CD95L-induced apoptosis, regardless of their increased expression of CD95L. From a retrospective point of view, it would have been ideal to measure the expression of both CD95 and CD95L in this work. In addition, it has been reported that activated CD95$^+$ cells can be refractory to cell death unless in contact with IL-2 for at least 48 h; this 'propriocidal' cell death is due to IL-2-induced cell cycle progression which is necessary to make T cells sensitive to TCR and CD95-induced apoptosis (Ramaswamy *et al*., 2009). This supports our hypothesis of cell death being promoted in *Ucp3*$^{-/-}$ T_H0 cells due to their increased production of IL-2 compared to *Ucp3*$^{+/+}$ T_H0 cells. AICD can also be induced by means independent of CD95, such as TNF ligation of the TNF receptor or exposure to ceramide and ROS (Maher *et al*., 2002; Roberts *et al*., 2003; Krammer *et al*., 2007). That ROS have been implicated in promoting T cell activation (Roth and Dröge, 1987; Los *et al*., 1995; Sena *et al*., 2013) and proliferation (Chang *et al*., 2013), as mentioned previously, as well as the induction of AICD, would strongly support the possibility of their involvement in the early activation and induced cell death observed in *Ucp3*$^{-/-}$ T_H0 cells. It is interesting to note that, while stimulated *Ucp3*$^{-/-}$ T_H0 cells do not survive as well as their WT counterparts, *Ucp3*$^{-/-}$ cells receiving no stimulation for up to 72 h (essentially still naive T cells) continue to survive better. It is possible that the fact that *Ucp3*$^{-/-}$ unstimulated T cells inherently survive better than their WT counterparts accounts for the increased IL-2 production and proliferation *etc*. observed in these cells.

We hypothesize that UCP3 acts to restrict T cell activation. Accordingly, following activation of naive T cells, UCP3 expression is downregulated rapidly. As naive T cells have not undergone any activation event, the effect of *Ucp3* ablation on them, as well as precursor cells to mature CD4$^+$ T cells, may be minimal. Correspondingly, after exploring their viability, size, cytokine production in response to stimulation and surface marker expression, it was noted that CD4$^+$CD8$^-$ thymocytes and naive T cells from both *Ucp3*$^{+/+}$ and *Ucp3*$^{-/-}$ mice appear to be similar. Moreover, CD4$^+$ memory and T_{reg} cell population

frequencies are also unaffected. It is evident that the effect of *Ucp3* knockdown on peripheral $CD4^+$ T cells does not transpire until after cell activation.

After observing the effect of *Ucp3* ablation on non-polarized, activated T (T_H0) cells, it was hypothesized that *Ucp3* ablation would also affect polarized T cell subsets. Intriguingly, no effect on *Ucp3*$^{-/-}$ T_H1 cell viability, cell size/activation or production of IFN-γ, the characteristic T_H1 cytokine, is apparent. These results were quite unexpected. On one hand, one may have predicted a decrease in IFN-γ production from the *Ucp3*$^{-/-}$ T_H1 cells, possibly due to AICD as in the *Ucp3*$^{-/-}$ T_H0 cells. Conversely, one could have also expected to observe an increase in survival and IFN-γ production from the *Ucp3*$^{-/-}$ T_H1 cells due to the increased IL-2 production observed in *Ucp3*$^{-/-}$ T_H0 cells as IL-2 induces IL-12Rβ2 subunit expression via STAT5 (augmenting responsiveness to IL-12 and promoting T_H1 cell differentiation), is capable of driving IFN-γ production and promotes cell survival (Boyman and Sprent, 2012; Liao *et al*., 2013), although this effect is not observed in T_H0 cells. That no difference altogether is observed was surprising. It is unclear as of yet why *Ucp3*$^{-/-}$ T_H1 cell activation, function and viability are unaffected by *Ucp3* ablation, in contrast to their non-polarized counterparts.

The effect of *Ucp3* ablation on T_H0 cells implies a role for UCP3 in restricting IL-2 production and T cell activation, thereby preventing AICD. Furthermore, IL-2 can play a significant role in influencing T_H17 and T_{reg} cell differentiation. In addition to TGF-β, high levels of IL-2 promote the induction and survival of T_{reg} cells and the expression of FoxP3 while inhibiting T_H17 cell polarization (Laurence *et al*., 2007; Boyman and Sprent, 2012; Liao *et al*., 2013). Indeed, in the absence of IL-2 signals, T_{reg} cell number declines substantially, whereas T_H17 cell number increases, leading to an enhanced susceptibility to autoimmune disease and inflammatory disorders (Boyman and Sprent, 2012). Therefore, although no effect of *Ucp3* ablation is observed in T_H1 cells, an effect of *Ucp3* ablation on T_H17 and T_{reg} polarized T cell subsets was hypothesized. Importantly, *Ucp3*$^{-/-}$ T_H17 cells display significantly less IL-17A secretion than *Ucp3*$^{+/+}$ T_H17 cells. Although not significant, a trend for decreased viability of *Ucp3*$^{-/-}$ T_H17 cells is also observed, presumably due to AICD. It is thought that the decrease in viable cells under T_H17 polarizing conditions accounts for the decrease in IL-17A production observed; however, IL-2 can also act to constrain IL-17A production (Laurence *et al*., 2007). FoxP3 expression is indicative of T_{reg} cell induction (Hori *et al*., 2003). $FoxP3^+$ *Ucp3*$^{-/-}$ cells are higher in number than $FoxP3^+$ *Ucp3*$^{+/+}$ cells under T_{reg} polarizing conditions and display higher cell

viability. These data advocate that, while *Ucp3*$^{-/-}$ T_H1 cells are unaffected by the altered IL-2 production following *Ucp3* ablation, the generation of T_H17 and T_{reg} cells is crucially affected. The IL-2 differential between *Ucp3*$^{+/+}$ and *Ucp3*$^{-/-}$ T cells appears to culminate in T_{reg} cell differentiation and survival being favoured over T_H17 cell differentiation and survival. Indeed, since neutralising IL-2 activity directs the *Ucp3*$^{-/-}$ cell phenotypes to return to a more WT-like state, it is convincing that IL-2 is responsible for the effects observed on *Ucp3*$^{-/-}$ T_H17 and T_{reg} cells. It should be noted that, while it is evident that *Ucp3*$^{-/-}$ T_{reg} cell survival and differentiation is enhanced, it is unclear whether this is due to the propagation of nT_{reg} cells already present in freshly isolated spleen samples or whether it is due to the *de novo* generation of iT_{reg} cells from FoxP3$^-$ conventional T cells. To confirm this, it may have been interesting to repeat the above investigation following the prior depletion of FoxP3$^+$ nT_{reg} cells from spleen samples.

T_H17 cells are extremely pro-inflammatory. The high inflammatory nature of T_H17 cells manifests in them being a main contributor to the pathogenesis of autoimmunity (Ivanov *et al*., 2006; Liao *et al*., 2013). T_{reg} cells, on the other hand, play a role in preventing autoimmunity. They are a specialized subpopulation of CD4$^+$ T cells that act to suppress helper T cells and activation of the immune system, thereby maintaining immune system homeostasis (Pulendran and Ahmed, 2006; Boyman and Sprent, 2012; Liao *et al*., 2013). They function in contrast to the other subsets, modulating inflammation and acting as key players in sustaining self-tolerance. This helps to prevent excessive tissue damage from too much inflammation and autoimmune responses to self-antigen, as supported by the occurrence of autoimmunity due to T_{reg} deficiencies (Gregori *et al*., 2012; Liao *et al*., 2013). That *Ucp3* ablation can tip the balance of T_H17 and T_{reg} cells in favour of the latter implicates *Ucp3* as a potential target for preventing or ameliorating autoimmune diseases such as multiple sclerosis (MS) and Crohn's disease. Hence, the potential of targeting *Ucp3* to modulate autoimmunity will need to be further investigated.

3.4 Conclusion

We have shown that *Ucp1*, *Ucp2* and *Ucp3* transcription is downregulated in activated $CD4^+$ T cells. We hypothesized that UCP3 would play a role in naive T cell maintenance or metabolism due to its expression in naive T cells and rapid downregulation following naive T cell activation. While no effects of *Ucp3* ablation are found on naive T cell viability, size or surface marker expression, $Ucp3^{-/-}$ T_H0 cells are majorly impacted. *Ucp3* ablation results in increased IL-2 production, upregulated CD25 and CD69 expression and greater proliferation. However, it also prompts the premature death of $Ucp3^{-/-}$ T_H0 cells. The favouring of T_{reg} cell generation over T_H17 cell generation also ensues from *Ucp3* ablation, while T_H1 cells are unaffected. Our data point towards a role for UCP3 in restricting TCR signalling and $CD4^+$ T cell activation. UCP3 acts as a rheostat to inhibit the magnitude of TCR activation and fine-tunes the TCR and CD28 signal, hence its expression in naive $CD4^+$ T cells and subsequent downregulation after cell stimulation. Following activation, TCR signals may block or switch off *Ucp3* gene expression within 4 h, as suggested by our RT-PCR data, in order to negate the dampening effect of UCP3 and allow for full activation. Ablation of *Ucp3* allows for uncontrolled early activation and appears to culminate in premature cell death, which we believe to be due to AICD. We conclude that UCP3 has a role in restricting T cell activation, thereby preventing AICD, and can perturb the T_H17:T_{reg} cell ratio. The altered T_H17:T_{reg} cell balance implicates *Ucp3* as a potential therapeutic target for autoimmune disease, although further investigation into how UCP3 is influencing this balance is required.

Chapter 4:

The Role of UCP3 in $CD4^+$ T Cell Metabolism

Chapter 4

The Role of UCP3 in $CD4^+$ T Cell Metabolism

4.1 Introduction

The role of UCP1, the archetypal uncoupling protein, is to dissipate the proton electrochemical gradient during NST by uncoupling electron transport and O_2 consumption from ATP synthesis in BAT mitochondria. UCP3 has an amino acid sequence more similar to that of UCP1 than any other member of the mitochondrial anion carrier superfamily (excluding UCP2), at 57 % homology (Boss *et al*., 1997). The six membrane-spanning α-helix structure of UCP1 is highly conserved in UCP3, including the three mitochondrial carrier protein motifs, consistent with a role as an ion transporter of the MIM (Boss *et al*., 1997; Fleury *et al*., 1997). Thus, it followed naturally that this protein was presumed to have uncoupling activity similar to that of UCP1 upon discovery. Indeed, UCP3 has been demonstrated to have uncoupling activity both in *in vitro* reconstitution systems (Jabůrek *et al*., 1999; Echtay *et al*., 2001) and in mitochondria isolated from SKM of 3,4-methylenedioxymethamphetamine (MDMA)-treated rats and mice (Kelly *et al*., 2012). However, while UCP3 is expressed in BAT (Cunningham *et al*., 2003), no role in NST is apparent (Nedergaard *et al*., 2001; Hilse *et al*., 2018). If there is any physiological/biochemical process that UCP3 has been correlated with, it is conditions under which FA mobilization and oxidation may be occurring (Hilse *et al*., 2018). When it comes to immune system-related cells, UCP3 protein is clearly detectable in thymocytes, splenocytes and the lymphocyte fraction of the spleen (Carroll and Porter, 2004) and its deficiency alters the T cell profile in both thymus and spleen, as reported by Kelly and Porter (2011). We have demonstrated in Chapter 3 that UCP3 is expressed in naive $CD4^+$ T cells at the mRNA level before being downregulated upon TCR and CD28-dependent T cell activation and that *Ucp3* ablation in mice perturbs $CD4^+$ T cell function. To this end, as a logical progression, the focus of the work presented in this chapter was to determine the role of UCP3 in $CD4^+$ T cell metabolism and investigate whether a skewed metabolism as a result of *Ucp3* ablation is the cause of the altered T cell function we have observed. We investigated the metabolism of $Ucp3^{+/+}$ and $Ucp3^{-/-}$ $CD4^+$ T cells using the Seahorse XF24 Analyzer, both at the naive cell stage and at different time points during and post-activation.

When naive $CD4^+$ T cells are activated to adopt a pro-inflammatory effector function, they undergo a metabolic switch from a relatively quiescent state utilising OxPhos as their predominant metabolic profile to a highly active state displaying a Warburg-like metabolism that relies predominantly on glycolysis as the primary pathway of energy generation (Chang *et al*., 2013; Pearce and Pearce, 2013). In contrast, when cells are activated to adopt an immunosuppressive function (T_{reg} cells), they switch to and primarily depend on lipid oxidation (Michalek *et al*., 2011). Interestingly, UCP3 has been implicated in the metabolic switch from OxPhos to FAO as it becomes upregulated in SKM (Garcia-Martinez *et al*., 2001) and thymus mitochondria (Carroll and Porter, 2004; Kelly and Porter, 2011) during times of starvation when FAs are the predominant fuel source. Thus, UCP3 may have a more important role in the metabolism and maintenance of T_{reg} cells than effector T cell subsets. For this reason, we investigated the role of UCP3 in T_{reg} cell metabolism, as well as in naive and effector T cell metabolism.

As discussed in Chapter 1, all cells have antioxidants, such as SOD, and physiological ROS defence mechanisms in place to counteract ROS production by mitochondria and reduce oxidative damage to DNA (Ježek and Hlavatá, 2005). However, this system is imperfect and ROS that evade it can continue to damage proteins, lipids and DNA directly (Brand *et al*., 2004). Additionally, this system targets existing ROS, whereas 'prevention rather than cure' would be a more logical way to decrease oxidative damage (Brand, 2000). A potential physiological mechanism to alleviate ROS production by mitochondria would be mild uncoupling, as mitochondrial ROS production is very sensitive to the PMF set up across the MIM by electron transport (Brand *et al*., 2004). This is where UCPs may be physiologically relevant; moderate uncoupling activity by UCPs and the generation of a controlled proton leak into the MM without ATP synthase involvement would lower the mitochondrial membrane potential and minimise the transfer of electrons to molecular O_2, the formation of O_2^- and oxidative damage to DNA (Brand, 2000; Miwa and Brand, 2003; Brand *et al*., 2004). Thus, this implicates an antioxidant function for UCPs within mitochondria. The role of the antioxidant defences would then be to mop up residual ROS that escape this primary control (Brand, 2000). Indeed, of the number of roles that have been postulated for UCPs, only the attenuation of ROS production and the associated protection against cellular degeneration and ageing would appear important enough to merit the energetic cost imposed by a proton leak (Brand, 2000). For this reason, in addition to investigating the metabolism of *Ucp3*$^{+/+}$ and *Ucp3*$^{-/-}$ $CD4^+$ T cells, we explored

the effect of *Ucp3* ablation on the mitochondrial membrane potential of, and ROS production by, naive $CD4^+$ T cells.

4.2 Results

4.2.1 *Ucp3* Ablation Does Not Affect the Mitochondrial Abundance of $CD4^+$ T Cells

Given that we have demonstrated that *Ucp3* gene expression is decreased upon T cell activation and that its ablation perturbs T cell function, as well as UCP3 activity being implicated in cellular metabolism as described previously, we next sought to examine whether UCP3 may play any role in mediating the metabolic activity of $CD4^+$ T cells. Firstly, to ensure that any potential differences observed between the metabolism of *Ucp3*$^{+/+}$ and *Ucp3*$^{-/-}$ $CD4^+$ T cells were not due to differences in mitochondrial content or abundance, the citrate synthase assay and flow cytometry analysing MitoTracker™ Green FM staining were carried out to confirm that cells of both genotypes possessed a similar amount of mitochondria. Citrate synthase is a MM protein commonly used as a marker of mitochondrial abundance within the cell (Spinazzi *et al*., 2012), while MitoTracker™ Green FM is a green fluorescent stain that localizes to mitochondria regardless of mitochondrial membrane potential (Puleston, 2015). These experiments ensure that detected differences in metabolism can be assigned to altered mitochondrial abundance where appropriate, preventing *a priori* assumptions of mitochondrial function.

The enzymatic activity of citrate synthase and staining of MitoTracker™ Green FM were measured in *Ucp3*$^{+/+}$ and *Ucp3*$^{-/-}$ T_H0 cells 8, 24, 48 and 72 h post-stimulation: time points matching those used in subsequent metabolic experiments. The activity of citrate synthase is significantly higher in *Ucp3*$^{-/-}$ T_H0 cells 72 h post-stimulation (Figure 4.1A) but this difference is not reflected by MitoTracker™ Green FM staining (Figure 4.1B and F). No differences are found at other time points (Figure 4.1B – E). This suggests that the mitochondrial abundance of *Ucp3*$^{+/+}$ and *Ucp3*$^{-/-}$ T_H0 cells is comparable. Similarly, the mitochondrial abundance of *Ucp3*$^{+/+}$ and *Ucp3*$^{-/-}$ naive (Figure 4.2), T_H17 (Figure 4.3) and T_{reg} (Figure 4.4) cells is not significantly different. Thus, it was assumed that, should any differences in metabolism be detected between naive, T_H0 or polarized T cells of each genotype in subsequent experiments, differences in mitochondrial content/abundance could be ruled out as the causative factor.

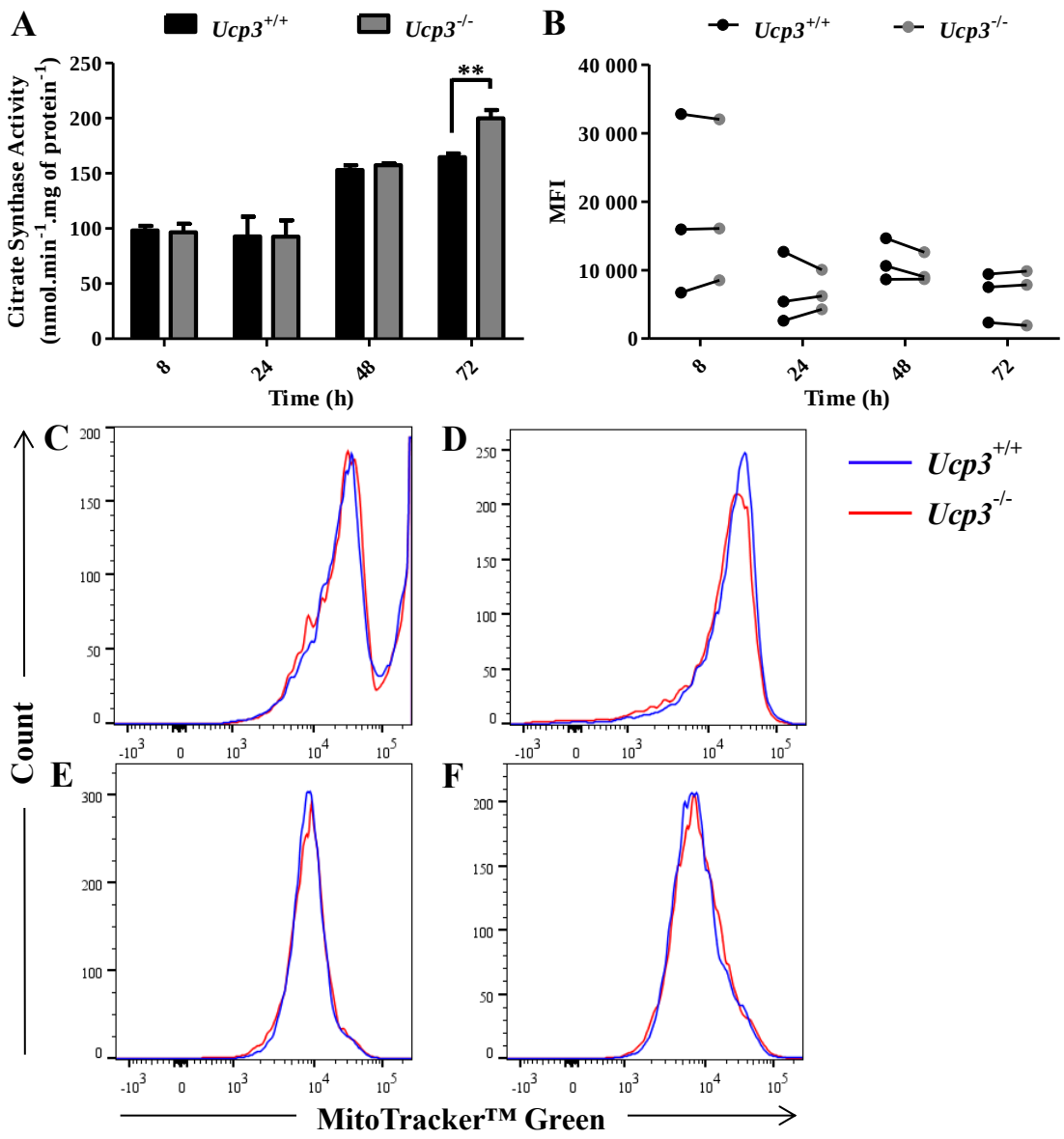

Figure 4.1: Mitochondrial abundance of *Ucp3*$^{+/+}$ and *Ucp3*$^{-/-}$ T_H0 cells is comparable

T_H0 cells were generated by incubating naive T cells in the presence of 1 and 2 µg.mL^{-1} of anti-CD3 and anti-CD28, respectively, for the time indicated. (A) Citrate synthase enzymatic activity of T_H0 cells at the time indicated. The citrate synthase activity assay was performed three times in triplicate. (B) MFI of MitoTracker™ Green FM staining of T_H0 cells from three individual experiments at the time indicated post-stimulation. All data were analysed using a two-way ANOVA with a *post hoc* Bonferroni test to quantify significance where detected. ** = $p < 0.01$. (C – F) Mitochondrial abundance of T_H0 cells 8 (C), 24 (D), 48 (E) and 72 (F) h post-stimulation. Data are presented as representative histograms of the viable, CD4$^+$ T cell population.

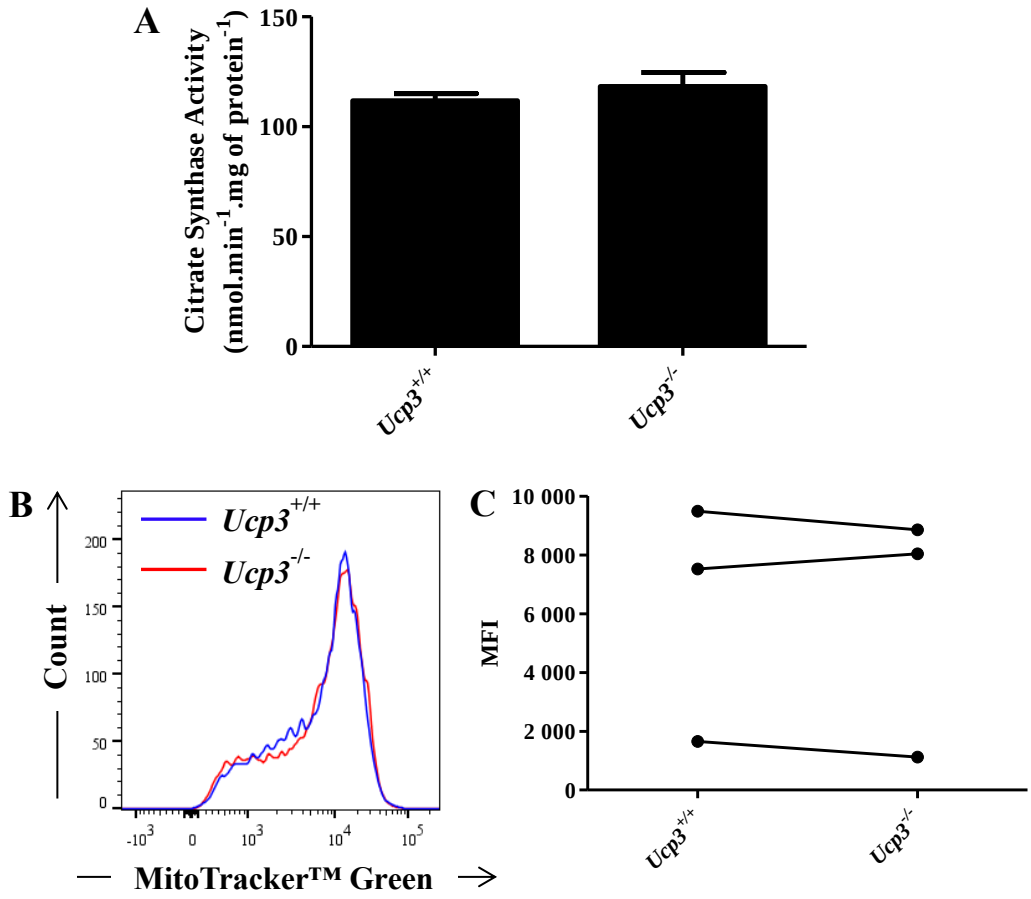

Figure 4.2: Mitochondrial abundance of *Ucp3*$^{+/+}$ and *Ucp3*$^{-/-}$ naive CD4^{+} T cells is comparable

Primary CD4^{+} T cells were isolated from a suspension of splenocytes and prepared for the citrate synthase assay (A) or flow cytometry (B and C) immediately. (A) Citrate synthase enzymatic activity of naive CD4^{+} T cells. The citrate synthase activity assay was performed three times in triplicate. (B) Mitochondrial abundance of naive CD4^{+} T cells. Data are presented as representative histograms of the viable, CD4^{+} T cell population. (C) MFI of MitoTracker™ Green FM staining of naive CD4^{+} T cells from three individual experiments. All data were analysed using a two-tailed, unpaired *t* test to quantify significance where detected.

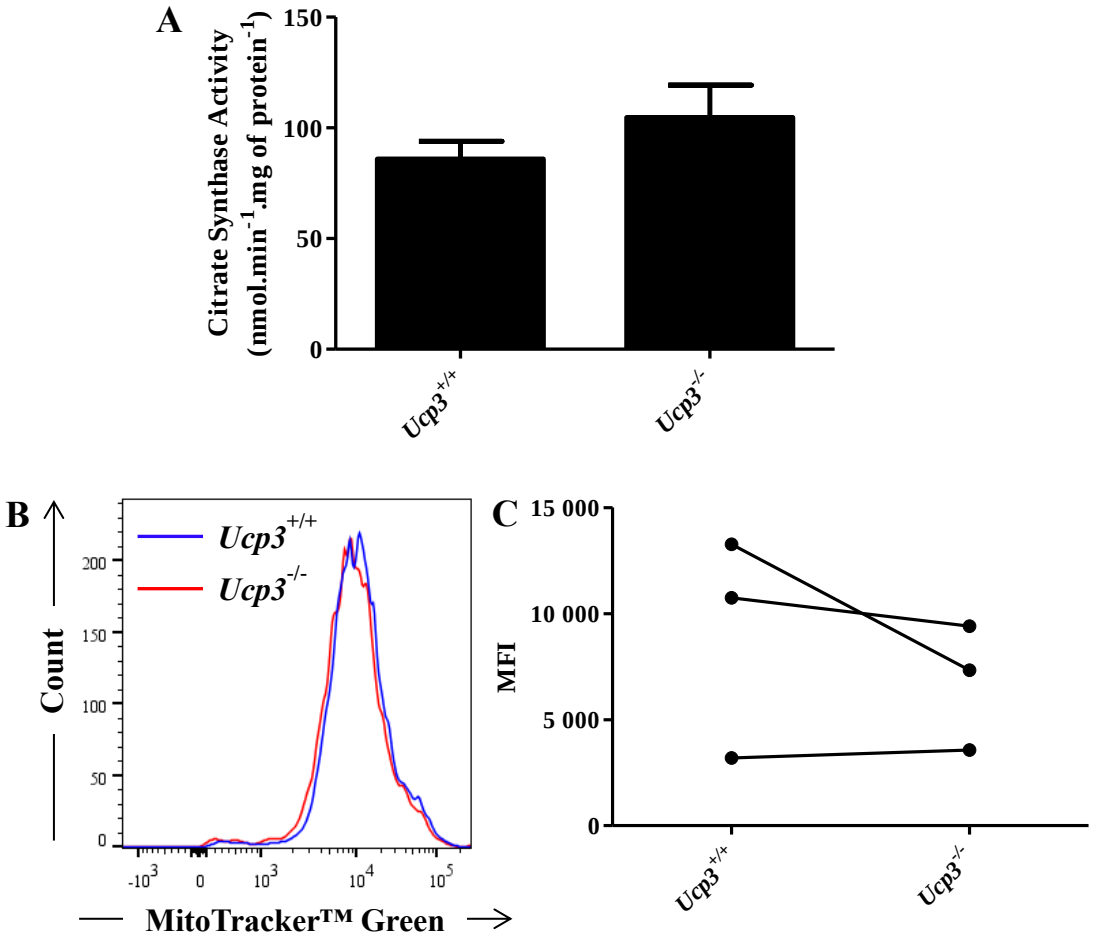

Figure 4.3: Mitochondrial abundance of *Ucp3*$^{+/+}$ and *Ucp3*$^{-/-}$ T_H17 cells is comparable

T_H17 cells were generated by incubating naive T cells in the presence of 5 µg.mL^{-1} of anti-CD3 and anti-CD28, 20 ng.mL^{-1} of anti-IL-4 and rIL-6, 10 µg.mL^{-1} of anti-IFN-γ and 2.5 ng.mL^{-1} of rhTGF-β1 for 72 h. (A) Citrate synthase enzymatic activity of T_H17 cells. The citrate synthase activity assay was performed three times in triplicate. (B) Mitochondrial abundance of T_H17 cells. Data are presented as representative histograms of the viable, CD4$^+$ T cell population. (C) MFI of MitoTracker™ Green FM staining of T_H17 cells from three individual experiments. All data were analysed using a two-tailed, unpaired *t* test to quantify significance where detected.

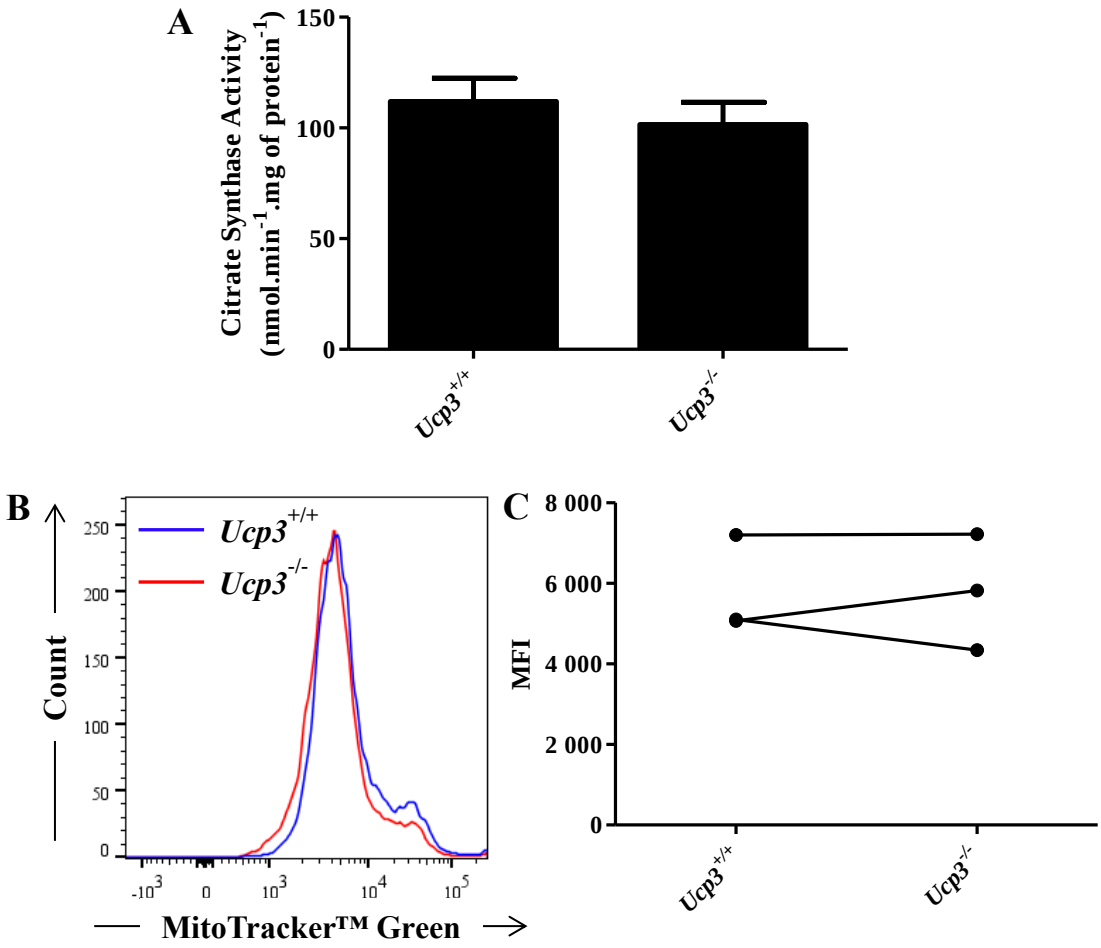

Figure 4.4: Mitochondrial abundance of *Ucp3*$^{+/+}$ and *Ucp3*$^{-/-}$ T_{reg} cells is comparable

T_{reg} cells were generated by incubating naive T cells in the presence of 1 µg.mL^{-1} of anti-CD3 and anti-CD28, 5 ng.mL^{-1} of rhTGF-β1 and 10 ng.mL^{-1} of rIL-2 for 120 h. (A) Citrate synthase enzymatic activity of T_{reg} cells. The citrate synthase activity assay was performed three times in triplicate. (B) Mitochondrial abundance of T_{reg} cells. Data are presented as representative histograms of the viable, CD4^{+} T cell population. (C) MFI of MitoTracker™ Green FM staining of T_{reg} cells from three individual experiments. All data were analysed using a two-tailed, unpaired *t* test to quantify significance where detected.

4.2.2 Optimization Results for the Seahorse XF Cell Mito Stress Test

In order to examine metabolic parameters of *Ucp3*$^{+/+}$ and *Ucp3*$^{-/-}$ T cells and the potential role of UCP3 in T cell metabolism, the Seahorse XF Cell Mito Stress Test was used. During a standard Seahorse XF Cell Mito Stress Test, four compounds are used to interrogate mitochondrial function: oligomycin, FCCP, antimycin A and rotenone. The experiment involves taking basal measurements of the OCR and ECAR followed by measurements taken after sequential injections of oligomycin, FCCP and a mix of rotenone and antimycin A. Oligomycin inhibits ATP synthase, the enzyme that generates ATP from ADP at the end of the ETC (Nicholls *et al*., 2010). By doing this, it shuts down the OxPhos energy pathway and the OCR should decrease. To avoid an energy crisis, the cell is forced to utilise glycolysis to meet its energy demands (Nicholls *et al*., 2010) and the rate of glycolysis is maximally increased to the cells 'glycolytic capacity'. If the ECAR increases, it suggests that cells can switch easily to glycolysis. It should be noted that the ECAR is not a direct measure of glycolysis and is used as an indirect measurement in all of these analyses. Injection of oligomycin shows how much of the OCR is linked to ATP synthesis.

When the mitochondrial uncoupler and protonophore, FCCP, is subsequently added, it allows a free flow of protons back into the MM independent of ATP synthase (Nicholls *et al*., 2010). This disrupts the proton gradient across the MIM which is coupled to electron transport. The ETC then works very hard to re-establish the electrochemical gradient again and to maintain the mitochondrial membrane potential by increasing the flow of electrons across the ETC at maximum speed and moving protons back into the IMS. Thus, in the presence of FCCP, the rate of OxPhos is maximally increased, allowing the maximum respiratory capacity of the ETC to be measured. The addition of FCCP allows one to observe how much O_2 consumption a cell can perform. In the case of T cells, the extent of the increase in the OCR after FCCP addition depends on the subset (van der Windt and Pearce, 2012). It is important to note that the ECAR can increase when FCCP is used, not only due to cells utilising glycolysis to generate ATP and maintain their energy balance (Nicholls *et al*., 2010), but also because they increase the TCA cycle as they try to recover and synthesize ATP. This leads to increased CO_2 production which can influence the pH/ECAR and give a false indication of higher glycolytic activity (Choi *et al*., 2009). Rotenone and antimycin A inhibit Complexes I and III, respectively, thereby completely inhibiting the ETC and, as such, any residual O_2 consumption measured after the addition of these compounds is non-mitochondrial – rotenone and antimycin A inhibit mitochondrial respiration only.

A number of parameters can be calculated following treatment with the above compounds, as described by Ruas *et al*. (2016) and on the Seahorse manufacturer website (Agilent Technologies). The basal mitochondrial OCR can be calculated by subtracting the non-mitochondrial respiration rate measured following rotenone and antimycin A injection from the basal OCR. The difference between the OCR after oligomycin injection and the non-mitochondrial respiration rate indicates the mitochondrial proton leak across the MIM. The ATP-linked mitochondrial OCR is calculated by subtracting proton leak from the basal mitochondrial OCR. The cell coupling efficiency is calculated by expressing the ATP-linked mitochondrial OCR as a percentage of the basal mitochondrial OCR. Maximal mitochondrial respiration is calculated by subtracting the non-mitochondrial respiration rate from the maximal respiration. The mitochondrial spare respiratory capacity is the extra mitochondrial capacity available beyond basal function; how much is 'on reserve' in a cell to produce energy under conditions of increased work or stress and is thought to be important for long-term cellular survival and function (Ferrick *et al*., 2008; Choi *et al*., 2009; Nicholls *et al*., 2010; van der Windt and Pearce, 2012; van der Windt *et al*., 2012). It can be calculated by subtracting the basal mitochondrial OCR from the maximal mitochondrial respiration and can also be expressed as a percentage of the basal rate. The OCR/ECAR ratio gives an indication of how oxidative or glycolytic a cell population is. It is calculated from the basal OCR and ECAR data obtained during the experiment. Alternatively, this can be calculated as an ECAR/OCR ratio. A graphic of these metabolic parameters and their equations are shown in Figure 4.5 and Table 4.1, respectively.

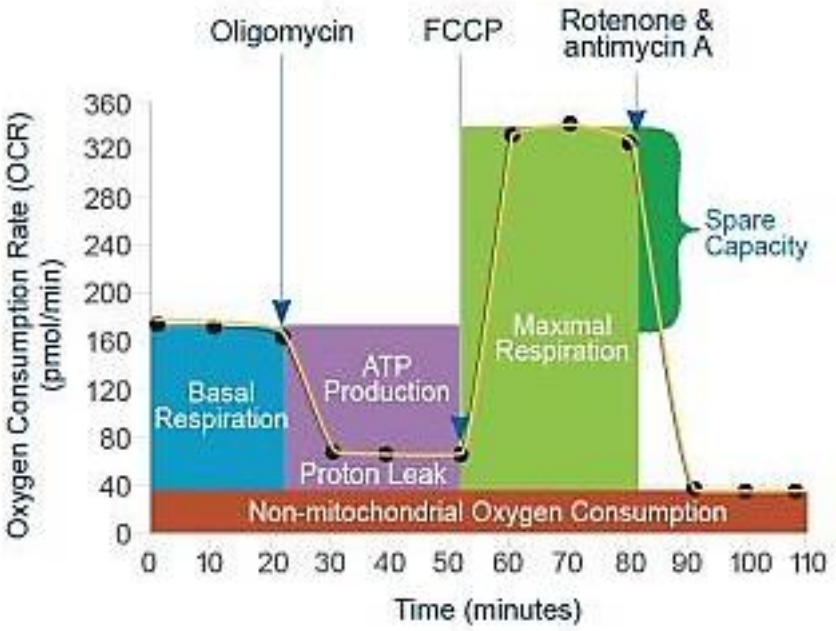

Figure 4.5: Seahorse XF Cell Mito Stress Test profile and measurement of mitochondrial parameters

Taken from the manufacturer website [https://www.agilent.com/en/products/cell-analysis-(seahorse)/seahorse-xf-consumables/kits-reagents-media/seahorse-xf-cell-mito-stress-test-kit].

Table 4.1: Parameters calculated from the Seahorse XF Cell Mito Stress Test

Parameter	Equation
OCR/ECAR Ratio	Basal OCR / basal ECAR
Non-mitochondrial respiration	Mean OCR following rotenone and antimycin A injection
Basal mitochondrial OCR	Mean basal OCR – non-mitochondrial respiration
Mitochondrial OCR linked to proton leak	Mean OCR following oligomycin injection – non-mitochondrial respiration
Mitochondrial OCR linked to ATP production	Basal mitochondrial OCR – proton leak
Coupling efficiency (%)	(Mitochondrial OCR linked to ATP production / basal mitochondrial OCR) x 100
Maximal respiration	Mean OCR following FCCP injection – non-mitochondrial respiration
Spare respiratory capacity	Maximal respiration – basal mitochondrial OCR
Spare respiratory capacity as a %	(Spare respiratory capacity / basal mitochondrial OCR) x 100

4.2.2.1 Cell Seeding Density Optimization

Before *Ucp3*$^{+/+}$ and *Ucp3*$^{-/-}$ T cell metabolism could be analysed using the Seahorse XF Cell Mito Stress Test, it was required that some optimization be carried out first. A seeding density optimization experiment was carried out to determine the seeding density that would give the best OCR and ECAR readouts. *Ucp3*$^{+/+}$ T_H0 cells were harvested from 96-well plates 24 h post-stimulation. Five different seeding densities were tested to determine the optimal seeding density for use with the Mito Stress Test: 250 000, 500 000, 750 000, 1 000 000 and 1 250 000 cells per well. The optimal seeding density was determined firstly by visual assessment; cells should be at 50 – 90 % confluence and evenly distributed within each individual well. Subsequently, three basal OCR and ECAR measurements were taken during a short trial assay and used to assess seeding density as the cells are offered an unlimited supply of substrate and have not yet been treated with mitochondrial inhibitors. A basal OCR and ECAR between 100 – 400 pmol.min^{-1} and 20 – 120 mpH.min^{-1}, respectively, are desired as these are recommended by the manufacturer. Figure 4.6 displays the results of the seeding density optimization experiment. 500 000 cells per well generates an OCR of over 100 pmol.min^{-1} and an ECAR of over 30 mpH.min^{-1} and is the only seeding density to satisfy the above criteria. Thus, a seeding density of 500 000 cells per well was used for all subsequent Seahorse experiments. That higher seeding densities display lower OCRs and ECARs is thought to be due to an excess of cells in the well causing some cells to lift from the well bottom or not adhere properly. Using too many cells can result in multiple cell layers and will increase disturbance of the cells during mixing (van der Windt *et al*., 2016). This may have lowered the OCR and ECAR as cells need to be in an adherent monolayer for the Seahorse XF24 Analyzer to take proper measurements.

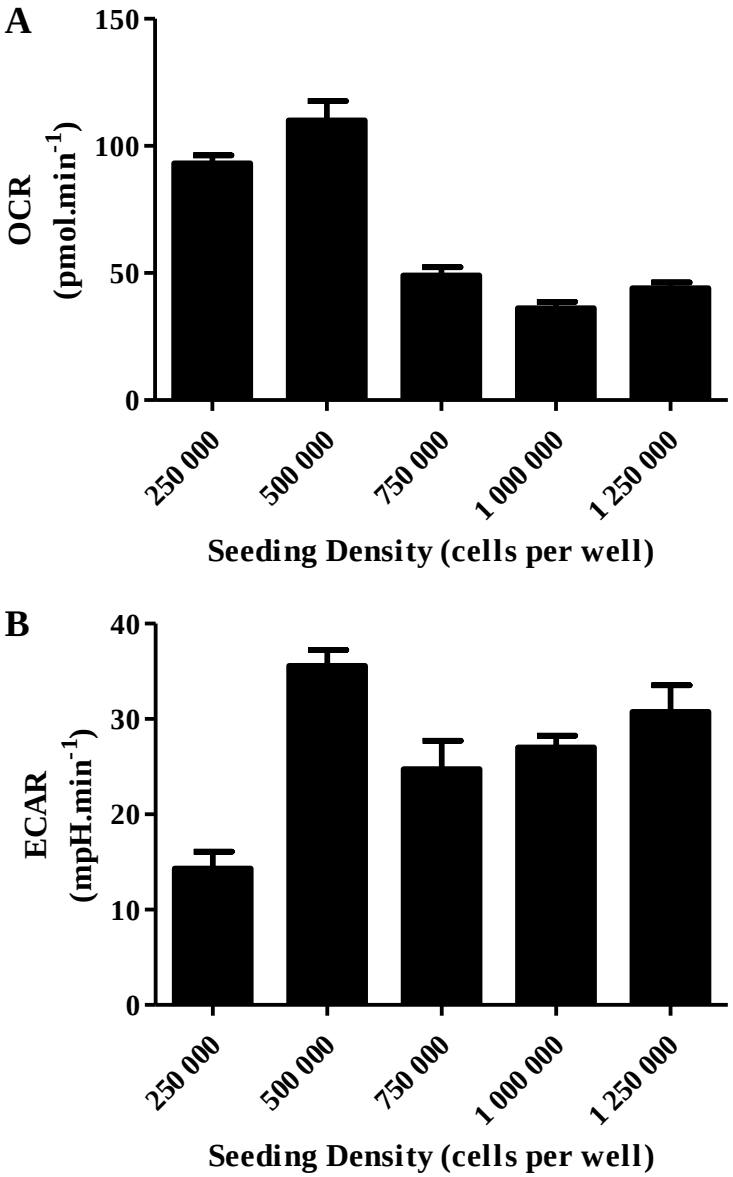

Figure 4.6: Seeding density optimization of *Ucp3*$^{+/+}$ T_H0 cells using the Seahorse XF24 Analyzer

T_H0 cells were generated by incubating naive T cells in the presence of 1 and 2 µg.mL^{-1} of anti-CD3 and anti-CD28, respectively, for 24 h before being seeded at the indicated densities in a Seahorse cell microplate and analysed on the Seahorse XF24 Analyzer. Seeding density optimization was performed once in quadruplicate. (A) Basal OCR of T_H0 cells 24 h post-stimulation at the seeding densities indicated. (B) Basal ECAR of T_H0 cells 24 h post-stimulation at the seeding densities indicated.

4.2.2.2 Seahorse XF Cell Mito Stress Test Compound Concentration Optimization

To optimize the use of the Seahorse XF Cell Mito Stress Test compounds described previously, they were first titrated in separate pilot experiments to determine the optimal concentration of each for use with $CD4^+$ T cells. *Ucp3*$^{+/+}$ T_H0 cells were harvested from 96-well plates 24 h post-stimulation and seeded at 500 000 cells per well in a Seahorse cell microplate for each experiment. Six working concentrations of oligomycin were tested: 0, 0.25, 0.5, 1, 1.5 and 2 µM. For the oligomycin optimization assay, 3 basal rate measurements were taken followed by compound (oligomycin) injection from port A and 3 more rate measurements to determine the optimal concentration. Figure 4.7 displays the OCR of T_H0 cells treated with titrated oligomycin. 1 µM was chosen as the optimal working concentration as higher concentrations of oligomycin do not decrease the OCR any further.

Six working concentrations of FCCP were tested: 0, 0.25, 0.5, 1, 1.5 and 2 µM. The FCCP optimization assay was carried out as follows: 3 basal rate measurements were taken followed by compound injection from Port A (1 µM oligomycin, working concentration), 3 rate measurements, compound injection from Port B (titrated FCCP) and 3 more rate measurements. Figure 4.8A displays the results of the FCCP optimization experiment. Unexpectedly, the OCR of cells following FCCP injection did not reach that of the basal OCR. Some cells may require sodium pyruvate supplementation as its absence can underestimate the maximum respiratory capacity (Nicholls *et al*., 2010; Ruas *et al*., 2016). However, the addition of 1 mM sodium pyruvate to the experimental media did not improve the response to 1.5 µM FCCP (Figure 4.8B). Ruas *et al*. (2016) demonstrated with human glioma and prostate cancer cells that, in the presence of oligomycin and other ATP synthase inhibitors, the maximum respiratory capacity of certain cell types following FCCP or protonophore addition can be underestimated by up to 45 %. Following their recommendation, the FCCP optimization experiment was repeated without a preceding injection of oligomycin, using media instead (Figure 4.8C). Interestingly, FCCP addition resulted in the expected OCR response only in the absence of a preceding oligomycin injection. In this experiment, the OCR following FCCP injection successfully reaches and surpasses that of the basal rate. Thus, it was decided that during the Seahorse XF Cell Mito Stress Test, wells would be treated with either oligomycin or FCCP followed by an antimycin A and rotenone mix so that the full effect of FCCP would be observed. 1.5 µM was chosen as the optimal working concentration of FCCP.

Two working concentrations of rotenone were tested mixed with 1 µM antimycin A: 0.1 and 1 µM. The rotenone optimization assay was carried out as follows: 3 basal rate measurements were taken followed by compound injection from Port A (1 µM oligomycin, working concentration), 3 rate measurements, compound injection from Port B (1.5 µM FCCP, working concentration), 3 rate measurements, compound injection from Port C (antimycin A and titrated rotenone mix) and 3 more rate measurements. Figure 4.9 displays the OCR of T_H0 cells treated with oligomycin, FCCP and antimycin A mixed with titrated rotenone. 0.1 µM was chosen as the optimal working concentration as this concentration decreases the OCR to a level that is not further decreased following addition of 1 µM rotenone.

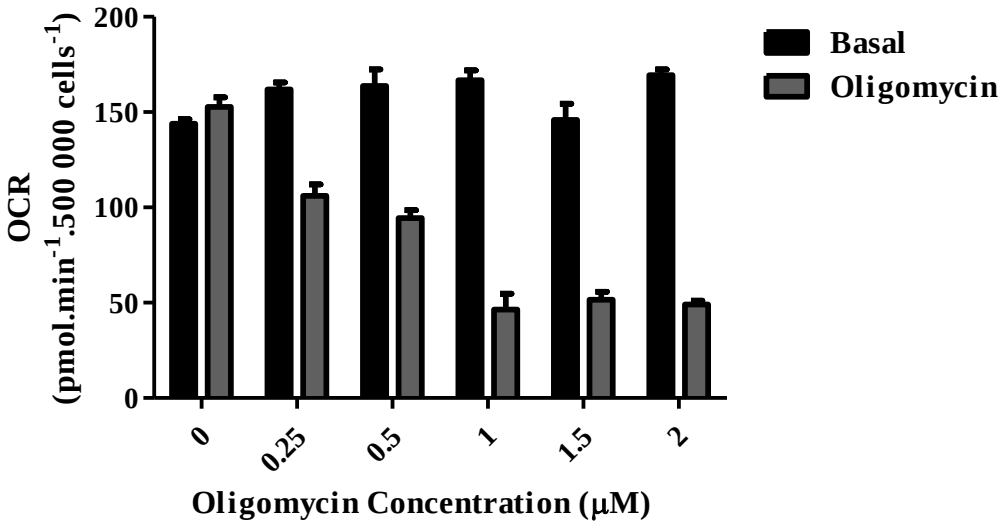

Figure 4.7: OCR of T_H0 cells 24 h post-stimulation during the oligomycin concentration optimization experiment

T_H0 cells were generated by incubating naive T cells in the presence of 1 and 2 µg.mL^{-1} of anti-CD3 and anti-CD28, respectively, for 24 h before being seeded at 500 000 cells per well in a Seahorse cell microplate and analysed on the Seahorse XF24 Analyzer. Basal measurements were taken 3 times followed by injection of the indicated concentration of oligomycin and 3 further rate measurements. Oligomycin concentration optimization was performed once in triplicate.

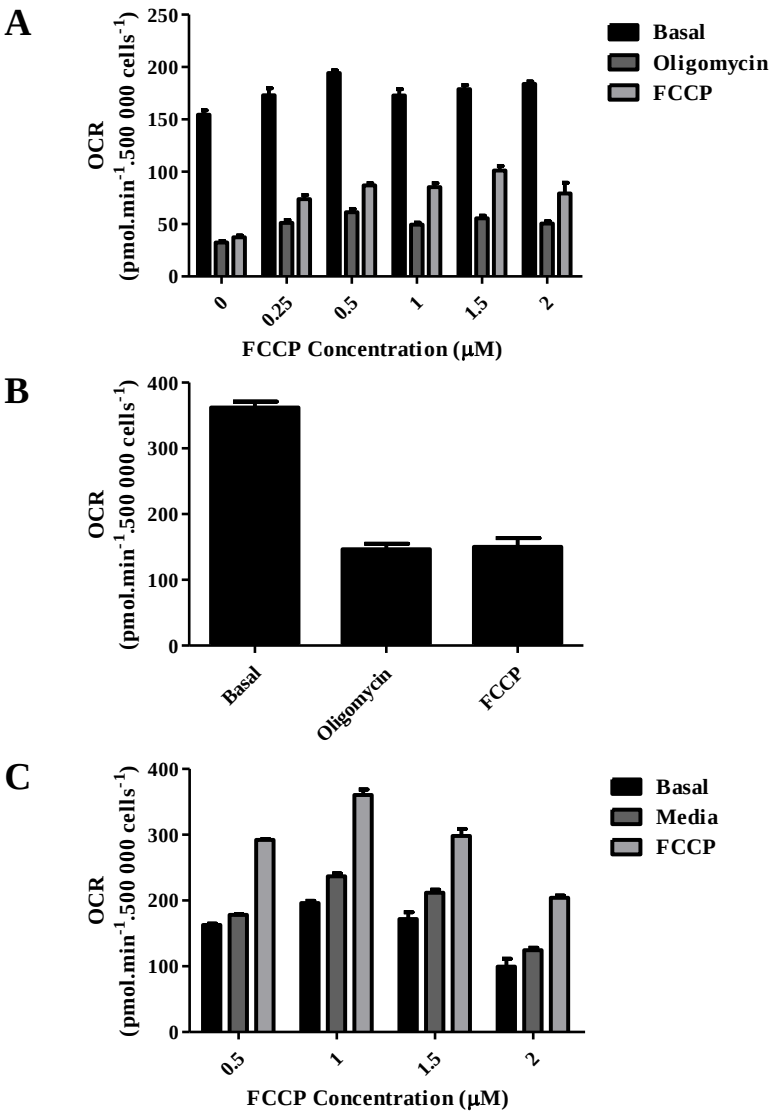

Figure 4.8: OCR of T_H0 cells 24 h post-stimulation during the FCCP concentration optimization experiment

T_H0 cells were generated by incubating naive T cells in the presence of 1 and 2 µg.mL^{-1} of anti-CD3 and anti-CD28, respectively, for 24 h before being seeded at 500 000 cells per well in a Seahorse cell microplate and analysed on the Seahorse XF24 Analyzer. Basal measurements were taken 3 times followed by injection of 1 µM oligomycin (A, B) or assay media (C), 3 further rate measurements, injection of the indicated concentration of FCCP and 3 final rate measurements. (B) FCCP concentration optimization in the presence of 1 mM sodium pyruvate and using 1.5 µM FCCP injection. FCCP concentration optimization was performed once in triplicate (A), quintuplicate (B) or single replicates (C).

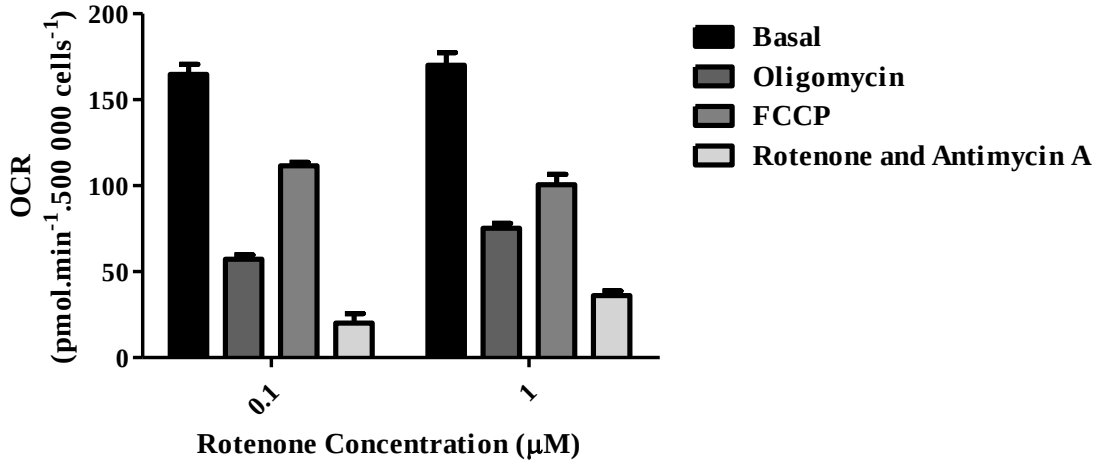

Figure 4.9: OCR of T_H0 cells 24 h post-stimulation during the rotenone concentration optimization experiment

T_H0 cells were generated by incubating naive T cells in the presence of 1 and 2 µg.mL^{-1} of anti-CD3 and anti-CD28, respectively, for 24 h before being seeded at 500 000 cells per well in a Seahorse cell microplate and analysed on the Seahorse XF24 Analyzer. Basal measurements were taken 3 times followed by injection of 1 µM oligomycin, 3 rate measurements, injection of 1.5 µM FCCP, 3 rate measurements, injection of 1 µM antimycin A mixed with 0.1 or 1 µM rotenone and 3 final rate measurements. Rotenone concentration optimization was performed once in duplicate.

4.2.3 Seahorse XF Cell Mito Stress Test Results

Having established the optimal seeding density and compound concentrations for *Ucp3*$^{+/+}$ T_H0 cells, the bioenergetic status of *Ucp3*$^{+/+}$ and *Ucp3*$^{-/-}$ CD4$^+$ T cells was explored using the Seahorse XF Cell Mito Stress Test. This allows one to dissect out O_2 consumption due to non-mitochondrial function and mitochondrial function in the form of the OCR linked to basal respiration, ATP production, proton leak and the maximal mitochondrial capacity.

4.2.3.1 UCP3 Does Not Play a Role in T_H0 Cell Metabolism

While our RT-PCR data suggest that UCP3 is not expressed or is significantly downregulated in activated T cells, the functional differences observed between *Ucp3*$^{+/+}$ and *Ucp3*$^{-/-}$ CD4$^+$ T_H0 cells (presented in Chapter 3) indicate that *Ucp3*$^{-/-}$ T_H0 cells undergo activation earlier and warranted investigation into the potential effect of *Ucp3* ablation on T_H0 cell metabolism. When naive CD4$^+$ T cells are activated, they move from a relatively quiescent state to a highly active state. Activated T cells require a demanding expenditure of energy as they undergo rapid clonal expansion, differentiation and initiate migratory functions, all of which involve the transcription of certain genes and a change in the expression of cytokines (Pearce and Pearce, 2013). This results in a metabolic switch from utilising OxPhos as the predominant metabolic profile to relying on glycolysis as the primary pathway of energy generation and displaying a Warburg-like metabolism (Chang *et al.*, 2013; Pearce and Pearce, 2013). This metabolic switch may occur sooner in *Ucp3*$^{-/-}$ T_H0 cells in line with their earlier activation, which would imply a potential role for UCP3 in T cell metabolism as well as function. Thus, the Seahorse XF Cell Mito Stress Test was performed to explore the metabolism of *Ucp3*$^{+/+}$ compared to *Ucp3*$^{-/-}$ T_H0 cells and to investigate whether a skewed metabolism is the cause of the altered *Ucp3*$^{-/-}$ T cell function. Primary *Ucp3*$^{+/+}$ and *Ucp3*$^{-/-}$ T cells were harvested direct from spleens and incubated for the desired time in the presence of anti-CD3 and anti-CD28 to generate T_H0 cells. The Seahorse XF Cell Mito Stress Test was carried out at different time points post-stimulation to ensure that any possible transient differences between the metabolic switch of *Ucp3*$^{+/+}$ and *Ucp3*$^{-/-}$ T_H0 cells following activation would be detected.

Figure 4.10 displays the OCR of *Ucp3*$^{+/+}$ and *Ucp3*$^{-/-}$ T_H0 cells 8, 24, 48 and 72 h post-stimulation. While a small significant difference is observed between the OCR of *Ucp3*$^{+/+}$ and *Ucp3*$^{-/-}$ T_H0 cells during the first rate measurement after FCCP addition 8 and 24 h post-stimulation (Figure 4.10A and B, respectively), this is not reflected by significance in the overall mean OCR after FCCP addition (Figure 4.10E and F, respectively). An increase

in the OCR is observed over time from 8 to 48 h in both strains. This is not unexpected as, although there is a known switch to a greater level of glycolysis in proliferating T cells, there can also be an increase in the overall global rate of OxPhos (Chang *et al*., 2013; Loftus and Finlay, 2016). No other significant differences in the OCR between genotypes are detected. Similar to the OCR, a small significant difference is observed in the ECAR of *Ucp3*$^{+/+}$ and *Ucp3*$^{-/-}$ T_H0 cells during the first basal rate measurement and the measurements following rotenone and antimycin A mix addition 8 h post-stimulation (Figure 4.11A). However, this is not reflected by significance in the overall mean basal ECAR and mean ECAR after rotenone and antimycin A addition (Figure 4.11E). An increase in the ECAR is observed over time from 8 to 48 h in *Ucp3*$^{+/+}$ and *Ucp3*$^{-/-}$ T_H0 cells, reflecting the increase in glycolytic activity of activated T cells as they undergo their metabolic switch; however, no other significant differences between genotypes are detected. The basal ECAR of T_H0 cells 24 h post-stimulation (Figure 4.11B and F) is similar to that reported by Sena *et al*. (2013).

Lower OCR/ECAR ratios than those calculated for naive $CD4^+$ T cells (see Figure 4.18) are observed in both strains 8, 24, 48 and 72 h post-stimulation (Figure 4.12). This is expected as $CD4^+$ T cells are known to increase their use of glycolysis following activation and to display a 'Warburg-like' metabolism. *Ucp3*$^{-/-}$ T_H0 cells have a significantly lower OCR/ECAR ratio than that of their WT counterparts 24 h post-activation (Figure 4.12B). This significant difference in the OCR/ECAR ratio indicates that the *Ucp3*$^{-/-}$ T_H0 cells are proportionally using more aerobic glycolysis than OxPhos for their energy needs; thus, they are more glycolytic at this time and this suggests that they become 'activated' earlier or faster than the *Ucp3*$^{+/+}$ cells. This is in line with the significant increases in IL-2 production and early activation marker expression observed in these cells within 24 h of stimulation, discussed in Chapter 3 (Figures 3.15 – 3.20). No significant differences in the OCR/ECAR ratio are detected between genotypes at other time points. Figure 4.13A – D displays the mitochondrial OCR, proton leak and maximal respiration of *Ucp3*$^{+/+}$ and *Ucp3*$^{-/-}$ T_H0 cells 8, 24, 48 and 72 h post-stimulation, respectively. No significant differences are found between genotypes. The fact that no difference in proton leak is observed would argue against an uncoupling role for UCP3.

No significant differences in the ATP-linked OCR are detected between *Ucp3*$^{+/+}$ and *Ucp3*$^{-/-}$ T_H0 cells 8, 24 and 48 h post-stimulation (Figure 4.14A – C, respectively), but *Ucp3*$^{-/-}$ T_H0 cells have a significantly lower ATP-linked OCR than *Ucp3*$^{+/+}$ T_H0 cells 72 h post-

stimulation (Figure 4.14D). This result is counterintuitive to UCP3 displaying an uncoupling role as its ablation would be expected to cause an increase in efficient ATP synthesis rather than a decrease. In line with this, the coupling efficiency (Figure 4.14H) and OCR (Figure 4.10D and H) of *Ucp3*$^{-/-}$ T_H0 cells are not significantly higher than *Ucp3*$^{+/+}$ T_H0 cells at that time, supporting a function other than uncoupling for UCP3. Despite no difference in the ATP-linked OCR (Figure 4.14A), *Ucp3*$^{-/-}$ T_H0 cells have a significantly lower coupling efficiency than *Ucp3*$^{+/+}$ T_H0 cells 8 h post-stimulation (Figure 4.14E). As the ablation of *Ucp3* does not result in an *increase* in coupling efficiency, this result is again unsupportive of an uncoupling role for UCP3 in $CD4^+$ T_H0 cells. No difference in coupling efficiency between *Ucp3*$^{+/+}$ and *Ucp3*$^{-/-}$ T_H0 cells is evident at later time points (Figure 4.14F – H). The spare respiratory capacities of *Ucp3*$^{+/+}$ and *Ucp3*$^{-/-}$ T_H0 cells 8, 24, 48 and 72 h post-stimulation (Figure 4.15) are not significantly different. Altogether, these data indicate that while *Ucp3* ablation distinctly impacts T_H0 cell function, as shown in Chapter 3, it does not affect T_H0 cell metabolism.

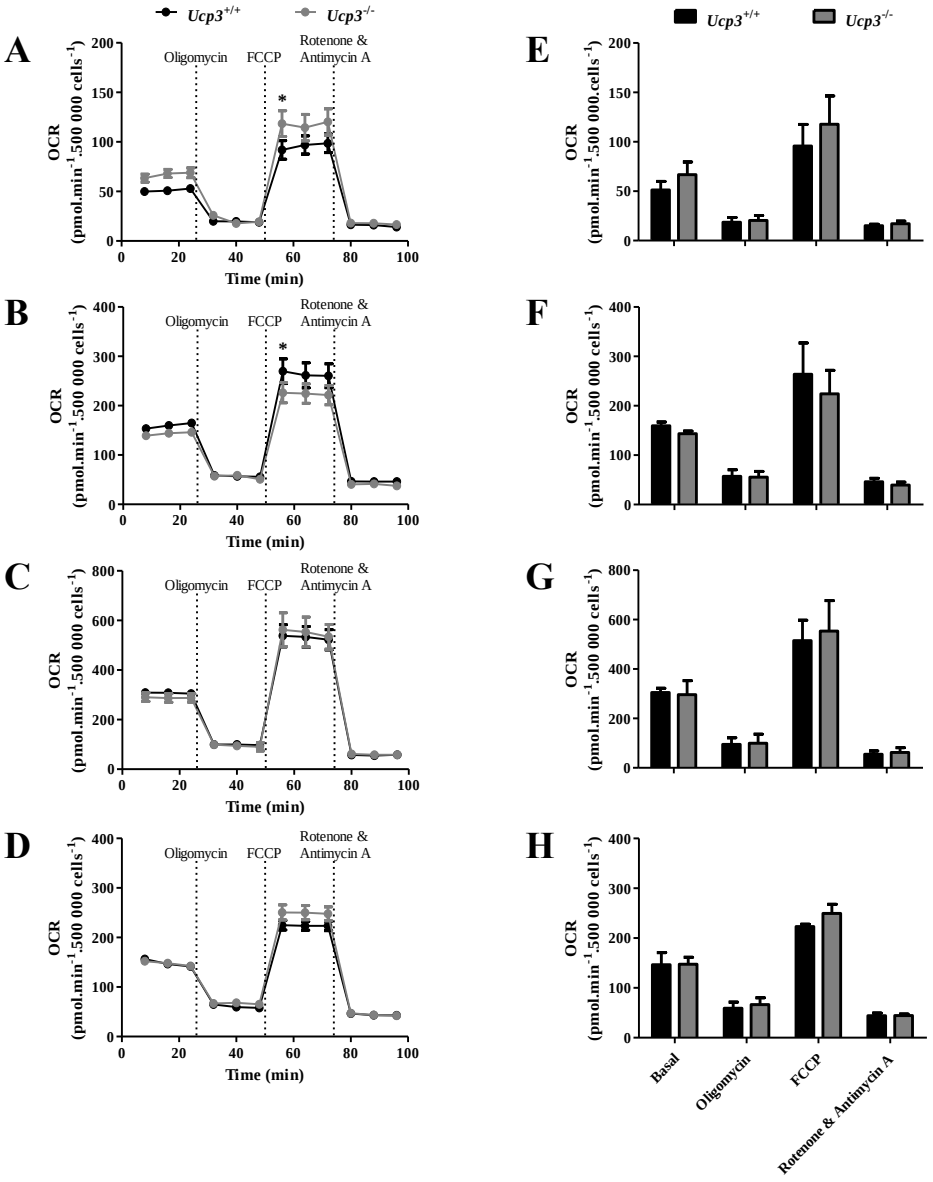

Figure 4.10: OCR of *Ucp3*$^{+/+}$ and *Ucp3*$^{-/-}$ T_H0 cells is comparable

T_H0 cells were generated by incubating naive T cells in the presence of 1 and 2 µg.mL^{-1} of anti-CD3 and anti-CD28, respectively, for 8 (A, E), 24 (B, F), 48 (C, G) or 72 (D, H) h before being seeded at 500 000 cells per well in a Seahorse cell microplate and analysed on the Seahorse XF24 Analyzer. Basal measurements were taken 3 times followed by injection of 1 µM oligomycin, 3 rate measurements, injection of 1.5 µM FCCP, 3 rate measurements, injection of 1 µM antimycin A mixed with 0.1 µM rotenone and 3 final rate measurements. Seahorse experiments were performed three times in quintuplicate. Data were analysed using a two-way ANOVA with a *post hoc* Bonferroni test to quantify significance where detected. * = $p < 0.05$. (A – D) Time graph of OCR of T_H0 cells during the Seahorse XF Cell Mito Stress Test. (E – F) Mean basal OCR and mean OCR following each compound injection.

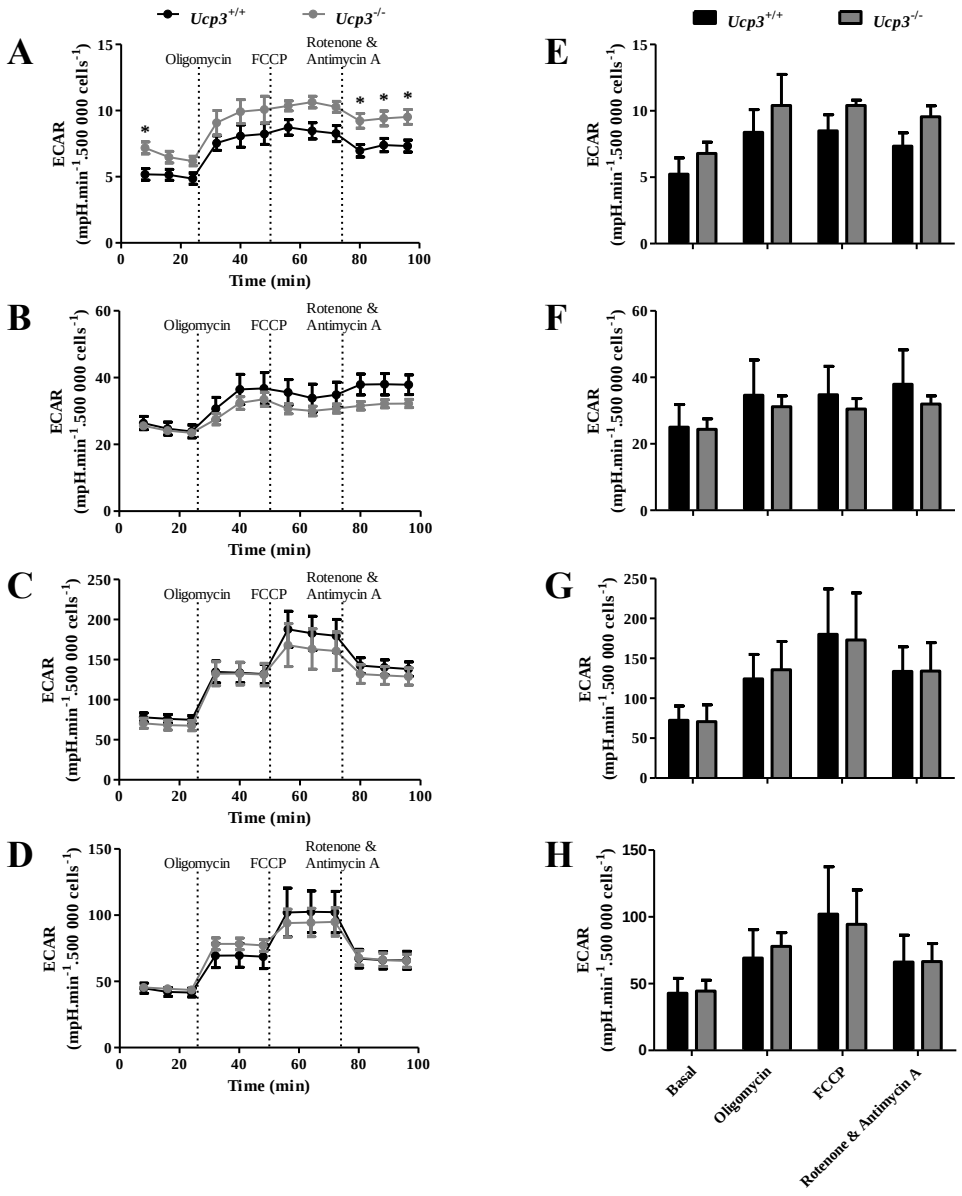

Figure 4.11: ECAR of *Ucp3*$^{+/+}$ and *Ucp3*$^{-/-}$ T_H0 cells is comparable

T_H0 cells were generated by incubating naive T cells in the presence of 1 and 2 µg.mL^{-1} of anti-CD3 and anti-CD28, respectively, for 8 (A, E), 24 (B, F), 48 (C, G) or 72 (D, H) h before being seeded at 500 000 cells per well in a Seahorse cell microplate and analysed on the Seahorse XF24 Analyzer. Basal measurements were taken 3 times followed by injection of 1 µM oligomycin, 3 rate measurements, injection of 1.5 µM FCCP, 3 rate measurements, injection of 1 µM antimycin A mixed with 0.1 µM rotenone and 3 final rate measurements. Seahorse experiments were performed three times in quintuplicate. Data were analysed using a two-way ANOVA with a *post hoc* Bonferroni test to quantify significance where detected. * = $p < 0.05$. (A – D) Time graph of ECAR of *Ucp3*$^{+/+}$ and *Ucp3*$^{-/-}$ T_H0 cells during the Seahorse XF Cell Mito Stress Test. (E – F) Mean basal ECAR and mean ECAR following each compound injection.

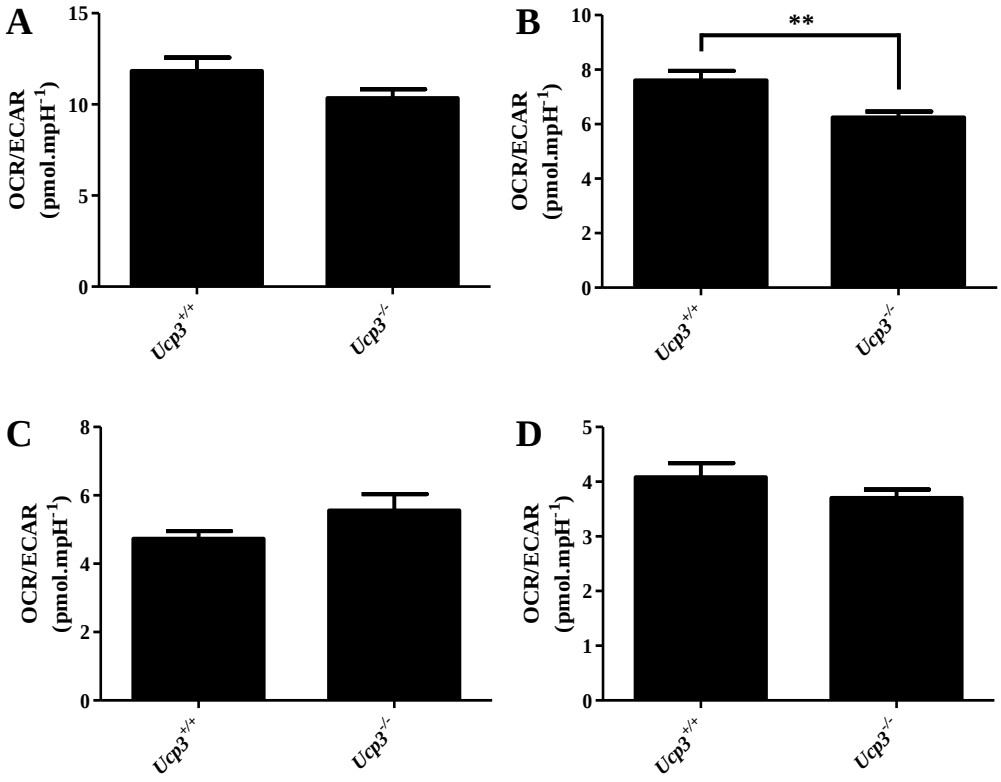

Figure 4.12: Basal OCR/ECAR ratio of *Ucp3*$^{+/+}$ and *Ucp3*$^{-/-}$ T_H0 cells is comparable

T_H0 cells were generated by incubating naive T cells in the presence of 1 and 2 µg.mL^{-1} of anti-CD3 and anti-CD28, respectively, for 8 (A), 24 (B), 48 (C) or 72 (D) h before being seeded at 500 000 cells per well in a Seahorse cell microplate and analysed on the Seahorse XF24 Analyzer. The OCR/ECAR ratio was calculated as in the text. Seahorse experiments were performed three times in quintuplicate. Data were analysed using a two-tailed, unpaired *t* test to quantify significance where detected. ** = $p < 0.01$.

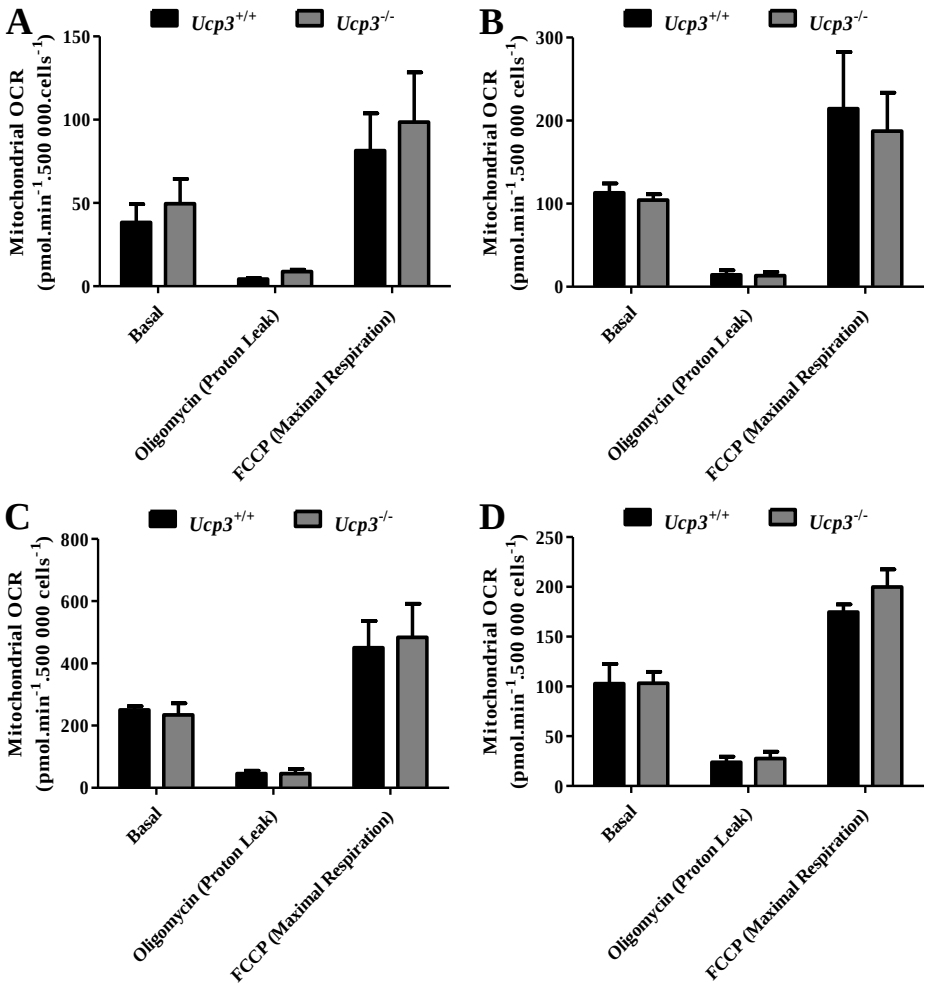

Figure 4.13: Basal mitochondrial OCR and mitochondrial OCR attributable to proton leak and maximal respiration of *Ucp3*$^{+/+}$ and *Ucp3*$^{-/-}$ T_H0 cells are comparable

T_H0 cells were generated by incubating naive T cells in the presence of 1 and 2 µg.mL^{-1} of anti-CD3 and anti-CD28, respectively, for 8 (A), 24 (B), 48 (C) or 72 (D) h before being seeded at 500 000 cells per well in a Seahorse cell microplate and analysed on the Seahorse XF24 Analyzer. Basal measurements were taken 3 times followed by injection of 1 µM oligomycin, 3 rate measurements, injection of 1.5 µM FCCP, 3 rate measurements, injection of 1 µM antimycin A mixed with 0.1 µM rotenone and 3 final rate measurements. Mitochondrial OCRs were calculated as in the text. Seahorse experiments were performed three times in quintuplicate. Data were analysed using a two-way ANOVA with a *post hoc* Bonferroni test to quantify significance where detected.

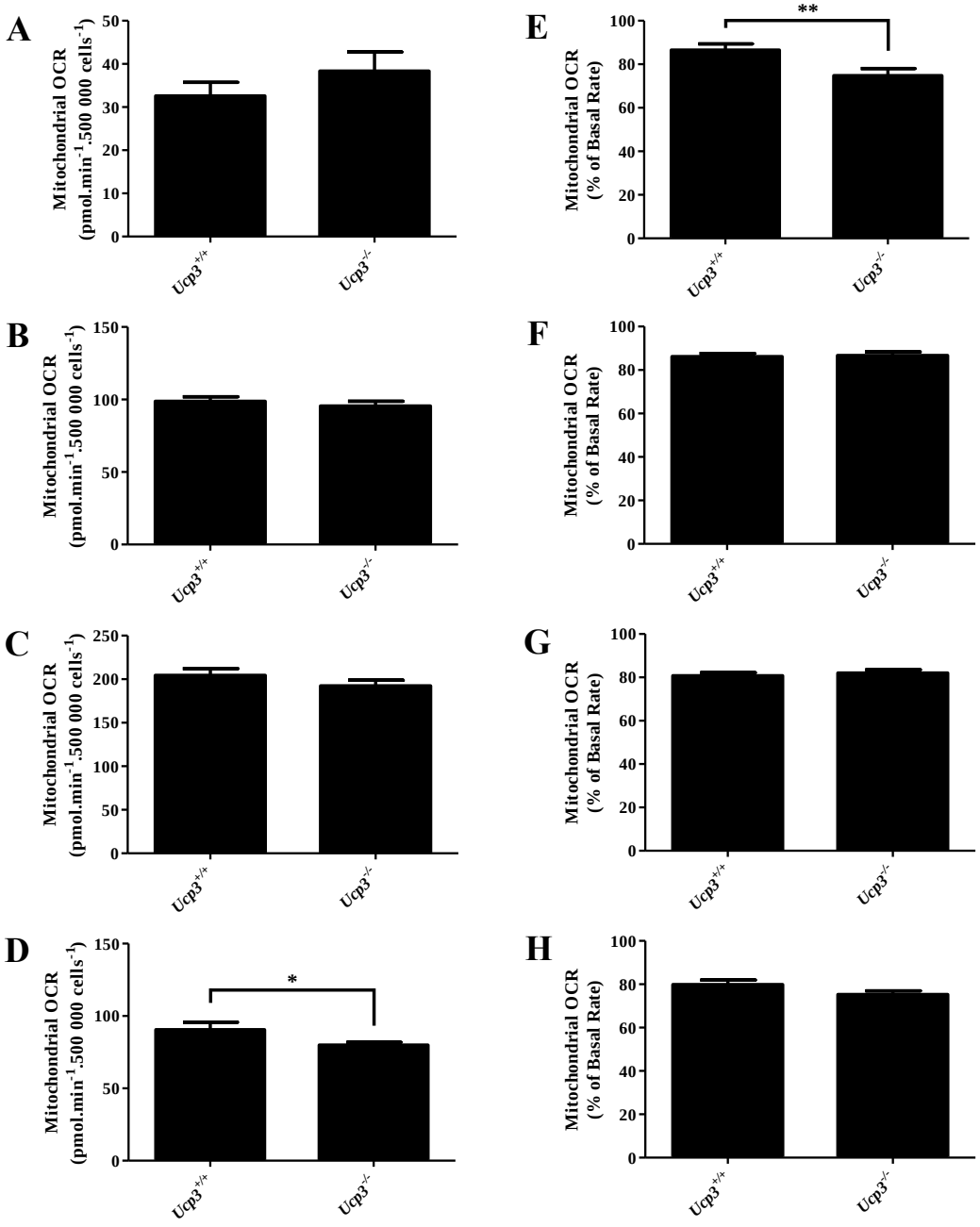

Figure 4.14: Mitochondrial OCR linked to ATP production and coupling efficiency of *Ucp3*$^{+/+}$ and *Ucp3*$^{-/-}$ T_H0 cells are comparable

T_H0 cells were generated by incubating naive T cells in the presence of 1 and 2 µg.mL^{-1} of anti-CD3 and anti-CD28, respectively, for 8 (A, E), 24 (B, F), 48 (C, G) or 72 (D, H) h before being seeded at 500 000 cells per well in a Seahorse cell microplate and analysed on the Seahorse XF24 Analyzer. The ATP-linked mitochondrial OCR (A – D) and coupling efficiency (E – H) were calculated as in the text. Seahorse experiments were performed three times in quintuplicate. Data were analysed using a two-tailed, unpaired *t* test to quantify significance where detected. * = $p < 0.05$.

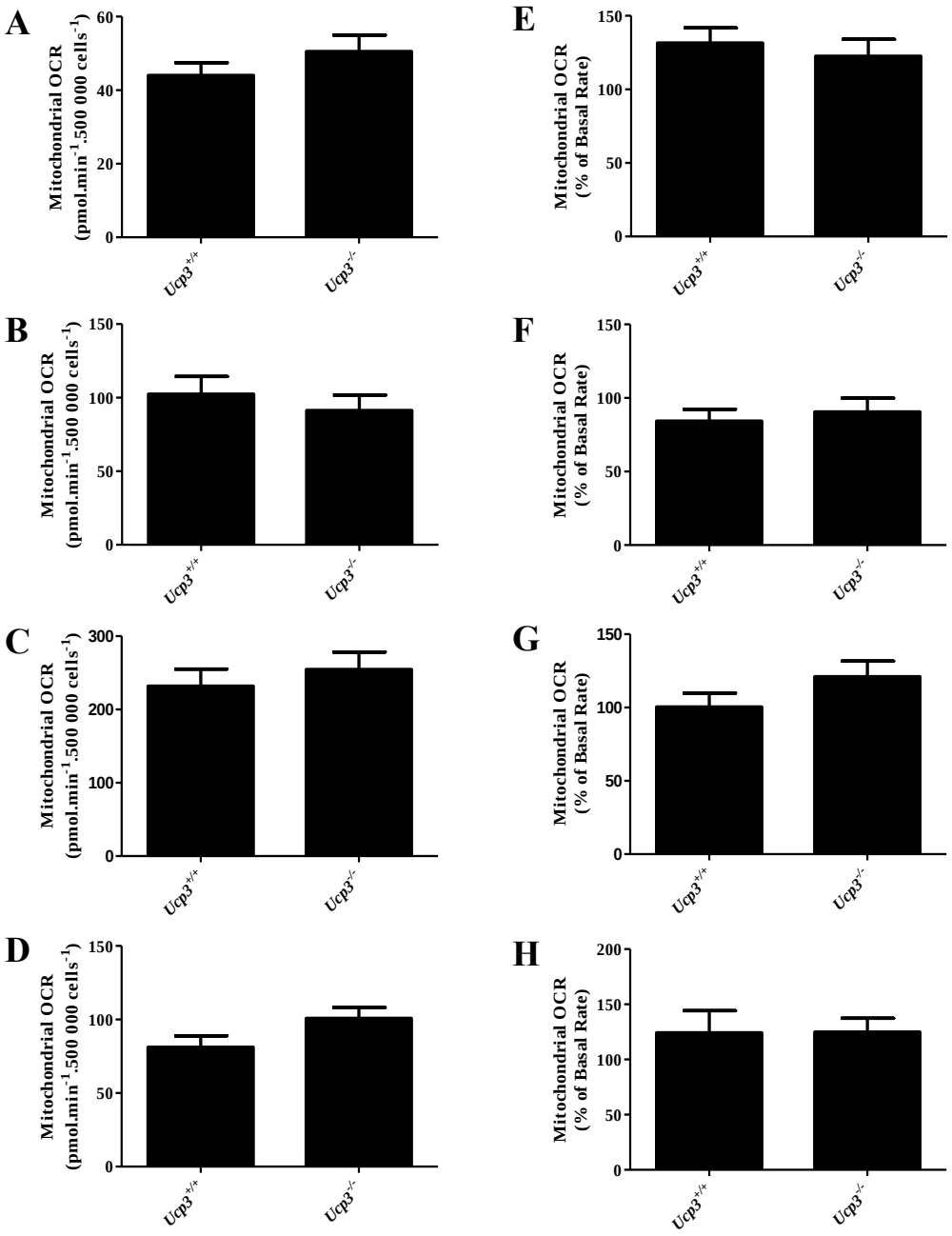

Figure 4.15: Spare respiratory capacity of *Ucp3*$^{+/+}$ and *Ucp3*$^{-/-}$ T_H0 cells is comparable

T_H0 cells were generated by incubating naive T cells in the presence of 1 and 2 µg.mL^{-1} of anti-CD3 and anti-CD28, respectively, for 8 (A, E), 24 (B, F), 48 (C, G) or 72 (D, H) h before being seeded at 500 000 cells per well in a Seahorse cell microplate and analysed on the Seahorse XF24 Analyzer. The spare respiratory capacity-associated mitochondrial OCR (A – D) and spare respiratory capacity as a percentage of basal mitochondrial OCR (E – H) were calculated as in the text. Seahorse experiments were performed three times in quintuplicate. Data were analysed using a two-tailed, unpaired *t* test to quantify significance where detected.

4.2.3.2 UCP3 Does Not Play a Role in Naive CD4$^+$ T Cell Metabolism

We have shown in Chapter 3 that *Ucp3* ablation does not impact naive T cell viability, surface marker expression or cytokine production but impressively alters activated T cell function, indicative of a role in hindering T cell activation. However, our RT-PCR data suggest that UCP3 is expressed in naive CD4$^+$ T cells but is not expressed or is at least downregulated in activated T cells. Additionally, if UCP3 indeed acts as an uncoupling protein, its knockdown would presumably alter metabolism. Thus, it was hypothesized that the ablation of this gene may have an effect on the overall metabolism of naive T cells more so than activated T cells. To further this investigation, we explored the metabolism of *Ucp3*$^{+/+}$ and *Ucp3*$^{-/-}$ naive T cells. Primary CD4$^+$ T cells were harvested direct from spleens and the Seahorse XF Cell Mito Stress Test was performed to explore the metabolism of *Ucp3*$^{+/+}$ compared to *Ucp3*$^{-/-}$ naive T cells immediately following isolation.

No significant differences in the OCR (Figure 4.16) or ECAR (Figure 4.17) are detected between *Ucp3*$^{+/+}$ and *Ucp3*$^{-/-}$ naive T cells. A high OCR/ECAR ratio is calculated for both *Ucp3*$^{+/+}$ and *Ucp3*$^{-/-}$ cells (Figure 4.18). While this is expected as naive T cells are known to rely predominantly on OxPhos as their primary metabolic pathway, the ratios are not significantly different. The basal OCR, basal ECAR and OCR/ECAR ratio calculated for naive CD4$^+$ T cells in this work are comparable to those reported by Chang *et al*. (2013). The basal ECAR is also similar to that reported by Sena *et al*. (2013). Figure 4.19 displays the mitochondrial OCR, proton leak and maximal mitochondrial respiration of *Ucp3*$^{+/+}$ and *Ucp3*$^{-/-}$ naive T cells. No significant differences are found between genotypes. Similar to that of T_H0 cells (Figure 4.13), the fact that no difference in proton leak is observed would argue against an uncoupling role for UCP3. In contrast to the significantly lower ATP-linked OCR of *Ucp3*$^{-/-}$ T_H0 cells 72 h post-stimulation (Figure 4.14D), *Ucp3*$^{-/-}$ naive CD4$^+$ T cells display a significantly higher ATP-linked OCR (Figure 4.20A). This result is in line with UCP3 displaying an uncoupling role. If UCP3 is uncoupling the mitochondria of naive T cells, its ablation would be expected to result in a more 'coupled' state of the mitochondria and, consequently, more efficient ATP production. However, the coupling efficiency (Figure 4.20B), as well as the OCR (Figure 4.16), of the *Ucp3*$^{+/+}$ and *Ucp3*$^{-/-}$ naive T cells are not statistically different which would argue against UCP3 carrying out uncoupling activity. Figure 4.21 displays the spare respiratory capacity of *Ucp3*$^{+/+}$ and *Ucp3*$^{-/-}$ naive CD4$^+$ T cells which is not significantly different. From these data, we can deduce that, similar to naive T cell viability, surface marker expression and cytokine

production examined in Chapter 3, as well as T_H0 cell metabolism, naive T cell metabolism is unaffected by *Ucp3* ablation.

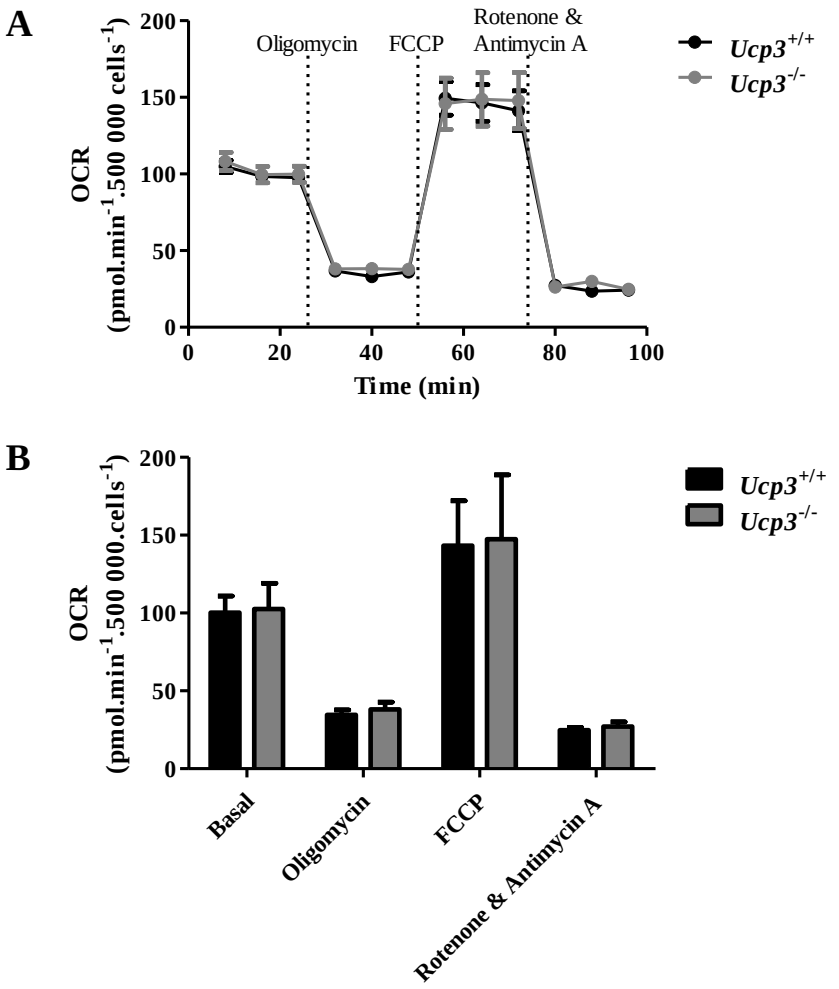

Figure 4.16: OCR of *Ucp3*$^{+/+}$ and *Ucp3*$^{-/-}$ naive CD4^{+} T cells is comparable

Primary CD4^{+} T cells were isolated from a suspension of splenocytes, seeded at 500 000 cells per well in a Seahorse cell microplate and analysed on the Seahorse XF24 Analyzer immediately. Basal measurements were taken 3 times followed by injection of 1 µM oligomycin, 3 rate measurements, injection of 1.5 µM FCCP, 3 rate measurements, injection of 1 µM antimycin A mixed with 0.1 µM rotenone and 3 final rate measurements. Seahorse experiments were performed three times in quintuplicate. Data were analysed using a two-way ANOVA with a *post hoc* Bonferroni test to quantify significance where detected. (A) Time graph of the OCR of *Ucp3*$^{+/+}$ and *Ucp3*$^{-/-}$ naive CD4^{+} T cells during the Seahorse XF Cell Mito Stress Test. (B) Mean basal OCR and mean OCR following each compound injection.

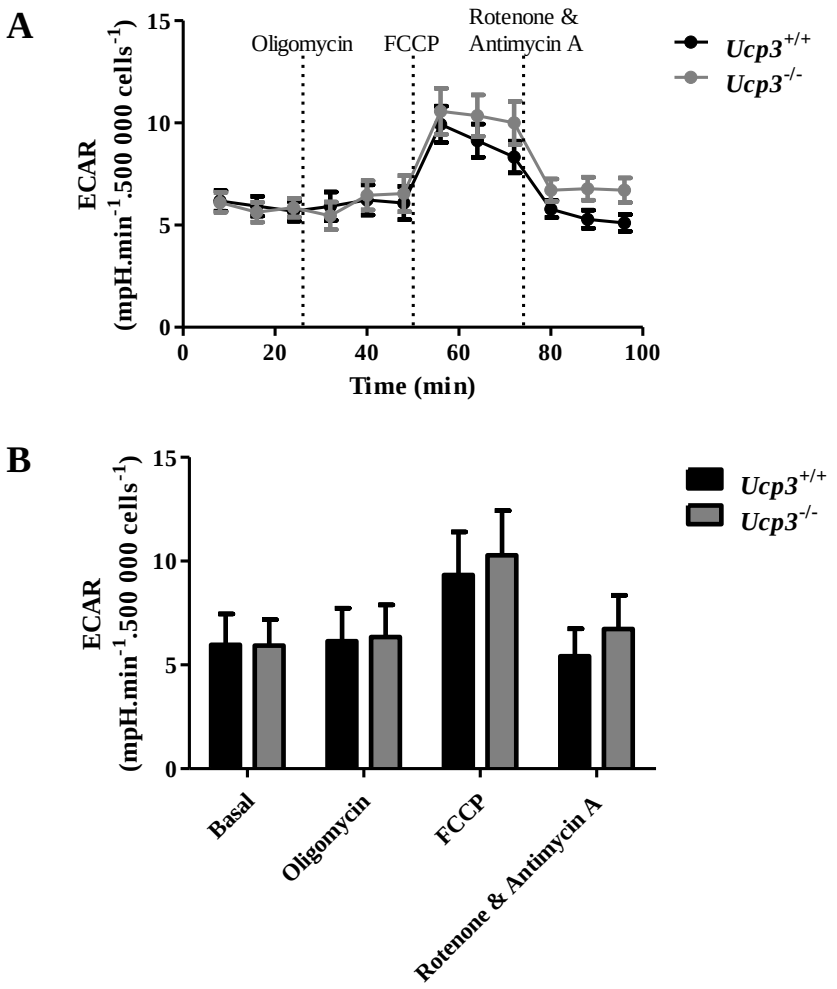

Figure 4.17: ECAR of *Ucp3*$^{+/+}$ and *Ucp3*$^{-/-}$ naive CD4^{+} T cells is comparable

Primary CD4^{+} T cells were isolated from a suspension of splenocytes, seeded at 500 000 cells per well in a Seahorse cell microplate and analysed on the Seahorse XF24 Analyzer immediately. Basal measurements were taken 3 times followed by injection of 1 µM oligomycin, 3 rate measurements, injection of 1.5 µM FCCP, 3 rate measurements, injection of 1 µM antimycin A mixed with 0.1 µM rotenone and 3 final rate measurements. Seahorse experiments were performed three times in quintuplicate. Data were analysed using a two-way ANOVA with a *post hoc* Bonferroni test to quantify significance where detected. (A) Time graph of the ECAR of *Ucp3*$^{+/+}$ and *Ucp3*$^{-/-}$ naive CD4^{+} T cells during the Seahorse XF Cell Mito Stress Test. (B) Mean basal ECAR and mean ECAR following each compound injection.

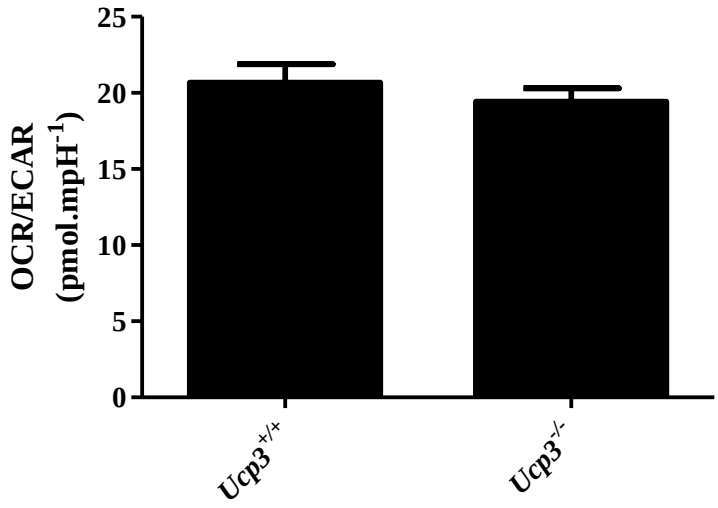

Figure 4.18: Basal OCR/ECAR ratio of *Ucp3*$^{+/+}$ and *Ucp3*$^{-/-}$ naive CD4^{+} T cells is comparable

Primary CD4^{+} T cells were isolated from a suspension of splenocytes, seeded at 500 000 cells per well in a Seahorse cell microplate and analysed on the Seahorse XF24 Analyzer immediately. The OCR/ECAR ratio was calculated as in the text. Seahorse experiments were performed three times in quintuplicate. Data were analysed using a two-tailed, unpaired *t* test to quantify significance where detected.

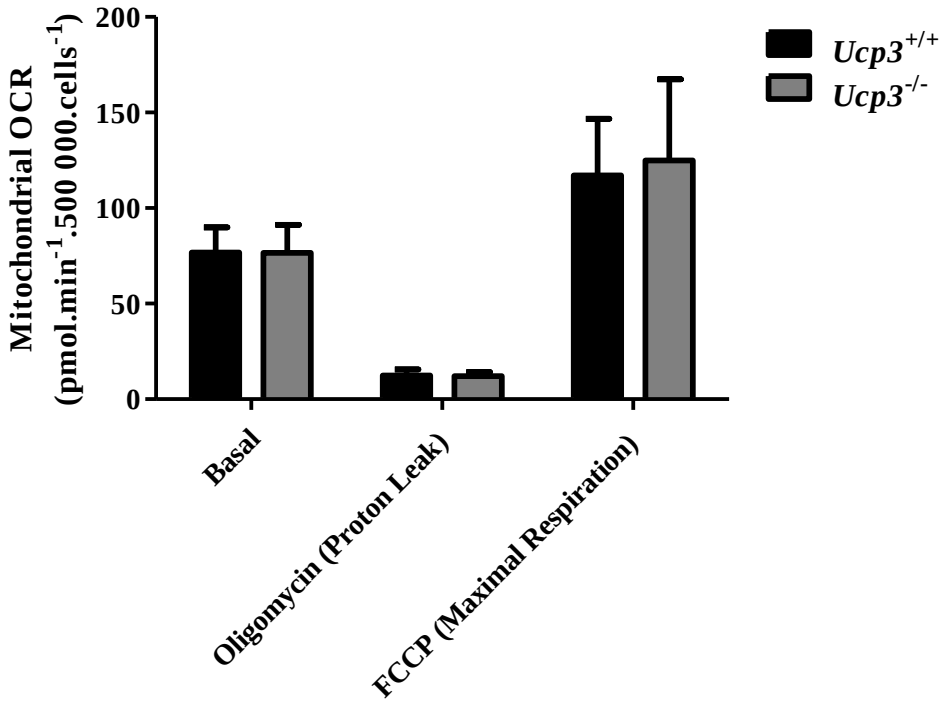

Figure 4.19: Basal mitochondrial OCR and mitochondrial OCR attributable to proton leak and maximal respiration of *Ucp3*$^{+/+}$ and *Ucp3*$^{-/-}$ naive CD4^{+} T cells are comparable

Primary CD4^{+} T cells were isolated from a suspension of splenocytes, seeded at 500 000 cells per well in a Seahorse cell microplate and analysed on the Seahorse XF24 Analyzer immediately. Basal measurements were taken 3 times followed by injection of 1 µM oligomycin, 3 rate measurements, injection of 1.5 µM FCCP, 3 rate measurements, injection of 1 µM antimycin A mixed with 0.1 µM rotenone and 3 final rate measurements. Mitochondrial OCRs were calculated as in the text. Seahorse experiments were performed three times in quintuplicate. Data were analysed using a two-way ANOVA with a *post hoc* Bonferroni test to quantify significance where detected.

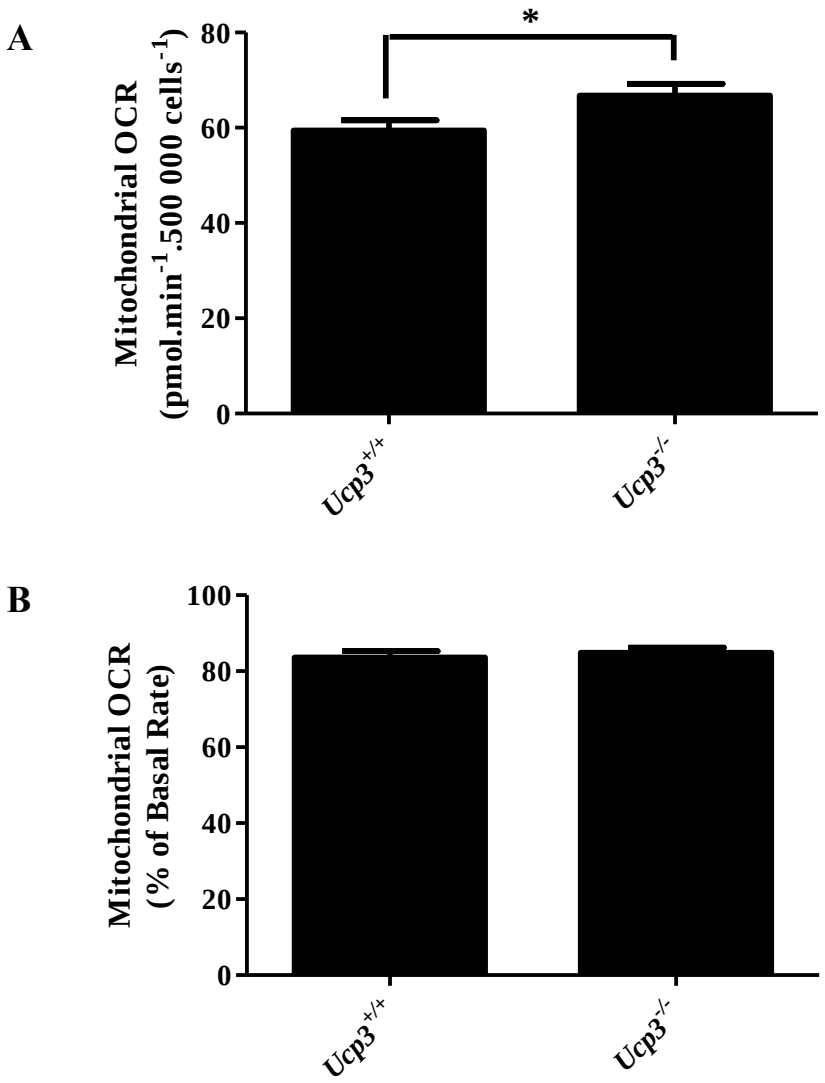

Figure 4.20: Mitochondrial OCR linked to ATP production and coupling efficiency of *Ucp3*$^{+/+}$ and *Ucp3*$^{-/-}$ naive CD4^{+} T cells

Primary CD4^{+} T cells were isolated from a suspension of splenocytes, seeded at 500 000 cells per well in a Seahorse cell microplate and analysed on the Seahorse XF24 Analyzer immediately. The ATP-linked mitochondrial OCR (A) and coupling efficiency (B) were calculated as in the text. Seahorse experiments were performed three times in quintuplicate. Data were analysed using a two-tailed, unpaired *t* test to quantify significance where detected. * = $p < 0.05$.

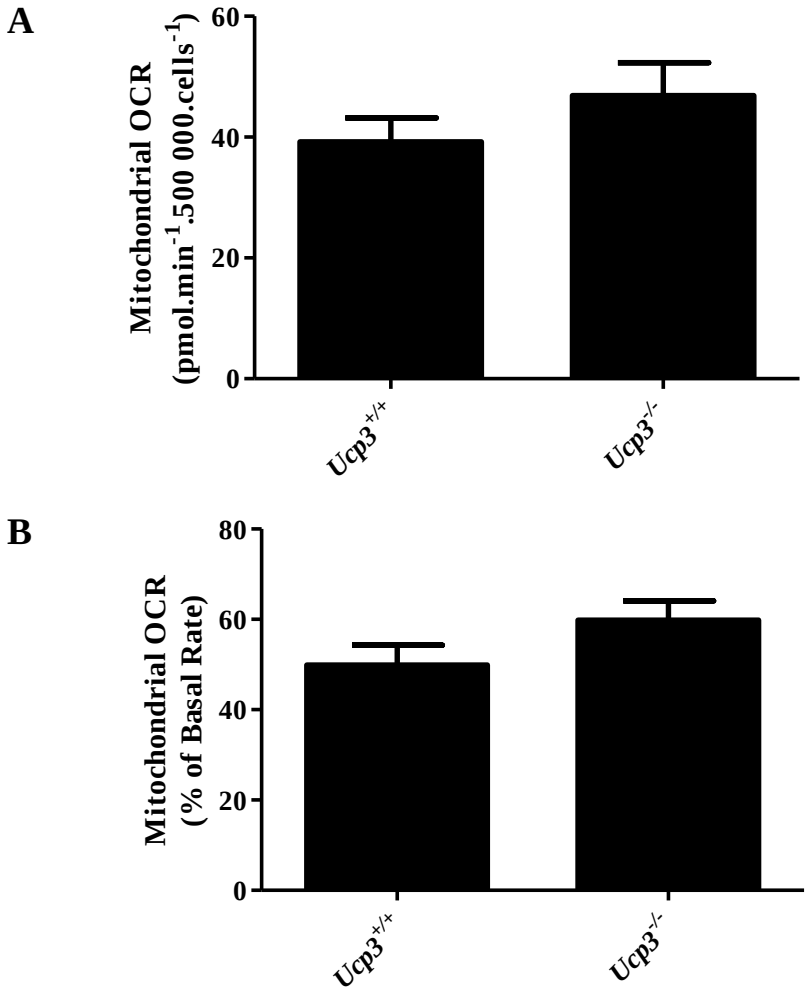

Figure 4.21: Spare respiratory capacity of *Ucp3*$^{+/+}$ and *Ucp3*$^{-/-}$ naive CD4^{+} T cells is comparable

Primary CD4^{+} T cells were isolated from a suspension of splenocytes, seeded at 500 000 cells per well in a Seahorse cell microplate and analysed on the Seahorse XF24 Analyzer immediately. The spare respiratory capacity-associated mitochondrial OCR (A) and spare respiratory capacity as a percentage of basal mitochondrial OCR (B) were calculated as in the text. Seahorse experiments were performed three times in quintuplicate. Data were analysed using a two-tailed, unpaired *t* test to quantify significance where detected.

4.2.3.3 UCP3 Does Not Play a Role in T_H17 Cell Metabolism

We have shown in Chapter 3 that, in addition to altering T_H0 cell function, *Ucp3* ablation impacts the viability and characteristic cytokine production of T_H17 cells. We hypothesize that this is a consequence of increased IL-2 production which can inhibit the generation of T_H17 cells. Although the metabolism of T_H0 cells is unaffected by *Ucp3* ablation despite their altered function, we decided to further our investigation into the effect of *Ucp3* ablation on T_H17 cells by conjointly exploring their metabolism. Primary *Ucp3*$^{+/+}$ and *Ucp3*$^{-/-}$ CD4$^+$ T cells were harvested direct from spleens and incubated for 72 h in the presence of anti-CD3, anti-CD28, anti-IL-4, anti-IFN-γ, rhTGF-β1 and rIL-6 to generate T_H17 cells before the Seahorse XF Cell Mito Stress Test was performed to explore their metabolism and to investigate whether a skewed metabolism is the cause of the altered T_H17 cell viability and function we observed.

No significant differences in the OCR (Figure 4.22) or ECAR (Figure 4.23) are detected between *Ucp3*$^{+/+}$ and *Ucp3*$^{-/-}$ T_H17 cells. Expectantly, a low OCR/ECAR ratio is calculated for both *Ucp3*$^{+/+}$ and *Ucp3*$^{-/-}$ T_H17 cells (Figure 4.24) similar to that calculated for T_H0 cells 72 h post-stimulation (Figure 4.12D), indicating the reliance of these cells on glycolysis as their main pathway of energy generation. Interestingly, the OCR/ECAR ratio of *Ucp3*$^{-/-}$ T_H17 cells is significantly higher than that of *Ucp3*$^{+/+}$ T_H17 cells, indicating that they are *less* glycolytic than their WT counterparts. This may be a reflection of the altered function and/or decreased viability of these cells, with a higher proportion of cells undergoing AICD/apoptosis potentially producing less lactic acid as a result of their glycolytic rate slowing down. However, as mentioned previously, no significant difference is observed in the ECAR of these cells compared to their WT counterparts (Figure 4.23). Figure 4.25 displays the mitochondrial OCR, proton leak and maximal mitochondrial respiration of *Ucp3*$^{+/+}$ and *Ucp3*$^{-/-}$ T_H17 cells 72 h post-stimulation. No significant differences are found between genotypes. Similar to that of T_H0 (Figure 4.13) and naive T cells (Figure 4.19), the fact that no difference in proton leak is observed would argue against an uncoupling role for UCP3.

Ucp3$^{-/-}$ T_H17 cells display a significantly higher coupling efficiency than that of *Ucp3*$^{+/+}$ T_H17 cells (Figure 4.26B). This result is in line with UCP3 displaying an uncoupling role. If UCP3 is uncoupling the mitochondria of T_H17 cells, its ablation would be expected to result in a more 'coupled' state of the mitochondria and, consequently, more efficient ATP production. However, the ATP-linked OCR (Figure 4.26A), as well as the OCR (Figure

4.22), of the *Ucp3*$^{+/+}$ and *Ucp3*$^{-/-}$ T_H17 cells are not statistically different which is unsupportive of UCP3 carrying out uncoupling activity. The spare respiratory capacity of *Ucp3*$^{+/+}$ and *Ucp3*$^{-/-}$ T_H17 cells is not significantly different (Figure 4.27A) unless calculated as a percentage of the basal mitochondrial OCR (Figure 4.27B). From these data, we can deduce that, despite its effect on T_H17 cell function, overall T_H17 cell metabolism is unperturbed by *Ucp3* ablation.

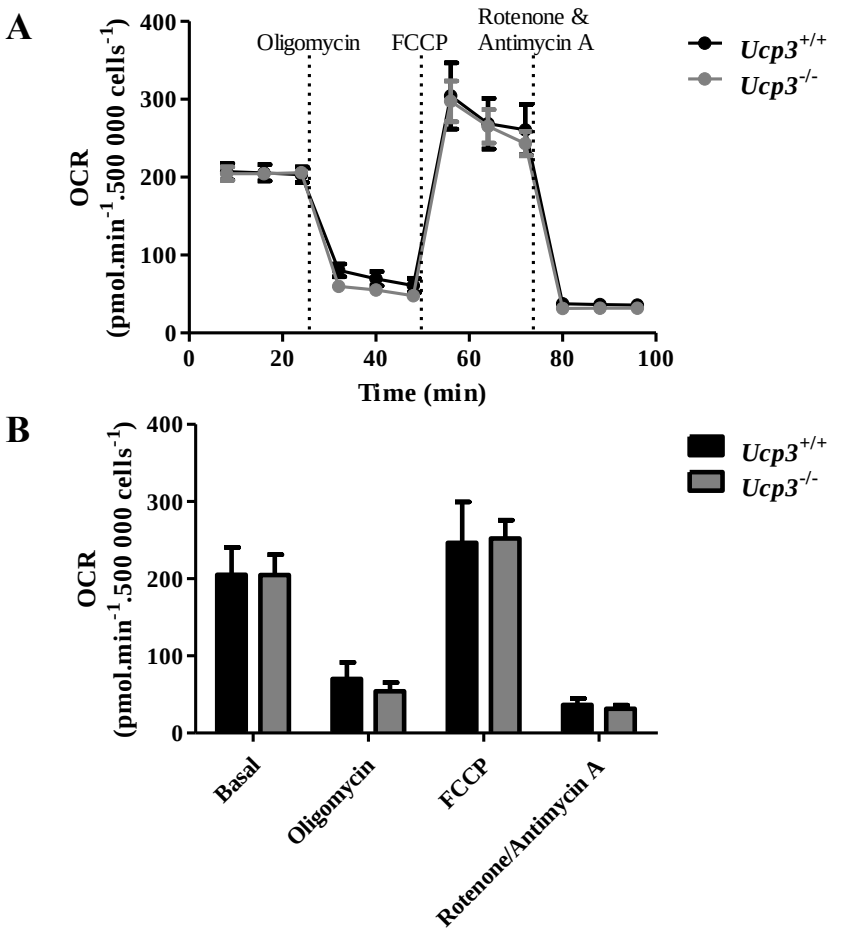

Figure 4.22: OCR of *Ucp3*$^{+/+}$ and *Ucp3*$^{-/-}$ T_H17 cells is comparable

T_H17 cells were generated by incubating naive T cells in the presence of 5 µg.mL^{-1} of anti-CD3 and anti-CD28, 20 ng.mL^{-1} of anti-IL-4 and rIL-6, 10 µg.mL^{-1} of anti-IFN-γ and 2.5 ng.mL^{-1} of rhTGF-β1 for 72 h before being seeded at 500 000 cells per well in a Seahorse cell microplate and analysed on the Seahorse XF24 Analyzer. Basal measurements were taken 3 times followed by injection of 1 µM oligomycin, 3 rate measurements, injection of 1.5 µM FCCP, 3 rate measurements, injection of 1 µM antimycin A mixed with 0.1 µM rotenone and 3 final rate measurements. Seahorse experiments were performed three times in quintuplicate. Data were analysed using a two-way ANOVA with a *post hoc* Bonferroni test to quantify significance where detected. (A) Time graph of the OCR of *Ucp3*$^{+/+}$ and *Ucp3*$^{-/-}$ T_H17 cells during the Seahorse XF Cell Mito Stress Test. (B) Mean basal OCR and mean OCR following each compound injection.

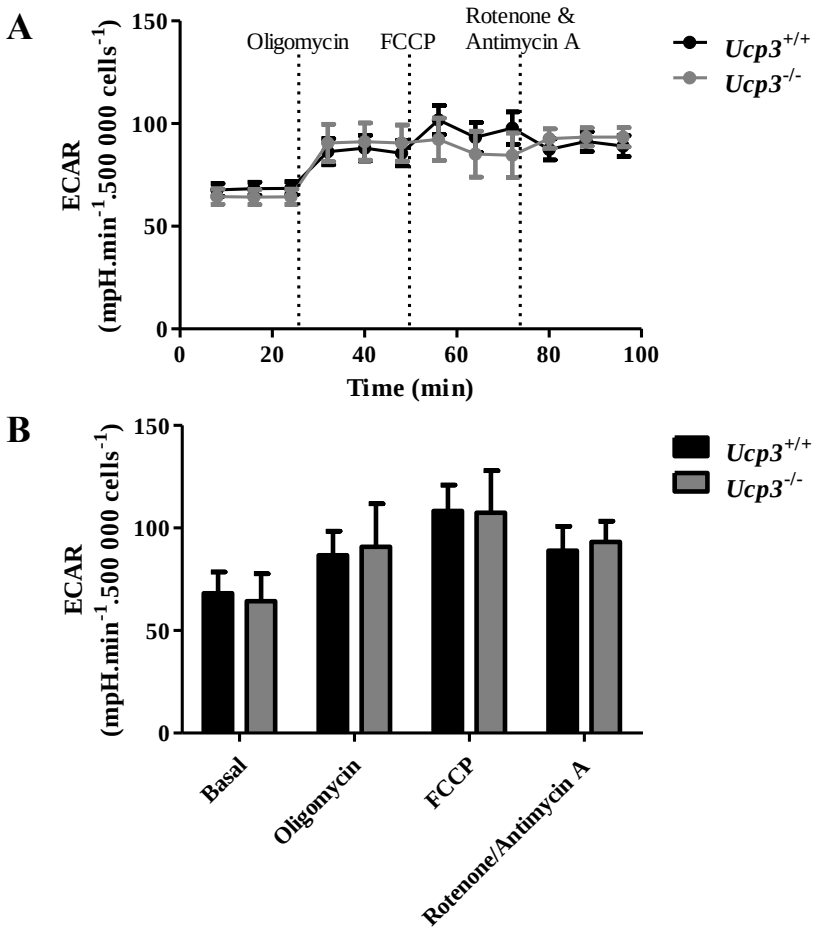

Figure 4.23: ECAR of *Ucp3*$^{+/+}$ and *Ucp3*$^{-/-}$ T_H17 cells is comparable

T_H17 cells were generated by incubating naive T cells in the presence of 5 µg.mL^{-1} of anti-CD3 and anti-CD28, 20 ng.mL^{-1} of anti-IL-4 and rIL-6, 10 µg.mL^{-1} of anti-IFN-γ and 2.5 ng.mL^{-1} of rhTGF-β1 for 72 h before being seeded at 500 000 cells per well in a Seahorse cell microplate and analysed on the Seahorse XF24 Analyzer. Basal measurements were taken 3 times followed by injection of 1 µM oligomycin, 3 rate measurements, injection of 1.5 µM FCCP, 3 rate measurements, injection of 1 µM antimycin A mixed with 0.1 µM rotenone and 3 final rate measurements. Seahorse experiments were performed three times in quintuplicate. Data were analysed using a two-way ANOVA with a *post hoc* Bonferroni test to quantify significance where detected. (A) Time graph of the ECAR of *Ucp3*$^{+/+}$ and *Ucp3*$^{-/-}$ T_H17 cells during the Seahorse XF Cell Mito Stress Test. (B) Mean basal ECAR and mean ECAR following each compound injection.

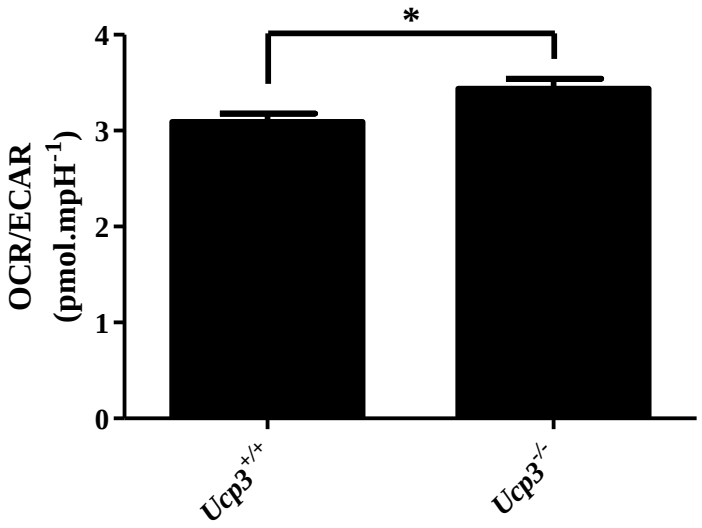

Figure 4.24: *Ucp3*$^{-/-}$ T_H17 cells display an increased basal OCR/ECAR ratio

T_H17 cells were generated by incubating naive T cells in the presence of 5 µg.mL^{-1} of anti-CD3 and anti-CD28, 20 ng.mL^{-1} of anti-IL-4 and rIL-6, 10 µg.mL^{-1} of anti-IFN-γ and 2.5 ng.mL^{-1} of rhTGF-β1 for 72 h before being seeded at 500 000 cells per well in a Seahorse cell microplate and analysed on the Seahorse XF24 Analyzer. The OCR/ECAR ratio was calculated as in the text. Seahorse experiments were performed three times in quintuplicate. Data were analysed using a two-tailed, unpaired *t* test to quantify significance where detected. * = $p < 0.05$.

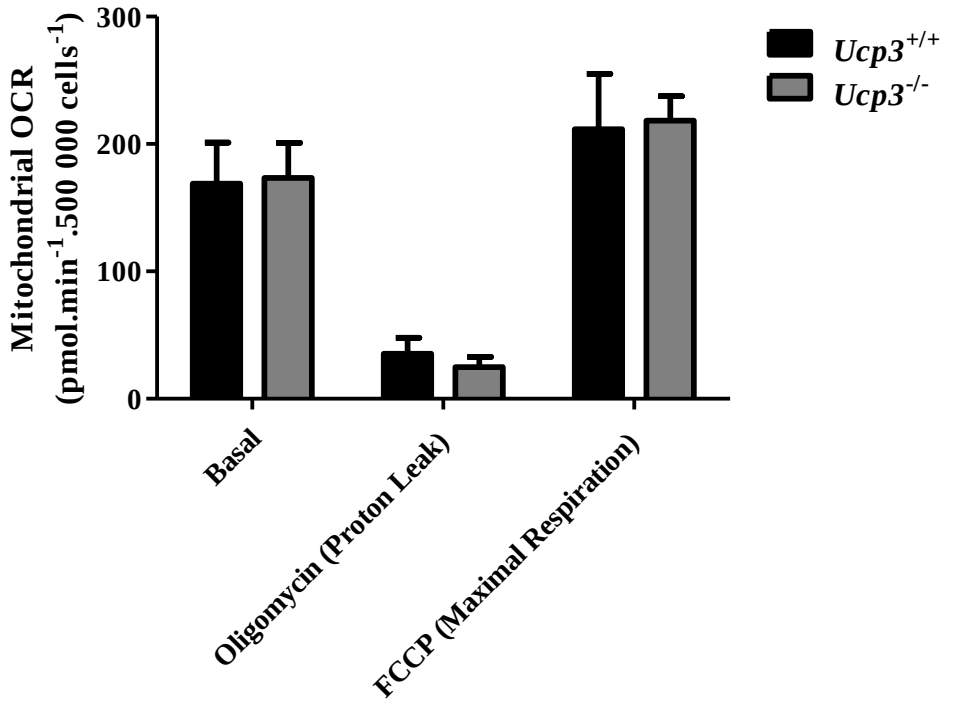

Figure 4.25: Basal mitochondrial OCR and mitochondrial OCR attributable to proton leak and maximal respiration of *Ucp3*$^{+/+}$ and *Ucp3*$^{-/-}$ T_H17 cells are comparable
T_H17 cells were generated by incubating naive T cells in the presence of 5 µg.mL^{-1} of anti-CD3 and anti-CD28, 20 ng.mL^{-1} of anti-IL-4 and rIL-6, 10 µg.mL^{-1} of anti-IFN-γ and 2.5 ng.mL^{-1} of rhTGF-β1 for 72 h before being seeded at 500 000 cells per well in a Seahorse cell microplate and analysed on the Seahorse XF24 Analyzer. Basal measurements were taken 3 times followed by injection of 1 µM oligomycin, 3 rate measurements, injection of 1.5 µM FCCP, 3 rate measurements, injection of 1 µM antimycin A mixed with 0.1 µM rotenone and 3 final rate measurements. Mitochondrial OCRs were calculated as in the text. Seahorse experiments were performed three times in quintuplicate. Data were analysed using a two-way ANOVA with a *post hoc* Bonferroni test to quantify significance where detected.

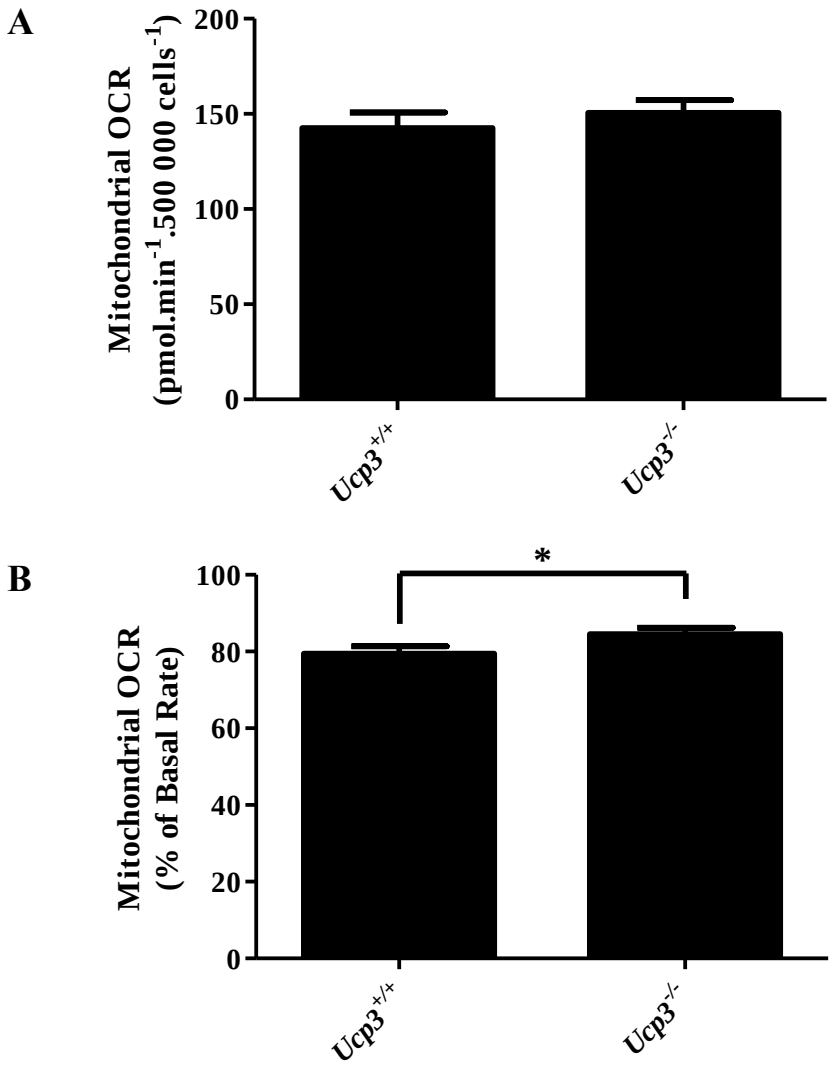

Figure 4.26: Mitochondrial OCR linked to ATP production and coupling efficiency of *Ucp3*$^{+/+}$ and *Ucp3*$^{-/-}$ T_H17 cells

T_H17 cells were generated by incubating naive T cells in the presence of 5 µg.mL^{-1} of anti-CD3 and anti-CD28, 20 ng.mL^{-1} of anti-IL-4 and rIL-6, 10 µg.mL^{-1} of anti-IFN-γ and 2.5 ng.mL^{-1} of rhTGF-β1 for 72 h before being seeded at 500 000 cells per well in a Seahorse cell microplate and analysed on the Seahorse XF24 Analyzer. The ATP-linked mitochondrial OCR (A) and coupling efficiency (B) were calculated as in the text. Seahorse experiments were performed three times in quintuplicate. Data were analysed using a two-tailed, unpaired *t* test to quantify significance where detected. * = $p < 0.05$.

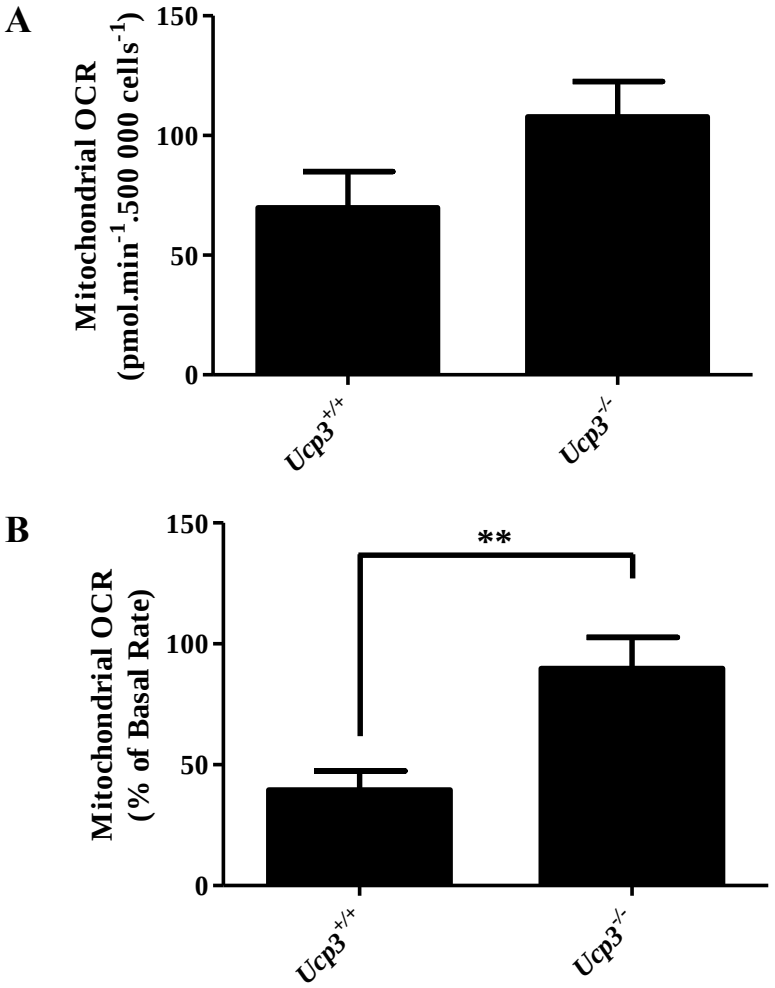

Figure 4.27: Spare respiratory capacity of *Ucp3*$^{+/+}$ and *Ucp3*$^{-/-}$ T_H17 cells

T_H17 cells were generated by incubating naive T cells in the presence of 5 µg.mL^{-1} of anti-CD3 and anti-CD28, 20 ng.mL^{-1} of anti-IL-4 and rIL-6, 10 µg.mL^{-1} of anti-IFN-γ and 2.5 ng.mL^{-1} of rhTGF-β1 for 72 h before being seeded at 500 000 cells per well in a Seahorse cell microplate and analysed on the Seahorse XF24 Analyzer. The spare respiratory capacity-associated mitochondrial OCR (A) and spare respiratory capacity as a percentage of basal mitochondrial OCR (B) were calculated as in the text. Seahorse experiments were performed three times in quintuplicate. Data were analysed using a two-tailed, unpaired *t* test to quantify significance where detected. ** = $p < 0.01$.

4.2.3.4 UCP3 Does Not Play a Role in T_{reg} Cell Metabolism

While our RT-PCR data suggest that UCP3 protein is not expressed or is significantly downregulated in $CD4^+$ T_{reg} cells, the differences observed in *Ucp3*$^{+/+}$ and *Ucp3*$^{-/-}$ T_{reg} cell number and viability (presented in Chapter 3) called for investigation into the potential effect of *Ucp3* ablation on T_{reg} cell metabolism. Moreover, it has been suggested that UCP3 plays a role in the metabolic switch from OxPhos to FAO as it is reportedly upregulated in SKM (Garcia-Martinez *et al*., 2001) and thymus mitochondria (Carroll and Porter, 2004; Kelly and Porter, 2011) during times of starvation when FAs are the predominant fuel source. T_{reg} cells are known to rely heavily on FAO as their main metabolic pathway in contrast to effector T cell subsets which display a predominantly glycolytic metabolic profile (Michalek *et al*., 2011). Thus, UCP3 may have a more important role in the generation and maintenance of T_{reg} cells than of effector T cells, which warranted the investigation into T_{reg} cell metabolism. Primary *Ucp3*$^{+/+}$ and *Ucp3*$^{-/-}$ $CD4^+$ T cells were harvested direct from spleens and incubated for 120 h in the presence of anti-CD3, anti-CD28, rhTGF-β1 and rIL-2 to generate T_{reg} cells. The Seahorse XF Cell Mito Stress Test was performed to explore the metabolism of *Ucp3*$^{+/+}$ compared to *Ucp3*$^{-/-}$ T_{reg} cells and to investigate whether a skewed metabolism is the cause of the altered T_{reg} cell viability and frequency we observed.

Ucp3$^{+/+}$ and *Ucp3*$^{-/-}$ $CD4^+$ T_{reg} cells are not significantly different in their OCR (Figure 4.28), ECAR (Figure 4.29) or basal OCR/ECAR ratio (Figure 4.30). Figure 4.31 displays the mitochondrial OCR, proton leak and maximal respiration of *Ucp3*$^{+/+}$ and *Ucp3*$^{-/-}$ T_{reg} cells 120 h post-stimulation. No significant differences between genotypes are detected, nor are any found between the ATP-linked mitochondrial OCR (Figure 4.32A) or coupling efficiency (Figure 4.32B) of these cells. The spare respiratory capacity of *Ucp3*$^{-/-}$ T_{reg} cells is significantly higher than that of *Ucp*3$^{+/+}$ T_{reg} cells (Figure 4.33A), although this is not reflected when the spare respiratory capacity is calculated as a percentage of the basal mitochondrial OCR (Figure 4.33B). The fact that no differences in OCR (Figure 4.28), proton leak (Figure 4.31), ATP-linked mitochondrial OCR (Figure 4.32A) or coupling efficiency (Figure 4.32B) are observed strongly supports an alternative function to uncoupling for UCP3 in $CD4^+$ T_{reg} cells. Overall, *Ucp3* ablation does not seem to perturb T_{reg} cell metabolism.

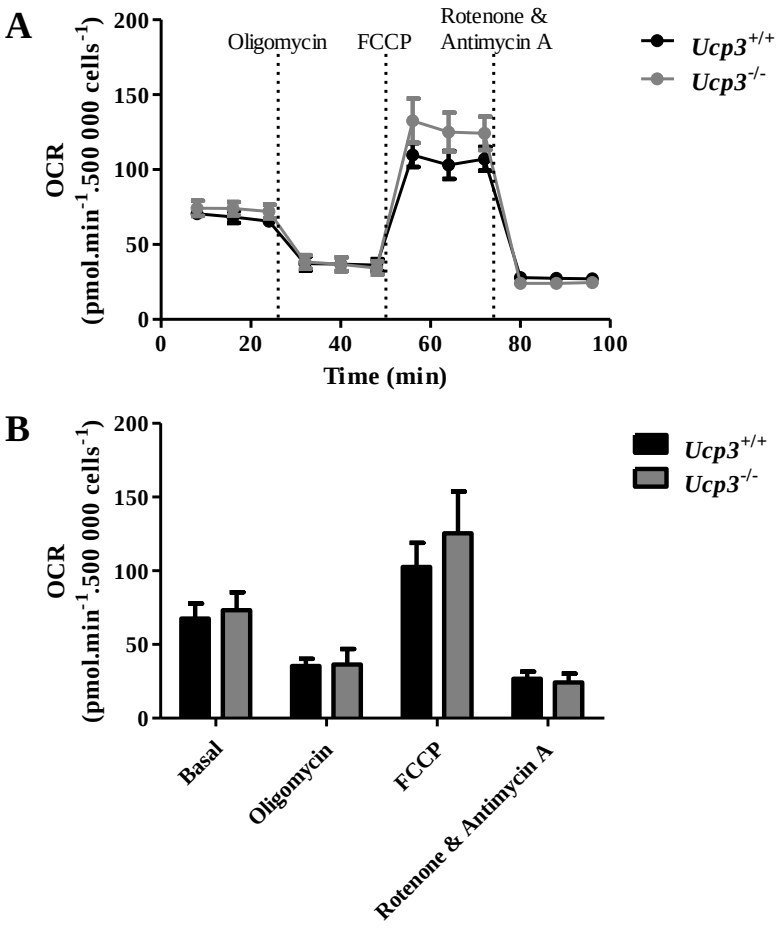

Figure 4.28: OCR of *Ucp3*$^{+/+}$ and *Ucp3*$^{-/-}$ T_{reg} cells is comparable

T_{reg} cells were generated by incubating naive T cells in the presence of 1 µg.mL^{-1} of anti-CD3 and anti-CD28, 5 ng.mL^{-1} of rhTGF-β1 and 10 ng.mL^{-1} of rIL-2 for 120 h before being seeded at 500 000 cells per well in a Seahorse cell microplate and analysed on the Seahorse XF24 Analyzer. Basal measurements were taken 3 times followed by injection of 1 µM oligomycin, 3 rate measurements, injection of 1.5 µM FCCP, 3 rate measurements, injection of 1 µM antimycin A mixed with 0.1 µM rotenone and 3 final rate measurements. Seahorse experiments were performed three times in quintuplicate. Data were analysed using a two-way ANOVA with a *post hoc* Bonferroni test to quantify significance where detected. (A) Time graph of the OCR of *Ucp3*$^{+/+}$ and *Ucp3*$^{-/-}$ T_{reg} cells during the Seahorse XF Cell Mito Stress Test. (B) Mean basal OCR and mean OCR following each compound injection.

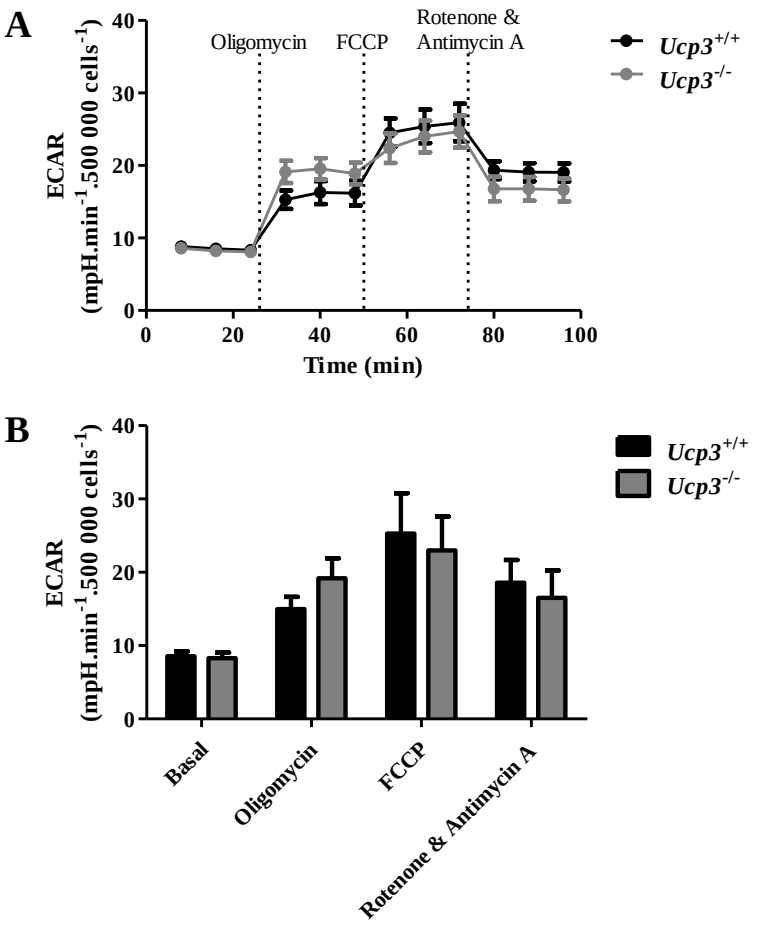

Figure 4.29: ECAR of *Ucp3*$^{+/+}$ and *Ucp3*$^{-/-}$ T_{reg} cells is comparable

T_{reg} cells were generated by incubating naive T cells in the presence of 1 µg.mL^{-1} of anti-CD3 and anti-CD28, 5 ng.mL^{-1} of rhTGF-β1 and 10 ng.mL^{-1} of rIL-2 for 120 h before being seeded at 500 000 cells per well in a Seahorse cell microplate and analysed on the Seahorse XF24 Analyzer. Basal measurements were taken 3 times followed by injection of 1 µM oligomycin, 3 rate measurements, injection of 1.5 µM FCCP, 3 rate measurements, injection of 1 µM antimycin A mixed with 0.1 µM rotenone and 3 final rate measurements. Seahorse experiments were performed three times in quintuplicate. Data were analysed using a two-way ANOVA with a *post hoc* Bonferroni test to quantify significance where detected. (A) Time graph of the ECAR of *Ucp3*$^{+/+}$ and *Ucp3*$^{-/-}$ T_{reg} cells during the Seahorse XF Cell Mito Stress Test. (B) Mean basal ECAR and mean ECAR following each compound injection.

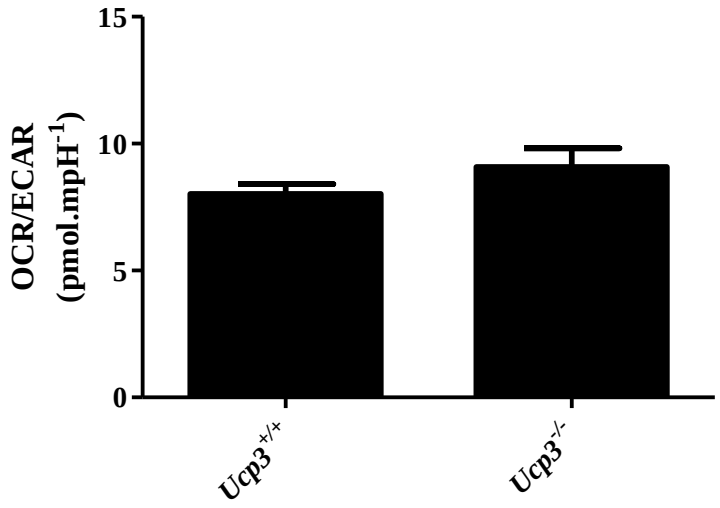

Figure 4.30: Basal OCR/ECAR ratio of *Ucp3*$^{+/+}$ and *Ucp3*$^{-/-}$ T_{reg} cells is comparable

T_{reg} cells were generated by incubating naive T cells in the presence of 1 µg.mL^{-1} of anti-CD3 and anti-CD28, 5 ng.mL^{-1} of rhTGF-β1 and 10 ng.mL^{-1} of rIL-2 for 120 h before being seeded at 500 000 cells per well in a Seahorse cell microplate and analysed on the Seahorse XF24 Analyzer. The OCR/ECAR ratio was calculated as in the text. Seahorse experiments were performed three times in quintuplicate. Data were analysed using a two-tailed, unpaired *t* test to quantify significance where detected.

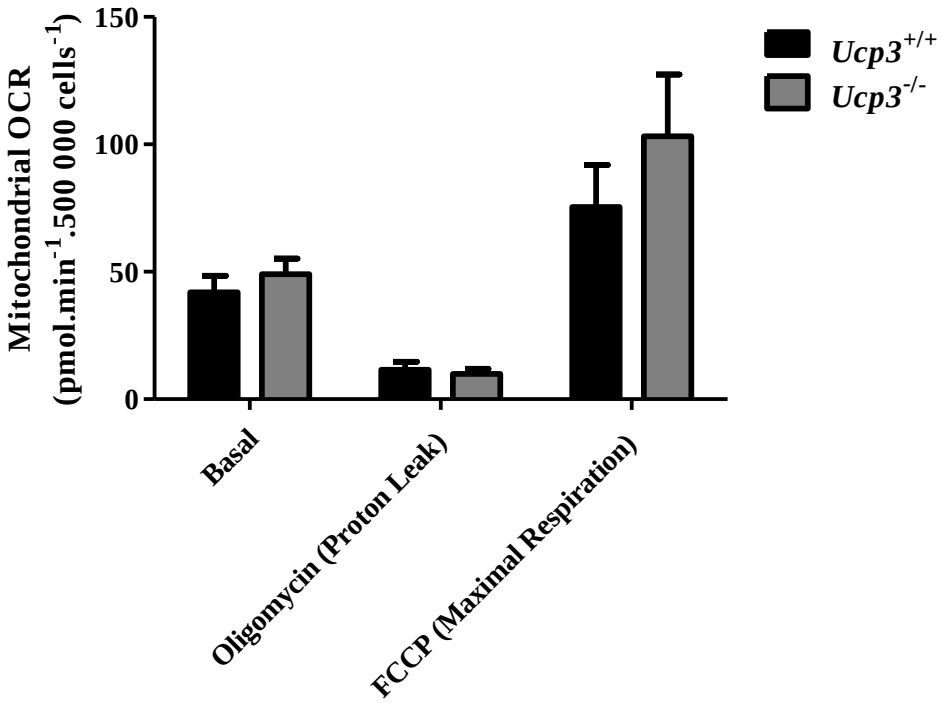

Figure 4.31: Basal mitochondrial OCR and mitochondrial OCR attributable to proton leak and maximal respiration of *Ucp3*$^{+/+}$ and *Ucp3*$^{-/-}$ T_{reg} cells are comparable

T_{reg} cells were generated by incubating naive T cells in the presence of 1 µg.mL^{-1} of anti-CD3 and anti-CD28, 5 ng.mL^{-1} of rhTGF-β1 and 10 ng.mL^{-1} of rIL-2 for 120 h before being seeded at 500 000 cells per well in a Seahorse cell microplate and analysed on the Seahorse XF24 Analyzer. Basal measurements were taken 3 times followed by injection of 1 µM oligomycin, 3 rate measurements, injection of 1.5 µM FCCP, 3 rate measurements, injection of 1 µM antimycin A mixed with 0.1 µM rotenone and 3 final rate measurements. Mitochondrial OCRs were calculated as in the text. Seahorse experiments were performed three times in quintuplicate. Data were analysed using a two-way ANOVA with a *post hoc* Bonferroni test to quantify significance where detected.

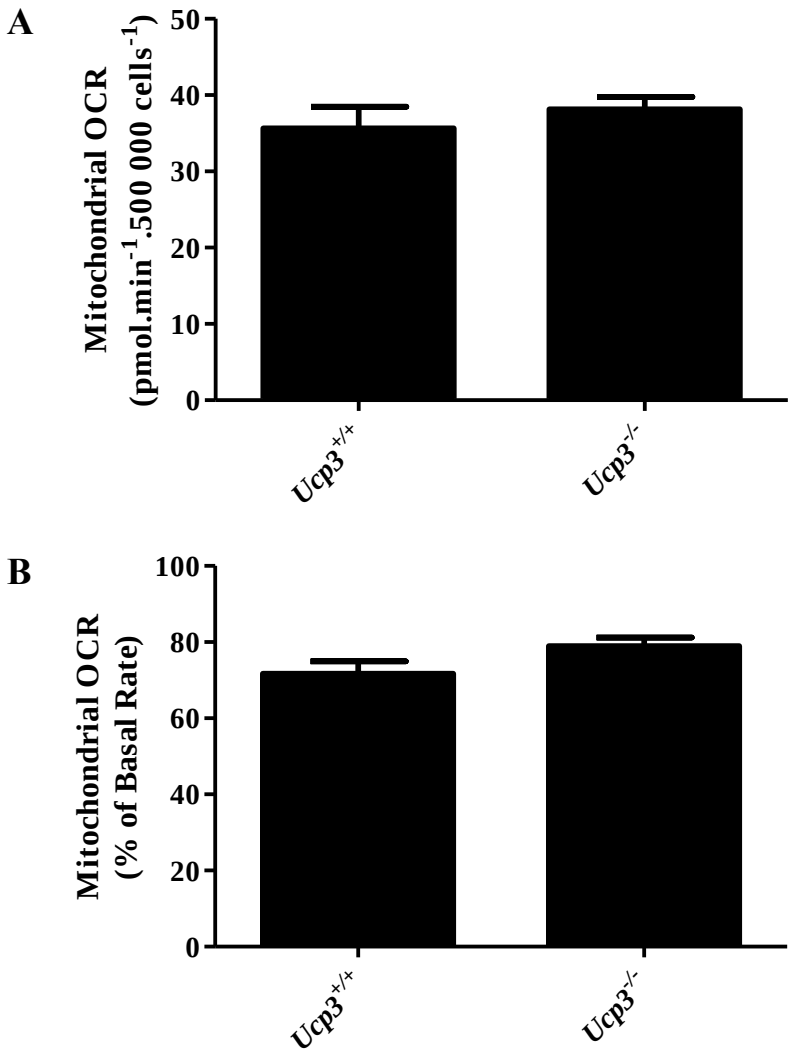

Figure 4.32: Mitochondrial OCR linked to ATP production and coupling efficiency of *Ucp3*$^{+/+}$ and *Ucp3*$^{-/-}$ T_{reg} cells are comparable

T_{reg} cells were generated by incubating naive T cells in the presence of 1 µg.mL^{-1} of anti-CD3 and anti-CD28, 5 ng.mL^{-1} of rhTGF-β1 and 10 ng.mL^{-1} of rIL-2 for 120 h before being seeded at 500 000 cells per well in a Seahorse cell microplate and analysed on the Seahorse XF24 Analyzer. The ATP-linked mitochondrial OCR (A) and coupling efficiency (B) were calculated as in the text. Seahorse experiments were performed three times in quintuplicate. Data were analysed using a two-tailed, unpaired *t* test to quantify significance where detected.

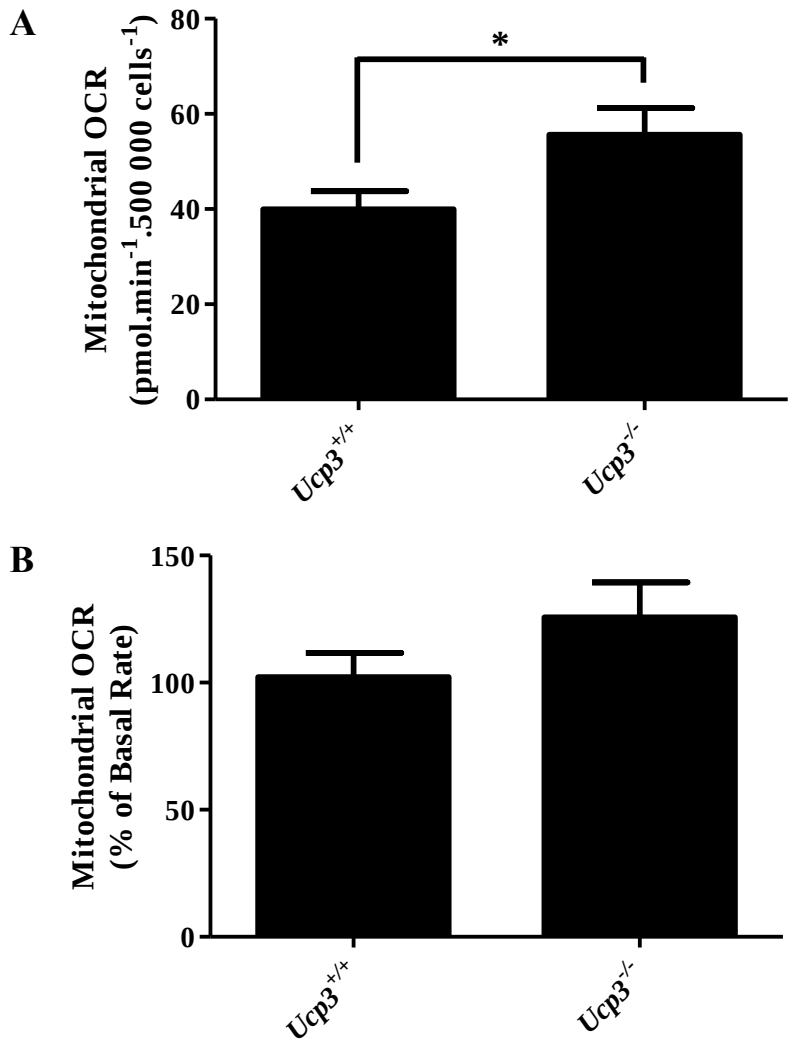

Figure 4.33: Spare respiratory capacity of *Ucp3*$^{+/+}$ and *Ucp3*$^{-/-}$ T_{reg} cells

T_{reg} cells were generated by incubating naive T cells in the presence of 1 µg.mL^{-1} of anti-CD3 and anti-CD28, 5 ng.mL^{-1} of rhTGF-β1 and 10 ng.mL^{-1} of rIL-2 for 120 h before being seeded at 500 000 cells per well in a Seahorse cell microplate and analysed on the Seahorse XF24 Analyzer. The spare respiratory capacity-associated mitochondrial OCR (A) and spare respiratory capacity as a percentage of basal mitochondrial OCR (B) were calculated as in the text. Seahorse experiments were performed three times in quintuplicate. Data were analysed using a two-tailed, unpaired *t* test to quantify significance where detected. * = $p < 0.05$.

4.2.4 *Ucp3* Ablation Does Not Affect Naive CD4$^+$ T Cell Mitochondrial Membrane Potential or ROS Production

From our results presented in Chapter 3, it is clear that *Ucp3* ablation has a prominent impact on T_H0, T_H17 and T_{reg} cell function, while intriguingly having no influence on their metabolism, as shown in Section 4.2.3. While we hypothesize that UCP3 is acting to restrict T cell activation and that its ablation evokes early activation of T_H0 cells, a skewed metabolism evidently does not play a role in inducing this effect. This is suggestive of a function other than uncoupling for UCP3. However, while the exact function of UCP3 has remained controversial up to this point, there are reports that UCP3 indeed carries out uncoupling activity (Jabůrek *et al*., 1999; Echtay *et al*., 2001; Jabůrek and Garlid, 2003). Moreover, UCPs have been implicated in the control of ROS production by carrying out mild uncoupling (Brand, 2000; Miwa and Brand, 2003; Brand *et al*., 2004) and, incidentally, ROS have been implicated in the priming of T cells for activation (Roth and Dröge, 1987; Los *et al*., 1995; Sena *et al*., 2013) and the promotion of T cell proliferation (Chang *et al*., 2013). Thus, we hypothesized that if UCP3 is acting to uncouple the mitochondria of CD4$^+$ T cells, its ablation may result in an increased mitochondrial membrane potential and a consequential increase in ROS production, which may be driving the early activation of T_H0 cells that we observe.

While activated T cells are predominantly glycolytic in their metabolic profile, an increase in the global rate of OxPhos is also observed, as mentioned previously (Chang *et al*., 2013; Loftus and Finlay, 2016). In line with this, mitochondrial ROS production by T cells increases following cell activation (Dumont *et al*., 1999; Hildeman, 2003; Sena *et al*., 2013; Yarosz and Chang, 2018). However, our RT-PCR data suggest that UCP3 is present in naive CD4$^+$ T cells before being subsequently downregulated following cell activation (Section 3.2.1). Thus, a difference in ROS production may be observed between *Ucp3*$^{+/+}$ and *Ucp3*$^{-/-}$ naive CD4$^+$ T cells before UCP3 expression is downregulated. Hence, to explore the possibility of *Ucp3*-ablated T cells generating more ROS than their WT counterparts, flow cytometry analysing MitoTracker™ Red CMXRos and DCFDA staining in *Ucp3*$^{+/+}$ and *Ucp3*$^{-/-}$ naive CD4$^+$ T cells, rather than activated cells, was carried out. Similar to MitoTracker™ Green FM, MitoTracker™ Red CMXRos is a red fluorescent dye that accumulates in mitochondria (Puleston, 2015). However, in contrast, its accumulation is mitochondrial membrane potential-dependent (Puleston, 2015). DCFDA is a fluorogenic dye that is deacetylated by cellular esterases into a non-fluorescent compound following its diffusion into a cell. This compound can then be

oxidized by ROS and form a fluorescent compound, 2',7'-dichlorofluorescein (DCF), which can be detected by flow cytometry and allow the rapid quantitation of ROS.

The mitochondrial membrane potential of *Ucp3*$^{+/+}$ and *Ucp3*$^{-/-}$ naive CD4^{+} T cells, as measured by MitoTracker™ Red CMXRos staining, is not significantly different (Figure 4.34A and B). Correspondingly, no difference is found between the ROS production of *Ucp3*$^{+/+}$ and *Ucp3*$^{-/-}$ naive CD4^{+} T cells (Figure 3.34C and D). Thus, it is apparent that a low level of uncoupling by UCP3 causing a decrease in the mitochondrial membrane potential of, and ROS production by, WT compared to KO naive CD4^{+} T cells may not be responsible for the differences in activation observed between *Ucp3*$^{+/+}$ and *Ucp3*$^{-/-}$ T_H0 cells.

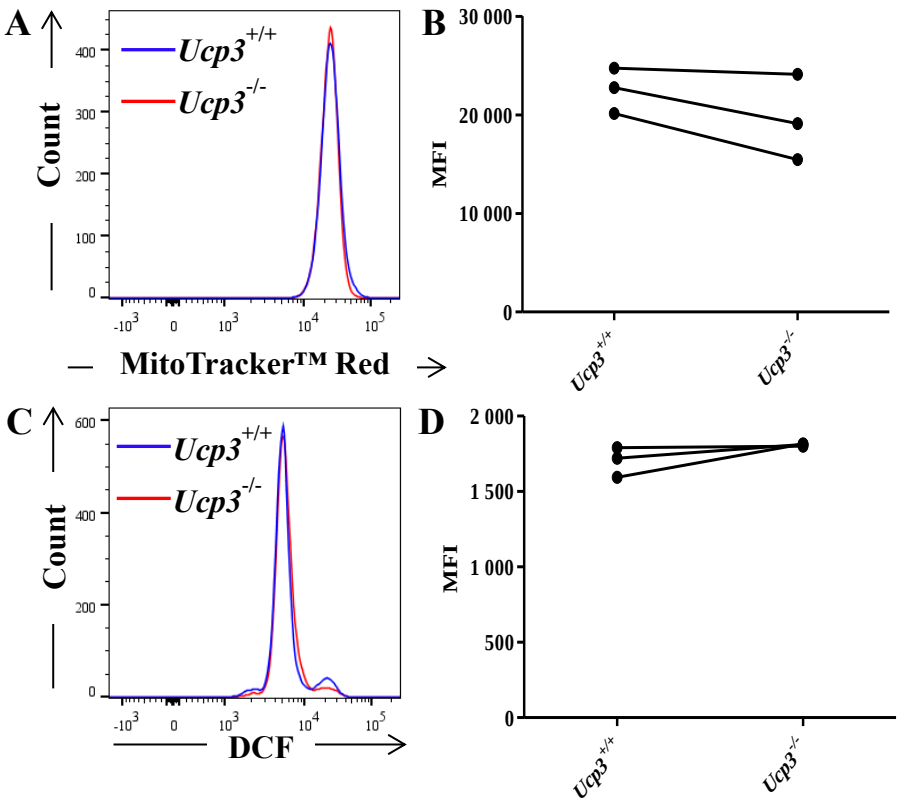

Figure 4.34: Mitochondrial membrane potential of, and ROS production by, *Ucp3*$^{+/+}$ and *Ucp3*$^{-/-}$ naive CD4^{+} T cells are comparable

Primary CD4^{+} T cells were isolated from a suspension of splenocytes and stained with LIVE/DEAD™, PE-Cy7:anti-CD4 and MitoTracker™ Red CMXRos (A and B) or DCFDA (C and D) before being analysed on a flow cytometer. Flow cytometry was performed three times. Histograms are representative of three different experiments and are of the viable, CD4^{+} T cell population. Graphs display MFI values from three individual experiments. (A and B) Mitochondrial membrane potential of naive CD4^{+} T cells. (C and D) ROS production by naive CD4^{+} T cells. All data were analysed using a two-tailed, unpaired *t* test to quantify significance where detected.

4.3 Discussion

We have shown in Chapter 3 that *Ucp3* ablation results in a marked alteration of activated T cell function by causing early activation and affecting T_H17 and T_{reg} cell generation. It is possible that *Ucp3* ablation would additionally impact activated T cell metabolism. When naive $CD4^+$ T cells are activated to adopt a pro-inflammatory effector function, they undergo a metabolic switch from a relatively quiescent state, utilising OxPhos as their predominant metabolic profile, to a highly active state displaying a Warburg-like metabolism that relies predominantly on glycolysis as the primary pathway of energy generation (Chang *et al*., 2013; Pearce and Pearce, 2013). This metabolic switch may occur sooner in *Ucp3*$^{-/-}$ T_H0 cells due to their earlier activation and/or may be skewed in *Ucp3*$^{-/-}$ T_H17 cells, resulting in their perturbed functioning, which would imply a potential role for UCP3 in T cell metabolism. If UCP3 is eliciting uncoupling activity, this may be evident in altered metabolic parameters of *Ucp3*$^{-/-}$ cells. Removal of a protein that has the potential to uncouple mitochondria would be expected to emanate in a decreased OCR, an increased OCR linked to ATP production, an increased coupling efficiency and, of course, a decreased proton leak. To this end, we set out to determine the role of UCP3 in the metabolism of activated *Ucp3*$^{+/+}$ and *Ucp3*$^{-/-}$ T_H0 and T_H17 cells and to investigate whether a skewed metabolism as a result of *Ucp3* ablation was responsible for the distorted T cell function we have observed.

Ucp3$^{-/-}$ T_H0 cells display a significantly lower OCR/ECAR ratio 24 h post-stimulation, indicating a more glycolytic phenotype which is in line with the earlier activation of these cells observed in Chapter 3. However, no other consistent differences are observed between the respiration or glycolysis of *Ucp3*$^{+/+}$ and *Ucp3*$^{-/-}$ T_H0 cells that would support a metabolic role or an uncoupling function of UCP3. In fact, a significant decrease in the mitochondrial OCR linked to ATP production of *Ucp3*$^{-/-}$ T_H0 cells 72 h post-stimulation contradicts an uncoupling function of UCP3. Our RT-PCR data in Chapter 3 suggest that UCP3 is downregulated in *Ucp3*$^{+/+}$ T_H0 cells following activation. If this is the case and if UCP3 is eliciting an uncoupling function, then indeed *Ucp3*$^{+/+}$ T_H0 cells would become more ‘coupled’ following activation and increase their OCR linked to ATP production. Nevertheless, this would not be expected to result in a significantly *higher* level of ATP-linked OCR in *Ucp3*$^{+/+}$ T_H0 cells and should result in an equal ATP-linked OCR at most. Therefore, this does not imply an uncoupling function for UCP3 in $CD4^+$ T_H0 cells. It is also possible that, while efforts were made to ensure only viable cells were used for all Seahorse experiments, this decrease is due to the *Ucp3*$^{-/-}$ T_H0 cells undergoing AICD, as

described in Chapter 3, although this was not reflected in any other metabolic parameter measured 72 h post-stimulation.

In the case of T_H17 cells, *Ucp3*$^{-/-}$ cells have a significantly higher OCR/ECAR ratio, indicating a more oxidative phenotype than their WT counterparts. This may suggest an altered metabolic profile of *Ucp3*$^{-/-}$ T_H17 cells as T_H17 cells are known to predominantly rely on glycolysis as their main metabolic pathway and potentially reflects their altered function reported in Chapter 3. *Ucp3*$^{-/-}$ T_H17 cells also display a significantly higher coupling efficiency than *Ucp3*$^{+/+}$ T_H17 cells which would underpin a role for UCP3 in uncoupling T_H17 cell mitochondria but, with no additional significant changes evident in the OCR or proton leak, this evidence for an uncoupling function remains weak. How *Ucp3*$^{-/-}$ T_H17 cells possess an increased spare respiratory capacity (when calculated as a percentage of basal mitochondrial OCR only), despite their decreased survival rate reported in Chapter 3, is also unclear.

While no clear function of UCP3 has yet been demonstrated in any UCP3-expressing tissue, claims of UCP3 uncoupling activity have been made (Jabůrek *et al*., 1999; Echtay *et al*., 2001; Jabůrek and Garlid, 2003). Having demonstrated that UCP3 is expressed in naive $CD4^+$ T cells at the mRNA level and decreases upon activation, we postulated that if UCP3 were to uncouple mitochondria, its ablation would affect the overall metabolism of naive T cells. Uncoupling of the mitochondria, through the addition of FCCP during the Seahorse XF Cell Mito Stress Test for example, usually results in increased O_2 consumption in order to restore the electrochemical gradient and synthesize ATP. Removal of an UCP from the mitochondria would be expected to result in a decreased OCR, an increased OCR linked to ATP production, an increase in coupling efficiency and, of course, a decreased proton leak due to the mitochondria being more ‘coupled’. In line with this, a small but significant difference is detected between the mitochondrial OCR linked to ATP production of *Ucp3*$^{+/+}$ and *Ucp3*$^{-/-}$ naive T cells. *Ucp3*$^{-/-}$ naive T cell mitochondria consume significantly more O_2 that is linked to ATP production than *Ucp3*$^{+/+}$ naive T cell mitochondria. This is in contrast to the previously mentioned *Ucp3*$^{-/-}$ T_H0 cells that display a significantly lower ATP-linked OCR compared to their WT counterparts, contradicting an uncoupling function for UCP3. However, as no other differences in metabolism are evident compared to the *Ucp3*$^{+/+}$ naive T cells, such as a decrease in O_2 consumption or proton leak or an increase in the coupling efficiency, this suggests that UCP3 does not have an uncoupling role. Alternatively, if acting to uncouple mitochondria of the WT cells, UCP3 may be

functioning at an extremely low level, low enough that its ablation does not result in marked changes in these parameters. Similar observations were made by Adams *et al*. (2010), who reported increased ATP levels in *Ucp1*$^{-/-}$ thymocytes but no difference in O_2 consumption, and Krauss *et al*. (2002), who reported a difference in proton leak and total cell ATP of *Ucp2*$^{+/+}$ and *Ucp2*$^{-/-}$ thymocytes but, again, no difference in O_2 consumption.

Although no clear uncoupling function of UCP3 is evident in our Seahorse XF Cell Mito Stress Test results, numerous reports have implicated UCPs in the attenuation of mitochondrial ROS production by generating a controlled proton leak (Brand *et al*., 2004). Indeed, of the number of roles that have been postulated for UCPs, only the attenuation of ROS production and the associated protection against cellular degeneration and ageing would appear important enough to merit the energetic cost imposed by a proton leak (Brand, 2000). Nègre-Salvayre *et al*. (1997) and Brand *et al*. (2004) reported that H_2O_2 generation was stimulated by the addition of the UCP inhibitor GDP to BAT, SKM, spleen and thymus mitochondria. Similarly, Dlasková *et al*. (2010) and Clarke and Porter (2013) showed that UCP1 has the potential to alleviate ROS production in BAT and thymocyte mitochondria, respectively. UCP2 in particular has been associated with a role in the alleviation of ROS production. Following macrophage stimulation through TLR4 with lipopolysaccharide (LPS), UCP2 deficiency promotes the expression of inducible NO synthase, ROS and reactive nitrogen species (RNS) production and the release of pro-inflammatory cytokines (Bai *et al*., 2005; Emre *et al*., 2007). *Ucp2*$^{-/-}$ mice have an increased pro-inflammatory response to infection with *Toxoplasma gondii*, triggered by elevated ROS and RNS production by infected *Ucp2*$^{-/-}$ macrophages (Arsenijevic *et al*., 2000; Bai *et al*., 2005) and pancreatic islet cells (Krauss *et al*., 2003), and are completely resistant to the normally lethal infection. The effect disappears upon the addition of a ROS or RNS scavenger. Similar results are seen in *Ucp2*$^{-/-}$ mice subjected to *Salmonella typhimurium* infection (Arsenijevic *et al*., 2000). Mitochondrial aconitase activity was decreased by 20 % in *Ucp3*$^{-/-}$ SKM (Vidal-Puig *et al*., 2000), indicative of increased ROS production. Mice lacking UCP3 have increased levels of oxidative damage to proteins and lipids (Brand *et al*., 2002), which further supports the role of UCPs in protecting against ROS production and oxidative tissue damage.

In line with this hypothesis, UCP1, UCP2 and UCP3 have been shown to be activated by ROS in a FA-dependent manner as a potential negative feedback mechanism (Echtay *et al*., 2002; Brand *et al*., 2004). These effects were confirmed in isolated mitochondria where a

GDP-sensitive proton leak was observed upon addition of polyunsaturated FAO/peroxidation products (HNE) formed from O_2^- (Echtay *et al*., 2003), but the specificity of the activation by FAO products was questioned by Shabalina *et al*. (2006). Using *in vivo* mouse models of acute activation of UCP1-dependent thermogenesis, Chouchani *et al*. (2016) reported ROS activated UCP1 activity through sulfenylation of a Cys residue (Cys253) in the protein that results in the sensitization of the protein to activation. Importantly, Cys253 is conserved in UCP2 and UCP3. Han *et al*. (2016) showed that adipocyte-specific *Sod2*$^{-/-}$ mice displaying elevated levels of O_2^- were extraordinarily resistant to weight gain on a high fat diet, which is thought to be due to chronically elevated thermogenic energy expenditure from UCP1 activation. Similarly, mice lacking nuclear factor-erythroid 2-related factor 2 (NRF2), a transcription factor controlling a broad range of ROS- and thiol-targeted antioxidant enzymes, are resistant to weight gain on a high-fat diet (Pi *et al*., 2010; Chartoumpekis *et al*., 2011), and these effects were attributed to chronically elevated energy expenditure (Schneider *et al*., 2016). Using the mitochondria-targeted antioxidant Mito-Q, which is well established to efficiently deplete mitochondrial lipid peroxides and O_2^- upon acute administration *in vivo*, Chouchani *et al*. (2017) reported that the capacity for BAT-mediated thermogenic respiration was substantially inhibited and induced hypothermia upon cold exposure.

We hypothesize that UCP3 is acting to restrict T cell activation and that its ablation evokes early activation of T_H0 cells, as evidenced by the increased IL-2 production, early activation marker expression and consequential increase in cell proliferation and cell death due to AICD. Interestingly, ROS have been implicated in enhancing T lymphocyte activation. O_2^- and H_2O_2 were shown to enhance the production of IL-2 in stimulated T lymphocytes, as well as expression of the IL-2R (Roth and Dröge, 1987; Los *et al*., 1995; Sena *et al*., 2013). Following oligomycin treatment of T cells, Chang *et al*. (2013) reported that mitochondrial ATP generated by OxPhos is a requirement for T cell proliferation and activation marker expression. However, the oligomycin treatment of activated T cells in the study by Chang *et al*. may have led to an increase in ROS production. ROS have also been shown to induce nuclear factor κ light chain-enhancer of activated B cells (NF-κB)-dependent apoptosis (Dumont *et al*., 1999). 'Coupled' *Ucp3*$^{-/-}$ naive $CD4^+$ T cells would be presumed to have a higher mitochondrial membrane potential than *Ucp3*$^{+/+}$ naive T cells and, thus, may produce more ROS. Due to these reports almost mirroring our own results, we hypothesized that UCP3 may be acting to uncouple the mitochondria of $CD4^+$ T cells and its ablation may result in an increased mitochondrial membrane potential and a

consequential increase in ROS production, thus driving the early activation and premature death of T_H0 cells. However, no difference in the mitochondrial membrane potential of, or ROS production by, *Ucp3*$^{+/+}$ and *Ucp3*$^{-/-}$ naive CD4$^+$ T cells is observed.

One explanation may be that, although ROS production may be increased by *Ucp3* ablation, it may simply not have been detected by the chosen method or the difference is just too small to detect due to such a low expression level of UCP3 in *Ucp3*$^{+/+}$ naive CD4$^+$ T cells, as suggested by our data in Section 3.2.2. Furthermore, mitochondrial ROS production by T cells increases following cell activation (Dumont *et al*., 1999; Hildeman, 2003; Sena *et al*., 2013; Yarosz and Chang, 2018). Hence, despite our RT-PCR data suggesting that UCP3 is only expressed in naive CD4$^+$ T cells, a difference in ROS production may only be observed following the exploration of ROS produced by activated T cells rather than naive T cells. An additional experiment that also could have been performed to check the levels of ROS production would be to measure the activity of enzymes containing iron-sulphur centres, such as aconitase or Complex I, which can be inactivated by the presence of ROS and, thus, may serve as an indicator for ROS production (Vidal-Puig *et al*., 2000). However, if *Ucp3* ablation resulted in increased ROS production in our experimental set up and caused the inactivation of Complex I, one would expect this to be reflected in our Seahorse XF Cell Mito Stress Test results. Mitochondrial antioxidant defences may also be upregulated in the mitochondria of *Ucp3*$^{-/-}$ animals to protect against the possibility of increased oxidative damage and, as such, differences in ROS production may be mopped up by antioxidants. In line with this, *Ucp2*-ablated animals display increased levels of SOD2 and decreased lipid peroxidation (de Bilbao *et al*., 2004). Indeed, a logical next step to confirm if this is the case would be to measure levels of SOD2. It may have also been worthwhile to measure the ATP/ADP ratio of *Ucp3*$^{+/+}$ compared to *Ucp3*$^{-/-}$ T cells in this work, as done by Chang *et al*. (2013). However, without an already obvious difference in the previously discussed metabolic parameters of these cells, a difference in the ATP/ADP ratio of *Ucp3*$^{+/+}$ and *Ucp3*$^{-/-}$ CD4$^+$ T cells may be unlikely. In line with our finding of no role for UCP3 in the attenuation of ROS production by CD4$^+$ T cells, Hilse *et al*. (2018) reported that UCP3 expression in cardiomyocytes does not coincide with the expression of ETC proteins, rendering UCP3 participation in ROS regulation unlikely. In addition, Pecqueur *et al*. (2008) reported no difference in ROS production or the mitochondrial membrane potential following *Ucp2* ablation, although these were examined in murine embryonic fibroblasts rather than T cells. It should be

noted, however, that it is possible that UCP3 was not activated in *Ucp3*$^{+/+}$ T cells in our experimental setup.

The lack of significant differences between the respiration of *Ucp3*$^{+/+}$ and *Ucp3*$^{-/-}$ naive CD4^{+} T cells, T_H0 and T_H17 cells suggests that UCP3 is not uncoupling the mitochondria of CD4^{+} T cells nor is it playing a role in their metabolism. This is in contrast to a number of reports that claim uncoupling action from UCP3. Vidal-Puig *et al*. (2000) reported that when UCP3 is reconstituted into proteoliposomes, it mediates proton transport across lipid bilayers similar to UCP1. UCP3 overexpression in cultured human muscle cells decreased the mitochondrial membrane potential (Garcia-Martinez *et al*., 2001). Human UCP3 decreased the mitochondrial membrane potential in transformed yeast (Gong *et al*., 1997) and transfected C2C12 mouse myoblasts, suggesting a function in line with proton transport across the MIM (Boss *et al*., 1998). However, it has been argued that artificial uncoupling may be associated with overexpression of UCP3 due to non-native insertion, folding or interactions of the protein in the MIM leading to compromised membrane integrity (Cadenas *et al*., 2002). Finally, SKM mitochondria lacking UCP3 were more coupled than those expressing UCP3 (Vidal-Puig *et al*., 2000). Nonetheless, none of these reports involved work carried out on CD4^{+} T cells and, as far as we are aware, no other research group is investigating the role of UCP3 in CD4^{+} T cells specifically. Furthermore, in line with our results, Kelly and Porter (2011), who reported the observation of an altered T cell profile in thymus and spleen of *Ucp3*$^{-/-}$ mice, also reported no differences in the basal OCR, the OCR linked to proton leak and the OCR following FCCP treatment of *Ucp3*$^{+/+}$ and *Ucp3*$^{-/-}$ thymocytes or splenocytes.

The fact that *Ucp3* is expressed in a variety of tissues suggests that it may have different functions that are tissue-dependent. This could be responsible for us not observing an uncoupling function of UCP3 in this work – UCP3 may not function as an uncoupler of CD4^{+} T cells but may function as something else. It should be noted, however, that the expression of UCP3 protein in SKM mitochondria is tiny compared to the UCP1 levels in BAT mitochondria and can be up to 1000-fold lower (Harper *et al*., 2001; Graier *et al*., 2008). Furthermore, SKM is reported to have the highest abundance of UCP3 expression than any other tissue [although this has been challenged by Hilse *et al*. (2016)], so any expression of UCP3 in CD4^{+} T cells is expected to be considerably less. Effector T cells are also known to have very few mitochondria, even compared to memory T cells (van der Windt and Pearce, 2012), and, in contrast, BAT contains many mitochondria with

abundant, densely packed cristae of the MIM – the location of UCP3 expression (Krauss *et al*., 2005). As a result, proton conductance or substrate transport, whatever the function of this protein may be, would presumably be much lower compared to UCP1 in BAT. Thus, any uncoupling effect of UCP3 may be only mild compared to the uncoupling observed in BAT and may be too small to detect. We have shown in Chapter 3 that the expression of *Ucp3* in naive $CD4^+$ T cells is almost 600-fold lower than the expression of *Ucp2* at the mRNA level. This may manifest in the lack of differences in the metabolic parameters of $Ucp3^{+/+}$ and $Ucp3^{-/-}$ naive T cells, T_H0 and T_H17 cells observed here.

It is also possible that the required activators of UCP3 function were absent in our experimental set up. UCP3 may not have been activated to catalyse a proton leak under the conditions used in our study. *In vitro* experiments and UCP3 reconstitution into vesicle membranes suggest that UCP3 facilitates a FA-dependent, nucleotide-inhibitable, UCP1-like proton leak (Jabůrek *et al*., 1999; Echtay *et al*., 2001). Additionally, while researching UCP1 activity in thymocytes, our laboratory demonstrated activation of O_2 consumption by palmitate and inhibition by GDP (Carroll *et al*., 2005). If UCP3 functions in a similar manner to UCP1 in thymocytes and T cells, palmitate or some other FA may be required for its activity. In our Seahorse XF Cell Mito Stress Tests, no FAs were present in the experimental media. Another important point is that UCP3 activation is still not fully understood and, even in the presence of FAs, no observable difference in metabolism would be guaranteed. This is supported by the fact that while increased levels of plasma FFAs are associated with upregulated *Ucp3* transcription and UCP3 expression in SKM mitochondria (Zhou *et al*., 2000), this is not reflected by an increase in proton leak (Cadenas *et al*., 1999). If UCP3 does in fact act as a proton transporter, this implies a more complex method of control such as covalent modification rather than simple protein abundance. In fact, our laboratory has recently reported serine and tyrosine phosphorylation of UCP3 following *in vivo* administration of MDMA to mice and rats, which was paralleled by an increase in O_2 consumption by isolated SKM mitochondria (Kelly *et al*., 2012). A requirement for covalent modification to activate UCP3 would make sense in that, although UCP3 has a short half-life of about 0.5 – 4 h (Azzu *et al*., 2010), its function needs to be under tight control as even small alterations in proton leak and, therefore, basal metabolic rate could manifest in significantly increased energy expenditure over time due to its high expression in a tissue (SKM) that boasts such a great mass in the body. In line with this, studies utilizing $Ucp3^{-/-}$ mice showed no difference in basal proton conductance in isolated mitochondria compared to WTs (Cadenas *et al*., 2002) but

differences were noted when other specific activators, such as HNE (Echtay *et al*., 2002, 2003; Brand *et al*., 2004), were used. HNE was not present in our experimental design. However, recent patch clamp studies on UCP1 regulation have shown that HNE is not sufficient to stimulate UCP1 protonophoric activity directly (Fedorenko *et al*., 2012) but can act synergistically with FAs, suggesting it to be an allosteric regulator of UCP1 activity (Malingriaux *et al*., 2013). Thus, its role in UCP3 activation may be similar.

That SKM alters its fuel substrate from glucose to lipids during starvation led to the proposal that the biological role for UCP3 is to regulate or play a role in lipid metabolism (Garcia-Martinez *et al*., 2001). UCP3 protein content is consistently upregulated in line with situations in which FA supply/delivery to SKM mitochondria exceeds the muscle's capacity to metabolize FAs, such as during fasting or starvation as mentioned previously [contrary to UCP1 and UCP3 expression in BAT, which are downregulated during fasting (Bonet *et al*., 1995; Gong *et al*., 1997)], T_3 treatment, acute exercise and high-fat feeding (Dulloo *et al*., 2001). This upregulation is most likely because FFAs are ligands for PPARγ and PPARδ, which have been shown to regulate *Ucp3* gene expression through their respective response elements in a manner similar to that for *Ucp1* (Boss *et al*., 1998; Schrauwen *et al*., 2002, 2006; Wang *et al*., 2003; Bezaire *et al*., 2005). In line with this, Carroll and Porter (2004) reported increased expression of UCP3 in the mitochondria of the thymus, thymocytes and splenic lymphocytes after fasting. In contrast, upon transition from starvation to refeeding, the expression of SKM UCP3 is found to be altered from a state of upregulation to one of downregulation below control levels (Dulloo *et al*., 2001). These findings could be interpreted as being consistent with a role for this UCP homologue in the switching of muscle substrate metabolism from a state of enhanced lipid utilization to one of reduced fat utilization (Dulloo *et al*., 2001). In fact, the downregulation of muscle expression of UCP3 during refeeding on a low fat diet is prevented by high fat refeeding, *i.e.* when the availability of dietary lipids is not a limiting factor (Dulloo *et al*., 2001). It has been reported that mice lacking UCP3 have an impairment in the starvation-induced switch in muscle FA partitioning between oxidation and storage (Garcia-Martinez *et al*., 2001).

$CD4^+$ T_{reg} cells are known to rely heavily on FAO as their main metabolic pathway in contrast to T_H cell subsets, such as T_H1 cells, that display a predominantly glycolytic metabolic profile (Michalek *et al*., 2011). Thus, it was hypothesized that UCP3 may have a role in the FAO metabolism of T_{reg} cells. In addition, while our RT-PCR data suggest that

UCP3 protein is not expressed or is significantly downregulated in T_{reg} cells (Figure 3.12), we have shown that *Ucp3* ablation indeed affects T_{reg} cell generation and viability (Chapter 3), which called for investigation into the potential effect of *Ucp3* ablation on T_{reg} cell metabolism. No significant metabolic or glycolytic differences are observed between *Ucp3*$^{+/+}$ and *Ucp3*$^{-/-}$ T_{reg} cells, except for a small significant difference in the spare respiratory capacity. *Ucp3*$^{-/-}$ T_{reg} cells have a significantly higher spare respiratory capacity than their WT counterparts. The spare respiratory capacity is the extra mitochondrial capacity available beyond basal function: how much is 'on reserve' in a cell to produce energy under conditions of increased work or stress, and is thought to be important for long-term cellular survival and function (Ferrick *et al*., 2008; Choi *et al*., 2009; Nicholls *et al*., 2010; van der Windt *et al*., 2012). In line with this, we previously observed an increase in T_{reg} cell survival 120 h post-stimulation (Section 3.2.6): the same time point used for the T_{reg} cell Seahorse XF Cell Mito Stress Test. The significantly greater spare respiratory capacity of the *Ucp3*$^{-/-}$ T_{reg} cells suggests that these cells have greater mitochondrial activity and that they are at somewhat of a metabolic advantage that would allow them to tap into a bigger metabolic reserve capacity, should these cells have to endure a metabolic stress or challenge. However, if the role of UCP3 is involved in FAO, how its ablation is connected to a metabolic advantage of T_{reg} cells which rely on FAO is unclear. As well as this, when calculated as a percentage of the basal mitochondrial OCR, the spare respiratory capacity of *Ucp3*$^{-/-}$ T_{reg} cells is not statistically significant.

It has been argued previously that the role of UCP3 is not quite in the oxidation of lipids but rather is in lipid handling and the protection against mitochondrial NEFA accumulation. Although the MIM provides a barrier for NEFAs, neutral NEFAs (but not anions) and FAs that cannot be esterified can accumulate in the cytosol in situations of surplus FA delivery to the cell, partition into the phospholipid bilayer of the MIM and, by a so-called 'flip-flop' mechanism, reach the matrix side of the membrane where they are deprotonated to FA anions due to the proton gradient across the MIM (Schrauwen *et al*., 2001, 2002, 2003). Once inside, these long-chain FA anions cannot be converted to fatty acyl CoA to be metabolized by β-oxidation due to a lack of fatty acyl CoA synthetase in the MM, nor can they flip-flop back across the MIM (Schrauwen *et al*., 2001, 2002). These NEFA anions are, thus, trapped and accumulate inside the MM. Here, they can have deleterious effects on mitochondrial function due to, for example, their proneness to lipid peroxidation (Schrauwen *et al*., 2001, 2002, 2003, 2006; Minnaard *et al*., 2006). Highly reactive lipid peroxides can damage mitochondrial DNA and ETC complexes in a process

termed lipotoxicity (Minnaard *et al*., 2006). Therefore, these NEFAs need to be transported out of the MM. It has been postulated that UCP3 performs uncoupling activity by facilitating the outward translocation of these NEFA anions from the MM to the IMS and, in this way, decreases the proton gradient across the MIM (Schrauwen *et al*., 2001, 2003). This is supported by reports of increased UCP3 content under conditions of elevated FAs and activation of UCP3 by the lipid peroxidation by-product, HNE (Minnaard *et al*., 2006). However, in this hypothesis, the uncoupling activity of UCP3 would be a side effect of its primary function which would be to protect mitochondria against lipotoxicity (Schrauwen and Hesselink, 2004). UCP3 protein expression is highest in type IIB muscle fibres, as reported by Schrauwen *et al*. (2002), which are characterized by a low capacity to oxidize FAs, and is lowest in type I muscle fibres which are characterized by a high fat oxidative capacity (Schrauwen *et al*., 2003). The former may need to be protected from mitochondrial NEFA accumulation while the latter, on the other hand, may be less prone to accumulation of NEFAs (Schrauwen *et al*., 2001, 2002). This is also underpinned by the fact that during high-fat feeding, the continuous delivery of FAs exceeds the oxidative capacity of SKM and not all FAs can be oxidized, resulting in a transient accumulation of FAs inside the muscle cell and the MM (Schrauwen *et al*., 2003). The observed upregulation of UCP3 may serve to facilitate the outward transport of these FAs from the MM (Schrauwen *et al*., 2003). The lack of upregulation of UCP3 on a medium-chain high fat diet versus a long-chain high fat diet, despite similar plasma NEFA levels, supports the hypothesis that UCP3 is specifically involved in the export of non-esterified, long-chain FA anions from the MM into the cytoplasm as medium-chain FAs that enter the MM can still be diverted to β-oxidation so there would be no need to upregulate UCP3 (Schrauwen *et al*., 2003). It was found that mice lacking UCP3 indeed have increased lipid peroxidation (Schrauwen *et al*., 2003). While we observed no differences in the metabolism of *Ucp3*$^{+/+}$ and *Ucp3*$^{-/-}$ T_{reg} cells, perhaps if we had carried out the experiment in an environment with a high concentration of long-chain FAs, the uncoupling effect of UCP3 may have been discerned. Indeed, according to Loftus and Finlay (2016), FoxP3^{+} T_{reg} cells metabolize *exogenously* derived FAs.

The general consensus is that UCP3 does not transport protons. For one thing, *Ucp3*$^{-/-}$ mice have no obvious physical or metabolic phenotype and there is no difference in whole body metabolic rate compare to WT animals, suggesting no role for UCP3 in determining basal metabolic rate (Carroll and Porter, 2004). While the structure of UCP1 is highly conserved in UCP3, one of the His residues proposed to be vital for proton transport in UCP1 is not

conserved (His147, FA proton-buffering model), indicating that UCP3 may not be a proton transporter, may use a different mechanism or may only sustain a reduced proton transport (Bienengraeber *et al*., 1998). The inhibition of UCP3 also appears to differ from that of UCP1. While almost all of the residues reported to be essential for the binding of GDP to UCP1 are conserved in UCP3, it has been reported that only UCP1 experiences nucleotide binding and this inhibitory regulation is not seen in UCP3 (Boss *et al*., 1998) or at least remains to be demonstrated [it has been reported in UCP2, however (Berardi and Chou, 2014)]. According to Vidal-Puig *et al*. (2000), UCP2 and UCP3 activities are inhibited by purine nucleotides but in contrast to UCP1, require much higher concentrations of purine nucleotides for inhibition and the maximal degree of inhibition is significantly less. Still, this would raise questions about the physiological relevance of this inhibition and support an alternative function for UCP3. Some studies have suggested that UCP3 can transport other molecules such as chloride anions, keto-acids (Robinson *et al*., 2008) and lipid hydroperoxides (Lombardi *et al*., 2010). *In vitro* work of UCP2 and UCP3 overexpressed in cells also found that Ca^{2+} was transported over the MIM into the MM (Trenker *et al*., 2007; Graier *et al*., 2008), although these reports were contested by Brookes *et al*. (2008). Further work is required to decipher the physiological substrate (if any) of this MIM 'transporter'.

4.4 Conclusion

The focus of the work presented in this chapter was to explore the role of UCP3 in $CD4^+$ T cell metabolism. Following our observations in Chapter 3 of perturbed *Ucp3*$^{-/-}$ T_H0 cell function, it was hypothesized that *Ucp3* ablation may impact T cell metabolism. If UCP3 were to act as an uncoupling protein, it was postulated that this would be evident in the metabolic parameters of *Ucp3*-ablated cells. On the contrary, no effects of *Ucp3* ablation are found on naive, T_H0 or T_H17 cell respiration or glycolysis for that matter. UCP3 has been implicated in FAO and lipid partitioning in SKM (Garcia-Martinez *et al*., 2001; Schrauwen *et al*., 2001). T_{reg} cells, which rely heavily on FAO as their primary metabolic pathway, are metabolically unaffected by *Ucp3* ablation, despite our observations of altered T_{reg} cell generation in Chapter 3. Additionally, in stark contrast to the numerous reports that claim a regulatory role in ROS production for the UCPs, the mitochondrial membrane potential of, and ROS production by, naive $CD4^+$ T cells are unaffected by *Ucp3* ablation. The lack of effect of *Ucp3* ablation on T cell metabolism shown here suggests that UCP3 does not uncouple T cell mitochondria nor does it demonstrably appear to participate in T cell energy metabolism. It may have an alternative role or even a redundant one or it simply may not have been activated in our experimental setup. In other research reports, it is still under debate whether UCP3 is a true uncoupling protein. As of yet, we are unsure as to how UCP3 functions to restrict TCR signalling and T cell activation and how *Ucp3* ablation emanates in altered T cell function through early activation without impacting the metabolism of these cells. The conclusion that can be drawn from our results is that it does not catalyse a proton leak in $CD4^+$ T cells and, therefore, does not act as an uncoupling protein in these cells.

Chapter 5:

Ucp3 Ablation Alters CD4^{+} T Cell Function *In Vivo*

Chapter 5

Ucp3 Ablation Alters CD4$^+$ T Cell Function *In Vivo*

5.1 Introduction

Our laboratory has reported evidence of UCP3 expression in murine thymocytes, spleen mitochondria and the lymphocyte fraction of the spleen (Carroll and Porter, 2004) and has previously shown that ablation of *Ucp3* alters the T cell profile of both thymus and spleen (Kelly and Porter, 2011). We have demonstrated in Chapter 3 that *Ucp3* is rapidly downregulated in mature CD4$^+$ T cells at the mRNA level following TCR and CD28 co-receptor stimulation and that *Ucp3* ablation alters the function of non-polarized and polarized CD4$^+$ T cells, whilst having no obvious effect on mature CD4$^+$ T cell metabolism, as shown in Chapter 4. Our data demonstrate that UCP3 plays a role in restricting TCR signalling and T cell activation. We hypothesize that UCP3 acts as a rheostat to inhibit the magnitude of TCR activation and fine-tunes the TCR and CD28 signal; hence its expression in naive CD4$^+$ T cells and subsequent downregulation after cell stimulation. Following activation, TCR signals may block or switch off *Ucp3* gene expression within 4 h, as suggested by our RT-PCR data, in order to negate the dampening effect of UCP3 and allow for full activation. Ablation of *Ucp3* allows for uncontrolled early activation and appears to culminate in premature cell death, which we believe to be due to AICD. Importantly, the augmented production of IL-2 by *Ucp3*$^{-/-}$ activated T cells can perturb and reciprocally affect the generation of T_H17 and T_{reg} cells, inhibiting the former and enhancing the latter.

The above data were generated from *in vitro* experimentation. *In vitro* experiments are often performed under ideal/optimized and static conditions. In contrast, the *in vivo* setting is intrinsically dynamic and more complex. While results obtained from *in vitro* experiments are often used to predict biological responses *in vivo*, they do not always transpose as expected to the *in vivo* setting and effects can be similar or completely different to those observed *in vitro*. Thus, to investigate whether the effect of *Ucp3* ablation on activated CD4$^+$ T cells that we observe *in vitro* would be mirrored in the *in vivo* setting and to further explore the role of UCP3 in CD4$^+$ T cell function, we examined the effect of *Ucp3* ablation on CD4$^+$ T cells following adoptive transfer to immunodeficient mice and following *in vivo* activation by immunizing *Ucp3*$^{+/+}$ and *Ucp3*$^{-/-}$ mice, the results of which are presented here.

5.2 Results

5.2.1 *Ucp3*$^{-/-}$ CD4^{+} T Cells Undergo Increased Homeostatic Proliferation *In Vivo*

We have shown that viable *Ucp3*$^{-/-}$ T_H0 cells proliferate at an increased rate compared to *Ucp3*$^{+/+}$ T_H0 cells *in vitro* (Section 3.2.3). To examine this phenomenon *in vivo*, we performed an adoptive transfer of CellTrace™ Violet-labelled *Ucp3*$^{+/+}$ and *Ucp3*$^{-/-}$ naive CD4^{+} T cells to immunodeficient *Rag1*$^{-/-}$ mice. Following an adoptive transfer to syngeneic immunodeficient mice, naive T cells are known to undergo homeostatic expansion and home towards the gut microbiome (Kieper *et al*., 2005). As mentioned previously, CellTrace™ Violet labelling permits the determination of the number of generations through which a cell has progressed since the label was applied. Seven days after the adoptive transfer was performed, splenocytes were extracted from host mice, labelled with PE-Cy7:anti-CD4 and the homeostatic proliferation of *Ucp3*$^{+/+}$ and *Ucp3*$^{-/-}$ cells was measured and compared by flow cytometry.

Ucp3$^{+/+}$ and *Ucp3*$^{-/-}$ CD4^{+} T cells undergo a number of rounds of cell division following adoptive transfer to host *Rag1*$^{-/-}$ mice, as seen by diluted CellTrace™ Violet labelling (Figure 5.1A). However, significantly more *Ucp3*$^{-/-}$ CD4^{+} T cells undergo a higher number of cell divisions than their WT counterparts, while significantly more *Ucp3*$^{+/+}$ CD4^{+} T cells undergo lower numbers of cell divisions than their KO counterparts *in vivo* (Figure 5.1B). This is in line with and supports our previous finding that *Ucp3*$^{-/-}$ T_H0 cells proliferate more than *Ucp3*$^{+/+}$ T_H0 cells *in vitro* (Section 3.2.3) and suggests that *Ucp3*$^{-/-}$ T cells may produce more IL-2 following activation *in vivo*, as seen *in vitro*, which would promote this increased proliferation effect.

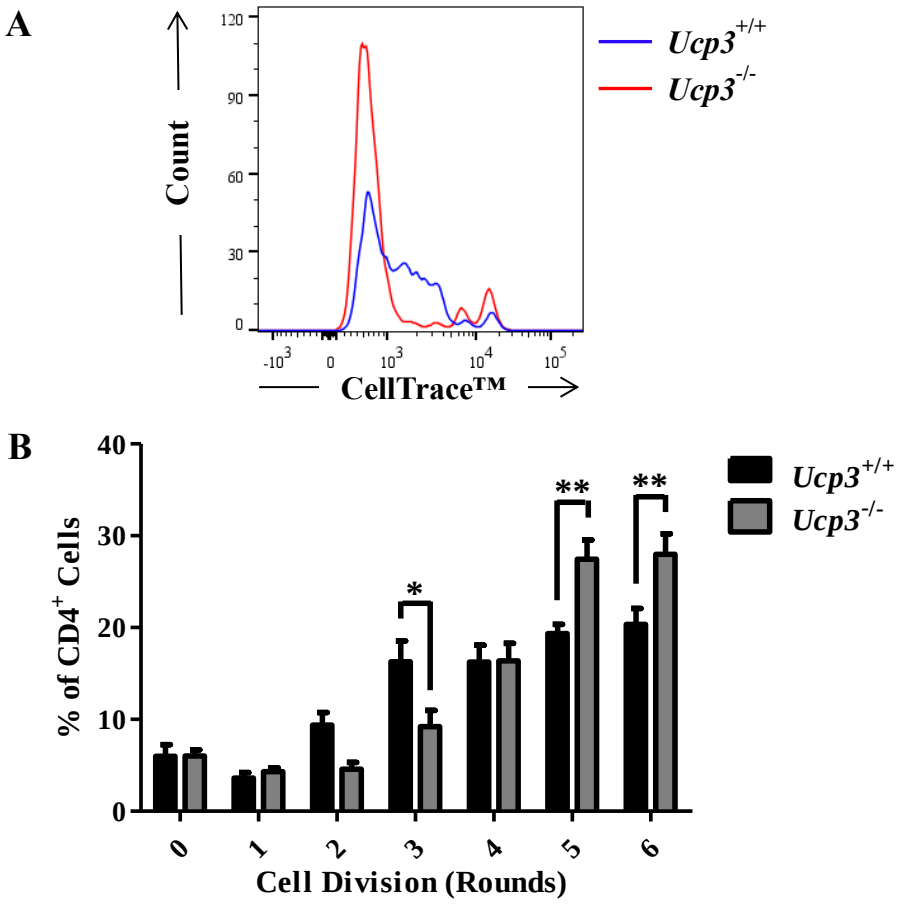

Figure 5.1: *Ucp3*$^{-/-}$ CD4^{+} T cells display greater proliferation 7 days post-adoptive transfer to *Rag1*$^{-/-}$ host mice

CD4^{+} T cells were isolated from *Ucp3*$^{+/+}$ and *Ucp3*$^{-/-}$ mice, labelled with CellTrace™ Violet and adoptively transferred to *Rag1*$^{-/-}$ mice (2 x 10^6 cells per mouse). After 7 days, splenocytes were isolated from host mice, stained with PE-Cy7:anti-CD4 and analysed on a flow cytometer. Flow cytometry was performed once in triplicate. (A) Histogram is representative of *Ucp3*$^{+/+}$ (n = 3 mice) and *Ucp3*$^{-/-}$ (n = 4 mice) samples. Data are of the total CD4^{+} T cell population. (B) Data are presented as a percentage of the total CD4^{+} T cell population. Data were analysed using a two-way ANOVA with a *post hoc* Bonferroni test to quantify significance where detected. * = $p < 0.05$. ** = $p < 0.01$.

5.2.2 *Ucp3* Ablation Alters T_{reg} Cell Frequency and $CD4^+$ T Cell Antigen Recall Responses *In Vivo*

We have shown that *Ucp3* ablation alters the T_H17:T_{reg} cell ratio *in vitro* by mitigating the function of T_H17 cells and enhancing the generation of $FoxP3^+$ T_{reg} cells (Section 3.2.6). We believe that this is due to increased IL-2 production by $Ucp3^{-/-}$ cells, as IL-2 is known to inhibit and promote the generation of T_H17 and T_{reg} cells, respectively (Laurence *et al*., 2007; Boyman and Sprent, 2012; Liao *et al*., 2013). However, it is important to confirm if this is the case *in vivo*. To explore whether this perturbation would translate to the *in vivo* setting, we immunized $Ucp3^{+/+}$ and $Ucp3^{-/-}$ mice with keyhole limpet hemocyanin (KLH) antigen with or without the adjuvant, cholera toxin (CT). Recent reports have described the strongly augmented production of IL-6 by DCs following *in vitro* and *in vivo* treatment with CT, culminating in the potent T_H17 cell-driving activity of CT (Lee *et al*., 2009; Tsai and Wu, 2015). Accordingly, as we have observed modulated $Ucp3^{-/-}$ T_H17 cell activity, CT was chosen as an appropriate adjuvant for this work.

Mice were immunized on days 0 and 14. On day 21, splenocytes and draining lymph node cells were isolated from immunized mice. Splenocytes were labelled with LIVE/DEAD™, PE-Cy7:anti-CD4, eFluor™ 660:anti-CD25, PerCP-eFluor™ 710:anti-LAP, FITC:anti-LAG3 and/or PE:anti-FoxP3 and analysed immediately *ex vivo* by flow cytometry for viability and $FoxP3^+$ T_{reg} cell frequency. Additionally, splenocytes and lymph node cells were incubated in the presence of media (negative control), anti-CD3 (positive control) or KLH for antigenic restimulation to detect antigen-specific recall responses. Supernatants were collected after 72 h and analysed by ELISA for the secretion of IFN-γ, IL-17A and IL-10, the characteristic cytokines produced by T_H1, T_H17 and regulatory T cells, respectively (Pulendran and Ahmed, 2006; Boyman and Sprent, 2012; Gregori *et al*., 2012; Liao *et al*., 2013). Lymph node cell viability and $FoxP3^+$ T_{reg} cell frequency were also analysed by flow cytometry following the 72 h incubation period, as outlined for splenocytes above.

Similar to our observations of freshly isolated $CD4^+$ T cells from non-immunized mice in Section 3.2.4, no differences in viability (Figure 5.2) or cell size (Figure 5.3) are observed between freshly isolated $Ucp3^{+/+}$ and $Ucp3^{-/-}$ splenic $CD4^+$ T cells from immunized mice, regardless of whether mice were immunized with antigen and adjuvant or antigen alone. In contrast, significant differences are observed in the frequency of $CD25^+FoxP3^+$ T_{reg} cells. The frequency of splenic $CD25^+FoxP3^+$ T_{reg} cells in $Ucp3^{-/-}$ mice immunized with antigen

plus adjuvant (KLH plus CT) is significantly higher than that observed in *Ucp3*$^{+/+}$ mice immunized with same, as well as *Ucp3*$^{-/-}$ mice immunized with antigen only (Figure 5.4). This corresponds to our *in vitro* observation of enhanced FoxP3^{+} T_{reg} cell generation from CD4^{+} T cells isolated from *Ucp3*-ablated mice (Section 3.2.6). As described in Chapter 3, FoxP3^{+} T_{reg} cells can regulate effector T cells by expressing TGF-β on their cell surface in complex with LAP (Duan *et al*., 2011; Gregori *et al*., 2012). Thus, TGF-β production can be measured indirectly by staining for LAP and analysing by FACS. Another mechanism often used by FoxP3^{+} T_{reg} cells to suppress inflammation is the prevention of DC activation by sending inhibitory signals through the interaction of T_{reg} cell-expressed LAG3 with MHC class II molecules on the DC surface (Gregori *et al*., 2012). No significant differences in the expression of LAP (Figure 5.5) or LAG3 (Figure 5.6) by *Ucp3*$^{+/+}$ and *Ucp3*$^{-/-}$ FoxP3^{+} T_{reg} cells are observed, irrespective of the immunization received previously, although this may be expected as no differences in LAP and LAG3 expression are evident *in vitro* following T_{reg} cell generation (Section 3.2.6).

IFN-γ secretion by splenocytes was measured 72 h post-incubation with 2, 10 or 50 μg.mL^{-1} of KLH (Figures 5.7A, B and C, respectively). Although there seems to be a trend for less IFN-y secretion by *Ucp3*$^{-/-}$ cells compared to the corresponding *Ucp3*$^{+/+}$ cells, this is not statistically significant. This is reflective of our *in vitro* observation in Section 3.2.5; IFN-γ secretion by *Ucp3*$^{+/+}$ and *Ucp3*$^{-/-}$ T_H1 cells generated *in vitro* is not significantly different. Additionally, CT is known to suppress a T_H1-type immunogenic response following immunization, even in the presence of a T_H1-promoting antigen such as LPS (Lavelle *et al*., 2003, 2004; Kang *et al*., 2016). Thus, a lack of enhanced secretion of IFN-γ by *Ucp3*$^{+/+}$ and *Ucp3*$^{-/-}$ cells is to be expected following immunization with KLH plus CT compared to KLH alone. In contrast to IFN-γ, marked differences in the secretion of IL-17A by *Ucp3*$^{+/+}$ and *Ucp3*$^{-/-}$ splenocytes are observed. *Ucp3*$^{+/+}$ cells from mice immunized with KLH plus CT secrete significantly more IL-17A than *Ucp3*$^{+/+}$ cells from mice immunized with KLH alone (Figure 5.8). This is observed consistently following incubation in the presence of 2, 10 and 50 μg.mL^{-1} of KLH for 72 h and indicates that the immune response of *Ucp3*$^{+/+}$ mice immunized with CT as well as KLH was successfully enhanced compared to those receiving KLH alone due to CT's promotion of a T_H17-type response, mentioned previously (Lee *et al*., 2009; Tsai and Wu, 2015). Interestingly, these differences are not observed in *Ucp3*$^{-/-}$ splenocytes. Additionally, IL-17A secretion by *Ucp3*$^{-/-}$ cells from mice immunized with both KLH and CT is significantly less than that by *Ucp3*$^{+/+}$ cells following incubation with 2 (Figure 5.8A) and 50 (Figure 5.8C) μg.mL^{-1} of KLH for 72 h. This

reflects our data of T_H17 cells generated *in vitro*; *Ucp3*$^{-/-}$ T_H17 cells secrete significantly less IL-17A than their WT counterparts, presumably due to the increased production of IL-2 by *Ucp3*-ablated cells inhibiting T_H17 cell differentiation and constraining IL-17A production (Section 3.2.6; Laurence *et al*., 2007; Boyman and Sprent, 2012; Liao *et al*., 2013). No significant difference in IL-10 secretion is observed between *Ucp3*$^{+/+}$ and *Ucp3*$^{-/-}$ cells, regardless of KLH concentration or the type of immunization that mice had received (Figure 5.9), although there seems to be a trend for less IL-10 secretion by *Ucp3*$^{-/-}$ cells than the corresponding *Ucp3*$^{+/+}$ cells. We previously observed decreased IL-10 production by *Ucp3*$^{-/-}$ $CD4^+$ T cells under T_{reg} polarizing conditions *in vitro* (Section 3.2.6). No significant differences may be observed in the *in vivo* immunization results presented here due to the presence of outliers that may be skewing the data and masking any potential significant differences.

Flow cytometry was performed on lymph node cells following 72 h of incubation in the presence of 50 $\mu g.mL^{-1}$ of KLH. *Ucp3*$^{+/+}$ and *Ucp3*$^{-/-}$ lymph node cell samples from mice immunized with KLH or mice immunized with KLH plus CT were pooled together. For this reason, no statistical analysis could be performed on flow cytometry data of lymph node cells. Viability of *Ucp3*$^{-/-}$ lymph node cells from both mice immunized with KLH and mice immunized with KLH plus CT is greater than that of *Ucp3*$^{+/+}$ lymph node cells (Figure 5.10A and B). It is possible that the cells isolated from lymph nodes of *Ucp3*$^{-/-}$ mice were not (yet) undergoing AICD as one might have expected following 72 h of stimulation with KLH and increased IL-2 production from these cells may have been promoting their survival similar to that observed in *Ucp3*$^{-/-}$ T_H0 cells 24 h post-stimulation *in vitro* (Section 3.2.3). From a retrospective viewpoint, measuring IL-2 secretion by ELISA would have been a useful, additional experiment to perform. Apart from the apparent difference in viability of *Ucp3*$^{+/+}$ and *Ucp3*$^{-/-}$ lymph node cells isolated from mice immunized with KLH alone or KLH plus CT, no other differences are apparent between these groups. Cell size (Figure 5.10C and D), $CD25^+FoxP3^+$ T_{reg} cell frequency (Figure 5.11), LAP and LAG3 expression of $FoxP3^+$ T_{reg} cells (Figures 5.12 and 5.13, respectively) and secretion of IFN-γ, IL-17A and IL-10 (Figures 5.14A – C, respectively) are comparable between groups with no significant differences evident. It is plausible that the *Ucp3*$^{-/-}$ cells displaying functional differences following immunization had migrated to the spleen by the time cell extraction was performed on day 21. Indeed, it may have been interesting to perform the above investigation at earlier and later time points after the final immunization.

The above data convey that *Ucp3* ablation alters $CD4^+$ T cell function *in vivo* in a manner similar to that observed *in vitro* and reported in Chapter 3. This indication is reassuring as *in vitro* experiment results do not always translate to the *in vivo* setting as one may predict. UCP3 appears to play a role in restricting TCR signalling and T cell activation and its ablation can perturb and reciprocally affect the generation of T_H17 and T_{reg} cells *in vivo*, inhibiting the former and enhancing the latter.

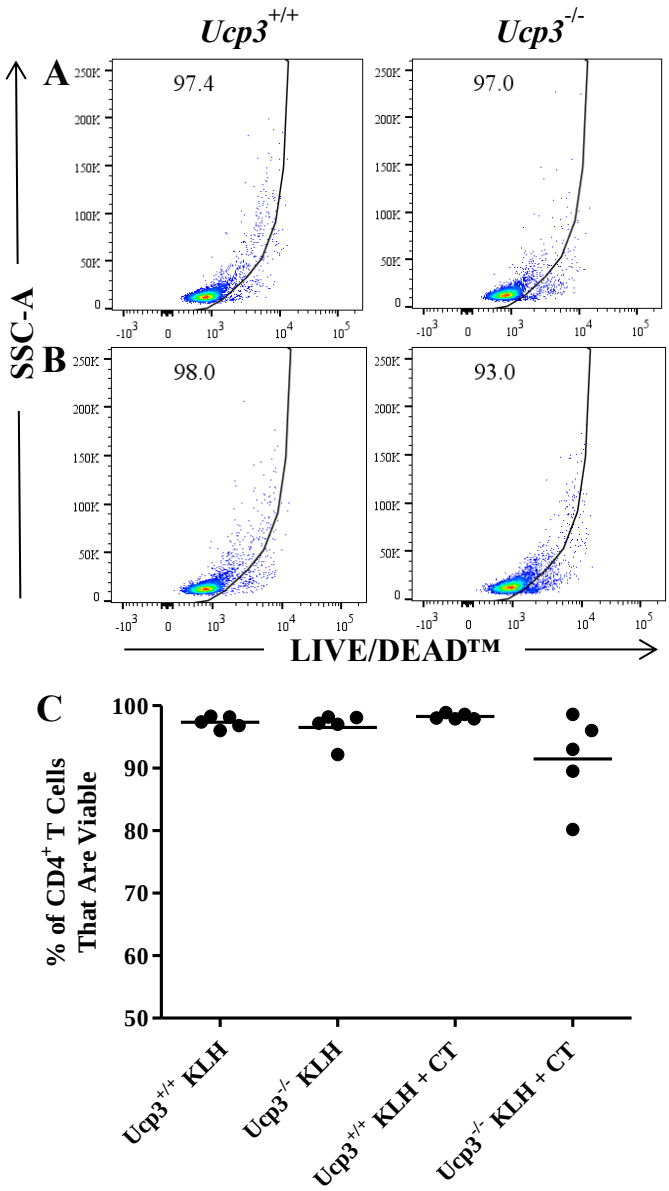

Figure 5.2: Viability of splenic CD4$^+$ T cells from *Ucp3*$^{+/+}$ and *Ucp3*$^{-/-}$ immunized mice is comparable

Ucp3$^{+/+}$ and *Ucp3*$^{-/-}$ mice were immunized with 1 µg of KLH (A) or 1 µg of KLH and CT (B) on day 0 and re-immunized on day 14. On day 21, splenocytes were isolated from immunized mice, stained with LIVE/DEAD™ and PE-Cy7:anti-CD4 and analysed on a flow cytometer. Flow cytometry was performed once in quintuplicate. Dot plots are representative of *Ucp3*$^{+/+}$ and *Ucp3*$^{-/-}$ samples (n = 5). All data are presented as a percentage of the total CD4$^+$ T cell population. (C) Data were analysed using a two-way ANOVA with a *post hoc* Bonferroni test to quantify significance where detected.

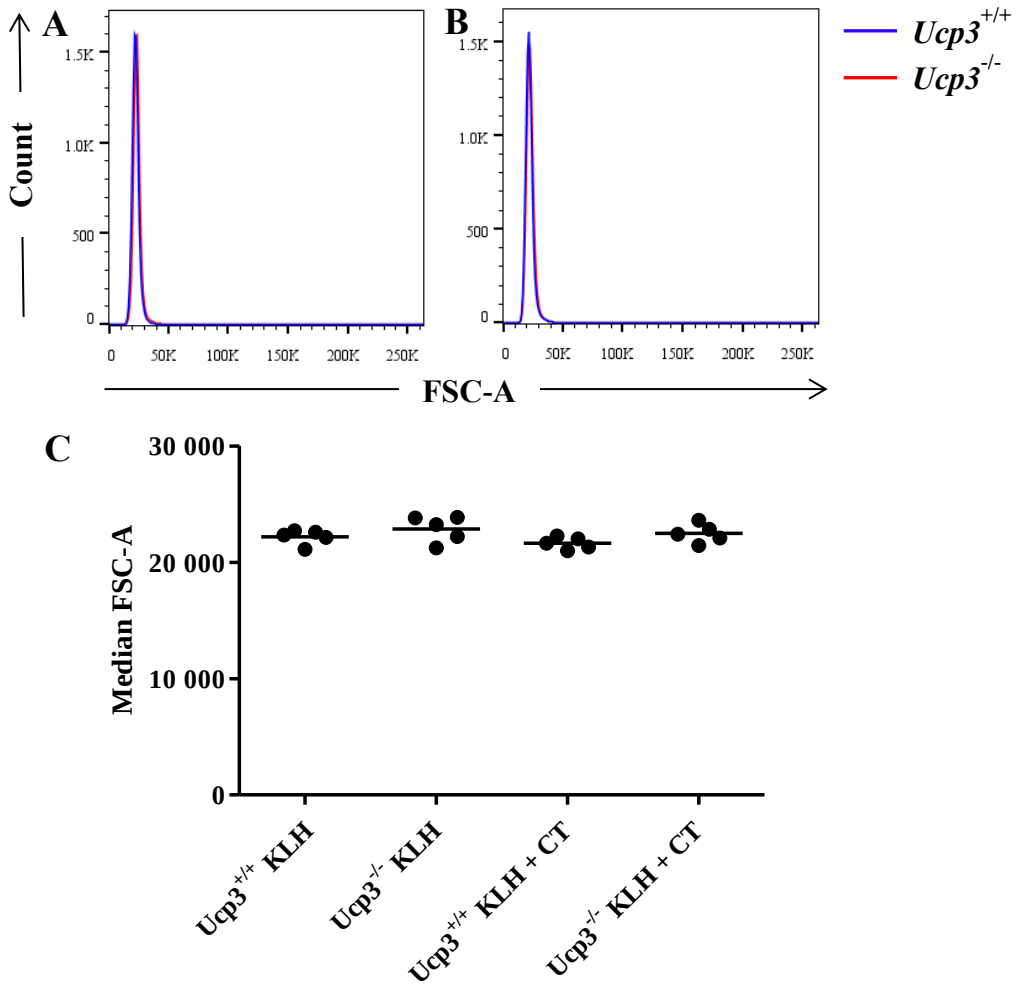

Figure 5.3: Size of splenic CD4$^+$ T cells from *Ucp3*$^{+/+}$ and *Ucp3*$^{-/-}$ immunized mice is comparable

Ucp3$^{+/+}$ and *Ucp3*$^{-/-}$ mice were immunized with 1 µg of KLH (A) or 1 µg of KLH and CT (B) on day 0 and re-immunized on day 14. On day 21, splenocytes were isolated from immunized mice, stained with LIVE/DEAD™ and PE-Cy7:anti-CD4 and analysed on a flow cytometer. Flow cytometry was performed once in quintuplicate. Histograms are representative of *Ucp3*$^{+/+}$ and *Ucp3*$^{-/-}$ samples (n = 5). All data are of the viable, CD4$^+$ T cell population. (C) Data were analysed using a two-way ANOVA with a *post hoc* Bonferroni test to quantify significance where detected.

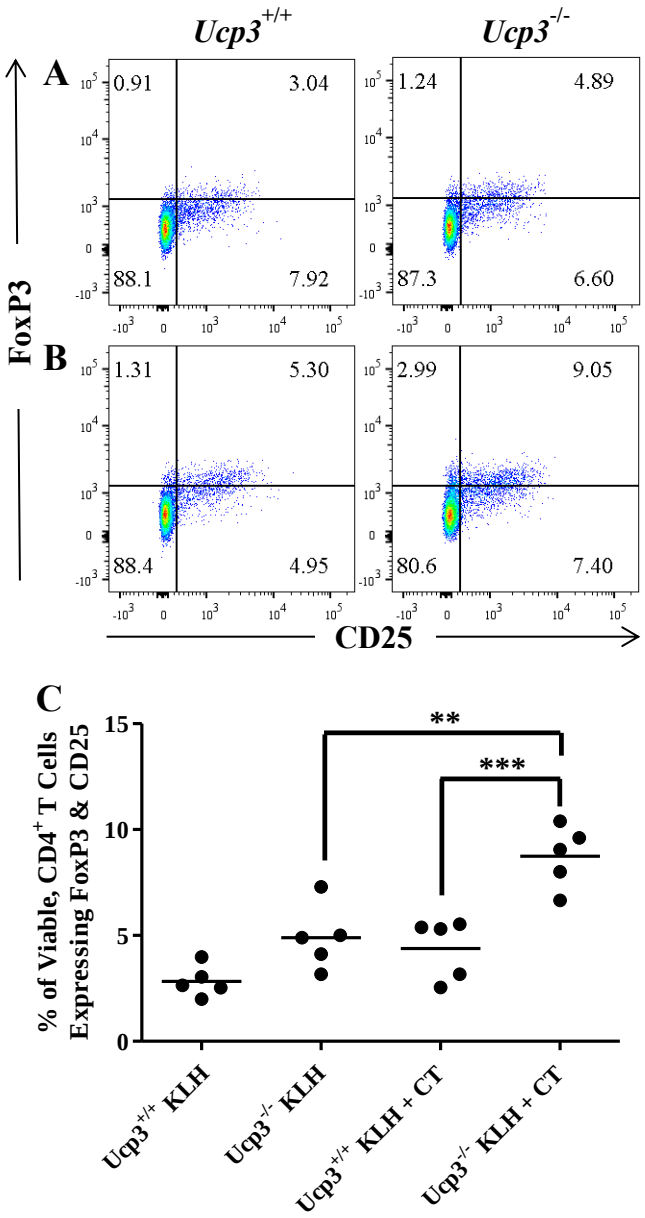

Figure 5.4: Frequency of splenic CD25$^+$FoxP3$^+$ T$_{reg}$ cells is higher in *Ucp3*$^{-/-}$ immunized mice

Ucp3$^{+/+}$ and *Ucp3*$^{-/-}$ mice were immunized with 1 µg of KLH (A) or 1 µg of KLH and CT (B) on day 0 and re-immunized on day 14. On day 21, splenocytes were isolated from immunized mice, stained with LIVE/DEAD™, PE-Cy7:anti-CD4, eFluor™ 660:anti-CD25 and PE:anti-FoxP3 and analysed on a flow cytometer. Flow cytometry was performed once in quintuplicate. Dot plots are representative of *Ucp3*$^{+/+}$ and *Ucp3*$^{-/-}$ samples (n = 5). All data are presented as a percentage of the viable, CD4$^+$ T cell population. (C) Data were analysed using a two-way ANOVA with a *post hoc* Bonferroni test to quantify significance where detected. ** = $p < 0.01$. *** = $p < 0.001$.

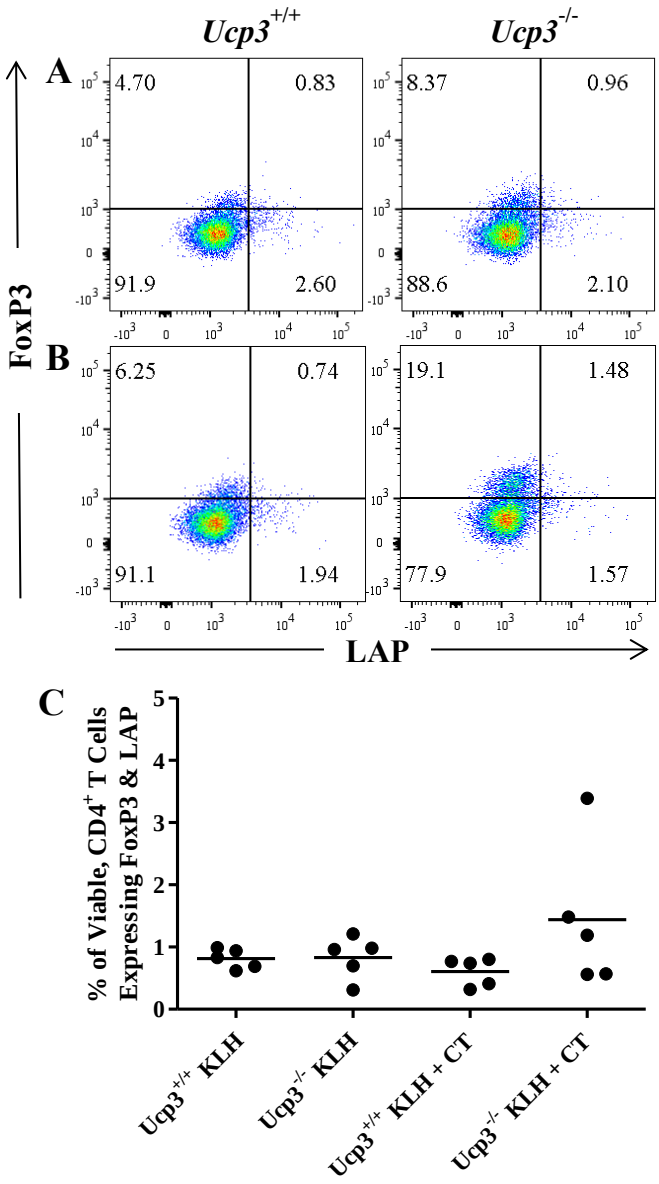

Figure 5.5: LAP expression of splenic FoxP3$^+$ T$_{reg}$ cells from *Ucp3*$^{+/+}$ and *Ucp3*$^{-/-}$ immunized mice is comparable

Ucp3$^{+/+}$ and *Ucp3*$^{-/-}$ mice were immunized with 1 µg of KLH (A) or 1 µg of KLH and CT (B) on day 0 and re-immunized on day 14. On day 21, splenocytes were isolated from immunized mice, stained with LIVE/DEAD™, PE-Cy7:anti-CD4, PerCP-eFluor™ 710:anti-LAP and PE:anti-FoxP3 and analysed on a flow cytometer. Flow cytometry was performed once in quintuplicate. Dot plots are representative of *Ucp3*$^{+/+}$ and *Ucp3*$^{-/-}$ samples (n = 5). All data are presented as a percentage of the viable, CD4$^+$ T cell population. (C) Data were analysed using a two-way ANOVA with a *post hoc* Bonferroni test to quantify significance where detected.

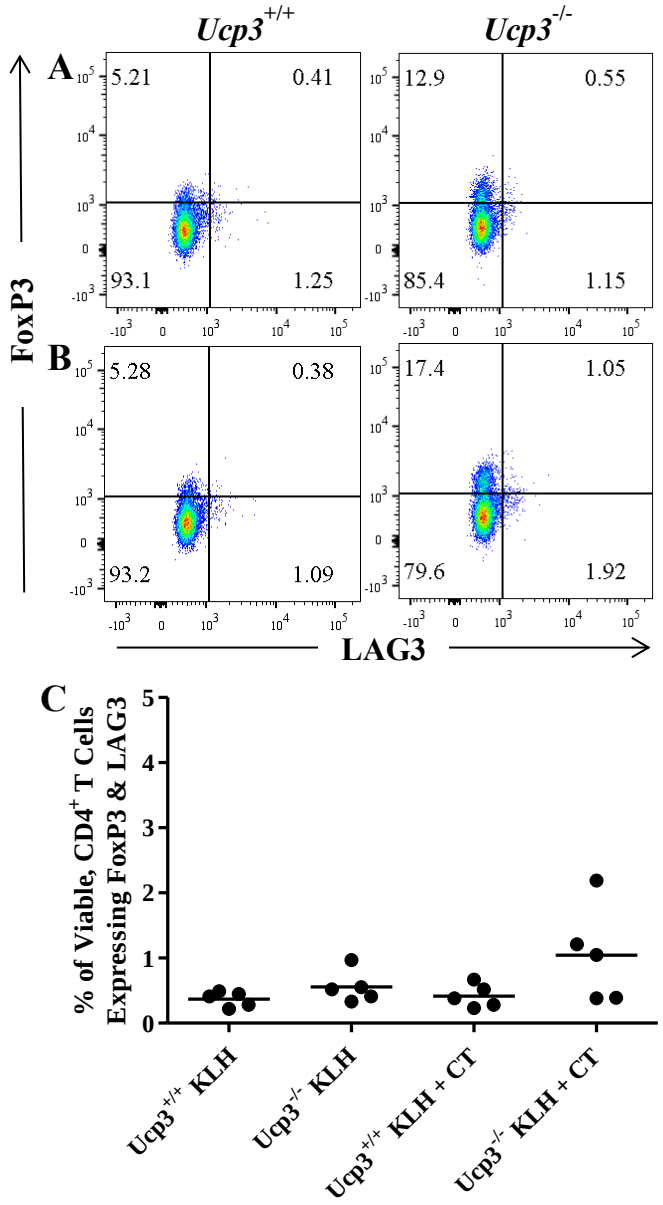

Figure 5.6: LAG3 expression of splenic FoxP3$^+$ T$_{reg}$ cells from *Ucp3*$^{+/+}$ and *Ucp3*$^{-/-}$ immunized mice is comparable

Ucp3$^{+/+}$ and *Ucp3*$^{-/-}$ mice were immunized with 1 µg of KLH (A) or 1 µg of KLH and CT (B) on day 0 and re-immunized on day 14. On day 21, splenocytes were isolated from immunized mice, stained with LIVE/DEAD™, PE-Cy7:anti-CD4, FITC:anti-LAG3 and PE:anti-FoxP3 and analysed on a flow cytometer. Flow cytometry was performed once in quintuplicate. Dot plots are representative of *Ucp3*$^{+/+}$ and *Ucp3*$^{-/-}$ samples (n = 5). All data are presented as a percentage of the viable, CD4$^+$ T cell population. (C) Data were analysed using a two-way ANOVA with a *post hoc* Bonferroni test to quantify significance where detected.

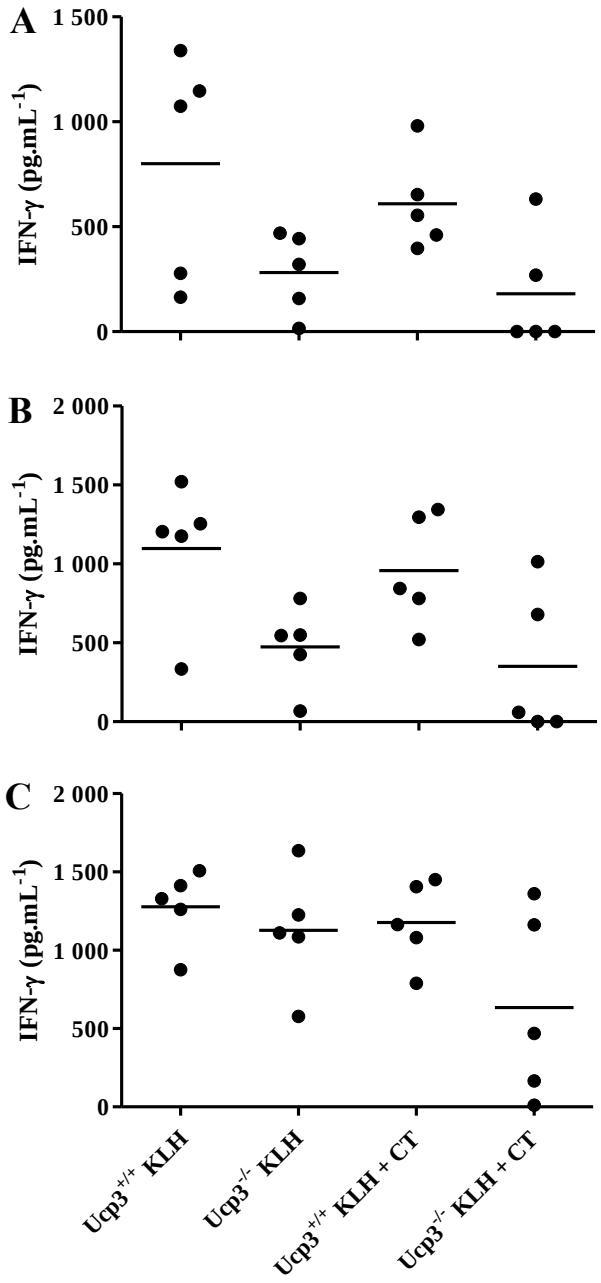

Figure 5.7: IFN-γ secretion by splenocytes from *Ucp3*$^{+/+}$ and *Ucp3*$^{-/-}$ immunized mice is comparable

Ucp3$^{+/+}$ and *Ucp3*$^{-/-}$ mice were immunized with 1 µg of KLH or 1 µg of KLH and CT on day 0 and re-immunized on day 14. On day 21, splenocytes were isolated from immunized mice and incubated in the presence of 2 (A), 10 (B) or 50 (C) µg.mL^{-1} of KLH for 72 h. ELISA was performed once in triplicate. Data are presented as mean concentration of IFN-γ. Data were analysed using a two-way ANOVA with a *post hoc* Bonferroni test to quantify significance where detected.

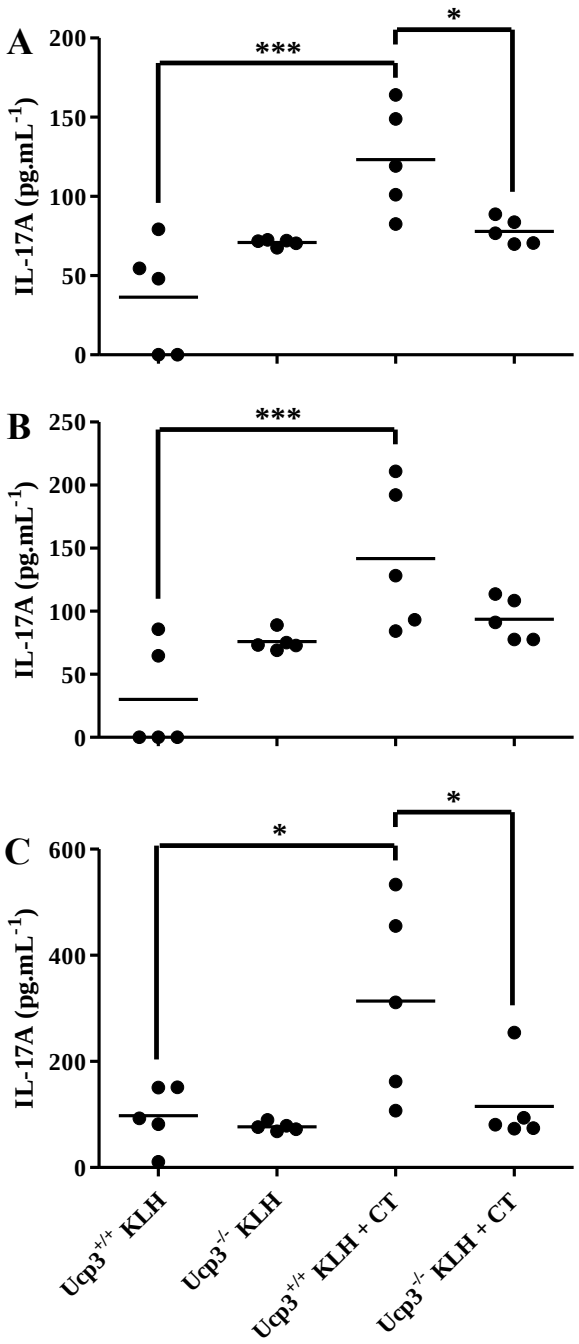

Figure 5.8: Splenocytes from *Ucp3*$^{-/-}$ mice immunized with KLH and CT secrete less IL-17A

Ucp3$^{+/+}$ and *Ucp3*$^{-/-}$ mice were immunized with 1 µg of KLH or 1 µg of KLH and CT on day 0 and re-immunized on day 14. On day 21, splenocytes were isolated from immunized mice and incubated in the presence of 2 (A), 10 (B) or 50 (C) µg.mL^{-1} of KLH for 72 h. ELISA was performed once in triplicate. Data are presented as mean concentration of IL-17A. Data were analysed using a two-way ANOVA with a *post hoc* Bonferroni test to quantify significance where detected. * = $p < 0.05$. *** = $p < 0.001$.

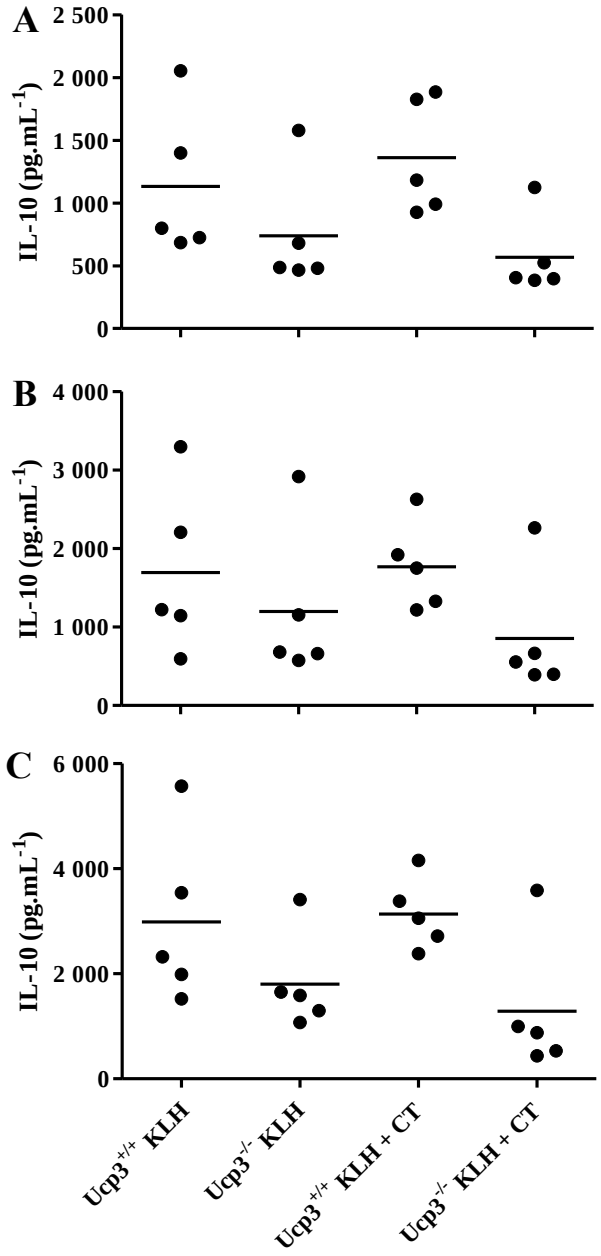

Figure 5.9: IL-10 secretion by splenocytes from *Ucp3*$^{+/+}$ and *Ucp3*$^{-/-}$ immunized mice is comparable

Ucp3$^{+/+}$ and *Ucp3*$^{-/-}$ mice were immunized with 1 µg of KLH or 1 µg of KLH and CT on day 0 and re-immunized on day 14. On day 21, splenocytes were isolated from immunized mice and incubated in the presence of 2 (A), 10 (B) or 50 (C) µg.mL^{-1} of KLH for 72 h. ELISA was performed once in triplicate. Data are presented as mean concentration of IL-10. Data were analysed using a two-way ANOVA with a *post hoc* Bonferroni test to quantify significance where detected.

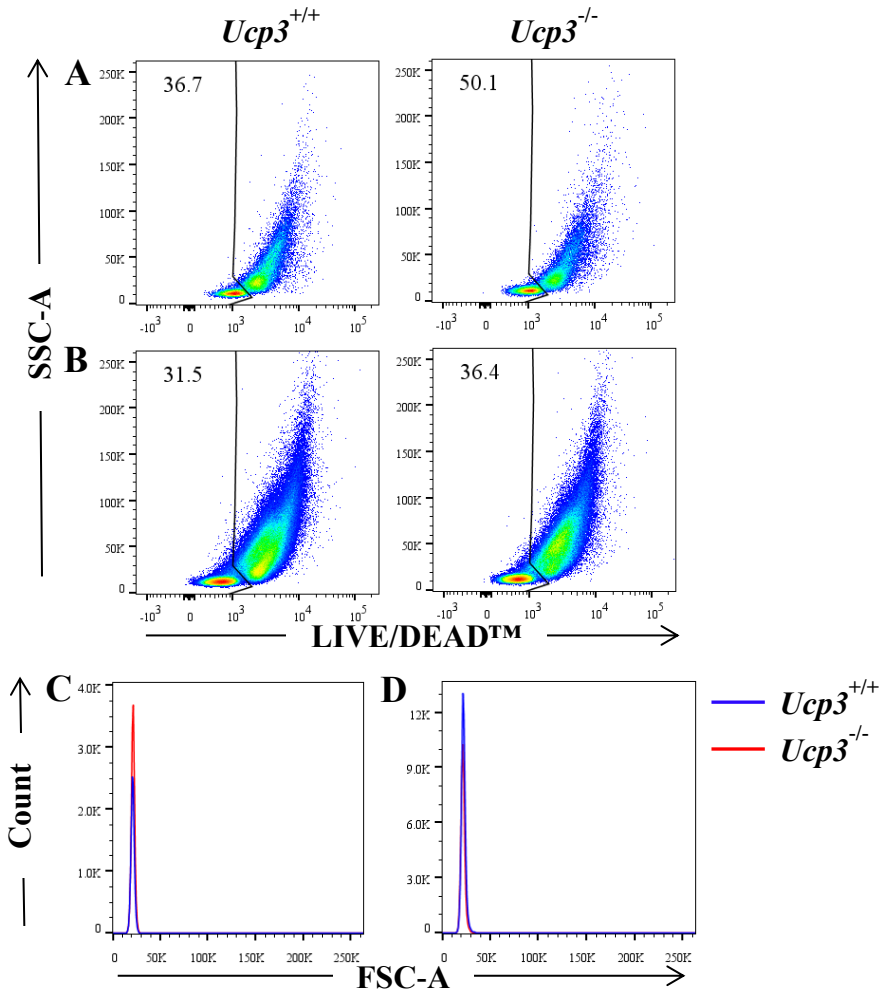

Figure 5.10: CD4$^+$ T cells isolated from lymph nodes of *Ucp3*$^{-/-}$ immunized mice display greater viability

Ucp3$^{+/+}$ and *Ucp3*$^{-/-}$ mice were immunized with 1 µg of KLH (A, C) or 1 µg of KLH and CT (B, D) on day 0 and re-immunized on day 14. On day 21, lymph node cells were isolated from immunized mice, incubated in the presence of 50 µg.mL^{-1} of KLH for 72 h and stained with LIVE/DEAD™ and PE-Cy7:anti-CD4 before being analysed on a flow cytometer. Flow cytometry was performed once. Dot plots and histograms are of pooled *Ucp3*$^{+/+}$ and *Ucp3*$^{-/-}$ lymph node cell samples (n = 5). (A, B) Data are presented as a percentage of the total CD4$^+$ T cell population. (C, D) Data are of the viable, CD4$^+$ T cell population.

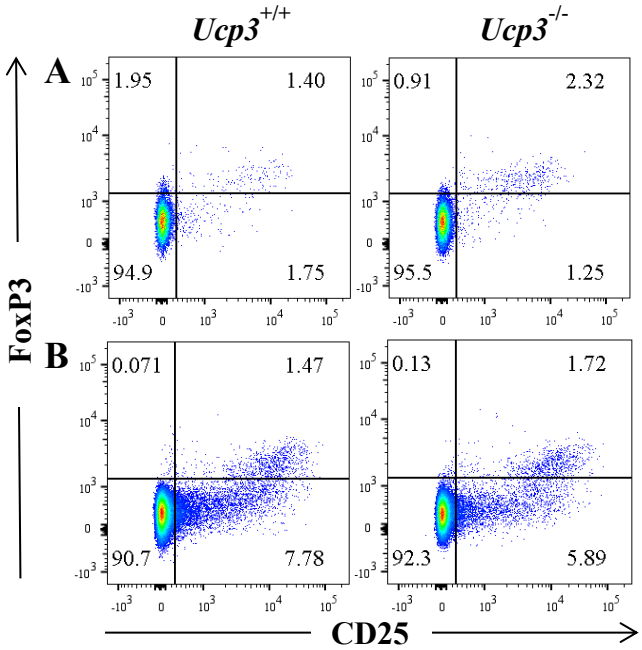

Figure 5.11: Frequency of CD25^{+}FoxP3^{+} T$_{reg}$ cells in lymph nodes of *Ucp3*$^{+/+}$ and *Ucp3*$^{-/-}$ immunized mice is comparable

Ucp3$^{+/+}$ and *Ucp3*$^{-/-}$ mice were immunized with 1 µg of KLH (A) or 1 µg of KLH and CT (B) on day 0 and re-immunized on day 14. On day 21, lymph node cells were isolated from immunized mice, incubated in the presence of 50 µg.mL^{-1} of KLH for 72 h and stained with LIVE/DEAD™, PE-Cy7:anti-CD4, eFluor™ 660:anti-CD25 and PE:anti-FoxP3 before being analysed on a flow cytometer. Flow cytometry was performed once. Dot plots are of pooled *Ucp3*$^{+/+}$ and *Ucp3*$^{-/-}$ lymph node cell samples (n = 5). Data are presented as a percentage of the viable, CD4^{+} T cell population.

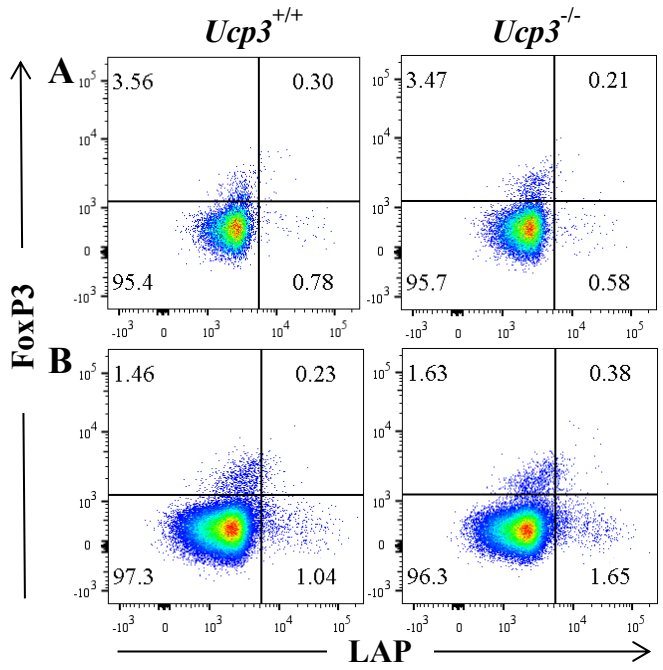

Figure 5.12: LAP expression of FoxP3$^+$ T$_{reg}$ cells from lymph nodes of *Ucp3*$^{+/+}$ and *Ucp3*$^{-/-}$ immunized mice is comparable

Ucp3$^{+/+}$ and *Ucp3*$^{-/-}$ mice were immunized with 1 µg of KLH (A) or 1 µg of KLH and CT (B) on day 0 and re-immunized on day 14. On day 21, lymph node cells were isolated from immunized mice, incubated in the presence of 50 µg.mL^{-1} of KLH for 72 h and stained with LIVE/DEAD™, PE-Cy7:anti-CD4, PerCP-eFluor™ 710:anti-LAP and PE:anti-FoxP3 before being analysed on a flow cytometer. Flow cytometry was performed once. Dot plots are of pooled *Ucp3*$^{+/+}$ and *Ucp3*$^{-/-}$ lymph node cell samples (n = 5). Data are presented as a percentage of the viable, CD4$^+$ T cell population.

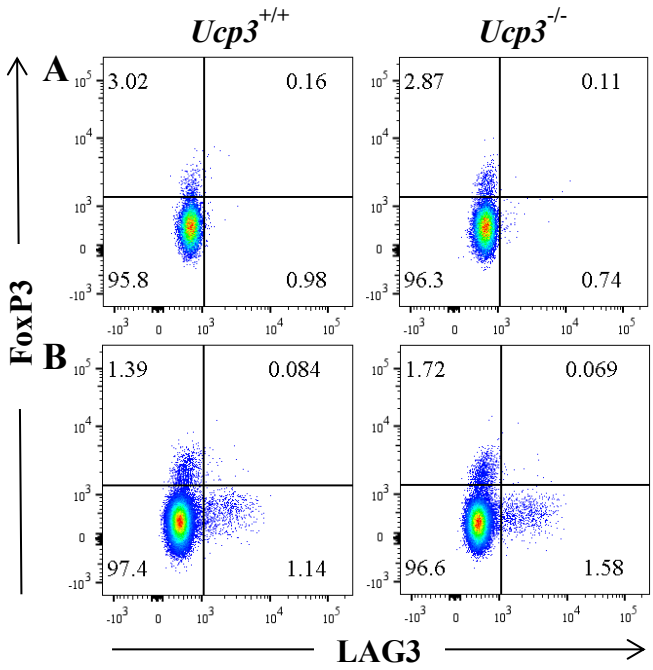

Figure 5.13: LAG3 expression of FoxP3$^+$ T$_{reg}$ cells from lymph nodes of *Ucp3*$^{+/+}$ and *Ucp3*$^{-/-}$ immunized mice is comparable

Ucp3$^{+/+}$ and *Ucp3*$^{-/-}$ mice were immunized with 1 µg of KLH (A) or 1 µg of KLH and CT (B) on day 0 and re-immunized on day 14. On day 21, lymph node cells were isolated from immunized mice, incubated in the presence of 50 µg.mL^{-1} of KLH for 72 h and stained with LIVE/DEAD™, PE-Cy7:anti-CD4, FITC:anti-LAG3 and PE:anti-FoxP3 before being analysed on a flow cytometer. Flow cytometry was performed once. Dot plots are of pooled *Ucp3*$^{+/+}$ and *Ucp3*$^{-/-}$ lymph node cell samples (n = 5). Data are presented as a percentage of the viable, CD4$^+$ T cell population.

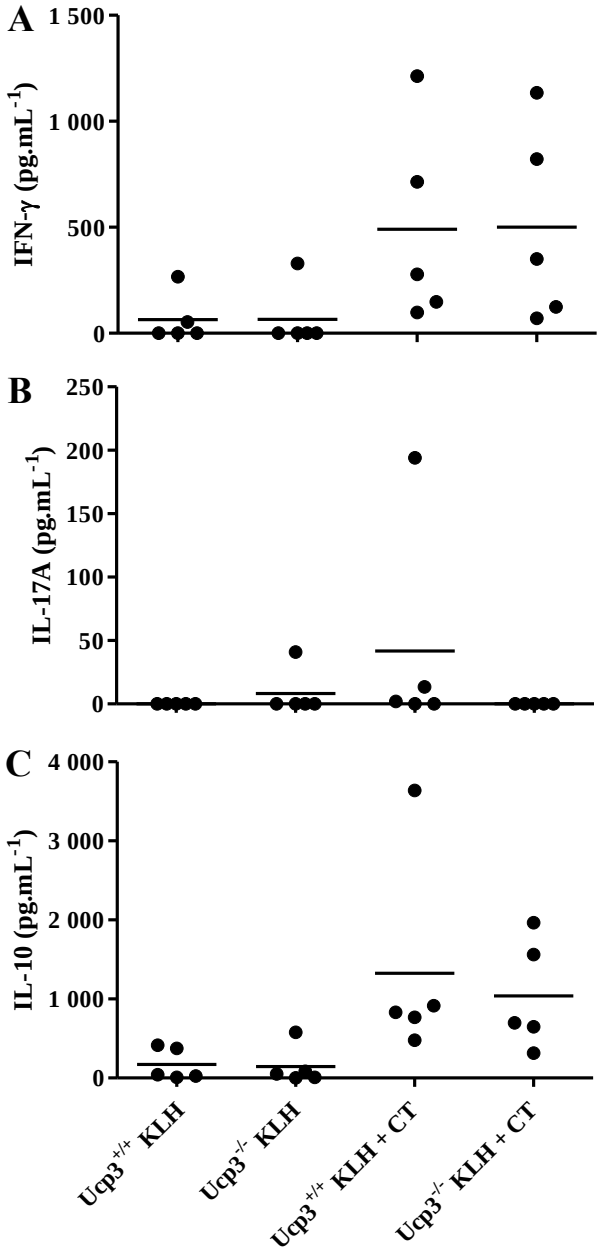

Figure 5.14: IFN-γ, IL-17A and IL-10 secretion by lymph node cells from *Ucp3*$^{+/+}$ and *Ucp3*$^{-/-}$ immunized mice is comparable

Ucp3$^{+/+}$ and *Ucp3*$^{-/-}$ mice were immunized with 1 µg of KLH or 1 µg of KLH and CT on day 0 and re-immunized on day 14. On day 21, lymph node cells were isolated from immunized mice and incubated in the presence of 50 µg.mL^{-1} of KLH for 72 h. ELISAs were performed once in triplicate. Data are presented as mean concentration of IFN-γ (A), IL-17A (B) or IL-10 (C). Data were analysed using a two-way ANOVA with a *post hoc* Bonferroni test to quantify significance where detected.

5.3 Discussion

We have shown in Chapter 3 that *Ucp3* ablation distinctly alters the function of $CD4^+$ T cells. Our *in vitro* data indicate that UCP3 plays a role in restricting TCR signalling and T cell activation. UCP3 acts as a rheostat to inhibit the magnitude of TCR activation and fine-tunes the TCR and CD28 signal, hence its expression in naive $CD4^+$ T cells and subsequent downregulation after cell stimulation. Following activation, TCR signals may block or switch off *Ucp3* gene expression within 4 h, as suggested by our RT-PCR data, in order to negate the dampening effect of UCP3 and allow for full activation. Ablation of *Ucp3* allows for uncontrolled early activation and appears to culminate in premature cell death, which we believe to be due to AICD. Importantly, *Ucp3* ablation can perturb and reciprocally affect the generation of T_H17 and T_{reg} cells, inhibiting the former and enhancing the latter. This is thought to be due to the augmented production of IL-2 by $Ucp3^{-/-}$ activated T cells. Our data mentioned above were generated by *in vitro* experiments and it is generally accepted that *in vitro* results may not always be replicated *in vivo*. Thus, the focus of the work presented in this chapter was to investigate whether these *in vitro* effects of *Ucp3* ablation would be mirrored in an *in vivo* setting.

We performed an adoptive transfer of $Ucp3^{+/+}$ and $Ucp3^{-/-}$ $CD4^+$ T cells to immunodeficient $Rag1^{-/-}$ mice to examine the homeostatic proliferation response of these cells. We also immunized $Ucp3^{+/+}$ and $Ucp3^{-/-}$ mice with KLH and CT to examine the effect of *Ucp3* ablation on $CD4^+$ T cell function *in vivo*. Adjuvants can alter the quantity and quality of adaptive immune responses, depending on the type of innate immune response they activate (Awate *et al*., 2013). For example, adjuvants can stimulate DC maturation and enhance their expression of MHC and co-stimulatory molecules which are required for efficient T cell activation (Awate *et al*., 2013). CT is an enterotoxin produced by *Vibrio cholera* consisting of an enzymatically active A subunit non-covalently linked to a pentamer of cell-binding B subunits (Lavelle *et al*., 2003, 2004). The B subunits facilitate intracellular entry of the A subunit after binding to ganglioside GM1 cell surface receptors, while the ADP-ribosylating A subunit activates the α subunit of a G_s protein, which subsequently activates adenylyl cyclase, leading to enhanced intracellular cAMP and inducing a multiplicity of biological effects (Lavelle *et al*., 2003, 2004). CT is a potent mucosal immunogen and adjuvant used in experimental animals that activates cellular immune responses to co-administered antigens and enhances the induction of $CD4^+$ T_H cell and CTL responses (Lavelle *et al*., 2004). It has been previously reported to modulate the stimulating potential of APCs, induce IL-4 and IL-10 production and inhibit IL-12 and

IFN-γ production, leading to a promotion of the induction of T_H2 cells and T cells with regulatory activity and suppression of the generation of T_H1 cells, respectively (Lavelle *et al*., 2003, 2004; Kang *et al*., 2016). Additionally, more recent reports have described the strongly augmented production of IL-6 by DCs following *in vitro* and *in vivo* treatment with CT, culminating in the potent T_H17 cell-driving activity of CT (Lee *et al*., 2009; Tsai and Wu, 2015). Accordingly, as we have observed modulated *Ucp3*$^{-/-}$ T_H17 and T_{reg} cell activity and generation, respectively, but no effect of *Ucp3* ablation on T_H1 cells, CT was chosen as an appropriate adjuvant for this work.

Importantly, *Ucp3* ablation indeed seems to perturb CD4$^+$ T cell function *in vivo*, mirroring our data generated by *in vitro* experiments. *Ucp3*-ablated CD4$^+$ T cells undergo increased homeostatic proliferation compared to *Ucp3*$^{+/+}$ cells following adoptive transfer to immunodeficient mice. This is assumed to be due to an increase in IL-2 production by these cells following activation, which promotes survival and proliferation (Boyman and Sprent, 2012). The viability of CD4$^+$ T cells 7 days post-adoptive transfer was not examined, however. While no effects of *Ucp3* ablation are found on LAP and LAG3 expression by T_{reg} cells or the secretion of IFN-γ and IL-10, *Ucp3*$^{-/-}$ mice display a higher frequency/enhanced generation of splenic CD25$^+$FoxP3$^+$ T_{reg} cells following immunization with KLH and CT compared to their WT counterparts, which is complementary to our data generated *in vitro*. Additionally, the production of IL-17A, the characteristic cytokine of T_H17 cells (Boyman and Sprent, 2012), by *Ucp3*$^{-/-}$ T cells following immunization with KLH plus CT appears to be hampered in comparison to WT controls, which also reflects our *in vitro* results. This was the only parameter measured that would indicate an alteration of *Ucp3*$^{-/-}$ T_H17 cell function following the immunization experiment. Thus, it may have been beneficial to compliment these data by additionally measuring RORγt levels, the characteristic transcription factor expressed by T_H17 cells, and/or STAT3 activation which is responsible for driving T_H17 cell differentiation (Ivanov *et al*., 2006; Boyman and Sprent, 2012; Liao *et al*., 2013; Kuhn *et al*., 2016). Nevertheless, our data are suggestive of altered T_H17 cell function *in vivo* following *Ucp3* ablation.

Although IL-2 secretion was not measured by ELISA in this experimental setup, we hypothesize that T_H17 and T_{reg} cells are reciprocally affected by *Ucp3* ablation *in vivo* due to increased production of IL-2, as seen *in vitro*. IL-2 can act to inhibit T_H17 cell differentiation and constrain IL-17A production by promoting STAT5 signalling which inhibits transcription from the *Il-17* gene locus (Laurence *et al*., 2007), as well as play a

prominent role in the generation of T_{reg} cells as it is crucial for T_{reg} cell maintenance, homeostasis and the enhancement of FoxP3 expression (Boyman and Sprent, 2012; Liao *et al*., 2013). Conditions in which IL-2 or its receptor subunits are absent lack T_{reg} cells (Crispin and Tsokos, 2009) and display a lack of peripheral immune tolerance mediated by T_{reg} cells, resulting in systemic autoimmunity (Boyman and Sprent, 2012). Additionally, where IL-2 deficiency is not absolute, T_{reg} cell function is still abnormal (Crispin and Tsokos, 2009).

T_H17 cells are extremely pro-inflammatory. The highly inflammatory nature of T_H17 cells manifests in them being the provocateur of many autoimmune disorders (Ivanov *et al*., 2006; Liao *et al*., 2013). T_{reg} cells, on the other hand, play a unique and important role in preventing autoimmunity. They are a specialized subpopulation of $CD4^+$ T cells that act to suppress pro-inflammatory immune cells and activation of the immune system, thereby maintaining immune system homeostasis (Pulendran and Ahmed, 2006; Boyman and Sprent, 2012; Liao *et al*., 2013). They function in contrast to the other subsets, modulating inflammation and acting as key players in sustaining self-tolerance. This helps to prevent excessive tissue damage from too much inflammation and autoimmune responses to self-antigen, as supported by the occurrence of autoimmunity due to T_{reg} deficiencies (Gregori *et al*., 2012; Liao *et al*., 2013). That *Ucp3* ablation can tip the balance of T_H17 and T_{reg} cells in favour of the latter *in vivo*, as well as *in vitro*, implicates *Ucp3* as a potential target for preventing or ameliorating autoimmune diseases such as MS and Crohn's disease. In the absence of IL-2 signals, T_{reg} cell number declines substantially, whereas T_H17 cell number increases, leading to an enhanced susceptibility to autoimmune disease and inflammatory disorders (Boyman and Sprent, 2012). In this work, we hypothesize that the opposite is occurring: increased IL-2 signals are promoting the generation of immunosuppressive T_{reg} cells and decreasing the number of T_H17 cells. Consequently, this may lead to enhanced protection from the development and/or progression of autoimmune disease and inflammatory disorders.

5.4 Conclusion

We have shown previously that *Ucp3* is rapidly downregulated in mature $CD4^+$ T cells at the mRNA level within 4 h of activation and that *Ucp3* ablation alters the function of non-polarized and polarized $CD4^+$ T cells, whilst having no obvious effect on mature $CD4^+$ T cell metabolism. We demonstrate here that our *in vitro* data generated exploring the role of UCP3 in $CD4^+$ T cell function translates to the *in vivo* setting. *Ucp3*$^{-/-}$ $CD4^+$ T cells undergo increased homeostatic proliferation following adoptive transfer to immunodeficient mice, similar to the increased proliferation of *Ucp3*$^{-/-}$ T_H0 cells observed *in vitro*. Additionally, *Ucp3*$^{-/-}$ mice immunized with KLH and CT display an augmented frequency of $CD25^+FoxP3^+CD4^+$ T cells, indicative of T_{reg} cells, and a marked decrease in the ability of their cells to secrete IL-17A, the characteristic cytokine of T_H17 cells. These data convey that *Ucp3* ablation perturbs the T_H17:T_{reg} cell ratio *in vivo*, as well as *in vitro*. The altered T_H17:T_{reg} cell balance *in vivo* implicates *Ucp3* as a potential target for the treatment of autoimmune disease.

Chapter 6:

Discussion

Chapter 6

Discussion

UCP3 was discovered in 1997 by Boss *et al*., almost 20 years after the discovery of the archetypical UCP, UCP1. UCP3 has the highest predicted amino acid sequence homology to UCP1 than any other member of the mitochondrial anion carrier superfamily at 57 % (except for UCP2 at 73 %; Krauss *et al*., 2005; Hilse *et al*., 2016). Similar to UCP1, UCP3 was thought to be exclusively expressed in one tissue, SKM, following its discovery (Boss *et al*., 1997). However, it has since been reported in BAT (Cunningham *et al*., 2003), spleen, thymus, reticulocytes, monocytes, lymphocytes (Carroll and Porter, 2004), pancreatic β-cells (Azzu *et al*., 2010) and heart (Hilse *et al*., 2018). Our laboratory has demonstrated UCP3 expression in murine thymocytes, spleen mitochondria and the lymphocyte fraction of the spleen using immunoblotting and confocal microscopy (Carroll and Porter, 2004; Kelly and Porter, 2011). Thymocytes are derived from lymphoid progenitor cells and develop into mature T lymphocytes in the thymus before migrating to peripheral lymphoid tissues, such as the spleen, where they wait to be activated by cells of the innate immune system and to carry out an immune response (Krammer *et al*., 2007). The spleen houses a significant proportion of the $CD4^+$ T cell pool following T cell exit from the thymus. The ablation of *Ucp3* changes $CD4^+$ and $CD8^+$ T cell frequencies in the thymus and spleen by affecting the apoptotic potential of these cells (Kelly and Porter, 2011). The role of UCP3 in T cells, however, has not been thoroughly investigated. Expression of UCP3 in thymocytes suggests its importance in thymic function, as well as a potential role in T cell selection, maturation, metabolism and/or function. Thus, the objective of this project was to build upon the aforementioned empirical evidence supplied by our laboratory of the existence of UCP3 in thymocytes by investigating the expression of UCP3 in peripheral $CD4^+$ T cells, both naive and polarized subsets, and to decipher the role, if any, of UCP3 in $CD4^+$ T cell metabolism and function.

We have shown that *Ucp3* is expressed in peripheral naive $CD4^+$ T cells but is quickly downregulated upon TCR and CD28-dependent T cell activation. Interestingly, Hilse *et al*. (2016) correlated UCP3 expression with UCP1 expression in BAT, although contradicted a role for UCP3 in BAT thermogenesis. Hence, a correlation between the expression of UCP1 and UCP3 in T cells may also be plausible and may be contributing to the similar effect on T cell profiles reported following *Ucp1* and *Ucp3* ablation (Adams *et al*., 2010;

Kelly and Porter, 2011). Due to the downregulation of *Ucp3* following T cell activation, it was perceived that, in addition to its potential role in thymic function and T cell selection mentioned previously, UCP3 may have an important role in naive T cell maintenance and/or metabolism, rather than in that of activated T cells. Interestingly, it is evident that UCP3 has a role to play in activated $CD4^+$ T cells, while naive $CD4^+$ T cells are unaffected by *Ucp3* ablation. We have shown that *Ucp3* knockdown affects activated T cells by resulting in significantly higher IL-2 production and secretion by T_H0 cells under a number of different stimulatory conditions. IL-2 is one of the first cytokines to be produced and secreted by all activated $CD4^+$ T cells in response to appropriate antigen presentation and co-stimulation through the TCR and CD28 co-receptor and is responsible for the promotion and modulation of T cell survival, activation, growth and proliferation (Crispin and Tsokos, 2009; Boyman and Sprent, 2012; Liao *et al*., 2013). In line with the above finding, *Ucp3*$^{-/-}$ T_H0 cells display elevated expression of CD25, the α subunit of the IL-2R. CD25 is absent or minimally expressed on resting T cells but its transcription and expression are potently induced following stimulation via the TCR or contact with IL-2 through the involvement of STAT5 binding to the *Cd25* gene locus, subsequently increasing cell responsiveness in a positive feedback mechanism (Boyman and Sprent, 2012; Liao *et al*., 2013; Preston *et al*., 2015). These data indicate that UCP3 plays a role in restricting activation and IL-2 production in response to TCR and CD28 co-stimulation. In agreement with this, *Ucp3*$^{-/-}$ T_H0 cells display upregulation of the early activation marker CD69, which is normally expressed at low levels on the surface of naive $CD4^+$ T cells and increases in expression following cell activation (Preston *et al*., 2015; Kang *et al*., 2016). Following secretion from activated $CD4^+$ T cells, IL-2 is known to modulate the proliferation of T and B lymphocytes (Boyman and Sprent, 2012). Accordingly, *Ucp3*$^{-/-}$ T_H0 cells also display higher frequencies of cells that have undergone more cell divisions. As a side note, it is interesting that Pecqueur *et al*. (2008) reported loss of *Ucp2* activated cell proliferation specifically in murine embryonic fibroblasts and T cells.

Our data demonstrate earlier activation and increased proliferation of *Ucp3*$^{-/-}$ T_H0 cells compared to *Ucp3*$^{+/+}$ T_H0 cells and point towards a role for UCP3 in restricting TCR signalling and T cell activation. In line with the above findings, it was predicted that earlier activated *Ucp3*$^{-/-}$ T_H0 cells of larger size would be greater in number than *Ucp3*$^{+/+}$ T_H0 cells and that they would additionally survive better due to the increase in IL-2 production which can promote cell survival and growth (Boyman and Sprent, 2012; Liao *et al*., 2013). Increased cell size, which occurs during lymphocyte blastogenesis (Preston *et al*., 2015), is

synonymous with increased cell growth and activation. However, fewer *Ucp3*$^{-/-}$ T_H0 cells are observed with a large FSC and *Ucp3*$^{-/-}$ T_H0 cell viability is decreased 72 h post-stimulation. As well as this, *Ucp3*$^{-/-}$ T_H0 cells secrete significantly less IFN-γ than their WT counterparts which is thought to be a reflection of their decreased viability. These results did not seem to coincide with *Ucp3*$^{-/-}$ T_H0 cells undergoing activation earlier and, thus, having a growth 'head start' and IL-2-linked promotion of cell survival and IFN-γ production (Liao *et al*., 2013). While these decreases in cell survival and cytokine production seem counterintuitive following the observations of increased IL-2 production, it is thought to be due to the triggering of a phenomenon known as AICD, an apoptotic form of cell death. In support of this, *Ucp3*$^{-/-}$ T_H0 cell viability is increased following incubation with an inhibitor of apoptosis, with no effect observed following incubation with an inhibitor of necrosis. Moreover, as well as acting as a T cell growth factor, IL-2 has been implicated in the priming of T cells for AICD following initial expansion (Maher *et al*., 2002; Roberts *et al*., 2003; Krammer *et al*., 2007; Boyman and Sprent, 2012; Liao *et al*., 2013). It is interesting to note that, while stimulated *Ucp3*$^{-/-}$ T_H0 cells do not survive as well as their WT counterparts, *Ucp3*$^{-/-}$ cells receiving no stimulation for up to 72 h (essentially still naive T cells) continue to survive better. Indeed, it is possible that the fact that *Ucp3*$^{-/-}$ unstimulated T cells inherently survive better than their WT counterparts accounts for the increased IL-2 production and proliferation *etc*. observed in these cells.

AICD is important for homeostasis and the elimination of potentially harmful autoreactive cells (Liao *et al*., 2013). Failure to produce normal amounts of IL-2 upon activation is a hallmark of T cells from patients with SLE and, indeed, SLE patients display defective AICD among other T cell defects (Crispin and Tsokos, 2009). AICD can be caused in part by the interaction of CD95 with CD95L, the expression of which can be promoted by IL-2 signalling (Maher *et al*., 2002; Roberts *et al*., 2003; Boyman and Sprent, 2012; Liao *et al*., 2013). This interaction triggers the clustering of CD95 and the recruitment of FADD (Maher *et al*., 2002). Pro-caspase 8 binds to FADD's death effector domain and is activated by self-cleavage, forming caspase 8 (Maher *et al*., 2002). Activated caspase 8 is released into the cytosol where it mediates apoptosis by either directly activating downstream effector caspases or by indirectly activating downstream effector caspases through cytochrome c release from mitochondria (Maher *et al*., 2002). CD95 is expressed ubiquitously in many tissues, whereas CD95L is described historically on activated T cells and is upregulated following T cell activation (Maher *et al*., 2002; Roberts *et al*., 2003). Transcription of CD95L is activated by c-Myc (Roberts *et al*., 2003). Importantly, IL-2

enhances the Jak/STAT and Akt signalling pathways which have been linked to c-Myc expression in T cells (Grumont *et al*., 2002; Preston *et al*., 2015). Thus, it was hypothesized that the increased IL-2 production of *Ucp3*$^{-/-}$ T_H0 cells could be enhancing c-Myc expression and indirectly promoting CD95L transcription, resulting in increased susceptibility to AICD. However, following our observation of decreased CD95L expression in *Ucp3*$^{-/-}$ T_H0 cells rather than increased expression, it is clear that AICD may be occurring by means other than the CD95:CD95L interaction. Indeed, Maher *et al*. (2002) reported that, although T cells constitutively express CD95, some apoptosis-resistant T cells can express lower levels or have defective CD95 signalling. It may be possible that *Ucp3*$^{+/+}$ T_H0 cells express lower levels of CD95 and, thus, are more resistant to CD95:CD95L-induced apoptosis, regardless of their increased expression of CD95L. From a retrospective point of view, it would have been ideal to measure the expression of both CD95 and CD95L in this work. In addition, expression levels of the apoptosis inhibitor, cellular [FADD-like IL-1β-converting enzyme (FLICE)]-inhibitory protein (c-FLIP), or anti-apoptotic B cell lymphoma-2 (Bcl-2) family members, such as Bcl-2 or Bcl-extra-large (Bcl-X_L), could have been measured as, for example, it has been reported that levels of c-FLIP are downregulated following T cell activation in an IL-2-dependent manner and correlate with sensitivity to CD95-induced AICD (Krammer *et al*., 2007; Brenner *et al*., 2008).

In addition to the interaction of CD95 with CD95L, AICD can be induced by other means, such as TNF ligation of the TNF receptor or exposure to ceramide and ROS (Maher *et al*., 2002; Roberts *et al*., 2003; Krammer *et al*., 2007). ROS have been shown to induce NF-κB-dependent apoptosis (Dumont *et al*., 1999). Interestingly, ROS have also been implicated in enhancing T lymphocyte activation. O_2^- and H_2O_2 were shown to enhance the production of IL-2 in stimulated T lymphocytes, as well as the expression of the IL-2R (Roth and Dröge, 1987; Los *et al*., 1995; Sena *et al*., 2013). We have hypothesized that UCP3 is acting to restrict T cell activation and that its ablation evokes early activation of T_H0 cells, as evidenced by the increased IL-2 production, early activation marker expression and consequential increase in cell proliferation and cell death due to AICD. That ROS have been previously implicated in promoting T cell activation (Roth and Dröge, 1987; Los *et al*., 1995; Sena *et al*., 2013) and proliferation (Chang *et al*., 2013), as well as the induction of AICD (Maher *et al*., 2002; Krammer *et al*., 2007), strongly supports the possibility of their involvement in the early activation and induced cell death observed in *Ucp3*$^{-/-}$ T_H0 cells. Moreover, UCPs have been implicated in the attenuation of

ROS production by carrying out moderate uncoupling activity and the generation of a controlled proton leak into the MM without ATP synthase involvement (Brand *et al*., 2004); this would lower the mitochondrial membrane potential and minimise the transfer of electrons to molecular O_2 and the formation of O_2^- (Brand, 2000; Miwa and Brand, 2003; Brand *et al*., 2004). Mitochondrial aconitase activity was decreased by 20 % in *Ucp3*$^{-/-}$ SKM (Vidal-Puig *et al*., 2000), indicative of increased ROS production. Mice lacking UCP3 have been reported to display increased levels of oxidative damage to proteins and lipids (Brand *et al*., 2002), which further supports the role of UCPs, and UCP3 in particular, in protecting against ROS production and oxidative tissue damage.

Due to the reports of ROS promoting T lymphocyte activation and cell death, which we observe in *Ucp3*-ablated cells, we hypothesized that UCP3 may be acting to uncouple the mitochondria of naive $CD4^+$ T cells, with its ablation resulting in an increased mitochondrial membrane potential and a consequential increase in ROS production. However, no difference in the mitochondrial membrane potential of, or ROS production by, *Ucp3*$^{+/+}$ and *Ucp3*$^{-/-}$ naive $CD4^+$ T cells is observed. One explanation may be that, although ROS production may be increased by *Ucp3* ablation, it may simply not have been detected by the chosen method or the difference is just too small to detect due to such a low expression level of UCP3 in *Ucp3*$^{+/+}$ naive $CD4^+$ T cells, as suggested by our data in Section 3.2.2. Furthermore, mitochondrial ROS production by T cells increases following cell activation (Dumont *et al*., 1999; Hildeman, 2003; Sena *et al*., 2013; Yarosz and Chang, 2018). Hence, despite our RT-PCR data suggesting that UCP3 is only expressed in naive $CD4^+$ T cells, a difference in ROS production may only be observed following the exploration of ROS produced by activated T cells rather than naive T cells. Therefore, it would have been wise to carry out this particular experiment on T_H0 cells, as well as naive T cells. An additional experiment that could have been performed to double check the levels of ROS production is the measurement of the activity of enzymes containing iron-sulphur centres, such as aconitase or Complex I, which can be inactivated by the presence of ROS and, thus, may serve as an indicator of ROS production (Vidal-Puig *et al*., 2000). However, if *Ucp3* ablation resulted in increased ROS production in our experimental set up and caused the inactivation of Complex I, one would expect this to be reflected in our Seahorse XF Cell Mito Stress Test results. Mitochondrial antioxidant defences may also be upregulated in the mitochondria of *Ucp3*$^{-/-}$ animals to protect against the possibility of increased oxidative damage and, as such, differences in ROS production may be mopped up by antioxidants. In line with this, *Ucp2*-ablated animals display increased levels of

SOD2 and decreased lipid peroxidation (de Bilbao *et al*., 2004). Indeed, a logical next step to confirm if this is the case in *Ucp3*$^{-/-}$ mice would be to measure levels of SOD2 in *Ucp3*$^{+/+}$ and *Ucp3*$^{-/-}$ CD4^{+} T cells. However, in agreement with our finding of no role for UCP3 in the attenuation of ROS production by CD4^{+} T cells, Hilse *et al*. (2018) reported that UCP3 expression in cardiomyocytes does not coincide with the expression of ETC proteins, rendering UCP3 participation in ROS regulation unlikely. In addition, Pecqueur *et al*. (2008) reported no difference in ROS production or the mitochondrial membrane potential following *Ucp2* ablation, although these were examined in murine embryonic fibroblasts rather than T cells.

Although no effect of *Ucp3* ablation on T_H1 cells is observed, it is known that IL-2 can play a significant role in influencing T_H17 and T_{reg} cell differentiation**.** High levels of IL-2 in the presence of TGF-β can promote the induction and survival of T_{reg} cells and the expression of FoxP3 and inhibit the generation of T_H17 cells, while lower levels of TGF-β in the presence of IL-6 favour T_H17 cell polarization (Laurence *et al*., 2007; Boyman and Sprent, 2012; Liao *et al*., 2013). Therefore, an effect of *Ucp3* ablation on T_H17 and T_{reg} polarized T cell subsets was hypothesized. Importantly, *Ucp3*$^{-/-}$ T_H17 cells display significantly less IL-17A secretion than *Ucp3*$^{+/+}$ T_H17 cells. It is thought that this decrease is due to IL-2 which can constrain IL-17A production by promoting STAT5 signalling, with STAT5 binding to the *Il-17* gene locus and inhibiting *Il-17* transcription (Laurence *et al*., 2007). FoxP3 expression is indicative of T_{reg} cell induction (Hori *et al*., 2003). FoxP3^{+} *Ucp3*$^{-/-}$ cells are higher in number than FoxP3^{+} *Ucp3*$^{+/+}$ cells under T_{reg} polarizing conditions and display higher cell viability. These data advocate that, while *Ucp3*$^{-/-}$ T_H1 cells are unaffected by the altered IL-2 production following *Ucp3* ablation, the generation of T_H17 and T_{reg} cells is crucially affected. Furthermore, these data are in line with many reports of the influence of IL-2 on T_H17 cell generation. Exposure of activated CD4^{+} T cells to IL-2 leads to lower cell surface expression of IL-6Rβ which, together with IL-6Rα, forms the IL-6R (Boyman and Sprent, 2012). As mentioned above, IL-2 activates STAT5 signalling which inhibits the binding of STAT3 to the *Il-17* locus by competing for the same sites on that gene; therefore, IL-2 reduces IL-6-mediated STAT3 activation, which is required for the development of RORγt^{+} T_H17 cells and the balance between STAT3 and STAT5 signalling is responsible for determining the extent of T_H17 cell generation (Boyman and Sprent, 2012). Measuring the expression of the IL-6R by *Ucp3*$^{+/+}$ and *Ucp3*$^{-/-}$ T_H17 cells may have been an interesting additional piece of datum to have. Since neutralising IL-2 activity directs the *Ucp3*$^{-/-}$ cell phenotype to return to a more WT-like

state, it is convincing that IL-2 is responsible for the effects observed on *Ucp3*$^{-/-}$ T_H17 and T_{reg} cells. These data support our previous findings of increased IL-2 production in *Ucp3*$^{-/-}$ T_H0 cells and highlight IL-2 as (one of) the main orchestrator(s) of the effects of *Ucp3* ablation on $CD4^+$ T cells.

The role of UCP1 in BAT is to dissipate the proton electrochemical gradient during NST by uncoupling electron transport and O_2 consumption from ATP synthesis. As mentioned previously, UCP3 has an amino acid sequence more similar to that of UCP1 than any other member of the mitochondrial anion carrier superfamily (excluding UCP2), at 57 % homology (Boss *et al*., 1997). The six membrane-spanning α-helix structure of UCP1 is highly conserved in UCP3, including the three mitochondrial carrier protein motifs, consistent with a role as an ion transporter of the MIM (Boss *et al*., 1997; Fleury et al., 1997). Thus, it followed naturally that this protein was presumed to have uncoupling activity similar to that of UCP1 upon discovery. However, while UCP3 is expressed in BAT, no role in NST is apparent as none of the expected phenotypes of cold sensitivity or obesity are observed in *Ucp3*$^{-/-}$ mice (Gong *et al*., 2000; Vidal-Puig *et al*., 2000; Hilse *et al*., 2016). UCP3 is also expressed in ectothermic fish and plants that do not require thermogenesis, so an exclusive thermogenic function of UCP3 is unlikely (Trenker *et al*., 2007; Graier *et al*., 2008). Its role in other tissues has been debated for the last two decades. If there is any physiological/biochemical process that UCP3 has been correlated with, it is conditions under which FA mobilization and oxidation may be occurring (Hilse *et al*., 2018).

Our RT-PCR data suggest that UCP3 is expressed in naive $CD4^+$ T cells before being downregulated following cell activation. If UCP3 elicits uncoupling activity in naive $CD4^+$ T cells, *Ucp3* ablation would have the potential to alter the metabolism of these cells. Removal of a protein that uncouples mitochondria would be expected to emanate in a decreased OCR, an increased OCR linked to ATP production, an increased coupling efficiency and a decreased proton leak. However, no consistent differences are observed between the respiration or glycolysis of *Ucp3*$^{+/+}$ and *Ucp3*$^{-/-}$ naive $CD4^+$ T cells or T_H0, T_H17 and T_{reg} cells that would support an uncoupling function of UCP3 or a role in FAO/FA transport (Dulloo *et al*., 2001; Garcia-Martinez *et al*., 2001; Schrauwen *et al*., 2001, 2003). Thus, in our hands, evidence of an uncoupling role for UCP3 in $CD4^+$ T cells is weak. However, it is possible that UCP3 is acting to uncouple the mitochondria of *Ucp3*$^{+/+}$ cells but is functioning at an extremely low level, low enough that its ablation does

not result in marked changes in metabolic parameters. Indeed, the expression of UCP3 protein in SKM mitochondria is tiny compared to the UCP1 levels in BAT mitochondria and can be up to 1000-fold lower (Harper *et al*., 2001; Graier *et al*., 2008). Furthermore, SKM is reported to have the highest abundance of UCP3 expression than any other tissue [although this has been contested by Hilse *et al*. (2016)], so any expression of UCP3 in $CD4^+$ T cells is expected to be considerably less. Effector T cells are also known to have very few mitochondria, even compared to memory T cells (van der Windt and Pearce, 2012), and, in contrast, BAT contains many mitochondria with abundant, densely packed cristae of the MIM – the location of UCP3 expression (Krauss *et al*., 2005). As a result, proton conductance or substrate transport, whatever the function of this protein may be, would presumably be much lower compared to UCP1 in BAT. Thus, any uncoupling effect of UCP3 may be only mild compared to the uncoupling observed in BAT and may be too small to detect. We have shown in Chapter 3 that the expression of *Ucp3* in naive $CD4^+$ T cells is almost 600-fold lower than the expression of *Ucp2* at the mRNA level. This may manifest in the lack of differences in the metabolic parameters of $Ucp3^{+/+}$ and $Ucp3^{-/-}$ naive T cells, T_H0, T_H17 and T_{reg} cells observed here. Indeed, observations were made by Adams *et al*. (2010) of increased ATP levels in $Ucp1^{-/-}$ thymocytes but no difference in O_2 consumption and Krauss *et al*. (2002) of a difference in the proton leak and total cell ATP of $Ucp2^{+/+}$ and $Ucp2^{-/-}$ thymocytes but, again, no difference in O_2 consumption.

There is a view in the literature that UCP3 does not transport protons *in vivo*. For one thing, $Ucp3^{-/-}$ mice have no obvious physical or metabolic phenotype and there is no difference in whole body metabolic rate compare to WT animals, contradicting a role for UCP3 in determining basal metabolic rate (Carroll and Porter, 2004). Although the structure of UCP1 is highly conserved in UCP3, a His residue proposed to be vital for proton transport activity in UCP1 is not conserved within UCP3 (His147; Bienengraeber *et al*., 1998). This suggests that, if UCP3 transports protons, it may use a different mechanism, may only sustain a reduced proton transport or simply may not be a proton transporter. The inhibition of UCP3 also appears to differ from that of UCP1. While almost all of the residues reported to be essential for the binding of GDP to UCP1 are conserved in UCP3, it has been reported that only UCP1 experiences nucleotide binding and this inhibitory regulation is not seen in UCP3 (Boss *et al*., 1998) or at least remains to be demonstrated [(it has been reported in UCP2, however (Berardi and Chou, 2014)]. According to Vidal-Puig *et al*. (2000), UCP2 and UCP3 activities are inhibited by purine nucleotides but, in contrast to UCP1, require much higher concentrations of purine

nucleotides for inhibition and the maximal degree of inhibition is significantly less. Still, this would raise questions about the physiological relevance of this inhibition and support an alternative function for UCP3. Some studies have suggested that UCP3 can transport other molecules such as chloride anions, keto-acids (Robinson *et al*., 2008) and lipid hydroperoxides (Lombardi *et al*., 2010). *In vitro* work of UCP2 and UCP3 overexpressed in cells found that Ca^{2+} was transported over the MIM into the MM (Trenker *et al*., 2007; Graier *et al*., 2008), although these reports were contested by Brookes *et al*. (2008). While the naming of UCP3 (and UCP2) is comprehensible, considering its homology to UCP1, in light of the accumulated experimental evidence that indicates an alternative function for UCP3 rather than an uncoupling role, Nedergaard and Cannon aptly suggested that its nomenclature might be misleading and may "*direct thoughts towards the implied function*" (Nedergaard and Cannon, 2003). Indeed, this is reflected by the many reports that deal with these proteins, discussing the contribution of UCP2 and UCP3 entirely on the basis of their uncoupling functions (Graier *et al*., 2008). The fact that UCP1, UCP2 and UCP3 are expressed in a variety of tissues suggests that UCPs have different functions. Not only may the inter-UCP function vary but also, as mentioned previously, the function of one UCP in a certain tissue compared to its function in another tissue may differ. One example of this is UCP1 which catalyses a proton leak in BAT mitochondria to generate heat during NST but is most probably not involved in thermogenesis in the thymus. This could be responsible for us not observing an uncoupling function of UCP3 in this work – UCP3 may not function as a *bona fide* uncoupler of $CD4^+$ T cells but may have an alternative function. There are a few well-known examples of proteins that have alternative functions besides their primary function. This phenomenon is called 'protein moonlighting' (Jeffery, 2015).

Ucp3 knockdown alters the function and/or generation of $CD4^+$ T_H0, T_H17 and T_{reg} cells. However, whether this effect is due to the absence of UCP3 in naive and/or activated $CD4^+$ T cells or due to its absence at an earlier point in T cell development is unclear. For example, it would not be impossible for the lack of UCP3 to impact thymocyte and T cell development in the thymus or even lymphoid progenitor cell development in bone marrow (cells that may be destined to mature into T cells), resulting in a 'reprogramming' or defect in the function of these cells that may only come to light following the mature T cell activation event. Indeed, while Kelly and Porter (2011) reported an alteration in the $CD4^+$ T cell frequency of thymus and spleen following ablation of the *Ucp3* gene, we have shown here that despite this effect, the lack of UCP3 does not perturb the function of thymocytes or naive $CD4^+$ T cells *ex vivo* but manifests only in activated mature $CD4^+$ T

cells. It should also be noted that compensatory mechanisms behind the effects observed in $CD4^+$ T cells following *Ucp3* ablation cannot be ruled out, as with all studies using KO mice. More research will be required to decipher how exactly this MIM protein can have such an effect on $CD4^+$ T cells. A potential method to address the above point would be to use an inducible Cre-Lox recombination system in which UCP3 is repressed specifically in peripheral $CD4^+$ cells (assuming mice containing a floxed sequence in the *Ucp3* gene are available). However, it may be extremely difficult/impossible to find a Cre system that is specifically targeted to peripheral $CD4^+$ T cells without cells at earlier stages of T cell development also being affected, *e.g.* $CD4^-CD8^-$ or $CD4^+CD8^+$ thymocytes. Thus, this may only be an effective system *in vitro,* by infecting isolated peripheral $CD4^+$ T cells with Cre-expressing lenti-, retro- or adenoviruses (Aghajani *et al*., 2012). If no differences are observed between WT and $Ucp3^{fl/fl}$ $CD4^+$ T cells, the effects described in this work could be attributed to the importance of UCP3 in thymic T cell development or the role of UCP3 in thymocytes and T cells could at least be determined less ambiguously.

That *Ucp3* ablation can tip the balance of T_H17 and T_{reg} cells in favour of the latter implicates *Ucp3* as a potential target for preventing or ameliorating autoimmune diseases. T_H17 cells are extremely pro-inflammatory. The high inflammatory nature of T_H17 cells manifests in them being a main contributor to the pathogenesis of autoimmunity (Ivanov *et al*., 2006; Liao *et al*., 2013). T_{reg} cells, on the other hand, play a role in preventing autoimmunity. They are a specialized subpopulation of $CD4^+$ T cells that act to suppress helper T cells and activation of the immune system, thereby maintaining immune system homeostasis (Pulendran and Ahmed, 2006; Boyman and Sprent, 2012; Liao *et al*., 2013). They function in contrast to the other subsets, modulating inflammation and acting as key players in sustaining self-tolerance. This helps to prevent excessive tissue damage from too much inflammation and autoimmune responses to self-antigen, as supported by the occurrence of autoimmunity due to T_{reg} deficiencies (Gregori *et al*., 2012; Liao *et al*., 2013). In the absence of IL-2 signals, T_{reg} cell number declines substantially, whereas T_H17 cell number increases, leading to an enhanced susceptibility to autoimmune disease and inflammatory disorders (Boyman and Sprent, 2012). As a logical progression to this project, the next step would be for one to examine the effect of *Ucp3* ablation on a suitable autoimmune disease model and investigate whether *Ucp*3 ablation would ameliorate disease pathogenesis. Similar to our adoptive transfer experiment described in Chapter 5, many groups have performed an adoptive transfer of naive, T_{reg}-depleted, $CD4^+$ T cells into syngeneic immunodeficient mice, such as severe combined immunodeficiency (SCID)

or *Rag1*$^{-/-}$ mice, and successfully induced inflammatory bowel disease (IBD; Kieper *et al*., 2005). Thus, as we have already performed this type of experiment, this would be quite a straightforward experiment to repeat. We examined cells following a short period of only 7 days *in vivo*. Leaving them *in vivo* for a longer period may allow an autoimmune disorder such as IBD to potentially develop. However, it is thought that the severe colitis that develops in this type of experimental setup reflects unregulated activation of naive donor CD4^{+} cells into IFN-γ- and TNF-α-secreting effector cells, as well as IL-17A-secreting effector cells, that infiltrate the colon (Kieper *et al*., 2005). This suggests that a T_H1-type immune response develops. Additionally, neutralisation of IL-17A has been shown to exacerbate colonic inflammation in an acute model of colitis (Ogawa *et al*., 2004), suggesting that IL-17A and T_H17 cells can play a protective role in some instances. As we have not observed significant differences *in vitro* or *in vivo* between *Ucp3*$^{+/+}$ and *Ucp3*$^{-/-}$ T_H1 cell function, it would be more ideal to use a T_H17 cell-mediated autoimmune disease model, such as experimental autoimmune encephalomyelitis (EAE) which is used as a murine model of MS.

MS is a chronic autoimmune disease of the central nervous system (CNS) in which the immune system targets neuronal myelin sheaths leading to demyelination of primary nerve axons (Vogler *et al*., 2006). EAE is a murine model of MS that has been used to characterise and study the underlying mechanisms involved in MS disease onset and progression and, more importantly, to develop and test potential treatments (Vogler *et al*., 2006). EAE is triggered by injection of myelin antigen together with an adjuvant to trigger a pronounced immune response. This leads to T cell activation against epitopes of autologous myelin proteins present in the CNS, the release of cytokines to recruit macrophages and more T cells and, consequently, myelin destruction. EAE was originally assumed to be mediated by T_H1 cells but is now accepted to be driven by IL-17A-producing T_H17 and γδ T cells (Sutton *et al*., 2006) and, consequently, may be an ideal model for this work. Clinical symptoms of EAE are ameliorated by blocking IL-17A; injection of anti-IL-17A delays onset of the disease and prevents the characteristic mononuclear cell infiltrate in spinal cord white matter (Sutton *et al*., 2006). Moreover, current therapies for MS include administration of glatiramer acetate which, among other mechanisms, is thought to restore the number of CD4^{+}CD25^{+}FoxP3^{+} T_{reg} cells generally deficient in MS patients (Hong *et al*., 2005). In this regard, targeting UCP3 may alleviate symptoms and/or progression of EAE (and potentially MS) by promoting the generation of FoxP3^{+} T_{reg} cells and inhibiting the function of T_H17 cells, as we have shown *in vitro* and

in vivo. In light of this, UCP3 may have therapeutic promise in the treatment of this chronic inflammatory disease and the potential of targeting *Ucp3* to modulate autoimmunity warrants further investigation.

6.1 Conclusion

We have shown that *Ucp1, Ucp2* and *Ucp3* are expressed in peripheral naive $CD4^+$ T cells and their transcription is downregulated following T cell activation. Following *Ucp3* ablation, T cells are capable of producing more IL-2, upregulating the activation markers CD25 and CD69 and increasing their proliferation rate. Subsequently, however, it is apparent that $Ucp3^{-/-}$ T_H0 cells die prematurely, as suggested by the lower frequency of viable cells, as well as the decrease in IFN-γ secretion and the number of cells of increased size compared to $Ucp3^{+/+}$ T_H0 cells. While this abrogation of cell survival and cytokine secretion seems counterintuitive following the observations of increased IL-2 production, it is thought to be due to the triggering of AICD. The favouring of T_{reg} cell over T_H17 cell generation also ensues from *Ucp3* ablation *in vivo,* as well as *in vitro,* while *Ucp3* knockdown in T_H1 cells is without effect. Surprisingly, *Ucp3* ablation has no effect on naive or activated $CD4^+$ T cell metabolism, which contradicts an uncoupling function for UCP3 in $CD4^+$ T cells, as well as a role in FAO or FA transport. Our data convey earlier activation of $Ucp3^{-/-}$ T_H0 cells compared to $Ucp3^{+/+}$ T_H0 cells and point towards a role for UCP3 in restricting TCR signalling and $CD4^+$ T cell activation. UCP3 acts as a rheostat to inhibit the magnitude of TCR activation and fine-tunes the TCR and CD28 signal; hence its expression in naive $CD4^+$ T cells and subsequent downregulation after cell stimulation. Following activation, TCR signals may block or switch off *Ucp3* gene expression within 4 h, as suggested by our RT-PCR data, in order to negate the dampening effect of UCP3 and allow for full activation. We conclude that UCP3 has a role in restricting T cell activation, thereby preventing AICD, and can perturb the T_H17:T_{reg} cell ratio. The altered T_H17:T_{reg} cell dichotomy implicates *Ucp3* as a potential target for the treatment of autoimmune disease. More investigation is required for us to decipher the role of this 'uncoupling' protein in $CD4^+$ T cells and the mechanism by which it restricts cell activation.

Chapter 7:
Future Work

Chapter 7

Future Work

We have shown that *Ucp3*$^{-/-}$ T_H0 cells undergo TCR and CD28 co-receptor-mediated activation earlier than their WT counterparts, as demonstrated by an increase in IL-2 production, early activation marker expression and proliferation. Numerous proteins have the potential to impact the production of IL-2 by and/or the activation of $CD4^+$ T cells. Thus, immunoblotting could be performed to explore whether the activity of transcription factors and signalling pathways have been influenced by *Ucp3* ablation and resulted in the observed altered function of these cells. Following co-receptor stimulation, p300/Creb-binding protein (CBP) molecules translocate to the *fos* promoter and induce *fos* transcription (an immediate early gene in T cell activation) by promoting histone-4 acetylation and RNA polymerase II binding (Crispin and Tsokos, 2009). This leads to the coupling of Fos and Jun which form activator protein-1 (AP-1), a transcription factor that associates with nuclear factor of activated T cells (NFAT) and induces IL-2 transcription (Hettmann *et al*., 1999; Crispin and Tsokos, 2009; Liao *et al*., 2013). Runt-related transcription factor 1 [RUNX1; also known as acute myeloid leukaemia 1 protein (AML1)] has also been shown to bind to a region upstream of the *Il-2* promoter and to stimulate IL-2 production in an NFAT-dependent fashion (Crispin and Tsokos, 2009). Mice lacking expression of lymphocyte NFAT, cytoplasmic 1 (NFATc1) and NFATc2 display no TCR-induced IL-2 production (Liao *et al*., 2013). FoxP2 also co-operates with NFAT to drive IL-2 expression (Liao *et al*., 2013). Hence, it may be important here to determine whether the activity of p300/CBP, AP-1, RUNX1, FoxP2 and/or NFAT have been modulated and increased in our *Ucp3*$^{-/-}$ T_H0 cells.

Additionally, Ras homologue gene family, member A (RhoA), a GTPase known for its role in cytoskeletal rearrangement, can inhibit IL-2 production in primary T cells by influencing the activity of NFAT (Crispin and Tsokos, 2009). It is possible that its activity is decreased in *Ucp3*$^{-/-}$ T_H0 cells. BOB.1/OBF.1 can form ternary complexes with octamer binding proteins (OCT-1 and OCT-2) and subsequently bind to the *Il-2* promoter in activated T cells in close association with AP-1 (Crispin and Tsokos, 2009; Liao *et al*., 2013). The absence of BOB.1/OBF.1 in BOB.1/OBF.1-deficient mice leads to impaired IL-2 production (Crispin and Tsokos, 2009), which suggests that its activity may be upregulated in our cells. BCL11B is a zinc finger protein expressed in $CD4^+$ T cells that

causes increased IL-2 production following T cell activation when overexpressed as it binds to the *Il-2* promoter of activated T cells, probably facilitating gene transcription (Crispin and Tsokos, 2009). The protein expression levels of early growth response 1 (EGR1), 2 and 3, increase after T cell activation (Crispin and Tsokos, 2009). EGR1 facilitates the expression of IL-2, whereas EGR2 and 3 have an inhibitory function over T cell activation and IL-2 production (Crispin and Tsokos, 2009). The transcription factor B lymphocyte-induced maturation protein-1 [BLIMP-1; also known as PR domain zinc finger protein 1 (PRDM1)] is activated by IL-2 and in turn represses IL-2 production by silencing the *Il-2* gene, thus providing a negative feedback mechanism (Boyman and Sprent, 2012; Liao *et al*., 2013). Prolonged exposure of T cells to antigen leads to the upregulation of BLIMP-1 expression, which in turn progressively reduces the capacity of the cells to secrete IL-2 as they become terminally differentiated or exhausted (Boyman and Sprent, 2012). Indeed, it would have been interesting to measure the expression of BLIMP-1 in activated *Ucp3*$^{+/+}$ and *Ucp3*$^{-/-}$ T_H0 cells in this case and to explore whether the ability of the *Ucp3*$^{-/-}$ T_H0 cells to produce IL-2 became downregulated by 72 h post-stimulation in line with an increased expression of BLIMP-1 and their decreased viability. NF-κB has also been associated with the induction of IL-2 expression and the promotion of proliferation following TCR-mediated T cell activation (Hettmann *et al*., 1999; Liao *et al*., 2013). In addition to immunoblotting, it may be interesting to transfect an NFAT and/or NF-κB luciferase reporter T cell line with a *Ucp3* cDNA vector to induce UCP3 overexpression or to inhibit UCP3 expression with small interfering RNA (siRNA), for example, in the same reporter cell line and monitor the effects on NFAT and NF-κB activity. As can be seen, a plethora of proteins and transcription factors and their respective signalling pathways could be investigated to explore the effect of *Ucp3* ablation on $CD4^+$ T cells, not to mention the transcription factors involved in the metabolic switch of activated T cells, although we observed no change in metabolism in this work.

Our data indicate that *Ucp3*$^{-/-}$ T_H0 cells are prone to AICD. However, it is apparent that the AICD observed in *Ucp3*$^{-/-}$ T_H0 cells is not due to the CD95:CD95L interaction as *Ucp3*$^{-/-}$ T_H0 cells display significantly decreased CD95L expression compared to *Ucp3*$^{+/+}$ T_H0 cells. Maher *et al*. (2002) and Roberts *et al*. (2003) reported that, in addition to the CD95:CD95L interaction, AICD can be induced by TNF ligation of the TNF receptor or exposure to ROS. It is possible that *Ucp3*$^{-/-}$ T_H0 cells produce significantly more TNF than their WT counterparts in a manner similar to their production of IFN-γ 24 h post-stimulation and/or that they produce more ROS due to their mitochondria being more

'coupled'. This may render these cells more susceptible to AICD and, thus, would be worth investigating. Programmed cell death protein 1 (PD-1) is a negative regulator of T cell function that is upregulated on T cells following activation and has been linked to T cell exhaustion (Chang *et al*., 2013) and to rendering T cells susceptible to apoptosis (Riley, 2009). PD-1 could be upregulated in *Ucp3*$^{-/-}$ T_H0 cells and may be an interesting additional parameter to measure.

In light of the fact that Adams *et al*. (2010) reported increased ATP levels in *Ucp1*$^{-/-}$ thymocytes but no difference in O_2 consumption and Krauss *et al*. (2002) reported a difference in proton leak and total cell ATP of *Ucp2*$^{+/+}$ and *Ucp2*$^{-/-}$ thymocytes but, again, no difference in O_2 consumption, additional experiments could be performed to ensure that no subtle differences in metabolism or ROS production were missed previously. One could measure the glucose uptake or GLUT1 expression of *Ucp3*$^{+/+}$ and *Ucp3*$^{-/-}$ T_H0 cells, with the expectation that one may observe increased uptake and/or GLUT1 expression by *Ucp3*$^{-/-}$ T_H0 cells sooner than *Ucp3*$^{+/+}$ T_H0 cells, as GLUT1 overexpression can enhance T cell IL-2 production (van der Windt and Pearce, 2012). ETC complex activity and lactate assays may be performed to compliment the Seahorse XF Cell Mito Stress Test data and the ATP/ADP ratio could be measured, as Chang *et al*. (2013) reported the importance of mitochondrial ATP generated by OxPhos for T cell proliferation and activation marker expression. SOD2 levels could also be measured as *Ucp2*-ablated animals display increased levels of SOD2 and decreased lipid peroxidation (de Bilbao *et al*., 2004). Mitochondrial antioxidant defences may be upregulated in the mitochondria of *Ucp3*$^{-/-}$ animals to protect against the possibility of increased oxidative damage and, as such, differences in ROS production may be mopped up by antioxidants.

UCP3 has been implicated in the metabolic switch from OxPhos to FAO as it becomes upregulated in SKM (Garcia-Martinez *et al*., 2001), as well as spleen and thymus mitochondria (Carroll and Porter, 2004), during times of starvation when FAs are the predominant fuel source. In contrast to effector T cells, $CD4^+$ T_{reg} cells rely predominantly on FAO as their primary form of energy production (Michalek *et al*., 2011). While we have shown that T_{reg} cells seem to be metabolically unaffected by *Ucp3* ablation, it may have been more appropriate to perform the T_{reg} cell Seahorse XF Cell Mito Stress Tests in a FAO-appropriate medium, such as one made using the Seahorse XF Palmitate-BSA FAO Substrate Kit supplied by the Seahorse manufacturer (Agilent Technologies). In this way, $CD4^+$ $T_{(reg)}$ cells may be forced to utilize FAO and the real effect of *Ucp3* ablation on

metabolism may be discerned, that is, if its role is *de facto* involved in FAO. The stimulants used under normal T cell culture conditions (anti-CD3, polarizing cytokines *etc*.) could also be included, as these were never present *during* the Seahorse experiments since cells were transferred from 96-well cell culture plates containing these stimulants to the Seahorse cell microplates without them. As well as this, it may be interesting, and indeed important, to explore the metabolism and function of $CD4^+$ T cells (each subset) under more physiological conditions. RPMI is the standard medium used for T cell culture; the concentration of glucose in the RPMI used in this work was 11 mM which is much higher than that found *in vivo*. Using a medium with a glucose concentration closer to that found under physiological conditions, such as 5 mM, may expose differences present in the metabolism of these cells. Indeed, Shi *et al*. (2011) investigated the effect of *Hif1α* knockdown on T_H17 cells and reported results similar to ours: dampened T_H17 cell differentiation and promotion of $FoxP3^+$ T_{reg} cell generation. They also reported a difference in the glycolytic activity of $Hif1\alpha^{+/+}$ and $Hif1\alpha^{-/-}$ T_H17 cells but had used a medium containing 5 mM glucose in contrast to the concentration of 11 mM glucose used in our study. In addition, our normal culture conditions could be performed in the complete absence of serum, as serum may contain substances with the potential to influence the activation and/or differentiation of both $Ucp3^{+/+}$ and $Ucp3^{-/-}$ T cells.

As a logical progression to this project, an important next step would be for one to examine the effect of *Ucp3* ablation on a suitable autoimmune disease model. Importantly, EAE, a murine model of MS, was originally assumed to be mediated by T_H1 cells but is now thought to be driven by IL-17A-producing T_H17 and γδ T cells (Sutton *et al*., 2006) and, consequently, may be an ideal model for this work. The clinical symptoms of EAE are ameliorated by blocking IL-17A; injection of anti-IL-17A delays onset of the disease and prevents the characteristic mononuclear cell infiltrate in spinal cord white matter (Sutton *et al*., 2006). Moreover, current therapies for MS include administration of glatiramer acetate which, among other mechanisms, is thought to restore the number of $CD4^+CD25^+FoxP3^+$ T_{reg} cells generally deficient in MS patients (Hong *et al*., 2005). In this regard, it would be worth investigating whether *Ucp3* ablation would result in the alleviation of symptoms and/or progression of EAE by promoting the generation of $FoxP3^+$ T_{reg} cells and inhibiting the function of T_H17 cells, as we have shown *in vitro* and *in vivo*. There is also extensive literature that claims that the production of granulocyte-macrophage colony-stimulating factor (GM-CSF) by pathogenic T_H17 cells is the driving force behind the development and progression of EAE (Codarri *et al*., 2011; El-Behi *et al*., 2011; McGeachy, 2011).

Thus, it may be worthwhile to measure the production of GM-CSF by *Ucp3*$^{+/+}$ and *Ucp3*$^{-/-}$ T_H17 cells, both *in vitro* and *in vivo*. In addition, it could be interesting to investigate the effect of *Ucp2* and *Ucp3* ablation (using double-KO mice) on the progression of EAE, as Vogler *et al*. (2006) reported a protective role for UCP2 in EAE, while our data suggest that *Ucp3* ablation may be protective. As well as this, polymorphisms in the *Ucp2* gene have been associated with increased susceptibility to the development of MS (Vogler *et al*., 2006). It would be of interest to explore whether polymorphisms of the *Ucp3* gene lead to a change in susceptibility to the development of MS, by examining the *Ucp3* gene of MS patients.

Chapter 8:

Courses, Conferences and Publications

Chapter 8

Courses, Conferences and Publications

8.1 Courses

Successfully completed the LAST-Ireland course, January 2015.

Successfully completed the Seahorse Biosciences Advanced Immunometabolism Workshop: Mitochondrial Function in T Cells, December 2015.

Successfully completed the Seahorse Workshop, TBSI, June 2016.

Successfully completed the Computer-Aided Drug Design Symposium and Workshop: Linking Design, Biology, Chemistry and Medicine, TBSI, May 2018.

8.2 Conferences

Second Joint Symposium of TBSI and the Weizmann Institute of Science, June 2015.
Oral presentation: 'Identification of Gb3-positive, drug-resistant cancer cells and their sensitivity to verotoxin-1'.

European Bioenergetics Conference, July 2016.
Poster presentation: Emma B. O'Connor, Richard K. Porter and Patrick T. Walsh (2016). 'A role for mitochondrial uncoupling protein 3 (UCP3) in T cell function'. *Biochimica et Biophysica Acta (BBA) – Bioenergetics, 1857* (Supplement), e98.

Integrating Metabolism and Immunity (E4), Keystone Symposia Conference, June 2017.
Poster presentation: Emma B. O'Connor, Richard K. Porter and Patrick T. Walsh. 'A role for mitochondrial uncoupling protein 3 (UCP3) in $CD4^+$ T cell function'.

European Bioenergetics Conference, August 2018.
Oral presentation: 'A role for mitochondrial uncoupling protein 3 in $CD4^+$ T cell function'. *Biochimica et Biophysica Acta (BBA) – Bioenergetics, 1859* (Supplement), e17.

8.3 Publications

Abstract from European Bioenergetics Conference, 2016:

O'Connor, E. B., Porter, R. K. and Walsh, P. T. (2016). A Role for Mitochondrial Uncoupling Protein 3 (UCP3) in T-cell function. *Biochimica et Biophysica Acta (BBA) – Bioenergetics*, *1857* (supplement), e98.

09.11

Palmitate-induced insulin resistance in rat and human skeletal muscle cells associates with inhibited ATP turnover

Raid B. Nisr, Charles Affourtit
School of Biomedical and Healthcare Sciences, Plymouth University, Plymouth, UK
E-mail address: charles.affourtit@plymouth.ac.uk (C. Affourtit)

Mitochondrial dysfunction correlates with the loss of skeletal muscle insulin sensitivity in obesity, but the causal relation between these pathologies remains subject of debate. At present, there is for example disagreement as to what extent the oxidative capacity of muscle cells may be insufficient to manage the elevated nutrient supply in obesity. Analogously with a market economy, the energy metabolism of muscle is largely controlled by ATP demand, which means that the *effective* capacity of mitochondrial oxidative phosphorylation is set indirectly by ATP turnover. The experiments reported here aimed to establish if ATP-consuming processes in rat and human myoblasts are altered when cells are exposed to palmitate, an abundant saturated fatty acid whose concentration increases in obesity. Measuring myocellular bioenergetics in real time we show that palmitate lowers the rate and efficiency of oxidative phosphorylation under the same conditions where it causes insulin resistance. Our data suggest that the decrease of ATP synthesis rate, at least partly, results from changed ATP demand. Direct measurement of *de novo* protein synthesis reveals that palmitate lowers this ATP-consuming process by 30%. This inhibition is reflected by a significantly decreased proportion of ATP supply allocated to protein synthesis: cycloheximide-sensitivity of oligomycin-sensitive respiration is decreased by 40%. Moreover, in both rat and human cells, palmitate lowers ATP supply used to drive the sodium pump by 60-70% and, in human cells only, decreases ATP supply reserved for DNA/RNA synthesis by almost 75%. These palmitate effects on ATP turnover shed new light on the 'mitochondrial insufficiency' debate and highlight that mitochondrial involvement in fatty-acid-induced insulin resistance is best evaluated in context of bioenergetics control.

doi: 10.1016/j.bbabio.2016.04.195

09.12

A Role for Mitochondrial Uncoupling Protein 3 (UCP3) in T-cell function

Emma B. O'Connor[a], Richard K. Porter[a], Patrick T. Walsh[b]
[a]*School of Biochemistry and Immunology, Trinity Biomedical Science Institute (TBSI), Trinity College Dublin, Dublin 2, Ireland*
[b]*Department of Clinical Medicine, School of Medicine, Trinity College Dublin, Ireland*
E-mail address: oconnoe6@tcd.ie (E.B. O'Connor)

Uncoupling proteins are inner mitochondrial membrane proteins belonging to the mitochondrial anion carrier superfamily. One of these transporters, UCP3, is found predominantly in skeletal muscle, with smaller amounts present in brown adipose tissue, heart, spleen and thymus. The exact function of UCP3 remains uncertain, although many reports suggest a role for UCP3 in lipid metabolism. We have shown that UCP3 is present in naïve $CD4^+$ T-cells. We also show that upon T-cell activation, expression of UCP3 decreases rapidly within the first 24 hours. The absence of UCP3 in $UCP3^{-/-}$ mice resulted in increased IL-2 production in non-polarised $CD4^+$ T-cells in the first 24 hours following activation, suggesting a possible role for UCP3 to restrict IL-2 levels before T-cell activation. One $CD4^+$ helper T-cell subset, namely T_H17 cells, play a prominent role in infection. T_H17 cells are highly inflammatory and are characterized by the production of the pro-inflammatory cytokine IL-17A, as well as IL-21 and IL-22 and the expression of their lineage-defining transcription factor, RORγt. Due to their inflammatory nature, they have been implicated as a main contributor to the pathogenesis of a number of autoimmune diseases, including multiple sclerosis and rheumatoid arthritis. UCP3 ablation in $UCP3^{-/-}$ mice resulted in a marked decrease in IL-17A production in T_H17 cells, 72 hours post-activation. This finding suggests UCP3 may be a potential target for the treatment of some forms of autoimmunity.

doi: 10.1016/j.bbabio.2016.04.196

09.13

Interactions of proteins with intracellular structures of glycogen

Paulina Patalas-Krawczyk, Jerzy Duszyński, Jędrzej Szymański
Laboratory of Bioenergetics and Biomembranes, Nencki Institute of Experimental Biology Polish Academy of Science, Warsaw, Poland
E-mail address: p.patalas@nencki.gov.pl (P. Patalas-Krawczyk)

The interior of a living cell is extremely crowded. One of the properties of such crowded environment is that diffusion is governed by different rules and should be described by viscosity which depends on the size of the diffusing object [1]. Glycogen could be considered as a platform integrating signals from different proteins involved in its metabolism [2]. We have determined that glycogenin (GN) (39,4 kDa), the primer of glycogen synthesis is evenly localized within the cell. Second important protein, glycogen synthase (GS) (83,7kDa) forms cytoplasmic granule-like deposits most probably corresponding to glycogen. By contrast, another enzyme involved in metabolism of this glucose polymer, glycogen branching enzyme (GBE1) (80 kDa) is uniformly distributed in the cell. We have found differences in the diffusion rates between those enzymes involved into the synthesis of glycogen. Measurements were based on Fluorescence Correlation Spectroscopy in several culturing conditions. This could tell us about the interactions of GN, GS and GBE1 with this large glucose polymer and estimate free and bound fractions for this enzymes. What is more, glycogen could be visualized by the means of fluorescence microscopy using different methods including 2-NBDG which is the most common possibility to indicate this particle or GS-GFP. Nevertheless, we have examined novel opportunity for live cell imaging of glycogen using constructs containing carbohydrate binding module, like CBM21 (p-mNeptune-C1-CBM21).

This work was supported from the source of the National Science Centre according to the decision number DEC-2013/08/W/NZ1/00687 (SYMFONIA grant).

References

1. T. Kalwarczyk, N. Ziębacz, A. Bielejewska, E. Zaboklicka, K. Koynov, J.Szymański, A.Wilk, A.Patkowski, J. Gapiński, H. Butt, R. Hołyst, Comparative Analysis of Viscosity of Complex Liquids and Cytoplasm of Mammalian Cells at the Nanoscale, *Nano Lett.* 2011, 11 (5), pp 2157–2163
2. P.J. Roach, A.A. Depaoli-Roach, T.D. Hurley, V.S. Tagliabracci, Glycogen and its metabolism: some new developments and old themes, Biochem. J. 2012, 441, 763–787.

doi: 10.1016/j.bbabio.2016.04.197

Abstract from European Bioenergetics Conference, 2018:

O'Connor, E. B., Walsh, P. T. and Porter, R. K. (2018). A Role for Mitochondrial Uncoupling Protein 3 in CD4$^+$ T Cell Function. *Biochimica et Biophysica Acta (BBA) – Bioenergetics*, *1859* (supplement), e17.

2. H. Guo, S.A. Bueler, J.L. Rubinstein. Atomic model for the dimeric F_O region of mitochondrial ATP synthase, Science 358 (2017) 936-940.

doi:10.1016/j.bbabio.2018.09.050

A Role for Mitochondrial Uncoupling Protein 3 in CD4$^+$ T Cell Function

Emma B. O'Connor[a], Patrick T. Walsh[b], Richard K. Porter[a]
[a]*School of Biochemistry and Immunology, Trinity Biomedical Sciences Institute, Trinity College Dublin, Dublin, Ireland*
[b]*Department of Clinical Medicine, School of Medicine, Trinity College Dublin, Ireland*

Uncoupling proteins (UCPs) are members of the mitochondrial anion carrier superfamily that can mediate the transfer of protons into the mitochondrial matrix from the intermembrane space. Our laboratory has previously reported evidence of UCP3 expression in thymocytes. Thymocytes develop into mature T cells before exiting the thymus and travelling to the periphery where they wait to carry out an immune response. Here, we demonstrate that *Ucp3* is expressed in peripheral naive CD4$^+$ T cells at the mRNA level before being markedly downregulated following cell activation. *Ucp3*$^{-/-}$ non-polarized, activated T cells (T_H0 cells) produce significantly more IL-2, which is reflected by an increase in CD25 and CD69 expression as well as an increase in cell proliferation. However, it is also followed by a decrease in cell viability and IFN-γ production 72 h post-stimulation. It is thought that the increased IL-2 levels observed in *Ucp3*$^{-/-}$ T_H0 cells are promoting early T cell activation but also subsequently inducing activation-induced cell death (AICD). The altered IL-2 expression observed between *Ucp3*$^{+/+}$ and *Ucp3*$^{-/-}$ T_H0 cells also appears to have a crucial impact on the generation of T_H17 and regulatory T (T_{reg}) cells *in vitro*. T_H17 cells are a subset of T cells that are highly pro-inflammatory, while T_{reg} cells act to suppress the immune response. An increased frequency of FoxP3$^+$ T_{reg} cells is generated *in vitro* from *Ucp3*$^{-/-}$ mice compared to *Ucp3*$^{+/+}$ mice, while *Ucp3*$^{-/-}$ T_H17 cells generated *in vitro* display lower cell survival/viability and decreased IL-17A production compared to their *Ucp3*$^{+/+}$ counterparts. We postulate that UCP3 is acting to restrict the activation of naive T cells. UCP3 may be acting as a rheostat to dampen signals following T cell receptor and CD28 co-receptor ligation, thereby preventing early activation and AICD. That *Ucp3* ablation alters the T_H17:T_{reg} cell balance implicates UCP3 as a potential target for the treatment of some forms of autoimmunity.

doi:10.1016/j.bbabio.2018.09.051

Tissue- and substrate-specific patterns in the oxygen kinetics of mitochondrial respiration

András T. Mészáros[a,b], Markus Haider[c], Erich Gnaiger[a,d]
[a]*Oroboros Instruments, Innsbruck, Austria*
[b]*Institute of Surgical Research, University of Szeged, Szeged, Hungary*
[c]*Steinhauser & Haider Technology Consulting OG, Innsbruck, Austria*
[d]*D. Swarovski Research Laboratory, Department of Visceral, Transplant and Thoracic Surgery, Medical University of Innsbruck, Innsbruck, Austria*

In most tissues mitochondria (mt) respire in a low oxygen (O_2) environment, where intracellular partial O_2 pressures (p_{O2}) may exert control over OXPHOS. It is well established that the affinity of cytochrome oxidase (CIV) for O_2 decreases with increasing enzyme turnover [1] and that mt p_{50} (p_{O2} at half-maximum O_2 flux, J_{O2}) is a function of coupling and J_{O2} [2]. In our study of tissue-specific O_2 kinetics, we investigated the influence of pathway and coupling control on mt p_{50} with various fuel substrates in OXPHOS-, LEAK- and ET-states in mt isolated from mouse brain, heart and liver.

Isolated mt were incubated in Oroboros O2k High-Resolution FluoRespirometers. Kinetic data was obtained during aerobic-anaerobic transitions with high time-resolution. p_{50} values were calculated using the **O2k**-kinetics software for automatic calibration and correction of O_2 signals, data processing and curve fitting.

p_{50} ranged from 0.006 to 0.07 kPa for NADH-linked LEAK respiration with glutamate&malate (GM), and NADH-&succinate-linked OXPHOS capacity with GM and pyruvate, in agreement with and extending the literature. p_{50} increased with an increase from 25 °C to 37 °C. In heart and liver, p_{50} was higher in OXPHOS- than in LEAK-states, increasing proportionally with CIV turnover. Surprisingly, however, brain mt did not follow this kinetic pattern in S-linked coupling control states, irrespective of rotenone addition, with p_{50} values in LEAK up to 2-times higher than in OXPHOS, despite a 3-4 fold decline of J_{O2}. Further studies are underway to elucidate the underlying mechanisms, and to address the question if mouse brain is an exception or representative of a general pattern.

1. K. Krab, H. Kempe, M. Wikström, Explaining the enigmatic K_M for oxygen in cytochrome c oxidase: A kinetic model, BBA 1807 (2011) 348–358
2. E. Gnaiger, R. Steinlechner-Maran, G. Méndez, T. Eberl, R. Margreiter, Control of mitochondrial and cellular respiration by oxygen, J. Bioenerg. Biomembr. 27 (1995) 583–96

doi:10.1016/j.bbabio.2018.09.052

Lunchtime special

New Mitochondrial Function Assay Technology

Barry R. Bochner
Biolog, Inc., Hayward, CA, USA

We have developed a new mitochondrial function assay technology that measures the rates of metabolism of mitochondrial substrates and the sensitivity of metabolism of these substrates to mitochondrial inhibitors. The technology employs saponin permeabilized cells and a redox dye added to 96-well microplates that contain mitochondrial substrates or inhibitors precoated and dried into the wells. The MitoPlate S-1™ has a triplicate repeat of a set of 31 substrates. Mitochondrial function is assayed by measuring the rates of dye reduction from electrons flowing into and through the electron transport chain from substrates whose oxidation produces NADH (e.g., L-malate) or $FADH_2$ (e.g., succinate). The electrons donated to complex 1 or complex 2 travel to the distal portion of the electron transport chain where a tetrazolium redox dye (MC) acts as a terminal electron acceptor and changes from colorless to a purple formazan upon reduction. All 96 assays in the MitoPlate are run concurrently, and each assay provides different information because each substrate follows a different metabolic route using different transporters to enter the mitochondria, and then different dehydrogenases to produce NADH or $FADH_2$. The MitoPlate S-1™ can also be used to assess the activity and specificity of substrate transport inhibitors, dehydrogenase inhibitors, or electron transport chain inhibitors. A second assay plate, the MitoPlate I-1™, provides another assessment of mitochondrial function by measuring the sensitivity of mitochondrial electron flow to a set of 22 diverse inhibitors titrated at 4 dilutions. The I-1 plates can be run using any of the NADH or $FADH_2$ producing substrates, each providing additional information.

Appendices

Appendix A

Supplier Names and Addresses

Abcam plc	330 Cambridge Science Park, Cambridge, CB4 0FL, United Kingdom
Agilent Technologies	Agilent Technologies Ireland Ltd., Unit 3, Euro House, Euro Business Park, Little Island, Co. Cork, Ireland
BD Biosciences	1030 Eskdale Road, Winnersh Triangle, Wokingham, RG41 5TS United Kingdom
Bio-Sciences Ltd.	3 Charlemont Terrace, Crofton Road, Dun Laoghaire, Co. Dublin, A96 K7H7, Ireland

Eurofins Genomics	Eurofins Genomics UK, i54 Business Park, Valiant Way, WV9 5GB, Wolverhampton, United Kingdom
Eurogentec	Parc Scientifique du Sart Tilman, 4102 Seraing, Belgium
Fisher Scientific Ltd.	Fisher Scientific Ireland Ltd., Suite 3, Plaza 212, Blanchardstown Corporate Park 2, Ballycoolin, Dublin 15, Ireland
ImmunoTools GmbH	Gladiolenweg 2, 26169 Friesoythe, Germany
List Biological Laboratories, Inc.	540 Division Street, Campbell, California 95008, United States of America
Medical Supply Company Ltd.	Damastown Industrial Estate, Mulhuddart, Dublin 15, D15 V293, Ireland

Merck Millipore Ireland B.V.	Tullagreen, Carrigtwohill, Co. Cork, Ireland
Miltenyi Biotec Ltd.	Almac House, Church Lane, Bisley, Surrey, GU24 9DR, United Kingdom
MyBio Ltd.	Kilkenny Research and Innovation Centre, St. Kieran's College Road, Kilkenny, Ireland
Sigma-Aldrich	Sigma-Aldrich Ireland Ltd., Vale Road, Arklow, Wicklow, Ireland
TCD Hazardous Materials Facility	East End Development 4/5, Trinity College Dublin, Dublin 2, Ireland
VWR	VWR International Ltd., Hunter Boulevard, Magna Park, Lutterworth, Leicestershire, LE17 4XN, United Kingdom

Appendix B

Agarose Gels from Genotyping Experiments

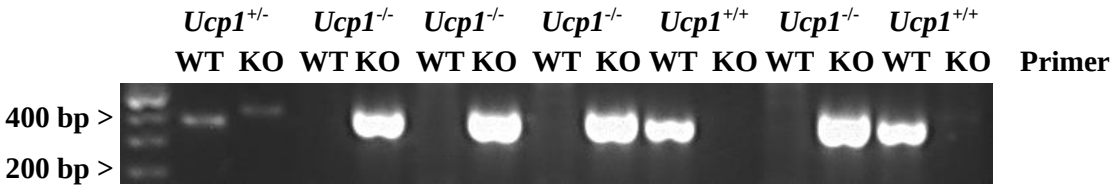

Figure A1: *Ucp1* genotyping agarose gel

Representative agarose gel of genomic DNA for *Ucp1* genotyping. 50 ng of genomic DNA isolated from ear punches or tail clips of alleged $Ucp1^{+/+}$, $Ucp1^{+/-}$ and $Ucp1^{-/-}$ mice underwent PCR and were electrophoresed on a 1.5 % (w/v) agarose gel at 110 V for 30 min. PCR reactions were performed with primers for WT and KO allele detection. WT and KO PCR product sizes are 378 and 400 bp, respectively. The proposed genotype of DNA, as assessed with GeneRuler™ DNA Ladder Mix, and primers used are written above the gel.

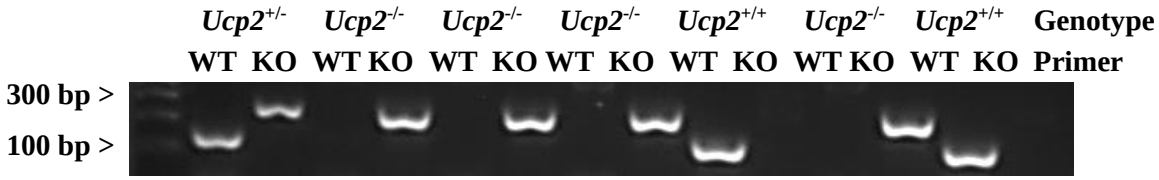

Figure A2: *Ucp2* genotyping agarose gel

Representative agarose gel of genomic DNA for *Ucp2* genotyping. 50 ng of genomic DNA isolated from ear punches or tail clips of alleged $Ucp2^{+/+}$, $Ucp2^{+/-}$ and $Ucp2^{-/-}$ mice underwent PCR and were electrophoresed on a 1.5 % (w/v) agarose gel at 130 V for 30 min. PCR reactions were performed with primers for WT and KO allele detection. WT and KO PCR product sizes are 156 and 280 bp, respectively. The proposed genotype of DNA, as assessed with GeneRuler™ DNA Ladder Mix, and primers used are written above the gel.

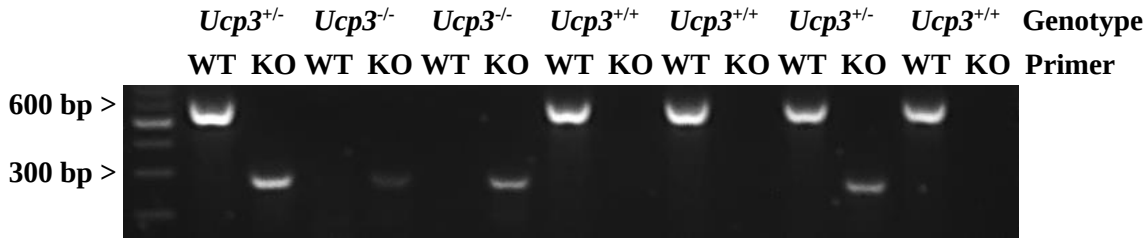

Figure A3: *Ucp3* genotyping agarose gel

Representative agarose gel of genomic DNA for *Ucp3* genotyping. 50 ng of genomic DNA isolated from ear punches or tail clips of alleged $Ucp3^{+/+}$, $Ucp3^{+/-}$ and $Ucp3^{-/-}$ mice underwent PCR and were electrophoresed on a 1.5 % (w/v) agarose gel at 90 V for 30 min. PCR reactions were performed with primers for WT and KO allele detection. WT and KO PCR product sizes are 600 and 300 bp, respectively. The proposed genotype of DNA, as assessed with GeneRuler™ DNA Ladder Mix, and primers used are written above the gel.

References

References

Adams, A. E., Carroll, A. M., Fallon, P. G. and Porter, R. K. (2008a). Mitochondrial uncoupling protein 1 expression in thymocytes. *Biochimica et Biophysica Acta*, *1777*, 772 – 776.

Adams, A. E., Hanrahan, O., Nolan, D. N., Voorheis, H. P., Fallon, P. and Porter, R. K. (2008b). Images of mitochondrial UCP 1 in mouse thymocytes using confocal microscopy. *Biochimica et Biophysica Acta*, *1777*, 115 – 117.

Adams, A. E., Kelly, O. M. and Porter, R. K. (2010). Absence of mitochondrial uncoupling protein 1 affects apoptosis in thymocytes, thymocyte/T-cell profile and peripheral T-cell number. *Biochimica et Biophysica Acta*, *1797*, 807 – 816.

Aghajani, K., Keerthivasan, S., Yu, Y. and Gounari, F. (2012). Generation of CD4CreER^{T2} transgenic mice to study development of peripheral CD4-T-cells. *Genesis*, *50* (12), 908 – 913.

Akira, S., Uematsu, S. and Takeuchi, O. (2006). Pathogen Recognition and Innate Immunity. *Cell*, *124*, 783 – 801.

Arsenijevic, D., Onuma, H., Pecqueur, C., Raimbault, S., Manning, B. S., Miroux, B., Couplan, E., Alves-Guerra, M.-C., Goubern, M., Surwit, R., Bouillaud, F., Richard, D., Collins, S. and Ricquier, D. (2000). Disruption of the uncoupling protein-2 gene in mice reveals a role in immunity and reactive oxygen species production. *Nature Genetics*, *26*, 435 – 439.

Awate, S., Babiuk, L. A. and Mutwiri, G. (2013). Mechanisms of action of adjuvants. *Frontiers in Immunology*, *4* (114), 1 – 10.

Azzu, V., Mookerjee, S. A. and Brand, M. D. (2010). Rapid turnover of mitochondrial uncoupling protein 3. *Biochemical Journal*, *426*, 13 – 17.

Bai, Y., Onuma, H., Bai, X., Medvedev, A. V., Misukonis, M., Weinberg, J. B., Cao, W., Robidoux, J., Floering, L. M., Daniel, K. W. and Collins, S. (2005). Persistent Nuclear Factor-κB Activation in *Ucp2*-/- Mice Leads to Enhanced Nitric Oxide and Inflammatory Cytokine Production. *Journal of Biological Chemistry*, *280* (19), 19062 – 19069.

Behrens, W. A. and Himms-Hagen, J. (1977). Alteration in Skeletal Muscle Mitochondria of Cold-Acclimated Rats: Association with Enhanced Metabolic Response to Noradrenaline. *Journal of Bioenergetics and Biomembranes*, *9*, 41 – 63.

Berardi, M. J. and Chou, J. J. (2014). Fatty Acid Flippase Activity of UCP2 Is Essential for Its Proton Transport in Mitochondria. *Cell Metabolism*, *20*, 541 – 552.

Berg, J. M., Tymoczko, J. L., Stryer, L. and Gatto Jnr., G. J. (2012). *Biochemistry* (Seventh). New York: W. H. Freeman and Company.

Betz, M. J. and Enerbäck, S. (2015). Human Brown Adipose Tissue: What We Have Learned So Far. *Diabetes*, *64*, 2352 – 2360.

Bezaire, V., Spriet, L. L., Campbell, S., Sabet, N., Gerrits, M., Bonen, A. and Harper, M.-E. (2005). Constitutive UCP3 overexpression at physiological levels increases mouse skeletal muscle capacity for fatty acid transport and oxidation. *FASEB Journal*, *19* (8), 977 – 979.

Bienengraeber, M., Echtay, K. S. and Klingenberg, M. (1998). H^+ Transport by Uncoupling Protein (UCP-1) Is Dependent on a Histidine Pair, Absent in UCP-2 and UCP-3. *Biochemistry*, *37* (1), 3 – 8.

Bonet, M. L., Serra, F., Matamala, J. C., García-Palmer, F. J. and Palou, A. (1995). Selective loss of the uncoupling protein from light versus heavy mitochondria of brown adipocytes after a decrease in noradrenergic stimulation *in vivo* and *in vitro*. *Biochemical Journal*, *311*, 327 – 331.

Boss, O., Muzzin, P. and Giacobino, J.-P. (1998). The uncoupling proteins, a review. *European Journal of Endocrinology*, *139*, 1 – 9.

Boss, O., Samec, S., Paoloni-Giacobino, A., Rossier, C., Dulloo, A., Seydoux, J., Muzzin, P. and Giacobino, J. P. (1997). Uncoupling protein-3: a new member of the mitochondrial carrier family with tissue-specific expression. *FEBS Letters*, *408*, 39 – 42.

Boyman, O. and Sprent, J. (2012). The role of interleukin-2 during homeostasis and activation of the immune system. *Nature Reviews Immunology*, *12*, 180 – 190.

Brand, M. D. (1990). The proton leak across the mitochondrial inner membrane. *Biochimica et Biophysica Acta*, *1018*, 128 – 133.

Brand, M. D. (2000). Uncoupling to survive? The role of mitochondrial inefficiency in ageing. *Experimental Gerontology*, *35*, 811 – 820.

Brand, M. D., Affourtit, C., Esteves, T. C., Green, K., Lambert, A. J., Miwa, S., Pakay, J. L. and Parker, N. (2004). Mitochondrial superoxide: production, biological effects and activation of uncoupling proteins. *Free Radical Biology and Medicine*, *37* (6), 755 – 767.

Brand, M. D., Chien, L.-F., Ainscow, E. K., Rolfe, D. F. S. and Porter, R. K. (1994). The causes and functions of mitochondrial proton leak. *Biochimica et Biophysica Acta*, *1187*, 132 – 139.

Brand, M. D., Pamplona, R., Portero-Otín, M., Requena, J. R., Roebuck, S. J.,

Buckingham, J. A., Clapham, J. C. and Cadenas, S. (2002). Oxidative damage and phospholipid fatty acyl composition in skeletal muscle mitochondria from mice underexpressing or overexpressing uncoupling protein 3. *Biochemical Journal*, *368*, 597 – 603.

Brand, M. D., Parker, N., Affourtit, C., Mookerjee, S. A. and Azzu, V. (2010). Mitochondrial uncoupling protein 2 in pancreatic β-cells. *Diabetes, Obesity and Metabolism*, *12* (2), 134 – 140.

Breen, E. P., Pilgrim, W., Clarke, K. J., Yssel, C., Farrell, M., Zhou, J., Murphy, P. V. and Porter, R. K. (2013). Lack of activation of UCP1 in isolated brown adipose tissue mitochondria by glucose-*O*-ω-modified saturated fatty acids of various chain lengths. *Journal of Chemical Biology*, *6*, 121 – 133.

Brennan, C. M., Breen, E. P. and Porter, R. K. (2006). Cold acclimation and oxygen consumption in the thymus. *Biochimica et Biophysica Acta*, *1757*, 1463 – 1468.

Brenner, D., Krammer, P. H. and Arnold, R. (2008). Concepts of activated T cell death. *Critical Reviews in Oncology/Hematology*, *66*, 52 – 64.

Broere, F., Apasov, S. G., Sitkovsky, M. V. and van Eden, W. (2011). 'T cell subsets and T cell-mediated immunity' in Nijkamp, F. P. and Parnham, M. J. (Eds.), *Principles of Immunopharmacology* (Third), 15 – 28. Berlin: Springer Science and Business Media.

Brookes, P. S., Parker, N., Buckingham, J. A., Vidal-Puig, A., Halestrap, A. P., Gunter, T. E., Nicholls, D. G., Bernardi, P., Lemasters, J. J. and Brand, M. D. (2008). UCPs - Unlikely Calcium Porters. *Nature Cell Biology*, *10* (11), 1235 – 1240.

Buttgereit, F. and Brand, M. D. (1995). A hierarchy of ATP-consuming processes in mammalian cells. *Biochemical Journal*, *312*, 163 – 167.

Cadenas, S., Buckingham, J. A., Samec, S., Seydoux, J., Din, N., Dulloo, A. G. and Brand, M. D. (1999). UCP2 and UCP3 rise in starved rat skeletal muscle but mitochondrial proton conductance is unchanged. *FEBS Letters*, *462*, 257 – 260.

Cadenas, S., Echtay, K. S., Harper, J. A., Jekabsons, M. B., Buckingham, J. A., Grau, E., Abuin, A., Chapman, H., Clapham, J. C. and Brand, M. D. (2002). The Basal Proton Conductance of Skeletal Muscle Mitochondria from Transgenic Mice Overexpressing or Lacking Uncoupling Protein-3. *Journal of Biological Chemistry*, *277* (4), 2773 – 2778.

Cannon, B. and Nedergaard, J. (2004). Brown Adipose Tissue: Function and Physiological Significance. *Physiological Reviews*, *84*, 277 – 359.

Carroll, A. M., Haines, L. R., Pearson, T. W., Brennan, C., Breen, E. P. and Porter, R. K. (2004). Immunodetection of UCP1 in rat thymocytes. *Biochemical Society*

Transactions, *32* (6), 1066 – 1067.

Carroll, A. M., Haines, L. R., Pearson, T. W., Fallon, P. G., Walsh, C. M., Brennan, C. M., Breen, E. P. and Porter, R. K. (2005). Identification of a Functioning Mitochondrial Uncoupling Protein 1 in Thymus. *Journal of Biological Chemistry*, *280* (15), 15534 – 15543.

Carroll, A. M. and Porter, R. K. (2004). Starvation-sensitive UCP 3 protein expression in thymus and spleen mitochondria. *Biochimica et Biophysica Acta*, *1700*, 145 – 150.

Carroll, A. M., Porter, R. K. and Morrice, N. A. (2008). Identification of serine phosphorylation in mitochondrial uncoupling protein 1. *Biochimica et Biophysica Acta*, *1777*, 1060 – 1065.

Chang, C.-H., Curtis, J. D., Maggi Jnr., L. B., Faubert, B., Villarino, A. V., O'Sullivan, D., Huang, S. C.-C., van der Windt, G. J. W., Blagih, J., Oiu, J., Weber, J. D., Pearce, E. J., Jones, R. G. and Pearce, E. L. (2013). Posttranscriptional Control of T Cell Effector Function by Aerobic Glycolysis. *Cell*, *153*, 1239 – 1251.

Chartoumpekis, D. V., Ziros, P. G., Psyrogiannis, A. I., Papavassiliou, A. G., Kyriazopoulou, V. E., Sykiotis, G. P. and Habeos, I. G. (2011). Nrf2 Represses FGF21 During Long-Term High-Fat Diet-Induced Obesity in Mice. *Diabetes, 60*, 2465 – 2473.

Choi, S. W., Gerencser, A. A. and Nicholls, D. G. (2009). Bioenergetic analysis of isolated cerebrocortical nerve terminals on a microgram scale: spare respiratory capacity and stochastic mitochondrial failure. *Journal of Neurochemistry*, *109*, 1179 – 1191.

Chouchani, E. T., Kazak, L., Jedrychowski, M. P., Lu, G. Z., Erickson, B. K., Szpyt, J., Pierce, K. A., Laznik-Bogoslavski, D., Vetrivelan, R., Clish, C. B., Robinson, A. J., Gygi, S. P. and Spiegelman, B. M. (2016). Mitochondrial ROS regulate thermogenic energy expenditure and sulfenylation of UCP1. *Nature*, *532*, 112 – 116.

Chouchani, E. T., Kazak, L. and Spiegelman, B. M. (2017). Mitochondrial reactive oxygen species and adipose tissue thermogenesis: Bridging physiology and mechanisms. *Journal of Biological Chemistry*, *292* (41), 16810 – 16816.

Clarke, K. J., Adams, A. E., Manzke, L. H., Pearson, T. W., Borchers, C. H. and Porter, R. K. (2012). A role for ubiquitinylation and the cytosolic proteasome in turnover of mitochondrial uncoupling protein 1 (UCP1). *Biochimica et Biophysica Acta*, *1817*, 1759 – 1767.

Clarke, K. J. and Porter, R. K. (2013). Uncoupling protein 1 dependent reactive oxygen species production by thymus mitochondria. *International Journal of Biochemistry and Cell Biology*, *45*, 81 – 89.

Codarri, L., Gyülvészi, G., Tosevski, V., Hesske, L., Fontana, A., Magnenat, L., Suter, T. and Becher, B. (2011). RORγt drives production of the cytokine GM-CSF in helper T cells, which is essential for the effector phase of autoimmune neuroinflammation. *Nature Immunology*, *12* (6), 560 – 567.

Cohen, P. and Spiegelman, B. M. (2016). Cell biology of fat storage. *Molecular Biology of the Cell*, *27*, 2523 – 2527.

Considine, M. J., Goodman, M., Echtay, K. S., Laloi, M., Whelan, J., Brand, M. D. and Sweetlove, L. J. (2003). Superoxide Stimulates a Proton Leak in Potato Mitochondria That Is Related to the Activity of Uncoupling Protein. *Journal of Biological Chemistry*, *278* (25), 22298 – 22302.

Costa, A. D. T., Nantes, I. L., Ježek, P., Leite, A., Arruda, P. and Vercesi, A. E. (1999). Plant Uncoupling Mitochondrial Protein Activity in Mitochondria Isolated from Tomatoes at Different Stages of Ripening. *Journal of Bioenergetics and Biomembranes*, *31* (5), 527 – 533.

Crispín, J. C. and Tsokos, G. C. (2009). Transcriptional regulation of IL-2 in health and autoimmunity. *Autoimmunity Review, 8* (3), 190 – 195.

Cunningham, O., McElligott, A. M., Carroll, A. M., Breen, E., Reguenga, C., Oliveira, M. E. M., Azevedo, J. E. and Porter, R. K. (2003). Selective detection of UCP 3 expression in skeletal muscle: effect of thyroid status and temperature acclimation. *Biochimica et Biophysica Acta*, *1604*, 170 – 179.

Cypess, A. M., Lehman, S., Williams, G., Tal, I., Rodman, D., Goldfine, A. B., Kuo, F. C., Palmer, E. L., Tseng, Y.-H., Doria, A., Kolodny, G. M. and Kahn, C. R. (2009). Indentification and Importance of Brown Adipose Tissue in Adult Humans. *New England Journal of Medicine*, *360* (15), 1509 – 1517.

de Bilbao, F., Arsenijevic, D., Vallet, P., Hjelle, O. P., Ottersen, O. P., Bouras, C., Raffin, Y., Abou, K., Langhans, W., Collins, S., Plamondon, J., Alves-Guerra, M.-C., Haguenauer, A., Garcia, I., Richard, D., Ricquier, D. and Giannakopoulos, P. (2004). Resistance to cerebral ischemic injury in UCP2 knockout mice: evidence for a role of UCP2 as a regulator of mitochondrial glutathione levels. *Journal of Neurochemistry*, *89*, 1283 – 1292.

Dlasková, A., Clarke, K. J. and Porter, R. K. (2010). The role of UCP 1 in production of reactive oxygen species by mitochondria isolated from brown adipose tissue. *Biochimica et Biophysica Acta*, *1797*, 1470 – 1476.

Drahota, Z., Chowdhury, S. K. R., Floryk, D., Mráček, T., Wilhelm, J., Rauchová, H., Lenaz, G. and Houštěk, J. (2002). Glycerophosphate-Dependent Hydrogen Peroxide

Production by Brown Adipose Tissue Mitochondria and Its Activation by Ferricyanide. *Journal of Bioenergetics and Biomembranes*, *34* (2), 105 – 113.

Duan, W., So, T., Mehta, A. K., Choi, H. and Croft, M. (2011). Inducible $CD4^{+}LAP^{+}Foxp3^{-}$ Regulatory T Cells Suppress Allergic Inflammation. *Journal of Immunology*, *187*, 6499 – 6507.

Dulloo, A. G., Samec, S. and Seydoux, J. (2001). Uncoupling protein 3 and fatty acid metabolism. *Biochemical Society Transactions*, *29* (6), 785 – 791.

Dumont, A., Hehner, S. P., Hofmann, T. G., Ueffing, M., Dröge, W. and Schmitz, M. L. (1999). Hydrogen peroxide-induced apoptosis is CD95-independent, requires the release of mitochondria-derived reactive oxygen species and the activation of NF-κB. *Oncogene*, *18*, 747 – 757.

Echtay, K. S., Esteves, T. C., Pakay, J. L., Jekabsons, M. B., Lambert, A. J., Portero-Otín, M., Pamplona, R., Vidal-Puig, A. J., Wang, S., Roebuck, S. J. and Brand, M. D. (2003). A signalling role for 4-hydroxy-2-nonenal in regulation of mitochondrial uncoupling. *EMBO Journal*, *22* (16), 4103 – 4110.

Echtay, K. S., Roussel, D., St-Pierre, J., Jekabsons, M. B., Cadenas, S., Stuart, J. A., Harper, J. A., Roebuck, S. J., Morrison, A., Pickering, S., Clapham, J. C. and Brand, M. D. (2002). Superoxide activates mitochondrial uncoupling proteins. *Nature*, *415*, 96 – 99.

Echtay, K. S., Winkler, E., Frischmuth, K. and Klingenberg, M. (2001). Uncoupling proteins 2 and 3 are highly active H^{+} transporters and highly nucleotide sensitive when activated by coenzyme Q (ubiquinone). *Proceedings of the National Academy of Sciences*, *98* (4), 1416 – 1421.

El-Behi, M., Ciric, B., Dai, H., Yan, Y., Cullimore, M., Safavi, F., Zhang, G.-X., Dittel, B. N. and Rostami, A. (2011). The encephalitogenicity of T_H17 cells is dependent on IL-1- and IL-23-induced production of the cytokine GM-CSF. *Nature Immunology*, *12* (6), 568 – 575.

Ellmeier, W., Sunshine, M. J., Losos, K., Hatam, F. and Littman, D. R. (1997). An Enhancer That Directs Lineage-Specific Expression of CD8 in Positively Selected Thymocytes and Mature T Cells. *Immunity*, *7*, 537 – 547.

Emre, Y., Hurtaud, C., Nübel, T., Criscuolo, F., Ricquier, D. and Cassard-Doulcier, A.-M. (2007). Mitochondria contribute to LPS-induced MAPK activation via uncoupling protein UCP2 in macrophages. *Biochemical Journal*, *402*, 271 – 278.

Enerbäck, S. (2010). Brown adipose tissue in humans. *International Journal of Obesity*, *34*, S43 – S46.

Enerbäck, S., Jacobsson, A., Simpson, E. M., Guerra, C., Yamashita, H., Harpers, M.-E. and Kozak, L. P. (1997). Mice lacking mitochondrial uncoupling protein are cold-sensitive but not obese. *Nature, 387*, 90 – 94.

Fedorenko, A., Lishko, P. V. and Kirichok, Y. (2012). Mechanism of Fatty-Acid-Dependent UCP1 Uncoupling in Brown Fat Mitochondria. *Cell, 151*, 400 – 413.

Feldmann, H. M., Golozoubova, V., Cannon, B. and Nedergaard, J. (2009). UCP1 Ablation Induces Obesity and Abolishes Diet-Induced Thermogenesis in Mice Exempt from Thermal Stress by Living at Thermoneutrality. *Cell Metabolism, 9*, 203 – 209.

Ferrick, D. A., Neilson, A. and Beeson, C. (2008). Advances in measuring cellular bioenergetics using extracellular flux. *Drug Discovery Today, 13* (5–6), 268 – 274.

Fleury, C., Neverova, M., Collins, S., Raimbault, S., Champigny, O., Levi-Meyrueis, C., Bouillaud, F., Seldin, M. F., Surwit, R. S., Ricquier, Daniel and Warden, C. H. (1997). Uncoupling protein-2: a novel gene linked to obesity and hyperinsulinemia. *Nature Genetics, 15*, 269 – 272.

Fox, C. J., Hammerman, P. S. and Thompson, C. B. (2005). Fuel feeds function: energy metabolism and the T-cell response. *Nature Reviews Immunology, 5*, 844 – 852.

Gandhi, R., Farez, M. F., Wang, Y., Kozoriz, D., Quintana, F. J. and Weiner, H. L. (2010). Cutting Edge: Human Latency-Associated Peptide^{+} T Cells: A Novel Regulatory T Cell Subset. *Journal of Immunology, 184*, 4620 – 4624.

García-Martínez, C., Sibille, B., Solanes, G., Darimont, C., Macé, K., Villarroya, F. and Gómez-Foix, A. M. (2001). Overexpression of UCP3 in cultured human muscle lowers mitochondrial membrane potential, raises ATP/ADP ratio, and favors fatty acid versus glucose oxidation. *FASEB Journal, 15* (11), 2033 – 2035.

Garlid, K. D., Jabůrek, M. and Ježek, P. (2001). Mechanism of uncoupling protein action. *Biochem Society Transactions, 29* (6), 803 – 806.

Garlid, K. D., Jabůrek, M. and Ježek, P. (1998). The mechanism of proton transport mediated by mitochondrial uncoupling proteins. *FEBS Letters, 438*, 10 – 14.

Garlid, K. D., Jabůrek, M., Ježek, P. and Vařecha, M. (2000). How do uncoupling proteins uncouple? *Biochimica et Biophysica Acta, 1459*, 383 – 389.

Garlid, K. D., Orosz, D. E., Modrianský, M., Vassanelli, S. and Ježek, P. (1996). On the Mechanism of Fatty Acid-induced Proton Transport by Mitochondrial Uncoupling Protein. *Journal of Biological Chemistry, 271* (5), 2615 – 2620.

Gimeno, R. E., Dembski, M., Weng, X., Deng, N., Shyjan, A. W., Gimeno, C. J., Iris, F., Ellis, S. J., Woolf, E. A. and Tartaglia, L. A. (1997). Cloning and Characterization of an Uncoupling Protein Homolog: A Potential Molecular Mediator of Human

Thermogenesis. *Diabetes*, *46*, 900 – 906.

Goldberg, M. V. and Drake, C. G. (2011). LAG-3 in Cancer Immunotherapy. *Current Topics in Microbiology and Immunology*, *344*, 269 – 278.

Golozoubova, V., Cannon, B. and Nedergaard, J. (2006). UCP1 is essential for adaptive adrenergic nonshivering thermogenesis. *American Journal of Physiology - Endocrinology and Metabolism*, *291*, E350 – E357.

Golozoubova, V., Hohtola, E., Matthias, A., Jacobsson, A., Cannon, B. and Nedergaard, J. (2001). Only UCP1 can mediate adaptive nonshivering thermogenesis in the cold. *FASEB Journal*, *15* (11), 2048 – 2050.

Gong, D.-W., He, Y., Karas, M. and Reitman, M. (1997). Uncoupling Protein-3 Is a Mediator of Thermogenesis Regulated by Thyroid Hormone, β3-Adrenergic Agonists, and Leptin. *Journal of Biological Chemistry*, *272* (39), 24129 – 24132.

Gong, D.-W., Monemdjou, S., Gavrilova, O., Leon, L. R., Marcus-Samuels, B., Chou, C. J., Everett, C., Kozak, L. P., Li, C., Deng, C., Harper, M.-E. and Reitman, M. L. (2000). Lack of Obesity and Normal Response to Fasting and Thyroid Hormone in Mice Lacking Uncoupling Protein-3. *Journal of Biological Chemistry*, *275* (21), 16251 – 16257.

Graier, W. F., Trenker, M. and Malli, R. (2008). Mitochondrial Ca^{2+}, the secret behind the function of uncoupling proteins 2 and 3? *Cell Calcium*, *44* (1), 36 – 50.

Gregori, S., Goudy, K. S. and Roncarolo, M. G. (2012). The cellular and molecular mechanisms of immuno-suppression by human type 1 regulatory T cells. *Frontiers in Immunology*, *3* (30), 1 – 12.

Grumont, R. J., Strasser, A. and Gerondakis, S. (2002). B Cell Growth Is Controlled by Phosphatidylinosotol 3-Kinase-Dependent Induction of Rel/NF-κB Regulated c-myc Transcription. *Molecular Cell*, *10*, 1283 – 1294.

Grundlingh, J., Dargan, P. I., El-Zanfaly, M. and Wood, D. M. (2011). 2,4-Dinitrophenol (DNP): A Weight Loss Agent with Significant Acute Toxicity and Risk of Death. *Journal of Medical Toxicology*, *7*, 205 – 212.

Gui, J., Mustachio, L. M., Su, D.-M. and Craig, R. W. (2012). Thymus Size and Age-related Thymic Involution: Early Programming, Sexual Dimorphism, Progenitors and Stroma. *Aging and Disease*, *3* (3), 280 – 290.

Han, Y. H., Buffolo, M., Pires, K. M., Pei, S., Scherer, P. E. and Boudina, S. (2016). Adipocyte-Specific Deletion of Manganese Superoxide Dismutase Protects From Diet-Induced Obesity Through Increased Mitochondrial Uncoupling and Biogenesis. *Diabetes*, *65*, 2639 – 2651.

Hanák, P. and Ježek, P. (2001). Mitochondrial uncoupling proteins and phylogenesis - UCP4 as the ancestral uncoupling protein. *FEBS Letters*, *495*, 137 – 141.

Harms, M. and Seale, P. (2013). Brown and beige fat: development, function and therapeutic potential. *Nature Medicine*, *19* (10), 1252 – 1263.

Harper, M.-E., Dent, R. M., Bezaire, V., Antoniou, A., Gauthier, A., Monemdijou, S. and McPherson, R. (2001). UCP3 and its putative function: consistencies and controversies. *Biochemical Society Transactions*, *29* (6), 768 – 773.

Heaton, G. M., Wagenvoord, R. J., Kemp Jr., A. and Nicholls, D. G. (1978). Brown-Adipose-Tissue Mitochondria: Photoaffinity Labelling of the Regulatory Site of Energy Dissipation. *European Journal of Biochemistry*, *82*, 515 – 521.

Henze, K. and Martin, W. (2003). Essence of mitochondria. *Nature*, *426*, 127 – 128.

Hesselink, M. K. C., Keizer, H. A., Borghouts, L. B., Schaart, G., Kornips, C. F. P., Slieker, L. J., Sloop, K. W., Saris, W. H. M. and Schrauwen, P. (2001). Protein expression of UCP3 differs between human type 1, type 2a, and type 2b fibers. *FASEB Journal*, *15* (6), 1071 – 3.

Hettmann, T., DiDonato, J., Karin, M. and Leiden, J. M. (1999). An Essential Role for Nuclear Factor κB in Promoting Double Positive Thymocyte Apoptosis. *Journal of Experimental Medicine*, *189* (1), 145 – 157.

Hildeman, D. A., Mitchell, T., Kappler, J. and Marrack, P. (2003). T cell apoptosis and reactive oxygen species. *Journal of Clinical Investigation*, *111* (5), 575 – 581.

Hilse, K. E., Kalinovich, A. V., Rupprecht, A., Smorodchenko, A., Zeitz, U., Staniek, K., Erben, R. G. and Pohl, E. E. (2016). The expression of UCP3 directly correlates to UCP1 abundance in brown adipose tissue. *Biochimica et Biophysica Acta*, *1857*, 72 – 78.

Hilse, K. E., Rupprecht, A., Egerbacher, M., Bardakji, S., Zimmermann, L., Wulczyn, A. E. M. S. and Pohl, E. E. (2018). The Expression of Uncoupling Protein 3 Coincides With the Fatty Acid Oxidation Type of Metabolism in Adult Murine Heart. *Frontiers in Physiology*, *9* (747), 1 – 11.

Hoffmann, L. S., Etzrodt, J., Willkomm, L., Sanyal, A., Scheja, L., Fischer, A. W. C., Stasch, J.-P., Bloch, W., Friebe, A., Heeren, J. and Pfeifer, A. (2015). Stimulation of soluble guanylyl cyclase protects against obesity by recruiting brown adipose tissue. *Nature Communications*, *6*, 1 – 9.

Hong, J., Li, N., Zhang, X., Zheng, B. and Zhang, J. Z. (2005). Induction of $CD4^{+}CD25^{+}$ regulatory T cells by copolymer-I through activation of transcription factor Foxp3. *Proceedings of the National Academy of Sciences*, *102* (18), 6449 – 6454.

Hori, S., Nomura, T. and Sakaguchi, S. (2003). Control of Regulatory T Cell Development by the Transcription Factor Foxp3. *Science*, *299* (5609), 1057 – 1061.

Huang, C.-T., Workman, C. J., Flies, D., Pan, X., Marson, A. L., Zhou, G., Hipkiss, E. L., Ravi, S., Kowalski, J., Levitsky, H. I., Powell, J. D., Pardoll, D. M., Drake, C. G. and Vignali, D. A. A. (2004). Role of LAG-3 in Regulatory T cells. *Immunity*, *21*, 503 – 513.

Huang, S.-G. and Klingenberg, M. (1995). Nature of the masking of nucleotide-binding sites in brown adipose tissue mitochondria: Involvement of endogenous adenosine triphosphate. *European Journal of Biochemistry*, *229*, 718 – 725.

Hurtaud, C., Gelly, C., Chen, Z., Lévi-Meyrueis, C. and Bouillaud, F. (2007). Glutamine stimulates translation of uncoupling protein 2 mRNA. *Cellular and Molecular Life Sciences*, *64*, 1853 – 1860.

Ivanov, I. I., McKenzie, B. S., Zhou, L., Tadokoro, C. E., Lepelley, A., Lafaille, J. J., Cua, D. J. and Littman, D. R. (2006). The Orphan Nuclear Receptor RORγt Directs the Differentiation Program of Proinflammatory IL-17^{+} T Helper Cells. *Cell*, *126*, 1121 – 1133.

Jabůrek, M. and Garlid, K. D. (2003). Reconstitution of Recombinant Uncoupling Proteins: UCP1, -2, and -3 have similar affinities for ATP and are unaffected by coenzyme Q_{10}. *Journal of Biological Chemistry*, *278* (28), 25825 – 25831.

Jabůrek, M., Vařecha, M., Gimeno, R. E., Dembski, M., Ježek, P., Zhang, M., Burn, P., Tartaglia, L. A. and Garlid, K. D. (1999). Transport Function and Regulation of Mitochondrial Uncoupling Proteins 2 and 3. *Journal of Biological Chemistry*, *274* (37), 26003 – 26007.

Jabůrek, M., Vařecha, M., Ježek, P. and Garlid, K. D. (2001). Alkylsulfonates as probes of uncoupling protein transport mechanism - ion pair transport demonstrates that direct H^{+} translocation by UCP1 is not necessary for uncoupling. *Journal of Biological Chemistry*, *276* (34), 31897 – 31905.

Jacobs, S. R., Herman, C. E., MacIver, N. J., Wofford, J. A., Wieman, H. L., Hammen, J. J. and Rathmell, J. C. (2008). Glucose Uptake Is Limiting in T Cell Activation and Requires CD28-Mediated Akt-Dependent and Independent Pathways. *Journal of Immunology*, *180* (7), 4476 – 4486.

Janeway Jnr., C. A. and Medzhitov, R. (2002). Innate Immune Recognition. *Annual Review of Immunology*, *20*, 197 – 216.

Jarmuszkiewicz, W., Sluse-Goffart, C. M., Hryniewiecka, L. and Sluse, F. E. (1999). Identification and Characterization of a Protozoan Uncoupling Protein in

Acanthamoeba castellanii. *Journal of Biological Chemistry*, *274* (33), 23198 – 23202.

Jeffery, C. J. (2015). Why study moonlighting proteins? *Frontiers in Genetics*, *6* (211), 1 – 5.

Ježek, P. and Hlavatá, L. (2005). Mitochondria in homeostasis of reactive oxygen species in cell, tissues, and organism. *International Journal of Biochemistry and Cell Biology*, *37*, 2478 – 2503.

Ježek, P., Modrianský, M. and Garlid, K. D. (1997a). A structure-activity study of fatty acid interaction with mitochondrial uncoupling protein. *FEBS Letters*, *408*, 166 – 170.

Ježek, P., Modrianský, M. and Garlid, K. D. (1997b). Inactive fatty acids are unable to flip-flop across the lipid bilayer. *FEBS Letters*, *408*, 161 – 165.

Jin, L., Alesi, G. N. and Kang, S. (2016). Glutaminolysis as a target for cancer therapy. *Oncogene*, *35* (28), 3619 – 3625.

Kang, J.-O., Lee, J.-B. and Chang, J. (2016). Cholera Toxin Promotes Th17 Cell Differentiation by Modulating Expression of Polarizing Cytokines and the Antigen-Presenting Potential of Dendritic Cells. *PLoS ONE*, *11* (6), 1 – 16.

Kelly, A. P., Finlay, D. K., Hinton, H. J., Clarke, R. G., Fiorini, E., Radtke, F. and Cantrell, D. A. (2007). Notch-induced T cell development requires phosphoinositide-dependent kinase 1. *EMBO Journal*, *26* (14), 3441 – 3450.

Kelly, O. M., McNamara, Y. M., Manzke, L. H., Meegan, M. J. and Porter, R. K. (2012). The preservation of in vivo phosphorylated and activated uncoupling protein 3 (UCP3) in isolated skeletal muscle mitochondria following administration of 3,4-methylenedioxymethamphetamine (MDMA aka ecstasy) to rats/mice. *Mitochondrion*, *12*, 110 – 119.

Kelly, O. M. and Porter, R. K. (2011). Absence of mitochondrial uncoupling protein 3: Effect on thymus and spleen in the fed and fasted mice. *Biochimica et Biophysica Acta*, *1807*, 1064 – 1074.

Kendrick, N. (2014). A gene's mRNA level does not usually predict its protein level. *www.kendricklabs.com*.

Kieper, W. C., Troy, A., Burghardt, J. T., Ramsey, C., Lee, J. Y., Jiang, H.-Q., Dummer, W., Shen, H., Cebra, J. J. and Surh, C. D. (2005). Cutting Edge: Recent Immune Status Determines the Source of Antigens That Drive Homeostatic T Cell Expansion. *Journal of Immunology*, *174*, 3158 – 3163.

Klaus, S., Casteilla, L., Bouillaud, F. and Ricquier, D. (1991). The uncoupling protein UCP: A membraneous mitochondrial ion carrier exclusively expressed in brown adipose tissue. *International Journal of Biochemistry*, *23* (9), 791 – 801.

Klingenberg, M. (1984). Characteristics of the uncoupling protein from brown-fat mitochondria. *Biochemical Society Transactions*, *12*, 390 – 393.

Klingenberg, M. (1990). Mechanism and evolution of the uncoupling protein of brown adipose tissue. *Trends in Biochemical Sciences*, *15*, 108 – 112.

Klingenberg, M. (2017). UCP1 - A sophisticated energy valve. *Biochimie*, *134*, 19 – 27.

Klingenberg, M. and Echtay, K. S. (2001). Uncoupling proteins: the issues from a biochemist point of view. *Biochimica et Biophysica Acta*, *1504*, 128 – 143.

Klingenberg, M. and Huang, S.-G. (1999). Structure and function of the uncoupling protein from brown adipose tissue. *Biochimica et Biophysica Acta*, *1415*, 271 – 296.

Krammer, P. H., Arnold, R. and Lavrik, I. N. (2007). Life and death in peripheral T cells. *Nature Reviews Immunology*, *7*, 532 – 542.

Krauss, S., Zhang, C.-Y. and Lowell, B. B. (2002). A significant portion of mitochondrial proton leak in intact thymocytes depends on expression of UCP2. *Proceedings of the National Academy of Sciences*, *99* (1), 118 – 122.

Krauss, S., Zhang, C.-Y. and Lowell, B. B. (2005). The mitochondrial uncoupling-protein homologues. *Nature Reviews Molecular Cell Biology*, *6*, 248 – 261.

Krauss, S., Zhang, C.-Y., Scorrano, L., Dalgaard, L. T., St-Pierre, J., Grey, S. T. and Lowell, B. B. (2003). Superoxide-mediated activation of uncoupling protein 2 causes pancreatic β cell dysfunction. *Journal of Clinical Investigation*, *112* (12), 1831 – 1842.

Kuhn, C., Rezende, R. M., M'Hamdi, H., da Cunha, A. P. and Weiner, H. L. (2016). IL-6 Inhibits Upregulation of Membrane-Bound TGF-β 1 on $CD4^+$ T Cells and Blocking IL-6 Enhances Oral Tolerance. *Journal of Immunology*, *198*, 1202 – 1209.

Lagresle, C., Gardie, B., Eyquem, S., Fasseu, M., Vieville, J.-C., Pla, M., Sigaux, F. and Bories, J.-C. (2002). Transgenic Expression of the $p16^{INK4a}$ Cyclin-Dependent Kinase Inhibitor Leads to Enhanced Apoptosis and Differentiation Arrest of $CD4^-CD8^-$ Immature Thymocytes. *Journal of Immunology*, *168*, 2325 – 2331.

Laloi, M., Klein, M., Riesmeier, J. W., Müller-Röber, B., Fleury, C., Bouillaud, F. and Ricquier, D. (1997). A plant cold-induced uncoupling protein. *Nature Scientific Correspondence*, *389*, 135 – 136.

Lambeth, J. D. (2002). Nox/Duox family of nicotinamide adenine dinucleotide (phosphate) oxidases. *Current Opinion in Hematology*, *9*, 11 – 17.

Larrouy, D., Laharrague, P., Carrera, G., Viguerie-Bascands, N., Levi-Meyrueis, C., Fleury, C., Pecqueur, C., Nibbelink, M., André, M., Casteilla, L. and Ricquier, D. (1997). Kupffer Cells Are a Dominant Site of Uncoupling Protein 2 Expression in Rat

Liver. *Biochemical and Biophysical Research Communications*, *235* (3), 760 – 764.

Laurence, A., Tato, C. M., Davidson, T. S., Kanno, Y., Chen, Z., Yao, Z., Blank, R. B., Meylan, F., Siegel, R., Hennighausen, L., Shevach, E. M. and O'Shea, J. J. (2007). Interleukin-2 Signaling via STAT5 Constrains T Helper 17 Cell Generation. *Immunity*, *26*, 371 – 381.

Lavelle, E. C., Jarnicki, A., McNeela, E., Armstrong, M. E., Higgins, S. C., Leavy, O. and Mills, K. H. G. (2004). Effects of cholera toxin on innate and adaptive immunity and its application as an immunomodulatory agent. *Journal of Leukocyte Biology*, *75*, 756 – 763.

Lavelle, E. C., McNeela, E., Armstrong, M. E., Leavy, O., Higgins, S. C. and Mills, K. H. G. (2003). Cholera Toxin Promotes the Induction of Regulatory T Cells Specific for Bystander Antigens by Modulating Dendritic Cell Activation. *Journal of Immunology*, *171*, 2384 – 2392.

Lee, J.-B., Jang, J.-E., Song, M. K. and Chang, J. (2009). Intranasal Delivery of Cholera Toxin Induces Th17-Dominated T-Cell Response to Bystander Antigens. *PLoS ONE*, *4* (4), 1 – 9.

Lee, Y., Willers, C., Kunji, E. R. S. and Crichton, P. G. (2015). Uncoupling protein 1 binds one nucleotide per monomer and is stabilized by tightly bound cardiolipin. *Proceedings of the National Academy of Sciences*, *112* (22), 6973 – 6978.

Liao, W., Lin, J.-X. and Leonard, W. J. (2013). Interleukin-2 at the Crossroads of Effector Responses, Tolerance, and Immunotherapy. *Immunity*, *38*, 13 – 25.

Loftus, R. M. and Finlay, D. K. (2016). Immunometabolism : Cellular Metabolism Turns Immune Regulator. *Journal of Biological Chemistry*, *291* (1), 1 – 10.

Lombardi, A., Busiello, R. A., Napolitano, L., Cioffi, F., Moreno, M., De Lange, P., Silvestri, E., Lanni, A. and Goglia, F. (2010). UCP3 Translocates Lipid Hydroperoxide and Mediates Lipid Hydroperoxide-dependent Mitochondrial Uncoupling. *Journal of Biological Chemistry*, *285* (22), 16599 – 16605.

Los, M., Dröge, W., Stricker, K., Baeuerle, P. A. and Schulze-Osthoff, K. (1995). Hydrogen peroxide as a potent activator of T lymphocyte functions. *European Journal of Immunology*, *25*, 159 – 165.

Maher, S., Toomey, D., Condron, C. and Bouchier-Hayes, D. (2002). Activation-induced cell death: The controversial role of Fas and Fas ligand in immune privilege and tumour counterattack. *Immunology and Cell Biology*, *80*, 131 – 137.

Malingriaux, E. A., Rupprecht, A., Gille, L., Jovanovic, O., Ježek, P., Jabůrek, M. and Pohl, E. E. (2013). Fatty Acids are Key in 4-Hydroxy-2-Nonenal-Mediated Activation

of Uncoupling Proteins 1 and 2. *PLoS ONE*, *8* (10), 1 – 7.

Mao, W., Yu, X. X., Zhong, A., Li, W., Brush, J., Sherwood, S. W., Adams, S. H. and Pan, G. (1999). UCP4, a novel brain-specific mitochondrial protein that reduces membrane potential in mammalian cells. *FEBS Letters*, *443*, 326 – 330.

Marko, A. J., Miller, R. A., Kelman, A. and Frauwirth, K. A. (2010). Induction of Glucose Metabolism in Stimulated T Lymphocytes Is Regulated by Mitogen-Activated Protein Kinase Signaling. *PLoS ONE*, *5* (11), 1 – 7.

Martinez-Botas, J., Anderson, J. B., Tessier, D., Lapillonne, A., Chang, B. H.-J., Quast, M. J., Gorenstein, D., Chen, K.-H. and Chan, L. (2000). Absence of perilipin results in leanness and reverses obesity in $Lepr^{db/db}$ mice. *Nature Genetics*, *26*, 474 – 479.

Matthias, A., Ohlson, K. B. E., Fredriksson, J. M., Jacobsson, A., Nedergaard, J. and Cannon, B. (2000). Thermogenic Responses in Brown Fat Cells Are Fully UCP1-dependent: UCP2 or UCP3 do not substitute for UCP1 in adrenergically or fatty acid-induced thermogenesis. *Journal of Biological Chemistry*, *275* (33), 25073 – 25081.

McGeachy, M. J. (2011). GM-CSF: the secret weapon in the T_H17 arsenal. *Nature Immunology*, *12* (6), 521 – 522.

Mebius, R. E. and Kraal, G. (2005). Structure and Function of the Spleen. *Nature Reviews Immunology*, *5*, 606 – 616.

Medzhitov, R. (2001). Toll-Like Receptors and Innate Immunity. *Nature Reviews Immunology*, *1*, 135 – 145.

Michalek, R. D., Gerriets, V. A., Jacobs, S. R., Macintyre, A. N., MacIver, N. J., Mason, E. F., Sullivan, S. A., Nichols, A. G. and Rathmell, J. C. (2011). Cutting Edge: Distinct Glycolytic and Lipid Oxidative Metabolic Programs Are Essential for Effector and Regulatory $CD4^+$ T Cell Subsets. *Journal of Immunology*, *186*, 3299 – 3303.

Mills, K. H. G. (1996). In A. Robinson, G. Farrar, and C. Wilbin (Eds.), *Methods in Molecular Medicine - Vaccine Protocols* (First), 197 – 221. New Jersey: Human Press.

Min, S. Y., Kady, J., Nam, M., Rojas-Rodriguez, R., Berkenwald, A., Kim, J. H., Noh, H.-L., Kim, J. K., Cooper, M. P., Fitzgibbons, T., Brehm, M. A. and Corvera, S. (2016). Human “brite/beige” adipocytes develop from capillary networks and their implantation improves metabolic homeostasis in mice. *Nature Medicine*, *22* (3), 312 – 318.

Minnaard, R., Schrauwen, P., Schaart, G. and Hesselink, M. K. C. (2006). UCP3 in muscle wasting, a role in modulating lipotoxicity? *FEBS Letters*, *580*, 5172 – 5176.

Mitchell, P. (1961). Coupling of Phosphorylation to Electron and Hydrogen Transfer by a

Chemi-Osmotic Type of Mechanism. *Nature*, *191* (4784), 144 – 148.

Miwa, S. and Brand, M. D. (2003). Mitochondrial matrix reactive oxygen species production is very sensitive to mild uncoupling. *Biochemical Society Transactions*, *31* (6), 1300 – 1301.

Murphy, M. P. (2009). How mitochondria produce reactive oxygen species. *Biochemical Journal*, *417*, 1 – 13.

Muzik, O., Mangner, T. J., Leonard, W. R., Kumar, A., Janisse, J. and Granneman, J. G. (2013). ^{15}O PET Measurement of Blood Flow and Oxygen Consumption in Cold-Activated Human Brown Fat. *Journal of Nuclear Medicine*, *54* (4), 523 – 531.

Nedergaard, J., Bengtsson, T. and Cannon, B. (2007). Unexpected evidence for active brown adipose tissue in adult humans. *American Journal of Physiology - Endocrinology and Metabolism*, *293*, E444 – E452.

Nedergaard, J. and Cannon, B. (2003). The "novel" "uncoupling" proteins UCP2 and UCP3: what do they really do? Pros and cons for suggested functions. *Experimental Physiology*, *88* (1), 65 – 84.

Nedergaard, J. and Cannon, B. (2010). The Changed Metabolic World with Human Brown Adipose Tissue: Therapeutic Visions. *Cell Metabolism*, *11*, 268 – 272.

Nedergaard, J., Golozoubova, V., Matthias, A., Asadi, A., Jacobsson, A. and Cannon, B. (2001). UCP1: The only protein able to mediate adaptive non-shivering thermogenesis and metabolic inefficiency. *Biochimica et Biophysica Acta*, *1504*, 82 – 106.

Nègre-Salvayre, A., Hirtz, C., Carrera, G., Cazenave, R., Troly, M., Salvayre, R., Pénicaud, L. and Casteilla, L. (1997). A role for uncoupling protein-2 as a regulator of mitochondrial hydrogen peroxide generation. *FASEB Journal*, *11*, 809 – 815.

Newton, R., Priyadharshini, B. and Turka, L. A. (2016). Immunometabolism of regulatory T cells. *Nature Immunology*, *17* (6), 618 – 625.

Nicholls, D. G., Darley-Usmar, V. M., Wu, M., Jensen, P. B., Rogers, G. W. and Ferrick, D. A. (2010). Bioenergetic Profile Experiment using C2C12 Myoblast Cells. *Journal of Visualized Experiments*, *46*, 1 – 6.

Nikolich-Žugich, J., Slifka, M. K. and Messaoudi, I. (2004). The many important facets of T-cell repertoire diversity. *Nature Reviews Immunology*, *4*, 123 – 132.

Ogawa, A., Andoh, A., Araki, Y., Bamba, T. and Fujiyama, Y. (2004). Neutralization of interleukin-17 aggravates dextran sulfate sodium-induced colitis in mice. *Clinical Immunology*, *110*, 55 – 62.

Page, D. M., Kane, L. P., Onami, T. M. and Hedrick, S. M. (1996). Cellular and

biochemical requirements for thymocyte negative selection. *Seminars in Immunology*, *8*, 69 – 82.

Palou, A., Picó, C., Bonet, M. L. and Oliver, P. (1998). The uncoupling protein, thermogenin. *International Journal of Biochemistry and Cell Biology*, *30*, 7 – 11.

Parascandola, J. (1974). Dinitrophenol and Bioenergetics: An Historical Perspective. *Molecular and Cellular Biochemistry*, *5* (1 – 2), 69 – 77.

Park, I.-K., Shultz, L. D., Letterio, J. J. and Gorham, J. D. (2005). TGF-β1 Inhibits T-bet Induction by IFN-γ in Murine $CD4^+$ T Cells through the Protein Tyrosine Phosphatase Src Homology Region 2 Domain-Containing Phosphatase-1. *Journal of Immunology*, *175*, 5666 – 5674.

Pearce, E. L. and Pearce, E. J. (2013). Metabolic Pathways in Immune Cell Activation and Quiescence. *Immunity*, *38*, 633 – 643.

Pearce, E. L., Walsh, M. C., Cejas, P. J., Harms, G. M., Shen, H., Wang, L.-S., Jones, R. G. and Choi, Y. (2009). Enhancing CD8 T-cell memory by modulating fatty acid metabolism. *Nature*, *460*, 103 – 107.

Pebay-Peyroula, E., Dahout-Gonzalez, C., Kahn, R., Trézéguet, V., Lauquin, G. J.-M. and Brandolin, G. (2003). Structure of mitochondrial ADP/ATP carrier in complex with carboxyatractyloside. *Nature*, *426*, 39 – 44.

Pecqueur, C., Alves-Guerra, M.-C., Gelly, C., Lévi-Meyrueis, C., Couplan, E., Collins, S., Ricquier, D., Bouillaud, F. and Miroux, B. (2001). Uncoupling Protein 2, *in Vivo* Distribution, Induction upon Oxidative Stress, and Evidence for Translational Regulation. *Journal of Biological Chemistry*, *276* (12), 8705 – 8712.

Pecqueur, C., Bui, T., Gelly, C., Hauchard, J., Barbot, C., Bouillaud, F., Ricquier, D., Miroux, B. and Thompson, C. B. (2008). Uncoupling protein-2 controls proliferation by promoting fatty acid oxidation and limiting glycolysis-derived pyruvate utilization. *FASEB Journal*, *22* (1), 9 – 18.

Pi, J., Leung, L., Xue, P., Wang, W., Hou, Y., Liu, D., Yehuda-Shnaidman, E., Lee, C., Lau, J., Kurtz, T. W. and Chan, J. Y. (2010). Deficiency in the Nuclear Factor E2-related Factor-2 Transcription Factor Results in Impaired Adipogenesis and Protects against Diet-induced Obesity. *Journal of Biological Chemistry*, *285* (12), 9292 – 9300.

Plecitá-Hlavatá, L., Lessard, M., Šantorová, J., Bewersdorf, J. and Ježek, P. (2008). Mitochondrial oxidative phosphorylation and energetic status are reflected by morphology of mitochondrial network in INS-1E and HEP-G2 cells viewed by 4Pi microscopy. *Biochimica et Biophysica Acta*, *1777*, 834 – 846.

Porter, R. K. (2001). Mitochondrial proton leak: a role for uncoupling proteins 2 and 3? *Biochimica et Biophysica Acta*, *1504*, 120 – 127.

Preston, G. C., Sinclair, L. V., Kaskar, A., Hukelmann, J. L., Navarro, M. N., Ferrero, I., MacDonald, H. R., Cowling, V. H. and Cantrell, D. A. (2015). Single cell tuning of Myc expression by antigen receptor signal strength and interleukin-2 in T lymphocytes. *EMBO Journal*, *34* (15), 2008 – 2024.

Pulendran, B. and Ahmed, R. (2006). Translating Innate Immunity into Immunological Memory: Implications for Vaccine Development. *Cell*, *124*, 849 – 863.

Puleston, D. (2015). Detection of Mitochondrial Mass, Damage, and Reactive Oxygen Species by Flow Cytometry. *Cold Spring Harbor Protocols*, *2015* (9), 830 – 834.

Qiu, Y., Nguyen, K. D., Odegaard, J. I., Cui, X., Tian, X., Locksley, R. M., Palmiter, R. D. and Chawla, A. (2014). Eosinophils and Type 2 Cytokine Signaling in Macrophages Orchestrate Development of Functional Beige Fat. *Cell*, *157*, 1292 – 1308.

Raimbault, S., Dridi, S., Denjean, F., Lachuer, J., Couplan, E., Bouillaud, F., Bordas, A., Duchamp, C., Taouis, M. and Ricquier, D. (2001). An uncoupling protein homologue putatively involved in facultative muscle thermogenesis in birds. *Biochemical Journal*, *353*, 441 – 444.

Ramaswamy, M., Cleland, S. Y., Cruz, A. C. and Siegel, R. M. (2009). Many checkpoints on the road to cell death: regulation of Fas-FasL interactions and Fas signalling in peripheral immune responses. *Results and Problems in Cell Differentiation*, *49*, 17 – 47.

Raud, B., Roy, D. G., Divakaruni, A. S., Tarasenko, T. N., Franke, R., Ma, E. H., Samborska, B., Hsieh, W. Y., Wong, A. H., Stüve, P., Arnold-Schrauf, C., Guderian, M., Lochner, M., Rampertaap, S., Romito, K., Monsale, J., Brönstrup, M., Bensinger, S. J., Murphy, A. N., McGuire, P. J., Jones, R. G., Sparwasser, T. and Berod, L. (2018). Etomoxir Actions on Regulatory and Memory T Cells Are Independent of Cpt1a-Mediated Fatty Acid Oxidation. *Cell Metabolism*, *28*, 504 – 515.

Rial, E., Poustie, A. and Nicholls, D. G. (1983). Brown-adipose-tissue mitochondria: the regulation of the 32 000-M_r uncoupling protein by fatty acids and purine nucleotides. *European Journal of Biochemistry*, *137*, 197 – 203.

Ricquier, D. and Bouillaud, F. (2000). The uncoupling protein homologues: UCP1, UCP2, UCP3, StUCP and AtUCP. *Biochemical Journal*, *345*, 161 – 179.

Ricquier, D., Bouillaud, F., Toumelin, P., Mory, G., Bazin, R., Arch, J. and Pénicaud, L. (1986). Expression of Uncoupling Protein mRNA in Thermogenic or Weakly Thermogenic Brown Adipose Tissue: Evidence for a Rapid β-Adrenoreceptor-

Mediated and Transcriptionally Regulated Step During Activation of Thermogenesis. *Journal of Biological Chemistry*, *261* (30), 13905 – 13910.

Ricquier, D., Mory, G., Bouillaud, F., Thibault, J. and Weissenbach, J. (1984). Rapid increase of mitochondrial uncoupling protein and its mRNA in stimulated brown adipose tissue: Use of a cDNA probe. *FEBS Letters*, *178* (2), 240 – 244.

Riley, J. L. (2009). PD-1 signalling in primary T cells. *Immunological Reviews*, *229* (1), 114 – 125.

Roberts, A. I., Devadas, S., Zhang, X., Zhang, L., Keegan, A., Greeneltch, K., Solomon, J., Wei, L., Das, J., Sun, E., Liu, C., Yuan, Z., Zhou, J.-N. and Shi, Y. (2003). The Role of Activation-Induced Cell Death in the Differentiation of T-Helper-Cell Subsets. *Immunologic Research*, *28* (3), 285 – 293.

Robinson, A. J., Overy, C. and Kunji, E. R. S. (2008). The mechanism of transport by mitochondrial carriers based on analysis of symmetry. *Proceedings of the National Academy of Sciences*, *105* (46), 17766 – 17771.

Rogers, G. W., Brand, M. D., Petrosyan, S., Ashok, D., Elorza, A. A., Ferrick, D. A. and Murphy, A. N. (2011). High Throughput Microplate Respiratory Measurements Using Minimal Quantities of Isolated Mitochondria. *PLoS ONE*, *6* (7), 1 – 12.

Rolfe, D. F. S., Hulbert, A. J. and Brand, M. D. (1994). Characteristics of mitochondrial proton leak and control of oxidative phosphorylation in the major oxygen-consuming tissues of the rat. *Biochimica et Biophysica Acta*, *1118*, 405 – 416.

Rosenwald, M., Perdikari, A., Rülicke, T. and Wolfrum, C. (2013). Bi-directional interconversion of brite and white adipocytes. *Nature Cell Biology*, *15* (6), 659 – 667.

Roth, S. and Dröge, W. (1987). Regulation of T-Cell Activation and T-Cell Growth Factor (TCGF) Production by Hydrogen Peroxide. *Cellular Immunology*, *108*, 417 – 424.

Rothwell, N. J., Saville, M. E. and Stock, M. J. (1984). Brown fat activity in fasted and refed rats. *Bioscience Reports*, *4*, 351 – 357.

Rousset, S., Alves-Guerra, M.-C., Ouadghiri-Bencherif, S., Kozak, L. P., Miroux, B., Richard, D., Bouillaud, F., Ricquier, D. and Cassard-Doulcier, A.-M. (2003). Uncoupling Protein 2, but Not Uncoupling Protein 1, Is Expressed in the Female Mouse Reproductive Tract. *Journal of Biological Chemistry*, *278* (46), 45843 – 45847.

Ruas, J. S., Siqueira-Santos, E. S., Amigo, I., Rodrigues-Silva, E., Kowaltowski, A. J. and Castilho, R. F. (2016). Underestimation of the Maximal Capacity of the Mitochondrial Electron Transport System in Oligomycin-Treated Cells. *PLoS ONE*, *11* (3), 1 – 20.

Rupprecht, A., Bräuer, A. U., Smorodchenko, A., Goyn, J., Hilse, K. E., Shabalina, I. G., Infante-Duarte, C. and Pohl, E. E. (2012). Quantification of Uncoupling Protein 2 Reveals Its Main Expression in Immune Cells and Selective Up-Regulation during T-Cell Proliferation. *PLoS ONE*, *7* (8), 1 – 9.

Rupprecht, A., Sittner, D., Smorodchenko, A., Hilse, K. E., Goyn, J., Moldzio, R., Seiler, A. E. M., Bräuer, A. U. and Pohl, E. E. (2014). Uncoupling Protein 2 and 4 Expression Pattern during Stem Cell Differentiation Provides New Insight into Their Putative Function. *PLoS ONE*, *9* (2), 1 – 10.

Saito, M., Okamatsu-Ogura, Y., Matsushita, M., Watanabe, K., Yoneshiro, T., Nio-Kobayashi, J., Iwanaga, T., Miyagawa, M., Kameya, T., Nakada, K., Kawai, Y. and Tsujisaki, M. (2009). High Incidence of Metabolically Active Brown Adipose Tissue in Healthy Adult Humans: Effects of Cold Exposure and Adiposity. *Diabetes*, *58*, 1526 – 1531.

Sanchis, D., Fleury, C., Chomiki, N., Goubern, M., Huang, Q., Neverova, M., Grégoire, F., Easlick, J., Raimbault, S., Lévi-Meyrueis, C., Miroux, B., Collins, S., Seldin, M., Richard, D., Warden, C., Bouillaud, F. and Ricquier, D. (1998). BMCP1, a Novel Mitochondrial Carrier with High Expression in the Central Nervous System of Humans and Rodents, and Respiration Uncoupling Activity in Recombinant Yeast. *Journal of Biological Chemistry*, *273* (51), 34611 – 34615.

Schmittgen, T. D. and Livak, K. J. (2008). Analyzing real-time PCR data by the comparative C_T method. *Nature Protocols*, *3* (6), 1101 – 1108.

Schneider, K., Valdez, J., Nguyen, J., Vawter, M., Galke, B., Kurtz, T. W. and Chan, J. Y. (2016). Increased Energy Expenditure, *Ucp1* Expression, and Resistance to Diet-induced Obesity in Mice Lacking Nuclear Factor-Erythroid-2-related Transcription Factor-2 (*Nrf2*). *Journal of Biological Chemistry*, *291* (14), 7754 – 7766.

Scholzen, T. and Gerdes, J. (2000). The Ki-67 Protein: From the Known and the Unknown. *Journal of Cellular Physiology*, *182*, 311 – 322.

Schrauwen, P. and Hesselink, M. K. C. (2004). The role of uncoupling protein 3 in fatty acid metabolism: protection against lipotoxicity? *Proceedings of the Nutrition Society*, *63*, 287 – 292.

Schrauwen, P., Hinderling, V., Hesselink, M. K. C., Schaart, G., Kornips, E., Saris, W. H. M., Westerterp-Platenga, M. and Langhans, W. (2002). Etomoxir-induced increase in UCP3 supports a role of uncoupling protein 3 as a mitochondrial fatty acid anion exporter. *FASEB Journal*, *16* (12), 1688 – 1690.

Schrauwen, P., Hoeks, J. and Hesselink, M. K. C. (2006). Putative function and

physiological relevance of the mitochondrial uncoupling protein-3: Involvement in fatty acid metabolism? *Progress in Lipid Research*, *45*, 17 – 41.

Schrauwen, P., Hoeks, J., Schaart, G., Kornips, E., Binas, B., van de Vusse, G. J., van Bilsen, M., Luiken, J. J. F. P., Coort, S. L. M., Glatz, J. F. C., Saris, W. H. M. and Hesselink, M. K. C. (2003). Uncoupling protein 3 as a mitochondrial fatty acid anion exporter. *FASEB Journal*, *17* (15), 2272 – 2274.

Schrauwen, P., Saris, W. H. M. and Hesselink, M. K. C. (2001). An alternative function for human uncoupling protein 3: protection of mitochondria against accumulation of nonesterified fatty acids inside the mitochondrial matrix. *FASEB Journal*, *15*, 2497 – 2502.

Schwarz, B. A. and Bhandoola, A. (2006). Trafficking from the bone marrow to the thymus: a prerequisite for thymopoiesis. *Immunological Reviews*, *209*, 47 – 57.

Seale, P., Bjork, B., Yang, W., Kajimura, S., Chin, S., Kuang, S., Scimè, A., Devarakonda, S., Conroe, H. M., Erdjument-Bromage, H., Tempst, P., Rudnicki, M. A., Beier, D. R. and Spiegelman, B. M. (2008). PRDM16 controls a brown fat/skeletal muscle switch. *Nature*, *454*, 961 – 967.

Sears, I. B., MacGinnitie, M. A., Kovacs, L. G. and Graves, R. A. (1996). Differentiation-Dependent Expression of the Brown Adipocyte Uncoupling Protein Gene: Regulation by Peroxisome Proliferator-Activated Receptor γ. *Molecular and Cellular Biology*, *16* (7), 3410 – 3419.

Sena, L. A., Li, S., Jairaman, A., Prakriya, M., Ezponda, T., Hildeman, D. A., Wang, C.-R., Schumacker, P. T., Licht, J. D., Perlman, H., Bryce, P. J. and Chandel, N. S. (2013). Mitochondria Are Required for Antigen-Specific T Cell Activation through Reactive Oxygen Species Signaling. *Immunity*, *38*, 225 – 236.

Shabalina, I. G., Petrovic, N., Kramarova, T. V., Hoeks, J., Cannon, B. and Nedergaard, J. (2006). UCP1 and Defence against Oxidative Stress: 4-Hydroxy-2-nonenal effects on brown fat mitochondria are uncoupling protein 1-independent. *Journal of Biological Chemistry*, *281* (20), 13882 – 13893.

Shi, L. Z., Wang, R., Huang, G., Vogel, P., Neale, G., Green, D. R. and Chi, H. (2011). HIF1α–dependent glycolytic pathway orchestrates a metabolic checkpoint for the differentiation of T_H17 and T_{reg} cells. *Journal of Experimental Medicine*, *208* (7), 1367 – 1376.

Shih, M.-F. and Taberner, P. V. (1995). Selective activation of brown adipocyte hormone-sensitive lipase and cAMP production in the mouse by β3-adrenoceptor agonists. *Biochemical Pharmacology*, *50* (5), 601 – 608.

Silva, J. E. and Rabelo, R. (1997). Regulation of the uncoupling protein gene expression. *European Journal of Endocrinology*, *136*, 251 – 264.

Skulachev, V. P. (1991). Fatty acid circuit as a physiological mechanism of uncoupling of oxidative phosphorylation. *FEBS Letters*, *294* (3), 158 – 162.

Smith, P. K., Krohn, R. I., Hermanson, G. T., Mallia, A. K., Gartner, F. H., Provenzano, M. D., Fujimoto, E. K., Goeke, N. M., Olson, B. J. and Klenk, D. C. (1985). Measurement of Protein Using Bicinchoninic Acid. *Analytical Biochemistry*, *150*, 76 – 85.

Solanes, G., Vidal-Puig, A., Grujic, D., Flier, J. S. and Lowell, B. B. (1997). The Human Uncoupling Protein-3 Gene: Genomic Structure, Chromosomal Localization, and Genetic Basis for Short and Long Form Transcripts. *Journal of Biological Chemistry*, *272* (41), 25433 – 25436.

Spinazzi, M., Casarin, A., Pertegato, V., Salviati, L. and Angelini, C. (2012). Assessment of mitochondrial respiratory chain enzymatic activities on tissues and cultured cells. *Nature Protocols*, *7* (6), 1235 – 1246.

Stock, D., Gibbons, C., Arechaga, I., Leslie, A. G. W. and Walker, J. E. (2000). The rotary mechanism of ATP synthase. *Current Opinion in Structural Biology*, *10*, 672 – 679.

Sutton, C., Brereton, C., Keogh, B., Mills, K. H. G. and Lavelle, E. C. (2006). A crucial role for interleukin (IL)-1 in the induction of IL-17–producing T cells that mediate autoimmune encephalomyelitis. *Journal of Experimental Medicine*, *203* (7), 1685 – 1691.

Suzuki, J., Gao, M., Ohinata, H., Kuroshima, A. and Koyama, T. (1997). Chronic Cold Exposure Stimulates Microvascular Remodelling Preferentially in Oxidative Muscles in Rats. *Japanese Journal of Physiology*, *47* (6), 513 – 520.

Tainter, M. L., Stockton, A. B. and Cutting, W. C. (1933). Use of Dinitrophenol in Obesity and Related Conditions. *Journal of the American Medical Association*, *101* (19), 1472 – 1475.

Thonberg, H., Fredriksson, J. M., Nedergaard, J. and Cannon, B. (2002). A novel pathway for adrenergic stimulation of cAMP-response-element-binding protein (CREB) phosphorylation: mediation via α_1-adrenoceptors and protein kinase C activation. *Biochemical Journal*, *364*, 73 – 79.

Toyomizu, M., Ueda, M., Sato, S., Seki, Y., Sato, K. and Akiba, Y. (2002). Cold-induced mitochondrial uncoupling and expression of chicken UCP and ANT mRNA in chicken skeletal muscle. *FEBS Letters*, *529*, 313 – 318.

Trayhurn, P. (2017). Origins and early development of the concept that brown adipose

tissue thermogenesis is linked to energy balance and obesity. *Biochimie*, *134*, 62 – 70.

Trenker, M., Malli, R., Fertschai, I., Levak-Frank, S. and Graier, W. F. (2007). Uncoupling proteins 2 and 3 are fundamental for mitochondrial Ca^{2+} uniport. *Nature Cell Biology*, *9* (4), 445 – 452.

Tsai, H.-C. and Wu, R. (2015). Mechanisms of Cholera Toxin in the Modulation of T_H17 Responses. *Critical Reviews in Immunology*, *35* (2), 135 – 152.

van der Windt, G. J. W., Chang, C.-H. and Pearce, E. L. (2016). Measuring Bioenergetics in T Cells Using a Seahorse Extracellular Flux Analyzer. *Current Protocols in Immunology*, *113*, 3.16B.1 – 3.16B.14.

van der Windt, G. J. W., Everts, B., Chang, C.-H., Curtis, J. D., Freitas, T. C., Amiel, E., Pearce, E. J. and Pearce, E. L. (2012). Mitochondrial Respiratory Capacity Is a Critical Regulator of $CD8^+$ T Cell Memory Development. *Immunity*, *36*, 68 – 78.

van der Windt, G. J. W. and Pearce, E. L. (2012). Metabolic switching and fuel choice during T-cell differentiation and memory development. *Immunological Reviews*, *249* (1), 27 – 42.

Vianna, C. R., Hagen, T., Zhang, C.-Y., Bachman, E., Boss, O., Gereben, B., Moriscot, A. S., Lowell, B. B., Bicudo, J. E. P. W. and Bianco, A. C. (2001). Cloning and functional characterization of an uncoupling protein homolog in hummingbirds. *Physiological Genomics*, *5*, 137 – 145.

Vidal-Puig, A. J., Grujic, D., Zhang, C.-Y., Hagen, T., Boss, O., Ido, Y., Szczepanik, A., Wade, J., Mootha, V., Cortright, R., Muoio, D. M. and Lowell, B. B. (2000). Energy Metabolism in Uncoupling Protein 3 Gene Knockout Mice. *Journal of Biological Chemistry*, *275* (21), 16258 – 16266.

Vidal-Puig, A., Solanes, G., Grujic, D., Flier, J. S. and Lowell, B. B. (1997). UCP3: An Uncoupling Protein Homologue Expressed Preferentially and Abundantly in Skeletal Muscle and Brown Adipose Tissue. *Biochemical and Biophysical Research Communications*, *235* (1), 79 – 82.

Virtanen, K. A., Lidell, M. E., Orava, J., Heglind, M., Westergren, R., Niemi, T., Taittonen, M., Laine, J., Savisto, N.-J., Enerbäck, S. and Nuutila, P. (2009). Functional Brown Adipose Tissue in Healthy Adults. *New England Journal of Medicine*, *360* (15), 1518 – 1525.

Vogler, S., Pahnke, J., Rousset, S., Ricquier, D., Moch, H., Miroux, B. and Ibrahim, S. M. (2006). Uncoupling Protein 2 Has Protective Function during Experimental Autoimmune Encephalomyelitis. *American Journal of Pathology*, *168* (5), 1570 – 1575.

Vozza, A., Parisi, G., De Leonardis, F., Lasorsa, F. M., Castegna, A., Amorese, D., Marmo, R., Calcagnile, V. M., Palmieri, L., Ricquier, D., Paradies, E., Scarcia, P., Palmieri, F., Bouillaud, F. and Fiermonte, G. (2014). UCP2 transports C4 metabolites out of mitochondria, regulating glucose and glutamine oxidation. *Proceedings of the National Academy of Sciences*, *111* (3), 960 – 965.

Wang, R., Dillon, C. P., Shi, L. Z., Milasta, S., Carter, R., Finkelstein, D., McCormick, L. L., Fitzgerald, P., Chi, H., Munger, J. and Green, D. R. (2011). The Transcription Factor Myc Controls Metabolic Reprogramming upon T Lymphocyte Activation. *Immunity*, *35*, 871 – 882.

Wang, S., Subramaniam, A., Cawthorne, M. A. and Clapham, J. C. (2003). Increased fatty acid oxidation in transgenic mice overexpressing UCP3 in skeletal muscle. *Diabetes, Obesity and Metabolism*, *5*, 295 – 301.

Winkler, E. and Klingenberg, M. (1994). Effect of Fatty Acids on H^+ Transport Activity of the Reconstituted Uncoupling Protein. *Journal of Biological Chemistry*, *269* (4), 2508 – 2515.

Wu, J., Boström, P., Sparks, L. M., Ye, L., Choi, J. H., Giang, A.-H., Khandekar, M., Virtanen, K. A., Nuutila, P., Schaart, G., Huang, K., Tu, H., van Marken Lichtenbelt, W. D., Hoeks, J., Enerbäck, S., Schrauwen, P. and Spiegelman, B. M. (2012). Beige Adipocytes Are a Distinct Type of Thermogenic Fat Cell in Mouse and Human. *Cell*, *150*, 366 – 376.

Yarosz, E. L. and Chang, C.-H. (2018). The Role of Reactive Oxygen Species in Regulating T Cell-mediated Immunity and Disease. *Immune Network*, *18* (1), e14.

Yoshida, T., Umekawa, T., Kumamoto, K., Sakane, N., Kogure, A., Kondo, M., Wakabayashi, Y., Kawada, T., Nagase, I. and Saito, M. (1998). β_3-Adrenergic agonist induces a functionally active uncoupling protein in fat and slow twitch muscle fibers. *American Journal of Physiology*, *274* (3), E469 – E475.

Yu, X. X., Mao, W., Zhong, A., Schow, P., Brush, J., Sherwood, S. W., Adams, S. H. and Pan, G. (2000). Characterization of novel UCP5/BMCP1 isoforms and differential regulation of UCP4 and UCP5 expression through dietary or temperature manipulation. *FASEB Journal*, *14* (11), 1611 – 1618.

Zacharchuk, C. M., Merćep, M. and Ashwell, J. D. (1991). Thymocyte Activation and Death: a Mechanism for Moulding the T Cell Repertoire. *Annals of the New York Academy of Sciences*, *636*, 52 – 70.

Zhang, C.-Y., Baffy, G., Perret, P., Krauss, S., Peroni, O., Grujic, D., Hagen, T., Vidal-Puig, A. J., Boss, O., Kim, Y.-B., Zheng, X. X., Wheeler, M. B., Shulman, G. I.,

Chan, C. B. and Lowell, B. B. (2001). Uncoupling Protein-2 Negatively Regulates Insulin Secretion and Is a Major Link between Obesity, β Cell Dysfunction, and Type 2 Diabetes. *Cell*, *105*, 745 – 755.

Zhang, Q., Chikina, M., Szymczak-Workman, A. L., Horne, W., Kolls, J. K., Vignali, K. M., Normolle, D., Bettini, M., Workman, C. J. and Vignali, D. A. A. (2017). LAG3 limits regulatory T cell proliferation and function in autoimmune diabetes. *Science Immunology*, *2*, 1 – 10.

Zheng, J. (2012). Energy metabolism of cancer: Glycolysis versus oxidative phosphorylation (Review). *Oncology Letters*, *4*, 1151 – 1157.

Zhou, M., Lin, B.-Z., Coughlin, S., Vallega, G. and Pilch, P. F. (2000). UCP-3 expression in skeletal muscle: effects of exercise, hypoxia, and AMP-activated protein kinase. *American Journal of Physiology - Endocrinology and Metabolism*, *279*, E622 – E629.

Zhu, R., Rupprecht, A., Ebner, A., Haselgrübler, T., Gruber, H. J., Hinterdorfer, P. and Pohl, E. E. (2013). Mapping the Nucleotide Binding Site of Uncoupling Protein 1 Using Atomic Force Microscopy. *Journal of the American Chemical Society*, *135*, 3640 – 3646.